Direct-drive inertial confinement fusion: A review

R. S. Craxton, K. S. Anderson, T. R. Boehly, V. N. Goncharov, D. R. Harding, J. P. Knauer, R. L. McCrory, P. W. McKenty, D. D. Meyerhofer, J. F. Myatt, A. J. Schmitt, J. D. Sethian, R. W. Short, S. Skupsky, W. Theobald, W. L. Kruer, K. Tanaka, R. Betti, T. J. B. Collins, J. A. Delettrez, S. X. Hu, J. A. Marozas, A. V. Maximov, D. T. Michel, P. B. Radha, S. P. Regan, T. C. Sangster, W. Seka, A. A. Solodov, J. M. Soures, C. Stoeckl, and J. D. Zuegel

Citation: Physics of Plasmas **22**, 110501 (2015); doi: 10.1063/1.4934714
View online: http://dx.doi.org/10.1063/1.4934714
View Table of Contents: http://scitation.aip.org/content/aip/journal/pop/22/11?ver=pdfcov
Published by the AIP Publishing

Direct-drive inertial confinement fusion: A review

R. S. Craxton,[1] K. S. Anderson,[1] T. R. Boehly,[1] V. N. Goncharov,[1] D. R. Harding,[1] J. P. Knauer,[1] R. L. McCrory,[1,2] P. W. McKenty,[1] D. D. Meyerhofer,[1,2] J. F. Myatt,[1] A. J. Schmitt,[3] J. D. Sethian,[3] R. W. Short,[1] S. Skupsky,[1] W. Theobald,[1] W. L. Kruer,[4] K. Tanaka,[5] R. Betti,[1,2] T. J. B. Collins,[1] J. A. Delettrez,[1] S. X. Hu,[1] J. A. Marozas,[1] A. V. Maximov,[1] D. T. Michel,[1] P. B. Radha,[1] S. P. Regan,[1] T. C. Sangster,[1] W. Seka,[1] A. A. Solodov,[1] J. M. Soures,[1] C. Stoeckl,[1] and J. D. Zuegel[1]
[1]*Laboratory for Laser Energetics, University of Rochester, Rochester, New York 14623-1299, USA*
[2]*Department of Physics and Astronomy and Department of Mechanical Engineering, University of Rochester, Rochester, New York 14623, USA*
[3]*Plasma Physics Division, Naval Research Laboratory, Washington, DC 20375, USA*
[4]*Lawrence Livermore National Laboratory, Livermore, California 94550, USA*
[5]*Department of Electric, Electronic, and Information, Graduate School of Engineering, Osaka University, Osaka, Japan*

(Received 6 February 2015; accepted 28 May 2015; published online 25 November 2015)

The direct-drive, laser-based approach to inertial confinement fusion (ICF) is reviewed from its inception following the demonstration of the first laser to its implementation on the present generation of high-power lasers. The review focuses on the evolution of scientific understanding gained from target-physics experiments in many areas, identifying problems that were demonstrated and the solutions implemented. The review starts with the basic understanding of laser–plasma interactions that was obtained before the declassification of laser-induced compression in the early 1970s and continues with the compression experiments using infrared lasers in the late 1970s that produced thermonuclear neutrons. The problem of suprathermal electrons and the target preheat that they caused, associated with the infrared laser wavelength, led to lasers being built after 1980 to operate at shorter wavelengths, especially 0.35 μm—the third harmonic of the Nd:glass laser—and 0.248 μm (the KrF gas laser). The main physics areas relevant to direct drive are reviewed. The primary absorption mechanism at short wavelengths is classical inverse bremsstrahlung. Nonuniformities imprinted on the target by laser irradiation have been addressed by the development of a number of beam-smoothing techniques and imprint-mitigation strategies. The effects of hydrodynamic instabilities are mitigated by a combination of imprint reduction and target designs that minimize the instability growth rates. Several coronal plasma physics processes are reviewed. The two-plasmon–decay instability, stimulated Brillouin scattering (together with cross-beam energy transfer), and (possibly) stimulated Raman scattering are identified as potential concerns, placing constraints on the laser intensities used in target designs, while other processes (self-focusing and filamentation, the parametric decay instability, and magnetic fields), once considered important, are now of lesser concern for mainline direct-drive target concepts. Filamentation is largely suppressed by beam smoothing. Thermal transport modeling, important to the interpretation of experiments and to target design, has been found to be nonlocal in nature. Advances in shock timing and equation-of-state measurements relevant to direct-drive ICF are reported. Room-temperature implosions have provided an increased understanding of the importance of stability and uniformity. The evolution of cryogenic implosion capabilities, leading to an extensive series carried out on the 60-beam OMEGA laser [Boehly *et al.*, Opt. Commun. **133**, 495 (1997)], is reviewed together with major advances in cryogenic target formation. A polar-drive concept has been developed that will enable direct-drive–ignition experiments to be performed on the National Ignition Facility [Haynam *et al.*, Appl. Opt. **46**(16), 3276 (2007)]. The advantages offered by the alternative approaches of fast ignition and shock ignition and the issues associated with these concepts are described. The lessons learned from target-physics and implosion experiments are taken into account in ignition and high-gain target designs for laser wavelengths of 1/3 μm and 1/4 μm. Substantial advances in direct-drive inertial fusion reactor concepts are reviewed. Overall, the progress in scientific understanding over the past five decades has been enormous, to the point that inertial fusion energy using direct drive shows significant promise as a future environmentally attractive energy source.
[http://dx.doi.org/10.1063/1.4934714]

TABLE OF CONTENTS

I. INTRODUCTION

It has been 55 years since the demonstration of the laser and the first proposal to use focused laser light to initiate thermonuclear (TN) fusion. Understandable optimism led to

early hopes and claims that breakeven (fusion energy out greater than laser energy in) was only a few years away. However, it is only in recent years that laser technology and understanding of the related physics have advanced to the point that laser-driven fusion energy can be seen as a realistic possibility for the future.

Inertial confinement fusion (ICF) is distinguished from magnetic confinement fusion in that the fusion fuel is compressed and maintained (briefly) at fusion densities and temperatures by its own inertia. There are two approaches to laser-driven ICF: direct drive, in which a spherical target containing fusion fuel is directly irradiated by laser beams,[1] and indirect drive, in which the laser beams heat the inside of a typically cylindrical enclosure known as a hohlraum, producing x rays that irradiate a spherical fuel-containing capsule.[2,3] This review is concerned solely with direct drive.

This review traces the history of direct-drive ICF from the earliest days to recent years, demonstrating the evolution of scientific understanding in a large number of areas critical to the success of the concept.

Target physics is the primary focus of this review. It is important to recognize that the growth of target-physics understanding has depended heavily on parallel developments in laser technology, experimental diagnostics, computer codes, and target fabrication, some of which have arisen from the indirect-drive program. However, descriptions of these areas are, with occasional exceptions, outside the scope of this review. It is assumed that the interested reader will refer to the bibliographies of the target-physics papers cited here for the pertinent information.

The evolution of the capabilities of high-power laser systems over the period of this review is remarkable. Multibeam spherical implosion facilities include the 20-beam Shiva,[4] the 10-beam Nova,[5] and the 192-beam National Ignition Facility (NIF)[6] lasers at Lawrence Livermore National Laboratory (LLNL); the 4-beam DELTA,[7] the 6-beam ZETA,[8] the 24-beam OMEGA,[9] and the 60-beam OMEGA[10] lasers at the Laboratory for Laser Energetics (LLE) at the University of Rochester; the 8-beam Helios laser[11] at Los Alamos National Laboratory (LANL); the 4-beam GEKKO IV[12] and the 12-beam GEKKO XII[13] lasers at the Institute for Laser Engineering at Osaka, Japan; the 6-beam Vulcan laser[14] at Rutherford Appleton Laboratory in the UK; the 8-beam OCTAL laser[15] at the Commissariat à l'énergie et aux énergies alternatives (CEA) at Limeil, France; the 9-beam Delfin laser[16] at the Lebedev Physics Institute in the USSR; the 12-beam Orion laser[17] at the Atomic Weapons Establishment, UK; and the 12-beam Iskra-5 laser[18] at the Russian Federal Nuclear Center. (In this review, unless otherwise stated, OMEGA refers to the 60-beam laser.) Implosion facilities that are planned or under construction include the Laser Mégajoule[19] near Bordeaux, France; the 128-beam Iskra-6 laser[20] at the Russian Federal Nuclear Center; and the SG-III (48-beam) and SG-IV lasers[21] at the Research Center of Laser Fusion in China. Many significant advances have resulted from work at other laser facilities such as the Nike laser[22] at the Naval Research Laboratory (NRL). The evolution of target-physics understanding has been very much an international effort; for example, results obtained on a relatively small laser facility at the Ecole Polytechnique in France[23] played an important part in the worldwide shift to shorter-wavelength lasers.

The outline of this review is as follows. Section II presents an overview of the main physics processes that are associated with direct-drive implosions. Section III describes the implosion process in more detail with reference to an ignition target design. This description is one dimensional (1-D), to illustrate how a target performs ideally. Later sections (Secs. XV and XVI) are concerned with two-dimensional (2-D) and 3-D effects, whose understanding is essential to target design.

Section IV reviews the early years of the laser fusion program, from the earliest concepts developed by Nuckolls[24] before the demonstration of the first laser until approximately 1980, when the field moved from infrared to short-wavelength lasers. The following sections are organized by topic: laser absorption (Sec. V), laser beam uniformity (Sec. VI), imprint (Sec. VII), implosion experiments (Sec. VIII), hydrodynamic stability (Sec. IX), coronal plasma physics (Sec. X), and thermal transport (Sec. XI). Implosion experiments include room-temperature implosions, used routinely to study most aspects of implosion physics, cryogenic implosions, which correspond more closely to ignition designs, and polar-drive implosions, developed for use on the NIF to study direct-drive physics on a system configured for indirect drive.

Section XII covers shock timing and equation-of-state studies motivated by the needs of ICF implosions. Section XIII reviews the evolution of cryogenic target systems and cryogenic target science from the early days when the need for the deuterium–tritium (DT) fuel to be in a solid (cryogenic) form was first recognized. Sections XIV (fast ignition) and XV (shock ignition) cover two alternative approaches to ignition. With a view toward the ultimate objective of inertial fusion energy (IFE), Sec. XVI reviews ignition and high-gain designs and Sec. XVII describes the evolution of concepts for IFE reactors.

While it is convenient to arrange much of the material by subject area, it must be recognized that there are strong interrelationships among the different areas, with many experiments depending on multiple physics processes, so that the categorization of some of the material can never be perfect. An attempt has been made to indicate many of these interrelationships through cross-referencing.

To provide a distinction between "mature" science, which is the focus of this review, and current developments, as well as for practical reasons, this review covers material published before October 2013.

Many texts and reviews on direct-drive ICF are available. Atzeni and Meyer-ter-Vehn[25] give a comprehensive treatment of ICF physics. An extensive review of the field prior to 1993 (in French) is contained in a three-part series of volumes edited by Dautray and Watteau.[26] Other texts include works by Duderstadt and Moses,[27] Kruer,[28] Yamanaka,[29] Velarde *et al.*,[30] Drake,[31] and Pfalzner.[32] Velarde and Carpintero-Santamaría[24] give an account of the history of ICF written by its pioneers. Early ICF work was reviewed in papers by Brueckner and Jorna,[33] McCall,[34] and McCrory and Soures.[35] More recently, Rosen[36] provided a useful tutorial and Lindl,[37] while focusing on indirect drive

reviewed much of the physics that is common to both approaches. A recent review of direct-drive ICF is given by McCrory *et al.*[38]

II. DIRECT-DRIVE PHYSICS OVERVIEW

The critical physical processes relevant to direct-drive implosions are summarized in Fig. 2-1, which schematically shows the four main stages of a typical implosion. The target is represented as a layer of cryogenic DT ice inside a CH shell but could include a DT-filled foam layer. Typical ignition and high-gain targets have diameters from 3 to 5 mm and ice layer thicknesses from 160 to 600 μm (Secs. III A and XVI). The interior of the DT ice layer contains low-density DT gas in thermal equilibrium with the ice. At early times [Fig. 2-1(a)], laser light is absorbed by the target, leading to the ablation of target material (at the "ablation surface") to form a hot plasma. The laser irradiation typically starts with a sequence of one to three low-intensity pulses, sometimes known as "pickets." The corresponding pressure pulses generated in the plasma launch a sequence of shock waves that propagate into the target, compressing it. The laser pulse intensity then increases rapidly, typically to an intensity of $\sim 10^{15}$ W/cm^2, launching a strong shock that merges with the earlier shocks around the time that the shocks break out of the inner surface of the ice layer (Sec. III A). During this shock-transit stage, target modulations [imperfections in fabrication or modulations imprinted by laser-beam nonuniformities (Sec. VII)] evolve as a result of a Richtmyer–Meshkov (RM)-like instability (Sec. VII C). After the shock reaches the inner surface, a rarefaction wave moves outward toward the ablation surface and the target shell and ice layer (collectively known as the shell) begin to accelerate inward toward the target center. Important issues during this initial stage include the development of ablation-surface modulations as a result of laser imprint, the "feedout" of inner-surface modulations carried by the rarefaction wave to the ablation surface (Sec. VII D), the timing of the sequence of shocks to minimize shock preheating of the fuel (Sec. XII B), and laser–plasma interactions in the coronal plasma (Sec. X). Laser–plasma interactions can have undesirable effects including the production of energetic electrons (also known as "fast," "hot," or "suprathermal" electrons), leading to fuel preheat. X rays from the hot plasma surrounding the target can also lead to preheat.

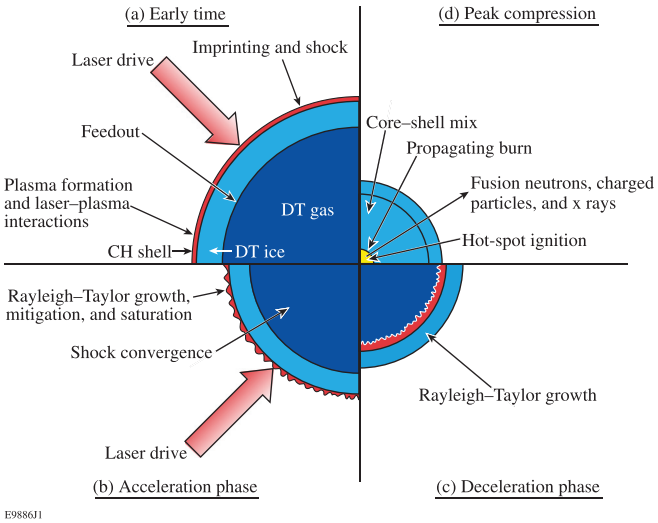

FIG. 2-1. Schematic of the four main stages of a direct-drive target implosion.

The laser intensity increases during the acceleration phase [Fig. 2-1(b)]. Ablation-surface modulations grow exponentially because of the Rayleigh–Taylor (RT) instability (Sec. IX), while the main shock within the DT gas converges toward the target center. Exponential growth continues until the perturbation amplitude reaches ~10% of the perturbation wavelength, when the instability growth becomes nonlinear. The greatest concern during the acceleration phase is the integrity of the shell. The ablation-surface modulations grow at a rate that depends in part on the shell adiabat α, defined as the electron pressure divided by the Fermi-degenerate pressure that the shell would have at absolute zero temperature. Larger adiabats result in thicker, lower-density imploding shells, larger ablation velocities, and better overall stability, but at the cost of lower overall performance. (The ablation velocity is the rate at which the ablation surface moves through the shell.)

The main shock wave moves ahead of the accelerating shell. Soon after it reflects from the target center and reaches the converging shell, the deceleration phase begins [Fig. 2-1(c)]. As the shell decelerates, its kinetic energy is converted into thermal energy and the DT fuel is compressed and heated. The attainable compression depends on the temperature of the DT at the start of the deceleration phase, and the maximum temperature depends on the kinetic energy of the shell. The greatest issue during the deceleration phase is the hydrodynamic instability of the inner surface of the shell. The deceleration instability is seeded by the feedthrough of ablation-surface modulations to the inner surface combined with the original inner-surface modulations. A major target design issue is the choice of α that optimizes performance by trading off stability with compressibility. Low values of α allow for high fuel compression, but at the cost of increased target instability.

Peak compression occurs in the final stage [Fig. 2-1(d)]. Fusion neutrons and x rays are produced together with charged particles (alpha particles for DT fuel) that, for NIF-scale targets, deposit their energy in the DT fuel, bringing more compressed fuel to fusion temperatures and leading to a propagating burn. This is commonly referred to as ignition.[2,3] In these targets, the first fusion reactions occur in a central "hot spot"—a high-temperature, low-density region surrounded by a lower-temperature, higher-density DT shell. The hot spot results from the compression of hot fuel in the deceleration phase and typically accounts for ~10% of the compressed fuel mass. It is critical that the hot spot has sufficient energy production and areal density ρR (where ρ is the density and R is the radius) for significant alpha-particle energy deposition to occur. From Refs. 2 and 3, this typically requires an ion temperature of 10 keV and $\rho R \gtrsim 300$ mg/cm^2, although an ion temperature of ~5 keV at the onset of ignition with a larger ρR is considered to be more realistic. Another concern at this stage is mixing between the hot fuel in the core and the cooler shell material, reducing the temperature of the hot fuel.

One of the most important issues for direct drive is laser beam uniformity (Sec. VI). Long-wavelength nonuniformities, which arise from considerations such as the number of beams and their placement around the target chamber, can limit the target convergence. These nonuniformities are typically required to be less than ~1% (rms). Shorter-wavelength nonuniformities, which are largely associated with the individual beam intensity profiles, are of concern as they can lead to laser imprinting (Sec. VII) during the initial stage of the laser–target interaction. Laser energy is deposited nonuniformly, according to the intensity distribution of each laser beam, resulting in ablation-surface modulations. Imprint occurs at early times until laser ablation produces a sufficiently large plasma in which the laser-absorption region becomes separated from the ablation surface. Thereafter, the shorter-wavelength laser-beam nonuniformities are smoothed by lateral thermal conduction (the "cloudy day" effect of Ref. 39) in the region between these surfaces. Imprint has been greatly reduced as a result of the development of laser beam-smoothing techniques (Sec. VI).

The properties of the hot coronal plasma surrounding the target are important for ensuring that the laser energy is efficiently absorbed and coupled to the imploding shell. The electron density n_e decreases with radius, passing through the so-called critical density n_c at the critical surface. At this surface, the electron plasma frequency, ω_p, defined by

$$\omega_p^2 = \frac{4\pi n_e e^2}{m_e}, \tag{2-1}$$

where n_e, e, and m_e are the electron number density, charge, and mass, respectively, equals the incident laser frequency ω_0. The incoming laser light can propagate only up to the critical density. Since [from Eq. (2-1)] n_c is proportional to ω_0^2, a reduction in the laser wavelength by a factor of 3 (as for the frequency-tripled glass lasers currently being used for fusion research) increases the critical density by a factor of 9. (The critical density is given by $n_c = 1.115 \times 10^{21}/\lambda_0^2\,\mathrm{cm}^{-3}$, where λ_0 is the laser wavelength in microns.) For frequency-tripled lasers, the main absorption process (inverse bremsstrahlung, Sec. V) involves electrons gaining directed energy through oscillations in the electromagnetic (EM) wave with this energy being thermalized through collisions. This process is most effective near the critical surface and favors short-wavelength lasers since the collision rate is larger at higher density. Energy is coupled more efficiently to the ablation surface of the imploding shell for short-wavelength lasers since it has a shorter distance to propagate; however, this shorter distance reduces the amount of thermal smoothing of laser nonuniformities, making laser beam smoothing particularly important. Energy transport from the absorption region to the ablation surface occurs through electron thermal conduction (Sec. XI), which is complicated by the existence of energetic electrons in the tail of the distribution function whose mean free paths between collisions are comparable to or larger than the temperature scale length.

A number of nonlinear laser–plasma interactions can take place in the portion of the plasma corona below the critical density (known as the "underdense" region) (Sec. X). Most notable are the two-plasmon–decay (TPD) instability, which occurs very close to the quarter-critical density and in which the incident EM wave excites two electron plasma waves (known as plasmons), and the stimulated Raman scattering (SRS) instability, which occurs below the quarter-critical density and in which the incident EM wave excites a scattered EM wave of lower frequency and a plasmon. These instabilities are of concern because electric fields associated with the plasmons can accelerate electrons to high energies. Another important process is stimulated Brillouin scattering (SBS), which is similar to SRS except that the plasmon is replaced by an ion-acoustic wave. This instability can occur anywhere below the critical density and can lead to a loss of energy. In one form of SBS, known as cross-beam energy transfer (CBET), laser energy can be lost by being scattered from incoming rays of one laser beam into outgoing rays of another. The effectiveness of these instabilities increases with laser intensity, imposing constraints on laser pulse-shape design.

Several nuclear reactions are of interest to laser-driven ICF. Most important are primary reactions from the DT fuel[40]

$$\mathrm{D} + \mathrm{T} \rightarrow {}^4\mathrm{He}\,(3.5\,\mathrm{MeV}) + \mathrm{n}\,(14.1\,\mathrm{MeV}). \tag{2-2}$$

The alpha particles ($^4He^{++}$) are reabsorbed in the fuel of igniting targets, but the neutrons substantially escape with some energy loss that can provide a diagnostic of the fuel ρR. For energy production, the neutrons would be captured in the blanket of an inertial fusion reactor (Sec. XVII). Many experiments have used D_2 fuel, in which the primary reactions comprise two branches with approximately equal probabilities[40]

$$\mathrm{D} + \mathrm{D} \rightarrow {}^3\mathrm{He}\,(0.82\ \mathrm{MeV}) + \mathrm{n}\,(2.45\ \mathrm{MeV}), \tag{2-3}$$

$$\mathrm{D} + \mathrm{D} \rightarrow \mathrm{T}\,(1.01\ \mathrm{MeV}) + \mathrm{p}\,(3.02\ \mathrm{MeV}). \tag{2-4}$$

The ^{3}He and triton products from these reactions can combine with fuel deuterium in the following "secondary" reactions:[41]

$$\mathrm{T}^* + \mathrm{D} \rightarrow {}^4\mathrm{He} + \mathrm{n}\,(11.8\,\mathrm{to}\,17.1\ \mathrm{MeV}), \tag{2-5}$$

$${}^3\mathrm{He}^* + \mathrm{D} \rightarrow {}^4\mathrm{He} + \mathrm{p}\,(12.5\,\mathrm{to}\,17.4\ \mathrm{MeV}), \tag{2-6}$$

where T^* and $^3He^*$ indicate tritons and ^{3}He nuclei that can have energies less than their corresponding birth energies [Eqs. (2-3) and (2-4)] because of slowing down in the compressed fuel. The primary reaction in D^3He fuel,[40]

$$\mathrm{D} + {}^3\mathrm{He} \rightarrow {}^4\mathrm{He}\,(3.6\ \mathrm{MeV}) + \mathrm{p}\,(14.7\ \mathrm{MeV}), \tag{2-7}$$

is also important. This can be used to diagnose the mix by filling the target with ^{3}He and placing deuterated plastic at some distance from the inner surface of a CH shell (Sec. VIII A).

III. ONE-DIMENSIONAL HYDRODYNAMICS AND IGNITION PHYSICS

To obtain hot-spot ignition of the DT fuel in an ICF implosion, a shell consisting of an inner cryogenic DT layer

and an outer layer of ablator material is accelerated inward by a temporally shaped pressure drive. This drive is created by laser energy absorbed in the lower-density coronal plasma via inverse bremsstrahlung, at some distance from the higher-density main shell. The absorbed energy is transported by electrons and radiation to the shell, causing its outer layer to ablate and creating a force that accelerates the shell inward. As the shell approaches peak compression and stagnation, a hotter, lower-density central region (hot spot) surrounded by colder, higher-density main fuel is formed. The ion temperature and areal density of the hot spot must be high enough to create alpha particles (produced as a result of fusing D and T) at a rate sufficient that the hot-spot self-heating is larger than the hot-spot cooling (by radiation and hydrodynamic expansion), resulting in a burn wave being launched into the main fuel.

The laser-driven ICF process leading to hot-spot ignition is described in Sec. III A, with reference to a triple-picket ignition design for the NIF. (The term "picket" refers to a short laser pulse delivered prior to the main laser pulse.) The physics of this process is common to ignition and high-gain target designs. Section III B summarizes a simple model describing the ignition phase of the implosion and its scaling with laser energy. Section III focuses on 1-D physics processes. Multidimensional aspects of ignition and high-gain designs are included in Sec. XVI. Two alternative modes of ignition that do not use the main laser drive to form a hot spot are described in Sec. XIV (fast ignition) and Sec. XV (shock ignition).

A. Triple-picket ignition design for the NIF

The basic physics of ignition and high-gain target designs is illustrated using a 1.5-MJ triple-picket design for the NIF, similar to that shown in Ref. 42. (Here and elsewhere, the energy associated with a design refers to the incident laser energy.) The target and the laser pulse that drives it are shown in Fig. 3-1. The target is a 37-μm-thick plastic (CH) shell surrounding a 160-μm-thick layer of DT ice, with a DT vapor density of 0.6 mg/cm^3 in the region inside the ice layer. The initial target radius is 1700 μm and the laser wavelength is 0.35 μm. The peak laser intensity is 8×10^{14} W/cm^2 relative to the initial target surface. The design assumes that the NIF is configured for spherically symmetric irradiation.

The required hot-spot pressure for a given drive energy can be achieved by shaping the laser pulse to increase the drive pressure and velocity of the main fuel as functions of time. Typically the drive pressure must reach ~100 Mbar to achieve the compressed fuel pressure required for ignition. A steep rise of the drive pressure to ~100 Mbar at the beginning of the pulse would lead to the formation of a very strong shock that would preheat the fuel, raise the shell entropy, and reduce the shell density resulting in a low final pressure. Therefore, the ignition target design strategy is to limit the strength of the initial shock launched into the fuel to a few Mbar to prevent a large increase in entropy. The first shock increases the fuel density by a factor of ~4, allowing subsequent shocks to only marginally increase the entropy since the entropy jump across a strong shock is proportional to

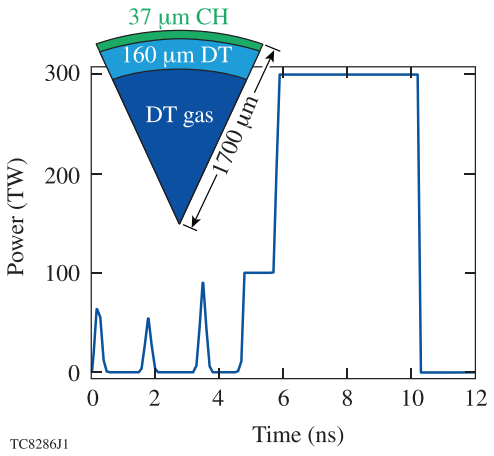

FIG. 3-1. Pulse shape and target dimensions for a 1.5-MJ triple-picket design for the NIF that is predicted to achieve a 1-D gain of 48.

$\Delta p/\rho^{5/3}$, where Δp is the pressure jump and ρ is the preshock density. As the density increases because of multiple shock compressions, the entropy increase becomes smaller and the compression approaches an adiabatic compression. Using a sequence of judiciously timed multiple shocks, it is possible to keep the shell at a relatively low entropy while raising the drive pressure to ~100 Mbar. This accelerates the shell to the required implosion velocity of $\geq 3 \times 10^7$ cm/s.

The pressure increase from a few Mbar to ~100 Mbar can alternatively be achieved adiabatically using a continuous-pulse design such as the "all-DT" design described in Sec. XVI. However, shock-velocity measurements in these designs[43] have shown that it is difficult to reproduce the adiabatic compression wave predicted by simulations. Because of this, current ignition designs are based on the generation of multiple shocks that can be accurately timed experimentally as described in Sec. XII.

In the ignition design of Ref. 42, the shocks are launched using a set of relatively short picket pulses followed by the main pulse. The picket pulses launch a sequence of decaying shocks that are experimentally timed to merge soon after they break out of the DT ice after propagating through the shell.

Precise shock timing is crucial to achieving high compression of the shell while it is in flight. A highly compressed shell acts like a rigid piston, efficiently transferring its kinetic energy to the central plasma contained within. Optimum shell compression is achieved when all shocks break out of the shell nearly simultaneously, minimizing the decompression resulting from rarefaction waves launched at each shock breakout. This requirement determines the picket amplitudes and timing. The use of multiple shocks has the additional benefit of reducing the shell nonuniformity growth factor associated with the Rayleigh–Taylor instability, as was pointed out by Lindl and Mead,[44] who presented the first multishock direct-drive design.

Figure 3-2 shows profiles of the mass density and pressure as functions of radius at a sequence of six times during the implosion from a simulation that excludes alpha-particle deposition to better illustrate the formation of the hot spot. In Fig. 3-2(a), just after the start of the main pulse, density and

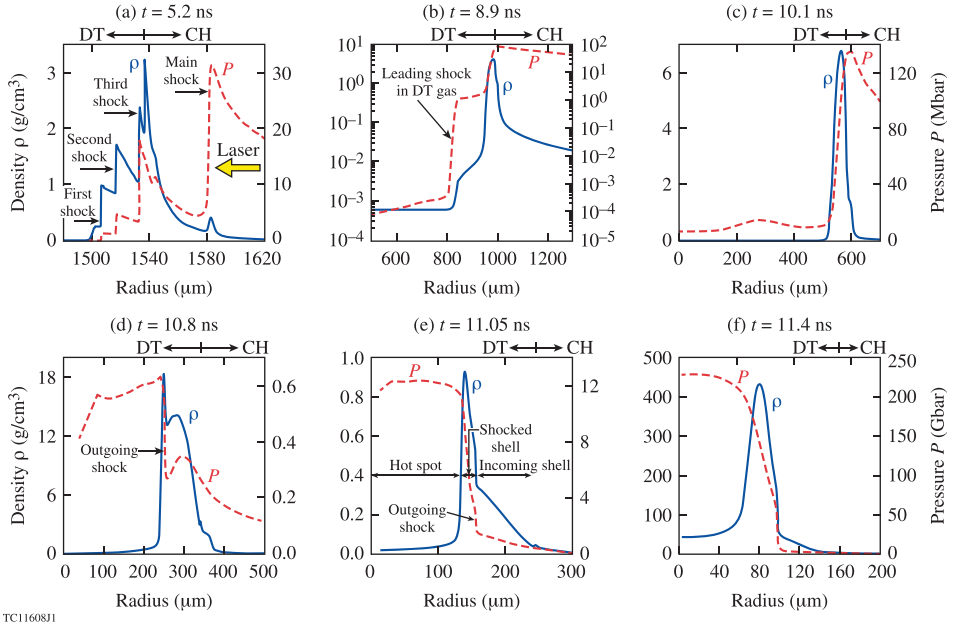

FIG. 3-2. Radial profiles of mass density (ρ) and pressure (P) of the 1.5-MJ design at times (a) 5.2 ns, just after the start of the main pulse; (b) 8.9 ns, after the leading shock is launched into the DT gas; (c) 10.1 ns, after the leading shock has reflected from the target center; (d) 10.8 ns, at the beginning of the main shell deceleration; (e) 11.05 ns, during shell deceleration; and (f) 11.4 ns, at stagnation.

pressure discontinuities indicate the positions of the first three shocks and the main shock. An additional density discontinuity (contact discontinuity) occurs at the CH/DT interface.

As the shell accelerates inward, a shock wave propagates into the vapor region ahead of the shell, as seen in Fig. 3-2(b). The shock pressure in the vapor (~1 Mbar) is much smaller than the ablation pressure (~100 Mbar) at this time. The leading shock pressure increases later because of convergence. As the leading shock wave approaches the target center and reflects, the pressure produced in the central region is not yet large enough to slow down the converging main shell [Fig. 3-2(c)]. The main shell has a maximum implosion velocity of 4×10^7 cm/s. The different stages of the deceleration phase and hot-spot formation are described in detail by Betti *et al.*[45,46] Continuous deceleration occurs when the vapor pressure has increased (because of convergence) to the level of the pressure of the main shell. As the shell continues to converge after that time, the vapor pressure keeps rising according to $P_{\text{vapor}} \sim V^{-5/3}$, where V is the volume of the vapor region, eventually exceeding the shell pressure and launching an outgoing shock (alternatively known as a return or rebound shock) through the incoming shell [Fig. 3-2(d)]. Before stagnation, the adiabatic approximation for the hot spot ($P \sim V^{-5/3}$) is valid because the thermal conduction losses are recycled by ablation back into the hot spot. The central temperature increases during the compression and heat flows out of the hot spot, driving mass ablation off the inner shell surface. This causes the hot-spot mass and areal density to increase while keeping the hot-spot pressure unaffected by heat-conduction losses.[45] Bremsstrahlung radiation leads to hot-spot energy losses, but does not significantly affect the adiabatic scaling law since the radiation cooling rate of the hot spot is smaller than the rate of PdV work of the converging shell.

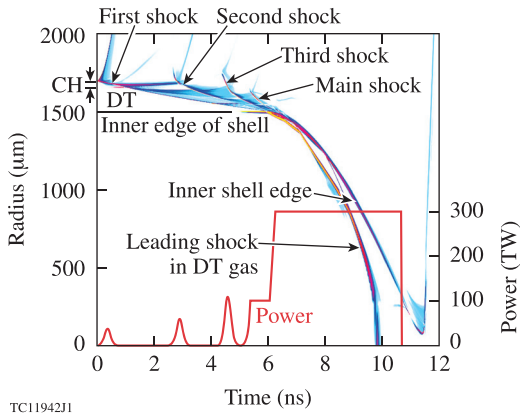

FIG. 3-3. Contour plot in the (radius, time) plane of the inverse pressure scale length $|\mathrm{d}(\ln P)/\mathrm{d}r|$ for a simulation almost identical to that of Fig. 3-2, showing the trajectories of the various shocks. The power in the incident laser pulse is included for reference.

As the shell converges and the hot spot is compressed, the outgoing shock propagates through the incoming shell and slows down the imploding shocked material. Further deceleration occurs in the shocked region because of the pressure gradient pointing from the shock front toward the target center [Fig. 3-2(e)]. The imploding shell comprises two regions: shocked material and an outer region of incoming material. Figure 3-2(f) shows the density and pressure profiles at stagnation. As the shocked material stagnates, its kinetic energy is transferred into the internal energy of the hot spot and the shocked shell. The hot-spot pressure reaches its maximum value at peak compression. At this time, ~1 mg of the initial fuel mass of ~1.2 mg is in the shocked shell and ~0.08 mg is in the hot spot.

The temporal behavior of the various shocks can be seen in Fig. 3-3, which shows contours of the inverse of the pressure scale length $|\mathrm{d}(\ln P)/\mathrm{d}r|$, where P is the total (electron plus ion) pressure. Since the pressure is discontinuous across a shock front, this plot is a convenient way of displaying shock trajectories from the simulation. (Numerically, the quantity plotted is never infinite because of the finite spatial resolution in the simulation.) The figure shows how the successive shocks are launched in response to sharp rises in the

laser power and how the shocks are timed to reach the inner edge of the shell at around the same time, just prior to shell acceleration.

The hydrodynamic efficiency of this design, defined as the kinetic energy of the imploding shell divided by the absorbed laser energy, is 6.7%. The absorbed laser fraction is 95%. Not all the shell kinetic energy is converted into internal energy of the stagnated fuel. As seen in Fig. 3-2(f), the shock has not yet reached the outer boundary of the shell at the time of stagnation, so there is some fraction of the shell that is unshocked and imploding (in "free fall"). The kinetic energy of this part of the shell is not converted into internal energy before the inner surface stagnates and the hot spot reaches its peak pressure. Figure 3-4 shows the evolution of the internal energy of the hot spot (red curve) and the combined internal energy of the shocked material and the hot spot during deceleration as functions of time. Out of the 100 kJ of shell kinetic energy, 40 kJ is transferred into the internal energy of the hot spot at stagnation. Since the inner part of the shocked shell starts to expand outward by the time the outgoing shock wave reaches the outer boundary of the shell at 11.5 ns, the total internal energy (blue curve in Fig. 3-4) never reaches the value of the peak shell kinetic energy.

When the hot-spot areal density exceeds ~0.2 g/cm^2, alpha particles start depositing a significant fraction of their energy inside the hot spot, raising its temperature and pressure. Once this self-heating is initiated, the adiabatic approximation is no longer valid. This is shown in Fig. 3-5, which gives profiles at 11.3 ns of mass density, ion temperature, and areal density, including alpha-particle deposition. A comparison of the temperature profile with the dashed curve (from a calculation with alpha deposition omitted) shows a rise in temperature resulting from alpha deposition. As the hot-spot temperature continues to rise and the number of alpha particles increases, the self-heating triggers a burn wave that propagates through the main fuel. The burnup fraction depends on the fuel areal density.[2,3,25] For this

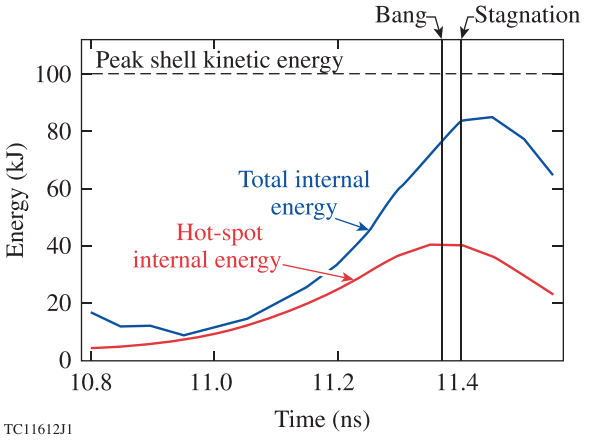

FIG. 3-4. Internal energy of the hot spot (red) and the combined internal energy of the shocked shell and hot spot (blue) during the deceleration phase. The two vertical lines indicate the bang time (the time of peak neutron production) and the time of peak pressure (stagnation). The horizontal dashed line shows the value of the shell's kinetic energy at peak shell velocity.

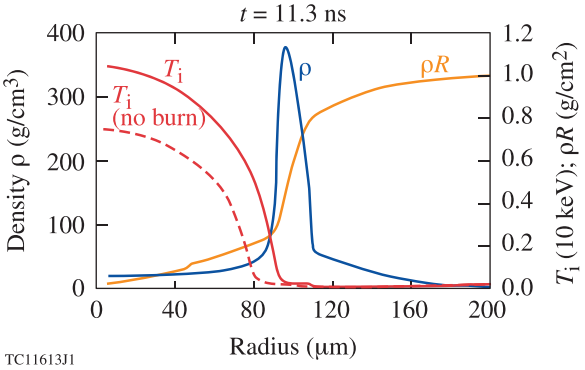

FIG. 3-5. Profiles of mass density (ρ), ion temperature (T_i), and areal density integrated from the origin (ρR) during the burn phase (solid curves) for a calculation including alpha-particle deposition. The dashed curve gives T_i for a simulation without alpha-particle deposition.

design, the target is predicted to ignite with a burnup fraction of 20% and produce a 1-D gain of 48.

Plots of electron density and temperature at the peak of the first picket (0.4 ns) and during the main pulse (8 ns) are shown in Fig. 3-6. The earlier density profile shows a small separation distance (standoff distance) $D_{ac} = 10\,\mu$m between the critical surface (radius R_c) and the ablation front (radius R_a). This is a concern for laser imprinting (Sec. VII) because little lateral smoothing can occur over this small distance. The distance D_{ac} increases with time, reaching 170 μm at $t = 8$ ns, keeping the laser nonuniformities from further distorting the shell. The electron density scale length at quarter critical (2.25×10^{21} cm^{-3} for the

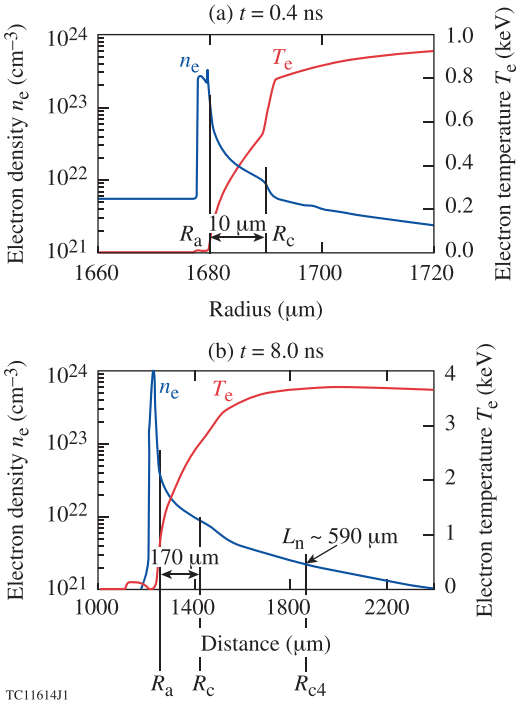

FIG. 3-6. Profiles of electron density (n_e) and temperature (T_e) at (a) 0.4 ns, at the peak of the first picket, and (b) 8.0 ns, during the main laser pulse. The ablation, critical, and quarter-critical surfaces are indicated by R_a, R_c, and R_{c4}, respectively. (The critical density for 0.35-μm light is 9×10^{21} cm^{-3}.)

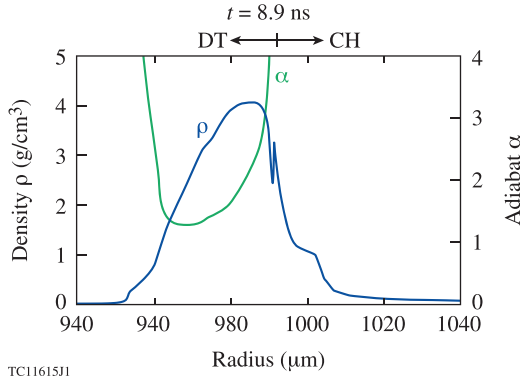

FIG. 3-7. Profiles of mass density (ρ) and adiabat (α) at 8.9 ns, during the shell acceleration. The adiabat decreases from the outside of the DT shell to the inside.

0.35-μm laser wavelength) is large (590 μm), leading to concerns about plasma instabilities producing hot electrons in this region (Sec. X).

Two important parameters of the 1-D design related to target stability, discussed further in Sec. XVI, are the in-flight aspect ratio (IFAR) and the convergence ratio. The IFAR (24.3 for this design) is defined near the beginning of shell acceleration, when the ablation-front radius is at 2/3 of the initial inner radius of the shell, as the ablation-front radius divided by the shell thickness. The convergence ratio (23 for this design) is defined as the initial inner radius of the shell divided by the inner shell radius at peak compression with alpha-particle deposition turned off.

Profiles of the in-flight shell density and the adiabat at $t = 8.9$ ns are shown in Fig. 3-7. The adiabat α is defined as the ratio of the shell pressure P_{shell} to the Fermi-degenerate pressure calculated at the shell density. It is a measure of the entropy added to the fuel by shocks and radiation. For DT fuel, the adiabat is given by

$$\alpha_{\text{DT}} \simeq \frac{P_{\text{shell}}}{2.2\,\rho^{5/3}}, \tag{3-1}$$

where the density ρ is in g/cm^3 and P_{shell} is in Mbar. As shown in Fig. 3-7, the adiabat is "shaped" inside the shell. The larger value of α at the outside of the shell is favorable for hydrodynamic stability (Sec. IX). An ICF target design is usually characterized by the mass-averaged fuel adiabat, which is ~1.6 for the design described here. The increase in α to the left of Fig. 3-7 results from the shock propagating in the DT gas shown in Fig. 3-2(b).

Adiabat shaping was suggested in 1991 by Gardner *et al.*[47] using controlled radiation deposition in the outer ablator, such that the ablation-front adiabat is raised (and the ablation-front density is lowered) without preheating the inner fuel layer. This radiative adiabat shaping has limitations, however, for typical ablator materials: the opacity is too low for DT, while the opacity of a solid-CH ablator is too high. Bodner *et al.*[48] pointed out that these problems could be avoided by using a CH-foam layer with DT wicked inside it as the ablator; the ablator would be covered with a thin high-Z layer, e.g., tungsten. Collins *et al.*[49] showed that the fluctuation decay lengths in the foam–fuel mixture are short enough that the shock jump (Rankine–Hugoniot) relations[50] are satisfied to within a few percent for shock strengths typical of ICF designs, validating the calculation of adiabats of shocked wetted foams with 1-D hydrodynamics codes. Goncharov *et al.*[51] proposed an alternative approach, showing that tailoring the spatial shape of the adiabat can be accomplished by launching a decaying shock into the ablator. The pressure of this shock is higher in the ablator than in the fuel, thereby setting the ablator on a higher adiabat than the fuel. Later, Anderson and Betti[52] found that a weaker decaying shock followed by a period of plasma relaxation and expansion would create a rarefaction density profile, which when shocked with a constant laser intensity yielded steeper adiabat gradients. Collins *et al.*[53] and Knauer *et al.*[54] confirmed this effect using 2-D simulations and experiments. Tabak independently investigated adiabat shaping using both the radiative and picket-pulse methods in the late 1990s.[55] Detailed calculations of both the decaying shock and relaxation methods of adiabat shaping were given by Anderson and Betti[56] and Betti *et al.*,[57] respectively.

The first picket provides the additional benefit of reducing laser imprint, as described in Sec. VII B 4.

B. Ignition physics

Hot-spot self-heating is initiated if the rate of alpha heating exceeds the rate of hot-spot energy loss. This ignition condition, known as a Lawson-type criterion, can be written as[58]

$$P_{\text{hs}}\tau > \frac{24}{\epsilon_\alpha S(T_{\text{i}})}, \tag{3-2}$$

where P_{hs} is the hot-spot pressure in Mbar, τ is the hot-spot confinement time in seconds (the time required to disassemble the hot spot through hydrodynamic motion), $\epsilon_\alpha = 3.5$ MeV is the alpha-particle birth energy, and $S(T_{\text{i}})$ is a function of the ion temperature T_{i} at the center of the hot spot as given in Ref. 58.

The function $S(T_{\text{i}})$ is approximately linear with T_{i} up to a central temperature of ~7 keV and reaches its maximum at ~15 keV (see Figs. 4 and 5 in Ref. 58). It would be desirable to operate at the 15-keV maximum of $S(T_{\text{i}})$ to reduce the $P\tau$ (product of pressure and confinement time) requirements for ignition. However, since the hot-spot temperature is approximately proportional to the implosion velocity, achieving ~15 keV through compression would require such high implosion velocities that hydrodynamic instabilities would severely compromise the integrity of the imploding shell. Typical ICF ignition designs use a maximum implosion velocity in the range of $3.5–4.0 \times 10^7$ cm/s, corresponding to an ion temperature of ~4 to 5 keV.

Equation (3-2) can be rewritten by introducing an ignition parameter

$$\chi = \frac{P_{\text{hs}}\tau\epsilon_\alpha S(T_{\text{i}})}{24}. \tag{3-3}$$

Igniting the hot spot requires $\chi > 1$. Assuming a perfectly spherical implosion and neglecting α-particle self-heating,

Eq. (3-3) can be rewritten, using the hydrodynamic relations derived in Ref. 59, to relate χ to observables

$$\chi \simeq [\rho R]^{0.8}(T_{\rm i}/4.7)^{1.6}, \tag{3-4}$$

where ρR is the total neutron-averaged areal density of the assembled fuel (including the hot spot and the main fuel) at peak compression in g/cm^2 and $T_{\rm i}$ is the neutron-averaged ion temperature of the hot spot in keV. Both areal density and ion temperature increase with the laser energy.[59]

To assess the progress of direct-drive implosions using sub-ignition–scaled laser facilities, such as OMEGA, Eq. (3-4) must be rewritten in terms of hydrodynamic quantities that remain constant for subscale designs hydrodynamically equivalent to ignition designs on MJ-scale facilities. One of the most important parameters is the hot-spot pressure $P_{\rm hs}$ at peak compression. To write the ignition criterion in terms of this pressure, hydrodynamic scalings[59] are first used to rewrite Eq. (3-4) in terms of the hot-spot areal density and temperature

$$\rho R_{\rm hs} \times T_{\rm i} > 0.3\,{\rm g/cm^2} \times 5\,{\rm keV}. \tag{3-5}$$

Since the DT fuel pressure (assuming equal ion and electron temperatures) is $P_{\rm DT} = 2\,\rho T_{\rm i}/2.5\,m_{\rm p}$, where $m_{\rm p}$ is the proton mass, Eq. (3-5) takes the form

$$P_{\rm hs} > 100\,{\rm Gbar}\left(\frac{100\,\mu{\rm m}}{R_{\rm hs}}\right), \tag{3-6}$$

where $R_{\rm hs}$ is the hot-spot radius. Assuming that a fraction $f_{\rm k}$ of the total kinetic energy of the shell $E_{\rm k}$ is converted into the internal energy of the hot spot at peak compression, $f_{\rm k}E_{\rm k} = 2\pi P_{\rm hs}R_{\rm hs}^3$, Eq. (3-6) can be rewritten in the form

$$P_{\rm hs} > 250\,{\rm Gbar}\left(\frac{f_{\rm k}E_{\rm k}}{10\,{\rm kJ}}\right)^{-1/2}. \tag{3-7}$$

Equation (3-7) shows that as the shell kinetic energy increases, the hot-spot pressure required for ignition decreases. For example, the target of Sec. III A couples ~100 kJ out of 1.5-MJ incident laser energy into shell kinetic energy with $f_{\rm k} \sim 0.4$ to 0.5. According to Eq. (3-7), this results in the minimum required hot-spot pressure exceeding 120–180 Gbar, which is smaller than the 215 Gbar predicted for this design. The maximum-allowed hot-spot size increases with the shell kinetic energy. This can be shown by combining Eqs. (3-6) and (3-7)

$$R_{\rm hs} < 40\,\mu{\rm m}\sqrt{\frac{f_{\rm k}E_{\rm k}}{10\,{\rm kJ}}}. \tag{3-8}$$

The condition on the minimum hot-spot pressure sets the requirements for laser pulse shaping and target dimensions. This can be understood using the following considerations: The hot-spot pressure increases by converting kinetic energy of the converging shell into internal energy of the stagnating fuel. Assuming that a fluid with velocity v and density ρ is stopped by a strong shock, the resulting pressure of the stagnated material is

$$P_{\rm stag} \sim \rho v^2. \tag{3-9}$$

This shows that the pressure at stagnation can be increased by increasing the shell density and velocity. For a given laser drive energy $E_{\rm L}$, the shell velocity scales as[43]

$$v \sim \frac{P_{\rm a}E_{\rm L}}{M_{\rm shell}I}, \tag{3-10}$$

where $P_{\rm a}$ is the drive (ablation) pressure created by the ablated plasma blowing off the target, $M_{\rm shell}$ is the shell mass, and I is the intensity of the incident laser during the main portion of the pulse. Equation (3-10) shows that the shell velocity increases by reducing the shell mass and increasing the drive pressure at a given laser intensity (by using, for example, more-efficient ablator materials).

The scaling for the target radius R comes from an argument that the shell velocity scales with target radius R and acceleration time $t_{\rm accel}$ as $v \sim R/t_{\rm accel}$, where $t_{\rm accel} \sim E_{\rm L}/R^2I$, so

$$R \sim (E_{\rm L}v/I)^{1/3}. \tag{3-11}$$

Using Eq. (3-11) and writing $M_{\rm shell} \sim \rho_0\Delta_0R^2$, where ρ_0 is the initial average shell density and Δ_0 is the initial shell thickness, Eq. (3-10) takes the form

$$v \sim \sqrt{\frac{P_{\rm a}}{\rho_0}\left(\frac{R}{\Delta_0}\right)}. \tag{3-12}$$

Equation (3-12) indicates that for a given ablator material (ρ_0 is fixed), the shell velocity can be increased by raising the laser intensity (which results in an increase in $P_{\rm a}$) or by increasing the initial aspect ratio of the shell R/Δ_0. Several design limitations control the maximum values of both quantities. The maximum laser intensity is limited by the excitation of laser–plasma instabilities such as the two-plasmon–decay instability (Sec. X A) and stimulated Raman scattering (Sec. X C), which reduce the laser coupling and lead to the generation of suprathermal electrons that can preheat the main fuel layer. The maximum value of the shell aspect ratio is determined by multidimensional effects, in particular instability growth, which potentially can break up the shell if it is too thin.

The second contributing factor to the stagnating hot-spot pressure [see Eq. (3-9)], the shell density, is determined mainly by the fuel adiabat α. The fuel adiabat is controlled primarily by shock and radiation heating. In addition, the generation of suprathermal electrons from laser–plasma instabilities can increase the adiabat in some designs when the laser intensity exceeds the instability thresholds. Calculations[43] show that ignition can fail if 1% to 2% of the shell kinetic energy is deposited in the main fuel due to suprathermal electron preheat. The design shown in Fig. 3-1 reaches a kinetic energy of ~100 kJ, leading to a limit of 1–2 kJ in preheat energy (or ~0.1% of the incident laser energy) to avoid quenching the burn. Suprathermal electron preheat is discussed further in Sec. X A 2.

IV. THE EARLY YEARS

The laser-driven ICF concept originated in classified environments, with the key physics concept of compression predating the invention of the laser. A brief history given by Atzeni and Meyer-ter-Vehn in Sec. 3.4 of Ref. 25 includes descriptions of (1) the role of compression on fusion reaction rates, from work by Eddington on stellar energetics to imploding fission weapons and to controlled thermonuclear micro-explosions; (2) the proposals of several scientists (Nuckolls, Kidder, and Colgate in the U.S., and Basov, Krokhin, and Sakharov in the Soviet Union) immediately after the operation of the first lasers to use pulsed lasers to drive implosions; (3) the initiation of secret experimental programs in the 1960s; (4) a talk delivered by Basov in 1971 that led to the declassification of the compression concept and the publication of the seminal 1972 Nature article by Nuckolls *et al.*;[1] and (5) the later declassification of research on indirect drive.

A more-detailed history of ICF is given in Ref. 24—a collection of personal recollections written by pioneers of the field. The chapter by Nuckolls in Ref. 24 is particularly useful for its description of the origins of ICF and the now-declassified work in the period up to 1972. As recognized by Lindl,[2,3] the concept of laser-driven ICF grew out of work by Nuckolls in the late 1950s on the challenge of creating small fusion explosions without the use of an atomic bomb. Nuckolls postulated that a "non-nuclear primary" might be able to energize a radiation-driven implosion. He considered several candidates for the radiation source including plasma jets, pellet guns, and charged particle beams. (Later, he advocated heavy-ion accelerators for ICF power plants.) He calculated quantities such as the required mass of DT and the required radiation energy and temperature. The importance of isentropic compression to high densities, the associated need for a shaped drive pulse, and the problem of fluid instabilities were all recognized at this time. Some of Nuckolls' calculations were for the radiation-driven implosion of a "bare drop" of DT. After the demonstration of the laser, Lindl[2,3] credits Nuckolls and Colgate with calculating implosions in laser-driven hohlraums and Kidder with calculations that applied a spherically symmetric pulse of laser light directly to the target—the first direct-drive simulations.

Significant work was reported in the open literature in the 1960s that, while omitting the concept of compression, developed some important theoretical understanding and set in motion experiments aimed at demonstrating laser-induced fusion. Possibly the earliest publication on this topic is a report from the International Solid-State Circuits Conference in February 1961 (Ref. 60) in which Peter Franken discussed the heating of small pellets of lithium hydride to fusion temperature by a laser. Franken is quoted as warning that "the physics of this scheme do not favor success, but the work has, nevertheless, been started."

In a 1962 conference abstract, Linlor[61] presented what may be the first report of a laser-produced plasma and mentioned its possible application to controlled fusion research. Soon thereafter, in 1964, Dawson[62] published ground-breaking theoretical work on laser-produced plasmas, covering many basic physics processes (such as inverse-bremsstrahlung absorption, thermal conduction, and electron–ion equipartition) that would subsequently be incorporated into hydrodynamic simulation codes. Dawson's main interest in this work was to use the laser to heat solid or liquid particles to fuel a magnetic-containment device. In what may be the first reference to the physical significance of the laser wavelength, he advocated higher-frequency lasers to heat the plasma at higher densities, improve the equipartition, and, thereby, heat the ions to higher temperatures.

In a later paper, Dawson *et al.*[63] considered the inverse-bremsstrahlung absorption process in more detail, including a finite density gradient in the plasma surrounding the solid particle. They recognized that efficient absorption is only possible with a sufficiently large scale length and estimated that a scale length of 1.4 mm would be needed to heat a deuterium plasma with a ruby laser (wavelength $\lambda_0 = 0.7\,\mu$m), assuming an electron temperature of 10 keV. Considering a 1.4-mm-radius sphere of electrons at the critical density, they estimated that an energy of the order of 100 kJ would be needed to accomplish this. (Of course, the density–radius product of this sphere, of the order of 1 mg/cm^2, would have been far too small for alpha-particle deposition.) They again advocated using higher-frequency lasers ("It might be advantageous to pass the light through a second harmonic generator"), noting that if the laser frequency is doubled, the density at the point where it is absorbed is 4× greater, allowing the radius of the particle to be reduced by a factor of 4.

While Dawson *et al.* did not take into account the need for compression and did not have appropriate hydrodynamic simulation codes available, their physical intuition that a deuterium plasma of a sufficient size, driven by a short-wavelength laser, could absorb a substantial fraction of the laser energy was correct and showed remarkable foresight. Their numerical estimates were mostly close, consistent with the parameters of the all-DT ignition design described in Sec. XVI, which has an outer radius of 1.7 mm and a coronal scale length of ∼0.5 mm, uses only inverse bremsstrahlung as an absorption mechanism, and is driven by a 0.35-μm laser. The only estimate that was a long way off was the laser energy (which is 1.5 MJ in the all-DT design); ignition designs account for the ∼10% conversion efficiency between the energy absorbed in the corona and the energy of imploding material and the energy cost associated with ensuring adequate target stability.

Unfortunately, the available laser energies, laser wavelengths, and target scale lengths in the 1960s and 1970s were such that the regime envisaged by Dawson *et al.* could not be realized. Instead, target physics was generally dominated by other absorption mechanisms and by their often undesired consequences.

A. The quest for neutrons

On the experimental side, leadership was provided by the work of Basov and others at the Lebedev Institute in the USSR. In 1964, Basov and Krokhin[64,65] reported on using lasers to heat hydrogen to fusion temperatures. (Reference 65 referred to a paper delivered by Basov at the Presidium of

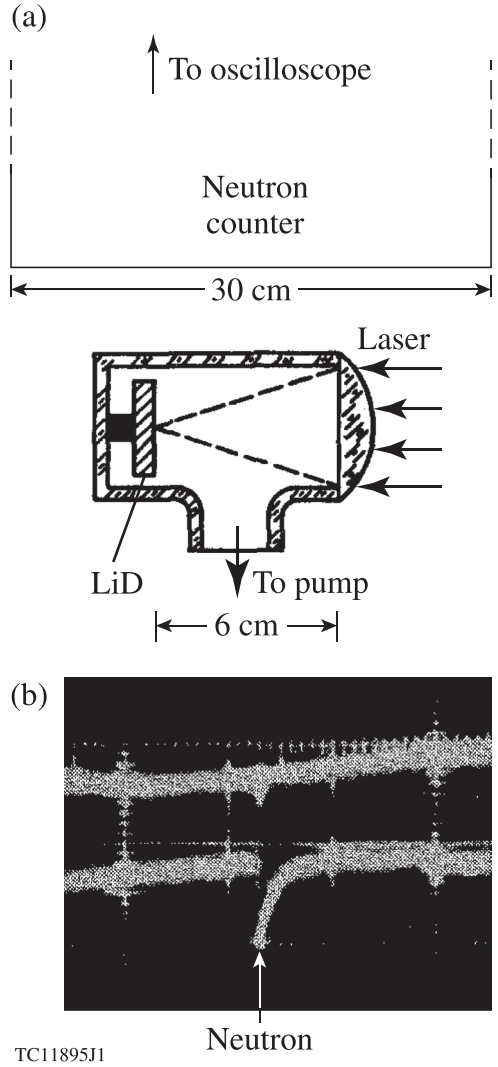

FIG. 4-1. (a) Setup of the first experiment to obtain fusion neutrons from a laser-heated target. (b) Scope traces indicating the production of a single neutron in coincidence with the laser pulse. Reprinted with permission from Basov *et al*., IEEE J. Quantum Electron. **4**, 864 (1968). Copyright 1968 IEEE.

the USSR Academy of Sciences as being one of the first suggestions to use lasers to initiate fusion.) In 1968, Basov *et al*.[66,67] reported the first observations of neutrons from solid LiD targets irradiated using short (~10-ps), 1-μm-wavelength Nd:glass laser pulses up to 20 J. Their experimental configuration is shown in Fig. 4-1(a). Their large plastic scintillator counter allowed them to measure neutrons in a large solid angle. On some shots, a single neutron was detected, such as shown on the scope trace of Fig. 4-1(b). Basov *et al*. claimed that these neutrons were thermonuclear, but this proved to be controversial.

Similar measurements were soon reported by other laboratories, also using Nd:glass lasers. Gobeli *et al*.[68] of Sandia Laboratories confirmed the Lebedev experiments, also using LiD targets and with similar laser parameters (up to 25 J in short laser pulses). They found "a somewhat higher rate of neutron production," meaning one to three neutrons per shot. Significantly, greater neutron counts were reported in 1970 by Floux *et al*.[69] at Limeil. They irradiated cryogenic D_2 targets using slightly larger energies (30–50 J) and substantially longer laser pulses (of ~10-ns duration), at focused intensities of a few times 10^{13} W/cm^2. They observed 100–150 neutrons per shot. They too claimed a thermonuclear origin. They estimated the electron temperature to be between 500 and 700 eV, based on x-ray signals, and estimated that if ions were at a similar temperature, they would produce some fusion reactions. In 1971, Basov *et al*.[70] repeated the long-pulse experiments of Floux *et al*., except that they used CD_2 targets. They quoted 10^3 neutrons per shot for a laser energy of 14 J.

In 1972, Mead *et al*.[71] at Livermore reported 10^3 to 10^4 neutrons from solid CD_2 targets, but only from pulses longer than 2 ns or double pulses. The reproducibility was poor and not understood. At the Max Planck Institute in Garching, Büchl *et al*.[72] observed up to 10^3 neutrons from a solid D_2 target at low intensities (5×10^{12} W/cm^2) and found on the basis of time-of-flight measurements that the neutrons came from the target. However, based on their hydrodynamic predictions of just 10^{-2} neutrons per shot and observations that the neutrons disappeared when a background gas was added, they concluded that the neutrons were not thermonuclear. An opposite interpretation came from further experiments at Limeil, in which Floux *et al*.[73] reported ~10^4 neutrons from solid D_2 targets heated by long pulses (~3.5 ns) and higher intensities (~8×10^{13} W/cm^2). They claimed that their yield was thermonuclear, coming from the overdense region of the corona where the ion temperature T_i was predicted to reach ~600 eV. They recognized that this explanation was consistent with the observations of lower yields for shorter pulses, where there was less time to heat the ions. Their claim must be considered to be highly plausible. Their results were supported by hydrodynamic calculations (incorporating the basic physics processes of inverse bremsstrahlung absorption, thermal conduction, and electron–ion equipartition described by Dawson[62]) that predicted yields reasonably close to what was observed as well as a time-dependent reflected light fraction that was remarkably close to observations (Sec. XB). This explanation is supported by earlier theoretical work of Shearer and Barnes,[74] who had carried out some preliminary simulations of the early Lebedev experiments and identified the basic physics processes.

A multibeam irradiation geometry was reported by Basov *et al*.,[75] who used the nine-beam Delfin laser of Ref. 16 to focus ~200 J onto a solid 110-μm-diam CD_2 target to obtain a yield of 3×10^6 neutrons. They suggested that this geometry was favorable because it avoided the spreading of the heated region beyond the spot diameter that occurs for planar targets. This was not presented as an implosion experiment, and it is plausible that the neutrons again came from the overdense coronal region.

A thermonuclear source for the neutrons was not universally accepted. McCall *et al*.[76] at Los Alamos argued that the neutrons could be produced in the blowoff plasma by fast ions generated through electrostatic acceleration. They showed that neutrons could arise from deuterium monolayers deposited on the chamber wall. They obtained neutrons using a short-pulse laser (17 J, 25 ps) at a high focused intensity of ~3×10^{16} W/cm^2, more likely to produce nonlinear interactions, and observed fast ions with velocities ~2×10^8 cm/s.

Yamanaka *et al.*[77] at Osaka obtained up to 2×10^4 neutrons from a solid D_2 target with 2-ns pulses at up to 10^{14} W/cm^2. This intensity is comparable to that of Floux *et al.*[73] and the pulse, although shorter, is long enough to establish a reasonable plasma scale length, so the plasma temperature must have been comparable and the similar observed neutron yield could also be consistent with a thermal origin. However, Yamanaka *et al.* observed fast ions (with an average speed of 10^8 cm/s) and invoked them as the source of the neutrons. They also invoked the parametric decay instability (PDI) (Sec. X E) for much of the absorption.

In Ref. 78, Basov *et al.* agreed with McCall *et al.*[76] that in the case of tight focusing on a solid target, the neutrons were produced external to the plasma from accelerated deuterons. However, they found that in a multibeam irradiation geometry with spherical targets, the neutrons were thermal, on the basis of the width of the energy spectrum of the neutrons. In Ref. 79, Soures *et al.* reported over 10^4 neutrons from a one-beam laser tightly focused onto solid spherical LiD targets; based on time-of-flight measurements, these neutrons originated from the target. This same conclusion was drawn by Basov *et al.*[80] from time-of-flight measurements in their multibeam system. Bodner *et al.*[81] proposed that the early fusion neutrons originated from ions directly heated to keV temperatures in a narrow turbulent region near critical, resulting from the parametric decay instability. Boyer[82] suggested that the SBS (Sec. X B) instability could have been responsible.

Spherical irradiation had been considered for some time. In 1966, Daiber *et al.*[83] proposed a laser-driven spherical implosion in which a first set of beams would be focused to a point in a gas, producing a spherical blast wave. A second set of beams would deposit their energy in the high-density shell of the blast wave, producing a spherically imploding shock wave. The intended application was fusion, and laser energies in excess of 10 MJ were envisaged for breakeven. Kidder[84] considered the implosion of a sphere of D_2 just above the critical density and found that a 100-kJ light pulse would produce 0.3 J of fusion energy. Mead[85] reported a spherically symmetric, 12-beam ruby laser system capable of 2 J per beam, in which 10-ns laser pulses were focused into a gas to produce spherical blast waves. Unfortunately, the energy had to be limited to 0.2 J per beam to avoid multiple breakdowns in the gas along the beam paths.

The field received a major impetus in 1972 with the Nature paper published by Nuckolls *et al.*[1] in which the concept of ablative compression to high densities was disclosed. This paper focused on solid DT spheres, although it was mentioned that shells could have some advantages as long as their aspect ratio was not too high. A central part of the concept, shown in Fig. 4-2(a), is a shaped laser pulse whose power increases rapidly in time over several orders of magnitude. (The peak power, 10^{15} W, exceeds that currently available on the National Ignition Facility by about a factor of 2.) The pulse shape was designed to isentropically compress the fuel to maximize the final density. Gain curves [Fig. 4-2(b)] were presented, showing that the required laser energy can be greatly reduced (e.g., to 1 kJ) if high compression can be obtained. Many important aspects of direct-drive physics

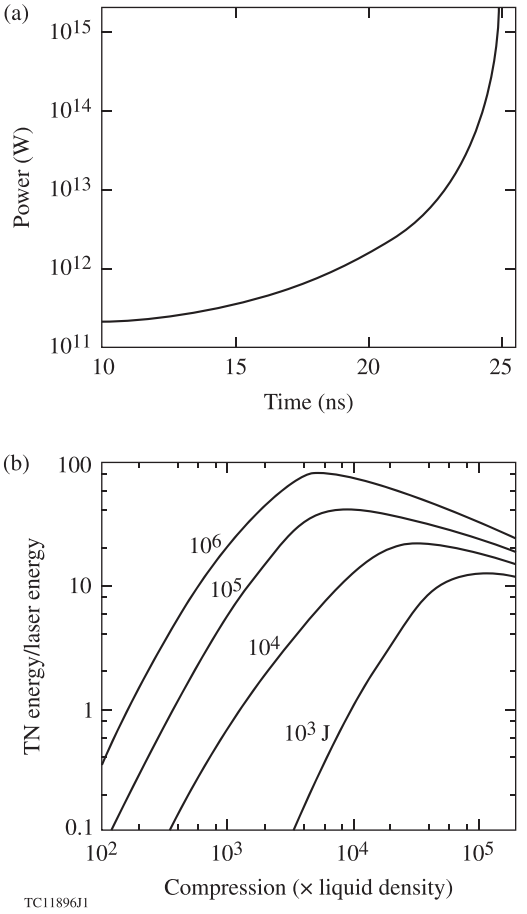

FIG. 4-2. (a) Shaped laser pulse proposed by Nuckolls *et al.*[1] to implode a solid sphere of DT. (b) Predicted gain [thermonuclear (TN) energy divided by incident laser energy] as a function of compression for various values of incident laser energy. Reprinted by permission from Nuckolls *et al.* Nature **239**, 139 (1972). Copyright 1972 Macmillan Publishers Ltd.

were identified, as is evident from the following findings: (a) a sequence of about ten pulses should suffice to create the shaped pulse; (b) 20% uniformity could be produced with six overlapping beams, and this could be reduced to $<1\%$ by thermal conduction; (c) absorption occurs via inverse bremsstrahlung and plasma instabilities; and (d) there are problems with suprathermal electrons generated by laser–plasma instabilities preheating the fuel, these problems being worse for longer-wavelength lasers such as CO_2 ($\lambda_0 = 10.6\,\mu$m) and minimized for ultraviolet lasers. The concepts described in Ref. 1 were expanded upon in Ref. 86.

In a commentary written just after Ref. 1 that reflects the partial physics understanding of the time, Rosenbluth and Sagdeev[87] stated, "Under conditions of interest for laser fusion (electron temperatures of many keV) the collision frequency in hydrogen is such that [inverse bremsstrahlung] absorption will be negligibly small." They added that, fortunately, the parametric decay instability "provides a very efficient mechanism for anomalous absorption." This view was shared by Brueckner,[88] who claimed that "strong nonclassical absorption occurs for laser power in excess of 10^{11} to 10^{12} W/cm^2," and anticipated that the absorption efficiency would approach unity. Indeed, for many years thereafter, simulations by many computer codes would deposit up to 100%

of the laser energy reaching the critical surface by assumed "anomalous mechanisms." Rosenbluth and Sagdeev were also concerned about SBS and advocated reducing this by going to shorter-wavelength lasers to increase the collisional damping of the SBS ion-acoustic waves.

The next major step forward came with the demonstration at KMS Fusion of thermonuclear neutrons resulting from laser-induced compression, reported by Johnson *et al.*[89] and Charatis *et al.*[90] A schematic of this experiment is shown in Fig. 4-3(a). KMS used a unique ellipsoidal clamshell optical system[91] to irradiate the spherical target with a high degree of uniformity. The targets were thin-walled glass microspheres, with diameter ~70 μm and wall thickness ~1 μm, filled with

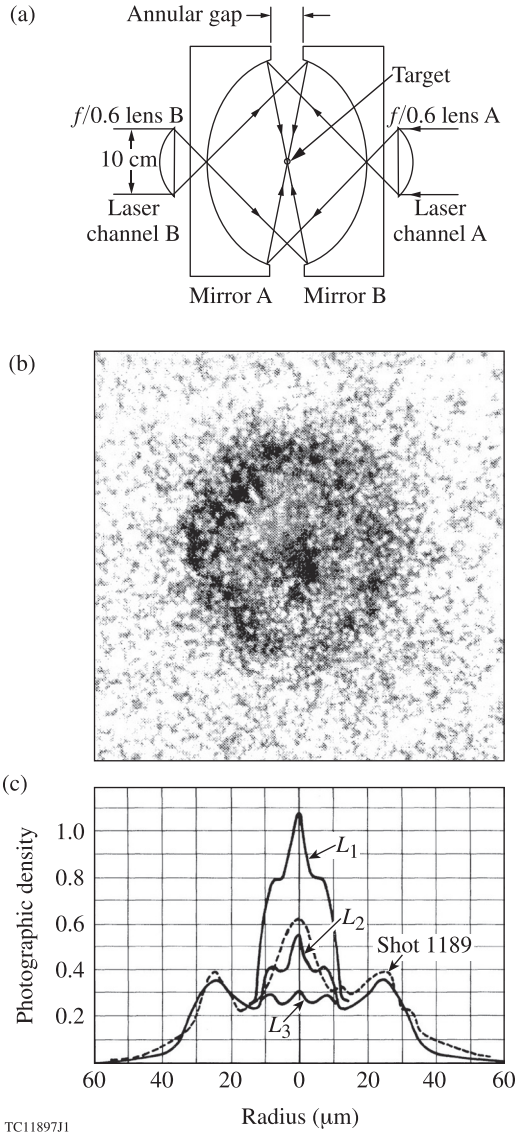

FIG. 4-3. (a) The KMS two-beam ellipsoidal-mirror target illumination system used for the first experiments to produce fusion through laser compression. Reproduced with permission from Charatis *et al.*, Plasma Phys. Controlled Nucl. Fusion Res. 1974 (IAEA, Vienna, 1974), Vol. II, pp. 317–335. Copyright 1975 International Atomic Energy Agency. (b) A typical x-ray pinhole camera image showing a hot compressed core. (c) Lineout through (b) (dashed curve), compared with three theoretical models (L_1 to L_3) including different levels of asymmetry. (b) and (c) Reprinted with permission from Campbell *et al.*, Phys. Rev. Lett. **34**, 74 (1975). Copyright 1975 American Physical Society.

13–18 atm of DT. Neutron yields were typically a few times 10^5. Evidence for target compression was provided by Campbell *et al.*,[92] who showed time-integrated x-ray pinhole camera images from empty glass microspheres (without the DT), such as the image in Fig. 4-3(b). The image shows emission from the outside of the target resulting from the hot coronal plasma and an intense central feature from the compressed core. Figure 4-3(c) compares a lineout of this image with three 1-D hydrodynamic simulations. The simulations incorporated angular momentum values L_1, L_2, and L_3 to represent deviations from spherical symmetry.

There was little doubt from the KMS experiments that the neutrons from microshell implosions were thermonuclear. This was confirmed by Slivinsky *et al.*,[93] who measured the ion temperature (~3 keV) from the broadening of the alpha-particle time-of-flight signal. They also showed an energy downshift of 0.2 MeV from the original 3.52 MeV, demonstrating that the neutrons originated from inside the glass shell. The final confirmation that the neutrons were generated in the central compressed core was provided by Ceglio and Coleman,[94] who imaged the alpha particles obtained from two-beam implosions on the Argus laser at Livermore. Their reconstructed images showed concentric elliptical contours with an *a/b* ratio of 1.1–1.2 and a volume compression of ~50. Ion-temperature measurements based on the neutron time-of-flight broadening (the neutrons were virtually unperturbed by passage through the compressed gas or glass shell) were reported by Lerche *et al.*[95]

B. Suprathermal electrons

Energetic particles and x rays had been observed from laser-produced plasmas for a long time. Energetic x rays are understood to result from the bremsstrahlung radiation emitted by energetic (suprathermal) electrons as they slow down. Here, "energetic" must be understood in the context of the time; the actual energies that were found noteworthy tended to increase as more powerful lasers became available. Linlor[96] noted ion energies up to 1 keV using a ruby laser. Langer *et al.*[97] measured electrons, ions, and x rays emitted from plasmas produced by ruby and Nd:glass lasers (albeit at the low intensity of $\sim 6 \times 10^{10}$ W/cm^2) and suggested a space-charge–separation accelerating electric field. Using a Nd:glass laser, Büchl *et al.*[72] observed a two-component x-ray spectrum with an ~2-keV nonthermal component that disappeared (along with the neutrons) when a background gas was added. Shearer *et al.*[98] irradiated plastic targets with a Nd:glass laser at $\sim 2 \times 10^{14}$ W/cm^2 and found 100-keV x rays with a temperature $T_H \sim 50$ keV; they suggested the parametric decay instability as the cause. Olsen *et al.*[99] reported 200- to 800-keV x rays, also from a Nd:glass laser. Ehler[100] observed proton energies reaching ~100 keV at a CO_2 laser irradiance up to 10^{14} W/cm^2.

A typical x-ray spectrum is shown in Fig. 4-4(a) from experiments at NRL by Ripin *et al.*[101] in which solid CH_2 targets were irradiated at $\sim 10^{16}$ W/cm^2 with 21-ps, 1-μm pulses. They claimed that magnetic fields, rather than a suprathermal electron component, were sufficient to explain the data (by inhibiting the thermal heat flux) and gave predictions of a magnetic-field model that came close to the

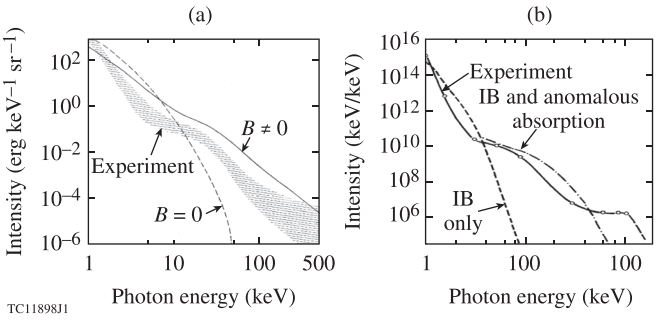

FIG. 4-4. Hard x-ray spectra from (a) Ripin *et al.*[101] and (b) Slivinsky *et al.*[107] showing suprathermal components that could not be modeled using classical physics. Magnetic fields (B) and anomalous absorption were offered as the respective explanations. IB: inverse bremsstrahlung. (a) Reprinted with permission from Ripin *et al.*, Phys. Rev. Lett. **34**, 1313 (1975). Copyright 1975 American Physical Society. (b) Reproduced with permission from J. Appl. Phys. **46**, 1973 (1975). Copyright 1975 AIP Publishing LLC.

data. Interestingly, the "thermal" temperature predicted by their model, ~60 keV, was higher than the maximum typically observed suprathermal temperature of ~20 keV.

The 60-keV temperature may have arisen from an assumption that all of the incident laser light was completely absorbed when it reached the critical density. This procedure, commonly referred to as a "dump-all," was routinely used in simulations at the time such as those of Refs. 102–105. In Ref. 103, all the energy was dumped in the first overdense zone, generating a sharp temperature gradient even though the mean free path of a 20-keV electron at $n_e = 10^{19}$ cm^{-3} is ~100 cm. Other simulation models allowed more flexibility; e.g., in the model described by

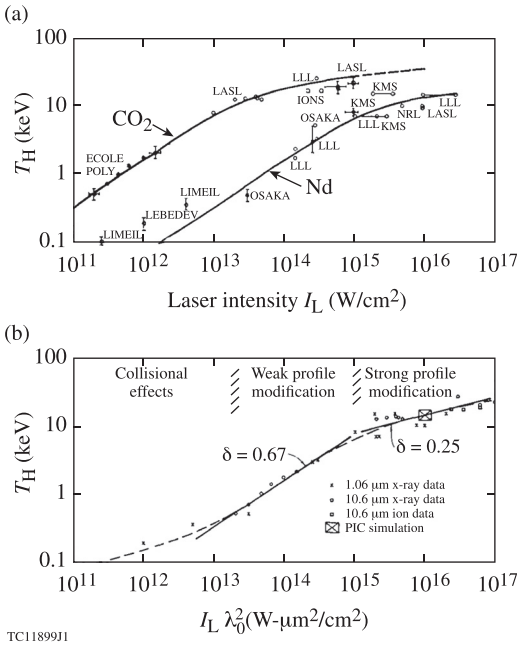

FIG. 4-5. (a) Hot-electron temperatures T_H (based mainly on the slopes of spectra such as shown in Fig. 4-4) obtained from many laboratories as a function of laser intensity I_L for CO_2 lasers (wavelength $\lambda_0 = 10.6\,\mu$m) and Nd:glass lasers ($\lambda_0 = 1.06\,\mu$m). (b) The same data as in (a) but plotted as a function of $I_L\lambda_0^2$. Reproduced with permission from E. L. Lindman, J. Phys. **38**, C6.9 (1977). Copyright 1977 EDP Sciences, see jphyscol.journaldephysique.org.

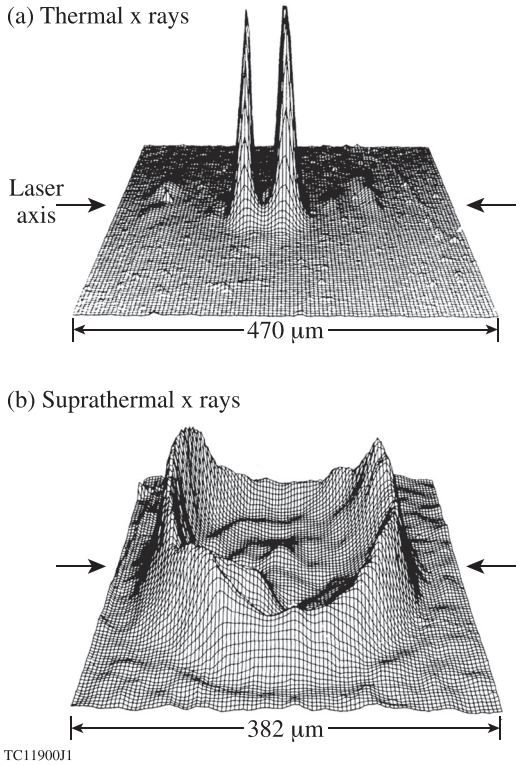

FIG. 4-6. Zone-plate images of x-ray emission from exploding-pusher glass-microshell targets irradiated on the Shiva laser. The images are in a plane containing the laser axis, about which the beams were clustered with ten beams on each side of the target. (a) Image in the spectral window 4 to 7 keV, indicating thermal emission from two disk-shaped regions of hot, stagnated glass near the target center. (b) Image in the spectral window 17 to 30 keV, indicating an origin near the irradiated portion of the surface of the ~300-μm-diam target. Reprinted with permission from N. M. Ceglio and J. T. Larsen, Phys. Rev. Lett. **44**, 579 (1980). Copyright 1980 Americal Physical Society.

Mead *et al.*,[106] the user was allowed to specify the fraction of a ray energy that was dumped and the density that the ray needed to reach for this to happen.

Another x-ray spectrum, obtained from CD_2 targets irradiated at 1-μm wavelength at the much lower intensity of $\sim 2 \times 10^{13}$ W/cm^2 by Slivinsky *et al.*,[107] is shown in Fig. 4-4(b). While the x-ray signal fell off faster with photon energy as a result of the lower irradiance, it exhibited similar behavior in that it could not be modeled using just classical inverse-bremsstrahlung absorption. Slivinsky *et al.* explained their results with "anomalous absorption," but they were unable to tell whether this was resonance absorption or a parametric instability. A third explanation was offered for similar results (Fig. 11-2 below) obtained in earlier work by Kephart *et al.*[108] in terms of thermal flux inhibition (Sec. XI).

A consensus emerged that the hard x rays resulted from suprathermal electrons produced by resonance absorption. In this absorption process, described in more detail in Sec. IV C, p-polarized light incident with a non-normal angle of incidence has a turning point below critical but tunnels to the critical density where it resonantly excites electron plasma waves, which accelerate electrons to high energies. Typically the hard x-ray spectrum showed an exponential

falloff with x-ray energy, characterized by a hot temperature T_H. (This is difficult to see in Fig. 4-4 because of the logarithmic x axes.) Brueckner[109,110] gave a convenient way of estimating the total hot-electron energy from the hard component in the spectrum.

A compilation of results by Lindman[111] for the T_H obtained from a large number of laboratories is shown in Fig. 4-5(a) for Nd:glass lasers ($\lambda_0 = 1.06\,\mu$m) and CO_2 lasers ($\lambda_0 = 10.6\,\mu$m). Remarkably, when plotted against $I_L\lambda_0^2$, where I_L is the laser intensity, all data lie very close to the same curve [Fig. 4-5(b)]. This curve and its interpretation as resonance absorption are consistent with particle-in-cell (PIC) simulations carried out by Forslund *et al.*[112,113] and by Estabrook and Kruer.[114] The parameter $I_L\lambda_0^2$ is important since it is proportional to the oscillatory energy of an electron in the electromagnetic field. Different scalings were noted for two regimes, described as "weak" and "strong" profile modification. Profile modification refers to the steepening of the density profile near critical. This was commonly ascribed to radiation pressure, sometimes described as the ponderomotive force, although there were alternative explanations (Sec. IV D). Early work on the ponderomotive force is described by Hora.[115] PIC simulations by Estabrook *et al.*[116] indicated that resonance absorption caused the steepening and was also enhanced by the steepening.

While scaling laws can be very informative, an understanding of their regimes of applicability is equally important. If one were to extrapolate the $I_L\lambda_0^2$ scaling of Fig. 4-5 to the $\lambda_0 = 0.35$-μm ignition design of Sec. III at 10^{15} W/cm^2, one would find T_H just below 2 keV, lower than the expected thermal temperature of $\sim$4 keV, in contradiction to the premise that T_H represents electrons hotter than thermal.

Very informative x-ray images of spherical glass microshells (diameter $\sim$300 μm, thickness $\sim$1.5 μm) imploded on the 1-μm-wavelength Shiva laser were obtained by Ceglio and Larsen[117] using zone-plate coded imaging. The laser delivered 17–20 TW in 90-ps pulses. The Shiva beams were arranged in two clusters of ten beams on either side of the target (in reality, above and below the target) with incidence angles up to 17.7°, so the target experienced strongly two-sided irradiation. Two (time-integrated) images are shown in Fig. 4-6: for thermal x rays [Fig. 4-6(a)] and for suprathermal x rays [Fig. 4-6(b)]. The thermal x rays come primarily from the hot compressed core, the two-lobed structure being associated with the two-sided irradiation. The suprathermal x rays come primarily from the outer target surface, with maximum emission from the portions of the target directly facing the laser beams.

From Fig. 4-6(b), it is evident that hard x rays also come from the less-irradiated region of the target in the center of the figure (the laser axis is horizontal in the figure, as indicated by the arrows). This is consistent with a picture in which the hot electrons can pass through the shell, fuel, and corona multiple times before slowing down. The electrons can lose their energy in two ways: (1) as a result of collisions in the shell, leading to x-ray emission and (2) as a result of reflections from a moving sheath on the outside of the corona, leading to the acceleration of fast ions. In this picture, the electrons provided considerable thermal smoothing of the deposited energy, enabling reasonably symmetric implosions of targets that were often irradiated with only two beams (or two clusters of beams as on Shiva).

These targets are known as "exploding pushers" because the glass shells, heated throughout their volume by the hot electrons, exploded. Exploding-pusher targets were typically irradiated at high laser intensities (to generate high temperatures) and were useful for producing neutrons. However, it was recognized that they would not scale to breakeven and gain because the large fuel preheat would preclude high compression. The short pulses used to drive these targets bore no resemblance to the shaped pulses required by Nuckolls *et al.*[1] for ablative compression. Storm[118] developed a model for exploding-pusher targets that enabled the dependence of yield on parameters such as laser pulse width, target diameter, wall thickness, and fill pressure, to be predicted without recourse to more-accurate hydrodynamic simulations that, at this time, required significant computational time even in one dimension. The model scaled with experiments and calculations to within a factor of 2 over several decades of neutron yield. Giovanielli and Cranfill,[119] Rosen and Nuckolls,[120] and Ahlborn and Key[121] also developed exploding-pusher models.

C. Resonance absorption

While the parametric decay instability had in earlier years appeared to be the primary laser-absorption mechanism, the success of the T_H scaling coupled with PIC simulations led to resonance absorption becoming the favored mechanism. The steepening of the density profile near critical worked against the parametric decay instability but helped resonance absorption because the incident wave had to tunnel through a shorter distance to reach critical. This was formalized by the basic resonance absorption function $\phi(\tau)$ [Fig. 4-7(a)], published by Denisov[122] in 1957 in the context of the propagation of electromagnetic radiation in the ionosphere and later by Ginzburg.[123] The quantity τ is defined as $\tau = (2\pi L/\lambda_0)^{1/3}\sin\theta$, where L is the scale length at critical and θ is the angle of incidence, and $\phi(\tau)$ represents the amplitude of the tunneled electric field. A similar curve is given by Friedberg *et al.*[124] for the absorption in cold plasmas. They found a maximum absorption of $\sim$40% at $\theta = 23°$ for $\lambda_0 = 1.06\,\mu$m and a steep density profile with scale length $L = 1.7\,\mu$m. They noted that the energy of the resonantly excited electron plasma waves could be transferred to energetic electrons by means of wave breaking and Landau damping. The work of Ref. 124 was extended to hot plasmas by Forslund *et al.*[112]

The theory of resonance absorption made several clear predictions: no absorption at normal incidence, no absorption for s polarization, and a strong angular dependence for p polarization. The results of one of the very limited number of experiments that set out to investigate these predictions are shown in Fig. 4-7(b), from Manes *et al.*[125] and Thomson *et al.*[126] They used a box calorimeter surrounding the target together with calorimetry of the light backscattered through the focus lens to measure the total scattered light, thereby obtaining an accurate measurement of the absorption. They

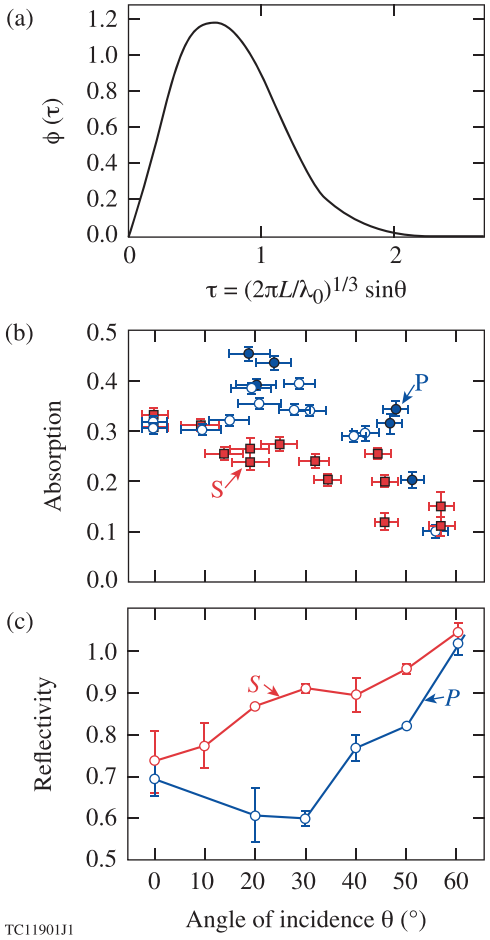

FIG. 4-7. (a) Resonance absorption function $\phi(\tau)$, where τ depends on the angle of incidence θ, the density scale length L, and the laser wavelength λ_0. Reproduced with permission from N. G. Denisov, Sov. Phys.-JETP **4**, 544 (1957). Copyright 1957 Russian Academy of Sciences. (b) Measured absorption of *p*- and *s*-polarized light as a function of angle of incidence θ, obtained on the Janus laser for CH targets. Data for *p* polarization (blue) are from Ref. 125, with solid circles indicating an intensity of $5.6 \pm 0.4 \times 10^{15}$ W/cm^2 and open circles $2.5 \pm 0.9 \times 10^{15}$ W/cm^2; data for *s* polarization (red) are from Ref. 126. Reprinted with permission from Manes *et al.*, Phys. Rev. Lett. **39**, 281 (1977). Copyright 1977 American Physical Society. (c) Reflectivity into 4π of *p*- and *s*-polarized light incident on Cu targets as a function of θ. Reprinted with permission from Godwin *et al.*, Phys. Rev. Lett. **39**, 1198 (1977). Copyright 1977 American Physical Society.

irradiated CH disk targets with ~30-ps, 1-μm-wavelength pulses at $\sim 10^{16}$ W/cm^2 with a small focal diameter of ~40 μm. They indeed observed a difference between the two polarizations in the angular dependence, indicating resonance absorption. However, the observed angular dependence for *p* polarization bore little resemblance to the curve of $\phi(\tau)$. The absorption fractions observed at normal incidence and for *s* polarization were much larger than would have been expected for inverse bremsstrahlung and were more difficult to explain. Thomson *et al.* offered the explanation that the critical surface was rippled, as postulated by Estabrook *et al.*[116] (More broadly, the whole density profile in the vicinity of critical could be considered to be strongly inhomogeneous.) However, the PIC simulations of Ref. 116 predicted ~15% absorption at normal incidence caused by the parametric decay and oscillating two-stream instabilities (Sec. X E), so the interpretation of Fig. 4-7(b) remains inconclusive.

Figure 4-7(c) shows data from an experiment at Garching by Godwin *et al.*,[127] who used an Ulbricht spherical photometer [similar to that shown in Fig. 5-1(b) below] to measure the scattered light. They irradiated Cu targets with 400-mJ, 30-ps pulses at a 1-μm wavelength over a wide range of intensities up to 10^{16} W/cm^2 and plotted the reflectance. Their results were similar to those of Fig. 4-7(b): there was about 30% absorption at normal incidence and the difference between *s* and *p* polarization was slightly larger. Similar experiments were reported for 0.5-μm irradiation by Maaswinkel *et al.*[128]

D. Plasma diagnostics

The plasma scale length L is of interest because it appears in the resonance absorption function $\phi(\tau)$ and, more broadly, because it affects the amount of inverse bremsstrahlung and the thresholds of parametric instabilities. An early measurement of the time-dependent scale length was provided by Jackel *et al.*[129] using the four-beam DELTA laser. By streaking the $2\omega_0$ and $3\omega_0/2$ emissions from ~40-μm-radius glass microballoon targets [Fig. 4-8(a)], where ω_0 is the incident laser frequency, they were able to plot the critical and quarter-critical surfaces as functions of time [Fig. 4-8(b)] and measure separation distances up to ~40 μm. [Second-harmonic emission, observed by Decroisette *et al.*[130] in 1971, is understood to result from nonlinear processes at the critical surface, and the $3\omega_0/2$ emission, a signature of the two-plasmon–decay instability (Sec. X A), comes from quarter critical.] Time-integrated images of the $2\omega_0$ and $3\omega_0/2$ emissions were first reported by Saleres *et al.*[131] for solid D_2 targets.

An interferometric measurement of the density profile was obtained by Attwood *et al.*[132] for the one-sided irradiation of 40-μm-diam glass microballoons with 30-ps pulses at $\sim 3 \times 10^{14}$ W/cm^2. A typical interferogram, obtained using a 15-ps, 0.266-μm, frequency-quadrupled probe, is shown in Fig. 4-9(a), with the laser incident from the right. Using Abel inversion in different planes perpendicular to the laser axis, they produced the reconstructed density profile of Fig. 4-9(b).

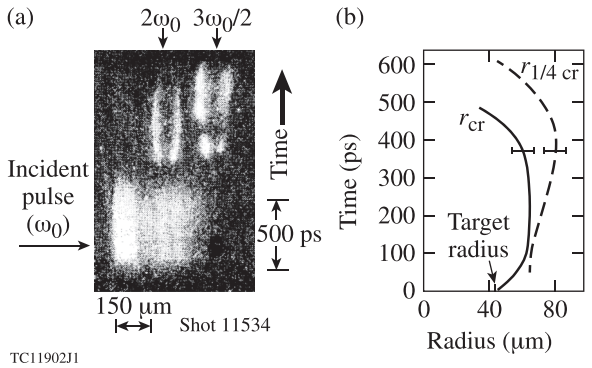

FIG. 4-8. (a) Streaked emission at $2\omega_0$ and $3\omega_0/2$ from a 42-μm-radius glass microballoon target irradiated by the four-beam DELTA laser, understood to originate from the critical and quarter-critical surfaces, respectively. (b) Trajectories of these surfaces obtained from the streaks in (a). Reprinted with permission from Jackel *et al.*, Phys. Rev. Lett. **37**, 95 (1976). Copyright 1976 American Physical Society.

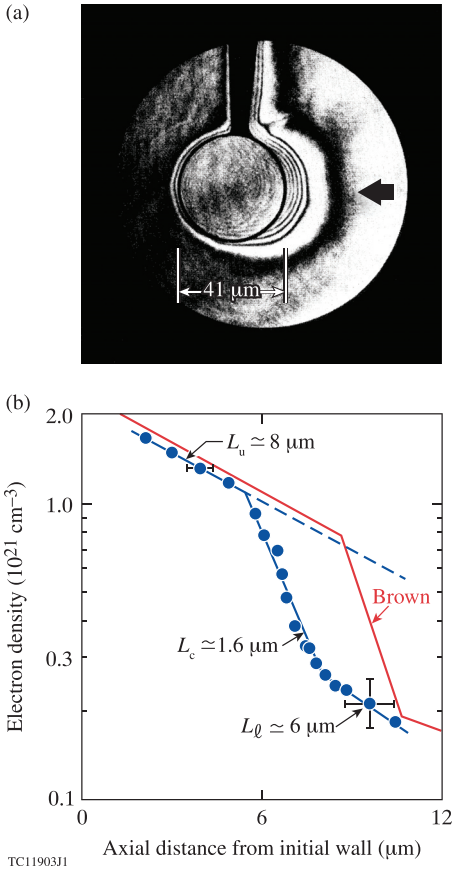

FIG. 4-9. (a) Interferogram at peak irradiation of a 41-μm-diam, 0.6-μm-thick, spherical glass microshell irradiated from the right by a laser beam at $\sim 3 \times 10^{14}$ W/cm^2, obtained with a 15-ps, 0.266-μm probe. (b) Reconstructed density profile on axis, fit by separate slopes in three regions with e-folding lengths L_u (upper), L_c (critical), and L_ℓ (lower), respectively. The red curve (from Ref. 134) is an alternative reconstructed profile that takes into account refraction of the probe beam. Reprinted with permission from Attwood *et al.*, Phys. Rev. Lett. **40**, 184 (1978). Copyright 1978 American Physical Society.

This showed the predicted steepened profile between critical and 0.3× critical, together with upper and lower density "shelves." Attwood *et al.* interpreted the steepened profile as confirmation of radiation-pressure effects, although Estabrook *et al.*[116] maintained that heating had a stronger effect on the profile. Also using interferometry, Fedosejevs *et al.*[133] observed steepening in CO_2 plasmas and claimed direct evidence of radiation pressure, but they recognized that momentum deposition from particles accelerated away from the critical region to lower densities could be a factor.

Attwood *et al.*[132] chose small targets to minimize refractive effects; however, the Abel inversion procedure neglects refractive effects. This was later investigated by Brown,[134] who analyzed the interferogram of Fig. 4-9(a) including refraction. He propagated rays through the reconstructed profile of Attwood *et al.* and found that no ray that was collected in the optical system reached a density higher than 7×10^{20} cm^{-3} and that the reconstructed profile could not have produced the interferogram. Brown then found another three-slope profile, shown in red in Fig. 4-9(b), which was consistent with the interferogram. The upper shelf started at a lower density, and the maximum density reached by the probe was 1.0×10^{21} cm^{-3}. Interestingly, he was unable to find any two-slope profile that matched the data. The more-accurate reconstruction confirmed the main observation of profile steepening but also made it clear that the role of refraction can be significant for the optical diagnosis of plasmas. Refraction would also have affected the observations of Jackel *et al.*[129]

In the context of the rippled-critical-surface scenario proposed for the resonance absorption data of Fig. 4-7, one might wonder whether the clear, smooth fringes of Fig. 4-9(a) are consistent with anything but a minimum of rippling. In addition, the experiments of Fig. 4-7 were both for very short laser pulses that are unrepresentative of most laser–plasma interaction experiments. While the consensus based on the x-ray spectra is that resonance absorption was dominant for both long- and short-pulse irradiation at high intensities with infrared lasers, the direct evidence for resonance absorption is minimal. One would need to create a 3-D model of a rippled critical surface and then pass a probe beam through, including refraction, to see the effect on the interferogram.

Although far removed from ignition conditions, implosions driven by infrared lasers stimulated the development of new diagnostics, some of which were reviewed by Attwood.[135] One such diagnostic was described by Attwood *et al.*,[136] who coupled an x-ray pinhole camera to an x-ray streak camera to diagnose an implosion. They obtained spatial and temporal resolutions of 6 μm and 15 ps, respectively. Sample output is shown in Fig. 4-10. It became possible to follow the implosion continuously, through the compression and disassembly phases, based on the self-emission of the target. Streaked x-ray imaging of imploding targets was also reported by Billon *et al.*[137]

Another advance, with far-reaching significance, was the development of x-ray backlighting at the Rutherford Laboratory using the Vulcan laser. This was reported by Key *et al.*,[138] who used the configuration shown in Fig. 4-11(a). A microballoon was imploded using two beams and radiographed by x rays produced from a brass (Cu + Zn) target, irradiated with a delayed laser pulse. The key feature of x-ray backlighting is that it makes it possible to diagnose cold dense plasmas such as imploding shells. A series of images obtained from a number of implosions with different

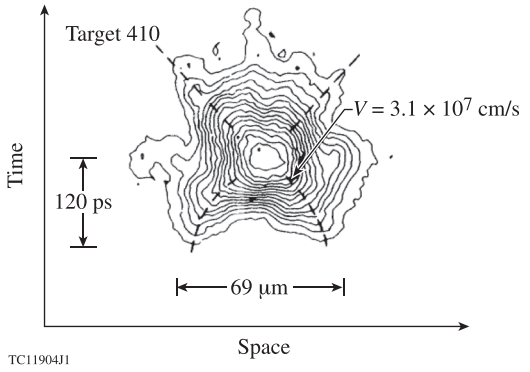

FIG. 4-10. First report of streaked x-ray emission from the two-sided implosion of a (69-μm-diam) microballoon with sufficient spatial and temporal resolutions to follow the implosion process continuously. Reprinted with permission from Attwood *et al.*, Phys. Rev. Lett. **38**, 282 (1977). Copyright 1977 American Physical Society.

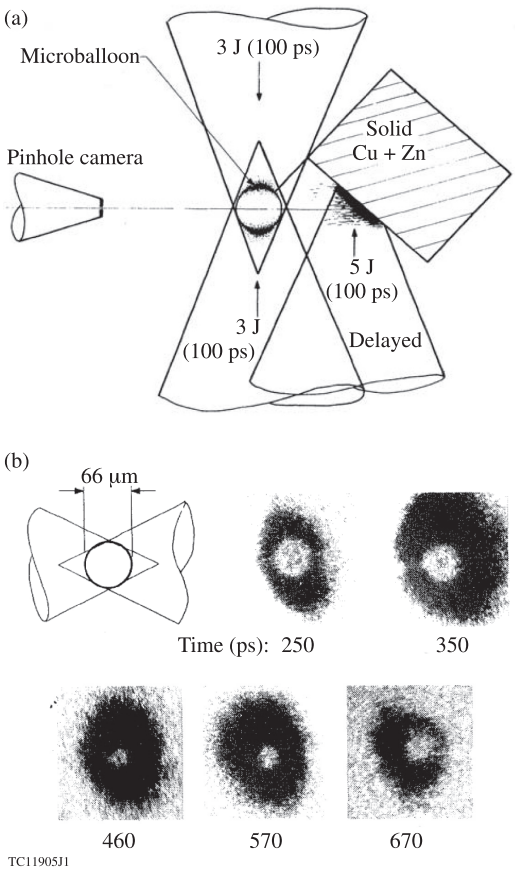

FIG. 4-11. (a) Experimental configuration used to demonstrate pulsed x-ray backlighting. A 66-μm-diam glass microballoon was imploded by two laser beams and radiographed by x rays from a solid brass target irradiated by a third beam with a variable timing delay. (b) A sequence of radiographic images for various delays of the backlighting beam. Reprinted with permission from Key *et al.*, Phys. Rev. Lett. **41**, 1467 (1978). Copyright 1978 American Physical Society.

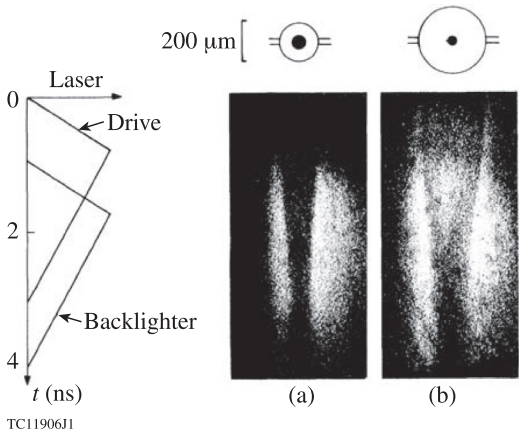

FIG. 4-12. Demonstration of streaked x-ray backlighting of the implosion of two targets driven by six laser beams: (a) 93-μm-radius, 1.1-μm-thick glass shell coated with 6.6 μm CH, aspect ratio 12; (b) 142-μm-radius, 1.3-μm-thick glass shell, aspect ratio 110. The sketches above the streaks show to scale the initial target diameter and the calculated minimum diameter of the core of opacity $\tau \geq 1$. Reprinted with permission from Key *et al.*, Phys. Rev. Lett. **45**, 1801 (1980). Copyright 1980 American Physical Society.

backlighter timings are shown in Fig. 4-11(b), following the implosion through compression. This was accomplished with just 5 J of backlighter energy. Today, tens of kilojoules of backlighter energy are available on the NIF.

Key *et al.*[139] reported the first demonstration of time-resolved x-ray backlighting, in which a slit across the image of an x-ray microscope was coupled to a streak camera with 80-ps temporal resolution. Results for two imploding microballoons of different aspect ratio (radius divided by thickness) are shown in Fig. 4-12. The shell (a) with a small aspect ratio of 12 imploded to a radius that was close to the predicted minimum diameter, while the shell (b), with an aspect ratio of 110, appeared to have broken up, presumably because of the Rayleigh–Taylor instability.

Many diagnostics were developed at LLNL in the 1970s beyond those described in Ref. 135. An extensive review of these diagnostics and the experiments that used them is given by Ahlstrom.[140]

E. The move to short wavelengths

Perhaps the most-significant advance in this period of time was the unequivocal demonstration at École Polytechnique by Fabre *et al.*[23] of improved absorption with short-wavelength lasers. With just 2.8 J of energy at the fourth harmonic of a Nd:glass laser, they obtained ~90% absorption in the range of 10^{14}–10^{15} W/cm^2. After years of experiments in which the absorption was dominated by mechanisms such as resonance absorption and parametric instabilities that were, at best, partially understood, it was refreshing to enter a regime, anticipated by Dawson,[62] in which the absorption was dominated by inverse bremsstrahlung. The benefits of short-wavelength lasers were also important for indirect drive.[2,3] The experiments of Fabre *et al.* along with others at different laboratories under a variety of target conditions are described in Sec. V.

The results of Fabre *et al.*,[23] reported at a conference in 1979, stimulated a change in focus at LLE from the second harmonic of the Nd:glass laser to the third harmonic. A few months later, Seka *et al.*[141] demonstrated third-harmonic generation with an efficiency of 80% using a tripling technique proposed by Craxton[142] that was subsequently implemented on the 24-beam OMEGA laser at LLE, the Nova laser at LLNL, the 60-beam OMEGA laser, and other laser systems. The 192-beam NIF used a different technique, also proposed in Ref. 142. The impact of a single 2.8-J UV beam was enormous. Conversion of large Nd:glass lasers to the fourth harmonic was not pursued because of the lack of suitable crystals to perform the frequency conversion at high fluence and low fourth-harmonic damage thresholds.

The problems encountered in the understanding of laser–plasma interactions at 1 μm did not impede progress in the production of larger numbers of neutrons as more powerful lasers were built. McCrory and Soures[35] compiled Fig. 4-13 from exploding-pusher experiments carried out at LLE, LLNL, and Osaka. It is notable that the highest yields were obtained for short laser wavelengths. The solid blue circle showing 10^{14} neutrons and a thermonuclear burn energy of ~1% of the laser energy, added subsequently to Ref. 35, is from the 60-beam OMEGA laser after its completion in 1995 (Ref. 143). Exploding-pusher implosions have received little

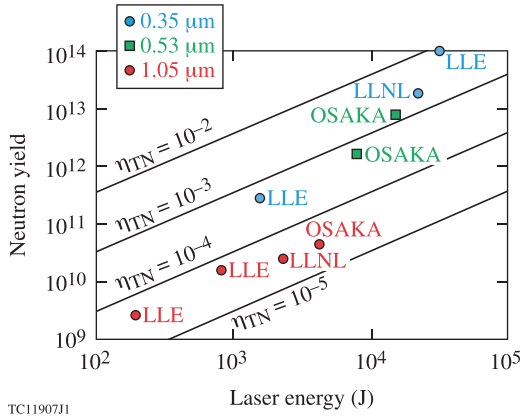

FIG. 4-13. Summary of high-neutron-yield implosion experiments from different laboratories. The straight lines delineate lines of constant thermonuclear yield efficiency, η_{TN} (thermonuclear burn energy/laser energy). Reprinted with permission from McCrory and Soures, "Inertially confined fusion," in Laser-Induced Plasmas and Applications, 1989, Marcel Dekker. The data point (10^{14} neutrons at 30 kJ from Ref. 143) is added for the 60-beam OMEGA laser.

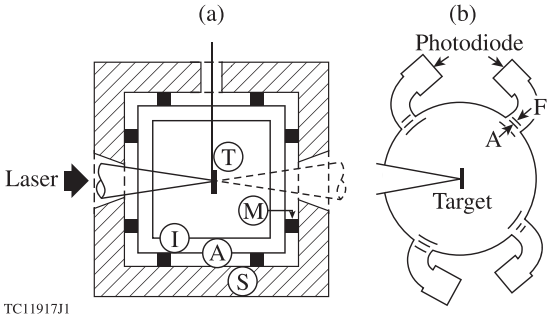

FIG. 5-1. Two experimental instruments used for making 4π measurements of the laser absorption. (a) The box calorimeter, which measures the scattered light and the combined particle and x-ray energies. I: quartz ion shield; A: volume-absorbing (color glass) calorimetric sensor; M: thermoelectric module; S: heat sink; T: target. Reprinted with permission from Seka *et al.*, Opt. Commun. **40**, 437 (1982). Copyright 1982 Elsevier. (b) The Ulbricht sphere, which is coated on the inside with scattering paint to isotropize the scattered light that is then measured by the photodiodes. A: attenuator; F: filter. Reproduced with permission from Fabre *et al.*, Plasma Phys. Controlled Nucl. Fusion Res. 1980 (IAEA, Vienna, 1981), Vol. II, pp. 263–272. Copyright 1981 International Atomic Energy Agency.

attention since, except as convenient sources of neutrons and other fusion products for various applications. After the work of Fabre *et al.*,[23] ICF experiments became focused on pursuing the ablative type of implosion envisaged by Nuckolls *et al.*[1] in 1972.

V. SHORT-WAVELENGTH ABSORPTION EXPERIMENTS

The observations by Fabre *et al.*[23] of dramatically increased absorption at short laser wavelengths (understood in this section to mean wavelengths $\leq 0.53\,\mu$m) stimulated several similar experiments at other laboratories in the early 1980s. The main conclusion of Fabre *et al.* was confirmed, and it became clear that the dominant absorption mechanism at short laser wavelengths, in the intensity regime of interest for ICF, is inverse bremsstrahlung. The observations of these experiments are reviewed in this section, together with later 0.35-μm experiments on OMEGA in spherical geometry.

Although it is basic to the understanding of laser-produced plasmas, the fraction of the incident laser energy that is absorbed in the target is very difficult to measure accurately. Basov *et al.*[16] recognized this problem and measured the absorbed energy by observing the time evolution of the expanding shock (blast) wave in the residual gas in their target chamber. Other workers relied on the light returning from the target through the focus lens (which was easy to measure), assuming that whatever light did not return into the focus lens was absorbed; however, this generally provides estimates of absorption of unknown accuracy since there is no measurement of light returning at other angles. The least-reliable estimates of the absorption are likely to be obtained for lenses of large *f* number (i.e., small solid angle), as discussed in Sec. X B with reference to Fig. 10-11.

The key to the accurate absorption measurements that were made on planar targets in the years around 1980 was the development of 4π calorimeters. Two such devices are shown in Fig. 5-1. Figure 5-1(a) shows a box calorimeter from Ref. 144, originally developed at LLNL by Gunn and Rupert[145] to measure the total unabsorbed light from experiments such as those of Fig. 4-7(b). The analysis of the calorimeter signals by Seka *et al.*[144] allowed the total plasma energy (ions plus x rays) to be measured, as well as the scattered light. Figure 5-1(b) shows an Ulbricht sphere, as used by Fabre *et al.*[23] The Ulbricht sphere was developed by Godwin *et al.*[127] at Garching and used for the measurements of Fig. 4-7(c). The inside of the sphere is coated with a scattering paint, allowing each photodiode to sample light scattered from the target into most of 4π steradians. For both devices, light returning into the focus lens is measured separately. Calibration of the Ulbricht sphere is described in Ref. 127.

The results from Ref. 23 were published by Garban-Labaune *et al.*[146] and are shown in Fig. 5-2 for a variety of laser wavelengths and for short and long pulses, all focused onto solid planar targets. Most data are for $C_{10}H_8O_4$, but the 0.26-μm-wavelength data include Al and Au. The increase in absorption as the laser wavelength decreases, in the intensity

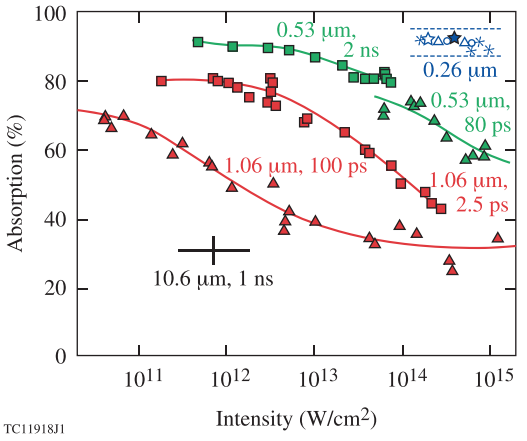

FIG. 5-2. Absorption measurements at Ecole Polytechnique at various laser wavelengths. The data at 0.26 μm include Al and Au targets and 60-ps and 170-ps pulse lengths; otherwise the targets are all $C_{10}H_8O_4$. The solid lines are fits to the data. Reprinted with permission from Garban-Labaune *et al.*, Phys. Rev. Lett. **48**, 1018 (1982). Copyright 1982 American Physical Society.

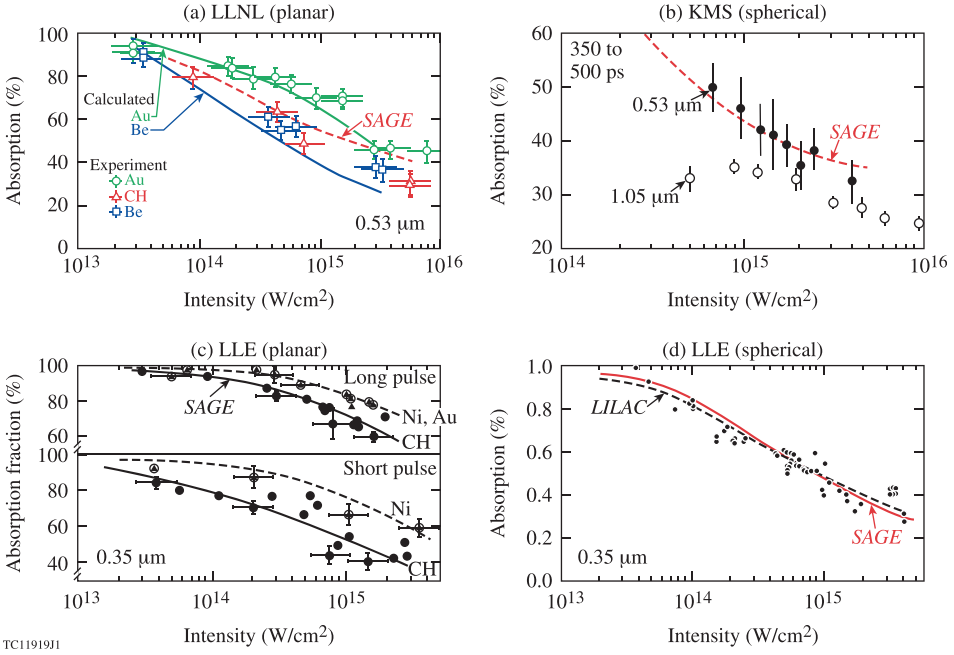

FIG. 5-3. Absorption data at submicron wavelengths from various laboratories. (a) Planar experiments at 0.53 μm on the Argus laser at LLNL. Reprinted with permission from Mead *et al.*, Phys. Rev. Lett. **47**, 1289 (1981). Copyright 1981 American Physical Society. (b) Spherical experiments at 0.53 μm at KMS with some data at 1.05 μm included for comparison. Reprinted with permission from Slater *et al.*, Phys. Rev. Lett. **46**, 1199 (1981). Copyright 1981 American Physical Society. (c) Planar experiments at 0.35 μm at LLE on the GDL laser. Reprinted with permission from Seka *et al.*, Opt. Commun. **40**, 437 (1982). Copyright 1982 Elsevier. (d) Spherical experiments at 0.35 μm at LLE using six beams of the OMEGA laser. Reprinted with permission from Richardson *et al.*, Phys. Rev. Lett. **54**, 1656 (1985). Copyright 1985 American Physical Society. The curves labeled "*SAGE*" in (a) and (b) are taken from Ref. 151.

range ($\lesssim 10^{15}$ W/cm^2) of interest to direct-drive ICF, is dramatic. Theoretical modeling of the data was reported by Garban-Labaune *et al.*[147]

Results from four other absorption experiments, carried out at three different laboratories in planar and spherical geometries and at 0.53 μm and 0.35 μm, are shown in Fig. 5-3. The results include 0.53-μm data obtained by Mead *et al.*[148] at LLNL and Slater *et al.*[149] at KMS Fusion, and 0.35-μm data obtained at LLE by Seka *et al.*[144] and Richardson *et al.*[150] Most datasets cover a large range of incident intensity, typically two to three orders of magnitude, by a combination of varying the laser energy and the focal-spot size.

The data in Fig. 5-3(a) were obtained from the irradiation of flat targets with one beam of the Argus laser in 600-ps pulses,[148] using a box calorimeter to measure the scattered light. Slightly higher absorption was found for Au compared with lower-Z targets (CH, Be), and in both cases the results were in agreement with hydrodynamics simulations using the code *LASNEX*. The low-Z results were also consistent with simulations using the hydrodynamics code *SAGE* carried out by Craxton and McCrory.[151] Mead *et al.*[148] found low levels of hot electrons—less than ~1% of the incident energy was converted into hot electrons for all target Z's at $\sim 2 \times 10^{15}$ W/cm^2.

The KMS experiments [Fig. 5-3(b)] were carried out in spherical geometry, using the ellipsoidal-mirror target irradiation system[91] shown in Fig. 4-3(a). The absorbed energy was determined with a differential plasma calorimeter at one location on the target chamber, so its accuracy depended on the assumption that the plasma blowoff was isotropic. Given the near-4π irradiation solid angle, this assumption is probably reasonable, although it would be hard to quantify. In addition to the 0.53-μm-wavelength data, which match the *SAGE* predictions, Fig. 5-3(b) shows data for 1 μm with the weaker dependence on intensity that was typically seen for experiments with a large (presumed) resonance absorption component.

The first measurements of absorption at 0.35 μm at LLE were reported by Seka *et al.*[144] and are shown in Fig. 5-3(c) together with *SAGE* simulations. They were carried out on the one-beam Glass Development Laser (GDL) System with UV energies up to 22 J at 90 ps and 60 J at 450 ps, using the box calorimeter of Fig. 5-1(a). The intensity was varied over two orders of magnitude by changing the spot diameter (100–800 μm) and the laser pulse energy. The absorption was generally found to be independent of spot size: no dependence on spot size was observed below 5×10^{14} W/cm^2, and small (~5%) differences between 1-D planar simulations and 2-D cylindrically symmetric simulations were noted at high intensities caused by spherical divergence effects from small focal spots. The simulations all used a flux limiter (Sec. XI) of $f = 0.03$ to model electron heat transport and, in addition to inverse bremsstrahlung, deposited an *ad hoc* fraction of 15% (representing additional absorption mechanisms such as resonance absorption) of whatever light reached critical. All the *SAGE* simulations shown in Fig. 5-3 used these same parameters, demonstrating consistency across the different experimental configurations. Almost identical predictions were obtained for the four data sets of Fig. 5-3(c) using $f = 0.04$ and no *ad hoc* deposition at critical.[144]

The data of Fig. 5-3(d), reported by Richardson *et al.*,[150] are from the original (24-beam) OMEGA Laser System after the conversion of six beams to the third harmonic. Solid-CH spherical targets of diameters between 50 and 400 μm were irradiated with 600- to 700-ps pulses in the intensity range 10^{13}–10^{15} W/cm^2. For optimal uniformity, the best focus of the beams was placed beyond the target center so that the edge rays of the beam were tangentially incident on the edge of the target. The absorption was measured by a set of 20 differential plasma calorimeters situated symmetrically about the target. With this large number of detectors, the overall absorption measurement should have been minimally affected by irradiation nonuniformities. The large dynamic range in intensity was possible because phase plates

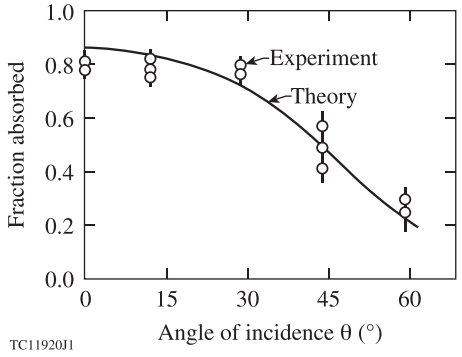

FIG. 5-4. Absorption measured on the Argus laser at LLNL at 0.53 μm as a function of angle of incidence, for Au disk targets at 3×10^{14} W/cm^2. Reproduced with permission from Phys. Fluids **26**, 2316 (1983). Copyright 1983 AIP Publishing LLC.

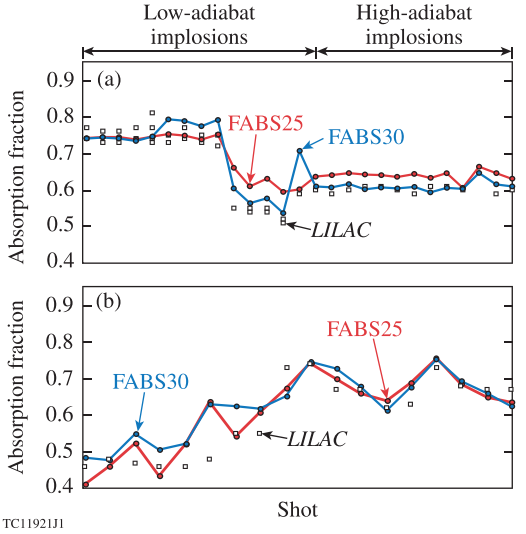

FIG. 5-5. Time-integrated absorption measurements obtained on OMEGA for a large number of shots with a variety of laser pulse shapes from (a) room-temperature implosion experiments from September 2005 to September 2006 and (b) cryogenic target implosions from March to September 2006. In both cases the measurements (from two backscatter stations, FABS25 and FABS30) and the *LILAC* simulations track each other closely. The peak laser intensities ranged from 3×10^{14} to 1.1×10^{15} W/cm^2 (from Ref. 154).

(Sec. VI A) were not implemented on the laser beams at the time. There were significant hot spots in the laser beams [see Fig. 6-11(a) below], but their effect on the overall absorption was probably minimal since a combination of thermal transport at densities below critical and refraction through the plasma of the obliquely incident laser rays could be expected to ensure a fairly uniform electron-temperature distribution in the corona. The data were consistent with the predictions of the hydrodynamics codes *LILAC* and *SAGE*, which used the same flux limiter of 0.03 and a 15% deposition factor at critical.

Overall, the results shown in Figs. 5-2 and 5-3 from different laboratories, under different experimental conditions and across a wide range of incident laser intensities, demonstrated conclusively that inverse bremsstrahlung is the dominant absorption mechanism in short-wavelength experiments.

Further confirmation of the inverse-bremsstrahlung process was provided by Mead *et al.*,[152] who measured the absorption of Au disk targets as a function of the angle of incidence (θ) using the Argus laser at 0.53 μm. Figure 5-4 shows results for an incident intensity of 3×10^{14} W/cm^2. The dependence of the absorption A on θ matches closely the prediction $A(\theta)=1-\exp(-\alpha_0\cos^3\theta)$ for inverse bremsstrahlung in an isothermal plasma with an exponential density gradient, where α_0 gives the absorption at normal incidence. (In contrast, Drake *et al.*[153] found no resolvable dependence of absorption on θ for all angles up to 50° for Au targets irradiated at 0.35 μm on one beam of the Nova laser; the reasons for this were not understood.)

Absorption on the 60-beam OMEGA laser has been routinely measured using scattered-light calorimeters placed at different angles around the target chamber. Two of these calorimeters are located in full-aperture backscatter stations (FABS), known as FABS25 and FABS30, which sample the light returning along the paths of Beamlines 25 and 30, respectively. The measurements in these calorimeters are adjusted to account for a small amount of "blow-by" light from the opposite beams, which is not intercepted by the target or the plasma. The accuracy of these measurements depends on the extent to which the scattered light is isotropic. While this can depend on the irradiation conditions, isotropy is generally a reasonable assumption. Examples of the absorption measured by these two backscatter stations[154] are shown for room-temperature implosions in Fig. 5-5(a) and for cryogenic implosions in Fig. 5-5(b). Each dataset spans a period of several months and includes data from a variety of laser pulse shapes with the peak laser intensity varying from 3×10^{14} to 1.1×10^{15} W/cm^2. The absorption fractions measured using the two different stations track each other closely as well as predictions of the code *LILAC*. While the pulse shape and target characteristics influence the absorption, the laser intensity was found to be the dominant factor with the higher absorption fractions being associated with the lower intensities.[154]

Streaked spectrometers on OMEGA have provided further insight into the absorption process. A typical streaked spectrum, obtained by Seka *et al.*,[155] is shown in Fig. 5-6(a) for an imploding cryogenic target irradiated by a single-picket pulse, observed in a port between beams that is not subject to blow-by effects. In this case, 1-THz, 2-D smoothing by spectral dispersion (SSD) (Sec. VI C) and polarization smoothing (Sec. VI D) were used with a ~0.4-nm UV bandwidth. The initial blue shift comes from the reduction in optical path for rays passing through the expanding plasma,[156] and the later red shift is associated with opposite changes to the optical path as the target implodes. (The refractive index $\mu=\sqrt{1-n_e/n_c}$, where n_e is the electron density and n_c is the critical density; the optical path $\int\mu ds$, where s is the distance along a ray path, therefore decreases when n_e increases along the path.) By integrating over the spectrum, the scattered-light power is obtained as a function of time [Fig. 5-6(b)]. This is shown together with the incident laser pulse and compared with the *LILAC* simulations using a flux-limited model with $f=0.06$ and a nonlocal heat-transport model.[157] The differences between the observations and the

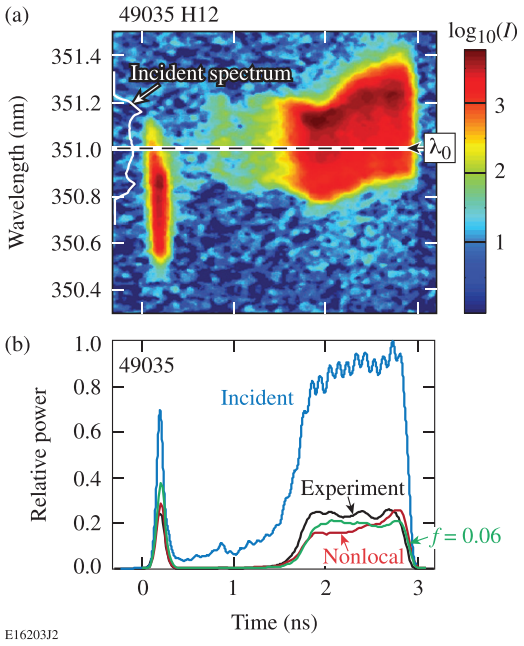

FIG. 5-6. (a) Streaked scattered-light spectrum, with λ_0 indicating the incident laser center wavelength, and (b) incident and scattered-light powers for a cryogenic target imploded on OMEGA with 17.7 kJ of laser energy including full beam smoothing [1-THz smoothing by spectral dispersion (SSD) and polarization smoothing]. The experimental scattered-light power in (b) is derived from (a). The green and red curves in (b) are from *LILAC* simulations with flux-limited transport ($f = 0.06$) and nonlocal heat transport, respectively. The power is given on a relative scale, with the peak incident power corresponding to a maximum incident intensity of 6×10^{14} W/cm^2 averaged over the initial target surface. Reproduced with permission from Phys. Plasmas **15**, 056312 (2008). Copyright 2008 AIP Publishing LLC.

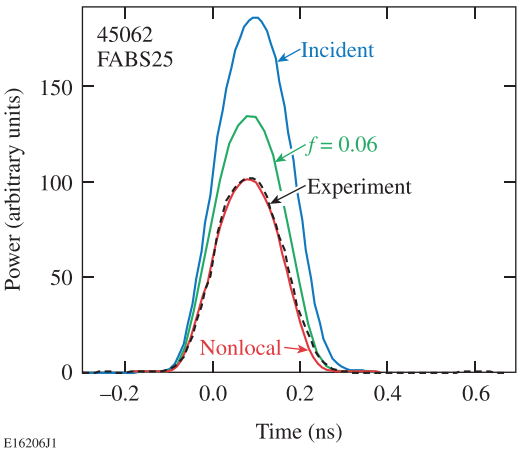

FIG. 5-7. Power histories of the incident and scattered light for a spherical target irradiated on OMEGA with a 200-ps laser pulse. Reproduced with permission from Phys. Plasmas **15**, 056312 (2008). Copyright 2008 AIP Publishing LLC.

predictions are typical for these experiments, but the details depend on target and irradiation parameters.

Seka *et al.*[155] made similar measurements for experiments using 200-ps pulses to investigate the physics associated with absorption in the picket portion (see Fig. 3-1) of implosion pulse shapes. Here, the nonlocal model provided a much better match to the experimental data (Fig. 5-7). Some work that advocates using a higher flux limiter at early times (which would decrease the predicted scattered light of the flux-limited curve in Fig. 5-7) is described in Sec. XI with reference to Fig. 11-8.

In more recent work, Igumenshchev *et al.*[158] have reported experiments in which the scattered light differs significantly from that predicted by the flux-limited model in *LILAC*, and cross-beam energy transfer has been identified as accounting for additional scattered light. This work is described in Sec. X B (see Fig. 10-18).

The dominance of inverse bremsstrahlung as the primary absorption mechanism is encouraging for ignition-scale designs since the absorption increases with scale length. For example, the predicted absorption for the design of Sec. III A is 95%. However, it is important to recognize that laser–plasma interaction processes in the associated longer-scale-length plasmas can be competing mechanisms, with the potential to reduce the absorption. It is therefore critical that absorption experiments continue to be made as larger plasmas are encountered.

VI. LASER BEAM UNIFORMITY

High-convergence, direct-drive implosions require extremely uniform irradiation to minimize the seeds for hydrodynamic instabilities. It is generally considered that the overall level of nonuniformity should be $\lesssim$1% rms (root mean square), but the details of the modal structure are crucial to determine the effect of nonuniformity on target performance. Shorter-wavelength nonuniformities that are imprinted on the target can grow rapidly during the acceleration phase of the implosion by the Rayleigh–Taylor instability and cause the target shell to break up. Longer wavelengths will grow more slowly, but they can feed through to the inner surface of the shell and continue to grow during the deceleration phase, disrupting formation of the hot spot. In addition, long-wavelength nonuniformities limit the attainable convergence. The level and spectrum of irradiation nonuniformity depend on a number of factors including the number of beams, beam placement around the target chamber, the lens f number, the beam intensity profile, the beam smoothing applied, and coronal plasma conditions that affect laser absorption.[159] Beam uniformity is also beneficial in reducing the amount of undesirable laser–plasma interactions.

Some processes involved in the calculation of irradiation uniformity (and the resultant uniformity of target drive) are illustrated in Fig. 6-1, taken from Ref. 159, which shows two of many overlapping beams at tangential focus, each beam irradiating half the target surface. Not shown in the figure, but included in the calculations, is the refraction of laser rays as they pass through the hot plasma atmosphere surrounding the target. After laser energy is deposited (which generally occurs close to the critical density), some of the nonuniformities are smoothed by thermal conduction as heat is transported inward to the ablation surface, where the implosion is driven. Shorter-wavelength nonuniformities are more easily smoothed. Therefore, in examining nonuniformity in laser deposition, considerable emphasis is placed on calculating the spatial wavelength of the nonuniformities in addition to their magnitude.

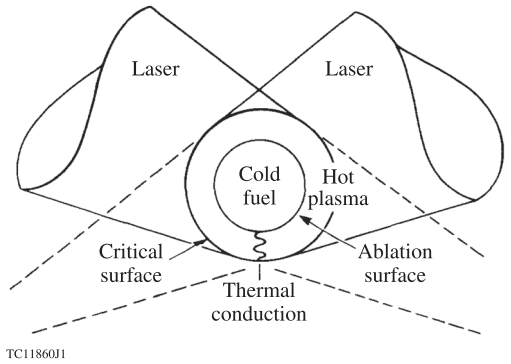

FIG. 6-1. Schematic of the corona of a laser-irradiated target, indicating elements that affect drive uniformity including beam overlap, transport of light through the plasma atmosphere, and thermal conduction to the ablation surface. Reproduced with permission from J. Appl. Phys. **54**, 3662 (1983). Copyright 1983 AIP Publishing LLC.

To estimate the magnitude and wavelength of nonuniformities from multiple overlapping laser beams, a simple model can be used in which all beams have identical, circular intensity profiles with all beam axes pointed toward the center of the target. (More-detailed calculations investigate deviations from these ideal conditions.) The nonuniformity in energy deposition can now be decomposed into spherical harmonics, σ_ℓ, as discussed by Skupsky and Lee,[159] with the geometrical contribution of the laser configuration clearly separated out

$$\sigma_\ell = \left|\frac{E_\ell}{E_0}\right| \left[(2\ell+1)\sum_{k,k'} P_\ell(\Omega_k \bullet \Omega_{k'})\frac{W_k W_{k'}}{W_T^2}\right]^{1/2}, \qquad (6\text{-}1)$$

where the total rms standard deviation over all modes $\sigma_{\rm rms}$ is defined as

$$\sigma_{\rm rms} = \left(\sum_{\ell\neq 0}\sigma_\ell^2\right)^{1/2}. \qquad (6\text{-}2)$$

The term in square brackets in Eq. (6-1) is a geometrical factor determined by the number and orientation of the beams (Ω_k) and the beam energies (W_k). The sum is over all beams, $W_T = \Sigma W_k$, and P_ℓ is a Legendre polynomial. The remaining factor on the right-hand side $|E_\ell/E_0|$ contains all the information about energy deposition by a single beam: focus position, f number, beam profile, and target conditions. The beam-smoothing techniques described in Secs. VI B–VI D are designed to reduce the E_ℓ.

Figure 6-2 (from Ref. 160) shows an example of how direct-drive uniformity depends on the number of overlapping laser beams uniformly distributed around a sphere. Each beam is treated as a converging cone whose tip is at the focal point of the lens, with the axis of each beam passing through the center of the target. The total rms nonuniformity $\sigma_{\rm rms}$ is plotted as a function of focus ratio for several beam configurations, all subtending a total solid angle of 2% of 4π. The focus ratio is defined as $R_{\rm beam}/R_{\rm target}$, where $R_{\rm beam}$ is the radius of the beam at the target location and $R_{\rm target}$ is the initial target radius. To a good approximation, a focus ratio of 1 corresponds to tangential focus (when the edge rays of the beam are aimed at the edge of the target). The beam profile was assumed to vary quadratically with radius r as $1-(r/R_{\rm beam})^2$. Only energy deposited between critical density and 1/3 critical was kept in the model and projected onto the surface of the sphere. Individual beam nonuniformities were not included. At the onset of irradiation, the focus ratio is generally chosen to be 1. During the time of irradiation, the target could implode to about 60% of its initial radius, resulting in a focus ratio of ~1.7 at the peak of the laser pulse for a constant laser spot size. Low levels of nonuniformity ($\sigma_{\rm rms} \lesssim 1\%$) are required over the entire range of focal conditions. Some laser systems employ "zooming," wherein the laser spot size is decreased as the target implodes; in this case, the focus ratio would remain approximately constant during the implosion. For a given focus ratio, the exact level of uniformity depends on the details of single-beam laser absorption in the target corona, but the qualitative dependence on the number of beams can be expected to be as shown in Fig. 6-2.

The possibility of obtaining a high level of uniformity with a small number of beams was considered by Schmitt.[161] He showed that perfect uniform illumination is possible with many aiming geometries and as few as six beams, provided that the absorption profile of each beam is proportional to $\cos^2\theta$, where θ is the angle between an incident ray and the target normal at the aim point of the ray on the target surface. This model treats the absorption profile as a function of the angular coordinates on the sphere, neglecting the dependence on radial distance from the target surface. In reality, energy is deposited continuously along ray paths, with energy from rays near the edge of the beam (which refract through the plasma toward lower densities) being deposited at larger radii (see Fig. 8-20 below for typical ray trajectories). Schmitt and Gardner[162] included refraction and a model of the ablation pressure that took into account the radius at which energy was deposited. They investigated the 32-beam configuration based on the faces of the truncated icosahedron that was proposed by Howard[163] and used in Fig. 6-2. Howard reported beam overlap calculations for 4–20 beams.

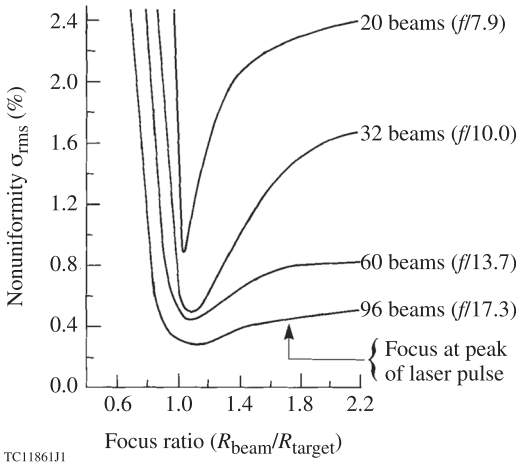

FIG. 6-2. Nonuniformity $\sigma_{\rm rms}$ as a function of focus ratio (beam radius $R_{\rm beam}$ divided by target radius $R_{\rm target}$) for various numbers of overlapping laser beams placed uniformly around the sphere. The f numbers of the beam cones are chosen such that the beam cones occupy a total solid angle fraction of 2% (From Ref. 160).

Figure 6-2 shows that good uniformity can be obtained with 32 beams, but this will occur over a limited range of laser–plasma conditions and will be very sensitive to variations among the beams such as pointing errors, energy imbalance, and spot shape variations. Moreover, Fig. 6-2 does not take into account the evolving plasma conditions. To maintain high levels of uniformity over a broad range of laser and target conditions, a 60-beam "stretched soccer-ball" configuration (based on the vertices of a truncated icosahedron)[164] was chosen for the current OMEGA laser.

The key factor that affects the level of uniformity in experiments without beam smoothing is the on-target laser-beam intensity profile that enters into the single-beam component of Eq. (6-1). Typically, an unsmoothed high-power laser beam focused onto the target will include high-modulation intensity structure resulting from phase aberrations that have accumulated through the laser chain. These aberrations are not reproducible, so they cannot be controlled by passive optical techniques. This section describes techniques that have been developed to control the laser-spot profile without relying on the detailed knowledge of the phase aberrations.

The first technique introduced to improve beam uniformity was the implementation of phase plates at the end of each beamline (Sec. VI A). Phase plates produce a well-defined intensity envelope in the target plane but contain a highly modulated speckle structure. The very short wavelength components of the speckle are smoothed by thermal conduction after laser deposition in the plasma corona. The longer wavelengths persist, however, and are large enough to seed hydrodynamic instabilities that can significantly degrade target performance. Two techniques developed to smooth the laser speckle in time are described in Secs. VI B [induced spatial incoherence (ISI)] and VI C [smoothing by spectral dispersion (SSD)]. Both techniques add bandwidth to the laser, causing the laser speckle to change rapidly in time compared with the hydrodynamic response time of the target, leading to a relatively smooth target drive. The nonuniformity can also be reduced instantaneously by an additional factor of $\sqrt{2}$ by dispersing the two components of laser polarization, as discussed in Sec. VI D.

A. Phase plates

When high-power laser beams are focused onto targets, significant distortions and amplitude modulations are found in the intensity profiles even when the near-field intensity profile is relatively smooth. Time-resolved focal measurements made by Holzrichter and Speck[165] on the Janus Nd:glass Laser System showed significant structure in the focused spot that was consistent with phase aberrations that accumulated throughout the laser chain (quantified in the so-called "*B*-integral"). For the 24-beam OMEGA Nd:glass laser, time-integrated equivalent-target-plane (ETP) images showed some structure, mostly of a long spatial wavelength, when operated in the IR, but highly modulated short-wavelength structure (hot spots) when frequency tripled to the UV[166] (Fig. 6-3). Skupsky and Kessler[166] reported high-power laser interferometry that was used to measure the

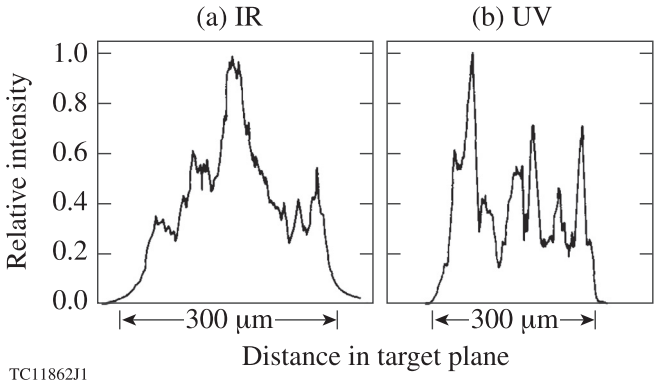

FIG. 6-3. Lineouts through the center of measured equivalent-target-plane intensity images on the 24-beam OMEGA laser for (a) a 1-μm IR beam and (b) a frequency-tripled UV beam. Reprinted with permission from S. Skupsky and T. Kessler, Opt. Commun. **70**, 123 (1989). Copyright 1989 Elsevier.

near-field phase front of one of the IR beams. The phase variations were found to explain the IR ETP intensity structure. Upon frequency tripling, the phase variation is tripled (i.e., the same optical path delay is measured in terms of wavelengths that are three times smaller). The structure in the UV ETP was found to be the result of small-scale-length phase errors. These errors were too small to significantly affect the IR beam but sufficiently large to strongly modulate the UV beam.

A technique to mitigate the effects of intrinsic phase errors, which was relatively insensitive to the details of the phase, was proposed in 1982 at Osaka by Kato and Mima[167] and described in more detail by Kato *et al.*[168] in 1984. The technique is illustrated schematically in Figs. 6-4(a) and 6-4(b). The spatial coherence of the beam is broken up by introducing a phase plate at the end of each beamline, before the focus lens. The initial implementation used a two-level phase plate of square elements with phases of 0 or π introduced at random across the beam. The element size was chosen so that the diffraction-limited focal-spot size associated with the element was equal to the target size. The beam is thereby broken into separate beamlets that overlap in the target plane, with each point in the target plane "seeing" each element of the phase plate. Phase-plate elements are typically much smaller than the spatial scale of the beam phase variations, making the irradiation pattern roughly independent of the phase variations. The intensity pattern on target [Fig. 6-4(c)] has a well-defined sinc^2 envelope (in two directions) produced by all phase-plate elements ($\mathrm{sinc}^2 x \equiv \sin^2 x/x^2$). Superimposed on this envelope is a highly modulated speckle structure resulting from interference between the beamlets. Essentially, the phase plate shifts nonuniformity energy toward shorter spatial wavelengths that can be more easily smoothed by thermal conduction after laser deposition in the target.

Following the original Osaka work, LLE and LLNL dedicated considerable effort toward the continued development of phase plates. LLE employed two-level phase plates similar to those of Fig. 6-4 except that a hexagonal pattern was used.[169] However, with two-level phase plates, close to 20% of the laser energy is diffracted outside the first zero of

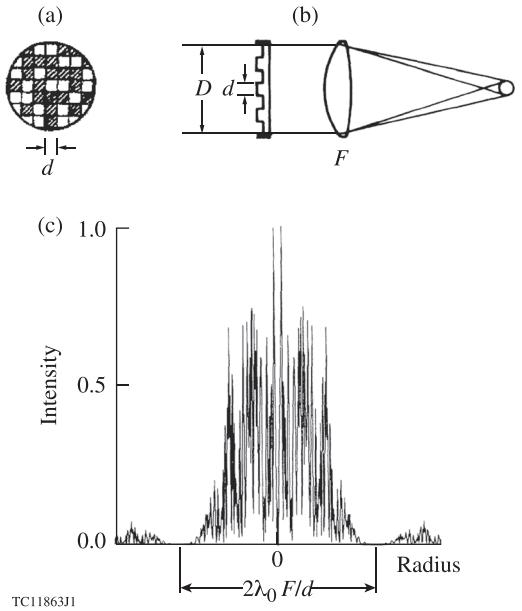

FIG. 6-4. (a) and (b) Schematic illustrating the earliest use of a phase plate to improve the uniformity on target. The phase plate, placed before a lens of focal length F, was divided into an array of elements, each of which produced a (random) phase shift of 0 or π. The size d of the element was chosen so that the diffraction-limited best-focus spot formed by the element (of diameter $\sim 2F\lambda_0/d$, where λ_0 is the laser wavelength) just overlapped the target. (c) Calculated intensity distribution in a focal plane. (a) Reprinted with permission from Y. Kato and K. Mima, Appl. Phys. B **29**, 186 (1982). Copyright 1982 Springer Science and Business Media. (b) and (c) Reprinted with permission from Kato *et al.*, Phys. Rev. Lett. **53**, 1057 (1984). Copyright 1984 American Physical Society.

the sinc^2 envelope and does not contribute to target drive. At LLE, two-level phase plates were replaced by continuous phase plates, developed by Kessler *et al.*,[170] in which the surface relief varied continuously, eliminating most of the diffraction losses and providing close to 100% of the beam energy on target. Initially, these phase plates were designed with phase distributions (translated into surface relief on fused-silica substrates) consisting of a random term combined with several spatial periodic terms. They provided the flexibility of being able to produce circular super-Gaussian beam profiles of various orders on target. They have the additional advantage of leading to minimal growth of intensity modulations during propagation through the final optical elements.

Phase-plate development work continued in parallel at LLNL. Large, 80-cm-diam phase plates were used on the Nova laser.[171] Dixit *et al.*[172] described a design procedure for "kinoform" phase plates, similar to the continuous phase plates of Ref. 170 except that they included some phase jumps (discontinuities in the surface relief) of $\sim 2\pi$ that limited the energy in the focal region to $\sim$95%. Continuous phase plates have become the norm for high-power glass lasers, with the phase plates used on the NIF manufactured by polishing the desired surface profile onto a substrate.[173]

An alternative approach to improve on the original two-level phase-plate concept was proposed by Deng *et al.*[174] in the form of a lens array. By replacing each phase-plate element with a lenslet, the diffraction problem associated with the phase-plate discontinuities was avoided. More flexibility could be provided by adding a small, random wedge angle to each lenslet. There were issues, however, relating to the manufacturability of these arrays. The current continuous phase plate includes all the benefits of a lens array but none of the disadvantages.

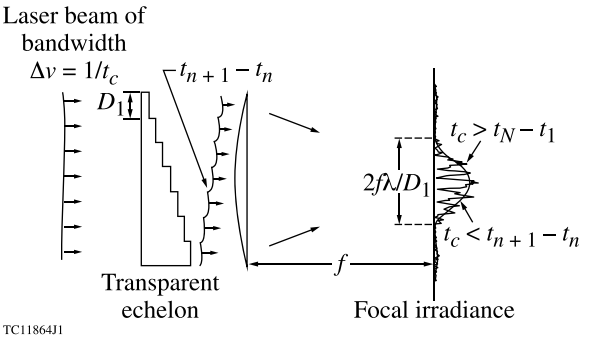

FIG. 6-5. Schematic illustrating the original concept of induced spatial incoherence (ISI), wherein spatial incoherence induced by a transparent echelon is used to smooth the focal-spot irradiance of a broadband laser in time as well as space. Reprinted with permission from R. H. Lehmberg and S. P. Obenschain, Opt. Commun. **46**, 27 (1983). Copyright 1983 Elsevier.

B. Induced spatial incoherence (ISI)

A novel technique known as ISI was developed by Lehmberg and Obenschain[175] at NRL to temporally smooth the beam intensity profile on target. In its initial form, an echelon was placed before the focus lens, as shown schematically in Fig. 6-5 for one dimension. The steps in the echelon delay different transverse sections of the beam by a laser coherence time (t_c) or larger, where t_c is related to the bandwidth ($\Delta\nu$) of the laser by $t_c = 1/\Delta\nu$. As with a phase plate, the echelon breaks up the beam into beamlets, each of which forms a well-defined intensity envelope on target. Instantaneously there is a high-modulation interference pattern (speckle) on target, but the speckle fluctuates randomly in time since the contributions to the interference pattern from different echelon steps are temporally incoherent. When averaged over many coherence times, the speckle structure becomes smoothed, with the nonuniformity decreasing in time as $\sqrt{t_c/t}$. The laser bandwidth must be sufficiently large (with a coherence time $\lesssim$2 ps, achievable on Nd:glass lasers) to smooth the beam before there is significant imprinting of nonuniformity onto the target. Obenschain *et al.*[22] quote a coherence time of $\sim$0.6 ps for the KrF Nike Laser System at NRL.

The ISI concept can be deployed in two dimensions by using either two perpendicular echelons or a structure of steps consisting, for example, of squares or closely packed hexagons. An extensive analysis of ISI was given by Lehmberg *et al.*[176] Complete ISI, in which the time delay constantly increases from step to step, could be problematic in a reactor where a large number of delays could make the pulse too long. In addition, rapidly rising pulses would be precluded. Partial ISI schemes have been investigated in which the delay repeats; in this case interference between elements with the same delay will not change in time. These elements would be chosen so that the spatial wavelength of the interference would be small and relatively easy to smooth in the plasma atmosphere.

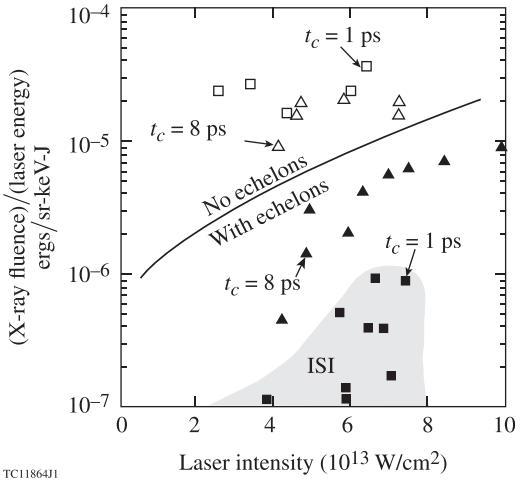

FIG. 6-6. Demonstration of the reduction of hard x rays from the first implementation of ISI. The x-ray emission near 25 keV is plotted as a function of (0.53-μm) laser intensity for narrowband (coherence time $t_c = 8$ ps) and broadband ($t_c = 1$ ps) irradiation with and without echelons. Reprinted with permission from Obenschain *et al.*, Phys. Rev. Lett. **56**, 2807 (1986). Copyright 1986 American Physical Society.

The ISI concept was demonstrated by Obenschain *et al.* in Ref. 177. Here the transmissive echelons of Fig. 6-5 were replaced by reflective echelons, and a frequency-doubled Nd:glass laser was used. In addition to providing smoother beams, ISI was found to reduce undesired laser–plasma interaction effects. Data for hard x rays, a signature of laser–plasma instabilities, are shown in Fig. 6-6. Without echelons, it was hard to differentiate between high bandwidth ($t_c = 1$ ps) and low bandwidth ($t_c = 8$ ps). However, with ISI (echelons plus high bandwidth), a dramatic reduction in the hard x-ray fluence was observed. Obenschain *et al.* also noted significant decreases in the hot-electron temperature, the laser light backscatter, and the $2\omega_0$ and $3\omega_0/2$ emissions, where ω_0 is the laser frequency. Lower levels of backscatter at both 1 μm and 0.53 μm were reported by Mostovych.[178] Peyser *et al.*[179] confirmed the reduction of $3\omega_0/2$ emission with ISI, as long as sufficient bandwidth was used. Obenschain *et al.*[177] suggested that ISI produced these benefits by preventing the seeding of the self-focusing (filamentation) instability.

Placing echelons at the end of each beamline would require a large number of optically coated steps that might not be practical for a fusion reactor. This problem was eliminated by the development of a greatly improved technique known as "echelon-free ISI." This was first suggested by Lehmberg *et al.*[176] and described more fully by Lehmberg and Goldhar[180] in 1987. The echelon-free ISI concept is shown schematically in Fig. 6-7. With this approach, the desired target-plane profile is generated early in the laser chain using broad-bandwidth light combined with a spatial beam shaper. An image of this input profile is then relayed through the laser chain and onto the target. A time-integrated target-plane beam profile from Ref. 22 is shown in Fig. 6-8 to be exceedingly smooth with variations of ~1% in the flat central portion. Another advantage of echelon-free ISI is that it allows the laser spot to be changed dynamically during the laser pulse. In particular, the spot can be zoomed to follow the inward-moving critical surface of a high-gain target design (see the discussion on Fig. 16-7 below), increasing the laser coupling to the target. The distribution of intensity in the laser spot can also be changed to dynamically minimize the nonuniformity.

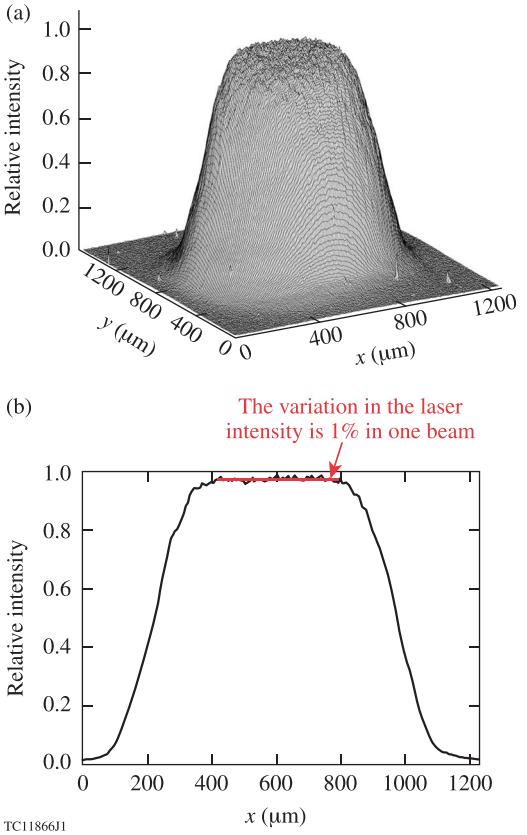

FIG. 6-8. (a) Focal distribution of a Nike KrF laser beam smoothed using echelon-free ISI, averaged over a 4-ns pulse. (b) A cross section of the beam, showing intensity variations of 1% in the flat central portion. (Reprocessed images of the beam data shown in Ref. 22.)

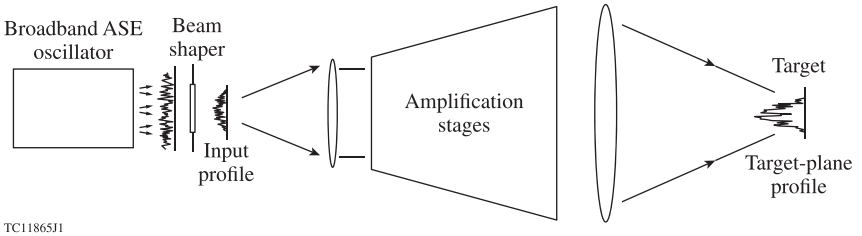

FIG. 6-7. Schematic of echelon-free ISI. A spatially shaped broadband input beam is imaged through the amplification stages of the laser to the target plane. This scheme is best suited to gas lasers such as KrF because of intensity modulations formed in the amplification stages. Reprinted with permission from R. H. Lehmberg and J. Goldhar, Fusion Technol. **11**, 532 (1987). Copyright 1987 American Nuclear Society.

This technique is appropriate for a gas laser such as KrF, but it cannot be used with a glass laser at full power because it produces amplitude modulations in the amplification stages and final optics that would damage the optical components. However, variants of ISI have been implemented on glass lasers at low power by Nakano *et al.* at Osaka,[181–183] where it is referred to as partially coherent light (PCL), and by Véron *et al.* at Limeil.[184,185]

Nakano *et al.*[181] implemented PCL in a 1-μm laser, producing 800 J per beam with 13 Å of bandwidth using an amplified spontaneous emission (ASE) source at the front end that introduced temporal bandwidth and transverse spatial modes. They observed some temporal spikes in the beam. Their output beam could be frequency doubled with a modest loss of conversion. In Ref. 182, a grating was added to the ASE beam before the beam was injected into the preamplifier and phase plates were added to the end of the system. Reference 182 presented data that indicated rapid smoothing. In Ref. 183, the bandwidth was introduced via self-phase modulation in a single-mode fiber and spatial incoherence was added in a multimode fiber. Véron *et al.*[184] obtained spatial incoherence by focusing the output of a broadband oscillator through a multimode fiber and demonstrated both a vastly improved target-plane profile and more-uniform x-ray emission from a gold target. A fuller description of this smoothing method was given in Ref. 185, where the laser output was found to be reduced to 4 TW—about half its level without smoothing.

C. Smoothing by spectral dispersion (SSD)

SSD was developed by Skupsky *et al.*[186] at LLE to provide the necessary temporal smoothing of phase-plate speckle and meet the damage constraints imposed on glass lasers such as OMEGA and the NIF. Like ISI, this approach uses broadband light and time delays to create temporally varying phase-front variations across the beam.

The basic SSD concept is shown in Fig. 6-9. Phase-modulated bandwidth imposed upon the laser beam by an electro-optic modulator is dispersed by a grating, resulting in color variations across the beam (shown as blue shifts to red shifts). The changing phase distribution across the beam combined with the use of a phase plate at the focus lens results in

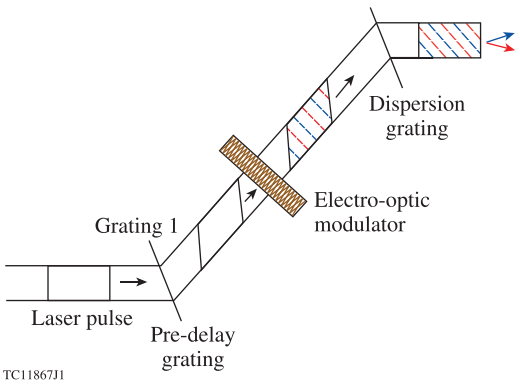

FIG. 6-9. Schematic of smoothing by spectral dispersion (SSD), showing the formation of color variations (blue to red) across the beam. Reproduced with permission from J. Appl. Phys. **66**, 3456 (1989). Copyright 1989 AIP Publishing LLC.

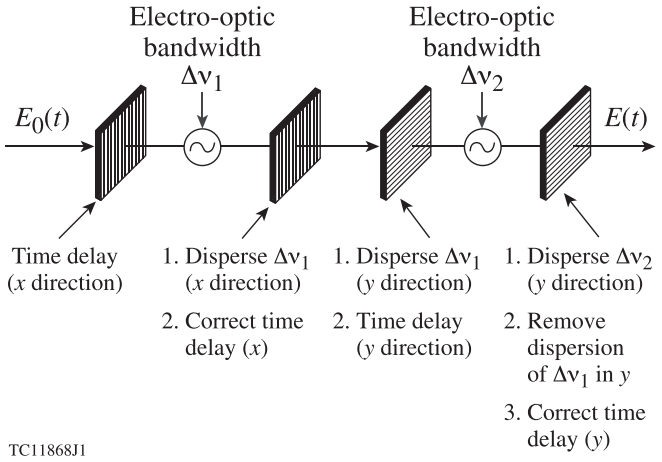

FIG. 6-10. Schematic of 2-D SSD, illustrating how the bandwidths from two modulators are dispersed in perpendicular directions. Reproduced with permission from Phys. Plasmas **6**, 2157 (1999). Copyright 1999 AIP Publishing LLC.

temporal smoothing. The pre-delay grating compensates for the delay that the dispersion grating imposes across the beam.

The phase plates are placed after the frequency-tripling crystals to minimize beam divergence through the crystals that would reduce tripling efficiency. Phase-modulated bandwidth is used, rather than the chaotic bandwidth of ISI, to minimize amplitude modulations in the laser pulse and avoid damage to optical components. The bandwidth is generated near the beginning of the laser chain using electro-optic modulators for OMEGA. For an early implementation on Nova for Rayleigh–Taylor experiments,[187] the bandwidth was generated through cross-phase modulation in an optical fiber; later,[188] an electro-optical modulator was used, as on OMEGA. The bandwidth is generated using fiber optics on the NIF.[6] This approach is convenient and allows one to use high modulation frequencies, but it precludes the pre-delay grating, limiting the ability of the laser to deliver rapidly changing pulse shapes.

The maximum bandwidth is determined by the constraints for efficient frequency tripling. For OMEGA, up to 1 THz (UV) is made possible by the use of dual tripler crystals,[189,190] providing an effective coherence time of 1 ps, similar to the ISI bandwidth used on Nike. However, longer-wavelength nonuniformities smooth faster with ISI for the same bandwidth. Long-wavelength smoothing by SSD is determined by the angular spread of the bandwidth. The maximum angular spread is limited by the laser pinholes, whose diameters are chosen to avoid self-focusing in the laser.

An extension of SSD to two dimensions was described by Skupsky and Craxton[191] and implemented on the 60-beam OMEGA laser. Two-dimensional SSD is shown schematically in Fig. 6-10. Here two modulators are used, with their bandwidths dispersed in orthogonal directions. Time-delay gratings are included for each modulator. The second and third gratings shown in Fig. 6-10 can be combined.

Equivalent-target-plane intensity distributions, integrated over time, are shown in Fig. 6-11 for a frequency-tripled beam (a) without beam smoothing, (b) with a continuous phase plate, (c) with 1-D SSD, and (d) with 2-D SSD. The phase plate by itself produces a static speckle pattern. With 1-D SSD, this is smoothed in the direction of dispersion. The smoothest beam is produced with 2-D SSD.

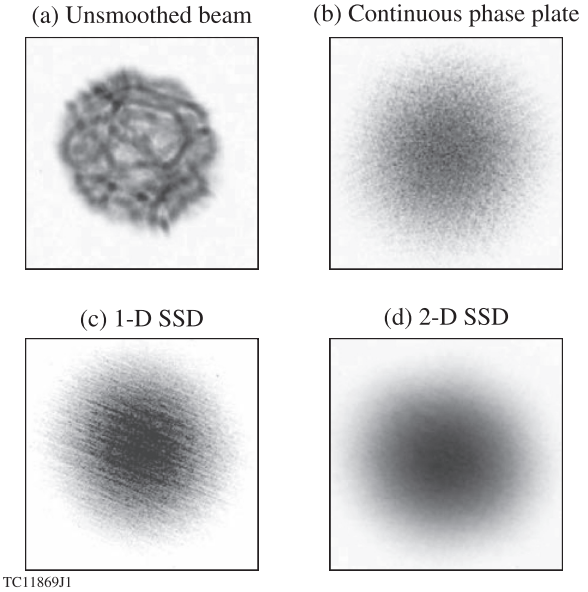

FIG. 6-11. Equivalent-target-plane images, integrated over an ~1-ns pulse width, of a single frequency-tripled OMEGA beam with four levels of smoothing: (a) unsmoothed; (b) continuous phase plate, no bandwidth; (c) bandwidth in only one modulator; and (d) bandwidth in both modulators.

The asymptotic uniformity of an SSD system can be estimated by recognizing that each spectral component of the bandwidth places the same speckle pattern on target, determined by the phase plate, but shifted in space because of the spectral dispersion. Smoothing occurs by superimposing multiple, statistically independent speckle patterns.[191] The number of such patterns depends on the maximum spatial shift (S_{max}) in the target plane imposed by the diffraction gratings and the smallest shift (S_{min}) that will produce statistical smoothing. The maximum shift is given by

$$S_{max} = F\Delta\theta, \tag{6-3}$$

where F is the focal length of the lens and $\Delta\theta$ is the angular spread of the bandwidth imposed by the diffraction gratings (referenced to the final aperture of the beam). The smallest shift that will produce smoothing (half a speckle size) is

$$S_{min} = F^{\#}\lambda_0 = \lambda_0 F/D, \tag{6-4}$$

where λ_0 is the wavelength of the light irradiating the target, D is the diameter of the near-field beam, and $F^{\#}$ is the f number of the focusing lens. The maximum number of statistically independent speckle patterns N_{stat} is then

$$N_{stat} = (S_{max}/S_{min})^2 = (D\,\Delta\theta/\lambda_0)^2, \tag{6-5}$$

where the ratio is squared because 2-D SSD allows the speckle pattern to be shifted in two perpendicular directions. As with 1-D SSD, the angular spread $\Delta\theta$ is limited by the laser pinholes. The two modulation frequencies must be incommensurate for all the modes to be independent. The speckle nonuniformity is reduced roughly by the factor $1/\sqrt{N_{stat}}$. As implemented on OMEGA with 1-THz bandwidth,[192] $N_{stat} \sim 10^4$, which reduces the speckle rms nonuniformity (taken to start at 100%) to the 1% level in the asymptotic limit. This estimate for N_{stat} is somewhat simplified because it assumes that all 2-D SSD spectral components have the same amplitude and are independent. A full simulation of this case in Ref. 192 gives $\sigma_{rms} = 3.9\%$, very close to the experimentally measured 3.8%.

Enhanced SSD smoothing can be achieved by using additional modulation frequencies. One variation on 2-D SSD, described as three-directional SSD, is given by Miyaji *et al.*[193] They use three phase modulators with incommensurate frequencies and disperse the bandwidths in directions 120° apart. Results are shown in Fig. 6-12. The images in the upper row (without phase plates) indicate the shifts in the target plane of the modes within the bandwidth. The images in the lower row show the progressive improvement as the number of modulators increases. The three-directional beam is smooth with a round focal-spot shape. This smoothing technique is used by Miyanaga *et al.*[194] on the GEKKO II–HIPER Laser System for the nine-beam, 0.35-μm main drive. This system includes three frequency-doubled beams for the foot, smoothed using PCL, and enables planar targets to be accelerated with good uniformity.

Multiple frequency modulators with independent frequencies were first proposed by Rothenberg.[195] Three such modulators are being considered for the implementation of SSD on the NIF for direct-drive experiments, but with only one direction of dispersion (to minimize modifications to existing hardware).[196,197] This achieves almost the same level of uniformity as 2-D SSD and should be adequate for direct-drive–ignition experiments. Rothenberg[195] examined multiple-frequency modulation in the limit of a large number of independent frequencies and found the result to be roughly equivalent to ISI smoothing for the same bandwidth at higher spatial frequencies. In the cross-phase-modulation implementation on Nova,[187] the resulting random phase modulations approximate SSD with multiple phase modulators.

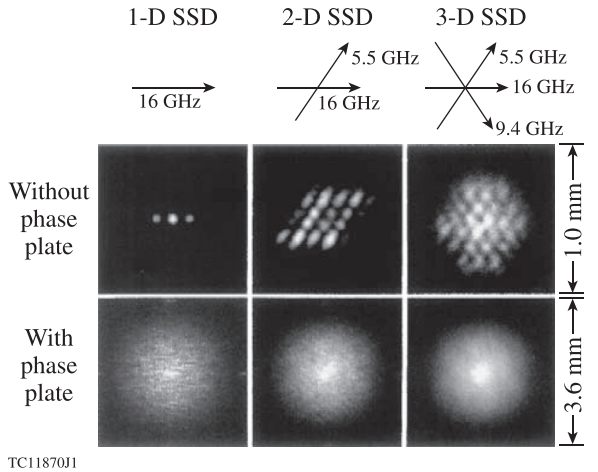

FIG. 6-12. Demonstration of three-directional SSD, wherein three phase modulators with incommensurate frequencies are given angular spectral dispersion in directions 120° apart. Reprinted with permission from Miyaji *et al.*, Opt. Lett. **27**, 725 (2002). Copyright 2002 Optical Society of America.

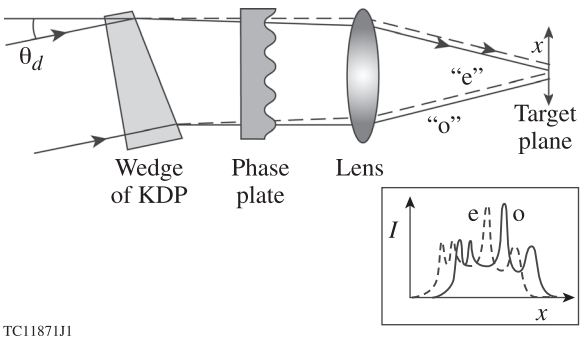

FIG. 6-13. Concept of polarization smoothing as implemented on OMEGA. A wedge of KDP is used to split the 0.35-μm beam into two orthogonally polarized beams ("o" and "e") propagating in slightly different directions. Their speckle patterns on target are shifted, providing an instantaneous $1/\sqrt{2}$ reduction in nonuniformity. Reproduced with permission from J. Appl. Phys. **85**, 3444 (1999). Copyright 1999 AIP Publishing LLC.

D. Polarization smoothing

Polarization smoothing was first proposed in 1984 by Kato,[198] who described a random-arrayed polarizer in which the near field is broken into a grid of elements, each with a polarization chosen at random, similar to the original phase-plate concept of Ref. 167. Kato found it sufficient to assign one of two orthogonal polarizations to each element. Since this has the effect of generating two independent speckle patterns (orthogonal polarizations do not interfere), the uniformity is improved (instantaneously) by a factor of $\sqrt{2}$.

The randomness of Kato's original concept is unnecessary. Regular checkerboard devices with orthogonal polarizations were proposed by Gunderman *et al.*,[199] using liquid crystals, and Tsubakimoto *et al.*,[200] using an array of half-wave plates, and produce the same uniformity improvement. However, a much simpler device was proposed in Ref. 201 employing a wedge filled with a birefringent material (a nematic liquid crystal in Ref. 201). Polarization smoothing was implemented on OMEGA using this concept. A wedge of potassium dihydrogen phosphate (KDP), a birefringent material, was placed near the end of each beamline after the frequency-tripling crystals,[191,202] as shown in Fig. 6-13. The wedge is inserted such that the beam polarization bisects the ordinary ("o") and extraordinary ("e") axes. The wedge deflects the two polarization components through slightly different angles, resulting in two spatially displaced speckle patterns in the target plane.

The most effective way to use this technique is to disperse the polarization over a distance larger than the spectral dispersion produced by SSD. In this way, the polarization shift smooths out nonuniformity modes that are not smoothed by SSD and overlap between the two techniques is avoided. This allows for the smoothing of some longer wavelengths of nonuniformity that would otherwise not be attenuated by the pinhole-limited spectral dispersion. (The longest wavelength of nonuniformity that can be smoothed is determined by the maximum separation of speckle patterns.) The predicted $\sqrt{2}$ reduction in nonuniformity was demonstrated in both ETP images and through-foil radiography of accelerated CH foils by Boehly *et al.*[202]

An analysis of ETP images on OMEGA after the implementation of 1-THz bandwidth and polarization smoothing was given by Regan *et al.*[192] A representative ETP image is shown in Fig. 6-14(a) for a 1-ns temporally flat laser pulse. Measured and modeled nonuniformity power spectra are shown in Fig. 6-14(b). The time-integrated σ_{rms} is 2.7% (measured) or 2.8% (modeled). The close agreement between the two spectra demonstrates that the optics of beam smoothing is very well understood, allowing one to confidently optimize smoothing schemes for future implementations.

VII. IMPRINT AND EARLY-TIME NONUNIFORMITY EVOLUTION

To achieve high performance, an ICF target must remain nearly spherically symmetric throughout the entire implosion. Small deviations from spherical symmetry are amplified by the Rayleigh-Taylor (RT) instability (Sec. IX), at the outer shell surface during acceleration and the inner shell surface during deceleration. The seeds for the instability are set during the early stages of implosion as nonuniformities in the target surfaces (inner and outer), within the bulk material,

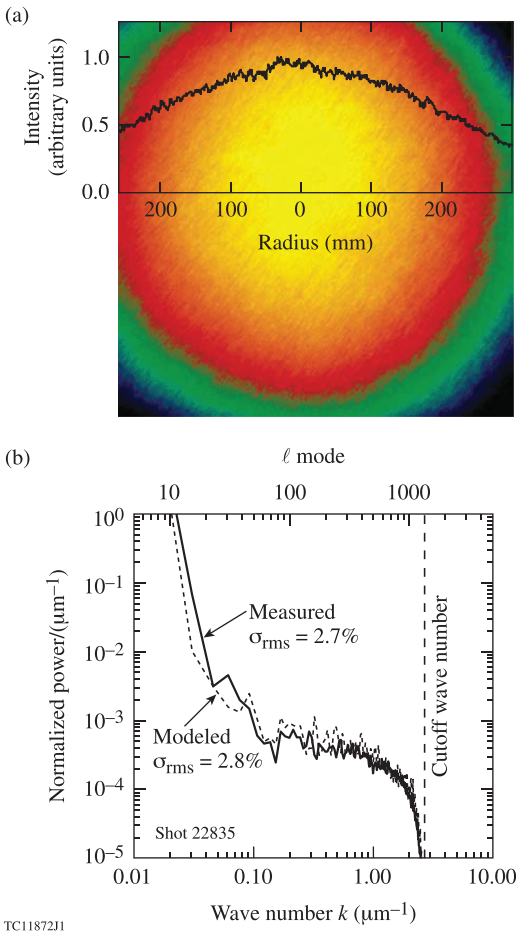

FIG. 6-14. (a) An equivalent-target-plane image of a 0.35-μm OMEGA beam smoothed with 1-THz, 2-D SSD and polarization smoothing together with a lineout through the center. (b) Measured and modeled power spectra based on (a). The wave number k is defined as $2\pi/\lambda_{SN}$, where λ_{SN} is the spatial nonuniformity wavelength, and the equivalent Legendre mode ℓ is defined as $\ell = kR$, where $R = 500\,\mu$m is the spherical target radius. Reprinted with permission from Regan *et al.*, J. Opt. Soc. Am. B **22**, 998 (2005). Copyright 2005 Optical Society of America.

or at material interfaces. Target nonuniformities can also be induced or "imprinted" by nonuniformities in the drive-laser intensity. The primary source for imprint is the laser-beam speckle pattern (Sec. VI).

Evolution of the initial outer surface roughness during the early stages of implosion is referred to as the ablative Richtmyer-Meshkov (RM) instability.[203] This has features in common with the classical RM instability,[204,205] which develops when a planar shock interacts with a corrugated interface between two materials. Rayleigh–Taylor seeding resulting from a shock interacting with a nonuniform inner ice surface is commonly referred to as "feedout."[206] Here, the perturbations at the inner ice surface feed out to the ablation front because of a rarefaction wave formed as the first shock breaks out of the shell. A comprehensive review of early-time nonuniformity evolution, including both theoretical and experimental aspects of the RM instability and the feedout process, is given by Aglitskiy *et al.* in Ref. 207.

Laser imprint is described in Sec. VII A and imprint mitigation strategies are discussed in Sec. VII B. The ablative RM instability is reviewed in Sec. VII C and feedout is described in Sec. VII D.

A. Laser imprint

The drive laser can produce both long- and short-scale-length nonuniformities in direct-drive target implosions. The RT instability produces significant growth in a range of modes with intermediate wavelengths; longer wavelengths grow more slowly and shorter wavelengths saturate (Sec. IX A). The configuration and number of beams and their overlap predominately affect the low-mode nonuniformities in the implosion. While they can lead to hot-spot and main-fuel distortion, they are not a concern for imprint. Laser imprint originates from the intensity distributions of the individual beams, which include significant speckle nonuniformities with wavelengths in the high-gain region of the RT instability. These speckle nonuniformities are reduced by beam overlap.

The physical mechanisms of imprint are reviewed in Sec. VII A 1, and several representative experimental measurements of imprint are described in Sec. VII A 2.

1. Physics of imprint

The main physical processes associated with laser-induced imprint are shown in Fig. 7-1. They have been described by Ishizaki and Nishihara[208,209] and Goncharov[210] and in Ref. 211. Laser energy absorbed in the corona is thermally conducted to the ablation front, where a shock is launched into the solid target shell. A perturbation δI in the incident laser intensity leads to a perturbation δP_a in the pressure P_a at the ablation front that, in turn, leads to a velocity perturbation (δv_x, δv_y) in the shocked solid. Transverse (y) mass modulations become imprinted in the target as the perturbed shock propagates.

Since the shock speed U_s scales as the square root of the pressure, stronger shocks launched in the regions where the ablation pressure is higher (point A in Fig. 7-1) propagate faster than the shocks launched in the lower-pressure regions (point B). This distorts the shock front and creates a perturbed

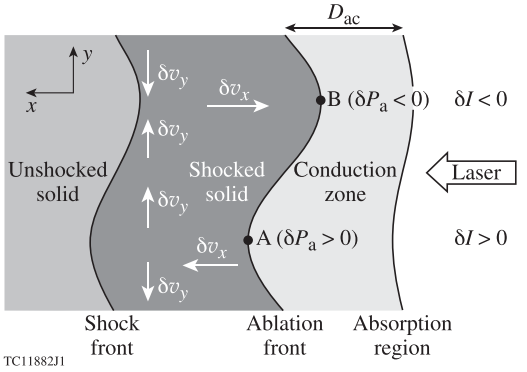

FIG. 7-1. Schematic illustration of the development of imprinted modulations in the target. Perturbations to the shock and ablation fronts result from a nonuniform laser intensity.

velocity field δv_x behind the shock. This leads to a linear-in-time growth in the ablation-front distortion η given by $\eta \sim \delta v_x t$, where $\delta v_x \sim (\delta P_a/P_a)U_s$, t is time, and the x axis points in the direction of shock propagation. This growth does not depend on the perturbation wavelength. Since the shock is rippled, it generates a mass flow component tangential to the shock front that moves mass from the regions where the shock is faster into the regions where the shock is slower (note the directions of δv_y in Fig. 7-1).

Modulations in the mass density lead to modulations in the pressure behind the shock, causing a pressure deficiency behind the faster parts of the shock and a pressure gradient from the shock front toward the ablation front. This pressure gradient accelerates fluid elements near the ablation front (point A in Fig. 7-1) toward the shock. At the parts of the shell driven by lower intensities, the picture is reversed. The hydrodynamic flow creates a pressure excess behind the shock and a pressure gradient from the ablation front toward the shock front. This accelerates the fluid elements near the ablation front (point B) toward the laser. The acceleration modulation leads to an additional growth of the ablation-front ripple $\eta \sim (1/\rho)(\partial_x \delta P_a)t^2$, where ρ is the compressed density. After the shock front has moved a distance of the order of the perturbation wavelength from the ablation front, the pressure modulation δP inside the compressed shell decays away from the ablation front as $\delta P \sim \delta P_a \exp[-k(x - x_a)]$, where k is the perturbation wave number and x_a is the position of the ablation front, leading to $\eta \sim (\delta P_a/\rho)kt^2$.

Combining the two contributing factors to the ablation-front distortion growth leads to[210]

$$\eta^{\text{hydro}} \simeq \frac{\delta P_a}{P_a}\left(0.7\, c_s t + 0.3\, k c_s^2 t^2\right), \tag{7-1}$$

where the numerical coefficients are obtained by solving the fluid equations in the strong shock limit assuming that the ratio of specific heats $\gamma = 5/3$, and c_s is the sound speed of the shock-compressed material. The superscript "hydro" indicates that only the effects of hydrodynamic flow are taken into account in deriving Eq. (7-1).

After the first shock breaks out of the shell, the back of the shell starts to expand, forming a rarefaction wave toward the ablation front. Soon after the leading edge of the

rarefaction reaches the ablation front, the ablation front starts to accelerate and the ablation-front modulations grow exponentially because of the RT instability. The imprint phase lasts from the start of the propagation of the first shock until the rarefaction wave reaches the ablation front. It takes $t = t_{\rm br} = \Delta_0/U_{\rm s}$, where Δ_0 is the initial shell thickness, for the first shock to travel through the shell and (in the strong shock limit) $t = t_{\rm rw} = \Delta_0/4\,c_s$ for the rarefaction-wave leading edge to propagate across the shell (the initial shell thickness is compressed by a factor of 4 because of the first shock). Since $U_{\rm s}/c_s \sim 1.8$ in the strong-shock limit, the imprint phase lasts for $t_{\rm imp} \simeq 0.8\,\Delta_0/c_s$. Substituting $t_{\rm imp}$ for time in Eq. (7-1) and assuming that the ablation pressure scales with the laser intensity as $P_{\rm a} \sim I^{2/3}$, the amplitude of the ablation-front ripple at the beginning of the shell acceleration is

$$\eta_{\rm imp}^{\rm hydro} \simeq \frac{\delta I}{I}\Delta_0(0.4 + 0.1\,k\Delta_0). \tag{7-2}$$

Introducing a normalized imprint amplitude defined by

$$\bar{\eta}_{\rm imp} = \frac{\eta_{\rm imp}}{\Delta_0(\delta I/I)} \tag{7-3}$$

and writing the wave number k as ℓ/R_0, where ℓ is the Legendre mode number and R_0 is the initial shell outer radius, Eq. (7-2) can be rewritten as

$$\bar{\eta}_{\rm imp}^{\rm hydro} \simeq 0.4 + 0.1\left(\frac{\ell}{A_0}\right), \tag{7-4}$$

where $A_0 = R_0/\Delta_0$ is the initial shell aspect ratio. (For a typical ignition design, A_0 varies between 4 and 5.) Equation 7-4 does not account for the effects of thermal conduction and mass ablation, which significantly reduce the imprint amplitude predicted by the equation.

Because of the high temperatures, pressure perturbations inside the conduction zone shown in Fig. 7-1 are smoothed by thermal conduction. The simplest theory, given by Bodner[39] and known as the "cloudy-day effect," predicts that pressure perturbations δP decay exponentially away from the critical surface as $\delta P \sim e^{-kx}$. Therefore, nonuniformities in the ablation pressure are reduced by a factor of $e^{-kD_{\rm ac}}$, where $D_{\rm ac}$ is the distance between the critical surface (representing the absorption region) and the ablation front (Fig. 7-1). This distance increases approximately as $D_{\rm ac} \sim V_{\rm c}t$, where $V_{\rm c}$ is the rate of growth of the width of the conduction zone, leading to an exponential decay in the ablation-pressure modulation with time, $\delta P_{\rm a} \sim \delta P_{\rm a}\ (t=0)\ \exp(-kV_{\rm c}t)$. After $t \sim (kV_{\rm c})^{-1}$, laser nonuniformities with the wave number k decouple from the ablation front. The k Fourier component of the perturbed acceleration goes to zero at this time and the ablation-front ripple subsequently grows linearly with time. The ripple velocity is estimated by calculating the time derivative of Eq. (7-1) at the decoupling time $t = (kV_{\rm c})^{-1}$, giving an asymptotic growth of the ablation-front amplitude,

$$\eta^{\rm th} \sim \frac{\delta I}{I}\frac{c_s}{V_c}c_s t. \tag{7-5}$$

The superscript "th" indicates that effects of thermal conduction smoothing in the conduction zone are taken into account. Larger values of $V_{\rm c}$ cause laser nonuniformities to decouple sooner from the ablation front, resulting in a smaller imprint amplitude. Since the sound speed $c_{\rm s}$ scales with the laser intensity as $c_{\rm s} \sim I^{1/3}$ while $V_{\rm c}$ scales as $V_{\rm c} \sim I^{4/3}$ (Ref. 212), Eq. (7-5) shows that the ablation-front modulations grow at a slower rate if the drive intensity is higher. This result is used in the imprint-mitigation schemes that introduce a high-intensity picket at the beginning of the laser drive (Sec. VII B 4). Taking into account numerical coefficients obtained from a solution of a full system of hydrodynamic equations[210] leads to the following normalized imprint amplitude at the onset of shell acceleration:

$$\bar{\eta}_{\rm imp}^{\rm th} \simeq 0.3\frac{A_0}{\ell}\left(\frac{\Delta_0}{\Delta_{\rm c}}\right)^2\left(1 - 1.4\frac{\Delta_{\rm c}}{\Delta_0}\right)(e^{-k\Delta_{\rm c}} - 1) + 0.3\frac{\Delta_0}{\Delta_{\rm c}}, \tag{7-6}$$

where $\Delta_{\rm c}$ is the size of the conduction zone at the beginning of the acceleration phase. For the all-DT design described in Sec. XVI, the shell thickness is $\Delta_0 = 325\,\mu$m and the size of the conduction zone $\Delta_{\rm c} \sim 60\,\mu$m. Compared with Eq. (7-4), which shows larger imprint amplitudes for shorter wavelengths, Eq. (7-6) indicates that thermal smoothing in the conduction zone causes laser nonuniformities for these modes to decouple from the ablation front, leading to reduced imprint amplitudes.

Mass ablation can further reduce imprint amplitudes by the dynamic overpressure or "rocket" effect[213,214] that results from modulations in the mass ablation rate and blowoff velocity across the rippled shock front. These modulations are caused by a slight increase in the temperature gradient near the parts of the ablation front that protrude toward the plasma corona (point B in Fig. 7-1) and a decrease in the valleys (point A). (Note that the ablation front is an isotherm.) An increase in the temperature gradient leads to an additional heat flow that speeds up the heat front and increases the velocity of the blown-off material $V_{\rm bl}$, so that $\delta V_{\rm bl} > 0$ at point B. Higher blowoff ("exhaust") velocity creates an excess in the dynamic pressure (i.e., a larger rocket effect). At the perturbation valleys, the picture is reversed. The modulation in the dynamic pressure therefore reduces the perturbation growth. The amplitude of the excess in dynamic pressure $\delta P_{\rm d}$ is proportional to the front distortion,[210] $\delta P_{\rm d} = \dot{m}V_{\rm bl}k\eta$, where $\dot{m}$ is the mass ablation rate. This modulation is opposite in sign to the ablation-pressure modulation caused by the nonuniformities in the laser intensity. Therefore, the ablation-front modulation continues to grow until it is balanced by the dynamic overpressure. At this point, the perturbation amplitude reaches the maximum value $\eta_{\rm sat}$ defined by $\delta P_{\rm a} \sim \dot{m}V_{\rm bl}k\eta_{\rm sat}$, giving $\eta_{\rm sat} \sim (\delta I/I)c_s^2/(kV_{\rm a}V_{\rm bl})$. After this time, the amplitude oscillates as for the ablative RM instability. Thermal conduction smoothing inside the conduction zone reduces the amplitude further to

$$\eta_{\rm sat} \sim \left(\frac{\delta I}{I}\right)\frac{c_s^2}{k\left(V_{\rm a}V_{\rm bl} + V_{\rm c}^2\right)}. \tag{7-7}$$

This saturation in the imprint amplitude was first predicted by Taylor[215] using numerical simulations and then theoretically explained by Goncharov.[203,210]

Even though the effects of thermal smoothing and mass ablation provide a significant reduction in the perturbation seeding caused by laser imprint, numerical simulations show that ignition targets require additional smoothing to prevent the shell from breaking up during acceleration. The laser-smoothing techniques described in Sec. VI are critical to target performance.

2. Imprint experiments

It is crucial for the success of direct-drive implosions to experimentally validate the predicted stabilizing mechanisms. Many measurements of imprint have been made by research groups at different laser facilities.

A typical experimental setup is shown in Fig. 7-2, similar to that used in Ref. 216. A planar-foil target is accelerated with several overlapping drive-laser beams. The growth of mass nonuniformities in the drive foil is diagnosed with through-foil x-ray backlighting, with 2-D radiographs recorded on an x-ray framing camera. The foil sometimes includes imposed mass modulations (as shown in Fig. 7-2) from which the growth rate of a single spatial mode can be determined. The use of through-foil backlighting of modulated targets was first demonstrated by Cole *et al.*[217] (see Fig. 9-4 below). Sometimes a streak camera is used instead of the framing camera to provide time resolution throughout the backlighter pulse with one dimension of spatial resolution.

An early imprint experiment carried out in the through-foil geometry was reported by Kalantar *et al.*[218] This experiment differed from subsequent imprinting experiments in that the x-ray backlighting was provided by an x-ray laser of 15.5-nm wavelength and 80-ps duration. A 3-μm-thick unmodulated Si foil was driven by one 0.35-μm beam in the Nova two-beam target chamber with a 400-ps pulse at 3×10^{12} W/cm^2. Smoothing by spectral dispersion (SSD) (Sec. VI C) was used with a bandwidth of up to 0.3 THz. The x-ray laser was timed to probe the foil at shock breakout, i.e., before RT growth occurs. Kalantar *et al.* found that most of the imprint reduction effected by SSD occurred in modes with wavelengths below 10 μm and suggested that the imprint with SSD is dominated by intensity modulations in the first 100 ps.

Glendinning *et al.*[219] described the growth of imprinted and preimposed modulations in laser-driven CH_2 foils at

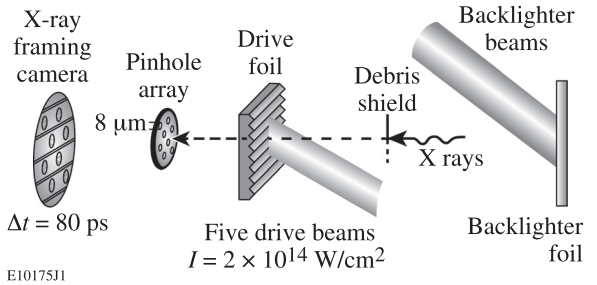

FIG. 7-2. Typical through-foil x-ray backlighting configuration used to measure imprint, similar to that used in Ref. 216.

10^{14} W/cm^2 and a laser wavelength of 0.53 μm, also in the Nova two-beam target chamber, using one beam to drive the foil and the other beam for x-ray backlighting. The drive beam was smoothed using SSD with three different bandwidths: 0.003 THz, 0.6 THz, and 0.9 THz. The pulse shape was a linear 1-ns ramp followed by a 2-ns constant drive. The target had a preimposed sinusoidal perturbation of 30-μm wavelength and 0.25-μm amplitude in one direction, and the laser was given an intensity modulation, also of 30-μm wavelength, in the other direction. The areal-density modulations were amplified by RT growth, which developed as a result of foil acceleration during the 2-ns portion of the pulse. The areal density was measured by x-ray backlighting using a gated pinhole camera with 8-μm spatial resolution and 100-ps temporal resolution, providing up to 12 frames per shot. The optical-depth modulations, separated into components associated with the target modulation and the imprinted modes, are plotted as functions of time in Fig. 7-3. Figure 7-3 shows that the growth rate of the foil modulations was the same for both target and imprinted modulations, allowing one to characterize imprint in terms of an equivalent surface finish. In many experiments the initial imprint modulations at the start of acceleration are so small that RT amplification is needed to measure them.

Pawley *et al.*[220] used up to 37 overlapping beams on the Nike laser to study laser imprint amplified by RT growth. The intensity of each beam was uniform to 1% (Fig. 6-8). When all 37 beams were overlapped, statistical averaging reduced this to 0.15% to 0.2% for spatial wavelengths greater than 7 μm. The targets were 40-μm-thick polystyrene (CH) with and without a preimposed outer surface modulation. The laser imprint was altered by the way the foot part of the drive pulse was generated. With the "multibeam foot," all 37 beams had similar pulse shapes including the foot part of the drive. This gave the best smoothing. Alternatively, the foot from the main pulse could be eliminated and the low-intensity part of the drive created by advancing one of the beams by 3.5 ns with respect to the remaining beams. This

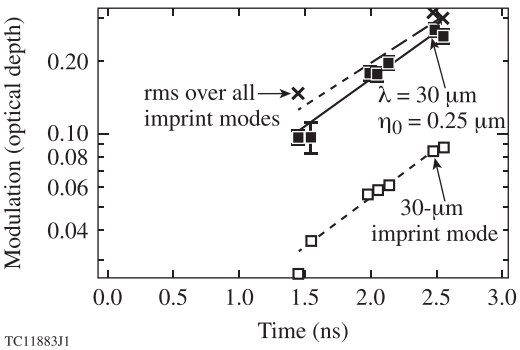

FIG. 7-3. Growth of modulations measured using through-foil radiography for 20-μm CH_2 targets accelerated on the Nova laser at 0.53 μm. The targets had preimposed modulations of wavelength $\lambda = 30$ μm and initial amplitude of $\eta_0 = 0.25$ μm in one direction; the laser had intensity modulations of the same wavelength in the orthogonal direction. Similar growth rates were observed for the target modulation (solid squares) and the imprinted modulations (the 30-μm laser-intensity mode and the rms over all modes), providing a basis for characterizing imprint in terms of an equivalent surface finish. Reprinted with permission from Glendinning *et al.*, Phys. Rev. E **54**, 4473 (1996). Copyright 1996 American Physical Society.

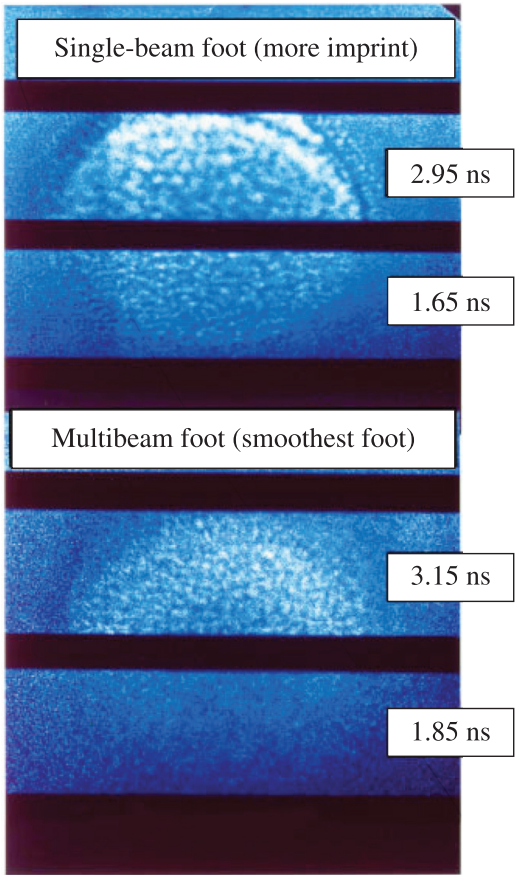

FIG. 7-4. Framing-camera images at 1.86 keV obtained on the Nike laser using a spherical crystal imager for two types of foot pulses. CH targets of 40-μm thickness were irradiated and accelerated with ~4-ns pulses at 0.248 μm. Reproduced with permission from Phys. Plasmas **4**, 1969 (1997). Copyright 1997 AIP Publishing LLC.

"single-beam" foot had larger imprint modulations than the multibeam foot by a factor of 6 ($\sqrt{37}$). Figure 7-4 shows high-resolution data obtained using a spherical crystal imager (Ref. 221; see also Fig. 7-7 below) for these two cases. The images from the multibeam foot pulse clearly show smaller perturbation amplitudes. The large magnification provided by the spherical crystal imager resulted in the images being spread across two strips of the framing camera in Fig. 7-4.

Boehly *et al.*[222] studied the effects of beam smoothing on laser imprinting using six OMEGA laser beams overlapped onto a 20-μm-thick CH foil. Figure 7-5 shows the equivalent surface roughness as a function of time for experiments without SSD [phase plates (Sec. VI A) only], with 2-D SSD (Sec. VI C) at bandwidths of 0.2 THz and 1 THz, and with 2-D SSD including polarization smoothing (Sec. VI D). The data separate into distinct sets associated with each uniformity condition and are constant in time, validating the concept of equivalent surface roughness. Figure 7-5 clearly demonstrates the improvements associated with the successive smoothing techniques.

Boehly *et al.*[222] also studied the effect of pulse shape on imprinting by using a slower rising ramp pulse. Their data showed that without SSD the ramp pulse produced ~50%

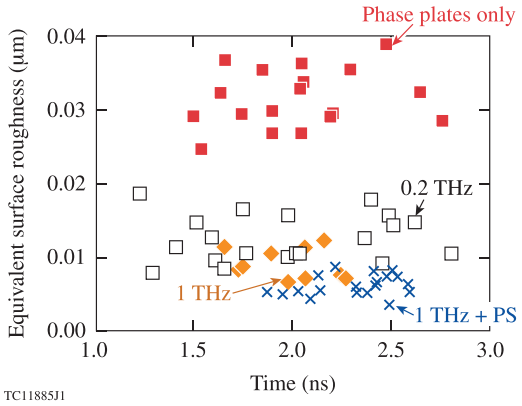

FIG. 7-5. Equivalent surface roughness at 60-μm wavelength derived from planar targets driven on OMEGA by a 3-ns square pulse and four levels of beam smoothing. PS: polarization smoothing. Reproduced with permission from Phys. Plasmas **8**, 2331 (2001). Copyright 2001 AIP Publishing LLC.

more imprinting than the square pulse. This can be explained by the longer time required by a slow-rising pulse to build up a sufficient plasma atmosphere and enable thermal smoothing.

The importance of beam smoothing in reducing imprint was confirmed by experiments carried out on the GEKKO XII laser by Nakai *et al.*[223] They imposed static and dynamic intensity modulations on the foot pulse used to provide imprinted perturbations on plastic foil targets and diagnosed the imprint using through-foil radiography. The dynamic modulations were produced by interfering two beams of slightly different wavelengths, resulting in a fringe pattern that moved rapidly across the target plane (typically at 2×10^7 cm/s). Lower imprint was found with the dynamic modulations.

B. Imprint mitigation

Beam-smoothing techniques are generally limited by the finite times required to average out the laser speckle pattern. This is a concern since imprint occurs primarily at early times when the length of the conduction zone D_{ac} is small. Accordingly, several additional means have been proposed to mitigate imprint, including foam, mid-Z dopants and high-Z layers, x-ray flashes, and intensity pickets. These proposals and experiments to test them are described in the following subsections. Foam on the outside of the target can be used to increase the standoff distance between the critical and ablation surfaces, sometimes aided by early-time heating from x rays. In addition, nonuniformities in a laser beam may be smoothed while propagating through the foam. Mid-Z dopants and high-Z layers also increase the standoff distance and can stabilize RT growth through the formation of double ablation fronts. X-ray flashes can be produced in indirect–direct hybrid targets, causing the initial plasma blowoff to be formed exclusively from (uniform) x-ray irradiation. A picket at the front of the laser pulse can produce a decaying shock that rapidly forms an initial plasma atmosphere without causing preheat of the main fuel. The picket can also minimize early-time RT growth.

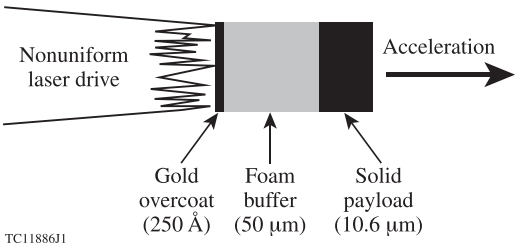

FIG. 7-6. Concept for mitigating imprint by placing a foam buffer covered with a thin gold layer on the outside of the target. Radiation from the gold heats the foam, providing a standoff distance for thermal smoothing. Reprinted with permission from Dunne *et al.*, Phys. Rev. Lett. **75**, 3858 (1995). Copyright 1995 American Physical Society.

1. Foam

Early implosion experiments using foam were carried out by Okada *et al.*[224] in tetrahedral geometry on the four-beam GEKKO IV laser. Glass microballoons of 100-μm diameter were overcoated with a 100-μm-thick foam layer with a density of 122 mg/cm^3 and imploded with 160 J of 1-μm light in a 120-ps pulse. The goal of the experiments was to separate the pusher surface from the laser-absorption region to improve the drive uniformity. They found that the foam layer significantly reduced the implosion nonuniformity and understood this in terms of the hydrodynamics of shock propagation through the foam.

Emery *et al.*[225] presented simulations of imprint mitigation using foam layers placed on the outside of a target, modeling the foam as a homogeneous low-density plasma. Another application of foam was proposed by Desselberger *et al.*[226] to achieve the faster-expanding conduction zone required by Sec. VII A 1: a layer of foam placed on the outside of the target was heated by a source of x rays. In one implementation of this concept, reported by Dunne *et al.*,[227] the foam was covered with a thin layer of a high-Z material such as gold (Fig. 7-6). This concept was tested in Ref. 227 by accelerating a plastic foil covered with a foam buffer of 50-mg/cm^3 density and 50-μm thickness coated with 250 Å of gold. Laser-imprinted modulations were dramatically reduced without compromising the foil acceleration. Foam-buffered implosion experiments at 0.53 μm on Nova, where the foam was made out of two hemishells, were reported by Watt *et al.*[228] Similar experiments showing reduced perturbation growth from rippled targets were reported by Watt *et al.*[229] for planar experiments at 0.35 μm on OMEGA.

An alternative way to provide smoothing using foam was proposed and demonstrated by Depierreux *et al.*[230] Here, a 500-μm-thick layer of underdense foam of 10-mg/cm^3 density placed on top of a solid target was irradiated with four beams of the Ligne d'Intégration Laser (LIL) (12 kJ energy at 0.35 μm). It was observed that the beam nonuniformities decreased after propagating through the foam plasma. This was ascribed to beam spreading as a result of filamentation and stimulated forward Brillouin scattering. The supersonic ionization wave created in the early part of the laser pulse was modeled by Gus'kov *et al.*,[231] who found the wave propagation velocity to be less than predicted for a homogeneous plasma. This was ascribed to the inhomogeneous nature of the foam as in earlier work by Tanaka *et al.*[232] on the propagation of 0.35-μm laser beams through underdense foam.

2. High-Z layers and mid-Z dopants

Mid- and high-Z materials convert some fraction of the laser energy into x-ray irradiation, preheating the outer layers of the ablator material. This increases the adiabat in this region and increases the standoff distance between the critical surface and the ablation front, increasing V_c and reducing the imprint. The relaxed ablation-front density leads to an increase in the ablation and blowoff velocities, reducing the maximum imprint level as shown by Eq. (7-7). Early work using high-Z layers on the Al targets was reported by Bocher *et al.*,[233] and the use of a high-Z coating irradiated by a very short burst of x rays was proposed by Emery *et al.*[225]

The use of a high-Z layer coated on CH targets was demonstrated on the Nike laser by Obenschain *et al.*[234] in an experiment shown schematically in Fig. 7-7(a). One of the Nike beams was used to provide a 3- to 3.5-ns foot laser pulse (at an intensity 2% to 3% of the peak). Another 40 beams provided a 4-ns main pulse with a peak intensity $\sim 7 \times 10^{13}$ W/cm^2 to accelerate the 40-μm-thick target. The growth of areal-density modulations in the accelerated target

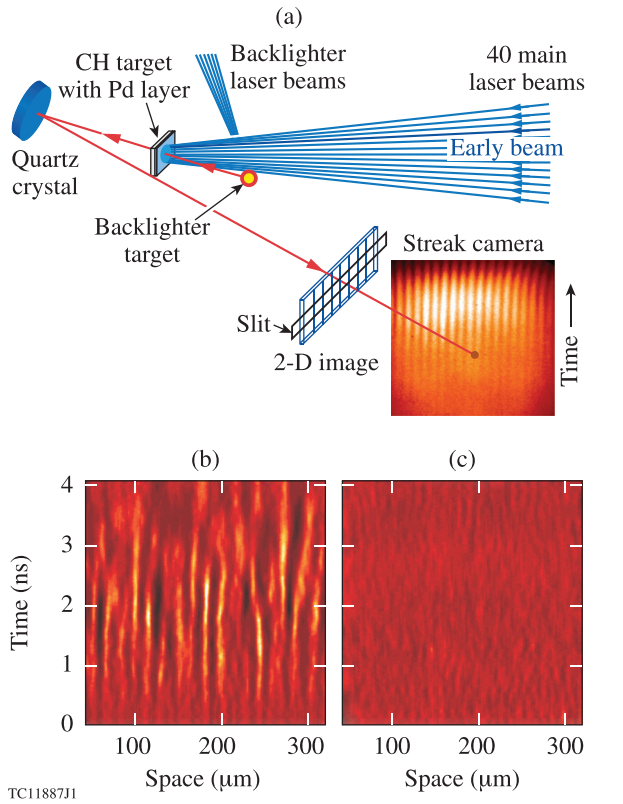

FIG. 7-7. (a) Configuration for an imprint experiment on the Nike laser diagnosed using through-foil x-ray backlighting, a spherical quartz crystal imager, and a streak camera. The target (a CH foil sometimes coated with a Pd layer) was irradiated by a low-intensity foot pulse provided by one early beam and then accelerated by 40 main laser beams. (b) A streaked image (at 1.86 keV) of a target without a Pd layer. (c) A streaked image with a 1200-Å Pd layer. Reproduced with permission from Phys. Plasmas **9**, 2234 (2002). Copyright 2002 AIP Publishing LLC.

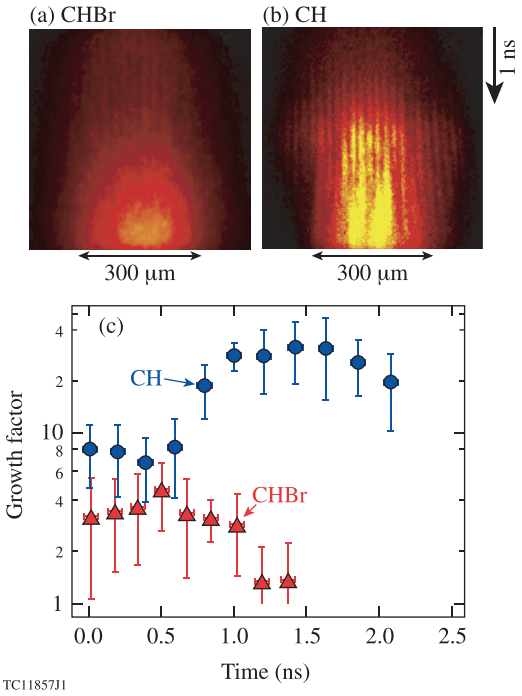

FIG. 7-8. Streaked face-on radiographs of perturbed laser-driven foils consisting of (a) brominated plastic (CH–Br) and (b) bare plastic (CH). (c) Comparison of the measured growth factors derived from each experiment. The time origin corresponds to the time of onset of the main laser drive. Reprinted with permission from Fujioka *et al.*, Phys. Rev. Lett. **92**, 195001 (2004). Copyright 2004 American Physical Society.

was diagnosed using through-foil x-ray backlighting as in Fig. 7-2, except that the pinhole imaging was replaced with high-spatial-resolution, monochromatic imaging provided by a spherical quartz crystal. One-dimensional imaging of the target was obtained along the slit of the streak camera. The streaked image shown in Fig. 7-7(a) is for an initially rippled target.

Streaked images of CH targets without and with a 1200-Å Pd coating are shown in Figs. 7-7(b) and 7-7(c), respectively. The imprinted perturbations grew to a large amplitude for the uncoated target, while no measurable RT-amplified imprint was seen for the coated target. This was understood to result from reduced imprint caused by a buffer plasma layer heated by x rays from the Pd. A minimum thickness of the high-Z layer was found to be necessary. Mostovych *et al.*[235] reported implosion experiments on the OMEGA Laser System using SSD beam smoothing and targets with Pd coatings of various thickness. They found improved performance as the coating thickness was increased from 0 to 400 Å: the neutron yield increased by a factor of 2 and the yield compared with 1-D simulations increased from 3% to 55%, suggesting increased stability. However, it was hard to make a definitive comparison between targets with and without the Pd coating since the targets with the coating imploded on a high adiabat as a result of radiation preheat and shock mistiming. The performance improvement was maintained for 600-Å Pd layers but degraded at 800 Å.

An experiment that demonstrated the benefit of mid-Z doping was reported by Fujioka *et al.*[236] They used planar brominated-plastic (CH–Br) foils to test the development of double ablation fronts to stabilize the RT growth seeded by mass perturbations and laser imprint. They used nine 0.35-μm GEKKO beams following three 0.53-μm foot-pulse beams to drive their foils. Results from these experiments are shown in Fig. 7-8, where streaked, 1-D spatially resolved radiographs are compared for the acceleration of CH–Br [Fig. 7-8(a)] and CH [Fig. 7-8(b)] foils with imposed spatial modulations. Growth factors obtained from these streaks, plotted versus time in Fig. 7-8(c), clearly demonstrate the suppression of RT growth. Fujioka *et al.* incorporated this concept into an ignition design that produced a gain of ~23.

An experiment that demonstrated the benefit of mid-Z dopants in spherical geometry was reported by Hu *et al.*[237] and Fiksel *et al.*[238] The setup is shown in Fig. 7-9(a), taken from Ref. 239 where it was used to measure RT growth in implosion experiments. Spherical plastic shell targets with various dopants were imploded using forty-eight 0.35-μm OMEGA beams. The shells had an outer diameter of 860 μm and a thickness of 22 μm. Each shell had a 400-μm-diam round opening into which a gold cone shield was inserted. A Ta x-ray backlighter was irradiated with six of the remaining OMEGA beams, making it possible to diagnose the growth of areal-density perturbations using an x-ray framing camera. The results [Fig. 7-9(b)] showed lower perturbation levels for the doped shells, consistent with predictions of hydrodynamic simulations.

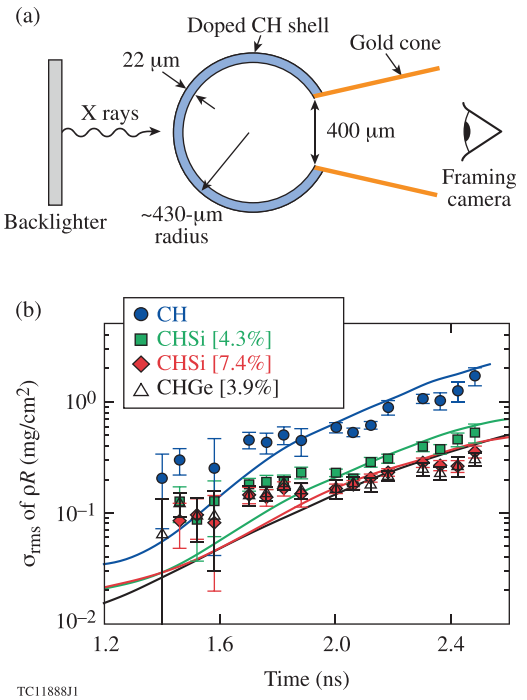

FIG. 7-9. (a) Schematic of an experiment that demonstrated lower imprint in an imploding plastic shell target doped with higher-Z elements. The shell had a round opening into which a gold cone shield was inserted. It was imploded by 48 OMEGA drive beams. Areal-density modulations were diagnosed using a Ta backlighter and an x-ray framing camera. Reprinted with permission from Smalyuk *et al.*, Phys. Rev. Lett. **103**, 105001 (2009). Copyright 2009 American Physical Society. (b) Measured and predicted perturbation growth for targets with various levels of doping. The solid lines are *DRACO* simulations. Reprinted with permission from Hu *et al.*, Phys. Rev. Lett. **108**, 195003 (2012). Copyright 2012 American Physical Society.

3. External x-ray flash

Two implementations of the x-ray flash concept proposed by Desselberger *et al.*[226] were reported by Nishimura *et al.*[240] and Nishikino *et al.*[241,242] In the first experiments, Nishimura *et al.*[240] investigated two types of targets that they described as indirect–direct hybrid targets: the foam hybrid of Ref. 226 and an external hybrid, in which the target is irradiated by an x-ray flash generated by a different laser beam. The external hybrid was based on an experiment by Desselberger *et al.*,[243] who found reduced structures in Au and Cu wire targets when a plasma atmosphere was formed by x-ray preheat from a burnthrough foil. Nishimura *et al.*[240] found reduced imprint for both target types in planar geometry. Neither scheme showed improvement, however, in preliminary spherical implosion experiments. The configuration for the indirect–direct hybrid implosion resembled a hohlraum with one laser entrance hole for each beam. An inner portion of each beam was deflected to irradiate the inner hohlraum wall to provide the x-ray prepulse.

The experiments reported by Nishikino *et al.*[242] used x rays generated by one beam of the GEKKO XII laser focused onto a gold target oriented ~45° from the normal of a CH foil target. Following the x rays, the imprint was imposed by another GEKKO beam, which provided a low-intensity foot pulse ($\sim 3 \times 10^{12}$ W/cm^2) and was sometimes given a spatial modulation. Finally, two main beams at $\sim 7 \times 10^{13}$ W/cm^2 were used to accelerate the foil, allowing the imprint to be measured after amplification by the RT instability. All beams were frequency doubled to 0.53 μm and smoothed using PCL (Sec. VI B). Nishikino *et al.*, like Obenschain *et al.*,[234] preferred to avoid the use of foam advocated in Ref. 226. Two streaked, spatially resolved images are shown in Fig. 7-10. They were obtained in a similar manner to those of Fig. 7-7, except that a slit rather than a spherical crystal was used for the imaging. In Fig. 7-10(a), without x-ray preirradiation, imprint imposed by the foot pulse and amplified during the main pulse is readily observable. With x-ray preirradiation [Fig. 7-10(b)], however, the nonuniformity in the areal mass modulations was dramatically decreased.

4. Intensity picket

Having a larger intensity at the beginning of the drive is beneficial for imprint mitigation, as described in Sec. VII A 1; however, a strong shock that fully traverses the shell will increase the main fuel adiabat. This can be prevented if the shock is unsupported so that it decays as it propagates. It is then possible to increase D_{ac} and reduce the growth of the most-damaging modes while avoiding an increase in the adiabat of the main fuel layer.

Since Nuckolls[244] advocated an initial spike on the laser pulse to improve the symmetry by preheating the atmosphere, many authors have included intensity spikes (pickets) in their designs. Iskakov *et al.*[245] and Krouský *et al.*[246] introduced an intensity picket at the beginning of the pulse to increase the standoff distance D_{ac} and demonstrated enhanced thermal smoothing when they used an optimal delay between the picket and the main laser pulse. They used the second harmonic of an iodine laser (fundamental wavelength 1.315 μm) for the picket and the third harmonic for the main pulse. Collins and Skupsky[247] proposed a picket pulse to minimize early-time RT growth at the DT–CH interface in cryogenic implosions. Experiments[54,248] confirmed imprint reduction using the picket. Smalyuk *et al.*[248] introduced a 5-μm-thick plastic layer on top of a thick, 180-mg/cm^3 foam to mimic the effect of the CD–DT interface in imprint growth. Such an interface leads to an early-time RT growth and enhances the imprint amplitude. It was shown that the intensity picket significantly reduces imprint growth for wavelengths 60 μm and shorter.

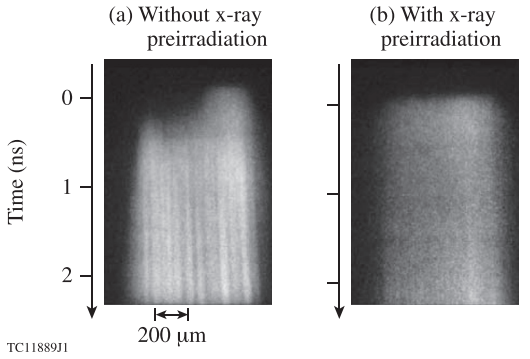

FIG. 7-10. Streaked, spatially resolved through-foil backlighting images for the indirect–direct hybrid irradiation scheme of Ref. 242, for CH foils accelerated (a) without and (b) with x-ray preirradiation. Reproduced with permission from Phys. Plasmas **9**, 1381 (2002). Copyright 2002 AIP Publishing LLC.

C. Richtmyer–Meshkov (RM) instability

1. Physical mechanism

The classical RM instability[204,205] involves the interaction of a planar shock with a corrugated interface between two fluids (Fig. 7-11). The transmitted shock created after this interaction becomes distorted, producing a pressure modulation in the shocked region. This creates a modulation in the acceleration of fluid elements near the material interface during a time of the order of the sound wave's transit time across the perturbation wavelength. The configuration in an ICF target is slightly different. Here, a rippled outer surface results in a rippled shock launched at the beginning of the pulse. The resulting pressure modulations increase the ablation-front ripple amplitude, in a manner similar to the classical RM case. The presence of thermal conduction in an ICF plasma, however, creates a restoring force (Sec. VII A 1). The RM instability drive (an early-time modulation in acceleration of the fluid near the ablation front) lasts for only a short period of time. The dynamic overpressure force, on the other hand, is present at all times, leading to stabilization of the perturbation growth. The restoring force stabilizes only the ablation surface modes localized inside the conduction zone ($kD_{ac} > 1$) shown in Fig. 7-1. For longer wavelengths, the distortion amplitudes at the critical surface (η_c) and the ablation front (η_a) are similar [the ratio $\eta_a/\eta_c \sim \exp(-kD_{ac})$ is of the order of unity for $kD_{ac} \ll 1$], resulting in a uniform temperature gradient along the ablation front and zero restoring force. In this limit, the ablation front is subject to the Landau–Darrieus instability.[249–251] The unstable

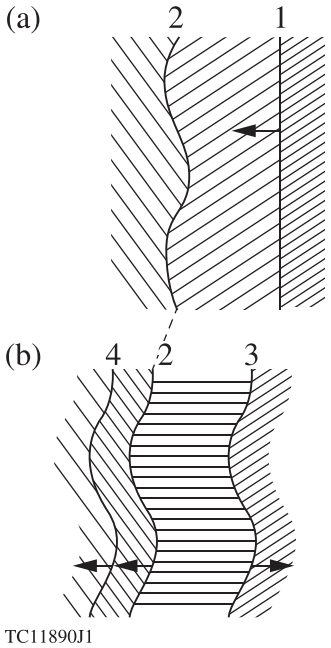

FIG. 7-11. Configuration of the classical Richtmyer–Meshkov instability. (a) A shock wave (1) traverses a rippled interface (2) from a lighter fluid toward a heavier fluid. (b) A reflected shock (3) and a transmitted shock (4) are formed, and the interface perturbation grows. Reprinted with permission from E. E. Meshkov, Fluid Dyn. 4(5), **101** (1969). Copyright 1969 Springer Science and Business Media.

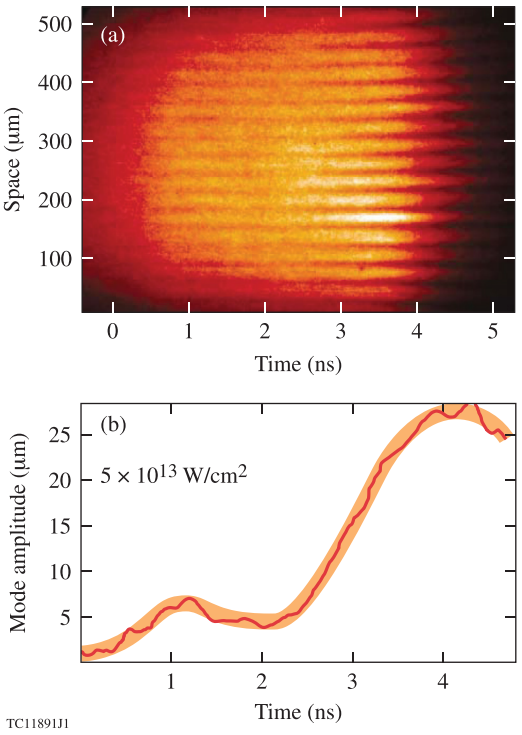

FIG. 7-12. First direct observation of the ablative Richtmyer–Meshkov instability. (a) Spatially resolved streak record obtained with a spherical crystal imager (at 1.86 keV) of areal-density modulations in a 47-μm-thick rippled CH target irradiated at 5×10^{13} W/cm^2. (b) Peak-to-valley amplitude of the dominant (30-μm) mode. The initial amplitude was 1 μm. Reprinted with permission from Aglitskiy *et al.*, Phys. Rev. Lett. **87**, 265001 (2001). Copyright 2001 American Physical Society.

modes in this case are expected to grow exponentially with the growth rate $\gamma_L \simeq \sqrt{(\rho_a/\rho_{bl})}\, kV_a$, where ρ_a and ρ_{bl} are the shell and blowoff plasma densities, respectively.

The analysis of Goncharov *et al.*,[157] Goncharov,[203] and Velikovich *et al.*[252] shows that the ablation-front perturbations oscillate in time because of both the dynamic overpressure and convection of the shock-induced vorticity. The dynamic overpressure acts as a restoring force, leading to amplitude oscillations with frequency $k\sqrt{V_a V_{bl}}$. Mass ablation causes the amplitude to decay in time as $\exp(-2kV_a t)$. The vorticity is imposed by the rippled shock inside the compressed shell[157,203] and is "frozen" into the shock-compressed fluid. In the ablation-front frame of reference, the ablator material travels with velocity V_a toward the ablation front, convecting the vorticity with it. The shock-induced vorticity oscillates in space with frequency $\sim 2k$ and the amplitude decays with distance x as $\sim 1/\sqrt{x}$ (Refs. 157, 208, and 209). Therefore, the ablation front oscillates because of the shock-induced vorticity with frequency $\sim 2kV_a$ and the amplitude decays as $\sim 1/\sqrt{t}$.

2. Richtmyer–Meshkov experiments

The first experimental observations of the dynamics of rippled shocks in plasmas were reported by Endo *et al.*,[253] who irradiated rippled CH foils with 0.53-μm laser light and observed phase inversion of the rippled shock front. The experimental results were successfully modeled by Ishizaki and Nishihara[208,209] and Matsui *et al.*[254]

The first observations of the ablative Richtmyer–Meshkov instability (using a monochromatic spherical crystal imager) were reported by Aglitskiy *et al.*[255] in the configuration shown in Fig. 7-7(a). They irradiated a 47-μm-thick CH target with 37 overlapping 0.248-μm, 4-ns Nike beams on a 750-μm-diam spot, producing an intensity of $\sim 5 \times 10^{13}$ W/cm^2. The target was rippled on its front side with a 30-μm perturbation wavelength of 1-μm peak-to-valley amplitude. A spatially resolved, streaked through-foil backlighting image is shown in Fig. 7-12(a). A reduction in contrast is apparent at ~ 2 ns and is confirmed in Fig. 7-12(b), which shows the amplitude of the dominant 30-μm mode.

The phase reversal and amplitude of the oscillations depend on many parameters of the hydrodynamic flow, including the ablation velocity, density scale length, and standoff distance. These parameters depend critically on the thermal conduction models used in the hydrocode simulations. To test this modeling, a series of RM experiments were carried out on OMEGA by Gotchev *et al.*[256] The experimental setup was similar to that of Aglitskiy *et al.*,[255] except that a high-resolution Kirkpatrick–Baez microscope was used for the imaging. A typical result for the time evolution of the modulation in optical density Δ(OD) is shown in Fig. 7-13 for a 20-μm modulation wavelength. Phase reversal was clearly observed. The observed behavior was not matched by simulations using a standard flux limiter f (Sec. XI) of 0.06. Better modeling was found using a time-dependent flux limiter based on the nonlocal model of Ref. 157, although the agreement with experiment was not as close for the 30-μm case of Ref. 256.

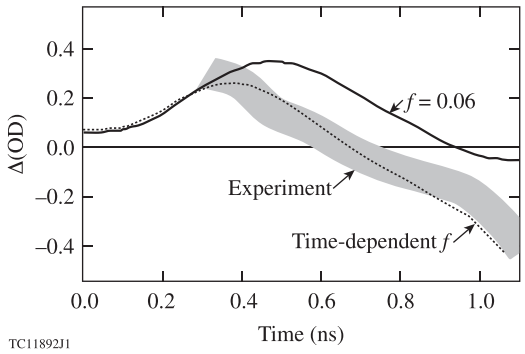

FIG. 7-13. Modulation in optical density Δ(OD) as a function of time observed for a ripple wavelength of 20 μm in a Richtmyer–Meshkov experiment carried out on the OMEGA laser. The data agree better with a simulation using a time-dependent flux limiter f determined from a nonlocal model. Reprinted from Gotchev *et al.*, Phys. Rev. Lett. **96**, 115005 (2006). Copyright 2006 American Physical Society.

D. Feedout

The feedout process describes the seeding of ablation-front instability growth by nonuniformities at material interfaces (other than the outer shell surface) and the inner ice surface. This process was originally discussed by Mikaelian[257] in relation to the RM instability in stratified fluids.

The physical mechanism of feedout was first explained by Betti *et al.*[206] and is illustrated in Fig. 7-14 (from Ref. 258). Figure 7-14(a) shows a slab of fluid with a shock wave S launched from the left end toward the rear surface of the slab, which is modulated with wavelength λ and amplitude δx_0. After the shock breaks out, a rippled rarefaction wave [with leading edge L in Fig. 7-14(b)] is reflected first from the valleys and then from the peaks. In the reference frame of the shocked mass, L propagates at a constant velocity a_1, the speed of sound in the unperturbed shocked material. Therefore, the leading edge of the reflected rarefaction wave is a sine wave of the same phase as the initial rear-surface ripple, with a time-independent amplitude [Fig. 7-14(c)]. The shocked material expands into vacuum, starting from the valleys, at a constant velocity u_e, which for an ideal gas equals $2a_1/(\gamma - 1)$, where γ is the ratio of specific heats, so that after the sine-shaped expansion front E is fully formed, its ripple amplitude is time independent. The expansion front propagates faster than the incident strong shock wave in the target, so the phase of the expansion front is inverted with respect to the initial rear-surface ripple [Fig. 7-14(c)]. Breakout of the rippled rarefaction wave occurs when its valleys (originated from the valleys at the rear surface of the target) reach the front surface, starting its acceleration. In other words, the thinner parts of the target start accelerating earlier and experience a higher acceleration under the same drive pressure because of the lower areal mass. During the RT growth phase that follows, these thinner parts evolve into bubbles, propagating ahead and transferring more of their mass into the spikes that trail behind.

The scenario shown in Fig. 7-14 is valid when the modulation wavelength is much larger than the thickness Δ of the shock-compressed region, i.e., when $k\Delta \ll 1$. When this condition does not hold, lateral mass redistribution in the rippled rarefaction wave can no longer be neglected. The lateral mass flow is driven as shown in Fig. 7-14(b). After the shock breaks out, expansion starts from the valleys, decreasing the pressure there, whereas near the peak locations, the pressure is maintained at the constant post-shock value. The resulting lateral pressure gradient drives mass from the peaks to the valleys, decreasing the pressure at the peaks and increasing it at the valleys. The mass flow continues when the pressure gradient vanishes, overshooting the equilibrium situation and building up a reversed pressure gradient. These sonic oscillations of areal mass in a rippled rarefaction wave, which continue until the rarefaction wave breaks out at the front surface of the target, were first described by Velikovich and Phillips.[259] In the context of the feedout problem, the oscillations were observed in simulations of hohlraum-driven experiments on Nova.[260]

The first demonstration of feedout in a direct-drive configuration was reported by Shigemori *et al.*[261] (Fig. 7-15). Initial perturbations of 10-μm peak-to-valley amplitude and 100-μm wavelength were imposed on the rear surface of CH foils that were driven with 0.53-μm laser radiation smoothed by PCL. The evolution of the perturbations was diagnosed using side-on and face-on radiography, leading to results consistent with the analytic model of Ref. 206. Figure 7-15 gives a sequence of four images (obtained from two nominally identical shots). The first image [Fig. 7-15(a)], at an early time, shows the initial ripple. The second and third images [Figs. 7-15(b) and 7-15(c)] are taken ~0.25 ns after the shock wave breaks out from the rear surface of the target at its thinnest portion (point A) and indicate phase reversal. The final image [Fig. 7-15(d)] is taken ~0.4 ns after the rarefaction wave from point A reaches the laser-irradiated surface (point B). Foil acceleration starts earliest at this point, resulting in the rippled accelerating foil shown in

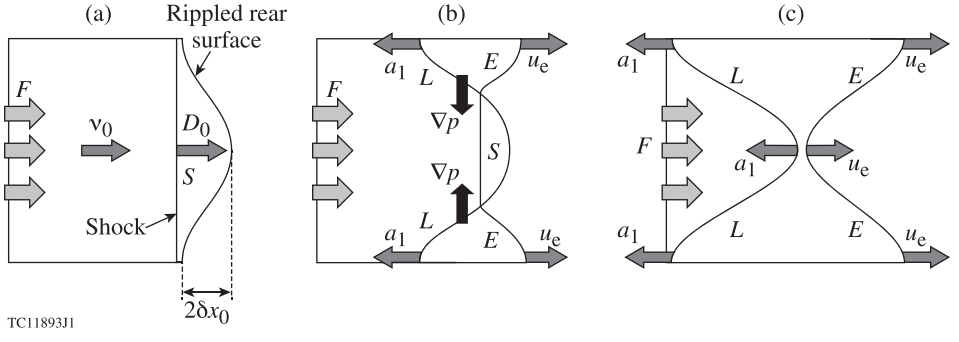

FIG. 7-14. Illustration of feedout. (a) A planar shock wave S driven by a constant force F approaches the valleys of the rear-surface ripples. (b) A rippled rarefaction wave with leading edge L and trailing edge E starts to form near the valleys. (c) The fully formed rarefaction wave approaches the front surface. Reproduced with permission from Phys. Plasmas **8**, 592 (2001). Copyright 2001 AIP Publishing LLC.

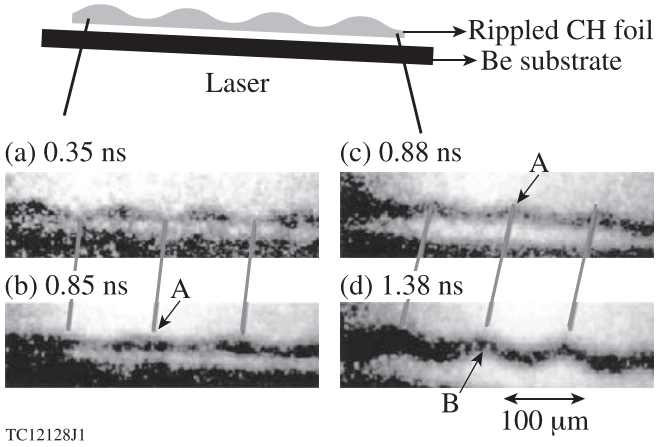

FIG. 7-15. A sequence of side-on framed x-ray backlighting images of a 0.53-μm laser-irradiated CH foil, demonstrating feedout from the rippled rear surface of the foil. The foil thickness varies from 20 μm to 30 μm. The lines between images indicate matching spatial positions. The dark shadow at the bottom of each image is the Be substrate used to support the foil. Phase reversal of the perturbation of the rear surface is seen at point A, resulting from the shock breaking out first from the valleys. The rarefaction reaches the front surface first at the corresponding point B, leading to a rippled foil in the acceleration phase with point B moving ahead. Reprinted with permission from Shigemori *et al.*, Phys. Rev. Lett. **84**, 5331 (2000). Copyright 2000 American Physical Society.

Fig. 7-15(d). Multiple phase reversals of the mass modulation amplitude in a rippled rarefaction wave were observed by Aglitskiy *et al.*[262]

VIII. IMPLOSION EXPERIMENTS

While many physics processes critical to direct-drive ICF can be studied in planar geometry, implosion experiments are at the heart of ICF research. The earliest such experiments operated in the exploding-pusher mode described in Sec. IV with the primary goal of maximizing the neutron yield. With the recognition that exploding pushers do not scale to ignition, the focus of research shifted to experiments aimed at generating high compressed fuel density. This section reviews these experiments with an emphasis on issues related to uniformity and stability.

The large majority of implosion experiments have been carried out at room temperature (Sec. VIII A), but the most significant are those carried out at cryogenic temperatures with frozen D_2 or DT fuel (Sec. VIII B). Section VIII C reviews polar-drive implosions, in which the non-spherically symmetric geometry of the NIF is compensated for by pointing the laser beams away from the target center, making it possible for direct-drive–ignition implosions to be carried out on the NIF.

Early implosion experiments were carried out at a number of facilities, often with a limited number of laser beams and often without beam smoothing. From the completion of the 60-beam OMEGA laser in 1995 and its implementation of beam smoothing soon thereafter, direct-drive–implosion physics has been advanced primarily on OMEGA by experimenters from LLE and many other institutions and on the 12-beam GEKKO XII laser.

A. Room-temperature implosions

Room-temperature implosions are important because they allow many physics processes critical to high-compression cryogenic implosions to be conveniently tested, often using diagnostic opportunities that are not available to cryogenic targets such as the addition of trace high-Z gases to the fuel for spectroscopic diagnostics. The fill pressure can be changed to vary the convergence ratio without changing the hydrodynamics of the acceleration phase, enabling stability issues to be addressed.

This section describes a number of implosion experiments aimed at diagnosing fuel compression and exploring the effects of various sources of drive nonuniformity. It starts with early experiments at LLE, LLNL, and LANL in which spectroscopic diagnostics were developed to measure the compressed density, at both 1-μm and 10-μm laser wavelengths. Experiments at Osaka at 0.53-μm wavelength follow, in which secondary reaction products were used to diagnose the fuel areal density (ρR) and study fuel–pusher mix. The implementation of phase plates (Sec. VI A) at Osaka made possible further experiments in which plastic shells with the hydrogen replaced by deuterium and tritium were compressed to high densities, diagnosed using neutron activation of Si doped into the plastic. Experiments are reported that demonstrated the benefits of smoothing by spectral dispersion (SSD) (Sec. VI C), with less burnthrough related to laser hot spots being observed on the 24-beam OMEGA laser and improved yield performance being found on the 60-beam OMEGA laser. Experiments at Osaka with the laser beams smoothed using partially coherent light (PCL) (Sec. VI B) showed a reduction of neutron yield with increased target offset. A variety of experiments are reported in which embedded layers placed near the inner CH shell surface were used to measure the shell areal density, study fuel–shell mix, and diagnose areal-density modulations in the shell. The embedded layers included Ti-doped CH for spectroscopic diagnostics and CD layers in conjunction with D^3He- or T-filled targets for mix diagnostics. Long-wavelength nonuniformities have been studied using proton diagnostics to measure the compressed target ρR at various locations around the target chamber, and using line emission from targets with Ar-doped fuel in experiments devoted to reconstructing the 3-D spatial structure of the electron temperature and density in the compressed core.

The importance of diagnosing fuel compression has long been recognized. In the early exploding-pusher experiments described in Sec. IV A, estimates of compression were made based on the central emission peak of (time-integrated) x-ray pinhole images, but these estimates were indirect. The first direct measurements of compressed density were made by Yaakobi *et al.*,[263] who imploded Ne-filled glass targets using 0.2-TW, 40-ps pulses from the four-beam, 1-μm DELTA laser. The compression was determined separately from the Stark broadening, the opacity broadening, and the spatial profiles of Ne^{9+} x-ray emission lines. Figure 8-1 shows the measured line emission around the optically thin, 9.7-Å Ne Lyman-γ line. This was well fitted by a calculated Stark profile for an electron density n_e of 7×10^{22} cm^{-3}, corresponding to a mass density of 0.26 g/cm^3. Assuming that the whole Ne mass was uniformly compressed, Yaakobi *et al.* inferred

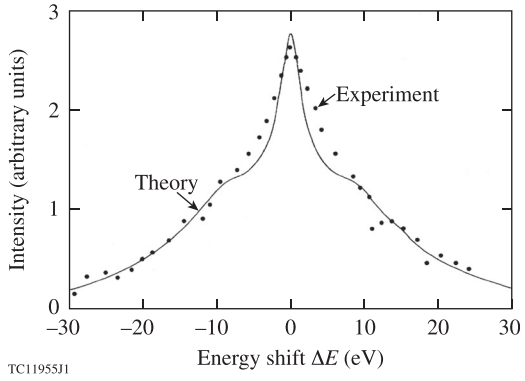

FIG. 8-1. Comparison of the measured Stark profile of the Lyman-γ line of Ne (9.7 Å) with the best-fit calculated profile for a Ne-filled glass microballoon imploded on the four-beam, 1-μm-wavelength DELTA laser, showing target compression to an electron density of 7×10^{22} cm^{-3}. Reprinted with permission from Yaakobi *et al*., Phys. Rev. Lett. **39**, 1526 (1977). Copyright 1977 American Physical Society.

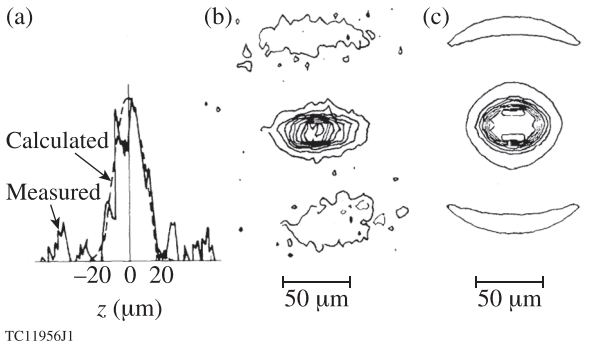

FIG. 8-2. X-ray images from polymer-coated glass microspheres filled with DT fuel and Ar seed gas, imploded on the 20-beam, 1-μm Shiva laser. (a) Measured and calculated Ar line-emission trace in the z (vertical) direction. (b) Measured and (c) calculated continuum x-ray microscope images at ~3.5 keV, indicating a DT density of ~2 g/cm^3. The initial target radius was ~90 μm. Reprinted with permission from Auerbach *et al*., Phys. Rev. Lett. **44**, 1672 (1980). Copyright 1980 American Physical Society.

an areal density ρR of 0.25 mg/cm^2. The ρR was separately inferred from the opacity of the optically thick He$_\alpha$ line. The Ne was compressed from its initial diameter of ~65 μm to an inferred diameter of 19 μm, corresponding to a convergence ratio of 3.4. Yaakobi *et al*. anticipated that trace amounts of Ne would be used to diagnose highly compressed thermonuclear fuel in future experiments. The Stark-broadening method was later extended to Ar fills for higher-temperature implosions carried out at 1-μm wavelength on the ZETA laser (which used the first six beams of the 24-beam OMEGA laser), and a density of 4–6 g/cm^3 was measured in these experiments.[264] A review of the application of plasma spectroscopy to laser-fusion experiments can be found in Ref. 265.

In earlier experiments on the DELTA laser, using similar Ne-filled targets, Yaakobi *et al*.[266] suggested using K$_\alpha$ emission to measure the number of suprathermal electrons and their preheating effect. They demonstrated this using Ne and Si K$_\alpha$ emission, estimating that suprathermal electrons accounted for at least 1 J of the 5- to 10-J absorbed energy. However, Hares *et al*.[267] suggested that the K$_\alpha$ emission in these experiments was dominated by radiation from the coronal plasma and used targets with a mylar layer in front of a K$_\alpha$ fluor layer to absorb this radiation. With the K$_\alpha$ emission pumped only by hot electrons, they were able to make absolute measurements of the hot-electron preheat. K$_\alpha$ fluorescence has been used in recent experiments to measure the preheat from hot electrons presumed to be generated by the two-plasmon–decay instability (Sec. X A).

Direct-drive compression experiments were also carried out at LLNL (at 1-μm laser wavelength) and at LANL (at 10.6 μm). At LLNL, Auerbach *et al*.[268] used the 20-beam, 4-kJ, 1-μm Shiva laser to implode DT-filled, polymer-coated glass shells with 200-ps pulses. Designed for indirect drive, the beams were clustered in rings at angles θ of 9.7° and 17.7° from the vertical (z) axis.[269] In an attempt to accommodate these direct-drive implosions, the beams were pointed away from the target center, but the resulting laser intensity on the target surface was far from uniform. Auerbach *et al*. estimated that it varied by a factor of 5, from 4×10^{15} to 2×10^{16} W/cm^2. The measured absorption fraction was 23%, understood to result primarily from resonance absorption. The DT fill included an Ar dopant for spectroscopic analysis. In contrast to Ref. 263, the compressed density was inferred from comparisons with hydrodynamic simulations, using the 2-D code *LASNEX*.[270] Figure 8-2(a) shows measured and calculated lineouts in the z direction of an Ar line-emission image; Figs. 8-2(b) and 8-2(c) show, respectively, measured and calculated continuum x-ray images of the compressed core. The images reflect the two-sided nature of the irradiation geometry. (As a result of suprathermal electron transport, they are probably rounder than might be expected from the variations of on-target laser intensity.) The inferred DT fuel density was 1–3 g/cm^3 or 5–15× liquid DT density.

At LANL, Tan *et al*.[271] performed implosion experiments using the eight-beam CO$_2$ laser system Helios, with ~3 kJ of laser energy in an ~1-ns pulse. The targets were 300-μm-diam, 1-μm-thick DT-filled glass microballoons overcoated with up to 100 μm of plastic. Irradiated at intensities of up to 5×10^{15} W/cm^2, the target absorbed approximately 26% of the laser energy. As the plastic thickness increased, the exploding-pusher character of the implosion changed to a more isentropic compression, with the neutron yield decreasing from mid-10^8 to ~10^6 and the ion temperature decreasing from 1 to ~0.3 keV. The final fuel density was determined in three ways, two involving spectroscopic diagnostics using a trace amount of Ar in the fuel and the other using x-ray pinhole camera images; it is plotted in Fig. 8-3 as a function of ablator thickness. The results are in good agreement with *LASNEX* simulations and indicate densities up to 2 g/cm^3. The estimated hydrodynamic efficiency (defined as the fraction of absorbed energy in the compressed fuel) was very low (~0.5%), indicating the very poor coupling characteristic of the long laser wavelength.

Density diagnostics based on secondary fusion reactions were demonstrated on the 12-beam GEKKO XII Laser Facility by Azechi *et al*.,[41] using the neutrons and protons generated by secondary reactions in D$_2$ fuel [Eqs. (2-5) and (2-6), respectively]. The yield ratio of secondary to primary

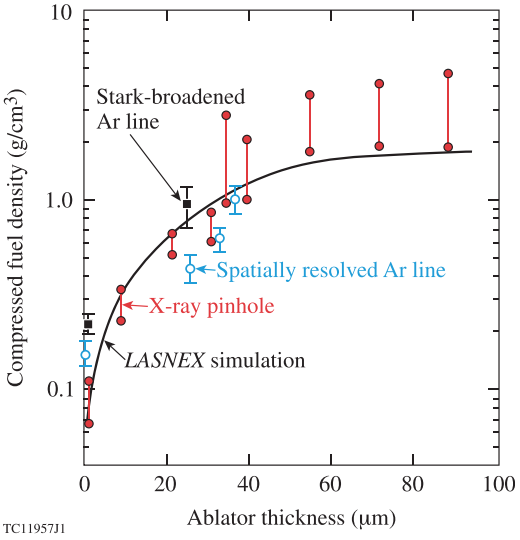

FIG. 8-3. Measured compressed fuel density as a function of ablator thickness from the implosion of plastic-coated glass microballoons filled with DT and sometimes a trace amount of Ar, imploded by the eight-beam, 10.6-μm Helios laser. The solid line is the result of *LASNEX* simulations. Reproduced with permission from Phys. Fluids **24**, 754 (1981). Copyright 1981 AIP Publishing LLC.

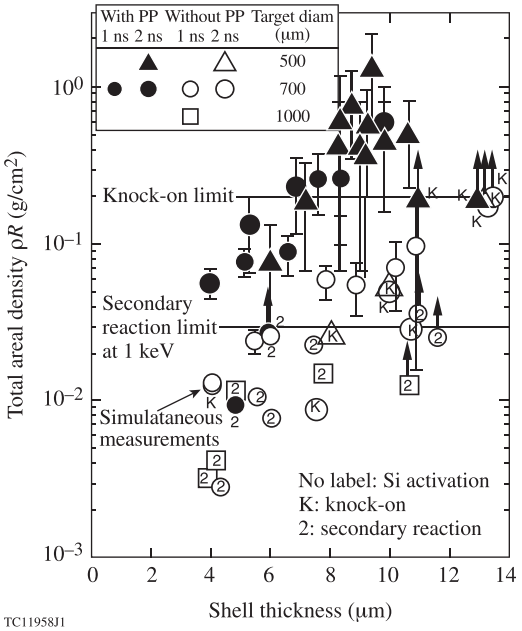

FIG. 8-4. Measured total areal density (ρR) as a function of shell thickness from a series of implosions of hollow CDT targets on the 12-beam, 0.53-μm GEKKO XII laser. The two horizontal lines show the limits of the knock-on and secondary-reaction techniques. Significantly larger values of ρR were obtained using phase plates (PP's). Reproduced with permission from Azechi *et al.*, Laser Part. Beams **9**, 193 (1991). Copyright 1991 Cambridge University Press.

reaction products increases with the fuel ρR. For a D_2-filled, ~700-μm-diam glass microballoon coated with a plastic ablator and imploded with ~7 kJ of 0.53-μm-wavelength laser energy in a 0.8-ns pulse, Azechi *et al.* obtained a fuel ρR of 2 mg/cm^2. They showed that (1) at higher values of ρR, the temperature could also be obtained and (2) the method is limited to values of ρR below ~300 mg/cm^2 (the range of a secondary 14.7-MeV proton). Earlier theoretical work proposing to use the ratio of DT to DD neutrons from D_2 fuel was reported by Gamaliĭ *et al.*[272]

These secondary reactions were also used by Azechi *et al.*[273] to study fuel–pusher mix in ablatively driven glass microballoon implosions on GEKKO XII under similar irradiation conditions. They used the enhanced slowing of the secondary triton by the higher-Z Si material mixed into the fuel to infer an electron temperature that was an order of magnitude less than that predicted by hydrodynamic simulations.

Around this time, it became clear that nonuniformities in the on-target laser-irradiation pattern were limiting the performance of implosions by seeding hydrodynamic instabilities (Sec. VI). Phase plates were added to the GEKKO XII laser, leading to a considerable improvement in target compression. This was clearly shown in a series of experiments reported by Azechi *et al.*[274] in which the GEKKO XII laser was used to implode plastic shells with the hydrogen replaced by deuterium and tritium. The CDT targets were 500–1000 μm in diameter with 4- to 13-μm thickness. They were imploded by 8–10 kJ of 0.53-μm laser energy in nominally 1- to 2-ns laser pulses. Results for the areal density ρR are shown in Fig. 8-4 as a function of shell thickness, for a variety of target diameters and pulse widths and for shots with and without phase plates. The primary diagnostic used for the areal density was neutron activation of Si doped into the plastic. (Neutron activation was developed by Campbell *et al.*[275] at LLNL and used to measure the areal density of the glass shells surrounding the fuel for exploding-pusher[275] and indirect-drive[2,3] targets.) Two other diagnostics (knock-ons[276,277] and secondary reactions) were used, but they were limited to values of ρR well below those of the best-performing shots. (Knock-ons are energetic deuterium and tritium ions elastically scattered by the 14.1-MeV neutrons.) Significantly higher values of ρR were obtained with phase plates (solid data points). The maximum total ρR found was ~1 g/cm^2, with the fuel ρR being 1/6 to 1/7 of the total ρR. The total density was inferred by assuming that all of the unablated mass was contained in a spherical region of uniform density ρ and radius R. The average density of the highest-performing targets was 600 g/cm^3, in agreement with simulations. This corresponded to a fuel density of ~600× liquid density. Azechi *et al.* noted, however, that the neutron yields were less than predicted by three orders of magnitude and suggested that the implosion uniformity was not sufficient.

Following the implementation of 1-D SSD (Sec. VI C) on the 24-beam OMEGA Laser System, to provide temporal smoothing of the static irradiation pattern produced by phase plates, Bradley *et al.*[278] demonstrated improved uniformity performance using ~265-μm-diam D_2-filled glass microballoons (with 3-μm wall thickness), overcoated with 6 μm of parylene. The onset of Si emission from the laser "burning through" the parylene was measured as a function of applied SSD bandwidth (Fig. 8-5). This is a good signature of uniformity as early burnthrough results from laser hot spots drilling through more rapidly than the desired uniform ablative process. Figure 8-5 shows that the burnthrough time is delayed as more smoothing is applied (higher bandwidth). The neutron yield increased from 10^{-3} to 10^{-2} of that

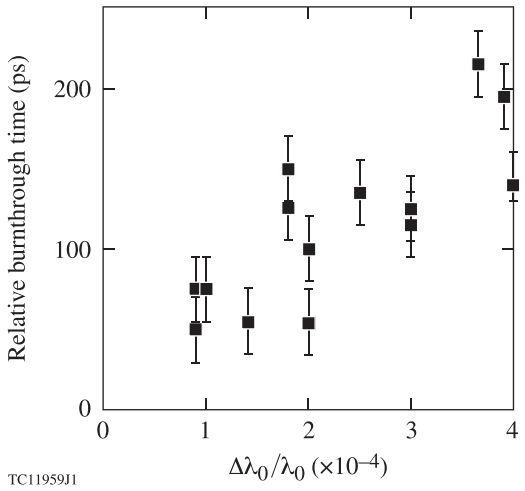

FIG. 8-5. Relative burnthrough times as a function of (1-D) SSD bandwidth $\Delta\lambda_0/\lambda_0$ for a series of implosions of plastic-coated glass microballoons on the 0.35-μm, 24-beam OMEGA laser. The burnthrough time is normalized to zero for the no-bandwidth case. Reprinted with permission from Bradley *et al*., Phys. Rev. Lett. **68**, 2774 (1992). Copyright 1992 American Physical Society.

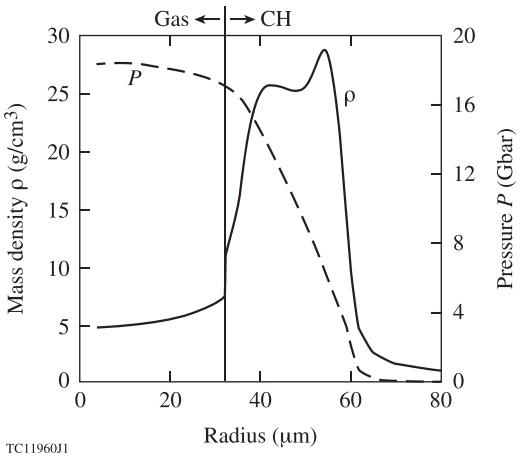

FIG. 8-6. Calculated density and pressure profiles at peak neutron production of a 20-μm-thick plastic shell filled with 15 atm of gas and imploded on the 60-beam OMEGA laser, indicating a region in the vicinity of the gas–CH interface with opposite density and pressure gradients that is subject to the deceleration-phase Rayleigh–Taylor instability and subsequent mix. Reproduced with permission from Phys. Plasmas **9**, 2208 (2002). Copyright 2002 AIP Publishing LLC.

predicted by the 1-D hydrocode *LILAC* with increasing bandwidth.

Heya *et al*.[279] followed up on the question of implosion uniformity raised by Azechi *et al*.[274] with more 0.53-μm-wavelength implosion experiments on GEKKO XII. By this time, PCL had been introduced into the laser along with phase plates to improve the single-beam uniformity. The targets were 500-μm-diam, 7-μm-thick plastic shells filled with hydrogen (6 atm) and deuterium (4 atm), with small fractions of Ar and tritium for x-ray and neutron diagnostics. The targets were driven with 3 kJ in a 1.6-ns temporally flat pulse with a 0.2-ns prepulse. Heya *et al*. made no attempt to impose nonuniformities on their targets, but found an $\ell = 1$ nonuniformity (where ℓ indicates the spherical-harmonic mode) whose level changed from shot to shot. The origin of this nonuniformity was not known, but target nonuniformity, beam power imbalance, target positioning errors, and beam pointing errors were listed as possibilities. Heya *et al*. showed time-integrated x-ray pinhole camera images of two compressed targets, one of which had a significantly larger offset (34 μm) than the second (14 μm). They also obtained 2-D x-ray images of the compressed core plasmas with high time resolution using a multichannel, multi-imaging x-ray streak camera method, from which they found that the x-ray emission from the core of the target with the larger offset was less symmetric and disappeared earlier in time. The neutron yield compared with 1-D simulations dropped from 12% for the small-offset case to 8% for the larger-offset case. They found that 2-D simulations including both $\ell = 1$ and $\ell = 6$ perturbations ($\ell = 6$ is characteristic of the dodecahedral GEKKO XII geometry) were required to model the experimental results, such as the rapid cooling of the hot core.

These conclusions were consistent with results reported around the same time by Meyerhofer *et al*.[280] from the 60-beam OMEGA laser with "full" beam smoothing [1-THz SSD (Sec. VI C) and polarization smoothing (Sec. VI D)]. They imploded ~940-μm-diam, ~20-μm-thick CH shells filled with D_2 using a 1-ns temporally flat laser pulse and found ratios of primary neutron yield to 1-D predicted yield [known as "yield over clean" (YOC)] up to 35%. The measured fuel and shell areal densities were close to 1-D predictions. The yields and fuel areal densities were ~70% larger than those obtained with less smoothing (0.35 THz and no polarization smoothing), consistent with the mitigation of instability growth. However, the marginal additional YOC obtained for 24-μm-thick shells led them to suggest that single-beam nonuniformities were no longer the dominant determinant of target performance, citing similar alternative causes to those listed by Heya *et al*.[279]

This work was extended by Meyerhofer *et al*.[281] and Radha *et al*.,[282] who demonstrated mixing between the fuel and the shell. Figure 8-6 shows simulated density and pressure profiles at peak neutron production. A region in the vicinity of the gas–CH interface is subject to the deceleration-phase Rayleigh–Taylor instability. Some of the targets used ^{3}He for the gas and included a 1-μm CD layer embedded at or near the inner surface of the CH shell; microscopic mix resulting from instability growth was then diagnosed by the production of primary D–^{3}He protons. (Similar targets were used in Ref. 283.) In other targets, filled with D_2, mix was diagnosed from the ratio of secondary neutrons [Eq. (2-5)] to primary D–D neutrons. This is possible because the D–T cross section (producing secondary neutrons) increases as the tritons slow down from their birth energy, and the presence of shell material in the fuel enhances the triton slowing down. An *ad-hoc* mix model matched the experimental observables, leading Radha *et al*. to conclude that ~30% of the compressed fuel areal density was in the modeled mix region.

The use of embedded-layer targets built upon earlier work involving spectroscopic diagnostics by Yaakobi *et al*.[284] and Bradley *et al*.[285] Yaakobi *et al*. showed that the areal density of the compressed shell can be inferred from Ti absorption lines. Bradley *et al*. used Ti-doped layers near the

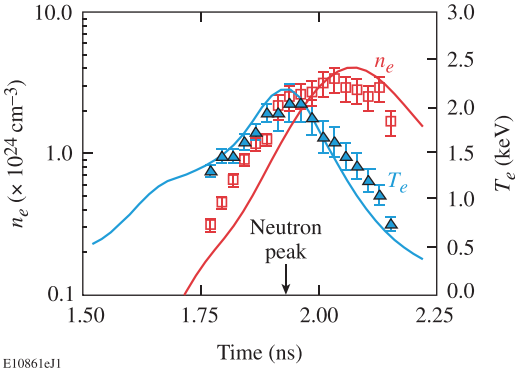

FIG. 8-7. Time-resolved, emissivity-averaged electron density n_e and temperature T_e in the hot spot inferred from Ar K-shell spectroscopy for an Ar-doped, D_2-filled CH target imploded on OMEGA. The solid lines are from 1-D simulations. The peak neutron production occurs at 1.93 ns, around the time of peak electron temperature. Reproduced with permission from Phys. Plasmas **9**, 1357 (2002). Copyright 2002 AIP Publishing LLC.

inside of the shell and observed He- and H-like line emission when the Ti-doped layer was on the inside of the CH layer but not when it was offset 0.5 μm from the interface. They also doped the fuel with Ar to measure its electron temperature and density spectroscopically, and found strong disagreement with 1-D simulations understood to be related to mix. However, these experiments were carried out before the implementation of beam smoothing.

Subsequent experiments with Ar-doped fuel, after the implementation of 1-THz SSD and polarization smoothing, were reported by Regan *et al.*[286,287] In contrast to the earlier work with unsmoothed beams,[285] the 1-D simulated time histories of electron temperature and electron density were closer to the experimental results (Fig. 8-7). However, the observation that the measured electron density was higher than simulated was attributed to hydrodynamic mixing of the inner wall of the plastic shell with the deuterium gas during the deceleration phase. Regan *et al.*[287] envisaged an inner core containing only fuel and an outer core containing a mix of fuel and CH shell material. They found that the electron density determined spectroscopically (and understood to come from the mix region) was approximately twice that of the inner core, obtained from a combination of nuclear measurements of fuel ρR and x-ray core images. On this basis, they estimated that ~0.4 μm of the initial CH thickness was contained in the mix region, where there were approximately equal mass densities of deuterium and CH. The inferred total pressure (electron plus ion) in the mix region was ~11 Gbar. In subsequent work, Regan *et al.*[288] showed that the mix correlated with the predicted feedthrough from the ablation surface to the inner shell surface.

The scenario envisaged by Regan *et al.*[287] was consistent with experiments using separated reactants. The 0.4-μm estimate for the mixed CH thickness was very close to the 0.5 μm reported by Li *et al.*[283] using ^{3}He-filled CH shells containing CD layers. Li *et al.* also found that the mix increased with convergence ratio. Rygg *et al.*[289] used the time dependence of the proton yield from similar targets to show that the neutron-production time is delayed, consistent with the amount of mix increasing in time. Wilson *et al.*[290] carried out similar experiments but with the shell filled with (nearly) pure tritium. From the time dependence of the D–T neutron production, they quantified the time-integrated and time-resolved amount of mix. They too found that the mix increased with time and, by comparing with a mix model, found that not all the mix was atomic.

One technique for reducing the mix levels resulting from laser imprint, the use of an intensity picket for adiabat shaping (Sec. VII B 4), was demonstrated by Knauer *et al.*[54] in experiments on OMEGA. They imploded ~910-μm-diam targets with ~30-μm plastic wall thicknesses, filled with 3–18 atm of D_2 or D^3He. The ~18-kJ laser pulses included a single picket, designed to keep the inner part of the shell on an adiabat of 2. The neutron yield was higher when adiabat shaping was used, as was the YOC.

In an extension of this work, Radha *et al.*[291] carried out triple-picket implosions of 27-μm-thick, ~860-μm-diam, D_2-filled plastic shells whose in-flight aspect ratio (IFAR) was varied by changing the picket energies and temporal separations and, to a lesser extent, the shell thickness. (In this work, the IFAR was defined as the average shell radius divided by the shell thickness when the shell has traveled 1/3 of the total distance through which it is accelerated. This definition gives higher values of IFAR by a factor of ~2 in comparison with the more commonly used definition of Sec. III, where the IFAR is calculated when the shell has moved to 2/3 of its initial radius.) Measured and simulated yields are shown in Fig. 8-8(a), plotted against the calculated IFAR. The measured

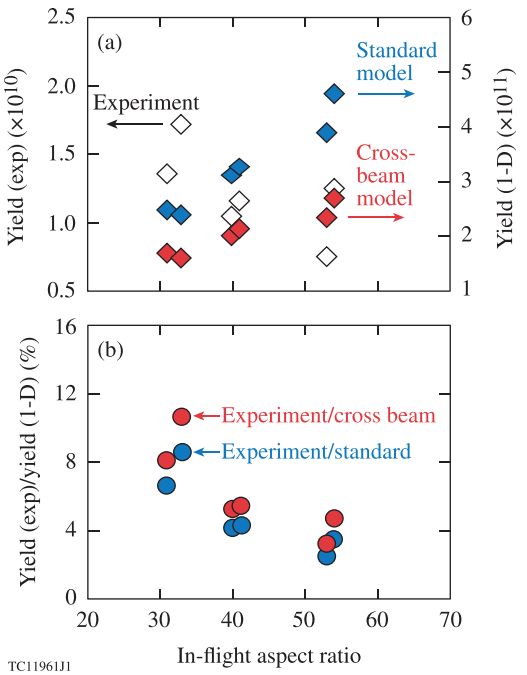

FIG. 8-8. (a) Measured neutron yield for a series of triple-picket implosions of gas-filled plastic shells on OMEGA as a function of the calculated in-flight aspect ratio (IFAR) (left axis) together with predictions (right axis) using the standard 1-D *LILAC* model and a model including cross-beam energy transfer. Note the different vertical scales. (b) Experimental yield relative to the predictions of the two models as a function of the IFAR. The data were taken for SSD beam smoothing with 1/3-THz bandwidth and three color cycles. Reproduced with permission from Phys. Plasmas **18**, 012705 (2011). Copyright 2011 AIP Publishing LLC.

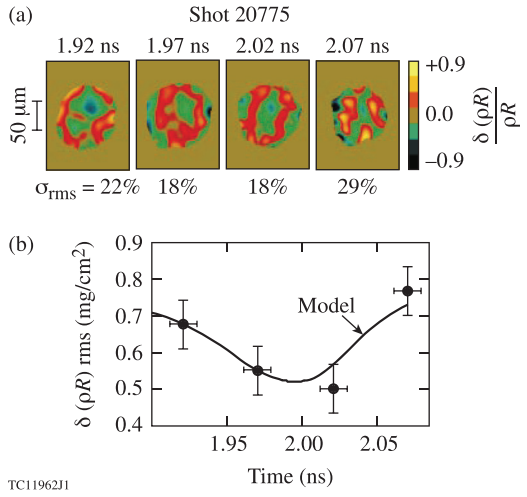

FIG. 8-9. (a) Normalized images showing the areal-density modulations at four times near peak compression of an ~2-μm Ti-doped layer on the inside of a 20-μm, D_2-filled CH shell imploded with a 1-ns temporally flat laser pulse on OMEGA. The images were obtained from framing-camera images above and below the Ti K edge of x rays emitted by the hot compressed D_2, which backlit the outer, colder shell. (b) Evolution of the rms modulation in ρR at the four times of (a) together with predictions of a model of Rayleigh–Taylor growth. (The results of the model are normalized to the experimental point at 1.97 ns.) Reprinted with permission from Smalyuk *et al.*, Phys. Rev. Lett. **87**, 155002 (2001). Copyright 2001 American Physical Society.

yields decrease with increasing IFAR. The simulated yields are based on two models: the standard *LILAC* model, which uses a flux limiter (Sec. XI) of 0.06, and an amended model that includes cross-beam energy transfer (Sec. X B). Both models show a trend counter to that of the experiment. The cross-beam model matches the experimental neutron bang time better and predicts a lower yield than the standard model because the laser absorption is lower. However, the difference between the two models is small in comparison with the difference between either model and the experimental data. The observed yield as a fraction of the simulated yield [Fig. 8-8(b)] decreases with increasing IFAR, independent of the simulation model, strongly suggesting that hydrodynamic instabilities cause the target performance to degrade with increasing IFAR. Radha *et al.* concluded that IFAR ≤ 40 is required to achieve adequate compression under the conditions of the experiment.

The evolution of nonuniformities with wavelengths longer than those thought to contribute to mix was studied in a series of experiments on OMEGA using a differential imaging technique proposed by Yaakobi *et al.*[292] These authors imploded D_2-filled, 20-μm-thick CH shell targets with 1-ns temporally flat laser pulses, under conditions similar to those of Ref. 280. The inner 2 μm of the shell was doped with Ti. As the target reached peak compression, a bright ~200-ps burst of x rays from the hot core backlit the compressed Ti layer. Time-integrated images above and below the Ti K edge were obtained using a pinhole-array spectrometer. The ratio of these images then reflected ρR modulations of the doped layer around the time of peak compression. Yaakobi *et al.* found that the shell maintained its integrity at peak compression and the observed ρR modulations agreed with 2-D simulations.

This work was followed by Smalyuk *et al.*,[293] who used time-integrated pinhole-camera imaging, and Smalyuk *et al.*,[294] who replaced the time-integrated pinhole camera with a pinhole camera coupled to an x-ray framing camera to obtain time resolution. Images of areal-density modulations from Ref. 294 are shown in Fig. 8-9(a), and the inferred rms areal-density modulation is plotted in Fig. 8-9(b) as a function of time. Smalyuk *et al.*[294] understood the early-time modulation to result from the front-surface (ablation front) shell distortion, the dip at intermediate times to result from a change in phase of the front-surface modulation after the laser is turned off and the ablation front becomes stable, and the growth at the latest time to reflect deceleration Rayleigh–Taylor growth at the unstable inner surface. They also showed that smaller SSD bandwidth resulted in greater areal-density modulation. In Refs. 295 and 296, Smalyuk *et al.* observed greater modulation growth during the deceleration phase for targets with higher convergence ratios (obtained using lower D_2 fill pressures). Extensive analysis of the differential-imaging technique is given in Refs. 293 and 297.

In Ref. 298, Smalyuk *et al.* extended the differential-imaging technique to compare time-integrated monochromatic images obtained with an x-ray microscope within (at ~4.60 keV) and outside (at ~4.87 keV) the spectral region of Ti 1*s*–2*p* absorption. The additional sensitivity of this technique permitted the central and outer parts of the shell, where the compression and modulations are smaller, to be diagnosed. As indicated in Fig. 8-10(a), Ti-doped layers were placed (on different shots) at 1, 5, 7, and 9 μm from the inner CH shell surface (~10 μm of the original 20-μm shell is ablated), allowing the rms modulation at peak compression to be compared at different locations in the shell [Fig. 8-10(b)]. The modulations are highest at the inner surface, which was unstable during the deceleration phase. These modulations decrease in the bulk of the shell and then increase near the outer surface (in the 9-μm layer), which was unstable during the acceleration phase.

In a collaboration among the University of Nevada (Reno), LLNL, and LLE, Tommasini *et al.*[299] extended the

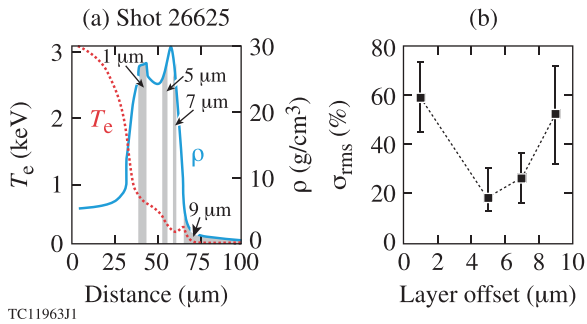

FIG. 8-10. (a) *LILAC*-simulated profiles of electron temperature T_e and target density ρ at peak compression for the implosion of a 20-μm CH shell filled with D^3He gas. The shaded areas indicate the locations of 1-μm-thick layers of Ti-doped CH initially placed with their inner radii at 1, 5, 7, or 9 μm from the inner CH surface. (b) Relative areal-density modulation σ_{rms} as a function of the layer offset, obtained from time-integrated x-ray microscope images inside and outside the Ti 1*s*–2*p* absorption spectral region. The dashed line connects the data points. Reproduced with permission from Phys. Plasmas **10**, 830 (2003). Copyright 2003 AIP Publishing LLC.

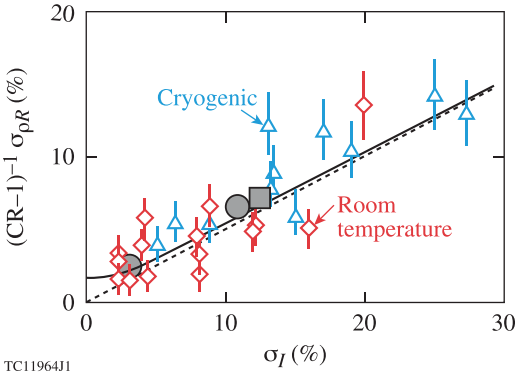

FIG. 8-11. Measured rms areal-density modulation $\sigma_{\rho R}$ (%) divided by (CR–1), where CR is the convergence ratio, as a function of the rms laser nonuniformity σ_I (%), from a large number of OMEGA room-temperature and cryogenic implosions. The solid line represents a best fit to the data, which agrees well with Eq. (8-1) (dashed line). The solid symbols are from 2-D simulations. Reprinted with permission from Li *et al.*, Phys. Rev. Lett. **92**, 205001 (2004). Copyright 2004 American Physical Society.

multi-pinhole spectral imaging technique described in Ref. 292 to multiple viewing axes. In these experiments, Nagayama *et al.*[300] used line emission from targets containing Ar-doped fuel to reconstruct the 3-D spatial structure of the electron temperature and density in the compressed core of OMEGA implosions.

Very low mode nonuniformities have been studied on OMEGA by Séguin *et al.*[301,302] and Li *et al.*[303] using proton diagnostics to measure the compressed target ρR at typically 8–11 locations around the target chamber. Measurements were made of primary protons from D^3He implosions and secondary protons from D_2 implosions, some of which were cryogenic. Li *et al.* analyzed a wide variety of implosions that were driven by both shaped (18-kJ) and 1-ns temporally flat (23-kJ) laser pulses. The laser nonuniformity on target was inferred from the offsets of the target from target chamber center (TCC) and energy and pulse-shape diagnostics. Li *et al.* postulated that the measured areal-density modulations averaged over angle $\sigma_{\rho R} = \langle \delta(\rho R) \rangle / \langle \rho R \rangle$ were proportional to the intensity nonuniformity $\sigma_I = \langle \delta I \rangle / \langle I \rangle$ and amplified through convergence according to

$$\sigma_{\rho R} \approx \frac{1}{2}(\mathrm{CR} - 1)\sigma_I, \tag{8-1}$$

where CR is the convergence ratio of the implosion. The results are shown in Fig. 8-11, where good agreement is seen. The fit to the data (solid line) does not go through the origin; the offset represents other sources of nonuniformity as σ_I approaches zero.

B. Cryogenic implosions

The use of cryogenic spherical targets containing layers of solid or liquid DT was proposed in the earliest publications on laser-induced compression. Nuckolls *et al.*[1] envisaged a hollow sphere of fusion fuel, Brueckner and Jorna[33] simulated a solid DT shell (obtaining a yield of 52 MJ from an incident laser energy of 680 kJ), Clarke *et al.*[104] found a gain of 4.7 for just 1.9 kJ of CO_2 energy incident on a DT shell, and Mason[105] reported parameter studies to optimize the performance of DT layers inside glass shells (microballoons). Mason noted that attempts to freeze DT inside microballoons resulted in the formation of a localized DT globule rather than the desired uniform layer and suggested that a transient state with a liquid layer might be preferable.

This section reviews cryogenic implosion experiments, starting with early experiments at KMS using 1-μm laser irradiation and DT layers of 1- to 2-μm thickness. These were followed by experiments on the 24-beam OMEGA laser at 0.35-μm wavelength using ~5-μm DT layers, at KMS at 0.53 μm using ~1-μm D_2 layers, and at Osaka at 0.53 μm using ~10-μm-thick foam layers wetted with liquid D_2. The OMEGA experiments yielded areal densities ρR of 20–35 mg/cm^2. The remainder of this section reviews an extensive series of cryogenic implosion experiments on the 60-beam OMEGA laser, spanning more than a decade and ongoing, using solid layers of thickness up to 100 μm. Initially, D_2 layers were used with the rms nonuniformity decreasing from ~9 μm to ~2 μm. Subsequently, DT layers have been used with the rms nonuniformity ~1 μm and below. The ρR has consistently increased, reaching ~100 mg/cm^2 for D_2 and ~300 mg/cm^2 for DT, as improvements have been made in layer uniformity, target positioning accuracy, and pulse shaping. The importance of shock timing in the design of pulse shapes, the most recent of which use triple pickets, has been identified.

The evolution of cryogenic systems that can produce uniform layers of DT in fusion targets is reviewed in Sec. XIII. Pioneering work was done at KMS Fusion, leading to the first report of direct-drive cryogenic implosions by Henderson and Johnson[304] in 1977. Henderson and Johnson condensed the DT fuel into a continuous liquid layer on the inner surface of small, ~60-μm-diam glass targets with an ~1-μm wall thickness. They used a point-contact conduction-cooling technique that allowed the target to be exposed to room-temperature radiation. Even though the DT layer was nonuniform, they found an increase of neutron yield compared with a similar target irradiated at room temperature (9×10^6 neutrons compared with 3×10^5). Further results from KMS were presented in 1982 by Storm *et al.*[305] They used two 1-μm laser beams in the ellipsoidal-mirror geometry of Fig. 4-3(a) to irradiate ~120-μm-diam glass microballoons, 2–5 μm thick, containing an ~2-μm layer of solid DT. The fast-refreeze technique used to form the layers is described in Sec. XIII. Storm *et al.* inferred compressed densities of ~1 g/cm^3 from the x-ray pinhole-camera images. They recommended the use of shorter-wavelength (0.53-μm) light to reduce the impact of hot electrons.

The KMS cryogenic system was adapted for use on the 24-beam OMEGA laser (Sec. XIII A). The OMEGA experiments were reported by McCrory *et al.*[306] and Marshall *et al.*[307] The targets used were spherical glass shells with a 3- to 5-μm wall thickness and a 100- to 150-μm outer radius. The solid DT layers were formed by using the fast-refreeze technique and were ~5 μm thick. The laser delivered 1–1.2 kJ of energy at a 0.35-μm wavelength in 650-ps Gaussian pulses with peak drive intensities up to 6×10^{14} W/cm^2. The targets were supported by three to five spider silks mounted on a U-shaped cradle.

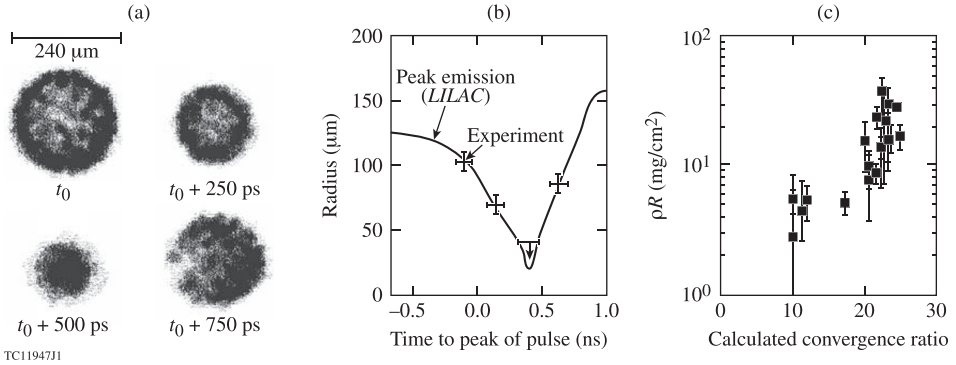

FIG. 8-12. (a) Time-resolved x-ray framing-camera images of an imploding cryogenic DT target of ~240-μm initial diameter, driven by the 24-beam OMEGA laser. (b) Comparison of measured and simulated x-ray radii as functions of time during the implosion. (c) Measured fuel areal density ρR as a function of calculated convergence ratio. Reprinted with permission from McCrory *et al.*, Nature **335**, 225 (1988). Copyright 1988 Macmillan Publishers Ltd.

The implosion trajectory was diagnosed with a four-frame x-ray framing camera.[308,309] A sequence of images of a cryogenic target implosion is shown in Fig. 8-12(a), covering both the implosion and disassembly phases. Figure 8-12(b) shows that the measured trajectory agrees very closely with the trajectory predicted by the 1-D hydrodynamics code *LILAC*. The areal density ρR was inferred using the knock-on technique.[276,277] The measured areal density, shown in Fig. 8-12(c) as a function of calculated convergence ratio, reached ~20–35 mg/cm^2 at the highest convergence ratios. The inferred fuel density was 20–40 g/cm^3, corresponding to 100–200× the density of liquid DT. These areal and mass densities were the highest measured at that time. However, the neutron yield was only ~10^{-3} of predicted, for which residual imperfections in the level of irradiation uniformity were offered as a probable explanation.[306,307]

Further cryogenic experiments at KMS, using deuterium fuel, were reported by Johnson *et al.*[310] A 0.53-μm laser wavelength and the shaped laser pulse shown in Fig. 8-13(a) were used to reduce the preheating of the compressing fuel. Two beams of the Chroma laser delivered ~200 J to target. The targets were spherical polyvinyl alcohol shells of 110- to 150-μm diameter and 3- to 7-μm shell thickness. They were filled with 8–12 ng of deuterium, which formed an ~1-μm-thick layer when cooled. The low laser energy precluded the observation of nuclear reaction products. A third laser beam with 60–120 J of energy irradiated an Al or Mo backlighter target; streaked x-ray backlighting (with ~1.6-keV x rays for Al and ~2.6-keV x rays for Mo) was then used to determine the shell trajectory and target compression. The compressed shell was completely opaque at peak compression. Figure 8-13(b) shows a streaked image of an imploding shell and a corresponding intensity lineout at peak compression, giving a compressed core diameter of 21 μm. The simulated implosion trajectories and coronal plasma scale lengths were in good agreement with the experimental measurements. Johnson *et al.* inferred compression up to 80–200× liquid deuterium density.

In the early 1990s, Nakai *et al.*,[311] Tanaka *et al.*,[312] and Kitagawa *et al.*[313] reported implosions of cryogenic foam targets wetted with liquid deuterium. Typical targets were 10-μm-thick, 500- to 700-μm-diam foam shells coated with a 4-μm plastic ablator. The targets were imploded with twelve 0.53-μm beams of the GEKKO XII Laser System. The energies ranged from 4 to 12 kJ in a 1.5- to 2.5-ns Gaussian laser pulse. The areal density ρR of the compressed deuterium fuel was determined by secondary neutron production in the deuterium fuel,[314] while the total ρR (fuel plus ablator) was obtained from the slowing down of the 3-MeV protons produced in the D–D reaction.[41] A typical proton spectrum is shown in Fig. 8-14(a). The peak occurs at ~1.8 MeV, indicating a downshift of ~1.2 MeV. Figure 8-14(b) shows areal densities inferred from each technique as functions of the simulated convergence ratio. Typical fuel areal densities were 6 mg/cm^2 with total areal densities ~12 mg/cm^2 (Ref. 312). The neutron yields were ~1% of those predicted by 1-D simulations.[311]

In 2000, a multi-year series of direct-drive cryogenic target implosions began on the 60-beam, 30-kJ OMEGA laser with pure deuterium layers. The goal of these experiments was to study the implosion of targets hydrodynamically equivalent to direct-drive NIF ignition targets. Early results were reported in 2002 by Stoeckl *et al.*[315] for ~1000-μm-diam, ~3-μm-thick CH shell targets, which were initially filled with up to 1000 atm of D_2 to provide 100-μm-thick ice layers when cooled. The best layers had an rms

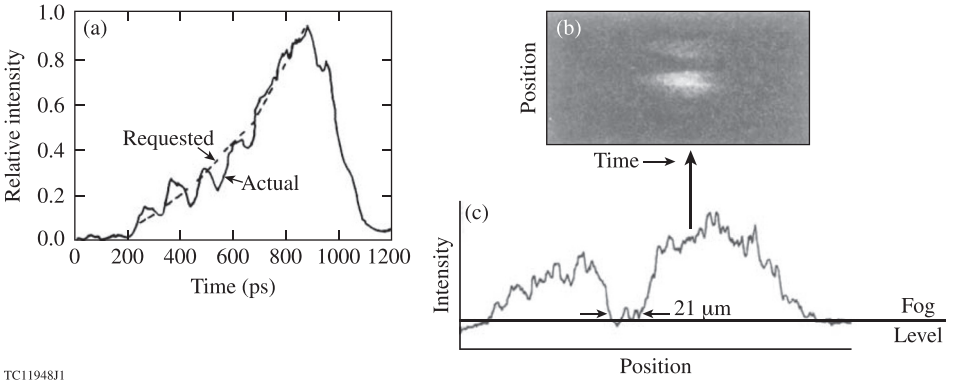

FIG. 8-13. (a) Ramped laser pulse used in KMS cryogenic D_2 implosions. (b) Streaked x-ray radiograph of an imploding shell using an Al backlighter. (c) A lineout of (b) taken at peak compression, indicated by the arrow in (b). The compressed target diameter is inferred to be 21 μm. Reprinted with permission from Johnson *et al.*, Phys. Rev. A **41**, 1058 (1990). Copyright 1990 American Physical Society.

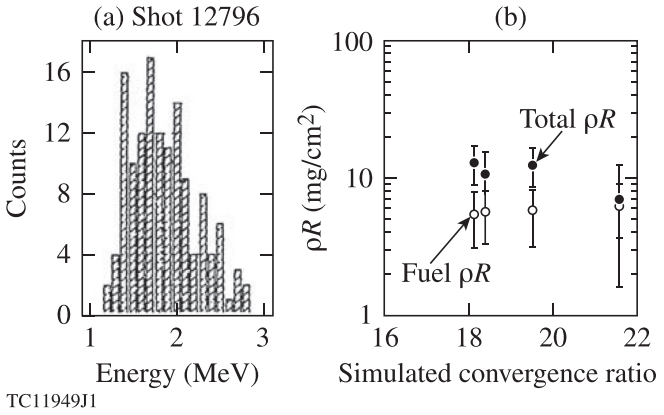

FIG. 8-14. (a) Proton spectrum for a cryogenic D_2 wetted-foam target imploded at Osaka, indicating a downshift of ~1.2 MeV from the birth energy of 3.0 MeV. (b) Measured areal density ρR versus simulated convergence ratio. The total ρR is obtained from proton spectra such as (a), while the fuel ρR is estimated from secondary neutrons. Reproduced with permission from Phys. Plasmas **2**, 2495 (1995). Copyright 1995 AIP Publishing LLC.

nonuniformity of 9 μm. Stoeckl *et al*. used a 1-ns temporally flat laser pulse, whose rapid rise put the fuel on a high adiabat α (electron pressure divided by Fermi pressure) of 25. They obtained a yield of 3×10^{10}, ~30% of the 1-D prediction, and an areal density ρR (determined from the energy downshift of secondary protons) of ~30 mg/cm^2, somewhat lower than the simulated 40 mg/cm^2. They suggested that layer quality was important, with imprint appearing to be less critical.

These experiments were extended in 2003 by Sangster *et al*.[316] to include targets irradiated with a lower-adiabat ($\alpha \sim 4$) laser pulse. Results for the primary neutron yield relative to the 1-D prediction, known as the YOC, and the areal density are shown in Fig. 8-15 as functions of the ice roughness and the target offset from TCC. The $\alpha \sim 4$ targets tended to have lower YOC but higher areal density (up to ~80 mg/cm^2), and the areal density decreased with target offset, but there was considerable scatter in the data. One shot with $\alpha \sim 25$ gave a YOC of 96% (1.3×10^{11} neutrons). The ice roughness affected the targets with $\alpha \sim 4$ but not those with $\alpha \sim 25$. Clear evidence of technical problems in correctly positioning the target at shot time is seen in Fig. 8-15(d), which includes offsets up to 130 μm (offsets of $\lesssim$10 μm are desired[317]). Target layers were improved over Ref. 315, with the best layers having an rms nonuniformity of ~3 μm, but the limitations of layering in D_2 (compared with DT) were noted. In 2004, McKenty *et al*.[318] reported lower target offsets within 40 μm of TCC, with many at ~20 μm. They also reported the first D_2 wetted-foam implosion on OMEGA, producing 1.8×10^{11} neutrons.

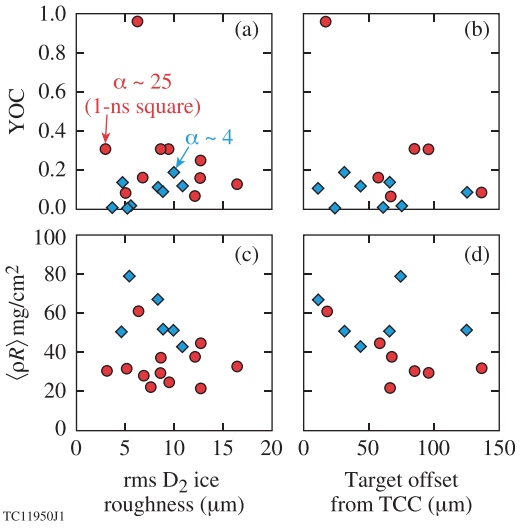

FIG. 8-15. Results from early cryogenic D_2 implosion experiments on the 60-beam OMEGA laser. (a) and (b) The ratio of the primary neutron yield to the 1-D predicted yield [the yield-over-clean (YOC)] plotted against the preshot inner D_2 ice layer roughness and the target offset from target chamber center (TCC), respectively. (c) and (d) Same as (a) and (b) but for the average areal density $\langle \rho R \rangle$. Reproduced with permission from Phys. Plasmas **10**, 1937 (2003). Copyright 2003 AIP Publishing LLC.

Further cryogenic D_2 experiments were reported in 2005 by Marshall *et al*.[319] for implosions with various values of α. The measured ρR reached ~100 mg/cm^2. The laser absorption, the neutron production time, images of the fuel core obtained from an x-ray microscope and an x-ray framing camera, and the continuum x-ray spectrum all agreed with 1-D simulations (using a flux limiter f of 0.06) of an $\alpha = 4$ implosion. The D_2 ice layer's nonuniformity was reduced further to ~2 μm rms. However, an increasing falloff in the ρR from predicted was observed with decreasing α, as shown in Fig. 8-16. Sangster *et al*.[320] suggested that one possible factor contributing to the low observed values of ρR could be "burn truncation," i.e., the fusion yield could have been terminated by inner-surface instability growth before the peak ρR was achieved. As a result, the proton-downshift method for measuring ρR would sample only lower densities. This suggestion was consistent with observations in Ref. 320 of reabsorption in the continuum x-ray spectrum, from which a much higher peak ρR in the compressed core of ~190 mg/cm^2 was inferred.

In late 2006, the focus of cryogenic experiments on OMEGA began to shift to DT targets. In 2007, Sangster *et al*.[320] reported DT layers with roughness below 1 μm (rms), the inner-surface smoothness requirement for ignition. They also provided a comprehensive description of the OMEGA cryogenic system and a historical review of cryogenic target development.

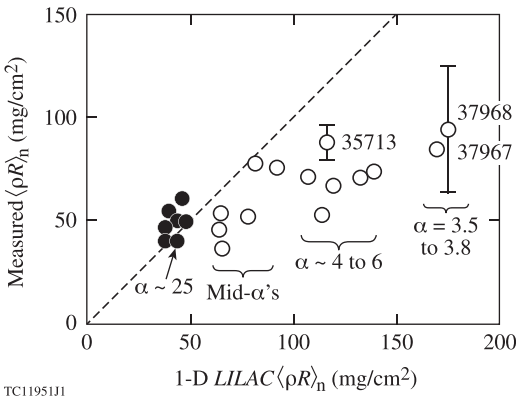

FIG. 8-16. Measured neutron-averaged areal density $\langle \rho R \rangle_n$ as a function of the 1-D predicted value. The ranges of fuel adiabat α are also indicated (mid-α's correspond to $\alpha \sim 6$ to 12). Reproduced with permission from Phys. Plasmas **12**, 056302 (2005). Copyright 2005 AIP Publishing LLC.

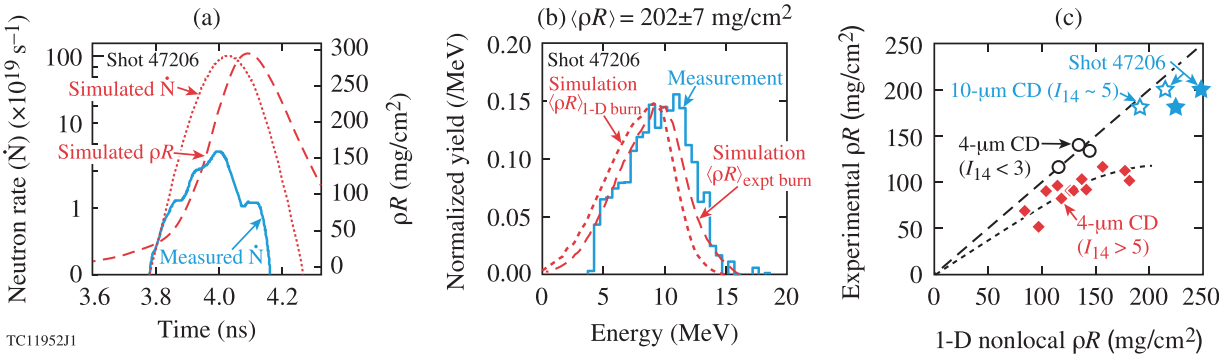

FIG. 8-17. (a) Simulated and measured neutron production rate $\dot{N}(t)$ and simulated ρR as functions of time t for the cryogenic D_2 shot 47206, which gave a ρR of $\sim$200 mg/cm^2. The target was a 10-μm-thick CD shell with a 95-μm-thick D_2 layer driven on an $\alpha = 2$ adiabat at 5×10^{14} W/cm^2. (b) Measured secondary proton spectrum from shot 47206 together with simulations averaged over the 1-D and experimental $\dot{N}(t)$. (c) Measured ρR and the ρR simulated using a 1-D nonlocal model for 4- and 10-μm-thick CD shells. I_{14} indicates the laser intensity in units of 10^{14} W/cm^2. The simulations used the 1-D $\dot{N}(t)$ except for the open stars, where the averaging was performed over the measured $\dot{N}(t)$ for the shots indicated by solid stars. (a) and (b) Reproduced with permission from Phys. Plasmas **15**, 056310 (2008). Copyright 2008 AIP Publishing LLC. (c) Reprinted with permission from Sangster *et al.*, Phys. Rev. Lett. **100**, 185006 (2008). Copyright 2008 American Physical Society.

Implosions with D_2 layers continued for a while. A dramatic increase in the maximum ρR to 200 mg/cm^2 was reported in 2008 by Sangster *et al.*[321] and Goncharov *et al.*[322] This was accomplished by increasing the CH shell thickness from $\sim$3 μm to 10 μm, adding a picket to the beginning of the pulse for adiabat shaping, and driving the target with a shaped pulse designed for $\alpha = 2.5$ with a peak intensity of $\sim 5 \times 10^{14}$ W/cm^2. Some results from these experiments are shown in Fig. 8-17. Burn truncation is demonstrated in Fig. 8-17(a), which shows the experimental and simulated neutron production rate $\dot{N}$ and the simulated ρR as functions of time t. The secondary proton spectrum of Fig. 8-17(b) implied a ρR of $\sim$202 mg/cm^2 and was matched better by a simulation that used the experimental $\dot{N}(t)$ rather than the simulated $\dot{N}(t)$. The predicted peak ρR reached $\sim$300 mg/cm^2 [Fig. 8-17(a)], but this could not be directly observed. The comparison between experimental and simulated ρR, shown in Fig. 8-17(c), is greatly improved over that of Ref. 319. The deviation from calculated values observed in the data of Fig. 8-17(c) for the 10-μm-thick shells is largely explained by burn truncation. Simulations using the experimental $\dot{N}(t)$ (open stars) show much better agreement with the data.

Insight into this improvement was provided by Goncharov *et al.*,[322] who identified two effects (in addition to burn truncation) as possible explanations for the results of Fig. 8-16: (1) shock mistiming caused the experimental ρR to be too low and (2) hot-electron preheating raised the adiabat above that calculated. Goncharov *et al.* described a nonlocal model for heat conduction (added to *LILAC*), which improved the calculation of shock timing (Sec. XII B). Later work reported by Goncharov[43] showed that short-scale mix caused by the Rayleigh–Taylor instability at the ablation front was not the cause of the ρR degradation—when beam smoothing was turned off, the yield dropped by a factor of 2 but the areal density remained unchanged.

Deviations from simulation seen in Fig. 8-17(c) for the 4-μm data at laser intensities above 5×10^{14} W/cm^2 led Sangster *et al.*[321] and Smalyuk *et al.*[323] to suggest that hot-electron preheat might play an important role in increasing the fuel adiabat at higher intensities. Sangster *et al.* found more hard x rays from the targets with thinner CD shells, which was consistent with expectations of greater hot-electron generation through the two-plasmon–decay instability (Sec. X A), once the quarter-critical surface moved into the DT. Other experimental data,[43] however, seemed to indicate that inaccuracy in the predicted shock timing was the dominant degradation mechanism. Difficulty in ensuring accurate shock timing also persisted in the design for the 10-μm-thick shell. While the 10-μm target shown in Fig. 8-17(c) (shot 47206) reached near 1-D compression, small deviations in the pulse shape or shell thickness led to drops in the measured areal density below predictions.[43] Smalyuk *et al.*[324] attempted to extend the ρR measurements to higher intensities (10^{15} W/cm^2) but found lower values of ρR, ascribed to a combination of shock mistiming and preheat.

Further success in increasing the areal density was reported in 2010 by Goncharov *et al.*[42] and Sangster *et al.*[317] Their targets ($\sim$860-μm-diam, 10-μm-thick CD shells surrounding an $\sim$65-μm-thick layer of DT ice) were irradiated with a triple-picket laser pulse with a peak intensity of $\sim 8 \times 10^{14}$ W/cm^2 designed to put the fuel on an adiabat $\alpha \sim 2$. The areal density was determined from the energy loss of primary 14-MeV neutrons as they passed through the dense fuel. These neutrons were diagnosed using a magnetic recoil spectrometer (MRS) (Ref. 325)—the neutrons produce forward-scattered deuterons from a CD foil placed close to the target, which are then energy resolved using a magnetic spectrometer. A representative deuteron spectrum is shown in Fig. 8-18(a), with a best fit indicating a ρR of 295 ± 66 mg/cm^2. From a comparison given by Frenje *et al.*[326] of this spectrum and two other spectra from shots with lower ρR, the ρR is determined primarily by the ratio of the two left-most points in Fig. 8-18(a) to the peak. This was the first time that DT fuel had been compressed to an areal density sufficient to initiate a thermonuclear burn wave.

The experimental and simulated ρR are compared in Fig. 8-18(b) for two sets of shots that used the different laser pulse shapes shown in the figure. The highest value of ρR was obtained for the case with a foot on the rising portion of the main pulse. The optimum pulse shape designs were based on simulations that matched data from shock-timing experiments (Sec. XII B). The experimental and simulated ρR match very

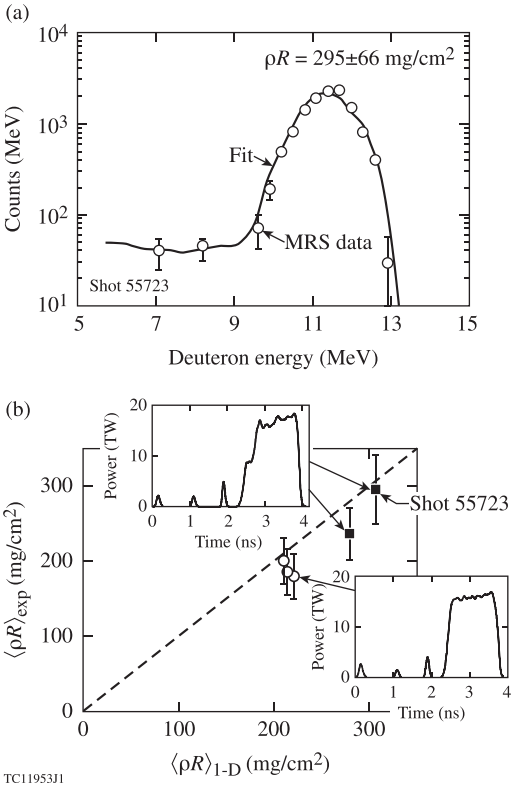

FIG. 8-18. (a) Deuteron spectrum obtained by a magnetic recoil spectrometer (MRS) for a cryogenic DT implosion on OMEGA, together with a fit indicating an areal density ρR of $\sim$300 mg/cm^2. Reproduced with permission from Phys. Plasmas **17**, 056312 (2010). Copyright 2010 AIP Publishing LLC. (b) Experimental and simulated $\langle \rho R \rangle$ for cryogenic targets with two triple-picket pulse shapes, one including a foot on the rising portion of the main pulse. Reprinted with permission from Goncharov *et al.*, Phys. Rev. Lett. **104**, 165001 (2010). Copyright 2010 American Physical Society.

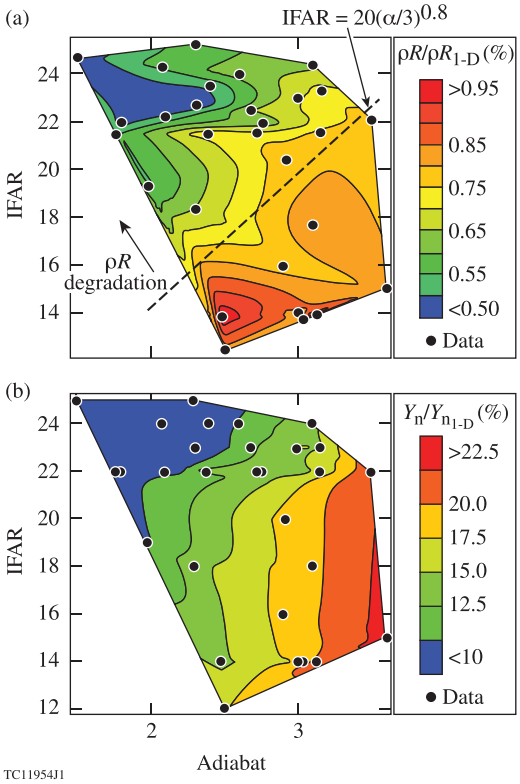

FIG. 8-19. Contour plots showing (a) the areal density ρR relative to 1-D predictions and (b) the yield relative to 1-D predictions as functions of adiabat and in-flight aspect ratio (IFAR) for cryogenic DT targets with ice roughness less than 1.5 μm and offsets from target chamber center less than 20 μm. The contours are obtained by interpolating among the experimental data points (represented by the black dots). Reproduced with permission from Phys. Plasmas **20**, 056317 (2013). Copyright 2013 AIP Publishing LLC.

closely. The predicted implosion velocity for these designs was 3×10^7 cm/s, higher than the 2.2×10^7 cm/s for the 10-μm CD shells of Fig. 8-17(c). The higher velocity was obtained by increasing the laser intensity from 5×10^{14} to 8×10^{14} W/cm^2 and reducing the ice thickness from 95 to 65 μm.

One other change implemented in these experiments was the replacement of silk mounts with stalks.[317] This made the targets less susceptible to vibration and easier to position accurately at TCC. On the shot that yielded 300 mg/cm^2, the target offset was $\leq$10 μm. Since the stalk is slightly cooler than the target, the ice was found to be slightly thicker in the vicinity of the stalk, leading to an average layer nonuniformity of 1.9 μm (rms), but modifications to the layering system were proposed to restore the submicron roughness obtained for silk-mounted targets. Another motivation for using stalk mounts was work by Marshall *et al.*,[327] who found a yield improvement by a factor of $\sim$2 for room-temperature targets when silks were replaced by stalks, and by Igumenshchev *et al.*,[328] who used hydrodynamic simulations to show that stalk mounts result in smaller perturbations to the imploding target.

The increased accuracy in target positioning and the reproducibility of good-quality ice layers made possible a systematic study of implosion performance reported in 2013 by Sangster *et al.*[329] They described a set of 29 DT implosions carried out over a period of 18 months, all of which had an offset of less than 15 μm from TCC, an ice-layer nonuniformity less than 2 μm, and acceptable pulse shape quality (typically the picket energies were within 10% of the design specification). They varied the IFAR, defined as the shell radius divided by the shell thickness, and the adiabat α. When they plotted the ratio of measured to predicted areal density ($\rho R/\rho R_{1\text{-D}}$) against each parameter separately, they found that the areal-density ratio generally dropped for IFAR above 17 and α below 2.5, but there was considerable scatter in the data. A clearer pattern emerged, however, when the data were plotted in the 2-D (α, IFAR) space, as shown in Fig. 8-19(a) for the areal-density ratio and in Fig. 8-19(b) for the YOC. Contours were drawn by using linear interpolation among the data points. The small-scale structures in the contour lines have no physical meaning since they reflect scatter in the experimental data, but the overall trends are clear. The dashed line in Fig. 8-19(a) bounds an area in which the experimental ρR is within 80% of predicted. For these shots, the yield degradation is largely a function of α.

Sangster *et al.*[329] ascribed much of the deviation from 1-D behavior for the better-performing targets to burn truncation and ^{3}He buildup in the target as a result of tritium β-decay. In addition, they found evidence for carbon mixing into the core (presumably caused by Rayleigh–Taylor growth) for adiabats below $\sim$2.3, based on enhanced core

x-ray emission for these shots. They suggested that the instability was seeded by contaminants in the DT fuel condensing on the target's outer surface. Imprint was not considered to be an issue since no difference in performance was observed for targets with the outer portion of the CD shells doped with Si to reduce imprint. Similar observations of enhanced x-ray emission were made by Ma *et al.*[330] for indirect-drive implosions.

A comprehensive account of the D_2 and DT cryogenic implosion experiments on OMEGA from a theoretical perspective is given by Goncharov,[43] who discusses issues related to fuel adiabat, implosion velocity, hot-electron preheat, laser coupling, thermal transport, shock timing, and stability. Design considerations for NIF-scale ignition targets are also covered.

C. Polar-drive implosions

From its earliest days, a spherically symmetric irradiation geometry for direct-drive implosions has been taken for granted. This is still the expectation for the long-term realization of direct-drive inertial fusion energy. However, at two times in the evolution of large laser systems, it has been desired to carry out direct-drive experiments on facilities built for indirect drive with irradiation geometries far from being spherically symmetric.

The first case arose with the 20-beam Shiva laser, where all laser beams were incident at angles θ less than 18° from the vertical (Sec. VIII A). Manes[331] described a 3-D uniformity code that was used to optimize the aim points of the laser beams on the target to improve the deposition at the equator and to avoid excessive heating at the poles. This was not totally successful, as can be seen from the x-ray images of Fig. 8-2. The implosion would probably have been much more nonuniform had it not been for the symmetrizing effect of suprathermal electrons.

The second and more-important case has arisen with the NIF, which was built with its beams incident at nominal angles θ of 23.5°, 30°, 44.5°, and 50°. The 192 beams are grouped into 48 "quads" (each containing four beams), entering the target chamber through what will be referred to as the 48 "indirect-drive ports." However, the as-built NIF did not meet the initial intention of providing a versatile irradiation facility that would accommodate both direct and indirect drive. In collaborative work between LLNL and LLE in 1995, Eimerl *et al.*[332] and Eimerl[333] proposed a 72-port configuration that would accomplish this goal. An additional 24 ports, known as the "direct-drive ports," would be added in two rings above and below the equator. Half of the beams (those with $\theta = 30°$ and 50°) would be diverted to the direct-drive ports to provide a spherically symmetric direct-drive option. The direct-drive ports were included in the NIF target chamber (with $\theta = 77.5°$), but the optics to route beams into these ports were never added.

As described in the introduction of Ref. 334, Eimerl *et al.*[332] had considered the option of repointing the beams from the indirect-drive ports so that some of the beams would not be directed radially, but dismissed this as ineffective. From Ref. 333, the uniformity of illumination would be compromised by the critical surface moving in as the target implodes, with the aim points (apparent positions) of the beams on the critical surface changing their θ values during the implosion. However, when it became apparent that the full implementation of direct drive on the NIF could be significantly delayed, Kilkenny[335] suggested that the option of using nonradial beams be reconsidered. This option is now known as polar drive (or equivalently, polar direct drive).

The first 2-D hydrodynamic simulations of polar drive [in (r,θ) geometry] were reported by Craxton[336] using the code *SAGE*, which included full 3-D ray tracing following the algorithm described in Ref. 337 for all the laser beams with the deposited energy averaged in the azimuthal direction. This approach, routinely used in subsequent hydrodynamic simulations of polar drive, overcomes some of the limitations of the simpler models of irradiation uniformity described in Sec. VI because the distributed absorption along ray paths and the thermal conduction of energy from its deposition radius to the ablation radius are included in the modeling. Consistent with the Shiva experience, Craxton found weak drive around the equator associated with the laser energy being refracted away from the critical surface. To overcome this, he proposed large repointings of some of the beams toward the equator and the use of phase plates that would produce elliptical focal spots (compressed in the θ direction) for these beams.

The primary physics issues associated with polar drive are illustrated in Fig. 8-20 (from Ref. 338), which shows laser ray trajectories through the underdense plasma for a representative NIF polar-drive simulation. The rays all enter at 50° from the vertical but with the center of the beam pointed close to the equator rather than at the center of the target. The beam repointing is equivalent to a spatial translation of the beam. The rays propagate according to geometrical optics, bending away from higher densities because the refractive index $[= \sqrt{(1 - n_e/n_c)}$, where n_e is the electron density and n_c is the critical density] is smaller than unity. Figure 8-20 illustrates four challenges that must be overcome in polar-drive designs: (1) as a result of the beam translation, some energy is lost from the edge of the beam; (2) once a plasma has formed, the energy in the equatorial region is deposited at larger radii, farther from the ablation surface, with no rays reaching the critical surface; (3) the irradiation pattern on the target is time dependent, with rays near the center of the beam in the figure having their turning point above the equator at the earlier time and below the equator at the later time; and (4) the large amount of ray crossing that occurs especially near the equator increases the possibility that effects associated with cross-beam energy transfer (CBET) (Sec. X B) will be important.

Skupsky *et al.*[339] followed with initial polar-drive designs for the NIF using wetted-foam targets. They proposed the configuration shown in Fig. 8-21(a) for repointing the NIF beams. The four beams within each quad are moved together. The resulting aim points (squares) correspond to the three rings in each hemisphere that would result from the direct-drive NIF configuration—four quads at 23.5°, eight quads at 44.5°, and 12 quads at 77.5°. They extended the specification of the focal spots of the equatorial beams to an asymmetric superposition of two super-Gaussian profiles,

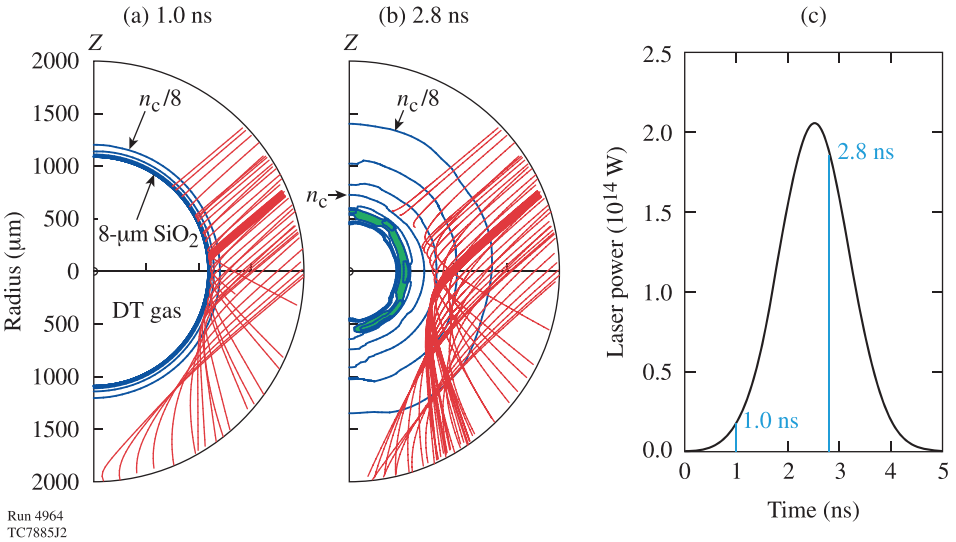

FIG. 8-20. Ray-trace plots for a representative polar-drive implosion on the NIF (a) at 1.0 ns, near the start of the laser pulse, and (b) at 2.8 ns, when the shell (density above $4n_c$, green shaded area) has imploded halfway. These plots show a selection of rays of the 50° ring of beams and some density contours, n_c indicating the critical density. The rays propagate in 3-D space, with their paths projected onto the plane of the figure. (c) Laser pulse shape, indicating the times of the ray-trace plots. Reproduced with permission from Phys. Plasmas **15**, 082705 (2008). Copyright 2008 AIP Publishing LLC.

including a highly elliptical profile to concentrate energy very close to the equator. They also proposed using different temporal pulse shapes in the different rings of quads to increase the power near the equator as the target imploded. They suggested that polar drive could achieve "at least near-ignition conditions" on the NIF.

Soon thereafter, Craxton *et al.*[334] reported initial polar-drive experiments on OMEGA using the 40-beam subset shown in Fig. 8-21(b). The OMEGA geometry has four rings of beams in each hemisphere, at angles θ of 21°, 42°, 59°, and 81°. With the equatorial (81°) beams removed, the OMEGA geometry provides a fairly close approximation to the NIF geometry. Some of the equatorial beams were used for x-ray backlighting. The targets—20-μm-thick, 865-μm-diam CH shells filled with 15 atm of D_2—were imploded with a 1-ns temporally flat laser pulse containing ~16 kJ of energy. Similar 40-beam configurations had been used earlier by Glendinning[340] and Kyrala *et al.*[341] to diagnose approximately spherical implosions with x-ray backlighting.

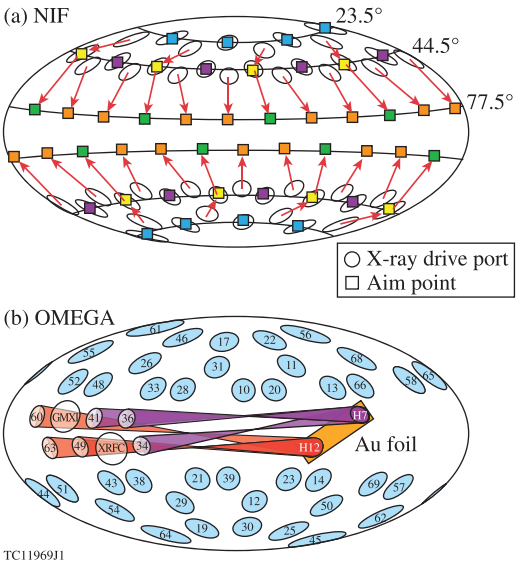

FIG. 8-21. (a) Polar-drive scheme proposed by Skupsky *et al.*[339] for repointing NIF quads from their x-ray-drive ports to direct-drive aim points closer to the equator. The angles indicated are lines of latitude containing the aim points. Reproduced with permission from Phys. Plasmas **11**, 2763 (2004). Copyright 2004 AIP Publishing LLC. (b) Geometry for polar-drive experiments on OMEGA, in which 40 of the 60 beams are used to drive the target and some of the 20 equatorial beams irradiate a gold x-ray backlighter foil, viewed, in particular, by an x-ray framing camera (XRFC). Reproduced with permission from Phys. Plasmas **12**, 056304 (2005). Copyright 2005 AIP Publishing LLC.

Typical x-ray framing-camera images at successive times, viewed from close to the equator, are shown in Fig. 8-22(a). The images include shadows resulting from absorption by the imploding shell. The first image, taken just before the end of the laser pulse at ~1 ns, shows a ring of self-emission from the hot corona. Figure 8-22(b) shows the trajectory of the imploding shell as obtained at earlier times from an imaging streak camera (which views the coronal self-emission) and at later times from x-ray framing-camera images. The trajectory was consistent with simulations using *SAGE* and the 1-D code *LILAC* post-processed with *Spect3D*.[342] The images of Fig. 8-22(a) at 1.25 and 1.5 ns look round to the eye, but when analyzed carefully [Fig. 8-22(c)], they show small variations in θ of the x-ray absorption radius, in close agreement with simulation. In particular, the equator is underdriven with respect to the mid-latitudes, which was perhaps not surprising since beams with elliptical focal spots were not available for the experiment.

Further polar-drive experiments on OMEGA were reported by Marozas *et al.*[343] They demonstrated that the 2-D code *DRACO* could accurately model the implosions, as illustrated in Fig. 8-23 for a shot in which non-optimum beam repointings were used. The implosion images [Fig. 8-23(a)] showed the pole moving somewhat faster than the equator and were well matched by the simulated images [Fig. 8-23(b)]. A similarly good agreement between simulated and experimental images was found by Radha *et al.*[344] for implosions driven by triple-picket pulse shapes. Marshall *et al.*[345] obtained framing-camera images through the time of peak compression, showed that the implosion was close to 1-D up to the time of core self-emission, and obtained density profiles through Abel inversion that agreed well with 1-D simulations. Cobble *et al.*[346] used polar drive to implode targets on OMEGA in a campaign aimed at studying the

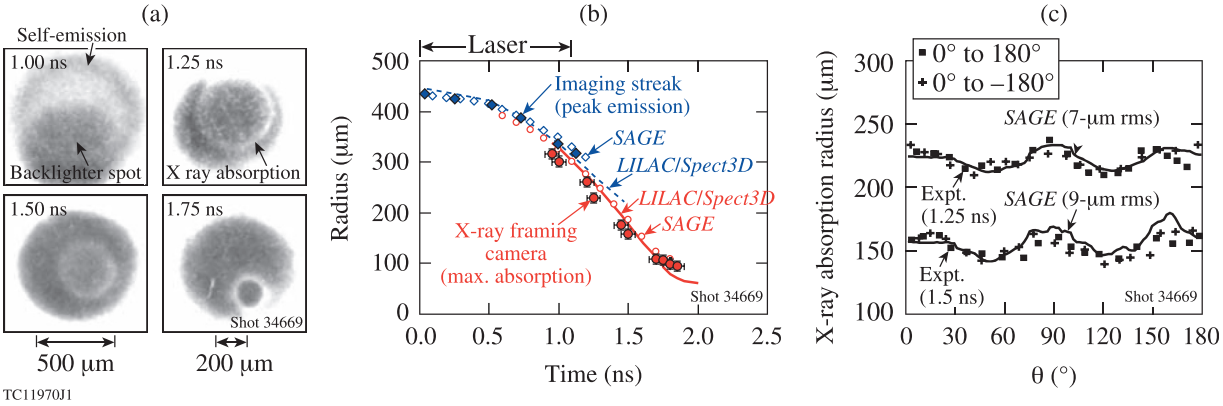

FIG. 8-22. A sequence of four backlit x-ray framing-camera images from the first polar-drive implosion experiments on OMEGA. The first image (at the end of the laser pulse, which delivered a steady 16 TW until it cut off at ~1.0 ns) shows a ring caused by self-emission from the corona, superposed on the smaller backlighter spot. The subsequent images show distinct rings of x-ray absorption, corresponding roughly to the inner edge of the imploding CH shell. (b) Measured trajectory of the imploding shell obtained from imaging streak and x-ray framing cameras and simulated using the codes *LILAC* and *SAGE*. (c) Measured and simulated variations of the radius of maximum x-ray absorption obtained from two of the images in (a) as functions of the polar angle θ. Reproduced with permission from Phys. Plasmas **12**, 056304 (2005). Copyright 2005 AIP Publishing LLC.

hydrodynamics associated with equatorial defects and found that both the trajectory and the pole-to-equator nonuniformity were well matched by *HYDRA*[347] simulations.

The demonstration that (a) polar drive can produce nearly round implosions and (b) the deviations from uniformity can be modeled was very encouraging and provided impetus for the continued development of polar-drive designs for the NIF. Marozas *et al.*[343] and Skupsky *et al.*[348] presented single-picket polar-drive designs for the NIF, incorporating concepts from Ref. 339. Marozas *et al.*[343] obtained a gain of 20 for a 1.36-MJ (incident energy) wetted-foam design. They described a procedure whereby the laser pulse shapes and focal-spot shapes of the different rings of beams were optimized for maximum time-dependent uniformity. They found it to be critically important for both shell and shock-front uniformity to be maintained at a high level throughout the drive pulse. An improperly timed shock front could cause a design to fail because of a small and distorted shock-heated hot spot, while small adjustments during the foot pulse could make the same target ignite by developing a large and minimally distorted hot spot. Skupsky *et al.*[348] used a wetted-foam target at 1 MJ, which ignited with a gain of ~30, and showed that the design was robust with respect to beam-pointing errors within the NIF capability. They also suggested the use of a "shimmed" target in which the equator is made thinner.

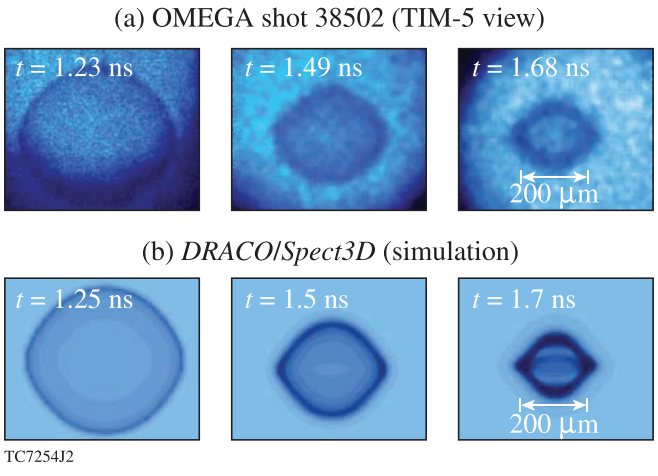

FIG. 8-23. (a) Experimental x-ray framing-camera images for a backlit polar-drive implosion on OMEGA with non-optimum beam pointings. (b) Corresponding images produced from *DRACO* simulations post-processed by *Spect3D*. The dark rings (minimum x-ray transmission) indicate the evolution of the shell distortion. Reproduced with permission from Phys. Plasmas **13**, 056311 (2006). Copyright 2006 AIP Publishing LLC.

This work was extended by Collins *et al.*,[197] who reported a polar-drive–ignition design for the NIF using an ~150-μm-thick DT ice layer inside a 3.3-mm-diam solid-CH ablator. The target was driven by 1.5 MJ of laser energy in a triple-picket pulse. The design achieved a gain of 32 in 2-D *DRACO* simulations including single-beam and multibeam nonuniformities and DT-ice and outer-surface roughness. The design had an in-flight aspect ratio of 36, a convergence ratio of 26, a peak implosion velocity of 4.3×10^7 cm/s, a peak fuel kinetic energy of 8.3 kJ, and a peak fuel pressure (from a simulation with alpha-particle transport switched off) of 305 Gbar. An important aspect of the design was the requirement that a 1-D multiple-frequency-modulator SSD scheme (Sec. VI C) be implemented on the NIF (2-D SSD being currently impractical). This scheme with its high bandwidth is employed only during the picket portion of the laser pulse, allowing safe laser operations during the high-intensity portion of the pulse. Collins *et al.* used asymmetric spot shapes as in earlier work, adding mask functions that operated near the edges of the beams to reduce the energy in the portion of the profile that would otherwise pass by the target substantially unabsorbed. The design called for an equatorial ice-layer shim as in Ref. 348. A target positioning accuracy of better than 20 μm was required.

A "Saturn" target design concept was proposed by Craxton and Jacobs-Perkins[349] in which a low-Z ring is placed around the target in the equatorial plane. Refraction through the expanding plasma formed around the ring allows the laser drive near the equator to be increased as the target implodes. Radiation from the ring to the target was later identified as an additional factor that increases the equatorial drive.[327] Saturn targets were demonstrated on OMEGA to increase the drive at the equator[334] and to produce yields close to those of energy-equivalent symmetric implosions

when the pointings were optimized.[327] However, because of the complexity of fielding a Saturn target in a cryogenic environment[343] and because the design of Ref. 197 without the ring produces uniformity consistent with a large gain, the Saturn concept has not been pursued further for the NIF.

One key aspect of all design work for polar-drive ignition on the NIF is the choice of appropriate phase plates. Recognizing the time involved in acquiring a full set of phase plates as well as the operational time required to change the phase plates on the laser system, Cok *et al.*[338] proposed that initial direct-drive experiments could be carried out conveniently by using the indirect-drive phase plates out of best focus and with appropriate repointings. (The best-focus NIF beams are too small to uniformly irradiate direct-drive targets.) Cok *et al.* used split quads, where different beams within a quad would be pointed to different aim points. For example, the upper two beams of a 44.5° quad would move only a short distance while the lower two beams would move closer to the equator. This achieves a similar effect in terms of energy balance to the configuration of Fig. 8-21(a) but retains the eightfold azimuthal symmetry of this ring of quads. Cok *et al.* also showed that the optimum repointings depend on the target material, with a higher-Z material such as SiO_2 requiring smaller shifts than a lower-Z material such as CH. Defocused indirect-drive phase plates have been used for implosions to calibrate NIF neutron diagnostics and subsequently for experiments devoted to studying direct-drive physics.

It is premature to review polar-drive implosion physics experiments on the NIF, which have just begun. It is important to note, however, that the validity of the fundamental concept of compensating for the NIF geometry by repointing the laser beams was demonstrated in multi-laboratory collaborative experiments involving LANL, LLE, General Atomics, and LLNL and reported by Schmitt *et al.*[350] Plastic-shell targets 2.2 mm in diameter and 42 μm thick were imploded with 700 kJ of energy in an ~2-ns temporally flat laser pulse and diagnosed using framed x-ray backlighting. A backlit image is shown in Fig. 8-24(a), taken when the shell had imploded to about 1/3 of its initial radius. The dark shadow, corresponding to absorption by the dense shell, looks round to the eye. The backlighting images were available only in a window of time after the end of the laser pulse and before peak compression; at other times the framing-camera images were dominated by self-emission. In Fig. 8-24(b), Schmitt *et al.* plotted backlighting and self-emission data together with the trajectory predicted using *HYDRA*, demonstrating good agreement. Azimuthal repointing of some of the laser quads to compensate for the two quads used for backlighting was described by Krasheninnikova *et al.*[351]

It should be noted that none of the experimental simulations shown in Figs. 8-22–8-24 included CBET. As polar-drive experiments proceed on the NIF it will be important to assess the extent to which CBET reduces the laser-energy coupling and affects the implosion uniformity.

Plans for polar-drive implosion experiments on the NIF are discussed by Radha *et al.* in Ref. 344. The targets are 2.2 mm in diameter, as in Ref. 350, but slightly thicker (80 μm). The laser pulses contain a foot portion at ~30 TW

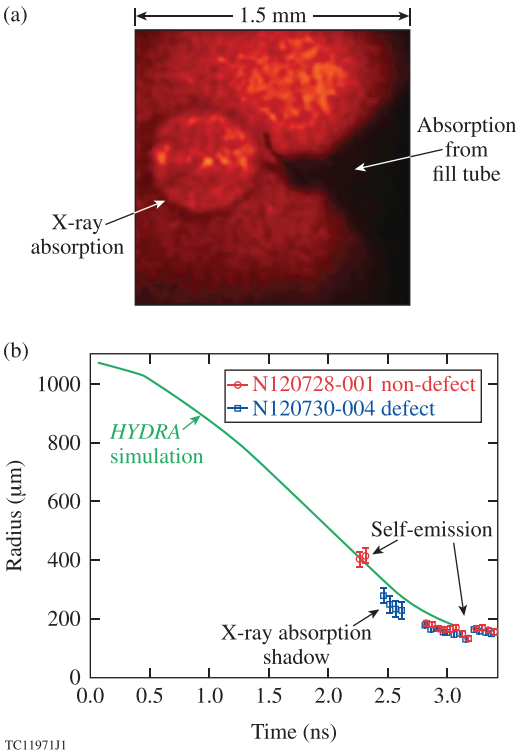

FIG. 8-24. (a) Backlit image of a CH shell imploded on the NIF using polar drive, viewed from the equator, at 2.62 ns. (b) Simulated target center-of-mass trajectory with data points indicating self-emission and backlighting measurements for two shots (one for a target with an imposed defect that was not expected to affect the implosion trajectory). Backlighting data were available only for a small time window. Reproduced with permission from Phys. Plasmas **20**, 056310 (2013). Copyright 2013 AIP Publishing LLC.

rising to a main portion at ~60 TW. Radha *et al.* gave a design that included different pulse shapes for the different rings of beams and proposed to investigate implosion uniformity by varying the peak-power portions of the pulse shapes. They proposed a first set of experiments at relatively low intensities to validate *DRACO* modeling in the absence of laser–plasma interaction (LPI) effects, followed by experiments at higher intensities to study LPI effects in the large-scale-length NIF coronal plasmas. Plans for supporting polar-drive experiments on OMEGA using low-adiabat, triple-picket pulses, including high-intensity cryogenic designs with smaller targets, are described by Radha *et al.* in Ref. 352. Low-adiabat room-temperature implosions on the NIF following the implementation of improved beam smoothing as described in Ref. 197 would be useful intermediate experiments prior to full-scale cryogenic ignition experiments.

Polar-drive experiments on the NIF are understood to be a necessary intermediate step on the road to direct-drive inertial fusion energy. There appears to be no obvious reason why a direct-drive reactor should not be spherically symmetric, as envisaged in Sec. XVII. However, the success of many years of polar-drive experiments on OMEGA in a geometry that appears at first sight to be highly unfavorable suggests that the design constraints on a reactor could be relaxed to allow some departure from spherical symmetry, which could very plausibly be compensated for by modest adjustments to the laser beams.

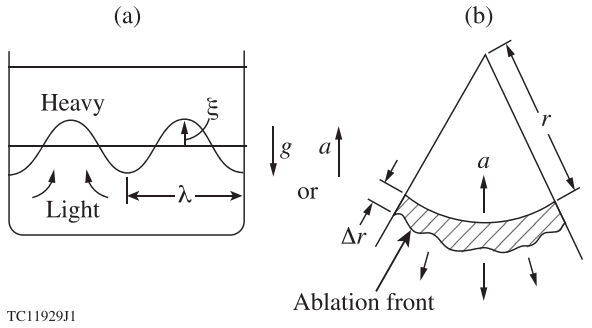

FIG. 9-1. (a) Configuration of the classical Rayleigh–Taylor instability of two fluids in a gravitational field; (b) analogous configuration in an ICF target, where a dense shell is accelerated toward the center of the target. Reprinted with permission from Springer Science + Business Media. From McCrory *et al.*, in Laser Interaction and Related Plasma Phenomena, 1981, Plenum Press.

IX. HYDRODYNAMIC STABILITY

The dominant hydrodynamic instability in ICF implosions is the Rayleigh-Taylor (RT) instability.[353,354] This occurs at the interface between two fluids of different densities in an acceleration field pointing toward the lighter fluid. This section reviews considerable theoretical (Sec. IX A) and experimental (Sec. IX B) work that has been done to understand the growth rate of this instability in direct-drive plasmas. This work is closely related to Sec. VII, which describes laser imprint and other seeds for the RT instability. A good review of early RT work is given by Kilkenny *et al.*[355]

A. Theory

Figure 9-1(a) (from Ref. 356) shows a schematic of the classical unstable configuration, in which a heavy fluid falls through a light fluid under the force of gravity (g). The amplitude ξ of a perturbation with wavelength λ (and wave number $k=2\pi/\lambda$) grows exponentially with a rate $\gamma_{\rm cl}=\sqrt{kg}$. Figure 9-1(b) shows the analogous situation for the ablatively driven RT instability, in which a dense shell experiences an acceleration a toward the target center. The outer surface of the shell is unstable during the acceleration phase because the higher-density shell is accelerated by the lower-density ablated plasma. In the frame of reference of the ablation front, the effective gravity g ($=a$) is directed from the heavier cold shell toward the lighter ablated plasma. The inner surface of the shell is unstable during the deceleration phase when the lower-density hot spot pushes against the higher-density shell. In the absence of thermal conduction and mass ablation, surface perturbations grow with the classical growth rate $\gamma_{\rm cl}$. In the acceleration phase of ICF experiments, however, thermal transport and mass ablation lead to a significant reduction in the growth rate and even total stabilization of the growth at shorter wavelengths.

The stabilizing roles of mass ablation and thermal conduction were first discussed by Nuckolls *et al.*[1] The stabilizing effect of ablation, however, was significantly overestimated. This led to an optimistic conclusion that an ICF implosion is "hydrodynamically stable, except for relatively long wavelength surface perturbations which grow too slowly to be damaging." The linear perturbation growth rate was estimated as

$$\gamma^2 = kg - \frac{k^2 P_{\rm a}}{\rho}, \tag{9-1}$$

where $P_{\rm a}$ is the ablation pressure and ρ is the density. If Δ is the shell thickness, Newton's law gives $g=P_{\rm a}/(\rho\Delta)$ and the perturbations become stable for $\lambda<2\pi\Delta$. Although Eq. (9-1) significantly overestimates the reduction in the growth, the stabilization mechanism was described very accurately: "the peaks of surface perturbations are effectively closer to the heat source… so that the temperature gradient is steeper. Consequently more rapid ablation occurs, and higher pressures are generated which reduce the amplitude of the perturbation. 'Fire polishing' may also be a significant mechanism."

Equation (9-1) was not rigorously derived but obtained using physical intuition. Different linear stability analyses were subsequently developed. Shiau *et al.*[357] showed that laser-driven spherical implosions are linearly unstable to perturbations at the ablation surface and found that the perturbations can be amplified through several orders of magnitude in a few nanoseconds. On the other hand, Henderson and Morse[358] claimed that "electron thermal conduction may be sufficiently symmetrizing to allow laser-driven fusion with a single beam." In an attempt to resolve the controversy, Bodner[359] carried out an analysis based on a sharp-boundary model in which the ablation region was approximated as a discontinuity surface. Bodner showed that the problem cannot be completely specified by the conservation equations using an incompressible fluid model, so that an additional closure equation (which depends on the details of the thermal conduction) is needed to match the number of unknowns with the number of equations. For the closure equation, Bodner used a relation between the perturbed pressure and ablation-front displacement but introduced a free parameter that depended on "the unspecified details in the energy transport." By setting this free parameter to zero (equivalent to neglecting pressure variations caused by modulations in the heat flux across the ablation front), Bodner obtained

$$\gamma = \sqrt{kg} - kV_{\rm a}, \tag{9-2}$$

where $V_{\rm a}$ is the ablation velocity (defined as the ratio of the mass ablation rate to the shell density, or equivalently the flow velocity across the ablation front). Bodner noted that "one cannot draw any overall conclusions at the present time about the importance of Rayleigh–Taylor instability in laser-fusion, except to note that there are stabilization mechanisms."

By the end of the 1970s, no clear picture existed on the importance of the RT instability in ICF implosions. Two-dimensional simulations by McCrory *et al.*[360] and Verdon *et al.*[361] found that small ablation-front perturbations grow but with growth rates less than classical. Other theoretical results in the 1980s generally agreed that the growth-rate reduction was related to the laser-driven ablation, but different researchers attributed the reduction to different physical mechanisms. The effect of finite thermal conduction, for example, was considered by Takabe and Mima,[362] who numerically solved the

system of linearized hydrodynamic equations. They argued that thermal conduction could not stabilize the instability but reduced the growth rate for short wavelengths. However, Baker[363] argued that large wave numbers were stabilized by lateral heat conduction. On the basis of numerical simulations, Emery *et al.*[364] explained the inhibited growth rate using another stabilizing mechanism—vortex shedding.

The need to use a self-consistent analysis of RT growth in ICF targets was first recognized by Takabe *et al.*[365,366] A self-consistent model is defined by a set of equations that can be used to determine the equilibrium hydrodynamic profiles (when perturbations are absent) and to carry out the stability analysis. Early analytic models of laser-accelerated targets considered mainly incompressible fluids. The incompressible model, however, is not self-consistent since the equilibrium configuration depends crucially on thermal conduction, leading to a nonzero velocity divergence. Retaining the effect of finite thermal conduction is therefore essential to describing the ablative flow.

The first solutions based on the self-consistent model were obtained numerically by Takabe *et al.*[365,366] in spherical geometry. In Ref. 366, the numerical results were fit with a Bodner-like formula

$$\gamma^{\text{fit}} = \alpha\sqrt{kg} - \beta k V_{\text{a}}, \tag{9-3}$$

where α and β were found to depend weakly on the normalized equilibrium parameters $G = gr_{\text{s}}/c_s^2$ and $R_\rho = \rho_{\text{a}}/\rho_{\text{s}}$, where c_{s} is the isothermal sound speed, ρ_{s} and r_{s} are the density and radius of the sonic point, respectively, and ρ_{a} is the density at the ablation front. For the values of G and R_ρ considered in Ref. 366 ($G \simeq 0.25$–4, $R_\rho = 12.5$–200), it was shown that the numerical results fit Eq. (9-3) with $\alpha \simeq 0.9$ and $\beta \simeq 3.1$. Tabak *et al.*[367] found that Eq. (9-3) with $\alpha = 0.9$ and $\beta = 3$ agreed remarkably well with *LASNEX* simulations. On the basis of Eq. (9-3), Takabe *et al.*[366] concluded that the main stabilizing mechanism causing the suppression of the short-wavelength modes with $k > \alpha^2 g/(\beta V_{\text{a}})^2$ was fluid flow across the ablation front. A modified form of Eq. (9-3) allowing for finite density scale lengths was given by Kilkenny *et al.*,[355] who used $\alpha = 1$ and $\beta = 3$

$$\gamma^{\text{fit}} = \alpha\sqrt{kg/(1+kL)} - \beta k V_{\text{a}}, \tag{9-4}$$

where L is the density scale length. This correction is unimportant for direct-drive designs (such as the all-DT design of Sec. XVI) in which electron thermal transport is the dominant energy transport mechanism. Here, radiation effects on the plasma profiles are usually small, L is small at the ablation surface as a result of the steep nonlinear thermal wave, and $kL \ll 1$ for relevant values of k. Radiation from plastic and mid-Z ablators tends to increase L (typically to 1–5 μm), reducing the RT growth rate according to Eq. (9-4).

The method developed in Ref. 366 was extended by Kull[368] to carry out a numerical stability analysis of subsonic ablation fronts in a much broader parameter space. This analysis showed that the growth rates scaled only with the dimensionless parameter Γ defined as $\Gamma = g\chi/V_{\text{a}}^3$, where χ is the thermal diffusivity at the ablation surface. This parameter characterizes the relative importance of acceleration, convection, and heat diffusion. If the growth-rate reduction is dominated by convection, then $\sqrt{kg} \sim kV_{\text{a}} \gg \chi k^2$ and $\Gamma \ll 1$. Conversely, if the instability growth rate is reduced mainly by thermal diffusion, then $\sqrt{kg} \sim \chi k^2 \gg kV_{\text{a}}$ and $\Gamma \gg 1$. The numerical results of Kull agreed with Eq. (9-3) only when $\Gamma < 1$. Significant discrepancies were observed for $\Gamma > 1$, suggesting that Takabe's formula has a limited applicability. In the same paper, Kull came to an important conclusion that the growth-rate reduction factor from classical for the most-damaging modes in ICF implosions varies between 0.4 and 0.5. He also found that the growth rate depends strongly on the power index ν for thermal conduction (heat flux $q \sim T^\nu \nabla T$, where T is temperature). If electron heat conduction is the dominant mechanism of energy transfer, then $\nu = 5/2$. However, in laser-accelerated targets using plastic or mid-Z ablators, radiation plays an important role, reducing the effective value of ν and significantly altering the unstable spectrum predicted by Eq. (9-3).

To obtain growth rate formulae valid for a wide range of ablator materials and drive conditions (including both direct and indirect drive), several researchers in the mid-1990s developed analytic solutions of the self-consistent model.[214,369–373] These models confirmed Kull's conclusion[368] that the most-important parameter characterizing the instability is the Froude number $\text{Fr} = V_{\text{a}}^2/(gL_0)$ (which is the inverse of Kull's parameter Γ), where $L_0 = \chi/V_{\text{a}}$ is the characteristic width of the ablation region. When Fr is large, the unstable spectrum consists of only long-wavelength modes [$kL_{\text{min}} \ll 1$, where $L_{\text{min}} = L_0\ (\nu+1)^{\nu+1}\nu^{-\nu}$ is the minimum density scale length within the interface region], while short wavelengths are stable (the cutoff wavelength is much longer than L_{min}). The growth rate in this regime has the form[214,371]

$$\gamma = \sqrt{\text{A}_{\text{T}} kg - k^2 V_{\text{a}} V_{\text{bl}} + (1+\text{A}_{\text{T}})^2 k^2 V_{\text{a}}^2} - (1+\text{A}_{\text{T}}) k V_{\text{a}}, \tag{9-5}$$

where $\text{A}_{\text{T}} = (\rho_{\text{a}} - \rho_{\text{bl}})/(\rho_{\text{a}} + \rho_{\text{bl}})$ is the Atwood number, $V_{\text{bl}} = V_{\text{a}}\rho_{\text{a}}/\rho_{\text{bl}}$ and $\rho_{\text{bl}} = \rho_{\text{a}}\mu(kL_0)^{1/\nu}$ are the blowoff velocity and density, respectively, at a distance $\sim 1/k$ from the ablation front, and $\mu = (2/\nu)^{1/\nu}/\Gamma(1+1/\nu) + 0.12/\nu^2$.

The main stabilizing mechanism is a combination of the dynamic overpressure term $k^2 V_{\text{a}} V_{\text{bl}}$ caused by differences in the heat flux and ablation pressure at the perturbation peaks and valleys, as described in Sec. VII. The term $(1+\text{A}_{\text{T}})kV_{\text{a}}$ results from a combination of "fire polishing" (peaks ablate faster than valleys) and vorticity convection (or vorticity shedding as discussed in Ref. 364), which reduces instability-generated vorticity at the ablation front by convecting it with the ablative flow into the lower-density blowoff region.

While fire polishing and vorticity shedding lead to a reduction in the growth rate, the cutoff is determined only by the dynamic overpressure. Comparing Eq. (9-5) with Eq. (9-1) given by Nuckolls *et al.*[1] shows that Eq. (9-1) overestimates the overpressure stabilization by a factor of c_s/V_{bl}, where the sound speed c_{s} is calculated at the critical density. The blowoff velocity, on the other hand, is the plasma velocity at a distance $\sim k^{-1}$ from the ablation front. Taking into

account the spatial profiles of mass density in the blowoff region, the factor can be expressed as $c_s/V_{\rm bl} \sim (kD_{\rm ac})^{1/\nu}$, where $D_{\rm ac}$ is the size of the conduction zone (the distance between the critical and ablation surfaces). Since ablative stabilization only acts on modes inside the conduction zone (modes with $kD_{\rm ac} \ll 1$ are unstable because of the Landau–Darrieus instability[249–251]), the factor is always large for the modes relevant to target stability.

When the Froude number is small, the unstable spectrum consists of long ($kL_{\rm min} < 1$), as well as short ($kL_{\rm min} > 1$) wavelengths.[373,374] The growth of short-wavelength perturbations is reduced by transverse thermal conduction, finite density scale length, and mass flow across the ablation region. It is well known (Ref. 375 and references therein) that finite density scale lengths L reduce the classical growth rate from $\sqrt{kg}$ to $\sqrt{g/L}$ when $kL \gg 1$. Including the effects of ablation and thermal conduction and using the minimum scale length $L_{\rm min}$, the growth rate in this regime is reduced further to

$$\gamma \simeq \sqrt{\frac{g}{L_{\rm min}} + \frac{k^4\chi^2}{4}} - \frac{k^2\chi}{2} - \beta_s k V_a, \tag{9-6}$$

where the coefficient β_s depends on ν (Ref. 373).

To apply the analytic theory to target designs relevant to ICF experiments, a simple procedure was given by Betti *et al.*[376] to determine ν, Fr, and $L_{\rm min}$ from fits to the hydrodynamic profiles obtained using one-dimensional codes. Because of the complexity of the analytic expressions for the growth rates, the growth rate was approximated by the simplified formula

$$\gamma^{\rm fit} = \alpha^{\rm fit}\sqrt{kg} - \beta^{\rm fit} k V_a, \tag{9-7}$$

where the coefficients $\alpha^{\rm fit}$ and $\beta^{\rm fit}$ are given as functions of Fr and ν in Ref. 376.

Mass ablation also plays an important role in stabilizing RT growth during the deceleration phase. Several analytic and numerical analyses[45,46,377,378] indicate that mass ablation stabilizes modes with $\ell \gtrsim 100$ during this phase for both NIF- and OMEGA-scale targets.

After perturbation amplitudes reach ~10% of the perturbation wavelength, the perturbations enter the nonlinear regime and their growth slows down. The subject of nonlinear RT evolution is beyond the scope of this review.

B. Experiments

This section reviews experiments that have been carried out since the early 1980s to measure the RT growth rates in ablatively driven targets to compare with the predictions described in Sec. IX A. The experimental techniques started with optical and double-foil diagnostics, but soon evolved into the now-standard procedure of using through-foil x-ray radiography to measure the growth rate of ablatively driven planar foils with preimposed sinusoidal surface modulations and side-on x-ray radiography to measure the foil trajectory and acceleration.

The earliest experiments used 1-μm laser drive, but most subsequent experiments have used wavelengths from 0.25 to 0.53 μm. Higher-quality data have been obtained since the advent of beam smoothing, and it has become possible to use preimposed perturbations of smaller amplitude to allow for a greater amount of growth in the linear regime. Improved experimental techniques, including moiré imaging and spherical-crystal x-ray imaging, have made it possible to extend the RT growth measurements to shorter-wavelength perturbations. Overall, the reduction in growth rate from the classical predictions has become well established, but significant differences remain in the interpretation, such as the role of nonlocal thermal transport.

Early measurements of planar-foil trajectories were made by Decoste *et al.*[379] using optical diagnostics (side-on shadowgraphy and the reflection of a 0.53-μm optical probe beam from the rear surface). These diagnostics had the disadvantage of being unable to penetrate beyond the underdense plasma on the rear of the foil. Obenschain *et al.*[380] then introduced the double-foil technique, which provided improved detection of the high-density accelerated material. They demonstrated this technique by accelerating thin CH foils (3.5–12 μm thick) with an ~0.5-kJ, 4-ns-duration, 1.05-μm laser beam into 7-μm-thick Al targets. The heating of the Al target from the impact was used to determine the arrival time and uniformity of the accelerated CH foil. By varying the distance between the two foils, the foil's trajectory was determined. This was first done using a relatively uniform 800-μm-diam focal spot. A large straight-line dip (140–220 μm wide) was then imposed in the center of the spot and the spatial variation in the arrival time was measured to study the lateral smoothing of laser drive nonuniformities. Extensions to these experiments were described by Grun,[381] who measured the mass ablation rate and ablation pressure and provided evidence of increased thermal smoothing in the corona at higher intensities, consistent with the "cloudy-day effect" described by Bodner.[39] Further foil-acceleration experiments including impact foils were reported by Obenschain *et al.*[382] on the Shiva laser at higher laser energies and irradiances.

In 1981, Raven *et al.*[383] used side-on x-ray radiography to measure the trajectories of 3-μm-thick mylar foils with the two-beam GEKKO II laser. One 1.05-μm beam was used to drive the target (with 27 J in 800 ps, at $\sim 4 \times 10^{13}$ W/cm^2), while the other beam irradiated an Al target to produce the x rays for radiography. The trajectories were measured using an x-ray framing camera to provide time-gated x-ray images of the accelerated foil [Fig. 9-2(a)]. The relative timings were varied to map out the trajectory over a significantly longer duration than the drive-pulse length. The composite trajectory is shown in Fig. 9-2(b). The solid line is a best fit to the measured locations of the center of the foil and the dashed lines show the front and rear surfaces. The growth of the width of the target suggested that its disassembly was dominated by thermal expansion and not by the RT instability. An upper limit on the RT growth was a factor of 6 less than that expected from the classical RT instability.

Since this early experiment, many trajectory measurements have been made of ablatively accelerated planar foils, using both framed and streaked x-ray radiography, on a number of laser systems and at various laser wavelengths. Examples include experiments at 1.06-μm wavelength on

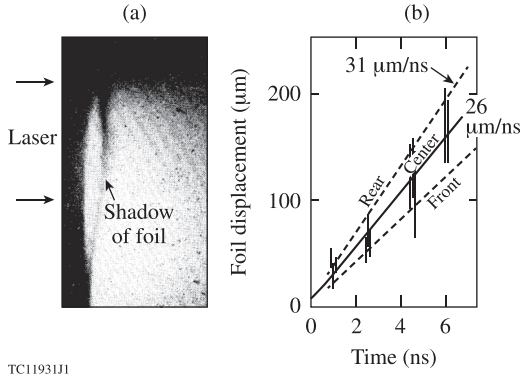

FIG. 9-2. (a) Side-on x-ray radiograph of a 3-μm-thick mylar foil accelerated by one beam of the GEKKO II Laser System taken 1 ns after the peak of the drive pulse. (b) Trajectory of the accelerated foil from a series of radiographs such as that of (a). Reprinted with permission from Raven *et al.*, Phys. Rev. Lett. **47**, 1049 (1981). Copyright 1981 American Physical Society.

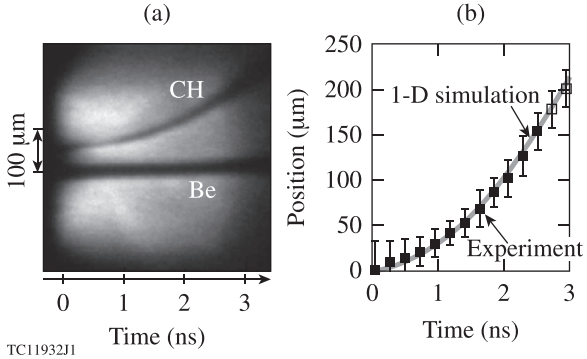

FIG. 9-3. (a) Streaked x-ray radiograph of a 40-μm-thick CH foil driven with a two-step laser pulse (0.53 μm followed by 0.35 μm) on the GEKKO XII Laser System. The horizontal shadow is from a Be support frame and $t = 0$ corresponds to the first half maximum of the 0.35-μm pulse. (b) Measured trajectory (foil position versus time) from (a) along with the results of a 1-D simulation. Reprinted with permission from Azechi *et al.*, Phys. Rev. Lett. **98**, 045002 (2007). Copyright 2007 American Physical Society.

Shiva,[382] at 1.05 μm on Pharos II at NRL,[381,384] at 0.53 μm on Vulcan,[217,385] at 0.53 μm on Nova,[187] at 0.35 μm on OMEGA,[386] and at 0.53 μm and 0.35 μm on GEKKO XII.[194,387–389] The targets were typically plastic with 10- to 40-μm thickness, driven at a range of laser intensities from $\sim 10^{13}$ W/cm^2 to a few times 10^{14} W/cm^2. Figure 9-3(a) shows a more recent example of a streaked x-ray radiograph, obtained by Azechi *et al.*[387] on the GEKKO XII laser. A 40-μm-thick CH foil was irradiated by a low-intensity, 0.53-μm foot pulse at 3×10^{12} W/cm^2, smoothed using partially coherent light (PCL) (Sec. VI B), followed by a higher-intensity, 0.35-μm main drive pulse at 7×10^{13} W/cm^2 employing smoothing by spectral dispersion (SSD) (Sec. VI C). Both pulses were nearly flat in time with widths $\sim$2.4 ns and all beams used phase plates. The measured trajectory agreed well with a 1-D simulation [Fig. 9-3(b)].

The first measurements of RT growth using through-foil streaked x-ray radiography were made by Cole *et al.*[217] They accelerated a 3-μm-thick Al target having a 0.5-μm-amplitude, 20-μm-wavelength corrugated perturbation [Fig. 9-4(a)]. The target was driven by three overlapped 1.2-ns, 0.53-μm laser beams with a total energy of $\sim$90 J. The x rays were generated by a fourth beam incident on a Cu target. The main target was imaged onto the slit of an x-ray streak camera through a 5-μm pinhole, producing a streaked radiograph as shown in Fig. 9-4(b). The growth of the modulations can be seen toward the bottom of the image. Figure 9-4(c) shows the measured areal-density modulation as a function of time. The growth is significantly lower than that expected for the classical RT instability but is similar to that predicted by a 2-D Eulerian simulation (which adjusted the absorbed energy to match the trajectory and included a convolution with the pinhole response). Through-foil radiography has become the standard technique for RT and imprint (Sec. VII) experiments.

Side-on x-ray radiography has also been used to measure the growth of target modulations through the RT instability. Whitlock *et al.*[390] reported experiments in which 4-ns pulses from the 1.05-μm Pharos-II laser were used to drive 10-μm-thick CH targets that had 50-μm-wavelength square-wave perturbations with amplitudes up to 2.7 μm on the rear side. The radiographs showed the development of bubbles and spikes, indicating that the instability had evolved into its nonlinear phase. Simulations using the 2-D *FAST2D* code were in good agreement with the measurements.

A variant on through-foil x-ray radiography was proposed by Grun and Kacenjar,[391] in which a thin Mg strip is embedded in a CH target to produce an x-ray flash when the ablation surface reaches it during the laser pulse, "self-

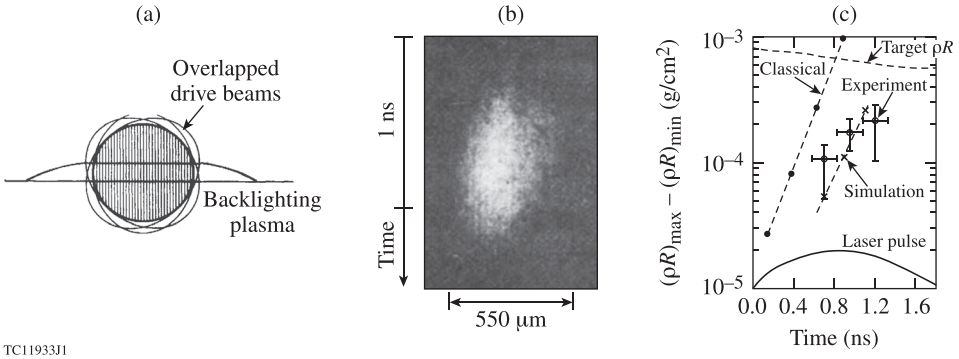

FIG. 9-4. (a) Configuration of the first Rayleigh–Taylor (RT) experiment diagnosed using through-foil x-ray backlighting. Three overlapped drive beams accelerated an Al disk with imposed thickness modulations. (b) Streaked radiograph showing modulation growth at later times. (c) Measured and simulated areal-density (ρR) modulations as functions of time, showing lower growth than expected for the classical RT instability. Reprinted with permission from Cole *et al.*, Nature **299**, 329 (1982). Copyright 1982 Macmillan Publishers Ltd.

backlighting" the target. Grun *et al.*[392] used this technique to diagnose targets with a square-wave perturbation on the rear surface with its wavelength varying from 30 to 100 μm, driven by a 5-ns, 1.05-μm laser pulse at an intensity of 10^{13} W/cm^2. They observed the growth of RT spikes to areal densities about twice that of the original foil. Two-dimensional *FAST2D* simulations were again in good agreement with the measurements.

The advent of beam smoothing in the 1980s (Sec. VI) allowed higher-quality RT growth data to be obtained. Grun *et al.*[384] used a 1.05-μm laser outfitted with ISI (Sec. VI B) to measure RT growth in ~10-μm-thick polystyrene foils with 2-μm-deep square-wave perturbations machined on the rear target surface with wavelengths of 50, 100, or 150 μm. The laser intensity was $2–6 \times 10^{12}$ W/cm^2 in a 4- to 5-ns pulse. The RT growth rates, measured with through-foil streaked x-ray radiography, were ~60% of classical RT predictions for the 100- and 150-μm wavelengths, in agreement with *FAST2D* simulations. However, no growth of the 50-μm-wavelength perturbation was observed, in disagreement with the simulations. It was postulated that ISI could delay the start of the growth for this perturbation.

Desselberger *et al.*[385] made RT growth measurements with a 0.53-μm laser that was equipped with phase plates and ISI. Six 1.8-ns laser beams drove 16-μm-thick CH_2 targets with an intensity of 1.5×10^{14} W/cm^2. The targets had sinusoidal perturbations with wavelengths of 30–100 μm and modulation depths of 1.8–4.6 μm. The growth rates were higher for the smaller modulation depth, suggesting that the targets with the larger modulations were entering the nonlinear RT regime. The growth rates were 25% to 50% of classical, but smaller than those predicted in 2-D *POLLUX* simulations. In contrast to the experiments of Ref. 384, these experiments saw clear growth of the 50-μm-wavelength perturbation with ISI employed.

Glendinning *et al.*[187] made RT growth-rate measurements in the two-beam Nova target chamber, accelerating ~20-μm-thick CH_2 targets with one 0.53-μm beam and using the other beam for backlighting. The drive beam was smoothed using SSD and split into nine segments that were independently steered with glass wedges to form a flattopped spatial intensity distribution. The drive pulse was a linear 1-ns ramp to a 2-ns flattop with an intensity of 8×10^{13} W/cm^2. The targets had 1-μm-amplitude sinusoidal perturbations at four wavelengths ranging from 20 to 70 μm. The growth rates, measured with though-foil x-ray radiography, were found to be ~70% of classical, in good agreement with 2-D *LASNEX* simulations and in good agreement with Eq. (9-3) with $\alpha = 0.9$ and $\beta = 3$.

In Ref. 355 Kilkenny *et al.* reviewed experiments through the early 1990s, addressing the ablative stabilization of the RT instability. Since then, planar RT experiments have continued to use through-foil x-ray radiography to measure the growth of sinusoidal, single-mode perturbations, and have focused on targets driven by 0.25- to 0.53-μm laser light with beam smoothing.

One example illustrating typical data from which the growth rate is determined is shown in Fig. 9-5 for 20-μm-thick CH targets accelerated on OMEGA by Knauer *et al.*[386] The targets included perturbations with amplitude ~0.5 μm and wavelengths 31 μm [Fig. 9-5(a)] and 20 μm [Fig. 9-5(b)]. Here, six overlapped 0.35-μm beams smoothed with SSD irradiated the target with a 3-ns flattop pulse at 2×10^{14} W/cm^2. Good agreement was generally found with simulations. The growth rate was determined from the slope of the data in the acceleration phase [starting at ~0.9 ns in Fig. 9-5(a) and ~0.7 ns in Fig. 9-5(b)]. The simulations, which used standard flux-limited thermal conduction, match the data very closely for the longer-wavelength case ($\lambda = 31$ μm) and quite closely for the 20-μm perturbation. It is harder to extract an accurate growth rate in the latter case since (a) nonlinear saturation occurs earlier (roughly when the perturbation amplitude reaches 10% of the perturbation wavelength) and (b) the experimental measurement becomes harder to make as the limit of spatial resolution set by the pinhole is approached.

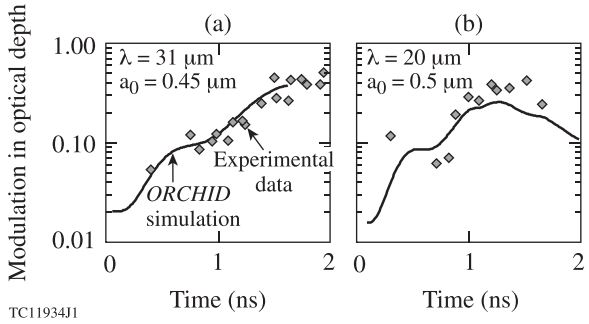

FIG. 9-5. Measured and simulated RT growth on OMEGA of targets with imposed perturbations of (a) 31-μm and (b) 20-μm wavelengths (λ). The initial perturbation amplitudes are indicated by a_0. The targets were driven at 2×10^{14} W/cm^2. Reproduced with permission from Phys. Plasmas **7**, 338 (2000). Copyright 2000 AIP Publishing LLC.

The results of growth-rate measurements obtained in this manner are shown in Fig. 9-6 for experiments carried out by Glendinning *et al.*[393] using two beams of the Nova laser with SSD beam smoothing [Fig. 9-6(a)] and by Azechi *et al.*[389] on the GEKKO XII laser with PCL beam smoothing [Fig. 9-6(b)], both using 0.53-μm irradiation to accelerate plastic foil targets at $\sim 7 \times 10^{13}$ W/cm^2. In each case, the growth rate is plotted as a function of the imposed perturbation wavelength. The experimental setup of Ref. 393 was similar to that of Ref. 187 except that lower perturbation amplitudes (in the range of 0.1–1.0 μm) were used.

Differences are found in the interpretations of the two experiments. In the Nova experiment, Glendinning *et al.*[393] speculated that the difference between the data and simulations at intermediate wavelengths might indicate a need to include Fokker–Planck (FP) modeling of thermal transport (Sec. XI) in the simulations. However, it is unclear why nonlocal transport would affect only the intermediate wavelengths. The growth rates on GEKKO were found to be significantly lower than predicted by integrating the modified Takabe growth-rate curve of Eq. (9-4) using the values of g, L, and V_a obtained from 1-D *ILESTA* simulations (and taking $\alpha = 1$ and $\beta = 3$). Azechi *et al.*[389] considered whether nonlocal effects could explain this difference. Figure 9-6(b) includes predictions by the 2-D code *KEICO-2D* using Spitzer–Härm (SH) and FP thermal transport, showing lower growth rates in the FP case that were ascribed to a lower density at the ablation front (and therefore higher V_a) resulting from energetic electron preheat. However, Azechi *et al.*

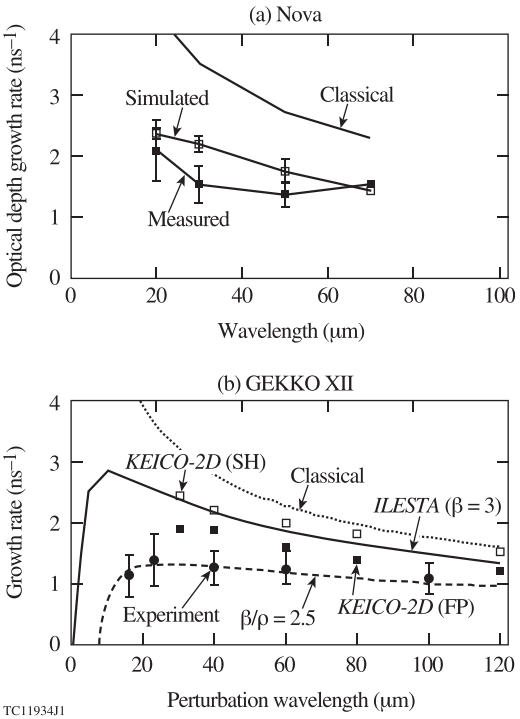

FIG. 9-6. Measured and simulated RT growth rates as functions of perturbation wavelength from experiments on (a) Nova and (b) GEKKO XII. The 2-D results in (b) cannot be compared directly with the data because of approximations within the model. The dashed curve is obtained from substituting experimental values into the Takabe formula and finding a best fit for β/ρ, where ρ is the density measured in g/cm^3. SH: Spitzer–Härm; FP: Fokker–Planck. (a) Reprinted with permission from Glendinning *et al.*, Phys. Rev. Lett. **78**, 3318 (1997). Copyright 1997 American Physical Society. (b) Reproduced with permission from Phys. Plasmas **4**, 4079 (1997). Copyright 1997 AIP Publishing LLC.

cautioned that quantitative comparisons with the experimental data could not be made because of the limitations in the computational model. The best agreement with the data (dashed curve) was found by substituting experimentally determined values into Eq. (9-4) and using $\beta/\rho = 2.5\,\text{cm}^3/\text{g}$, where ρ is the ablation density ($\beta \sim 4$ for $\rho = 1.5$ g/cm^3). The low growth rates were consistent with earlier work at Osaka reported by Shigemori *et al.*,[388] who also used frequency-doubled PCL to minimize the effect of imprint on RT growth-rate measurements.

With through-foil x-ray radiography, the shortest wavelength that can be measured with pinhole-based x-ray framing and streak cameras is usually limited to $\sim 20\,\mu$m to maintain adequate x-ray throughput. Sakaiya *et al.*[394] described a technique, shown in Fig. 9-7(a), to extend x-ray radiography to shorter wavelengths using a moiré grid added to the through-foil x-ray setup.[395] When the grid has a slightly different wavelength from that of the preimposed sinusoidal modulation, the shorter-wavelength perturbation is converted to a longer wavelength through the difference between the k vectors. In Ref. 394, 16-μm-thick polystyrene targets were driven at intensities of $7 \times 10^{13}\,\text{W/cm}^2$ with beams from the GEKKO XII laser smoothed using PCL. This made it possible to measure RT growth rates for preimposed modulations as short as 4.7 μm. A streaked radiograph is shown in Fig. 9-7(b) for an 8.5-μm target perturbation. Figure 9-7(c) shows the measured RT growth rate dispersion curve, extending to a short wavelength limit of 4.7 μm. The SH and FP simulation curves are calculated by first using the 1-D hydrodynamics code *ILESTA-1D* (with a flux limiter of $f = 0.1$ in the SH case) to obtain the growth rate as a function of time and then integrating the perturbation amplitude with respect to time. The growth rate is obtained from the modified Takabe formula [Eq. (9-4)] as a function of time based on the values of acceleration, scale length, and ablation velocity calculated by the code ($\alpha = 1$ and $\beta = 1.7$ are assumed). Sakaiya *et al.* explained the reduction in growth rate at short wavelengths by preheating from nonlocal heat transport. The lack of agreement between the FP simulation and the data from Ref. 389, which were matched well in Fig. 9-6(b) using a different β, is unclear.

Further experiments were carried out at Osaka at the GEKKO XII–HIPER Facility[194] by Azechi *et al.*,[387] using an SSD-smoothed 0.35-μm beam at $7 \times 10^{13}\,\text{W/cm}^2$ preceded by a 0.53-μm PCL-smoothed foot pulse at $3 \times 10^{12}\,\text{W/cm}^2$, in which they accelerated CH targets with 20- and 50-μm-wavelength perturbations and measured all the quantities in the growth-rate formula [Eq. (9-4) with $\alpha = 1$] (except for the scale length, for which they relied upon simulations) to obtain the coefficient β of the ablative stabilization term. They found that β was consistent with theory for the 20-μm perturbation ($\beta = 1.2 \pm 0.7$), but larger than predicted at 50 μm ($\beta = 3.3 \pm 1.1$).

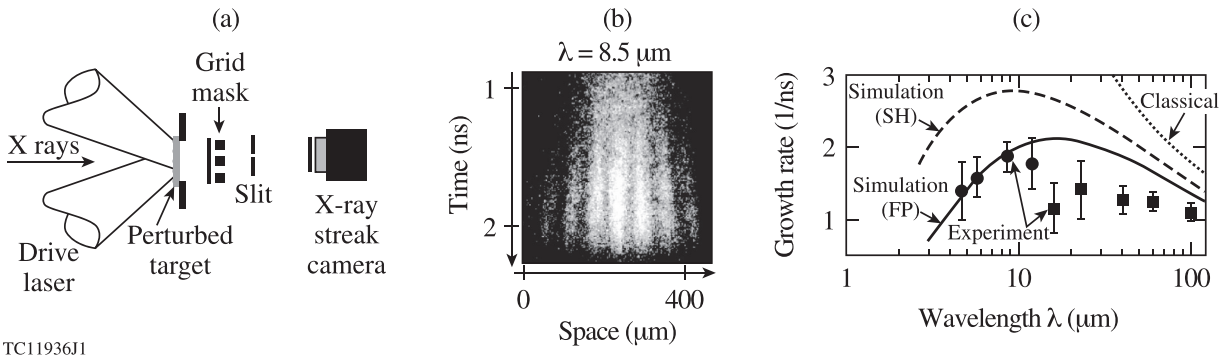

FIG. 9-7. (a) Experimental setup to measure the RT growth on polystyrene targets using through-foil x-ray backlighting combined with moiré interferometry. (b) A streaked radiograph for a target perturbation wavelength λ of 8.5 μm. (c) Measured and simulated RT growth rates as functions of λ, with the experimental data extending to a short-wavelength limit of 4.7 μm. The square data points are from earlier work [Fig. 9-6(b)]. Reprinted with permission from Sakaiya *et al.*, Phys. Rev. Lett. **88**, 145003 (2002). Copyright 2002 American Physical Society.

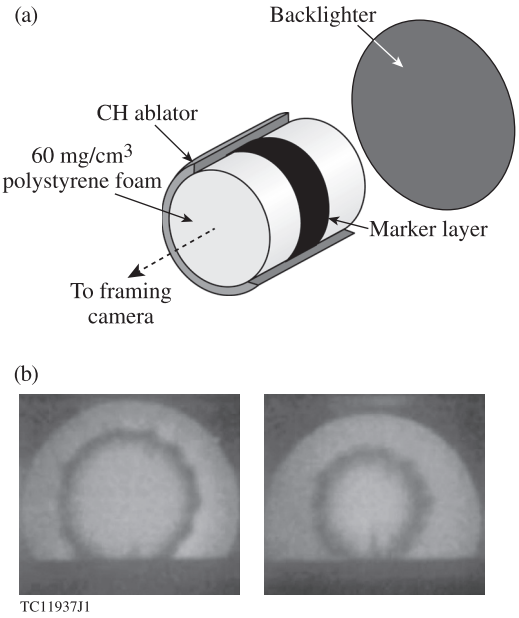

FIG. 9-8. (a) Experimental configuration for an RT experiment carried out on OMEGA in cylindrical geometry, diagnosed using axial radiography. (b) Axial radiographs (at successive times) of a cylindrical target with preimposed $m = 14$ sinusoidal target modulations. Reproduced with permission from Phys. Plasmas **6**, 2095 (1999). Copyright 1999 AIP Publishing LLC.

Dual-wavelength experiments at the GEKKO XII–HIPER Facility were also reported by Otani *et al.*[396] at laser intensities of $\sim 10^{14}$ W/cm^2. They found reduced growth rates ascribed to nonlocal heat transport whereby electrons in the tail of the distribution deposit their energy near the ablation surface, increasing the ablation velocity and scale length.

Another technique to extend RT growth measurements to shorter-wavelength perturbations was described by Pawley *et al.*[397] They used the improved spatial resolution of a spherical-crystal x-ray imager[221] (see Fig. 7-7) at 1.48 keV to measure the growth of 12.5-μm-wavelength sinusoidal perturbations in 40-μm-thick CH targets on the 0.25-μm-wavelength Nike laser. The nominal peak laser intensity was 7.5×10^{13} W/cm^2. Their results were in good agreement with 2-D hydrodynamic simulations that did not include nonlocal thermal transport.

In high-intensity (10^{15}-W/cm^2) experiments with planar foils on OMEGA, Smalyuk *et al.*[398,399] measured the RT growth for preimposed modulations of wavelength 60, 30, and 20 μm. The growth for the 60-μm modulation agreed very well with *DRACO* simulations using a flux-limited thermal-transport model; the growth in the 30-μm case was somewhat lower than predicted; however, no growth was observed for the 20-μm case, in disagreement with simulations. In contrast, at a lower intensity ($\sim 5 \times 10^{14}$ W/cm^2), experiments and simulations agreed very well at all three perturbation wavelengths. Smalyuk *et al.* suggested that nonlocal thermal heating of the ablation surface could be responsible for the observed growth stabilization at high intensity for the 20-μm-wavelength perturbation.

Hager *et al.*[400] reported RT growth measurements at 0.35-μm wavelength on OMEGA for SiO_2 targets irradiated with high intensities (up to 9×10^{14} W/cm^2) obtained by overlapping 11 drive beams. They imposed a 60-μm-wavelength modulation on a single drive beam using a special phase plate and observed growth rates that were well modeled by the 2-D code *DRACO* using only flux-limited thermal transport.

It is evident that there are significant differences of interpretation in the various RT growth-rate experiments that have been carried out to date, not only between different laboratories, but on the same experimental platforms at different perturbation wavelengths. Nonlocal effects may be more important at 0.53 μm than at 0.35 μm and shorter wavelengths, but Richtmyer–Meshkov experiments at 0.35 μm (Fig. 7-13) indicate the presence of nonlocal thermal transport. Azechi *et al.*[387] made a particularly careful attempt to compare with the growth-rate formula by measuring all but one of the quantities required by the formula, but the result at the longer perturbation wavelength was somewhat inconclusive. In short, it has not been possible to explain all the data with a single theoretical model.

All the experiments described above were carried out in planar geometry. The effects of convergence were investigated by Tubbs *et al.*[401] in cylindrical geometry using the OMEGA laser. A 20-μm-thick cylindrical CH shell with a diameter of 900 μm and a length of 2.25 mm was imploded with $\sim$19 kJ of 0.35-μm light in a 2.5-ns ramped laser pulse. The pointing of the 50 drive beams was optimized to maximize azimuthal symmetry and produce a flat illumination flux over the central 500 μm of the cylinder. The targets were radiographed end-on using the configuration of Fig. 9-8(a). A 4-μm-thick marker layer of $C_8H_6Cl_2$ was placed inside the CH shell in the central 500 μm of the irradiated area, where uniform compression is expected, to enhance the contrast in the radiographic images, two of which are shown in Fig. 9-8(b). Modulations were preimposed on the outer target surface, in this case an $m = 14$ azimuthal mode with an initial amplitude of 0.5 μm. Growth factors of 10–14 were observed, roughly half of what was expected from 2-D *LASNEX* simulations. The measured target trajectories were consistent with simulations. It was suggested that preheat from the chlorine doping may have put the target onto a higher adiabat, thereby reducing the growth rate.

X. CORONAL PLASMA PHYSICS

This section reviews several plasma-physics processes that can take place in the corona of a direct-drive target. Most of these processes must be avoided or controlled within acceptable limits if the implosion is to be successful. A good introduction to the physics of these processes is given in Ref. 28.

Section X A reviews the two-plasmon–decay instability, in which the incident electromagnetic wave decays into two electron plasma waves (plasmons). This instability is a major concern because the plasmons produce energetic electrons (also known as "hot," "fast," or "suprathermal" electrons) that can preheat the fuel. It is important for target designs to maintain the incident laser intensity at a level that will produce minimal preheat. Sections X B and X C describe stimulated Brillouin scattering (SBS) and stimulated Raman scattering (SRS),

respectively. These instabilities lead to some of the laser energy being reflected from the target together with the generation in the plasma of ion-acoustic waves (Brillouin) or electron plasma waves (Raman). Section XB includes an account of cross-beam energy transfer—a form of stimulated Brillouin scattering, wherein energy is scattered from one beam to another. One concern with Brillouin and Raman scattering is the potential loss of laser energy, while an additional concern with Raman scattering is hot-electron generation. Raman scattering generally requires plasmas with long scale lengths. It was a major problem at 1-μm wavelengths in hohlraum plasmas on Shiva, but it appears to be less important at 0.35 μm in OMEGA-scale direct-drive plasmas.

Section XD reviews self-focusing in plasmas (often referred to as filamentation when the associated scale length is small). This process can dramatically increase the intensity modulations within a laser beam, reducing the uniformity of the laser drive and increasing other undesired plasma processes by enhancing the local laser intensity. With the advent of laser-beam smoothing (Sec. VI), filamentation is no longer considered to be a significant concern. Section XE covers the parametric decay instability, once thought to be the primary laser-absorption mechanism but now thought to be insignificant. Finally, Sec. XF reviews the generation of magnetic fields in laser-produced plasmas. While large magnetic fields can be generated under suitable irradiation conditions with a magnitude sufficient to affect the electron thermal conductivity, they are believed to be unimportant in the corona of a uniformly irradiated spherical target.

A. Two-plasmon decay (TPD)

The TPD instability is the decay of a coherent EM wave of frequency ω_0 into two plasma waves (also known as electron plasma waves, plasmons, or Langmuir waves) of frequency $\omega_e \approx \omega_0/2$, close to the local electron plasma frequency ω_p [defined in Eq. (2-1)]. Since ω_p scales as the square root of the electron density n_e, the TPD instability occurs at densities close to $n_c/4$, where n_c is the critical density at which $\omega_p = \omega_0$.

Figure 10-1 shows a wave-vector diagram of the decay. The incident EM wave ($\mathbf{k}_0$, ω_0) decays into two plasma waves ($\mathbf{k}_{e1}$, ω_{e1}) and ($\mathbf{k}_{e2}$, ω_{e2}), satisfying the wave-vector and frequency-matching equations

$$\mathbf{k}_0 = \mathbf{k}_{e1} + \mathbf{k}_{e2} \tag{10-1}$$

and

$$\omega_0 = \omega_{e1} + \omega_{e2}. \tag{10-2}$$

Since the plasma waves satisfy the dispersion equation (for $\alpha = 1,2$)

$$\omega_{e\alpha}^2 = \omega_p^2 + 3v_{th}^2 k_{e\alpha}^2, \tag{10-3}$$

where $v_{th} = \sqrt{k_B T_e/m_e}$, k_B is Boltzmann's constant, T_e is the electron temperature, and m_e is the electron mass, the TPD instability occurs at plasma densities slightly below $n_c/4$.

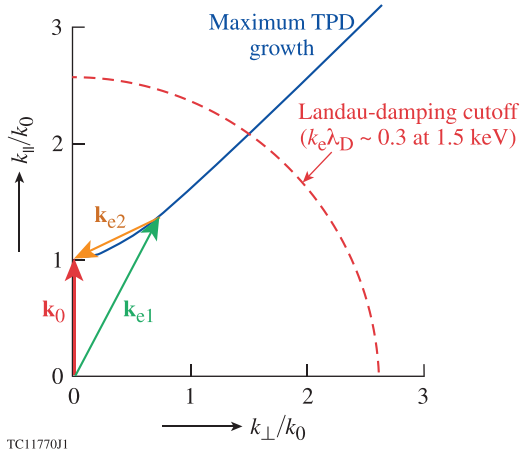

FIG. 10-1. Decay diagram for the two-plasmon–decay (TPD) instability of a plane wave pump, in a homogeneous plasma, shown in the plane of polarization. An incident photon with wave vector $\mathbf{k}_0$ and frequency ω_0 decays into two plasmons with wave vectors $\mathbf{k}_{e1}$ and $\mathbf{k}_{e2}$ and frequencies ω_{e1} and ω_{e2}. The solid hyperbola corresponds to the most-unstable decays.

The linear stability analysis of a plane EM wave subject to TPD in a homogeneous plasma, of uniform density $n_e < n_c/4$, is well known. Decays having the largest growth rate correspond to the wave vector $\mathbf{k}_{e1}$ lying in the plane of polarization of the EM wave and falling on a hyperbola (the solid line in Fig. 10-1). Points on the maximum-growth-rate hyperbola correspond to different values of n_e. From Eq. (10-3), it is clear that decays involving smaller wave vectors occur at densities closer to $n_c/4$ than decays involving larger wave vectors. Damping of the decay waves is generally very weak (and a result of electron–ion collisions) unless the decay wave vectors are large enough to be close to the Debye wave number k_D, when strong wave-particle interactions (Landau damping) set in. (Here, $k_D = 2\pi/\lambda_D$, where the Debye length $\lambda_D = v_{th}/\omega_p$.) This occurs around the so-called Landau-damping cutoff shown in Fig. 10-1. Values of $k_e\lambda_D \sim 0.2$ to 0.3 are typically taken to represent the cutoff, where k_e is the plasmon wave number. In the example given, an electron temperature of 1.5 keV and a laser wavelength of 0.35 μm are assumed. The threshold for the TPD instability in a homogeneous plasma occurs when the growth rate exceeds the plasma-wave damping rate ν_c. Since ν_c is usually small, the collisional threshold is easily exceeded in direct-drive implosions. The instability can be classified as absolute or convective. An absolute instability occurs when a perturbation grows exponentially in time at a fixed location in space. If no such location exists, but a suitable moving (or convecting) point can be found such that the amplitude of the perturbation grows exponentially, the instability is convective.

The TPD instability was first identified by Goldman,[402] on investigation of the Green's function for the longitudinal electric field in an irradiated plasma, and by Jackson,[403] who adopted an approach based on the Vlasov equation. The significance of the TPD instability was soon recognized. It was argued by Galeev *et al.*[404] and Rosenbluth[405] that the collisional damping of plasma waves produced in the decay would transfer energy to thermal electrons and provide an anomalous

absorption mechanism. It was also recognized that stochastic heating caused by the resulting electrostatic turbulence,[406,407] or wave breaking,[408] would lead to energetic electrons and the possibility of target preheat. Preheat would reduce the fuel compressibility and therefore the target gain.

From a theoretical standpoint, a linear variation in plasma density (i.e., inhomogeneity) can be shown to lead to convective instability—a result obtained by Rosenbluth[405] in 1972. This introduced a threshold, known as the convective threshold, that can be higher than the collisional threshold found earlier for a homogeneous plasma. The convective threshold depends on the laser intensity I, the laser wavelength λ_0, the density scale length L_n, and the plasma temperature in the combination $I\lambda_0 L_n/T_e$. A careful linear stability analysis of small-wave-number decays near their turning point (invalidating the WKB analysis used by Rosenbluth) revealed the possibility of absolute instability (temporal growth). The threshold for the absolute instability was calculated most completely by Simon *et al.*,[409] correcting deficiencies in earlier pioneering work by Lee and Kaw,[410] Liu and Rosenbluth,[411] and Lasinski and Langdon.[412] A good review of the technical problems and mathematical techniques that are used to solve this problem can be found in the work by Afeyan and Williams.[413]

1. Single-beam experiments

The experimental signatures of TPD are typically indirect. They include the generation of optical emission at $\omega_0/2$ and $3\omega_0/2$, a hard component (typically > 20 keV) in the x-ray bremsstrahlung spectrum, an energetic tail in the electron spectrum, and K_α emission from cold materials (usually mid-Z) resulting from the energetic electrons.

Early observations of harmonic and subharmonic emission were reported by Bobin *et al.*[414] in Nd:glass laser–solid target experiments at a 1-μm wavelength. Figure 10-2 shows spectra at $2\omega_0$, $3\omega_0/2$, and $\omega_0/2$. Later experiments by Pant *et al.*,[415] again employing a Nd:glass laser at a 1-μm wavelength, determined the threshold laser intensity for the onset of $3\omega_0/2$ emission and found it to be consistent with the threshold for the excitation of the TPD instability as given by Jackson[403] and Rosenbluth.[405] As proposed by Avrov *et al.*,[416] $3\omega_0/2$ emission is generated by Thomson upscattering of the incident laser light by plasma waves near the quarter-critical density (i.e., self-Thomson scattering), or possibly by higher-order nonlinear processes such as the combination of three plasma waves.

Figure 10-2(c) shows the first observation of half-harmonic emission and has been cited as possibly the first observation of SRS. However, $\omega_0/2$ emission can also be generated from the TPD instability and other mechanisms such as the high-frequency hybrid instability of Afeyan and Williams.[417] All mechanisms require plasma waves to be present near $n_c/4$. Similarly, it is generally not obvious from hard x-ray spectra whether the hot electrons were produced by the TPD instability, SRS, or some other mechanism.

Perhaps the most-direct experimental observations of TPD have been obtained by Thomson-scattering measurements using a probe beam with higher frequency than the

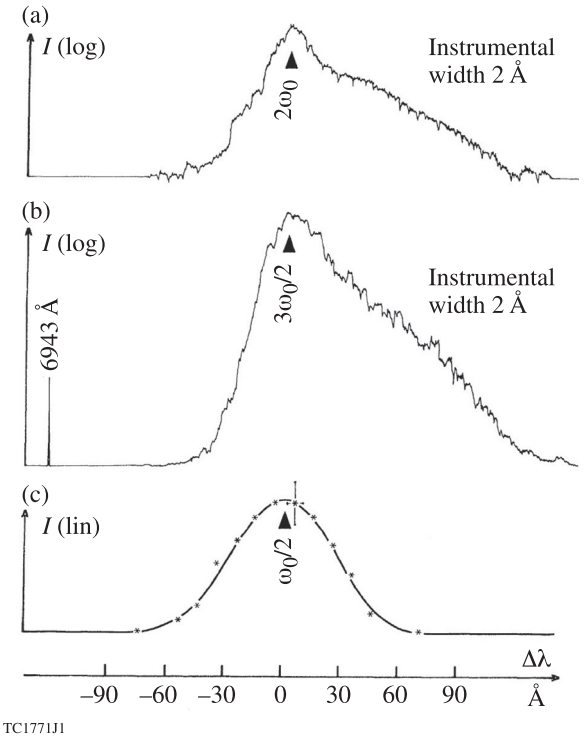

FIG. 10-2. Spectra of harmonic emission at (a) $2\omega_0$, (b) $3\omega_0/2$, and (c) $\omega_0/2$ emitted along a direction 45° from the laser beam's axis when a Nd:glass laser was focused on a solid target. The vertical scales are arbitrary. Reprinted with permission from Bobin *et al.*, Phys. Rev. Lett. **30**, 594 (1973). Copyright 1973 American Physical Society.

interaction beam. The first such observations of TPD plasma waves were made by Schuss *et al.*,[418] using a ruby-laser Thomson probe on a plasma formed from the CO_2 laser irradiation of a hydrogen gas jet target, and by Baldis *et al.*[419] The latter authors employed a frequency-doubled Nd:glass Thomson probe together with a CO_2 interaction beam that was incident on a preformed plasma, which was generated by the interaction of a 4-J, 30-ns ruby laser with a solid target and characterized by interferometry. In both cases, an enhancement in the intensities of the electron Thomson-scattering satellites was seen at frequencies $\sim\omega_0/2$ only when the peak plasma density probed was near $n_c/4$. This provided strong evidence for the TPD instability.

The first experimental demonstration of hot-electron generation resulting from the TPD instability was reported in 1980 by Ebrahim *et al.*[420] They irradiated a plasma with a large density scale length $L_n \sim 300\,\mu$m with CO_2 light at $\sim 4\times 10^{14}$ W/cm^2 using the experimental configuration shown in Fig. 10-3(a). A solid carbon target was irradiated by a long-pulse 1.06-μm laser to form the plasma, whose density was interferometrically determined using a 0.53-μm probe beam. This plasma was then irradiated transversely by the CO_2 laser at a known density. The maximum density n_0 was typically just above quarter critical for the CO_2 laser wavelength, allowing the hot electrons generated by the TPD instability to be isolated from electrons generated by resonance absorption (Sec. IV C) or the parametric decay instability (Sec. X E) near the critical density.

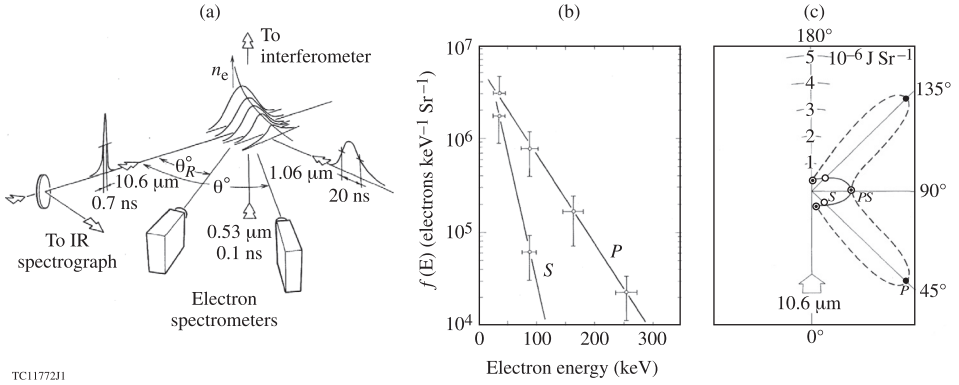

FIG. 10-3. (a) Experimental configuration used to isolate hot electrons generated by the TPD instability. A long-scale-length plasma was preformed by a 1.06-μm laser pulse (2 to 4 J in 20 ns). The 10.6-μm (CO_2) interaction beam was incident transverse to the 1.06-μm beam, permitting a choice of maximum electron density n_0 in the range $n_c/10 < n_0 < n_c$. (b) Hot-electron spectra for directions parallel (P) and perpendicular (S) to the laser electric field for collection angles $\theta = 45°$ and 135° and peak densities between 0.25 n_c and 0.4 n_c. (c) Angular distribution of hot electrons (having energies between 35 and 400 keV) for both S (open circles) and P directions (closed circles). Reprinted with permission from Ebrahim *et al.*, Phys. Rev. Lett. **45**, 1179 (1980). Copyright 1980 American Physical Society.

Figure 10-3(b) shows hot-electron spectra measured in directions parallel (P) and perpendicular (S) to the laser electric vector for a maximum density between 0.25 n_c and 0.4 n_c. The angular dependence of the hot electrons is shown in Fig. 10-3(c). It is notable that the largest signals were observed at ±45° to the laser direction. Figure 10-3(b) corresponds to this case—at other angles, the difference between the P and S directions was not observed. The slope of the P component of Fig. 10-3(b) corresponds to a temperature of ~60 keV. On the basis of the angular distribution of the electrons and their polarization dependence, Ebrahim *et al.* identified the electrons as originating from the TPD instability rather than processes such as SRS.

The preferred angles of observation were consistent with the expected direction of the most-unstable TPD wave vectors for the parameters of the experiment ($n_0 \sim 3 \times 10^{18}$ cm^{-3}, $T_e \sim 200$ eV). From Fig. 10-1, large-wave-number decays consist of two plasmons propagating at angles of almost 45° and 135° with respect to the pump wave vector. Similar single-beam experiments performed later with a shorter-wavelength (0.35-μm) interaction beam saw much weaker directionality, although emission was again stronger in the plane of polarization.[421] In general, the directionality and energy spectrum of hot electrons produced by the TPD instability at 0.35 μm have proven difficult to predict because neither the saturated plasmon wave-number spectrum nor the electron acceleration processes are well understood. Additionally, most of these electrons do not escape the target and the relationship between the source direction and emission direction is unclear.

Further evidence for the TPD instability was obtained from the x-ray spectrum. In 1.06-μm and 10.6-μm laser experiments, a two-temperature spectrum was commonly observed (Sec. IV B), explained by a thermal component and a suprathermal component with a temperature T_H resulting from resonance absorption that scaled in a well-established way with $I\lambda_0^2$ (where I is the laser intensity and λ_0 is the laser wavelength). However, in 0.35-μm single-beam interaction experiments reported by Keck *et al.*,[422] there was no evidence of such a component. Instead, the x-ray spectrum was well fit by a "superhot" electron component with a temperature T_{SH} greatly in excess of the T_H expected for resonance absorption. This understanding was consistent with experiments reported in the same paper for the irradiation of targets in spherical geometry at 1 μm with the 24-beam OMEGA laser, where three Maxwellian components (thermal, resonance absorption, and superhot) were required to fit the data. The temperature T_{SH} was found to be somewhat higher for 1-μm irradiation, and it was reasonable to assume the same origin for the superhot component.

The superhot temperature from Keck *et al.*[422] is plotted as a function of I in Fig. 10-4 for 0.35-μm irradiation and shows an approximate scaling with $I^{0.2}$ from 2×10^{14} to 10^{15} W/cm^2. This scaling should be treated with caution because the changes in density scale length (L_n) with irradiation conditions were not reported. The TPD threshold is known to decrease as L_n increases [Refs. 405, 409, and 411; see also Eq. (10-4) below], and it is reasonable to assume that T_{SH} should also depend on L_n. The energy in superhot electrons was estimated to be a fraction of 10^{-4} of the incident energy at the highest intensities. A similar superhot component was found by Mead *et al.*[423] for flat targets irradiated at 0.35 μm. While both papers recognized that it was difficult to identify whether SRS or the TPD instability was responsible,

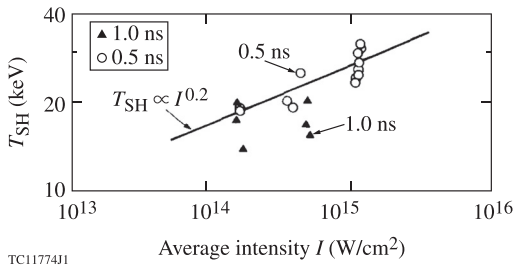

FIG. 10-4. "Superhot" electron temperature T_{SH}, attributed to the two-plasmon decay, as a function of laser intensity for a single 0.35-μm laser beam incident on a planar plastic target. Reproduced with permission from Phys. Fluids **27**, 2762 (1984). Copyright 1984 AIP Publishing LLC.

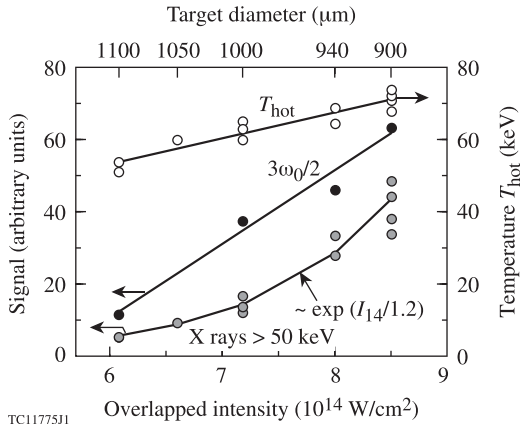

FIG. 10-5. Hot-electron temperature T_{hot}, $3\omega_0/2$ emission, and hard x rays (>50 keV) as functions of overlapped laser intensity for spherical implosion experiments on OMEGA. Reprinted with permission from Stoeckl *et al.*, Phys. Rev. Lett. **90**, 235002 (2003). Copyright 2003 American Physical Society.

Keck *et al.*[422] found the TPD instability to be the probable cause. This conclusion was consistent with earlier work by Phillion *et al.*,[424] who found, for 1-μm laser irradiation, simultaneous occurrence of $3\omega_0/2$ light and hard x rays.

2. Overlapping-beam experiments

Experiments designed to explore hot-electron production for the long density scale lengths applicable to ignition-scale, direct-drive NIF experiments were first carried out by Stoeckl *et al.*[425] using the 0.35-μm, 60-beam OMEGA laser. Both spherical and planar geometries were used.

In the spherical experiments, the density scale length was limited to the range 100–150 μm—substantially shorter than the ~500-μm scale length expected on the NIF. (The design shown in Fig. 3-6 has $L_n \sim 590\,\mu$m.) Figure 10-5 shows the scaling of hot-electron temperature, $3\omega_0/2$ emission, and hard (>50-keV) x-ray signal with overlapped laser intensity for these experiments. (The hot-electron temperatures shown here should be reduced by 40% because of an error in the analysis of the hard x-ray diagnostic identified by Froula *et al.*[426]) In these experiments, the overlapped intensity was changed by varying the target diameter. The laser energy was maintained constant and the beams irradiated the target at best focus, so the individual beam intensity was the same for all cases. The experiments thereby indicated that multibeam interactions are important for TPD.

The planar experiments were configured as shown in Fig. 10-6(a). A sequence of defocused primary and secondary beams was used to generate the long-scale-length plasma from planar CH targets. These beams were followed by up to six overlapping interaction beams. A density scale length of ~350 μm was expected for low-to-moderate overlapped intensities ($\lesssim 1 \times 10^{15}$ W/cm^2) using standard phase plates, while to achieve high intensities (>10^{15} W/cm^2), smaller laser spots were obtained for the interaction beams by using different phase plates. The smaller laser spots were predicted to produce shorter density scale lengths (180 μm), as a result of the preformed plasma being perturbed by the interaction beams, and higher plasma temperatures (~4.5 keV). Results for the hard x-ray emission, together with estimates of the fractional preheat (relative to the incident laser energy), are shown in Fig. 10-6(b), plotted against the overlapped laser intensity as in Fig. 10-5. For combinations of two to six interaction beams, the signals track the overlapped intensity.

The maximum inferred hot-electron fraction seen in Fig. 10-6(b) was ~0.1%. Stoeckl *et al.*[425] commented, "It is encouraging that the preheat level lies below 0.1% for intensities around 1.3×10^{15} W/cm^2, the peak intensity required for NIF direct-drive experiments." Interestingly, the hot-electron fraction in the planar experiments of Fig. 10-6 showed a significantly weaker scaling with intensity for intensities above 10^{15} W/cm^2. This may have been a result of the factor-of-2 reduction in scale length that occurred at the highest overlapped intensities. The most-intense interaction beams also significantly increased the temperature of the preformed plasma.

The planar experiments were consistent with the spherical experiments in providing evidence that, when using multiple overlapping beams, the overlapped intensity, and not the single-beam intensity, governed the threshold and scaling of hot-electron production by the TPD instability. Stoeckl *et al.*[425] suggested that multiple overlapping beams might contribute to instability by sharing a common decay plasma wave. Similar behavior has been predicted for the stimulated Brillouin and Raman scattering instabilities by DuBois *et al.*[427]

On the basis of overlapped intensity, Seka *et al.*[428] analyzed TPD signatures observed in OMEGA spherical

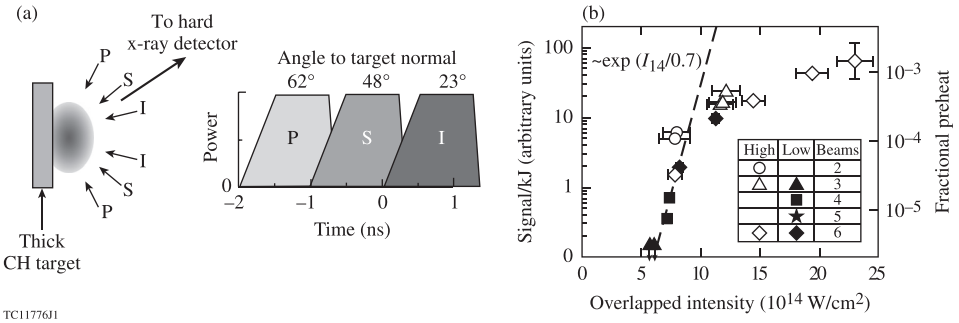

FIG. 10-6. (a) Schematic of planar experiments on OMEGA using three sets of beams with different timings: nine primary (P) beams, six secondary (S) beams, and two to six interaction (I) beams with smaller focal spots. (b) X-ray signal and fractional hot-electron preheat plotted against overlapped laser intensity for various numbers of interaction beams, including standard ("low") and high-intensity ("high") phase plates. Reprinted with permission from Stoeckl *et al.*, Phys. Rev. Lett. **90**, 235002 (2003). Copyright 2003 American Physical Society.

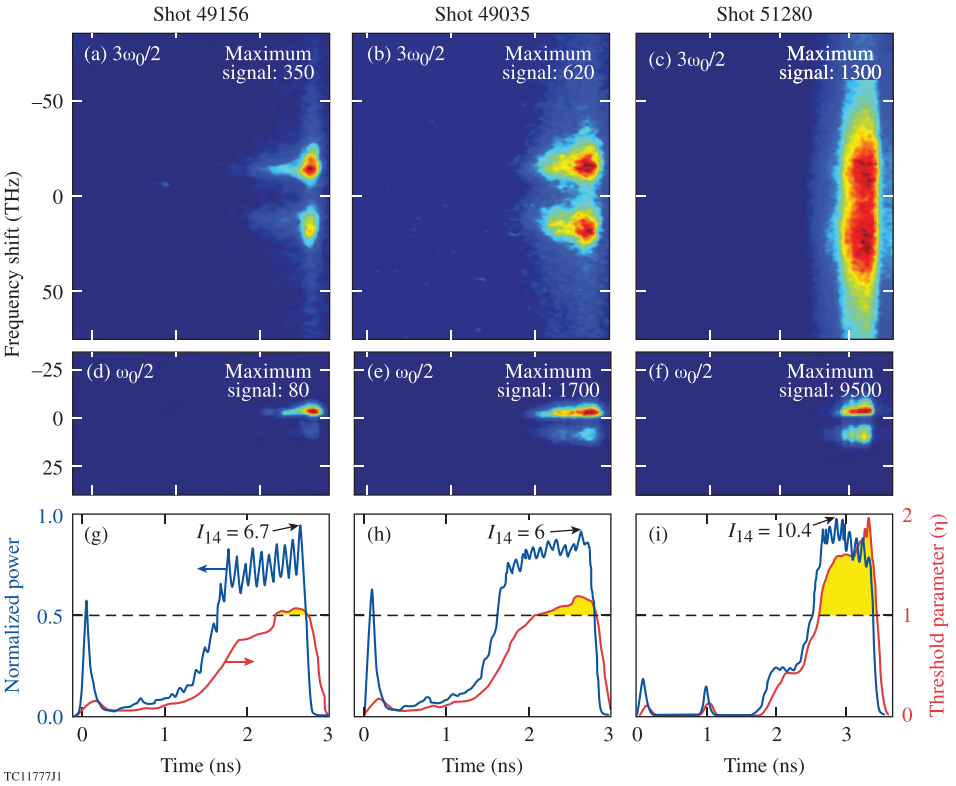

FIG. 10-7. Time-resolved spectra of $3\omega_0/2$ emission (top row) and $\omega_0/2$ emission (middle row) for three cryogenic implosions on OMEGA. Each column corresponds to one particular shot. For each shot, the normalized laser power histories and the computed TPD threshold parameter η are shown in the bottom row. The peak incident laser intensities I_{14} are given in units of $10^{14}\,\mathrm{W/cm^2}$. The $3\omega_0/2$ and $\omega_0/2$ emissions are observed when η exceeds unity. Reproduced with permission from Phys. Plasmas **16**, 052701 (2009). Copyright 2009 AIP Publishing LLC.

implosion experiments, for the first time accounting for the effects of scale length and plasma temperature in the analysis. This was done in an *ad hoc* way by substituting the total overlapped laser intensity into the theoretical expression for the TPD threshold derived by Simon *et al.*[409] for the onset of absolute instability of a single plane EM wave. This can be written as $\eta = 1$, where the threshold parameter η is given in the relevant regime by

$$\eta = \frac{I_{14} L_n(\mu\mathrm{m})}{230 T_e(\mathrm{keV})} \left(\frac{\lambda_0}{0.351\,\mu\mathrm{m}}\right), \tag{10-4}$$

where I_{14} is the laser intensity in units of $10^{14}\,\mathrm{W/cm^2}$ and L_n is the density scale length at quarter critical in microns. In these experiments, the coincidence of TPD signatures, combined with the absence of SRS backscattered light, was considered evidence for the dominance of the TPD instability over other potential sources of hot electrons or harmonic emission in direct-drive implosions.

Figure 10-7 shows time-resolved $3\omega_0/2$ [Figs. 10-7(a)–10-7(c)] and $\omega_0/2$ [Figs. 10-7(d)–10-7(f)] harmonic emission spectra obtained from three representative cryogenic implosions. The time-dependent threshold parameter η is shown in red in Figs. 10-7(g)–10-7(i). It was evaluated from the overlapped intensity, density scale length, and temperature (at the quarter-critical surface) predicted by 1-D *LILAC* hydrodynamic simulations. During the high-intensity portion of the laser pulse [normalized laser pulse shapes are shown in Figs. 10-7(g)–10-7(i)], the scale length varied between 100 and 150 μm, while T_e varied between 2 and 3 keV. Remarkably, for all three implosions, the harmonic signatures were observed only at times during which the threshold parameter was predicted to exceed unity.

The targets all contained 77- to 100-μm-thick DT or D_2 ice layers inside plastic (CH or CD) shells, one of which (shot 49156) was doped with 5% (atomic) Si over the outer half of the shell. The Si-doped shell increased the peak incident laser intensity required for the onset of harmonic emission; however, this was consistent with the expected behavior based on the threshold parameter. The effect of the Si dopant was to increase the coronal temperature, which raises the threshold intensity. This is consistent with reductions in the amount of energy in suprathermal electrons observed for targets with higher Z by Smalyuk *et al.*[429] and Hu *et al.*[430]

Figure 10-8 [from Ref. 428] shows time-resolved $\omega_0/2$, $3\omega_0/2$, and hard x-ray signatures for the high-intensity target shown in Fig. 10-7 (shot 51280). Notice that all three signals begin when η is greater than unity. By analysis of the harmonic emission, it is demonstrated in the same work that the unstable plasmon spectrum is much broader than would be expected on the basis of linear theory, but the Landau cutoff is respected (i.e., plasma waves were not observed with wave numbers greater than 0.25 λ_D). Similar broad plasma wave spectra were inferred by Meyer and Zhu[431] in earlier single-beam CO_2 laser experiments.

Further long-scale-length experiments investigating the TPD instability in planar geometry were carried out with four 0.35-μm beams on the OMEGA EP laser by Yaakobi *et al.*[432] and Froula *et al.*[426] Figure 10-9(a), from Ref. 432, shows the plasma conditions predicted by a 2-D *SAGE* simulation at the end of the laser pulse for a typical experiment with a peak overlapped laser intensity of $5.8 \times 10^{14}\,\mathrm{W/cm^2}$. Density contours spaced by a factor of 2 are shown together with a subset of 3-D laser ray trajectories projected into the (r, z) plane. In the simulation, the laser energy is predicted to

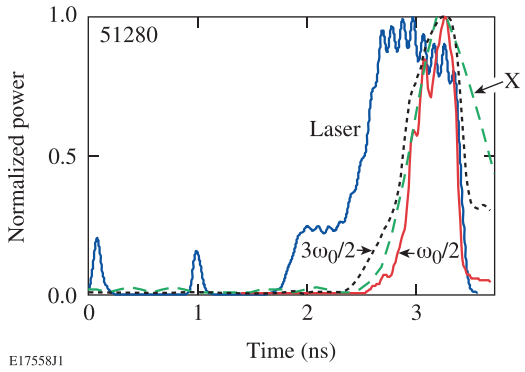

FIG. 10-8. Power histories of the incident laser pulse, the $\omega_0/2$ and $3\omega_0/2$ emissions, and hard x rays above 40 keV (X) for a high-intensity cryogenic implosion experiment at 10.4×10^{14} W/cm^2 (corresponding to the right-hand column in Fig. 10-7). The correlation of the hard x-ray and harmonic emissions provides evidence that the electrons are generated by the TPD instability. Reproduced with permission from Phys. Plasmas **16**, 052701 (2009). Copyright 2009 AIP Publishing LLC.

be nearly totally absorbed. Laser rays are attenuated to 70% of their initial energy by the time they reach quarter critical (for lower incident intensities this fraction is reduced to ~50%). The plasma scale length saturates at ~400 μm near $n_c/4$ halfway through the 2-ns laser pulse (limited by the laser spot diameter of ~1100 μm). The coronal plasma temperature is ~2.6 keV through most of the laser pulse.

Using the time- and space-integrated K_α line emission as a diagnostic, the energy in fast electrons as a fraction of the incident laser energy was found to increase from 0.01% at incident intensities of 2×10^{14} W/cm^2 to ~1% at intensities of 6.5×10^{14} W/cm^2 [Fig. 10-9(b)] for a density scale length that was approximately constant at ~350 to 400 μm. This level of hot-electron production [greater than the ~0.1% limit that can be coupled into the compressed fuel (Sec. III B)] has led to a renewed concern regarding the amount of preheat that might be present in the OMEGA implosions and future ignition designs on the NIF if, indeed, the hot-electron production is a function of the overlapped beam intensity regardless of the number of beams. It is possible that planar target experiments overestimate the coupling to a spherical target implosion.

To investigate this further, Michel *et al.*[433] carried out a series of experiments in three configurations: (a) up to four overlapped OMEGA EP beams incident on a planar target; (b) 18 overlapped OMEGA beams on a planar target (in three rings of six at incidence angles of 23°, 48°, and 63°); and (c) 60 overlapped OMEGA beams on a spherical target. The hot-electron fractions were measured from K_α emissions from Mo layers embedded in the targets. The hot-electron fraction, when plotted as a function of overlapped intensity, depended on the beam configuration. Michel *et al.* recognized that the intensity threshold depends on the hydrodynamic parameters at the quarter-critical surface and the configuration of the laser beams. However, they found that all their data fell on a single curve when plotted against a quantity known as the common-wave gain,[434] which is similar to the parameter η but includes adjustments calculated for each configuration that are based on the beam polarizations and the sum of the intensities of the beams that share the same angle with the common electron plasma wave vector.

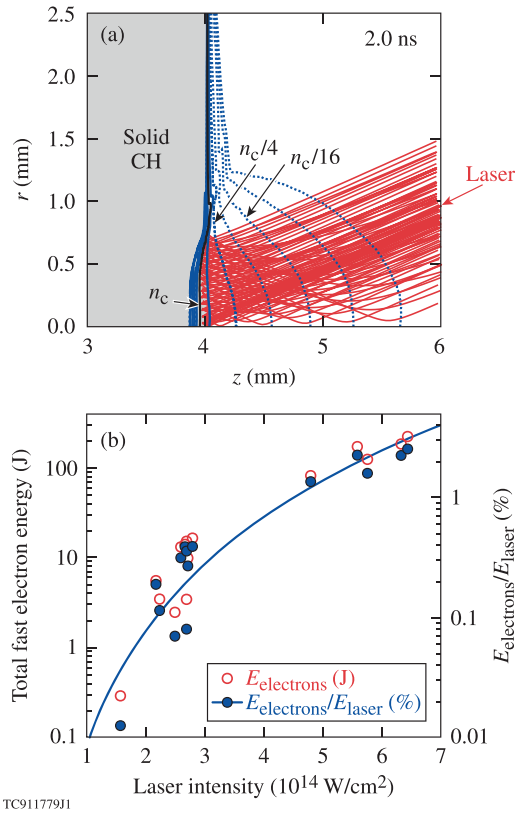

FIG. 10-9. (a) *SAGE* simulation of long-scale-length planar target experiments on OMEGA EP. Electron density contours are shown at the end of the laser pulse (2.0 ns) together with the projection onto the (r,z) plane of a subset of laser rays for an 1100-μm-diam beam. (b) Total energy in fast electrons $E_{\text{electrons}}$ and relative energy $E_{\text{electrons}}/E_{\text{laser}}$ versus incident overlapped laser intensity. Reproduced with permission from Phys. Plasmas **19**, 012704 (2012). Copyright 2012 AIP Publishing LLC.

One further step is necessary to relate the measured hot-electron fraction to the preheat experienced by a cryogenic implosion target. The amount of preheat for a given implosion design depends on the details of the hot-electron source. For example, a large angular spread of the hot electrons at their generation point would lead to less preheat based on geometrical considerations (assuming straight-line trajectories). This is because the quarter-critical surface is at a larger radius than the cold fuel shell and the solid angle subtended by the fuel will be significantly less than 2π. The hot-electron source temperature is another factor as the less-energetic electrons in the distribution undergo more attenuation in the shell.

An experimental technique was recently developed by Yaakobi *et al.*[435] to estimate the angular divergence of hot electrons for conditions relevant to directly driven implosions. Molybdenum-coated glass balls of varying diameters were suspended concentrically inside CH shell targets, which were then irradiated on the OMEGA laser at intensities $I \sim 1 \times 10^{15}$ W/cm^2. The hot-electron divergence was inferred from the dependence of the hot-electron–produced Mo K_α signal on the diameter of the Mo shell (while maintaining similar interaction conditions in the underdense corona). The absolute K_α signal was best fit by a widely divergent hot-electron source, even after considerations of hot-electron scattering and return-current instabilities were

taken into account. These results suggest that only ~25% of the hot electrons generated contribute to preheat in spherical implosions.

3. Numerical simulations

Several numerical methods have been used to investigate the nonlinear evolution of the TPD instability when excited by a single plane EM wave. Since the TPD growth rate vanishes for decay wave vectors that are parallel to the pump wave vector, the instability must be studied in at least two dimensions. The first such calculations were performed by Langdon *et al.*[436] using the particle-in-cell (PIC) technique. These simulations highlighted the importance of density profile steepening and the role played by ion fluctuations in the nonlinear evolution of the instability. Hot-electron tails were formed with an effective temperature of ~100 keV.

The majority of single-beam calculations performed since have been 2-D calculations in the plane of polarization. These generally fall into two categories: explicit PIC calculations[437] and reduced models that employ time enveloping. Examples of the latter include reduced-description PIC,[438] extended Zakharov,[439,440] and Zakharov models with quasi-linear evolution of the electron distribution function.[441] All of these calculations have confirmed the importance of ion turbulence in determining the nonlinear saturation of the instability. Generally speaking, explicit PIC calculations tend to overpredict the fraction of hot electrons relative to experimental observations, but they have demonstrated that this fraction is sensitive to the collisional damping of plasma waves,[442] an effect also observed in reduced models.[441] Work with reduced PIC models has attempted to describe nonlinear saturation and hot-electron production in terms of cavitating Langmuir turbulence,[443] where hot electrons are accelerated by collapsing Langmuir wave packets. The reduced PIC calculations have also validated some of the assumptions used in the quasi-linear Zakharov models.[444]

B. Stimulated Brillouin scattering (SBS) and cross-beam energy transfer (CBET)

Brillouin scattering[445] was proposed in 1922 as an interaction between an electromagnetic wave and an acoustic wave (phonon) in a solid. In laser-produced plasmas, the process occurs as the scattering of an incident photon ($\mathbf{k}_0$, ω_0) from an ion-acoustic wave ($\mathbf{k}_{ia}$, ω_{ia}) to produce a scattered photon ($\mathbf{k}_s$, ω_s), satisfying the wave-vector matching equation ($\mathbf{k}_0 = \mathbf{k}_s + \mathbf{k}_{ia}$), as shown in Fig. 10-10. The respective frequencies satisfy $\omega_0 = \omega_s + \omega_{ia}$, with the scattered frequency ω_s slightly less than ω_0 because ω_{ia} is small. The process is frequently encountered as an instability, known as stimulated Brillouin scattering (SBS), when the ion-acoustic wave is generated through the beating of the incident and scattered waves via the nonlinearity of the ponderomotive force.

A treatment of SBS in the context of a high-intensity electromagnetic wave interacting with a solid, where the nonlinear coupling occurs through the elasto-optic effect, was given by Kroll.[446] Kroll recognized the analogy between

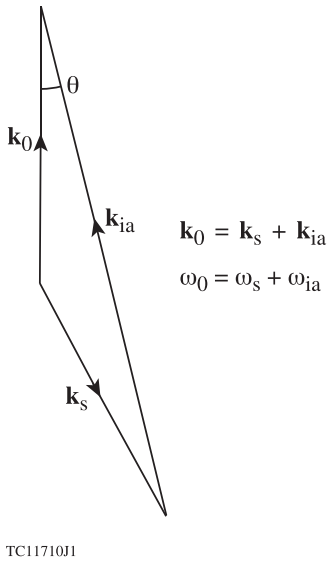

FIG. 10-10. Wave-vector diagram for stimulated Brillouin scattering (SBS). An incident photon ($\mathbf{k}_0$, ω_0) scatters off an ion-acoustic wave ($\mathbf{k}_{ia}$, ω_{ia}) to produce a scattered photon ($\mathbf{k}_s$, ω_s). Backscattering occurs for $\theta = 0$ and sidescattering for $\theta \neq 0$. The ion-acoustic wave is generated by the beating of the incident and reflected waves.

SBS and optical parametric amplification. Comprehensive treatments of SBS in plasmas are given by Liu *et al.*[447] and Forslund *et al.*[448] Early simulations of SBS are described by Forslund *et al.*[449,450] and Kruer *et al.*[451] A treatment of sidescattering is given by Galeev *et al.*,[452] who found maximum gain for scattering through 90°, a result for which no experimental evidence ever seems to have been offered.

The SBS process has always been recognized as a potential threat to ICF because of its ability to scatter light from the plasma before it can propagate to high densities and be absorbed, and it was widely investigated from the early days of laser–plasma experiments. It has, however, been consistently difficult to observe SBS unambiguously. While it is straightforward to measure light scattered from the plasma, most conveniently through a focus lens, it is nontrivial to distinguish between the unabsorbed light (meaning light that has simply not been absorbed while refracting through the plasma and reflecting from near the critical surface) and light that is a result of stimulated scattering. (The terms "reflected" and "scattered" are used interchangeably when experimental observations are reported and so should not be understood as statements of origin.) Many early experiments at 1-μm laser wavelength saw a variety of scattered-light signatures that suggested SBS; however, predictive models of SBS that explained the wide range of experimental observations were never developed. After the move to short-wavelength lasers in the early 1980s, and as plasmas with larger scale lengths (which should be more susceptible to SBS since they enable phase matching to be maintained over larger distances) were generated from larger laser systems, it was found that the fraction of scattered light was lower and broadly in agreement with models that included inverse bremsstrahlung as the dominant absorption mechanism (Sec. V). The concern that SBS would become worse proved unfounded for conditions relevant to direct drive. Fewer

claims were made of significant SBS and the limited observations of SBS were generally at very low levels. It is only recently that interest in the relevance of SBS to direct-drive ICF has been revived because of its potential to scatter energy from one beam to another in spherical irradiation geometry—a process known as cross-beam energy transfer.

Two early observations of the time-resolved light reflected from the target into the focusing lens are shown in Fig. 10-11. The experiment of Fig. 10-11(a), from Floux *et al*. at Limeil,[73] was one of the first from which thermonuclear neutrons were reported. A solid D_2 target was irradiated by a long pulse (3.5 ns) of 1-μm light focused onto a small spot (150 μm) using an *f*/0.9 lens (29° half-angle). Approximately one third of the incident light was reflected into the lens. Figure 10-11(a) also shows the simulated reflected light, which agrees remarkably well with the observation. This was calculated using a 1-D hydrodynamics code (with an adaptation to approximate the divergence of the flow) that included only basic physics, in particular, inverse-bremsstrahlung absorption, electron thermal conduction, and separate electron and ion temperatures, but no parametric processes such as SBS. The actual absorption might have been less than implied since light reflected outside the (large) lens solid angle was not taken into account. Indeed, few experiments over the years have collected anywhere close to 100% of the scattered light. However, the experimental results are consistent with the reflected light being just the light that is not absorbed by inverse bremsstrahlung. The decrease of reflectivity early in the pulse is consistent with an increasing plasma scale length, and the steady reflectivity during the main part of the pulse is consistent with a steady divergent flow being established. There is no sudden onset of reflection as might be expected when an intensity threshold or a minimum scale length is reached. The neutron yield was also fairly close to predictions.

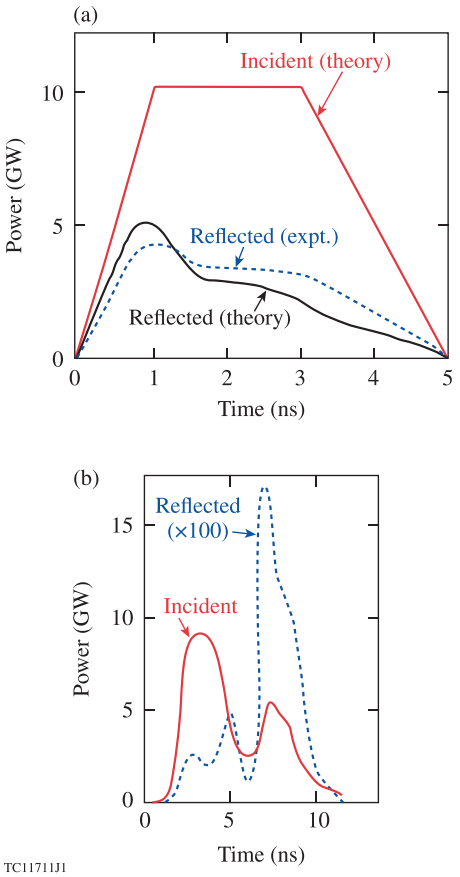

FIG. 10-11. Incident laser power and power reflected through the focus lens for two experiments, both using 1-μm wavelength at $\sim 1 \times 10^{14}$ W/cm^2. (a) Solid D_2 target, *f*/0.9 lens. Reprinted with permission from Springer Science + Business Media. From Floux *et al*., "Nuclear DD reactions in solid deuterium laser created plasma," in Laser Interaction and Related Plasma Phenomena, 1972, Plenum Press. (b) Polyethylene target, *f*/7 lens. Reprinted with permission from Shearer *et al*., Phys. Rev. A **6**, 764 (1972). Copyright 1972 American Physical Society. In (a) the reflected power is compared with the prediction of a 1-D hydrodynamic model.

In the other experiment [Fig. 10-11(b)], plastic targets were irradiated at LLNL by Shearer *et al*.[98] at a comparable intensity of $\sim 2 \times 10^{14}$ W/cm^2 and a wavelength of 1 μm. Bursts of reflected light were seen, with up to 3% of the incident laser power observed in the *f*/7 lens (4° half-angle). The authors ascribed this light to SBS, claiming that several nanoseconds were required to set up the right plasma conditions. They also suggested that the reflected light rays were retracing the paths of the incident rays. However, if this were true, very close to 100% of the incident light seen in Fig. 10-11(b) would have been absorbed, in total contradiction to the large body of later work that found nowhere near 100% absorption of 1-μm radiation at these intensities. It is likely that the bulk of the scattered light emerged in a much larger solid angle than that of the focus lens. The bursts of light into the lens could then be associated with changes in the shape of the plasma density profile near critical, sometimes referred to as a rippled critical surface, which could result from a variety of mechanisms including hot spots (speckle) in the laser beam and/or filamentation.

Ray retracing was investigated in the "question mark" experiment carried out at Garching by Eidmann and Sigel.[453] They focused a long-pulse (5-ns), 1-μm laser onto a small focal spot. Their beam was strongly edge-peaked except at best focus, where the spot diameter was $\sim$40 μm. A notable result is shown in Fig. 10-12. The incident beam [Fig. 10-12(a)] passed through a mask on its way to the target. A portion of the reflected beam was sampled by a beamsplitter (encountered before the reflected beam reached the mask) and recorded on burn paper [Fig. 10-12(b)]. This result was obtained away from best focus for solid D_2 and the effect was also present although less strong for other materials. Low levels of scattering outside the mask were hard to see because of the strong nonlinearity of the burn paper. While quantitative measurements of the scattered light were not given, the close reproduction of the question mark provided strong evidence for ray retracing, ascribed to SBS.

Very limited corroboration for ray retracing was provided from other experiments. Most notable was an experiment at NRL by Ripin *et al*.[454] in which large direct backscatter into an *f*/1.9 lens (15° half-angle) was observed when a plasma preformed by a prepulse was irradiated by a short, 1-μm, 75-ps pulse focused to a small spot (30 μm) at an average intensity up to 7.5×10^{15} W/cm^2. The backscatter remained high ($\sim$30% to 40%) even at angles of incidence above 75°, leading to the conclusion (based on the assumption of a 1-D planar preformed plasma) that SBS was taking place below $0.1 n_c$.

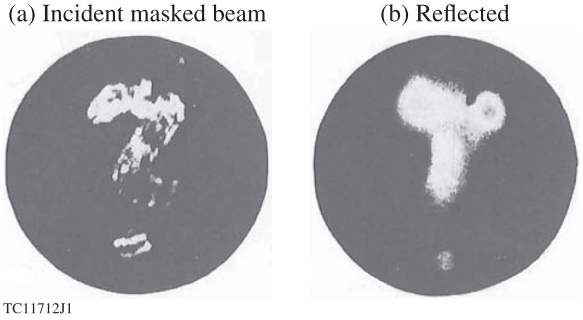

FIG. 10-12. Demonstration of ray retracing from a solid D_2 target. (a) An aperture in the shape of a question mark was placed in the incident beam. (b) This shape was reproduced in the reflected beam. Reprinted with permission from Springer Science and Business Media. From Eidmann and Sigel, "Backscatter experiments," in Laser Interaction and Related Plasma Phenomena, 1974, Plenum Press.

A theory of optical ray retracing in support of this experiment was provided by Lehmberg.[455] It is notable that Ripin's result was obtained only when there was a prepulse. The aspect of this experiment that might provide commonality with the Garching experiment is the use of a tightly focused beam on a large plasma; in the Garching experiment, the large plasma resulted from the use of a long pulse. Otherwise, most experiments (including those of Ref. 454 when the prepulse was absent) did not observe ray retracing; rather, the scattered light (whether or not ascribed to stimulated processes) emerged with a broader range of angles than the incident lens cone. For example, Godwin *et al.*[127] found very little direct backscatter without a prepulse, but a lot of direct backscatter when there was a prepulse. Experiments at LLNL, where the angular dependence of scattered light was generally well characterized,[456–459] showed differences in scattering parallel and perpendicular to the laser polarization, beyond what might be expected from resonance absorption, suggesting stimulated sidescattering.

Many experiments at 1-μm wavelength had unintentional prepulses, which were hard to eliminate because of limitations of laser technology in the early years of interaction physics experiments. Such prepulses could affect the interpretation of these experiments; for example, a high-intensity laser incident on a preformed plasma can channel through the plasma by heating and ablating the material, resulting in the critical surface moving back toward the solid and thereby producing a red shift in the reflected light. This was seen in an experiment by Goldman *et al.*,[460] where a prepulse of ~0.6% of the (1-μm) laser energy preceded the main pulse by 6 ns. Goldman *et al.* irradiated spherical targets through an *f*/2 lens and found that the scattered light was red shifted and spectrally broadened. They interpreted this as SBS and, based on the red shift, estimated that the SBS was occurring between 0.90 and 0.98 of critical (in contrast to Ref. 454). They recognized that the fraction of light reflected back along the incident beam is difficult to estimate since it is a sensitive function of the shape and position of the reflecting surfaces.

Spectral analysis of the scattered light was commonly used. Examples of two such spectra, obtained by Phillion *et al.*[457] at high intensities (mid-10^{15} W/cm^2) at 1-μm-wavelength on the Argus laser at LLNL, are shown in Fig. 10-13, one for a glass microshell, which showed a red shift, and the other for a parylene disk, which showed a blue shift. Since the frequency of the scattered SBS wave is downshifted from the incident frequency by the ion-acoustic frequency, a red shift has sometimes been understood to be a signature of SBS. However, as was recognized by Büchl *et al.*,[461] this shift must be combined with the Doppler shift corresponding to the interaction region. (Büchl *et al.* observed a red shift in the backscattered light from a solid D_2 target and interpreted it as resulting from the shock wave moving into the solid.) The red shift of Fig. 10-13(a) could be interpreted as resulting from the implosion of the microshell target, and, as recognized in Ref. 457, the blue shift of Fig. 10-13(b) could result from the Doppler shift associated with the expanding critical surface. (This would include a blue component resulting from the change of optical path in an expanding plasma, which is present even if the critical surface is stationary.[156]) Phillion *et al.*[457] interpreted both spectra as SBS, however, citing the significant spectral broadening as additional evidence for SBS. No simulations were given of the broadening or the shifts. Since both spectra were time integrated, it was impossible to tell whether the broadening was present at all times or whether it reflected changing plasma conditions.

In the experiment of Ref. 457, a large fraction of the incident light (~30% to 50%) was reflected back into the *f*/1 focus lens, so the spectra seen in Fig. 10-13 should include both stimulated scattering and classically unabsorbed light, but it is hard to distinguish the two components. On the simple basis of normal incidence on a planar plasma, one would expect a significant amount of incident light to reach the critical surface, provide the resonance absorption that accounted for most of the small (~12%) absorption observed in these high-intensity experiments, and return from the critical surface to be seen as a relatively unbroadened component of the spectrum. However, this simple picture appears not to apply, and one should not rule out other broadening mechanisms such as might be associated with laser hot spots, filamentation, and plasma inhomogeneities.

A different interpretation was provided by Tarvin and Schroeder,[462] who reported experiments at KMS Fusion also

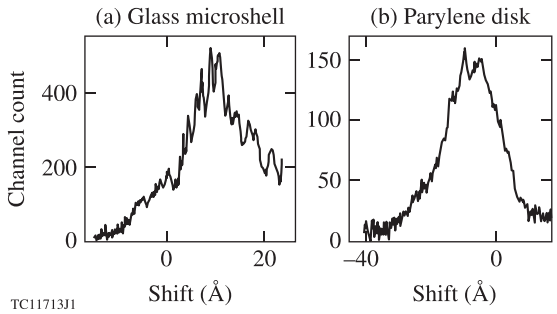

FIG. 10-13. Backscatter spectra at mid-10^{15} W/cm^2 for (a) a glass microshell and (b) a parylene disk irradiated on Argus with 1-μm laser light. Zero shift corresponds to the incident laser wavelength. The microshell showed a red shift and the disk a blue shift; both spectra are broadened. The data were interpreted as SBS. Reprinted with permission from Phillion *et al.*, Phys. Rev. Lett. **39**, 1529 (1977). Copyright 1977 American Physical Society.

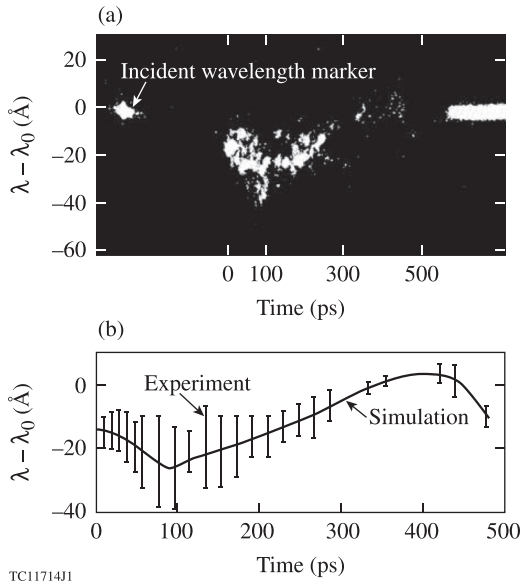

FIG. 10-14. (a) Time-resolved spectrum (deviation from the 1-μm laser wavelength λ_0) from a spherical glass target irradiated at 6.6×10^{15} W/cm^2 on the KMS Chroma laser using a pair of *f*/0.2 ellipsoidal mirrors. (b) Simulation of the data. The length of the bar at each time gives the visible extent of the spectrum in the streak record. The spectrum was understood to shift to the blue as a Doppler effect associated with the expanding critical surface and return toward zero after 250 ps as the critical surface became nearly stationary. Reprinted with permission from Tarvin and Schroeder, Phys. Rev. Lett. **47**, 341 (1981). Copyright 1981 American Physical Society.

at high intensity (6.6×10^{15} W/cm^2) and 1-μm wavelength, in which the spherical targets were irradiated using two *f*/0.2 ellipsoidal mirrors. Figure 10-14(a) shows a streaked backscattered-light spectrum, which is compared with a simulation in Fig. 10-14(b). The most-notable feature is an initially growing blue shift, understood to be a Doppler shift associated with the expanding plasma,[156] followed by a return to zero shift as the plasma profiles become more stationary (i.e., change less with time). Tarvin and Schroeder offered two explanations for the broadening: (1) the laser rays encounter the target at different angles, experiencing a range of Doppler shifts; and (2) different parts of the critical surface move with different velocities at any given time. Their simulations show very little SBS because of large gradients of density and velocity outside the critical surface.

In more recent years, experiments were carried out on the OMEGA laser in which high-intensity 0.35-μm interaction beams were used to irradiate long-scale-length plasmas, formed from flat, solid targets using low-intensity, defocused beams, in an attempt to access parameters relevant to NIF ignition designs. One such experiment was reported by Regan *et al.*[463] Exploding-foil and solid-target plasmas were created with parameters approximating those expected at the peak of ignition pulses. The temperature (~4 keV) was diagnosed spectroscopically and the evolution of the peak density in the exploding-foil plasmas was determined from streaked SRS measurements. Both measurements were consistent with 2-D hydrodynamic simulations. No SBS of any significance was seen from the interaction beam, with an upper limit of 0.1% for the exploding foils and an estimate of 0.2% for the solid targets.

A similar experiment, reported by Myatt *et al.*,[464] was designed to generate a region with a flat velocity profile, favorable for SBS as the Doppler shift is constant along the path of the stimulated wave. Figure 10-15 (from Ref. 464) shows a streaked spectrum of the backscattered light at normal incidence. Of note is the component whose blue shift increases with time. This is understood to be SBS generated in the region, predicted to move away from the target, where the velocity profile is flat. The square points are predictions for the maxima in the backscattered spectrum based on an SBS code being used to post-process profiles from hydrodynamic simulations. Classical absorption is strong in these experiments, and the amount of SBS (backscattered into an *f*/6 focus lens) is typically less than a few percent.[465] The redshifted feature in Fig. 10-15 is associated with nonlinear SBS in the dense plasma near the critical surface.[466] In Ref. 466, the reflected light spectra have features associated with both SBS and unabsorbed refracted light, addressing the long-standing question about the relative roles of these two effects.

Some insight into the origin of the SBS observed in these experiments is provided by Fig. 10-16, which shows the time-integrated reflectivity through a focus lens measured as a function of interaction beam intensity by Seka *et al.*[467] A significant difference is observed depending on whether or not polarization smoothing (PS) (Sec. VI D) is used. Peak speckle intensities within the beam are reduced by a factor of 2 with PS, as the two polarizations are independent. When the PS points are plotted with their intensity reduced by a factor of 2, they lie together with the points without PS. This consistency suggests that the reflectivity is a result of SBS occurring in hot spots (high-intensity laser speckles).

More recently, much attention has been directed to seeded SBS. "Pure" SBS results from the amplification of thermal noise, requiring a large velocity-gradient scale length to provide a sufficient number of *e* foldings for significant reflection unless the absolute threshold is exceeded. As

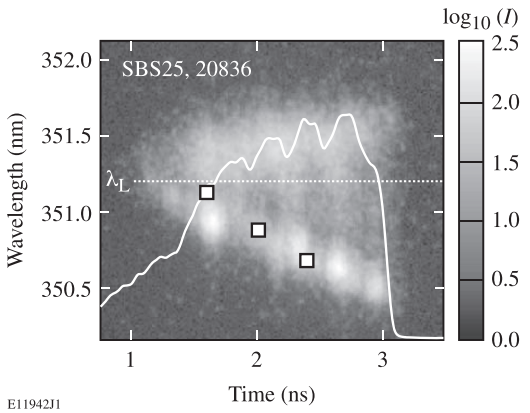

FIG. 10-15. Time-resolved backscatter spectrum of a high-intensity ($\sim 8.5 \times 10^{14}$ W/cm^2) interaction beam from a long-scale-length plasma experiment on OMEGA. The white curve gives the incident laser pulse shape on a linear scale. The squares give the predicted locations of maxima on the backscattered frequency spectrum based on the evolving plasma profiles. Reproduced with permission from Phys. Plasmas **11**, 3394 (2004). Copyright 2004 AIP Publishing LLC.

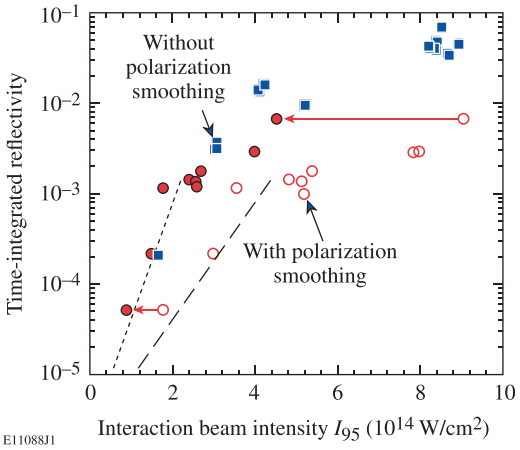

FIG. 10-16. Time-integrated reflectivity through the focus lens as a function of interaction beam intensity with and without polarization smoothing (PS), from long-scale-length plasma experiments on OMEGA. The solid circles are obtained from the open circles with the intensity reduced by a factor of 2; their consistency with the square points suggest that the reflectivity is due to SBS occurring in hot spots, which are a factor of 2 less intense with PS. The dashed lines are to guide the eye. Reprinted with permission from Springer Science and Business Media. From Seka *et al.*, "Laser-plasma interaction diagnostics for ICF fusion research," in Advanced Diagnostics for Magnetic and Inertial Fusion, 2002, Kluwer Academic/Plenum.

early as 1972, it was recognized that SBS could be seeded by backscattered light from the target for laser beams with a large bandwidth.[98] (The seed beam must have the correct wavelength to satisfy the frequency-matching conditions.) This was subsequently recognized by Begg and Cairns[468] and Randall *et al.*[469] Using a 1-D model with the laser at normal incidence, Randall *et al.* noted that there is a region with the appropriate Mach number at which the reflected light from the critical surface seeds SBS backscatter and offered this as an alternative to the phase-conjugate explanation of Lehmberg.[455]

Essentially the same physics occurs when the seed is not a portion of the incident beam that is reflected from near critical but light from another laser beam. In this case, seeded SBS is more commonly known as cross-beam energy transfer (CBET). This process was predicted to be important for NIF conditions by Kruer *et al.*[470] Kirkwood *et al.*[471] presented the first observation of energy transfer between frequency-mismatched laser beams and a stimulated ion-acoustic wave. Another demonstration of CBET is shown in Fig. 10-17, from long-scale-length plasma experiments carried out on OMEGA by Seka *et al.*[472] Here, six overlapping high-intensity interaction beams irradiated a preformed plasma. The target was oriented so that specular reflections from Beamline 23 would enter the focus lens of Beamline 25, where there was a backscatter station that recorded the time-resolved backscattered light. In all cases the other four interaction beams (shown in blue) were used. The specular reflection from just Beamline 23 and the backscatter from just Beamline 25 were small, but with both beams present the backscatter from Beamline 25 was considerably greater, providing evidence of seeded SBS. The short duration of the backscatter is understood on the basis of changing plasma conditions associated with the motion of a velocity plateau similar to that discussed in relation to Fig. 10-15. The CBET process has been observed by Glenzer *et al.*[473] and Michel *et al.*[474] in recent indirect-drive experiments, where it was demonstrated to be possible to tune the implosion symmetry on the NIF by shifting the wavelength of the outer beams with respect to the inner beams.

Recent work by Igumenshchev *et al.*[158] has examined the effect of CBET on direct-drive implosions. The configuration of interest is shown in Fig. 10-18(a), where incoming energy in one beam (represented as Ray 1) is sidescattered into the outgoing path of another beam (represented as Ray 2). Assuming that both beams have the same frequency, phase matching requires the interaction to occur in the vicinity of the Mach-1 surface. [In practice, both beams have some imposed spectral broadening due to SSD (Sec. VI C) and some additional broadening resulting from propagation through the plasma.] While the scattering process can occur between different rays within a single beam, a more-important situation occurs when central rays of one beam, incident near normal and therefore potentially capable of experiencing high absorption, are scattered into the emerging paths of near-tangential rays from another beam.

Figure 10-18(b) shows the incident and scattered power from the implosion of an 830-μm-diam plastic shell on OMEGA. Two simulations without CBET (one using a flux-limited model with $f = 0.06$ and the other using a nonlocal model) underestimate the scattered power, while a simulation that includes both the nonlocal model and CBET agrees very closely with observations. The neutron bang time (time of peak neutron generation) predicted for this shot using CBET is also in better agreement with experiment than the other models, which predict a bang time $\sim$150 ps earlier. Igumenshchev *et al.*[158] estimate that CBET can reduce the laser absorption by 10% to 20%. While the scattered light is matched well in Fig. 10-18(b), for an incident intensity of 5×10^{14} W/cm^2 (corresponding to a power of 11 TW), the CBET model predicts more scattered light than measured at $\sim 10^{15}$ W/cm^2 (Ref. 475); this discrepancy was ascribed to an additional absorption mechanism such as the two-plasmon–decay instability.

A time-resolved spectrum of scattered light from a similar plastic-shell implosion is shown in Fig. 10-18(c). As in

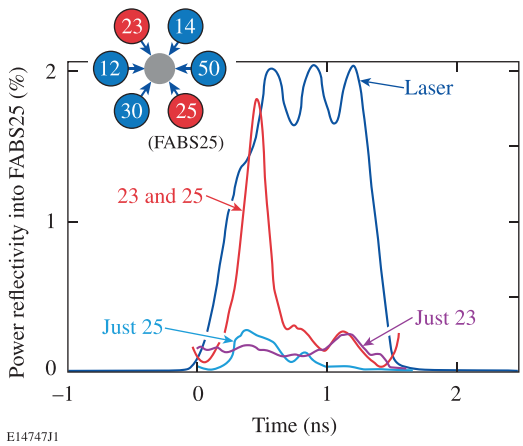

FIG. 10-17. Demonstration of seeded SBS from long-scale-length plasma experiments on OMEGA, where six overlapping interaction beams (inset) irradiate a preformed plasma. The power reflectivity into the FABS25 backscatter station is shown for single-beam backscattering ("Just 25"), single-beam reflection ("Just 23"), and seeded backscattering ("23 and 25"). The laser intensity (in arbitrary units) is also shown (from Ref. 472).

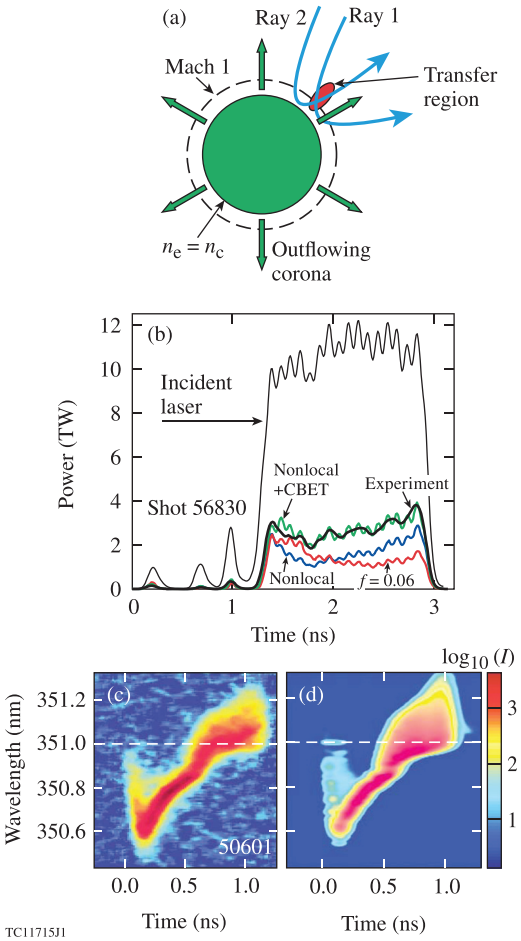

FIG. 10-18. (a) Schematic of cross-beam energy transfer (CBET) in the corona of a spherical target, where incoming energy in one beam (Ray 1) is scattered into the outgoing path of another beam (Ray 2). (b) Incident and (lower curves) scattered laser power from a plastic-shell implosion, including predictions of three models. (c) Measured time-resolved spectrum of the backscattered light from a similar implosion. (d) Simulation of (c) using nonlocal transport and CBET (with the parameter η described in Ref. 158 equal to 0.75). Reproduced with permission from Phys. Plasmas **17**, 122708 (2010). Copyright 2010 AIP Publishing LLC.

Fig. 10-14, one sees an early-time blue shift resulting from the initial plasma expansion followed by a later-time red shift as the target implodes. A simulation of the spectrum including the nonlocal model and CBET and incorporating the formulation of Dewandre *et al.*[156] for the changing optical path through the plasma [Fig. 10-18(d)] agrees well with the experiment.

The estimate of Ref. 158 that 10% to 20% of laser drive energy can be lost because of CBET in OMEGA implosions motivated further work to test the predictions of CBET models and to search for mitigation strategies. Experiments were performed on OMEGA that demonstrated the predicted enhancement in laser coupling in implosions with beams smaller than the target size.[475,476] Narrowing the laser beam reduced the electromagnetic seed caused by light refracting through the corona near the edge of the target and mitigated the CBET losses. However, this method has a limitation on systems such as OMEGA since the drive uniformity becomes worse when there is less beam overlap on the target. Future laser systems could overcome this limitation by using a large number of beams.[475] Another possible CBET mitigation strategy is to introduce a frequency shift between different laser beams to move the resonant coupling from the Mach-1 surface (Fig. 10-18) to regions with lower density and correspondingly lower SBS gain. Calculations performed in Refs. 158 and 475 indicate that frequency shifts equal to or larger than 5 Å (at $3\omega_0$) have a mitigating effect. While such shifts are challenging to realize on current laser systems, they may be feasible for future laser systems. Additionally, the CBET gain can be reduced by increasing the plasma temperature, which could be brought about by the use of higher-Z ablators or ablators with higher-Z layers.

Many examples of cross-beam interactions are closely related to CBET, including the beat-wave generation of electron plasma waves and ion-acoustic waves by crossing EM beams, four-wave mixing, and phase conjugation. More recently, there has been great interest in the use of cross-beam interactions under conditions not directly relevant to direct-drive ICF to achieve laser pulse compression or Raman amplification, for example. These topics are described in two recent review articles by Kirkwood *et al.*[477,478]

C. Stimulated Raman scattering (SRS)

Early in the development of quantum mechanics it was realized that a photon could be inelastically scattered by a molecule, resulting in a transition of the molecule to a higher-frequency vibrational state and a photon downshifted in frequency by the same amount. This effect was predicted by Smekal[479] in 1923 and observed in 1928 in liquids by Raman[480] and in crystals by Landsberg and Mandelstam.[481] The transition probability increases with the number of downshifted photons present; because of this stimulated emission, the downshifted photons tend to form a coherent wave that amplifies exponentially. This SRS was analyzed and proposed as a possible basis for a laser by Hellwarth[482] in 1963.

In laser-irradiated coronal plasmas, SRS arises from the parametric resonance between the incident laser light with the normal modes of the plasma (electron plasma waves, also known as Langmuir waves) rather than the vibrational states of molecules. The incident and scattered light waves satisfy the electromagnetic dispersion relations $\omega_0^2 = \omega_p^2 + c^2k_0^2$ and $\omega_s^2 = \omega_p^2 + c^2k_s^2$, where $(\mathbf{k}_0, \omega_0)$ and $(\mathbf{k}_s, \omega_s)$ are the wave vector and frequency of the incident and scattered light waves, respectively, ω_p is the electron plasma frequency, and c is the speed of light. The plasma wave $(\mathbf{k}_e, \omega_e)$ satisfies the Bohm–Gross dispersion relation $\omega_e^2 = \omega_p^2 + 3v_{th}^2k_e^2$ [Eq. (10-3)], where v_{th} is the electron thermal velocity. The basic geometry is shown in Fig. 10-19 for near-backscatter, sidescatter, and near-forward scatter. The frequency and wave-vector matching conditions are given by $\omega_0 = \omega_s + \omega_e$, $\mathbf{k}_0 = \mathbf{k}_s + \mathbf{k}_e$. It is apparent from the dispersion relations and the frequency-matching condition that SRS cannot occur at plasma densities above quarter-critical (ω_p above $\omega_0/2$). Another restriction is that the plasma wave should not be suppressed by Landau damping, which requires $k_e\lambda_D \lesssim 0.25$, where $\lambda_D = v_{th}/\omega_p$ is the Debye length.

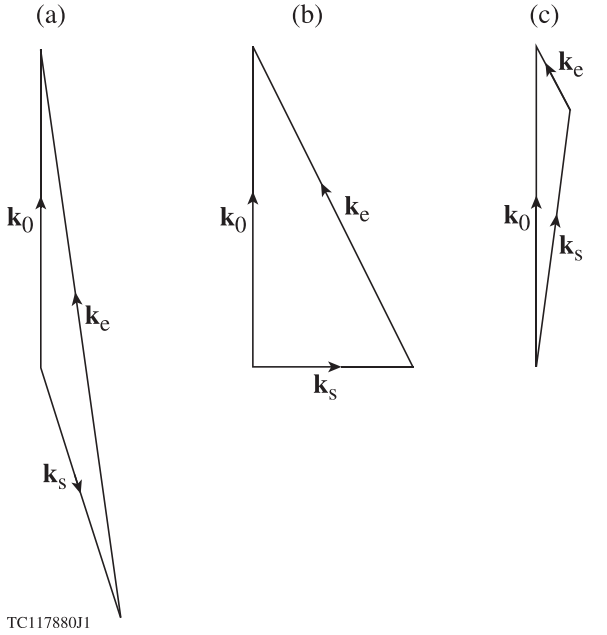

FIG. 10-19. Wave-vector matching diagrams for stimulated Raman scattering (SRS) resulting from the decay of an incident photon ($\mathbf{k}_0$, ω_0) into a scattered photon ($\mathbf{k}_s$, ω_s) and an electron plasma wave ($\mathbf{k}_e$, ω_e). (a) Near-backscatter, (b) sidescatter, and (c) near-forward scatter. Angles shown are at the location of the SRS decay; the scattered light will be refracted closer to the density gradient as it propagates out of the plasma.

The Landau constraint becomes more restrictive for lower densities and higher temperatures, with backscatter being suppressed first since k_e is largest in this case (Fig. 10-19). Collisional damping can also suppress SRS, although in direct-drive coronas this is usually not a primary suppression mechanism. As will be seen below, plasma inhomogeneity is usually the dominant factor in determining SRS thresholds in direct-drive plasmas.

Amplification growth rates and thresholds for SRS in homogeneous plasmas were studied theoretically using various approaches in the 1960s (Refs. 483–485). Not until the 1970s, however, did lasers become powerful enough to allow experimental observation of SRS. Bobin *et al.*[414] observed down-scattered light at $\omega_0/2$ using a Nd:glass laser and a solid hydrogen target (Fig. 10-2), although it was unclear whether this was actually SRS. The first definitive observations of SRS were not made until the work of Phillion and Banner,[486] reported in the literature by Phillion *et al.*[269] Meanwhile, it was recognized that, since laser-produced plasmas in the laser-fusion context would necessarily be small, spatial inhomogeneity would play a significant role in determining the threshold and gain of SRS.

During the 1970s, an extensive effort began to understand SRS in inhomogeneous plasmas using both theory and computer simulations. In inhomogeneous plasmas the distinction between absolute and convective growth becomes important. Owing to the inhomogeneity, the SRS gain for a given pair of daughter waves is confined to a limited spatial region where the matching conditions for the decay are approximately satisfied. Once the waves convect out of this region, they cease to grow, resulting in a finite amplification as the waves propagate through the resonance region. Under certain conditions, however, energy may be transferred to the growing waves faster than they can convect it out of the resonant region, resulting in growth that is saturated only by nonlinear effects. Rosenbluth[405] gave the first comprehensive analysis of parametric instabilities in inhomogeneous plasmas, using a three-wave WKB approximation. He found that in this analysis absolute growth cannot occur in a linear density profile and parametric instabilities are limited to spatial amplification.

Unfortunately, Rosenbluth applied this analysis to the TPD instability and incorrectly concluded that TPD cannot be absolute; however, both TPD and SRS can be absolute near the quarter-critical density. The absolute SRS instability was studied by Drake and Lee[487] and Liu *et al.*,[447] both of whom gave approximate expressions for its threshold. It is interesting to compare this threshold with the threshold of the absolute TPD instability given by the definitive analysis of Simon *et al.*[409] The absolute SRS threshold can be expressed as $I_{14}\lambda_\mu^{2/3}L_\mu^{4/3} > 1549$ (Ref. 487) and >1433 (Ref. 447), while for TPD it is $I_{14}\lambda_\mu L_\mu/(81.86T_{\rm keV}) > 1$ (Ref. 409), where I_{14} is the incident intensity in units of 10^{14} W/cm^2, λ_μ is the laser wavelength in microns, L_μ is the plasma density scale length in microns, and $T_{\rm keV}$ is the electron plasma temperature in keV. TPD has the lower threshold at smaller scale lengths and temperatures, but for the larger scale lengths and temperatures relevant to current and future direct-drive fusion experiments, absolute SRS may become increasingly important.

Early particle simulation work was carried out by Forslund *et al.*[449,450] Reference 450 was accompanied by a comprehensive theoretical treatment of the linear and nonlinear evolution of SRS in Ref. 448. Further simulation work was reported by Kruer *et al.*[488] and Estabrook *et al.*[489] Estabrook *et al.* found a hot-electron temperature T_H in the 10- to 100-keV range, depending on the phase velocity of the Raman-generated wave (a function of the plasma density and electron temperature) rather than on the laser intensity. They recognized that large plasma regions with low gradients are needed for significant SRS. A discussion on the importance of plasma scale length for SRS and other plasma instabilities is given by Max *et al.*[490]

Unlike TPD, SRS can occur as a convective instability at densities significantly below quarter-critical. The convective SRS gain for $L_\mu = 300$, $T_{\rm keV} = 2.0$, $I_{14} = 1.0$, and a laser wavelength of 0.351 μm is shown in Fig. 10-20, as calculated from the analysis of Rosenbluth.[405] The axes of the plot are the x and y components (k_{sx}, k_{sy}) of the scattered electromagnetic wave vector $\mathbf{k}_s$; decays at larger values of k_s occur at lower densities. Note that the gain is strongly maximized for sidescatter ($k_{sx} = 0$); this is because the scattered electromagnetic wave has a larger group velocity than the plasma wave and therefore is responsible for most of the energy convection away from the resonant region. The gain is therefore highest when the scattered electromagnetic wave propagates perpendicular to the density gradient. Along the y axis, it is found that the spatial gain diverges; a more-complete calculation by Liu *et al.*[447] shows that this represents the onset of absolute instability for the SRS sidescatter.

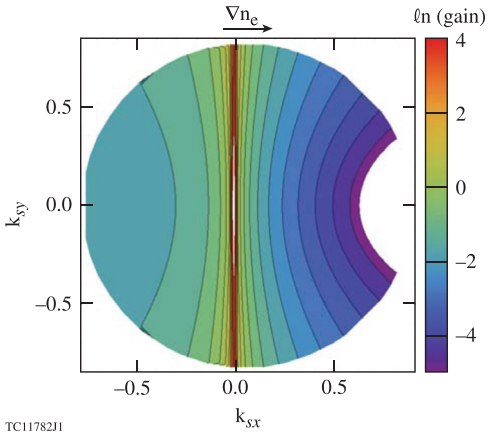

FIG. 10-20. Convective SRS gain as a function of the scattered electromagnetic wave vector (k_{sx}, k_{sy}) *for* $L_n = 300\,\mu$m and $T_e = 2$ keV. The electron density gradient ∇n_e is along the x axis. The gain becomes singular along the k_y axis, where the sidescatter instability may become absolute.

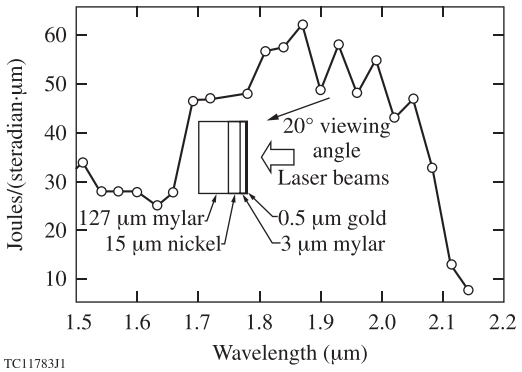

FIG. 10-21. Early observation of SRS on Shiva at 1.06-μm wavelength across a broad wavelength range. Assuming a planar plasma, the oblique observation angle of 20° to the target normal would have suppressed detection of TPD emission from the quarter-critical density. Reproduced with permission from Phys. Fluids **25**, 1434 (1982). Copyright 1982 AIP Publishing LLC.

The pioneering measurements of SRS made by Phillion and Banner[486] and Phillion *et al.*[269] were carried out on the 1.064-μm Shiva laser and depended on the development of suitable diagnostics in the difficult infrared wavelength range. An example of an observed SRS spectrum is shown in Fig. 10-21. A gold disk target was irradiated at 3.3×10^{15} W/cm^2 with the upper ten Shiva beams, which were incident in two rings with angles of 9.7° and 17.7° to the vertical axis. An energy of 3.25 kJ was delivered to the target in a 600-ps pulse. The SRS emission was measured with a liquid-nitrogen–cooled InAs detector array, a pyroelectric detector for time resolution, and a Czerny–Turner spectrograph. A broad spectrum of Raman emission was observed up to a falloff seen just before the 2.1-μm quarter-critical cutoff. Since the target was viewed at 20° to the normal, emission close to $\omega_0/2$ would not be expected to reach the detector (assuming a planar plasma) as the emission refracts toward the target normal. Phillion *et al.*[269] estimated that several percent of the incident light was Raman scattered and found that the SRS emission came late in the pulse when the scale length was large. (At this time the instantaneous SRS reflectivity would have been higher than several percent.) Further work by Phillion *et al.*[424] used exploding CH foil targets, also irradiated at 1-μm wavelength. These targets produced a density plateau in the center of the plasma, and the (time-integrated) SRS increased to 10% of the incident laser energy. On account of the Manley–Rowe relations[491] (which state that when a photon of frequency ω_0 decays into two waves of frequencies ω_s and ω_e, the energies of the product waves are proportional to their frequencies), a comparable amount of energy went into plasma waves. Since these plasma waves can generate hot electrons, which result in undesirable target preheating, these large levels of SRS caused considerable concern. Indeed, high levels of SRS in long-scale-length hohlraum plasmas degraded the achievable density and neutron yield on Shiva.[2,3]

Phillion and Banner[486] and Phillion *et al.*[269] suggested that irradiation at shorter wavelengths could reduce SRS. They reported experiments using the Argus laser at 0.53 μm (Fig. 10-22) to irradiate gold disk targets at a nominal intensity of 5×10^{14} W/cm^2. Here the target was viewed along its normal, and, in addition to the dominant broad feature characteristic of convective SRS, the spectrum showed a double-peaked structure at twice the laser wavelength (near 1064 nm). This is now known to be characteristic of TPD,[492,493] although it was not identified as such at the time.

In other 0.53-μm experiments on Argus, Mead *et al.*[148] irradiated disk targets of Be, CH, and higher-Z materials with energies up to 35 J in 600-ps pulses at intensities from 3×10^{13} to 4×10^{15} W/cm^2. They claimed that just 10^{-5} of the incident energy emerged as SRS from 0.6 to 1 μm, and they estimated that less than 1% of the laser energy was converted to hot electrons for all values of Z, even at 2×10^{15} W/cm^2. Turner *et al.*[494] reported 0.53-μm experiments on Argus in which the time-resolved SRS emission was measured for solid Be and Au planar targets. They estimated that $\sim 10^{-4}$ of the incident energy emerged as SRS in near-backscatter directions. They observed temporal pulsations simultaneously across the spectrum, corresponding to densities from 0.02 n_c to 0.15 n_c, where n_c is the critical density. The pulsations lacked a clear explanation although

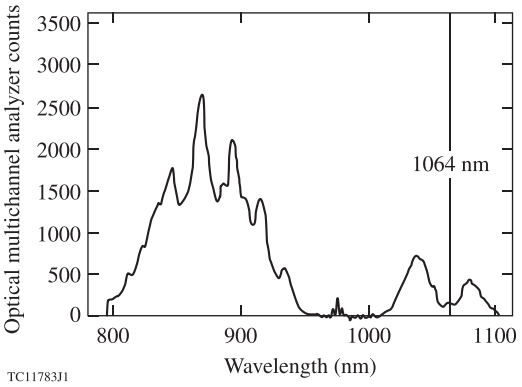

FIG. 10-22. Early observation of SRS and TPD spectra from a gold disk irradiated at 0.53 μm on the Argus laser at an angle of incidence of 30° by a 28-J, 700-ps laser pulse. This observation was made in the target normal direction, so the TPD emission, with its characteristic double-peak structure around 1064 nm, is clearly visible. Reproduced with permission from Phys. Fluids **25**, 1434 (1982). Copyright 1982 AIP Publishing LLC.

Turner *et al*. suggested that the SRS could come from hot spots in the laser beam enhanced by filamentation. The small spot sizes used in these energy-limited experiments and their commensurate short plasma scale lengths may have been responsible for the low levels of SRS that were observed.

Drake *et al*.[495] used the much larger energy available on the Novette laser (up to 4 kJ) to irradiate Au targets at 0.53-μm wavelength with focal spots of 150- to 1880-μm diameter. They integrated the angular distribution of the SRS to obtain the Raman-scattered light fraction and found that this correlated very closely over nearly three orders of magnitude with the hot-electron fraction obtained from the hard x-ray spectrum (Fig. 10-23). They found up to a few percent of the incident energy in each of the Raman light and hot electrons.

The first observations of SRS at 0.35 μm were reported by Tanaka *et al*.[496] on the GDL laser at LLE. Two spectra from this work are shown in Fig. 10-24, corresponding to incident intensities 1.1× and 3× the estimated threshold for the absolute SRS instability. The large gap between the bulk of the SRS emission and the TPD signal at twice the laser wavelength (7000 Å) was ascribed to steepening of the density profile near quarter-critical caused by SRS, but this seems doubtful since the SRS conversion fraction in these experiments was very low ($\sim 10^{-5}$). It is conceivable that profile steepening might have occurred as a result of the TPD instability, which has a lower threshold than SRS for the conditions of this experiment and is confined to the quarter-critical region. Another possible explanation for the gap was given by Drake *et al*.,[497] who irradiated 3-μm-thick (exploding foil) CH targets at 0.35 μm and observed SRS spectra that broadened as the incident intensity increased from 2×10^{13} to 10^{14} W/cm^2 but consistently showed a gap. They found that after the plasma has developed a sufficiently long scale length, collisional absorption of the scattered light wave when it originates close to its critical density can be significant. Further observations of SRS at 0.35 μm were made in experiments on GDL by Figueroa *et al*.[498] in which

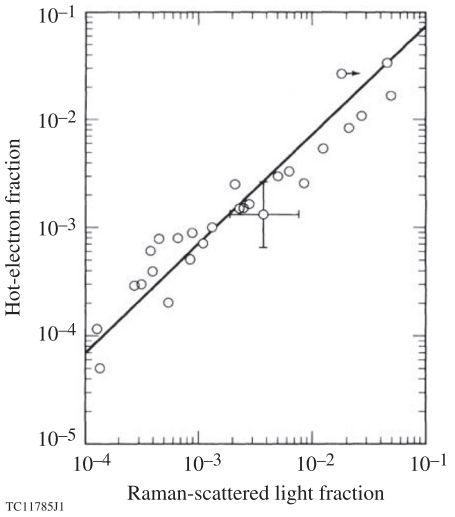

FIG. 10-23. Correlation between Raman-scattered and hot-electron fractions measured from Au disks on Novette with up to 4 kJ of 0.53-μm light. Reprinted with permission from Drake *et al*., Phys. Rev. Lett. **53**, 1739 (1984). Copyright 1984 American Physical Society.

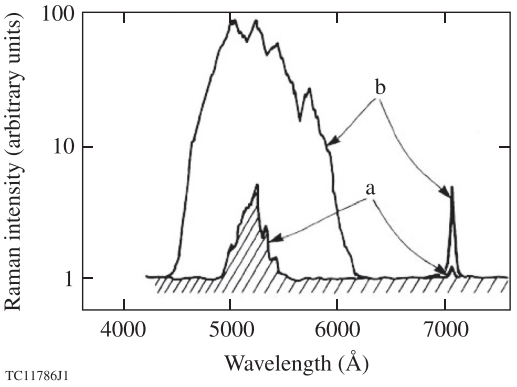

FIG. 10-24. First observation of SRS with 0.35-μm irradiation. Planar CH targets were irradiated at 4.6×10^{14} W/cm^2 ($1.1 \times I_{\text{SRS-A}}$) (curve a) and at $3 \times I_{\text{SRS-A}}$ (curve b), where $I_{\text{SRS-A}}$ is the threshold intensity for the absolute SRS instability. Reprinted with permission from Tanaka *et al*., Phys. Rev. Lett. **48**, 1179 (1982). Copyright 1982 American Physical Society.

a defocused 1-μm pulse exploded a submicron foil and a tightly focused third-harmonic interaction beam irradiated the preformed plasma.

Exploding-foil targets were also employed by Turner *et al*.[499] for SRS experiments at a 0.26-μm wavelength on Novette. They used 6-μm-thick CH targets and 0.4-μm-thick Au targets, chosen on the basis of hydrodynamic simulations to produce density profiles with the maximum electron density on axis just below quarter critical by the peak of the laser pulse. The targets were irradiated at normal incidence at $(1–2) \times 10^{15}$ W/cm^2, with focal diameters of 300–350 μm. With CH targets, Turner *et al*. found ~2% SRS, compared with ~10% for 0.5-μm irradiation. In contrast, they found no detectable SRS for Au targets, with the SRS from Au at least three orders of magnitude lower than that from CH. They ascribed this to strong collisional damping. This showed for the first time that SRS could be suppressed by collisionality in high-Z targets using short-wavelength irradiation. However, SRS has remained a concern for the lower-Z targets typically used in direct-drive experiments.

In the experiments of Tanaka *et al*.,[496] SRS was observed at intensities well below the threshold for the absolute instability predicted by hydrodynamic simulations of the plasma conditions. Filamentation of hot spots in the beam, resulting in localized regions of high intensity, was proposed by Short *et al*.[500] as an explanation. Such filamentation was also proposed as an explanation of the simultaneous appearance of SRS emission over a wide range of wavelengths reported by Turner *et al*.[494] Filamentation could lead to a rapid increase of intensity throughout the length of the filament.

Further support for the filamentation hypothesis was provided after the development of beam smoothing (Sec. VI) in the 1980s. Beam smoothing changes the laser speckle pattern incident on the target on a time scale comparable to (or shorter than) that of the small-scale density perturbations in the plasma associated with filamentation, thereby reducing or eliminating filamentation. Shortly after the implementation of ISI (Sec. VI B) on the 1-μm Pharos III laser at NRL (using etalons), Obenschain *et al*.[501] irradiated plastic (CH) targets

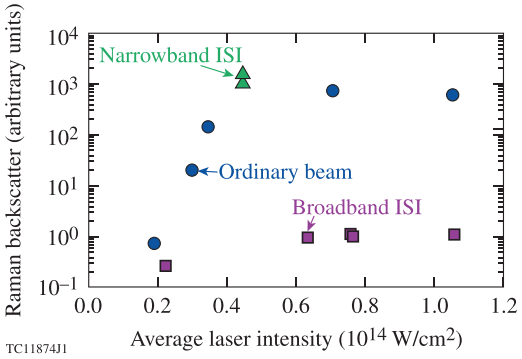

FIG. 10-25. Peak Raman backscatter in the 1350- to 1750-nm band as a function of laser intensity for the 1-μm irradiation of planar CH targets, comparing broadband ISI, narrowband ISI, and an ordinary laser beam with narrow bandwidth. The ISI was implemented using reflective echelons. Reprinted with permission from Obenschain *et al.*, Phys. Rev. Lett. **62**, 768 (1989). Copyright 1989 American Physical Society.

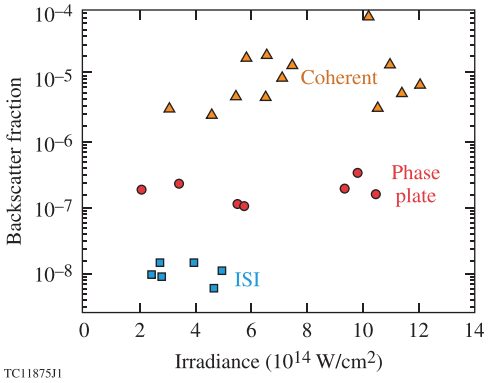

FIG. 10-26. SRS backscatter fraction from a long-scale-length, underdense plasma ($n_e \lesssim n_c/10$) as a function of laser irradiance for a coherent beam ($f/10$), a phase-plate beam ($f/2.5$), and ISI ($f/10$). The laser wavelength was 0.53 μm. Reproduced with permission from Coe *et al.*, Europhys. Lett. **10**, 31 (1989). Copyright 1989 EDP Sciences, see http://iopscience.iop.org/epl/.

with ~2-ns pulses at $\sim 10^{14}$ W/cm^2 with a spot diameter of ~300 μm and reported a reduction of SRS with broadband ISI by three orders of magnitude (Fig. 10-25). This result was understood to be a consequence of the suppression of filamentation. The coherence time τ_c was 2 ps for broadband ISI. For narrowband ISI ($\tau_c = 2$ ns), there was, as expected, no significant difference compared with the ordinary beam.

Corroboration of the NRL result was provided by experiments at the Rutherford Laboratory reported by Coe *et al.*[502] in which a 0.5-μm interaction beam irradiated a long-scale-length, low-density plasma (electron density $n_e \lesssim 0.1\ n_c$) formed from the explosion of a thin Al strip in line-focus geometry. [See Fig. 10-33(a) below for the configuration.] The results (Fig. 10-26) showed an SRS signal that decreased first with the introduction of phase plates and further with ISI. Again, this was attributed to the suppression of filamentation.

Seka *et al.*[503] found that SRS was strongly reduced by SSD (Sec. VI C), as shown in Fig. 10-27. In these experiments at 0.35 μm on the 24-beam OMEGA laser, CH foils were exploded with plasma-forming beams and irradiated with a high-intensity interaction beam. The application of SSD bandwidth was found to reduce the SRS level by three orders of magnitude. In contrast, TPD (as evidenced by the $3\omega_0/2$ emission) was only slightly affected. Since the speckle pattern changes too slowly to affect the growth rate of electron plasma wave instabilities directly, the implication is that the SSD beam modulation is suppressing filamentation (which occurs on the ion-acoustic time scale) and therefore indirectly suppressing SRS within filaments. TPD, which is necessarily a multidimensional phenomenon, is not expected to be confined to filaments and therefore would not be affected by SSD.

As a result of beam smoothing, the levels of SRS observed in spherical direct-drive experiments on OMEGA were generally found to be negligible, i.e., less than the detection threshold of 5×10^{-4} of the incident beam energy.[504] In the unlikely event that the SRS emission from a spherical target were isotropic, the applicable detection threshold would be raised to 5×10^{-3} of the total incident energy. Interest in the topic of SRS for direct drive declined, although SRS remained a concern for indirect-drive plasmas with their larger scale lengths. To assess whether SRS would be important in conditions relevant to ignition-scale direct-drive designs, long-scale-length plasmas have been used on OMEGA to study SRS. A typical streaked SRS spectrum from these experiments[505] is shown in Fig. 10-28 from a plasma formed by irradiating a solid planar CH target with defocused primary and secondary beams in the configuration shown in Fig. 10-6(a). SRS is observed during the presence of five overlapped interaction beams, each with an intensity of $\sim 1.2 \times 10^{14}$ W/cm^2, whose temporal shape is given by the red curve. The emission just above and below 700 nm, coming from the vicinity of the quarter-critical density, is understood to result from the TPD instability and is consistent with the 0.53-μm experiment on Argus shown in Fig. 10-22. The feature whose wavelength decreases with time is consistent with the motion of a density plateau that propagates to lower densities as a result of the increased ablation rate that occurs with the onset of the high-intensity interaction beams. The yellow circles are predictions of an SRS model that post-processes 2-D hydrodynamic simulations using

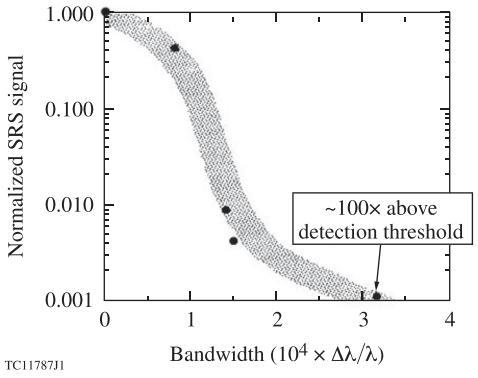

FIG. 10-27. Reduction of SRS by SSD bandwidth in long-scale-length CH plasmas irradiated at 0.35 μm on the 24-beam OMEGA laser. The bandwidth is believed to suppress filamentation, thereby preventing SRS from occurring in high-intensity filaments. The shaded area is to guide the eye. Reproduced with permission from Phys. Fluids B **4**, 2232 (1992). Copyright 1992 AIP Publishing LLC.

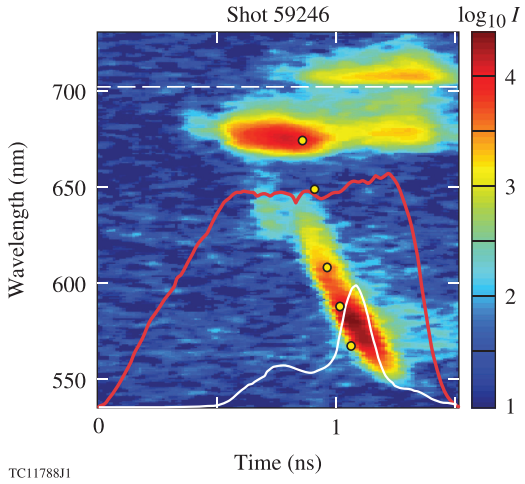

FIG. 10-28. Time-resolved SRS spectrum recorded from a long-scale-length plasma on the 60-beam OMEGA laser. The red curve indicates the interaction-beam laser intensity and the white line represents the signal integrated over the spectrum. The yellow circles correspond to predicted wavelengths of peak SRS emission (from Ref. 505).

SAGE and show good agreement with the observations. Similar streaked SRS spectra have been widely used to diagnose the maximum (plateau) density of exploding-foil plasmas (see, e.g., Refs. 503 and 506).

As direct-drive experiments extend into conditions of larger scale length and higher temperature appropriate to the NIF, SRS may play a larger role even with smoothed beams since filamentation will no longer be necessary to reach the SRS threshold. SRS therefore remains a concern, and further experimental and theoretical investigations, including the effects of multibeam irradiation, are required.

D. Self-focusing and filamentation

1. Theory

Laser light propagating through a plasma can undergo self-focusing because the plasma index of refraction changes in response to variations in the local light intensity, supporting perturbations in the direction perpendicular to the beam. In a plasma, the index of refraction μ is related to the electron density n_e as $\mu = \sqrt{1 - n_e/n_c}$, where n_c is the critical density. A locally increased intensity can lower the electron density (through the ponderomotive force or local plasma heating) and increase the index of refraction, leading to ponderomotive or thermal self-focusing, respectively. Ponderomotive self-focusing was described in 1962 by Askar'yan.[507]

Thermal self-focusing is illustrated in Fig. 10-29 (from Ref. 337). Here, a 0.35-μm-wavelength laser beam is incident on a cold CH plasma with a 500-μm scale length, heating the plasma in a channel near the axis. The plasma expands radially, reducing the density in the channel and thereby causing light rays to refract (or focus) into the intense region, further increasing the intensity and producing the instability. The locally intense region initiating the process can be a perturbation within a larger (nominally smooth) beam, in which case the process is known as filamentation or small-scale self-focusing, or it can be the entire beam, in

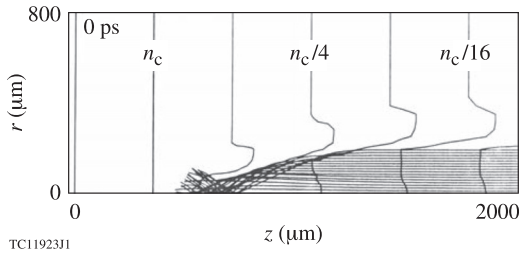

FIG. 10-29. Illustration of thermal self-focusing of light using the 2-D hydrodynamics code *SAGE* with ray tracing. Laser rays heat a channel near the axis, reducing the density there. The rays are then refracted toward the axis and increase the on-axis intensity. Contour lines show the electron density in the plasma relative to the critical density n_c, and the rays indicate the direction of light propagation. Reproduced with permission from J. Appl. Phys. **56**, 108 (1984). Copyright 1984 AIP Publishing LLC.

which case the process is known as whole-beam self-focusing. The physical mechanism is essentially the same.

There are two particularly important aspects of this instability: (1) the intensity threshold is relatively low and (2) the resulting intensity enhancement can induce other instabilities (which would otherwise be below threshold). The second point may explain why many early laser–plasma instability experiments with unsmoothed laser beams exhibited puzzling and sometimes irreproducible results (see, for example, early observations of backscattered light described in Sec. X B). It is also believed to be the reason why optical beam smoothing has been effective in reducing instabilities such as SRS (Sec. X C), which has a growth rate significantly greater than the laser bandwidth. Early examples of this effect are given in Sec. VI B, with Fig. 6-6 illustrating the reduction in hot electrons with beam smoothing.

The linear filamentation threshold is determined by equating the focusing effect of a plane-wave perturbation with diffraction, which counteracts the focusing by broadening the perturbation. Different intensity thresholds in a homogeneous plasma are found for the ponderomotive[508] and thermal[509] mechanisms. A useful threshold intensity I_{14} can be calculated by requiring that the intensity in the filament exponentiate once inside the plasma for the fastest-growing spatial mode, with the plasma assumed to have a length L. This results in[510]

$$I_{14} \geq 20 \frac{n_c}{n_e} \frac{T_e\,(\mathrm{keV})}{L\,(\mu\mathrm{m})\lambda_0\,(\mu\mathrm{m})} \tag{10-5}$$

for ponderomotive filamentation and

$$I_{14} \geq 2 \times 10^5 \left(\frac{n_c}{n_e}\right)^3 \frac{T_e(\mathrm{keV})^5 \lambda_0\,(\mu\mathrm{m})^2}{Z^2 L^2 (\mu\mathrm{m})} \tag{10-6}$$

for classical thermal filamentation. Here, I_{14} is given in units of 10^{14} W/cm^2, Z is the plasma ionization, T_e is the electron temperature, λ_0 is the laser wavelength, and it is assumed that $n_e \ll n_c$.

Because both diffraction and the laser-induced nonlinear plasma response depend on the wavelength λ of the perturbation, the resulting filamentation growth rates can depend

sensitively on the perturbation wave number k ($=2\pi/\lambda$). The spatial growth rates K are found by Fourier analysis of the nonlinear wave equation, and representative examples of the dependence of K on k are shown in Fig. 10-30 (taken from Ref. 511) for three mechanisms, using the experimental parameters of Refs. 512 and 513. No growth occurs in any case for wave numbers larger than a critical value since diffraction will stop any focusing. As the wave number decreases below this critical value, the ponderomotive filamentation growth rate peaks and then decreases. In contrast, classical thermal filamentation is insensitive to the wave number as long as the perturbation wavelength is much larger than the threshold wavelength. Its largest growth rate occurs for long wavelengths (small wave numbers).

The classical result for thermal filamentation can be substantially modified in the underdense plasma corona when the mean free path of a thermal electron is greater than a small fraction ($\sim$1/100) of the perturbation size.[511] In this case, the nonlocal nature of thermal conduction (Sec. XI) effectively decreases the local conductivity, sharpens small-scale temperature perturbations, and enhances the filamentation effect for shorter wavelengths. An example of this modified dispersion relation is shown in Fig. 10-30, where nonlocal thermal filamentation dominates ponderomotive filamentation.

Rose and DuBois[514] questioned the applicability of the linear filamentation stability analysis to laser beams smoothed by phase plates. Such beams contain a distribution of hot spots (local maxima) of the laser intensity within the focal volume that are assumed to act as seeds for filamentation. Rose and DuBois argued that the evolution of self-focusing/filamentation in a laser hot spot is nonlinear from its inception if the hot spot contains more than a certain critical power. The concept of a critical power for self-focusing arises from the appearance of self-localized solutions to the cubic nonlinear Schrödinger equation, which has been used for a long time as a model for self-focusing.[515]

2. Simulations

Ray tracing coupled to hydrodynamics simulations was first used to simulate thermal self-focusing in plasmas by Craxton and McCrory[337] and Estabrook *et al.*[516] However, since diffraction and interference of the electromagnetic wave are not included in this treatment, neither ponderomotive filamentation nor saturation of self-focusing was properly represented. Simulations of filamentation including interference and diffraction effects were developed in two dimensions by Nicholas and Sajjadi,[517] Schmitt,[518] and Rankin *et al.*[519] These studies coupled parabolic-wave-equation representations with simple models for the hydrodynamics of the background plasma. They showed that optical beam smoothing using phase plates, ISI, or SSD (Sec. VI) could greatly reduce or eliminate filamentation in typical ICF plasmas, while unsmoothed beams would filament and significantly enhance the energy at intensities many times the average. With phase plates, although the incident intensity pattern is stationary, filamentation can be reduced by the decreased perturbation amplitude driving the most rapidly growing modes and by the disruption of filament growth accomplished by decreasing the speckle length. For this, smaller $f/\#$ optics (which produce smaller hot spots) perform best. Methods using finite laser bandwidth (ISI or SSD) were shown to further suppress filamentation by changing the position of the laser speckles ("hot spots") more quickly than the plasma can respond.

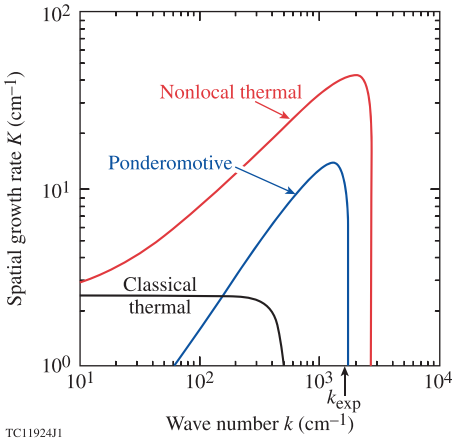

FIG. 10-30. Spatial growth rate K as a function of wave number k for ponderomotive, classical thermal, and nonlocal-thermal-conduction–dominated filamentation, for the experimental conditions of Refs. 512 and 513: $I=4.2\times10^{13}$ W/cm^2, $T_e=0.8$ keV, $n_e/n_c=0.1$, $\lambda_0=1.06$ μm, and $Z=3.5$. The arrow marked k_{exp} denotes the wave vector of the applied perturbation in the experiment of Refs. 512 and 513. Reprinted with permission from E. M. Epperlein, Phys. Rev. Lett. **65**, 2145 (1990). Copyright 1990 American Physical Society.

These results were confirmed when the model was subsequently improved by Schmitt[520] and Berger *et al.*[521] with increasingly complex hydrodynamic modeling of the background plasma including three dimensions and nonlocal electron thermal transport. Further development of these wave-based filamentation models included axial hydrodynamic coupling (which produced an interaction between filamentation and both forward Brillouin smoothing and plasma-induced incoherence[522]) and explicit coupling to other instabilities such as backward Brillouin and stimulated Raman scattering.[523,524] This work showed that filamentation can generate and interact with laser–plasma instability processes in very complex ways.

Figure 10-31 shows two typical examples of 3-D simulations of filamentation, based on Ref. 520. In the simulation of Fig. 10-31(a), the laser is spatially incoherent from phase plates but has no bandwidth. The figure shows intensity contours in cross sections of the beam at the incident plane $z=0$ and after propagation through 500 μm of CH. Ponderomotive filamentation dominates any thermal effects, and the incoming beam (which initially has peak-to-average intensity variations of $\sim$8:1) filaments to produce intensity peaks more than 600$\times$ the average local intensity. Fine-scale diffraction features are also seen. In contrast, a simulation using ISI beam smoothing [Fig. 10-31(b)] shows that filamentation is eliminated as the beam propagates through a large-scale plasma without intensity enhancement. In this simulation the beam propagated through a large DT plasma whose density increased from $0.01n_c$ (top) to $0.75n_c$ (bottom). [The density

profile is shown in Fig. 22(c) of Ref. 518.] This figure shows the intensity averaged over 100 coherence times (90 ps); there was also no evidence of filamentation from images of the instantaneous intensity.

3. Experiments

Filamentation can be difficult to observe experimentally because the desired starting point—a high-power plane wave with a small perturbation—is difficult to produce. All high-power laser systems exhibit phase distortions in the amplifying chain that cause large "hot spots" in the irradiation plane in the absence of beam smoothing. These hot spots may have intensities many times larger than the average beam intensity. Therefore, many of the signatures that could be associated with filamentation can be caused by the incident light structure.

The first claimed experimental evidence of filamentation in plasmas was the observation of apparent density striations or channels and localized radiation emission in underdense plasmas, starting in CO_2 laser interactions.[525–527] In the early 1980s, Willi *et al.*[528] and Willi and Rumsby[529] observed clear light and dark streaks in the underdense corona of a spherical target exemplified by the schlieren (dark-field) image of Fig. 10-32, published in Refs. 528 and 529. These features provided evidence for long, narrow density perturbations and were seen with schlieren imaging, shadowgraphy, and interferometric diagnostics using probe beams that propagated nearly orthogonal to the direction of the laser and

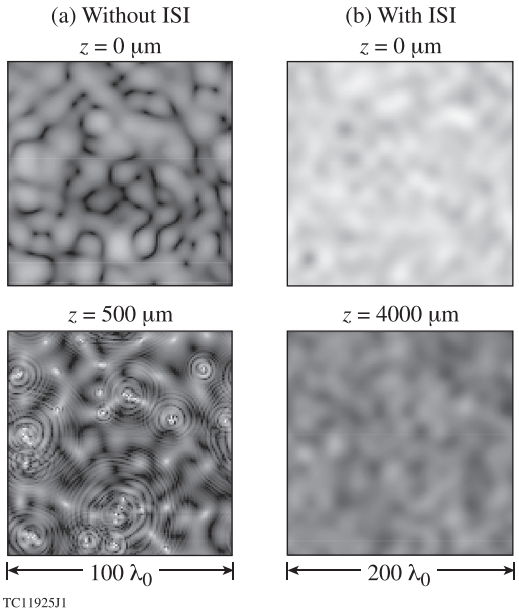

FIG. 10-31. Three-dimensional simulations of filamentation showing the behavior of laser propagation (a) without and (b) with ISI. All images show slices of the intensity in the plane orthogonal to the laser propagation direction z. In simulation (a), a 0.53-μm narrowband laser beam at an intensity of 2×10^{14} W/cm^2 propagates through an inhomogeneous CH plasma with a density scale length of 120 μm. Peak-to-average intensity variations increase from ~8:1 at $z = 0$ to ~600:1 at $z = 500\,\mu$m. In simulation (b), an ISI-smoothed 0.25-μm beam with a coherence time of 0.9 ps and at an intensity of 3×10^{14} W/cm^2 propagates through a DT plasma. The images (averaged over 100 coherence times) show no evidence of filamentation. (The figures show reprocessed data based on the simulations reported in Ref. 520.)

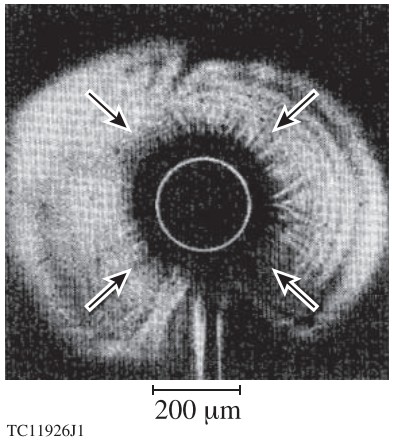

FIG. 10-32. A schlieren image of a plastic-coated microballon irradiated at 3×10^{13} W/cm^2. Arrows indicate the directions of the heating laser beams; the original target position is marked by a white circle. Reprinted with permission from Willi *et al.*, IEEE J. Quantum Electron. **17**, 1909 (1981). Copyright 1981 IEEE.

the filaments. Structures aligned with the laser were interpreted as filaments and structures normal to the target were interpreted as jets. Some structures were interpreted as arising from an electrothermal instability.[530]

Early evidence of filamentation included various nonlinear electromagnetic emissions that were localized and therefore attributed to filamentation. Localized x-ray emission spots were ascribed to filamentation,[526,531,532] although in some experiments they were re-identified as target contaminants.[533,534] Localized $2\omega_0$ emission[535,536] and $3\omega_0/2$ emission[537] were also observed.

However, there is a fundamental difficulty in identifying any of these measurements as filamentation, as summarized by Young *et al.*:[512] "indirect identification of filaments, such as x-ray photographs, imaging of backscattered light, angular distribution of $3/2\omega$ emission, and imaging and angular distribution of 2ω emission, are unsatisfactory since the relation between these processes and filaments is unclear. Direct identification of filaments with use of interferometry and shadowgraphy, has not distinguished between filamentation and stable perturbations of the plasma density by structure in the beam." The relationship between these observations and filamentation was particularly tenuous because the intense hot spots in the incident laser beam could cause these effects without filamentation. Young gave a good review of early filamentation experiments in Ref. 513.

In their experiment, Young *et al.*[512] addressed these issues by using a laser with 1-D perturbations to drive the filamentation, and an orthogonal probe beam to measure the depth of the resulting density channels using dark-field imaging. The experiment was designed to isolate ponderomotive filamentation (see the placement of the wave number k_{exp} of the applied perturbation beyond the cutoff for thermal filamentation in Fig. 10-30). Young *et al.* estimated that the intensity fluctuations (without filamentation) would produce channels with ~0.3% less density; however, the channels observed were consistent with ~10% density fluctuations, implying filamented intensity increases of ~100×. Epperlein[511] later found that thermal filamentation with nonlocal (as opposed to classical) thermal

conduction probably dominated for these experimental conditions. Young extended this work with experiments using interferometry in spherical geometry at KMS.[538] He found it was harder to observe filaments propagating obliquely to the plasma flow, suggesting that filamentation will be even less likely to be a concern in spherical geometry with multiple, overlapped, smoothed laser beams.

Perhaps the most-direct evidence of filamentation comes from experiments by Coe *et al.*[539,540] and Willi *et al.*,[541] who imaged the (0.53-μm) light transmitted through preformed plasmas formed by narrow and thin exploding foils [Fig. 10-33(a)]. In these experiments, unsmoothed beams with phase plates and optically smoothed ISI beams were propagated through the long-scale-length, underdense plasmas (typically with $n_e/n_c \sim 0.08$) created by an exploding foil, typically a 700-nm-thick Al stripe supported on a 100-nm-thick formvar substrate. The transmitted laser pulses were imaged by a framing camera or a streak camera with spatial resolution at the exit from the plasma. The streaked image of Fig. 10-33(b), taken for an unsmoothed beam propagating through a high-Z plasma (created from a 250-nm-thick Bi stripe) at an earlier time when the plasma is more dense, provides evidence for whole-beam self-focusing through the reduced size of the image during the second half of the pulse.[540] In addition, Fig. 10-33(b) shows evidence for some finer-scale breakup of the beam late in time that could be a result of filamentation.

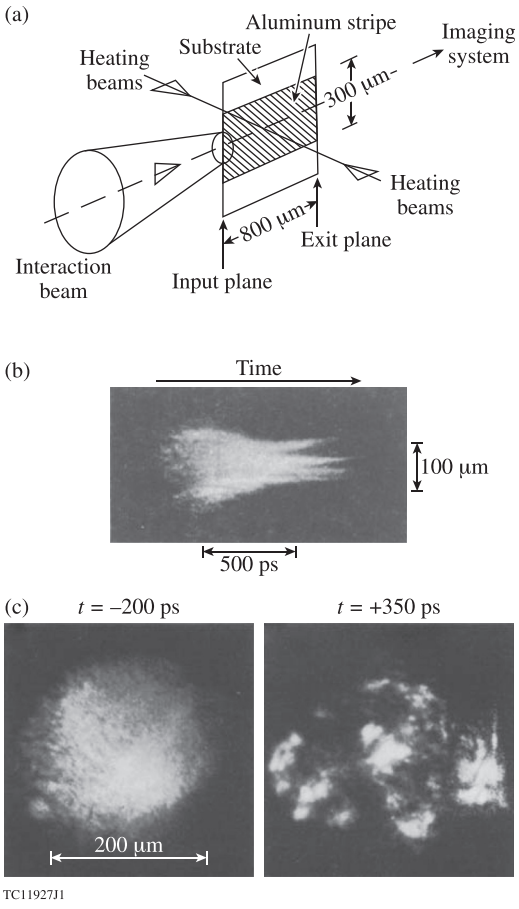

FIG. 10-33. (a) Setup of a filamentation experiment in which a 0.53-μm interaction beam propagates through an underdense plasma formed by the irradiation of a thin Al foil by a pair of line-focused 0.53-μm heating beams. Filamentation is observed by imaging the transmitted light. Reproduced with permission from Phys. Fluids B **2**, 1318 (1990). Copyright 1990 AIP Publishing LLC. (b) A streaked record of the spatial profile of light transmitted through a Bi target showing evidence at later times of both whole-beam thermal self-focusing (beam narrowing) and filament formation (discrete spots). Reprinted with permission from Coe *et al.*, Europhys. Lett. **13**, 251 (1990). Copyright 1990 EDP Sciences, see http://iopscience.iop.org/epl. (c) Two-dimensional 120-ps gated images of the transmitted beam at two different times t in the interaction laser pulse relative to the peak of the interaction pulse, for an Al plasma and an intensity of 4.5×10^{14} W/cm^2. Reprinted with permission from Coe *et al.*, Opt. Commun. **73**, 299 (1989). Copyright 1989 Elsevier.

Figure 10-33(c) shows the framing-camera images of the transmitted interaction beam through an Al plasma, obtained by Coe *et al.*[539] The images were obtained from similar laser shots with different camera timings. The image at the earlier time is relatively uniform, but by the later time the beam has broken up into intense hot spots, consistent with filamentation. Coe *et al.* characterized beam uniformity in terms of the quantity I_{max}/I_{av}, the peak-to-average intensity ratio from a typical 1-D scan across the profile. In Fig. 10-33(c), I_{max}/I_{av} increased from 1.3 at the earlier time to 7.4 at the later time, when the peak-to-valley intensity variations were ~50:1. Another interesting observation is that the beam at the earlier time was significantly more uniform than the beam with no plasma present, which was described as being extremely nonuniform with $I_{max}/I_{av} \sim 3.8$. Coe *et al.* found this early-time smoothing effect to be present on all shots and suggested that it may result from refraction in local plasma density perturbations.

Willi *et al.*[541] found no beam breakup effects in the same experimental configuration when they smoothed the interaction beam with ISI. They also observed stimulated Brillouin and Raman backscattering by imaging and streaking the input plane, and, since these emissions correlated with the onset of filamentation, they inferred that they were growing in filaments. With optically smoothed beams, these processes were substantially suppressed. Similar results were reported by Afshar-rad *et al.*[542]

The development of optical beam smoothing finally allowed experimental control and characterization of the incident beam, at least in a statistical sense. Although the instantaneous intensity fluctuations can still be as large as for unsmoothed beams, the distribution of the scale lengths of intensity variations is broadened and the dwell time of the hot spots is limited. Experiments with optically smoothed beams saw a significant reduction of nonlinear effects (see Fig. 6-6 for example); this is often cited as strong (albeit indirect) evidence of filamentation suppression.

Even with the highest-bandwidth lasers available today (~1 THz), plasmon-generating instabilities such as SRS and TPD have such rapid growth rates that they are not expected to be directly affected by the temporally changing intensity structure of optical beam smoothing. Yet experimental results show that such instabilities are greatly reduced with ISI (see the discussion of Fig. 6-6) or SSD (Fig. 10-27). Similar results are found in the measurements of SBS from optically smoothed beams, even when the SBS growth rates are much larger than the applied bandwidths.[178] Bandwidth alone did not appreciably affect SBS in these experiments.

On the basis of these experimental results, filamentation is not currently considered an issue for direct-drive ICF because of the availability of beam smoothing.

E. Parametric decay instability (PDI)

The PDI, sometimes referred to as the ion-acoustic decay instability, attracted a lot of attention in the 1960s and 1970s when it was commonly believed to be a primary mechanism for the absorption of laser energy in a plasma. Interest in the instability declined after resonance absorption and then inverse-bremsstrahlung absorption became established as the dominant absorption mechanisms. The role of the PDI in laser absorption was never established, but, equally, it was never proven that the PDI was not occurring at some significant level. This section provides a brief review of the PDI including one laser-driven experiment in which the PDI was observed.

The basic process, in simplified form, is illustrated in Fig. 10-34. A homogeneous plasma is assumed together with an imposed oscillating electric field $E_0 e^{i\omega_0 t}$. The instability occurs when the electron plasma frequency ω_p is just below ω_0. If one starts with a small-amplitude electron plasma wave of frequency ω_e and wave vector $\mathbf{k}_e$, and if the amplitude of the imposed field is large enough, a nonlinear polarization is produced that drives an ion-acoustic wave with frequency ω_{ia}, equal to the difference frequency ω_0–ω_e, and wave vector $\mathbf{k}_{ia} = -\mathbf{k}_e$. Here, $\omega_e^2 = \omega_p^2 + 3v_{th}^2 k_e^2$ [Eq. (10-3)] and $\omega_{ia} = k_{ia} c_s$, where v_{th} is the electron thermal velocity $\sqrt{k_B T_e / m_e}$, c_s is the acoustic velocity, k_B is Boltzmann's constant, T_e is the electron temperature, and m_e is the electron mass. The interaction of the imposed field with the ion-acoustic wave feeds back through the nonlinear current on the electron plasma wave to provide growth of the two waves, provided that the strength of the imposed field is enough to overcome the damping of the waves. This is in analogy to parametric interactions in optical media that, for example, form the basis of the harmonic generation of Nd:glass lasers to shorter wavelengths.[543] Given this broad context, the common use of the term "parametric" to describe the instability is unfortunate. Another identification as "the decay instability" is also unfortunate because of its failure to distinguish this instability from other decay processes such as the two-plasmon–decay instability.

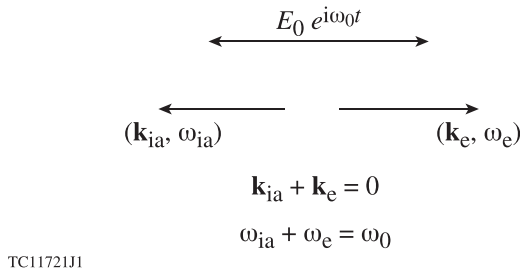

FIG. 10-34. Schematic of the parametric decay instability (PDI). In its simplest form, a homogeneous oscillating electric field $E_0 e^{i\omega_0 t}$ applied to a uniform plasma excites an ion-acoustic wave ($\mathbf{k}_{ia}$, ω_{ia}) and an electron plasma wave ($\mathbf{k}_e$, ω_e), propagating in opposite directions parallel to the electric field polarization.

The earliest work on the PDI is usually credited to Silin[544] and DuBois and Goldman,[545] although earlier work by Oraevskii and Sagdeev[546] has been noted. Comprehensive theoretical treatments of the PDI were given by Goldman.[402,547] In Ref. 547, Goldman suggested that the instability could be demonstrated at microwave frequencies. In Ref. 402, he noted that the theory requires the plasma to be relatively free from density gradients and questioned whether the theory would apply to laser-produced high-density plasmas. The first reported evidence for the PDI instability was given by Stern and Tzoar,[548] who beamed a microwave signal at a mercury discharge plasma whose plasma frequency was approximately equal to the microwave frequency. They observed ion-acoustic oscillations above a sharp threshold for a microwave power of just 3 W. They noted that the parametric excitation of plasma oscillations by means of transverse electromagnetic radiation was discussed in an unpublished report by Yariv in 1959.

Extensive theoretical work was reported by DuBois and Goldman,[549] Jackson,[403] and Nishikawa.[550] Nishikawa also noted a related instability, known as the oscillating two-stream instability.[551] In this instability, which applies for $\omega_0 < \omega_e$, a high-frequency mode oscillating at ω_0 and a non-oscillatory low-frequency mode grow at the same rate. Nishikawa found this instability not to be of practical interest because it is hard to propagate an electromagnetic wave to the required density. Amano and Okamoto[552] and Rosenbluth[405] developed the theory of the PDI in the presence of density gradients. Kruer and Dawson[553] carried out particle-in-cell simulations of the PDI and the oscillating two-stream instability and predicted efficient coupling from the laser to electron plasma waves, which in turn would generate suprathermal electrons.

Another experimental observation of the PDI was reported by Wong *et al.*,[554] who applied a 350-MHz radio-frequency field (tuned to the plasma frequency) to an argon discharge plasma through a capacitor embedded in the plasma. As with Stern and Tzoar,[548] their conditions (electron density $n_e \sim 10^9$ cm^{-3}, $T_e = 2$ eV, ion temperature $T_i = 0.1$ eV) were far removed from laser plasmas of interest. Further microwave experiments were carried out by Mizuno *et al.*[555,556] in similar low-density conditions ($n_e \sim 2 \times 10^{10}$ cm^{-3}, $T_e \sim 3$ eV, $T_i \sim 0.3$ eV). In Ref. 555, hot-electron heating was seen in agreement with PDI simulations, and in Ref. 556 it was observed that the ion-acoustic waves were initially peaked in the pump wave direction but soon became almost isotropic. Mizuno *et al.*[557] later attempted to diagnose the PDI in laser-produced plasmas through the second-harmonic emission but found[558] that very little can be inferred from this emission.

Perhaps the most-unambiguous observation of the PDI in a laser-produced plasma is reported by Mizuno *et al.*[558] for an experiment on the 24-beam OMEGA laser. Long-scale-length (~1-mm), hot (~1-keV) plasmas were formed by exploding 6-μm-thick CH foils using 16 beams at a 0.35-μm wavelength. One beam at 1.054 μm (the interaction beam) was delayed and focused through the preformed plasma at $\sim 1.25 \times 10^{14}$ W/cm^2. The predicted plasma profiles at the peak of the interaction beam [Fig. 10-35(a)] show a maximum density close to critical. The slightly skew

temperature plot is due to heating by the interaction beam. Another 0.35-μm beam was used as a Thomson-scattering probe, and the fourth-harmonic light scattered off the electron plasma wave was detected by a streaked spectrometer. The ion-acoustic–wave frequency ω_{ia} was determined from the position of the peak of the spectrum, which is plotted in Fig. 10-35(b) as a function of the normalized frequency shift $(\omega_0 - \omega_e)/\omega_{ia}$. The measured spectrum was consistent with the predicted growth rate curve, also shown in Fig. 10-35(b). The electron temperature was estimated from the phase velocity of the ion-acoustic wave as 1.5 keV, in reasonable agreement with the predicted 1.1 keV.

This experiment did not provide an estimate of how much laser energy was absorbed through the PDI. Since the PDI occurs only very close to the critical density, one might expect a steep drop in absorption above some critical angle of incidence if the PDI were a significant absorption mechanism. Such a behavior was never demonstrated experimentally and was certainly not seen in Fig. 4-7. Whether the continuous dependence of absorption on the angle of incidence that was usually observed was a result of a rippled critical surface or the PDI not providing significant absorption may remain unknown. Significant PDI absorption in spherical geometry could have adverse uniformity implications if those parts of the target surface irradiated by light at normal incidence experienced strong additional absorption, but no evidence to date suggests that this is the case.

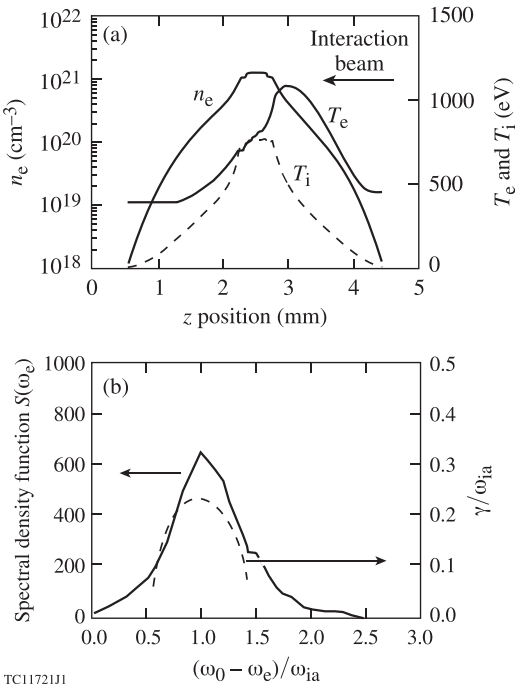

FIG. 10-35. (a) Calculated spatial profiles of the electron density n_e and the electron and ion temperatures (T_e, T_i) at the peak of the interaction beam for the PDI experiment of Ref. 558. The interaction beam enters from the right. (b) The spectral density function of the electron plasma wave (solid line) measured by collective Thomson scattering at the peak of the interaction beam. Dashed line: the normalized PDI growth rate γ/ω_{ia} calculated for a laser intensity five times threshold. Reprinted with permission from Mizuno *et al.*, Phys. Rev. Lett. **73**, 2704 (1994). Copyright 1994 American Physical Society.

F. Self-generated magnetic fields

One important process that attracted much attention, especially when 1-μm lasers were widely used, was the generation of magnetic fields within laser-produced plasmas. Interest in these fields was stimulated by their potential to impede thermal conduction in the target corona, possibly reducing drive uniformity or contributing to the generation of suprathermal electrons.

An early observation of laser-produced magnetic fields was reported by Korobkin and Serov,[559] who formed a plasma spark with a focused 2-J, 30-ns ruby laser and detected the magnetic field through the current induced in a coil. Similar observations were made by Askar'yan *et al.*,[560] who found currents in the azimuthal direction about the target normal corresponding to a magnetic-field component along the normal (a geometry different from what was standard in later work). They found an order-of-magnitude increase in the magnetic field with a prepulse. However, it was the observation of azimuthal magnetic fields by Stamper *et al.*[561] in 1971, together with a proposed mechanism for magnetic-field generation in laser-produced plasmas, that proved seminal in stimulating interest in the subject. Stamper *et al.* used a generalized Ohm's Law to determine the electric field **E**, leading to an equation for the magnetic field **B** through Faraday's Law, $\partial\mathbf{B}/\partial t = -\nabla \times \mathbf{E}$. From the term $-\nabla P_e/n_e e$ in the expression for **E**, they found a magnetic-field source term proportional to $\nabla T_e \times \nabla n_e$, assuming an ideal gas with $P_e = n_e k_B T_e$. Here, P_e, n_e, and T_e are the electron pressure, density, and temperature, respectively, e is the electron charge, and k_B is Boltzmann's constant. The magnetic-field–generating mechanism is sometimes known as the "Biermann battery," which has its origin in astrophysics. As described by Biermann and Schlüter,[562] one can find a $\nabla P_e/n_e e$ that is not curl-free in a star with nonrigid rotation. A comprehensive account of other sources of magnetic fields in laser-produced plasmas is given by Haines.[563] The growth of magnetic fields with time usually saturates by a combination of convection and resistive diffusion. Theoretical and experimental work on laser-produced magnetic fields was reviewed by Stamper.[564]

A simplified picture of the generation of magnetic fields caused by the $\nabla T_e \times \nabla n_e$ source is given in Fig. 10-36, taken from Schwirzke.[565] The laser is incident from the right upon a solid target, producing a plasma that is assumed to be azimuthally symmetric. (The plasma of Ref. 560 may have lacked this symmetry.) The density increases toward the target and the temperature increases toward the axis, providing a contribution to the magnetic-field source. There is also a contribution from the product of $\partial T_e/\partial z$ and $\partial n_e/\partial r$. The magnetic field is generated in the azimuthal direction, with the corresponding current flow **J** in the (r, z) plane.

Results from Stamper *et al.*[561] are shown in Fig. 10-37. The authors measured the azimuthal magnetic field using an inductive probe (inset) for an experiment in which a $C_5H_8O_2$ target was irradiated at $\sim 4 \times 10^{12}$ W/cm^2 with a 1-μm laser in a 200-mTorr background of N_2. They plotted the maximum field B_{max} (with respect to time) as a function of radius and found a maximum field of $\sim$1 kG at a radius of a few

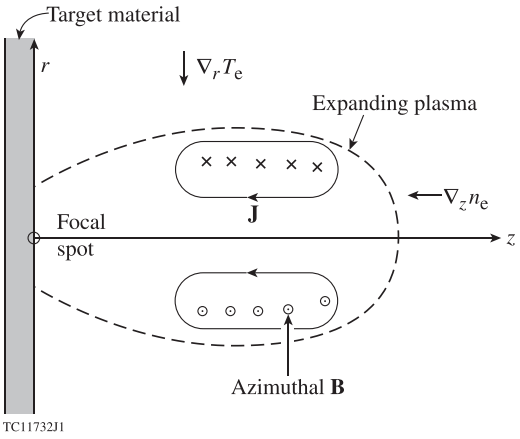

FIG. 10-36. Schematic of the $\nabla T_e \times \nabla n_e$ thermal source mechanism for the generation of magnetic fields in laser-produced plasmas. A laser beam irradiates a solid target, producing a plasma that is symmetric about the z axis. Radial temperature gradients coupled with axial density gradients result in an azimuthal magnetic field **B**. The associated current **J** lies in the (r, z) plane. Reprinted with permission from Springer Science and Business Media. From Schwirzke, "Measurements of spontaneous magnetic fields in laser-produced plasmas," in Laser Interaction and Related Plasma Phenomena, 1974, Plenum Press.

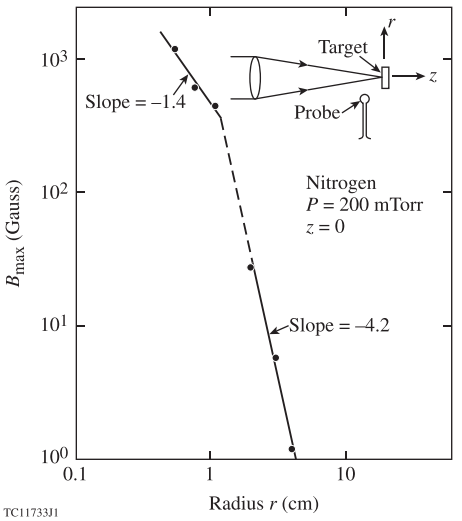

FIG. 10-37. Radial dependence of the maximum magnetic field B_{max} recorded by a probe (inset) placed just outside the focal spot for a $C_5H_8O_2$ target irradiated at $\sim 4 \times 10^{12}$ W/cm^2 in a 200-mTorr background of N_2. Larger fields appear to exist at smaller radii, but they cannot be measured by the probe. The two solid lines are fits to the radial dependence of the magnetic field ($B \propto r^{-1.4}$ and $B \propto r^{-4.2}$); the dashed line connects the two regions. Reprinted with permission from Stamper *et al.*, Phys. Rev. Lett. **26**, 1012 (1971). Copyright 1971 American Physical Society.

millimeters. The scaling with radius suggested higher fields within the plasma, which was produced by a beam of ~250-μm diameter. Another series of experiments using inductive probes was reported by Schwirzke,[565] who irradiated solid targets in a gas background of various pressures, also with a 1-μm laser, at $\sim 10^9$ W/cm^2. This work showed that the field topology was consistent with the $\nabla T_e \times \nabla n_e$ source.

A major advance in the diagnosis of magnetic fields was made by Stamper and Ripin,[566] who used the Faraday rotation of the polarization of an optical probe beam to estimate the magnetic field within the focal spot. Their setup is shown in Fig. 10-38(a). The target was irradiated by a 1.06-μm laser at $\sim 1 \times 10^{15}$ W/cm^2, forming a plasma plume. A linearly polarized second-harmonic (0.53-μm) probe beam was passed through the plasma and then through a polarizer with its axis oriented at an angle $\Delta\phi$ to the direction that would extinguish the incident probe in the absence of a plasma. Probe rays accumulate a phase shift $\Delta\phi_R \propto \int B n_e dl$, where the integral is taken along the probe path. The sign of $\Delta\phi_R$ is different above and below the horizontal plane containing the z axis. If this phase shift matches the rotation of the polarizer, the probe beam appears bright on one-half of the image and dark on the other. Such an image from Ref. 566 is shown in Fig. 10-38(b). The dark, curved region in the center of the image corresponds to dense plasma that refracts the probe beam out of the collection optics. Since the product of the magnetic field and the electron density appears inside the path integral, it was necessary for Stamper and Ripin to make estimates of the electron density in order to estimate the magnetic field. They found the fields to be of the order of 1 MG, claiming the first direct observations of megagauss fields in laser-produced plasmas.

Similar measurements were made by Raven *et al.*[567] at an incident laser intensity of $\sim 1 \times 10^{16}$ W/cm^2. They used an adaptation of the setup of Fig. 10-38(a), the main changes being that a frequency-doubled, Raman-shifted, 0.633-μm probe beam was used and a portion of the emerging probe beam was split off into a folded-wave interferometer. The Raman-shifted wavelength avoided second-harmonic emission from the plasma and the interferometer was used to determine the density profile. This enabled Raven *et al.* to find both the density and magnetic field as functions of r and z. A representative Faraday-rotation image from their experiment is shown in Fig. 10-38(c), and typical radial magnetic-field and density profiles are shown in Fig. 10-39. Not surprisingly, the peak magnetic field was observed off-axis since it has to pass through zero on the axis. The field peaked at ~2 MG. Further measurements were reported by Stamper *et al.*,[568] for slab and spherical targets with and without prepulses, and Raven *et al.*,[569] who measured no magnetic fields for spheres below 100-μm diam. Perhaps, on this scale, thermal conduction was sufficient to smooth out the temperature gradients.

All the above Faraday-rotation measurements were carried out with single beams focused at high laser intensities onto small spots. Recognizing that these experiments were in a regime not necessarily relevant to direct-drive implosions, Willi *et al.*[570] reported the first measurements of magnetic fields in the ablative regime just below the threshold for the production of hot electrons. They used 1-ns, 1-μm pulses at 10^{13}–10^{14} W/cm^2 focused onto 240- to 280-μm-diam glass microballoons. When four beams were used without beam overlap, they observed megagauss magnetic fields (again through Faraday rotation). When the beams were overlapped, however, the magnetic fields were reduced to below 0.1 MG. This constitutes the best experimental evidence that magnetic fields are unlikely to be a concern for uniform spherical irradiation.

Magnetic-field measurements using optical probing never proved feasible after the shift to submicron laser

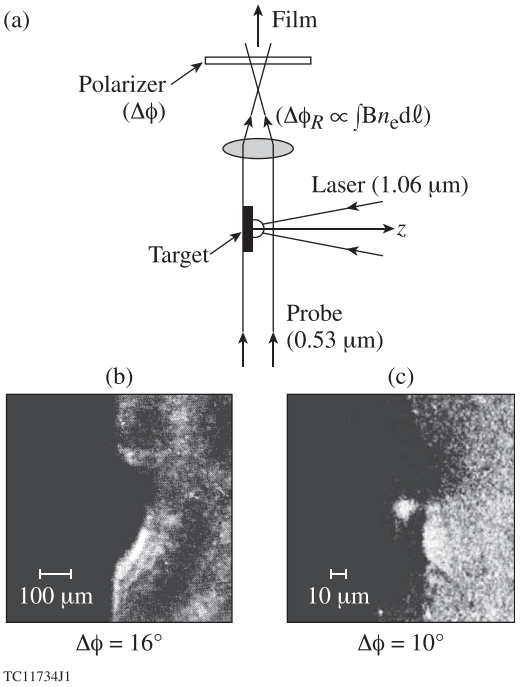

FIG. 10-38. (a) Configuration for the measurement of self-generated magnetic fields using Faraday rotation.[566] A probe beam passing through the plasma generated by the main (1.06-μm) laser experiences opposite rotations of its polarization $\Delta\phi_R$ above and below the z axis, leading to asymmetric images when the polarizer is oriented at an angle ($\Delta\phi$) from the position at which an unrotated probe would be extinguished. (b) Faraday rotation image from Ref. 566. (c) Faraday rotation image from Ref. 567. Both images indicate magnetic fields of the order of 1 MG. The image in (b) is reproduced with a left–right reflection so that the laser enters consistently from the right in each image. (a) and (b) Reprinted with permission from J. A. Stamper and B. H. Ripin, Phys. Rev. Lett. **34**, 138 (1975). Copyright 1975 American Physical Society. (c) Reprinted with permission from Raven *et al.*, Phys. Rev. Lett. **41**, 554 (1978). Copyright 1978 American Physical Society.

wavelengths because of the extreme difficulty in reaching the relevant densities close to critical. The impact of magnetic fields on thermal conduction, which depends on $\Omega_e\tau_{ei}$, where Ω_e is the electron gyro frequency and τ_{ei} is the electron–ion collision time, is expected to be less at shorter laser wavelengths since τ_{ei} is smaller at higher densities. In view of the results of Willi *et al.*[570] for just four overlapped beams, there is little reason to be concerned about magnetic fields at UV wavelengths in reactor designs with large numbers of overlapping beams.

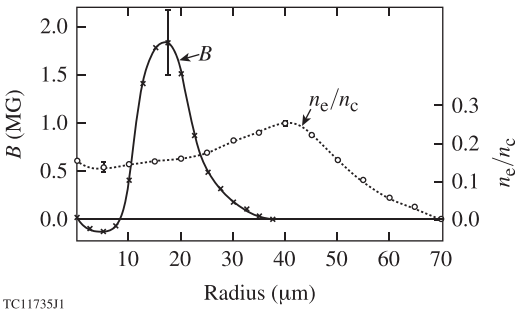

FIG. 10-39. Profiles of magnetic field B and electron density relative to critical (n_e/n_c) at a distance z of 12.5 μm from an Al wire target irradiated at 10^{16} W/cm^2, 60 ps after the peak of the 100-ps main pulse. The peak magnetic field is observed off-axis. Reprinted with permission from Raven *et al.*, Phys. Rev. Lett. **41**, 554 (1978). Copyright 1978 American Physical Society.

An alternative magnetic-field diagnostic, the Zeeman splitting and broadening of spectral lines, was demonstrated by McLean *et al.*[571] and found to give results consistent with Faraday rotation measurements. The diagnostic gives an average magnetic field along the line of sight. McLean *et al.* recognized that while it has the potential to allow observations at densities higher than those accessible to optical probing, it requires other spectral broadening mechanisms such as thermal Doppler and Stark broadening as well as Doppler shifts resulting from mass motion to be taken into account.

The topology of self-generated magnetic fields was illustrated in an experiment carried out by Yates *et al.*[572] at Los Alamos. Two CO_2 laser beams from the Helios laser irradiated a flat Au target in a ~1-ns pulse at an intensity of $\sim 10^{16}$ W/cm^2, with ~120-μm-diam focal spots separated by 1 mm. The geometry of the experiment is shown in Fig. 10-40(a). The magnetic fields generated by the two beams interfere in the center, producing a field null. According to simulations by Forslund and Brackbill,[573] energy is convectively transported away from the laser spots in the corona by fast electrons magnetically insulated from the target surface. However, in the vicinity of the magnetic-field null, the electrons are expected to deposit their energy into the target. This prediction was confirmed in the x-ray pinhole-camera image of Fig. 10-40(b). The hot electrons in the experiment were measured via bremsstrahlung to have a temperature of ~200 keV. Yates *et al.* presented similar results obtained with up to eight beams.

While magnetic fields are unlikely to affect implosion dynamics, they can be generated as a result of nonuniform hydrodynamic behavior such as the Rayleigh-Taylor (RT) instability[574] and have the potential to be used as a

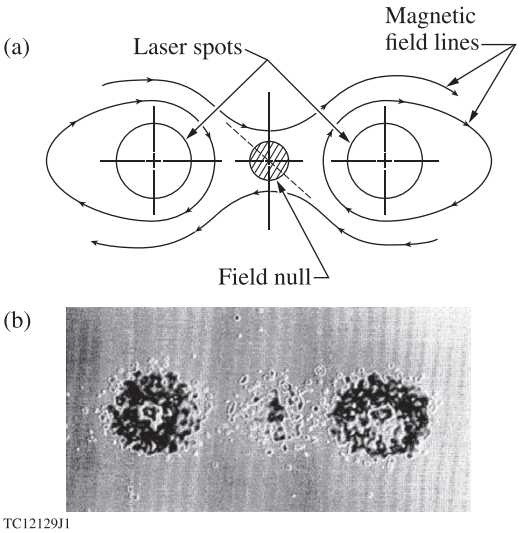

FIG. 10-40. Evidence for self-generated magnetic fields from an Au target irradiated by two 10-μm-wavelength laser beams. (a) Schematic of predicted magnetic-field geometry, showing a field null between two laser-irradiated spots. (b) An x-ray pinhole-camera image showing emission in the vicinity of the field null understood to result from convective electron transport. The beams were spaced 1 mm apart. Reprinted with permission from Yates *et al.*, Phys. Rev. Lett. **49**, 1702 (1982). Copyright 1982 American Physical Society.

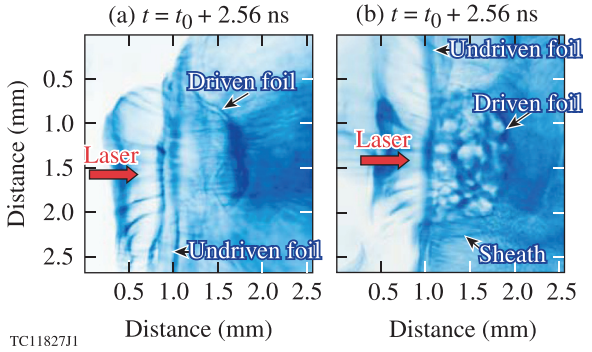

FIG. 10-41. Proton radiographs of laser-accelerated CH foils of thickness (a) 25 μm and (b) 15 μm taken with 13-MeV protons on the OMEGA EP laser. The targets were irradiated at $\sim 10^{14}$ W/cm^2 with an ~4-kJ, 2.5-ns, 0.35-μm laser pulse. The protons were generated from a 20-μm-thick Cu foil irradiated with an ~1-kJ, 10-ps pulse at 1.053 μm. The thinner target in (b) broke up as a result of the Rayleigh–Taylor instability. Reprinted with permission from Gao *et al.*, Phys. Rev. Lett. **109**, 115001 (2012). Copyright 2012 American Physical Society.

diagnostic. In recent work, Manuel *et al.*[575,576] and Gao *et al.*[577,578] have reported proton-probing observations of magnetic fields associated with the RT instability. Manuel *et al.* used D^3He protons from an implosion source, while Gao *et al.* used protons accelerated from the rear surface of a target irradiated with a short (~10-ps) pulse from one beam of the OMEGA EP laser. Two typical proton radiographs from Ref. 577 are shown in Fig. 10-41, both taken under the same irradiation conditions. Figure 10-41(a) is for a 25-μm-thick target that is unbroken by instability formation; Fig. 10-41(b) is for a thinner, 15-μm-thick target that has broken up because of the RT instability. The structures seen in the image are consistent with proton deflection in MG-level magnetic fields.

XI. THERMAL TRANSPORT

An understanding of the process of thermal transport, which governs the transfer of energy deposited by the laser to the high-density DT fuel, is essential to the design of ICF targets. Equally important is the incorporation of this understanding into hydrodynamic simulation codes. However, both a basic understanding of thermal transport and comprehensive simulation models have long been elusive.

The basic processes appear simple. Electrons are heated through interactions with the laser in the underdense corona and then move into the higher-density region, undergoing collisions with ions and other electrons. This process leads to a high pressure at the ablation surface that drives the implosion. In an ideal and somewhat-simplified picture, the transport is described by a diffusion process, wherein the electron heat flux Q_{SH} is given by

$$Q_{SH} = -\kappa_{SH} \nabla T_e, \tag{11-1}$$

where κ_{SH} is the thermal conductivity, given for unmagnetized plasmas by the Spitzer–Härm conductivity.[579] The thermal conductivity depends on the electron density n_e and temperature T_e as $\kappa_{SH} \propto n_e T_e \tau_{ei}$, where τ_{ei} is the electron–ion collision time, which scales as $\tau_{ei} \propto T_e^{3/2}/(Zn_e)$, where Z is the ion charge. Combining these two scalings, $\kappa_{SH} \propto T_e^{5/2}/Z$ and the density dependence disappears. This is easy to understand: if τ_{ei} were a constant, the heat flux would be proportional to the number density of carrier electrons n_e, but since the collision rate of an individual electron is proportional to n_e, n_e cancels out.

It is natural to ask what happens in the limit of zero density, when the diffusion equation gives a finite heat flux even though there are no particles to carry it. Parker[580] encountered this issue in the context of the solar wind, finding that Spitzer's conductivity broke down a long way from the sun, perhaps inside the orbit of the earth. He gave an absolute upper limit to the heat flux Q_A defined as $f_A Q_{fs}$, where

$$Q_{fs} = n_e k_B T_e \sqrt{k_B T_e / m_e}, \tag{11-2}$$

with $f_A = 3\sqrt{3}/2 = 2.598$ obtained by assuming that all the electrons are moving in the direction of the heat flow with the rms thermal velocity. Here, k_B is Boltzmann's constant and m_e is the electron mass. The quantity Q_{fs} is generally referred to as the "free-streaming" flux.

A second limitation of the diffusive formula was recognized by Harrington[581] in the simpler context of Fourier heat flow (where the conductivity is constant). He showed that the heat flux is not necessarily determined by a locally defined temperature gradient because the mean free paths of the heat-carrying particles must be considered in relation to the scale length of temperature variations. In Fig. 11-1, he gave two different temperature distributions that have the same temperature gradient at the point x_0 but produce different heat fluxes across that point. His Appendix gave a nonlocal treatment showing that 41% of classical heat flow comes from within one mean free path in the direction of the temperature gradient and 98% from five mean free paths. Salzmann[582] applied Harrington's results to laser plasmas by giving the conductivity a temperature dependence.

The first limitation was addressed by Shearer[583] in the context of how to treat heat flow in a numerical code. He advocated limiting the heat flow to a maximum of $f_B Q_{fs}$, a variant of Parker's upper limit, where $f_B = 3\sqrt{3}/8 = 0.6495$:

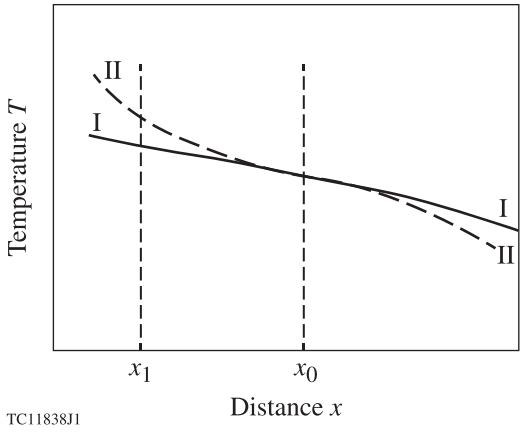

FIG. 11-1. Illustration of hypothetical temperature distributions, curves I and II, yielding different thermal transports across isothermal plane, x_0, even though both curves have the same value of dT/dx at x_0. Figure and caption reproduced with permission from J. Appl. Phys. **38**, 3266 (1967). Copyright 1967 AIP Publishing LLC.

$$\frac{1}{Q} = \frac{1}{Q_{SH}} + \frac{1}{f_B Q_{fs}}. \quad (11\text{-}3)$$

This was obtained by considering a half-plane problem for which the temperature is T_e on the hot side and negligible on the cold side. [The integral was performed incorrectly. The correct integral for a one-sided 3-D Maxwellian is $f_C Q_{fs}$, where $f_C = \sqrt{2/\pi} = 0.798$ (Ref. 584).] Equation (11-3) provides a smooth transition, but sometimes a "sharp cutoff" is used, given by

$$Q = \min(Q_{SH}, f_B Q_{fs}). \quad (11\text{-}4)$$

As pointed out by Delettrez,[585] the difference between the two forms can be significant in some regimes of interest. Shearer recognized that his upper limit was probably too high since it neglected electric-field effects, so Eq. (11-3) might still overestimate the heat flux. [In 1-D spherical geometry, a one-sided heat flux would violate charge neutrality; an electric field (included in the Spitzer–Härm description) arises to ensure no net current.]

The second limitation soon became clear in the context of hot electrons generated in laser-produced plasmas, as evidenced, in particular, by the hard x-ray bremsstrahlung radiation that they emitted. Morse and Nielson[586] recognized that the energy associated with hot electrons is deposited deep into the target, violating the basic premises of diffusive conductivity. They considered non-Maxwellian distribution functions and their associated heat flow, in particular two-component electron velocity distributions. They also recognized that hot electrons could be generated from electric-field fluctuations resulting from plasma instabilities.

Around the same time, Bickerton[587] noted the breakdown of Spitzer conductivity when the electron mean free path is comparable to the temperature scale length, and claimed that the flux could not possibly exceed a value equivalent to $f_B Q_{fs}$. He also suggested that the ion-acoustic instability could be excited for an electron distribution very far from Maxwellian, leading to a more-severe flux limit (by $\sqrt{m_e/m_i}$, where m_e and m_i are the electron and ion masses, respectively) if $T_e \gg T_i$. This suggestion was consistent with the work of Forslund,[588] who showed that large heat flows in the solar wind can result in the excitation of ion-acoustic waves. While Forslund did not solve the self-consistent problem of the effect of these waves on the distribution function, he suggested that weak ion-acoustic turbulence could reduce the thermal conductivity. A comprehensive treatment of the ion-acoustic instability and its effect on thermal transport was given by Dum.[589]

Ehler *et al.*[590] offered inhibited heat conduction resulting from the ion-acoustic instability as an explanation for a variety of observations from experiments at 10^{16} W/cm^2 at a 1-μm laser wavelength and 10^{14} W/cm^2 at 10 μm. These observations included electrons with energies greater than 50 keV, a large fraction of the laser energy appearing as fast ions, and less laser energy than expected being transmitted through thin foils. In related experiments, Kephart *et al.*[108] reported x-ray spectra up to 50 keV, indicating a clear suprathermal electron component. A number of these observations were then modeled by Malone *et al.*[591] They used a 1-D hydrodynamics code with a single electron temperature in which the heat flux was given by Eq. (11-3), except that f_B was replaced by a much smaller number, f, now known as the "flux limiter." Figure 11-2 shows one example of their modeling for a typical x-ray spectrum I_ν [curve (d) of Fig. 1 of Kephart *et al.*[108]]. Reasonable matches to the data were obtained with values of f in the range of 0.03–0.1, while Spitzer–Härm conductivity ($f = \infty$) came nowhere close to the data.

Malone *et al.* also matched, in a phenomenological way, the energy fraction transmitted through a thin foil and the percentage of energy in fast ions and, following Ehler *et al.*,[590] offered ion-acoustic turbulence as a possible explanation. They suggested heat-flux limitation by magnetic fields (Sec. X F) as another possibility. Their simulations had the limitation that they modeled a single-temperature distribution; therefore, inhibiting the transport of energy deposited at the critical-density surface led to sufficiently high temperatures to produce the observed hard x rays. However, their work led to a recognition that (1) there was no reason why the then commonly used values of $f \sim 0.6$ in formulae like Eq. (11-3), only ever derived as crude upper limits on the heat flux, should give the actual heat flux; and (2) experiments with substantial energy in hot electrons cannot be modeled with a single, locally defined thermal temperature.

It became widely recognized that a different treatment was required for suprathermal electrons, which showed few signs of being inhibited in their transport and consistently preheated the fuel making high compression impossible. Gitomer and Henderson[592] found that hard x-ray spectra such as those of Kephart *et al.*[108] could be fit with appropriate assumptions for the absorption fraction into hot electrons and their temperature. However, suprathermal electron models that could provide quantitative predictions of data such as the observations considered by Malone *et al.*[591] were never developed before the move to short-wavelength lasers in the 1980s, when interest in such models declined as a result of the dramatic decrease in the energy observed in hot electrons. Hot-electron

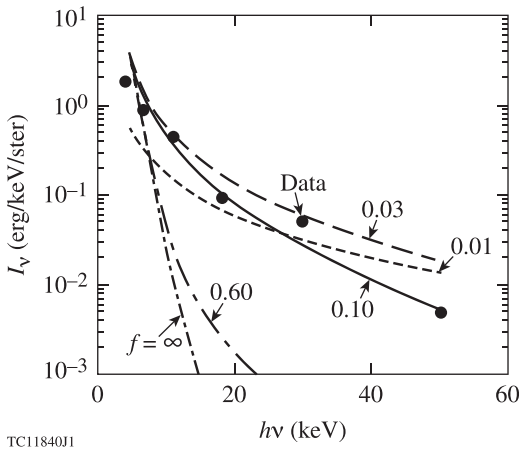

FIG. 11-2. Calculated bremsstrahlung spectra I_ν from a thick CH_2 target versus photon energy $h\nu$ for different values of the flux limiter f, compared with experimental data. The target was irradiated by a 1.06-μm laser in a 25-ps pulse at $\sim 10^{16}$ W/cm^2. Reprinted with permission from Malone *et al.*, Phys. Rev. Lett. **34**, 721 (1975). Copyright 1975 American Physical Society.

modeling has since become important in the context of fast ignition (Sec. XIV) and shock ignition (Sec. XV) and in the coupling of parametric-instability–generated hot electrons to the compressed fuel (Sec. X A).

Interest in heat-flux inhibition continued with an experiment by Gray *et al.*[593] in which they attempted to isolate heat flow from the complications associated with high-intensity lasers such as fast-electron transport, magnetic-field generation, and resonant absorption. They heated a hydrogen *Z* pinch[594] of initial density 6×10^{16} cm^{-3} and initial temperature 4 eV with a 300-MW, 3-ns CO_2 laser focused to a 350-μm-diam spot and used ruby-laser scattering to measure the evolution of T_e and n_e transverse to the direction of the heating laser. They modeled their data with two adjustable parameters—the flux limiter and a multiplier w on the classical absorption rate—obtaining results such as those shown in Fig. 11-3(a) for the temperature profile. Without strong inhibition of the heat flux, they predicted that heat would flow away from the heated region faster than was observed. They found best fits to the data with $w=1$ (classical absorption) and $f=0.016$–0.04. [Note that their definition of f, shown as f^* in Fig. 11-3(a), was higher than f by a factor of $\sqrt{\pi/2}$.] Their care in considering possible deviations from classical absorption makes the point that uncertainties in absorption modeling can lead to uncertainties in transport modeling and vice versa.

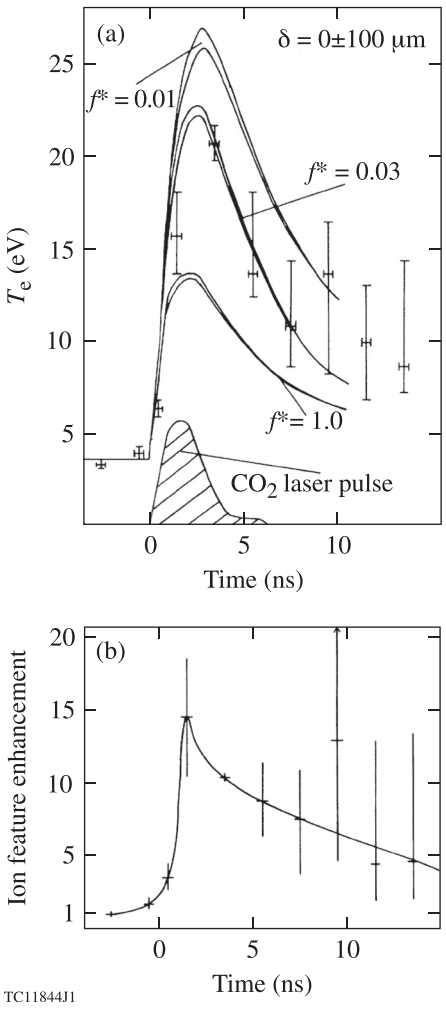

FIG. 11-3. (a) Calculated temperature profiles for a *Z* pinch heated by a 300-MW, 3-ns, CO_2 laser pulse for three values of the flux limiter f^*, compared with experimental data. [Note that $f^*=f\sqrt{\pi/2}$, where f is the standard definition of the flux limiter.] For each simulation the two solid lines indicate the band of temperatures possible within the ±100-μm alignment error. (b) Enhancement of the ion feature above thermal $(S_{i0}/S_{i,th})$ measured by ruby-laser scattering, indicating ion-acoustic turbulence. Reprinted with permission from Gray *et al.*, Phys. Rev. Lett. **39**, 1270 (1977). Copyright 1977 American Physical Society.

Gray *et al.*[593] also measured an enhancement up to a factor of 14× thermal in the ion feature of their scattering results [Fig. 11-3(b)]. This provided evidence for ion-acoustic turbulence, which they claimed was the source of the observed low heat flux. Gray *et al.* noted that the first-order perturbation theory of Spitzer and Härm breaks down when the ratio of the electron mean free path λ_e to the temperature-gradient scale length L exceeds 0.02. A full report of this work is found in Ref. 584.

An alternative interpretation to ion-acoustic turbulence was provided in 1981 by Bell *et al.*[595] Until this time, thermal transport was routinely modeled in an *ad hoc* manner with Eq. (11-3) or (11-4), usually with a small value of f as advocated by Malone *et al.*[591] Bell *et al.* solved the Fokker–Planck equation to obtain solutions for the electron distribution function for a simple 1-D heat flow problem in which the Spitzer–Härm theory broke down. In this approach, the electron distribution function $f(v,x,\theta)$ is expressed as a Legendre polynomial expansion $\sum_\ell f_\ell(v,x)P_\ell(\cos\theta)$, where θ is the angle in velocity space to the direction of heat flow, with each $f_\ell(v,x)$ solved as a function of space (x) and velocity (v). In contrast to the Spitzer–Härm model, which uses the perturbation approximation $[f(v,x,\theta)=f_0(v,x)+f_1(v,x)\ \cos\theta]$, $f_0(v,x)$ does not need to be Maxwellian. The different velocities are coupled by an appropriate collision operator. The density was uniform in the simulation region, and a temperature difference between the two ends of the region was created by raising the temperature at one end. Figure 11-4(a) shows the evolution of the temperature profile and the associated heat flux.

From plots such as Fig. 11-4(a), Bell *et al.*[595] were able to scan from one end of the region to the other, plotting for each point the ratio of the heat flux Q to Q_{fs} and the ratio L/λ_e. An example (for a normalized time of 5260) is shown in Fig. 11-4(b), demonstrating that the heat flux is not simply a function of the local plasma state. In this example, the heat flux near the top of the heat front (immediately to the right of the heated region) was ~0.1 times the free-streaming limit and the heat flux at the base of the heat front exceeded the Spitzer–Härm flux. The temperature gradient scale length was a few times the mean free path of a thermal electron in the most-extreme case considered. (The mean free path of a heat-carrying electron, which typically has a velocity 2–3× thermal, is considerably larger than that of a thermal electron as the mean free path of an electron scales with v^4.) Bell *et al.* also found that while the perturbed part of the distribution function f_1 in the Spitzer–Härm model exceeds the unperturbed (Maxwellian) part f_0 at large velocity, the amplitude of f_1/f_0 was limited to just below unity in the Fokker–Planck calculations. Using an *ad-hoc* (local) model with a simplified collision operator, Shvarts *et al.*[596] showed

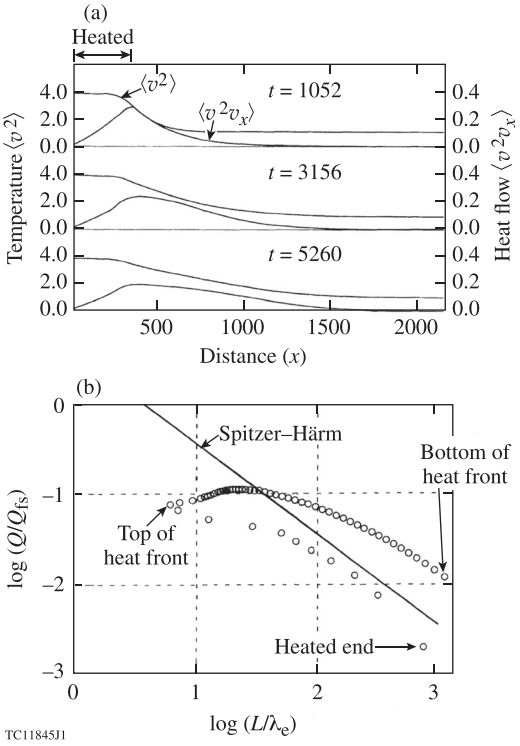

FIG. 11-4. (a) Plots of temperature $\langle v^2 \rangle$ and heat flux $\langle v^2 v_x \rangle$ as functions of distance x (in units of Debye lengths) from a Fokker–Planck calculation of the heat flow, at three successive times t. The calculation started with the region $0 \leq x \leq 350$ being heated to $4\times$ the initial temperature. (b) Plot of heat flow (Q/Q_{fs}) against inverse temperature gradient (L/λ_e) at $t = 5260$, each point corresponding to a different value of x. Different points experience heat fluxes that can be below or above Spitzer–Härm. Reprinted with permission from Bell *et al.*, Phys. Rev. Lett. **46**, 243 (1981). Copyright 1981 American Physical Society.

that by limiting f_1 to $0.75\,f_0$, some of the results of Bell *et al.* could be reproduced to within a factor of 2.

Other approaches were tried at around the same time. Khan and Rognlien[597] obtained a Monte Carlo solution to the Fokker–Planck equation (essentially following the collisions of individual electrons) in a model temperature profile (heat baths at 30 eV and 40 eV separated by 60 cm at a density of 10^{13} to 10^{15} cm^{-3}). They showed a transition from the collisional limit, where Q is independent of n_e, to the collisionless limit, where Q is proportional to n_e. However, the conditions were far removed from those of laser-fusion plasmas, and it appears that the Monte Carlo method is not useful for relevant densities. Shirazian and Steinhauer[598] considered a plasma slab confined between two boundaries, one hot and one cold, and attempted to solve for the heat flow (assumed to be a single value independent of position) by expressing the distribution function in terms of trial functions. However, they encountered considerable difficulty in the collisional limit, where they were unable to match the Spitzer–Härm solution. The field subsequently followed the Fokker–Planck approach introduced by Bell *et al.*[595]

Matte and Virmont[599] described Fokker–Planck simulations very similar to those of Bell *et al.*,[595] finding that just the $n = 1$ term of the Legendre polynomial expansion of the perturbed distribution function (Bell *et al.* used eight terms) was sufficient. Albritton[600] presented Fokker–Planck calculations for plasmas with $Z > 10$ in which the non-Maxwell–Boltzmann distributions resulting from inverse-bremsstrahlung laser absorption were included. Matte *et al.*[601] extended the work of Matte and Virmont[599] to include inverse bremsstrahlung absorption and a model for ion motion. Luciani *et al.*[602] introduced a delocalization model (based on a suggestion by Bell[603]), wherein the heat flux at one point is given by a weighted average (convolution integral) of the Spitzer–Härm heat flux at all other points, appropriately weighted according to the electron mean free path. As shown in Fig. 11-5, they obtained results that agreed with a 1-D Fokker–Planck code for a test problem. Their model can describe the preheating effects beyond the base of the heat front and has the merit of being far easier to implement in a hydrodynamics code than a Fokker–Planck model. Delettrez[585] pointed out some limitations of this approach. An extensive mathematical analysis of the convolution method was given by Luciani *et al.*[604]

Delettrez[585] provided a comprehensive review of many experiments, especially layered-target–burnthrough and charge-collector measurements of mass ablation, that have typically indicated effective values of f in the range of 0.03–0.1. There were some exceptions, but Delettrez pointed out that the conclusions of some of these experiments, carried out before beam smoothing (Sec. VI) became routine, may have been affected by laser nonuniformity. For example, Goldsack *et al.*,[605] who reported the first measurements of the mass ablation rate in spherical geometry (both at 1 μm and 0.5 μm), had only six beams available and the combination of beam defocus with the lack of beam smoothing would have resulted in significant irradiation inhomogeneities. Another exception was provided by Mead *et al.*,[423] who irradiated Be-on-Al disks at 1 μm and 0.35 μm with $\sim 10^{14}$ W/cm^2 absorbed and, based on time-integrated soft x-ray signals, found it necessary to use f in the range of 0.01–0.03; here, the target-plane laser profiles had substantial modulation, especially at 0.35 μm, and there were many uncertainties in both the modeling and experimental conditions.

One example of an experiment that found the need for flux inhibition is shown in Fig. 11-6. Fechner *et al.*[606] used an all-reflective focusing system (that formed each of two 1-

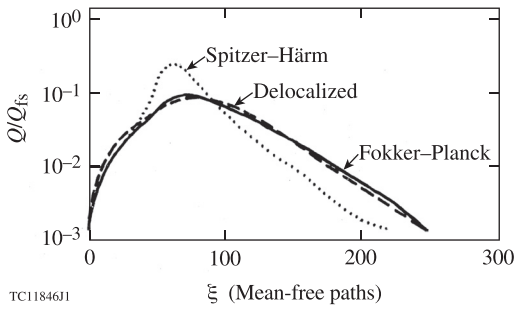

FIG. 11-5. Normalized heat-flux profiles Q/Q_{fs} calculated by a Fokker-Planck simulation, Spitzer-Härm, and a delocalization model. The horizontal coordinate ξ is a "reduced position," measured in mean free paths, that would be proportional to the actual distance in a uniform-density plasma. Reprinted with permission from Luciani *et al.*, Phys. Rev. Lett. **51**, 1664 (1983). Copyright 1983 American Physical Society.

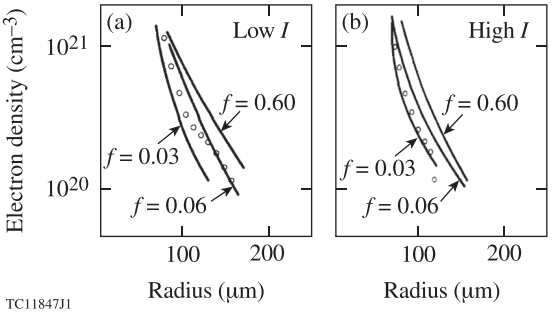

FIG. 11-6. Electron density profiles determined from holographic interferometry for ~100-μm-diam spherical targets irradiated with a 1-μm laser, at (a) low intensity ($I < 3 \times 10^{14}$ W/cm^2) and (b) high intensity ($I > 6 \times 10^{14}$ W/cm^2). The data are compared with simulations using three different values of the flux limiter f. Reproduced with permission from Phys. Fluids **27**, 1552 (1984). Copyright 1984 AIP Publishing LLC.

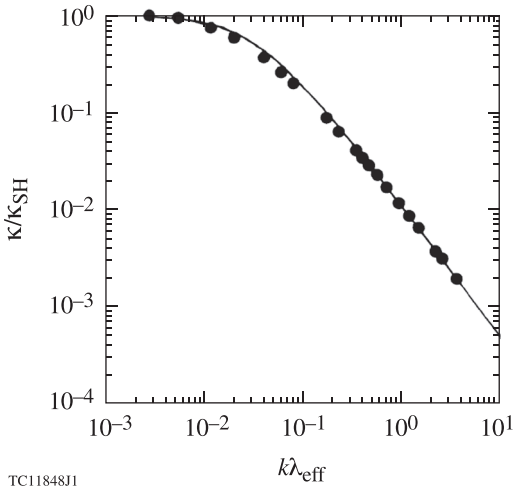

FIG. 11-7. Ratio of the effective thermal conductivity κ to the Spitzer–Härm conductivity κ_{SH} as a function of $k\lambda_{eff}$, obtained from calculations (solid circles) using the Fokker–Planck code *SPARK* for low-amplitude perturbations. Here, k is the perturbation wave number and λ_{eff} is the effective stopping length of the electron. The reduced conductivity for small perturbation wavelengths (large k) enhances the growth of thermal filamentation. The solid curve is a fit to the simulation data. Reprinted with permission from E. M. Epperlein, Phys. Rev. Lett. **65**, 2145 (1990). Copyright 1990 American Physical Society.

μm laser beams into a 140° cone) to irradiate spherical targets, which were diagnosed using holographic interferometry. The interference fringes were to a good approximation circular, implying that the plasma density profiles were close to spherically symmetric. The density profiles were determined using Abel inversion, compared with simulations using various values of f, and found to fit predictions for f in the range of 0.03–0.06. Figures 11-6(a) and 11-6(b) give examples for intensities identified as low and high. The data appeared to be fairly reproducible, with minor variations from shot to shot. Fechner *et al*. gave four other examples, three of which were well fit by $f = 0.03$ and one by $f = 0.06$. Absorption experiments carried out around this time were also consistent with values of f in this range (Sec. V). McCrory *et al*.[607] successfully modeled the absorption, implosion trajectory, x-ray conversion, and shell areal density for targets imploded on the 24-beam, 0.35-μm OMEGA laser using a (sharp cutoff) flux limiter of 0.06.

Another aspect of nonlocal heat transport was demonstrated by Fokker–Planck calculations of Bell[603] in a regime where Spitzer–Härm transport broke down not because of large heat fluxes but because of nonlocal effects. In examining electron energy transport in ion waves intermediate between isothermal and adiabatic, Bell found that the conductivity is reduced when the wavelength of the ion wave is less than 1000 electron mean free paths, independent of the amplitude of the temperature gradient. A similar effect was found by Epperlein,[511] who extended the theory of thermal self-focusing to include the effects of nonlocal heat transport. His results (Fig. 11-7) show that that the thermal conductivity calculated by the Fokker–Planck code *SPARK* is greatly reduced compared with the Spitzer–Härm model when the perturbation wavelength approaches the electron mean free path. (It begins to be reduced when the wavelength is a few hundred times the mean free path defined at the temperature T, but the heat-carrying electrons have energy ~7 T, or a mean free path ~49× longer.) This effect cannot be treated using a flux limiter since the perturbations in the stability analysis are all small, as in Bell.[603] Epperlein applied his theory to the experiment of Young *et al*.[512] and found that thermal self-focusing is expected to dominate over ponderomotive self-focusing as a result of this effect (Sec. X D). The calculations of Epperlein[511] were confirmed with an improved model of *SPARK*[608] that included a hydrodynamic model.

Since the work of Malone *et al*.,[591] the flux-limiter model has been routinely used in hydrodynamic simulations for target design, experimental design, and the interpretation of experimental data. It has the advantage of computational efficiency and ease of use in both 1-D and multidimensional codes, and it provides a reasonable means of modeling the amount of heat that flows from the corona to the interior of the target. However, it cannot be relied upon to predict detailed profiles of quantities such as temperature, and it cannot model nonlocal effects that are important in many situations. Work has therefore been pursued to incorporate a Fokker–Planck treatment into hydrodynamic codes. Two examples are given by Nishiguchi *et al*.,[609] who present 1-D implosion simulations including a Fokker–Planck model, and Li *et al*.,[610] who compared flux-limiter and Fokker–Planck models in 1-D planar simulations for a square temporal pulse of varying intensity on an ionized Al slab, finding that the flux-limiter model breaks down at or above 10^{15} W/cm^2.

An example of a simpler treatment is provided by Goncharov *et al*.,[157] who described a 1-D nonlocal model based on the BGK (Bhatnagar, Gross, and Krook) collision operator[611] and found it able to model both shock transit times and the Richtmyer–Meshkov instability. Hu *et al*.[612] found that planar-foil acceleration experiments at high intensity (~10^{15} W/cm^2) could be matched with this model.

A model intended for use in multidimensional hydrodynamics codes, known as the SNB (Schurtz, Nicolaï, and Busquet) model, was proposed in Ref. 613. This is a 2-D diffusion model derived from the convolution models. It

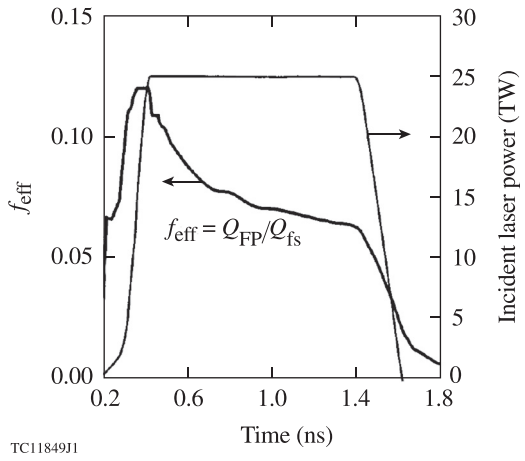

FIG. 11-8 Time dependence of the effective flux limiter $f_{\rm eff}$ obtained from a simulation of an implosion in which a Fokker–Planck model is incorporated into the 1-D hydrodynamics code *LILAC*. The parameter $f_{\rm eff}$ is defined at the critical surface as the ratio of the Fokker–Planck heat flux $Q_{\rm FP}$ to the free-streaming flux $Q_{\rm fs}$. Reprinted with permission from Sunahara *et al.*, Phys. Rev. Lett. **91**, 095003 (2003). Copyright 2003 American Physical Society.

computes the nonlocal heat flux as a correction to the Spitzer–Härm flux using the local electron mean free path. Unlike the convolution models and those based on the BGK collision operator, it can easily be used in codes in which diffusion solvers already exist. The model also assumes that the source of the heat-carrying electrons is Maxwellian, so it does not take into account tail depletion in the corona.

Another approach, advocated by Sunahara *et al.*,[614] is to use a time-dependent flux limiter in hydrodynamic simulations. Sunahara *et al.* incorporated a 1-D Fokker–Planck solver into the 1-D hydrocode *LILAC*. From their simulations of an implosion, they plotted the effective flux limiter $f_{\rm eff}$ at the critical surface, defined as the ratio of the Fokker–Planck heat flux to $Q_{\rm fs}$, as a function of time (Fig. 11-8). They found that $f_{\rm eff}$ peaked at $\sim$0.12 early in the pulse and then decreased to $\sim$0.06. This time-dependent flux limiter could then be used in 1-D or multidimensional simulations.

Marocchino *et al.*[615] reviewed two nonlocal electron thermal conduction models, the SNB model and the CMG (Colombant–Manheimer–Goncharov) model,[616–618] and compared them with Vlasov–Fokker–Planck simulations. The CMG model is derived from first principles based on the BGK collision operator. Unlike the convolution models and the SNB model, which do not limit the diffusion of electrons and so are expected to produce too much preheat, it limits the electrons to their range. Also, the CMG model computes the self-consistent electric field by assuming zero current conditions. The model compares well with the results of the Fokker–Planck code *SPARK*.[511]

In view of the large experience gained from Fokker–Planck simulations, there can be little doubt as to the importance of nonlocal effects on heat flow. The possibility remains, however, that nonlocal effects may not be the complete explanation and that magnetic-field or ion-acoustic inhibition may also be significant.

Self-generated magnetic fields resulting from nonparallel temperature and density gradients (Sec. XF) have been considered as a means for inhibiting the heat flux, but, as shown in Sec. XF, they are not large enough in conditions relevant to spherically uniform irradiation, especially for submicron laser wavelengths. Magnetic fields generated through instabilities driven by electron fluxes (e.g., the Weibel instability[619] or the electrothermal instability proposed by Haines[530]) might inhibit the flow of heat-carrying electrons. However, the Weibel instability grows with a very small characteristic scale length $c/\omega_{\rm p}$, where c is the speed of light and $\omega_{\rm p}$ is the electron plasma frequency. Electron scattering by the turbulent magnetic fields associated with the instability is expected to be relatively ineffective since an electron must pass through many turbulent cells (in each of which its direction changes by a small amount) before its direction changes through 90°. Similar arguments apply to the electrothermal instability, which also occurs on short scale lengths.

It is hard to confirm or rule out ion-acoustic turbulence because it has not been possible to make direct experimental measurements in the overdense plasmas of interest. The *Z*-pinch measurements of Gray *et al.*[593] were made at densities many orders of magnitude lower that were accessible to optical probing.

The possibility that ion-acoustic turbulence and nonlocal effects are operating simultaneously has been explored by Tikhonchuk *et al.*[620] They started with work by Bychenkov *et al.*,[621] who found that the effect of ion-acoustic turbulence on the inhibition of the heat flux can be expressed by a flux limiter

$$f_{\rm ia} = 0.18\left(\frac{Z}{A}\right)^{1/2}\beta, \tag{11-5}$$

where Z is the ion charge number, A is the ion mass number, and β is a parameter that depends on the electron distribution function [$\beta = 1$ for a Maxwellian, while $\beta \approx 0.3$ for an $\exp(-\text{const}\ v^5)$ distribution such as was found by Langdon[622] when considering the reduction in inverse bremsstrahlung absorption at high laser intensities and large Z]. For a typical ratio $Z/A = 1/2$, $f_{\rm ia} = 0.12$ for a Maxwellian and 0.04 for the $\exp(-\text{const}\ v^5)$ distribution. Tikhonchuk *et al.* then performed Fokker–Planck simulations (for a laser wavelength of 0.35 μm and $Z = 6$) that matched hydrodynamic simulations using $f = 0.16$. From their calculated distribution function, they obtained a value of 0.32 for β, implying a flux limiter $f_{\rm ia}$ of 0.04 resulting from ion-acoustic turbulence. In this case, ion-acoustic turbulence predicted additional inhibition beyond that found from the Fokker–Planck simulation. However, the laser intensity of the simulation (10^{16} W/cm^2), chosen to be sufficiently high to produce a significant deviation of the distribution from Maxwellian, was unrepresentative of typical direct-drive conditions. The electron density was homogeneous at 0.02 times the critical density and the simulation was run for $\sim$10 ps.

While flux-limited Spitzer–Härm transport is generally agreed to be adequate for most 1-D aspects of spherical implosions, there are many circumstances in which it does not correctly model lateral heat flow along the target surface. For example, the reduction of thermal conductivity perpendicular

to the laser direction found by Epperlein[511] in the context of thermal self-focusing is not modeled at all since the heat fluxes are all perturbation quantities well below Q_{fs}. The complexity introduced by the second dimension was illustrated by Rickard *et al.*,[623] who used a 2-D Fokker–Planck calculation of a 3.5-ps, 0.25-μm laser pulse incident on an exponential density gradient of 3-μm scale length to show that the heat flux is not necessarily parallel to $-\nabla T_e$. They found angles of up to 34° between the two vectors. This situation cannot be handled by 2-D nonlocal models or 2-D flux-limiter models in which an equivalent thermal conductivity is obtained using the heat flux and used to solve the 2-D thermal diffusion equation. The radial and lateral heat flows are related in a complex way: nonlocal heat flow into the target results in a depletion of the high-energy tail of the distribution in the absorption region, providing fewer electrons with high energy and long mean free path to distribute energy laterally. Similar considerations are expected to apply in polar-drive implosions (Sec. VIII C), where the electron temperature varies with polar angle and lateral heat flow is important. Unfortunately, Fokker–Planck simulations are too computationally expensive for routine implementation in 2-D hydrodynamic simulations. Two-dimensional nonlocal models provide a computationally viable improvement on 2-D flux-limiter models, but it should be recognized that they are unable to capture the full 2-D nature of thermal conduction.

It may never be feasible to obtain an accurate modeling of heat flow in ICF plasmas. However, the insight provided by simulations using the flux-limiter model and Fokker–Planck models has made it possible to obtain reasonable predictions of experimental performance over close to four decades.

XII. SHOCK TIMING AND EQUATION OF STATE (EOS)

An ideal ICF implosion is driven by a continuous drive profile with increasing power that isentropically compresses the fuel, imparting maximum PdV work with no increase in entropy. This is difficult to realize in experiments because the fuel begins at low density, is easily compressed, and has a sound speed that rapidly increases with compression. Subsequent increases in pressure create compression waves that travel at higher velocities. If the drive profile is not controlled with high precision, these compression waves can overtake their predecessors creating shock waves that impart considerable entropy to the fuel, raising the adiabat of the implosion and degrading its efficiency.

Instead of attempting the formidable precision required to control such a drive profile, isentropic compression is approximated by a series of weak shocks that compress the fuel without excessive increases in entropy. This is done by using a precisely timed sequence of shocks that incrementally (and quasi-isentropically) compress the shell and fuel as described in Sec. III A. Each shock adds the correct amount of entropy to produce the desired adiabat. Target designs typically use two or three shocks to compress the DT ice to a state where an intense compression wave can implode the assembly along the desired trajectory with only a small increase in its entropy. These initial shocks are produced by short (~100-ps) laser pulses ("pickets") separated by nanoseconds. The pickets are followed by an intense pulse, several nanoseconds in length, which drives the implosion. The strength and timing of the initial shocks are critical to target performance, so their diagnosis is of primary importance for assessing the quality of an implosion and for validating the simulations used to create the target design.

Precise measurement of multiple shocks in a spherical target is made possible by the development and refinement of the imaging VISAR (velocity interferometry system for any reflector). The modern system was developed for diagnosing laser-driven shocks in deuterium[624] and thereafter shown to be ideal for timing shocks for ICF targets.[625] Section XII A describes VISAR and a related diagnostic: the streaked optical pyrometer (SOP), which measures shock self-emission and temperature. Section XII B presents the use of VISAR and SOP to measure shock timing in spherical targets.

Hydrodynamic simulations of shock strength and timing as well as target compression require knowledge of the shocked materials' EOS. The development of VISAR has facilitated an extensive effort in the study of materials at extreme conditions to support efforts both in direct-drive ICF and in high-energy-density physics. Section XII C reviews the significance of EOS research to ICF implosions and experiments that have been used to measure the EOS of deuterium and CH—two materials that are especially important for direct drive.

A. VISAR and SOP diagnostics

Figure 12-1 is a schematic of the VISAR and SOP diagnostics currently implemented at OMEGA.[626,627] The diagnostics share an optical telescope. They provide simultaneous time-resolved velocity and self-emission data from shock waves within a transparent material. The VISAR diagnostic detects the Doppler shift of a probe beam reflected off the shock front moving to the rear (right) of the target. Originally developed as a single-point detection system[628] that observed the rear (free) surface of shock-compressed opaque samples, VISAR evolved to multi-point and line-imaging systems.[629] Modern VISAR systems use imaging through a Mach–Zehnder interferometer, as shown in Fig. 12-1, developed by Celliers[626] to provide the velocity as a function of space and time with high precision. The shock pressures in ICF targets are sufficiently strong to melt and partially ionize the compressed material, forming a conductive (metalized) material. That and the steepness of the shock front produce a localized surface from which the VISAR probe can reflect.

The VISAR system on OMEGA comprises three primary components: a probe laser, an imaging system, and two interferometers of which one is shown in Fig. 12-1. The probe is a frequency-doubled Nd:YAG laser that produces 50- to 200-ns pulses that are fiber optically coupled to the VISAR system. The imaging system relays an image of the rear target surface to the output beam splitter (BS) of the interferometer. It also conveys the probe beam to and from the target. Each interferometer has an optical etalon (delay) in one leg, providing a comparison of the phases of the

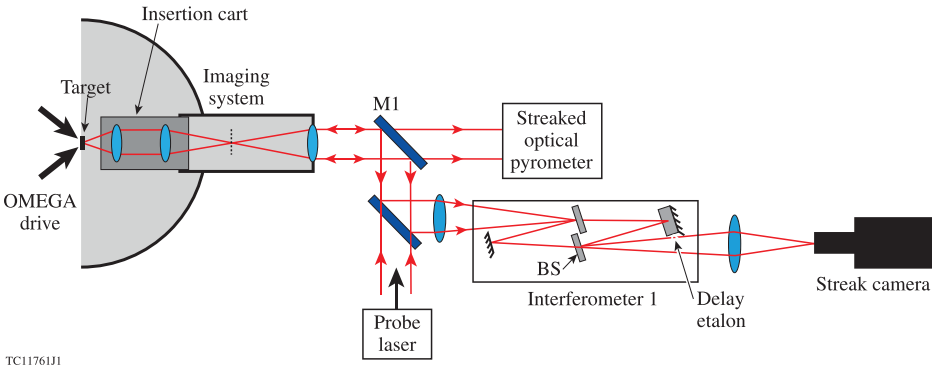

FIG. 12-1. Schematic of the velocity interferometer system for any reflector (VISAR) and streaked optical pyrometer (SOP) diagnostics. BS: beam splitter.

reflected probe-beam signal at two different times. The difference in phase between the legs results from the Doppler shifts in wavelength accumulated during the preset time difference between the legs. The result is a series of fringes (imposed onto the target image), as shown in Fig. 12-3 below, whose displacements are proportional to the velocity of the rear target surface, resolved in space along the face of the target transverse to the direction of shock propagation. These fringe patterns are detected with an optical streak camera to provide a velocity record as a function of space and time, with ~5-μm spatial resolution and ~10- to 50-ps temporal resolution. The second channel has a different velocity sensitivity to resolve the modulo-2π ambiguities that result when instantaneous velocity jumps (from shocks) are greater than one fringe period. Simultaneously, the SOP detects self-emission in the 590- to 850-nm wavelength band to obtain time-resolved brightness temperatures.

B. Shock-timing measurements

The use of VISAR to diagnose the shock waves in liquid (cryogenic) deuterium was first demonstrated by Munro *et al.*[625] They measured multiple planar shocks in liquid deuterium driven by hohlraums. The deuterium is a surrogate for the deuterium–tritium ice layer in an ICF target, providing an extended, uniform medium through which the shocks can propagate. Munro *et al.* were able to measure shock velocities in the deuterium of 12–65 km/s with 2% precision. They also detected multiple shocks with stronger ones overtaking weaker ones, precisely as required for shock timing for ignition capsules. This technique was refined for hohlraums with re-entrant cones[630] and then demonstrated in spherical geometry on directly driven cryogenic spheres.[324,630–632]

The measurements of Refs. 631 and 632 were made on OMEGA for deuterium in direct-drive spheres as shown in Fig. 12-2. The velocity and timing of multiple converging shock waves were measured inside spherical CD targets filled with liquid deuterium. The targets were fitted with a re-entrant diagnostic cone similar to that used in fast-ignition experiments (Sec. XIV B). The spherical shell and cone were filled with liquid deuterium; VISAR and the SOP observed the shocks on the inside of the shell through an aperture in the end of the cone, with the VISAR probe beam incident and reflected in the directions of the arrows in Fig. 12-2. The sphere was irradiated by 36 OMEGA beams on the hemisphere opposite the VISAR line of sight. Two-dimensional simulations indicate that this configuration produces a uniform intensity distribution that replicates the 60-beam irradiation uniformity in a region within ~±20° about the VISAR axis. These experiments were therefore an accurate surrogate for the shock-transit portion of a spherically symmetric ICF implosion.

The technique shown in Fig. 12-2 was used to detect all four shocks in NIF indirect-drive shock-timing experiments in which ignition-scale targets were employed with re-entrant cones that extended out beyond the hohlraum and its thermal mechanical package.[633] These targets were later extended to multi-axis measurements and used successfully to diagnose various aspects of ignition target physics.[634,635]

Using pulses based on the triple-picket design of Sec. III A, the drive laser produced a sequence of up to four shocks whose strength and timing were designed so that later shocks overtake earlier weaker ones at specific times and locations in the target to produce multiply shocked deuterium with a predefined adiabat. Figure 12-3(a) shows VISAR data for a three-shock experiment in a 900-μm-diam,

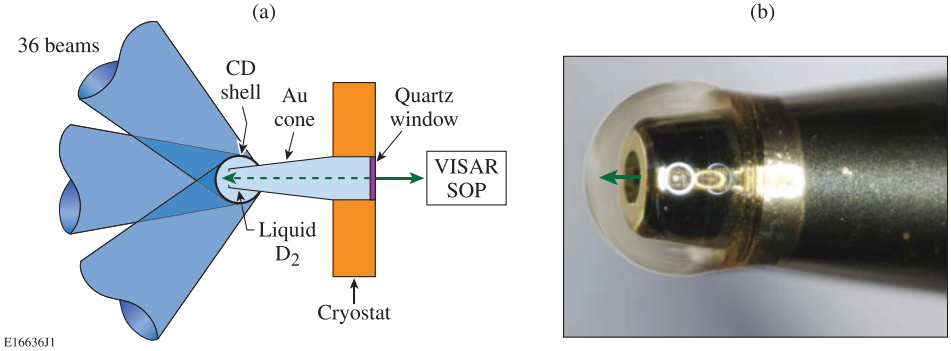

FIG. 12-2. (a) Schematic of cryogenic shock-timing experiments in convergent geometry, showing a 900-μm-diam CD shell with a re-entrant Au cone. The shell is irradiated with 36 OMEGA beams. (b) Photograph of the capsule and cone. Both are filled with cryogenic liquid deuterium. The arrow indicates the direction of the incident VISAR beam. Reproduced with permission from Phys. Plasmas **18**, 092706 (2011). Copyright 2011 AIP Publishing LLC.

10-μm-thick CH shell filled with liquid deuterium and driven by three 100-ps laser pulses, shown as the white overlay. The VISAR record is a 1-D image of the target (vertical axis) that is streaked in time (horizontal axis). Imposed on this image is a series of fringes whose vertical position (fringe phase) varies linearly with the shock velocity.

The image in Fig. 12-3(a) provides a view of the shocks in the liquid deuterium contained within the shell. The liquid deuterium is transparent to the VISAR probe. When shocked to ~Mbar pressures, the deuterium is compressed and heated sufficiently to produce free electrons, undergoing an insulator-to-conductor transition that is common at high pressures and producing a reflecting surface for the VISAR probe. The shock waves spherically converge along the VISAR axis, ultimately coalescing to form a single strong shock that converges toward the center of the target. VISAR is able to track this convergence until the shock impacts the front of the cone, which is 200 μm from the inside of the sphere.

Before time $t = 0$, the fringes in Fig. 12-3(a) are horizontal because there is no shock or movement in the target. At

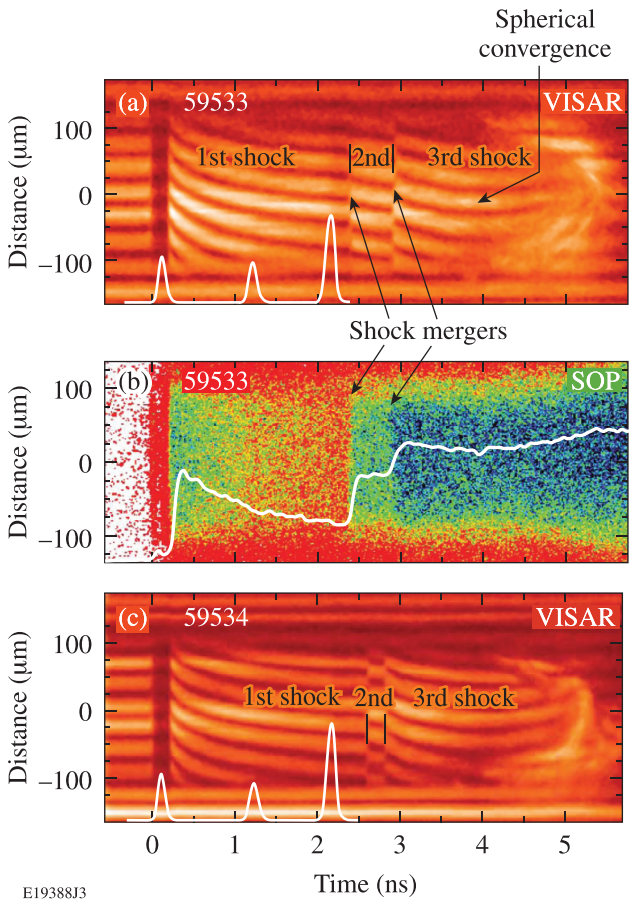

FIG. 12-3. (a) VISAR data record (space versus time) for shot 59533, with fringes that represent the velocities of the shocks produced by the triple-picket laser pulse shown in white. The three shocks are observed as well as the jumps in fringe position that occur when the shocks merge. (b) SOP data for the same shot, showing that the self-emission intensity (white overlay) follows the shock velocity and shock mergers, providing corroboration of shock timing. (c) VISAR data for a shot (59534) with a less-intense second pulse and a more-intense third pulse; this causes the first merger to be delayed and the second merger to be advanced, illustrating the ability of the technique to provide accurate shock timing. Reproduced with permission from Phys. Plasmas **18**, 092706 (2011). Copyright 2011 AIP Publishing LLC.

$t = 0$ the signal disappears because the VISAR probe is absorbed by the 10-μm CD shell, photoionized by x rays from the laser-produced plasma. After the shock transits the CD and reaches the deuterium (which remains transparent because it has lower x-ray absorption), the VISAR signal returns and the fringes abruptly shift in response to the shock velocity in the deuterium. The shock produced by the short laser pulse is unsupported and decelerating; the resulting VISAR fringes, therefore, exhibit curvature in time with a decreasing gradient. At 2.4 ns, the shock produced by the second laser pulse (incident on the target at ~1.2 ns) overtakes the first shock. (VISAR does not detect the second shock until it overtakes the first because the first shock is reflective and opaque.) At that point, the coalesced shock (the first and second shocks) is stronger and has a higher velocity; VISAR detects this sudden increase in velocity as a jump in fringe position. Since this shock is also unsupported, it decelerates as it travels through the deuterium and the fringes are seen to slope downward. (The decay rate of this second shock is different from that of the first because the rarefaction wave associated with its production now encounters doubly shocked deuterium.)

At 2.9 ns, the shock from the third pulse (at ~2 ns) overtakes the coalesced shock and another velocity jump occurs. This final shock (the sum of three coalesced shocks) is also unsupported and begins to decay, producing a downward motion of the fringes in time. At ~4 ns, the fringes curve upward, indicating acceleration of the shock as a result of spherical convergence. Finally, at ~5 ns, the shock impinges on the face of the cone, producing a disturbance that propagates into the cone aperture and the VISAR line of sight. This produces the brighter signal at 5 ns that moves toward the center of the image as it fills the aperture at ~5.5 ns.

Figure 12-3(b) shows the SOP data acquired simultaneously with the VISAR data in Fig. 12-3(a). This is a color-scaled image of the self-emission intensity imaged along the vertical axis and streaked in time (horizontal axis). The solid white line overlaid on the image is a plot of the intensity (horizontal lineout) that represents the temporal profile of shock brightness. The SOP intensity decays and jumps in response to the various shocks in a fashion similar to the VISAR velocity data. The SOP therefore provides an independent, corroborative measure of shock timing. When calibrated, the SOP also provides the shock temperature.

Figure 12-3(c) shows a VISAR image of a similar experiment with a slightly modified laser drive. The second pulse was a bit weaker and the third stronger. Compared with Fig. 12-3(a), the first merger now occurs later (at 2.6 ns) and the second earlier (at 2.8 ns), demonstrating an accurate technique to produce a tight sequence of shock arrivals for an ICF target design. In the VISAR data shown here, the shock mergers cause a fringe jump that occurs over, at most, two of the 10.6-ps pixels (i.e., ~21 ps). Using the temporal optical fiducials on these data, the streak cameras can be calibrated to a precision of better than 1%. This makes it possible to time shock waves with <50-ps precision.

Figure 12-4 shows the measured velocity profile from the experiment corresponding to Fig. 12-3(a), together with a *LILAC* simulation (which uses the *SESAME* equation of state

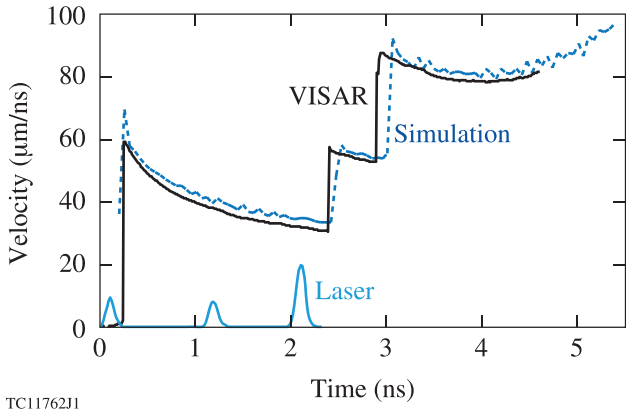

FIG. 12-4. The shock-velocity profile obtained by VISAR (solid) for the three-shock experiment of Fig. 12-3(a). The laser pulse shape is shown in light blue. The dashed line is the velocity profile simulated by *LILAC* (using a nonlocal transport model and including the effect of convergence). The velocities and merger times of the three shocks are modeled with good accuracy.

and the nonlocal model for electron transport described in Ref. 157). The simulation matches the experiment well.

C. Equation of state

Hydrodynamic simulations, such as those used in Fig. 12-4 or used to design ICF ignition targets, require accurate models for the behavior of materials at high pressures because an ICF implosion compresses the ablator and fuel to several tens of Mbar with shocks and ultimately to ~150-Gbar pressures at peak compression. The material response in each pressure range is important. The initial shock-transit stage is of particular importance because the response to single and multiple shock waves determines the adiabat of the implosion.

Numerous models and methods have been used to construct an EOS. Two models frequently used for ICF simulations are the *SESAME* compilation of EOS tables and the quotidian EOS (QEOS). These are global EOS models that attempt to describe material conditions over a wide range of densities and temperatures. *SESAME*, based on early work by Kerley,[636] started as a library of tabular EOS data compiled for use in hydrodynamics simulation codes at Los Alamos National Laboratory.[637] It has subsequently been maintained and updated numerous times as additional needs arose and new data was obtained.[638]

The *SESAME* EOS includes the zero-temperature electronic-state (cold curve), thermal-electronic, and thermal-ionic contributions. Each contribution is modeled independently, and the total EOS is obtained by the summation of these three terms. The QEOS model[639] applies an additive assumption, where the Helmholtz free energy is expressed as $F(\rho, T_i, T_e) = F_i(\rho, T_i) + F_e(\rho, T_e) + F_b(\rho, T_e)$, where ρ is the mass density, T_i is the ion temperature, T_e is the electron temperature, and each term is computed independently. Here F_i corresponds to the ion or nuclear contribution, F_e is the electron contribution, and F_b represents a semi-empirical chemical bonding correction. Alternatively, F_b can represent quantum or exchange corrections.

In contrast to EOS models such as *SESAME* and QEOS, first-principles methods have been used to predict the behavior of hydrogen and its isotopes at extreme conditions. These methods are based on either density functional theory (DFT) or the path-integral Monte Carlo (PIMC) approach. Using the tight-binding approximation, Lenosky *et al.*[640] performed quantum-molecular-dynamics (QMD) simulations for the shock Hugoniot of deuterium. (The Hugoniot is the set of states accessible as a result of a single shock.[641]) With DFT-based QMD calculations, the Hugoniot of deuterium has been studied to a maximum pressure of ~1.5 Mbar in Refs. 642–644. Other DFT–QMD calculations[645–647] have extended the Hugoniot studies to higher pressures of 5 Mbar and to the reshock situation.[648] The restricted PIMC method[649–652] has been used to study the principal Hugoniot for pressures from 1 Mbar to ~100 Mbar, while direct PIMC calculations[653,654] have been used for shock Hugoniot pressures in the range of 1–60 Mbar. Off the principal Hugoniot, Caillabet *et al.*[655] have used the DFT-based QMD calculations to build a multiphase EOS of deuterium for densities and temperatures up to 5 g/cm^3 and 10 eV, respectively, and Morales *et al.*[656] have used similar simulations to examine the hydrogen EOS up to 3 g/cm^3 and ~3.6 eV. Using the PIMC method, Hu *et al.*[657] have extended the first-principles calculations of the deuterium EOS to a wide range of densities (0.002–1600 g/cm^3) and temperatures (1.35–5500 eV). Applying this EOS to hydrodynamic simulations of ICF implosions, Hu *et al.*[658] found a neutron-yield reduction of up to ~50% for low-adiabat implosions, in comparison with simulations using the *SESAME* model. Caillabet *et al.*[659] showed that such a reduction of yield can be recovered by retuning the laser pulse shape.

The high-pressure EOS for a material encompasses a huge phase space depending upon the application of interest. Experimental tests are necessarily limited. Studies at high pressure have historically been performed using shock waves because they are easily produced with a variety of drivers, they are localized events, and they can be characterized with the conservation equations across a shock (often known as the Rankine–Hugoniot equations).[50] Knowledge of a material's Hugoniot provides information in a comparatively narrow but highly useful region of high-pressure phase space. Other methods at high pressure for off-Hugoniot studies include static compression with diamond anvil cells (DACs) and ramp compression. DACs statically compress submillimeter-sized volumes between the culets of two opposing diamonds, producing pressures of $\lesssim$1 Mbar that are used to study isentropes of materials with applications to planetary physics. Adding laser drive to a DAC allows one to access shocked states of precompressed materials.[660–663]

Ramp compression can be achieved by driving a target with the forward-moving ejecta that are released from a shock-compressed material[664] or with a slowly rising laser pulse that acts to continually increase the pressure on the target.[665–668] By controlling the rate of rise, one can ensure that the waves of increasing compression will not overtake earlier ones, producing a shockless compression of the material. Diamond is a favored material because its high strength allows it to be compressed without shocks.[669] In many other

materials, the sound speed increases rapidly with compression and, when ramp compressed, these materials readily produce shocks. One technique to overcome this is to sandwich a material between two planes of diamond that can be ramp compressed, forcing the enclosed material to be similarly compressed.[670] Also described in Ref. 670 is the use of x-ray diffraction to measure the atomic structure of compressed matter. Considerable effort has been performed in support of ICF material studies using magnetically driven experiments on the Z machine at Sandia National Laboratories. The properties of D_2 (Ref. 671), Be,[672] carbon,[673] and quartz[674] (used as a standard in EOS experiments) have been studied with both shock- and ramp-compression experiments.

It is only recently that high-pressure drivers and diagnostics have been available in the laboratory to make accurate and repeatable measurements at >1 Mbar. The laser ablation process readily produces extreme pressures (>1 Mbar) that rapidly compress the irradiated material. Depending on the temporal profile of the drive pulse, the compression can be a ramp (or quasi-isentropic) compression wave or a shock wave. At pressures and strain rates pertinent for ICF implosions, the first response of a material is typically a shock wave.

The EOS of liquid deuterium has been studied using laser-driven shock waves at megabar pressures. Initial experiments[675–677] showed compressions of deuterium to ~6× its initial density, indicating that deuterium is significantly more compressible than expected. These results generated considerable interest and controversy, which was addressed with more experiments and models. Subsequent experiments with magnetic drive, albeit at slightly lower pressures, contradicted these results by indicating that shocks up to ~1 Mbar compressed deuterium to ~4× its initial density, in agreement with the refined *SESAME* table *Kerley03*.[678] Laser-driven double-shock experiments by Mostovych *et al.*[679,680] appeared to confirm the sixfold compression but the results were later rescinded.[681] Later, double-shock experiments by Boehly *et al.*[682] and single-shock experiments by Hicks *et al.*[683] at pressures between 0.6 and 2.5 Mbar showed deuterium compressions intermediate between the two.

Considerable work ensued, attempting to resolve these discrepancies. Hicks *et al.*[683] performed a reanalysis of several experiments, addressing the importance of using a consistent model for the reference materials (aluminum and quartz) in the impedance-matching analysis used to calculate the deuterium compression. Their results are shown in Fig. 12-5, together with predictions of three models: *SESAME72*,[636] *Kerley03*, and Ross.[684] They found compressions of ~4.2 below 1 Mbar that (within the error bars) reconciled the differences between magnetically driven, explosively driven, and laser-driven experiments. At higher pressures in the range of 1.0–2.2 Mbar, a maximum compression of ~5 was observed, less than the sixfold compression observed on the earliest laser-shock experiments (similar to the Ross curve) but greater than expected from simple extrapolations of the lower-pressure data. These results and the interest generated by them underscore both

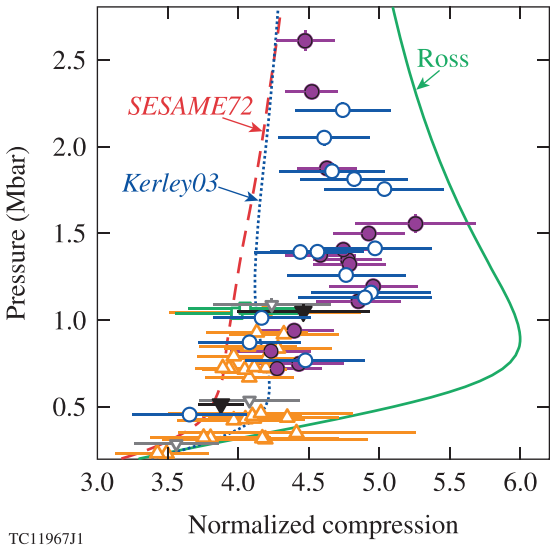

FIG. 12-5. Experimental and calculated single-shock Hugoniot data for deuterium obtained using lasers (open blue circles), magnetic fields (orange triangles), and high explosives (inverted black open and solid triangles and open green squares). The purple solid circles indicate results inferred from double-shock data. Reprinted with permission from Hicks *et al.*, Phys. Rev. B **79**, 014112 (2009). Copyright 2009 American Physical Society.

the difficulty and importance of obtaining precise EOS data using multiple methods and platforms. As yet a comprehensive explanation for the remaining discrepancies has not been formulated. These results are somewhat important for ICF research because the initial shocks used to set the adiabat of the implosion reside in this pressure range. To account for such uncertainties, experimental shock-timing measurements are used to set the drive pulses such that the shock waves traverse the ablator and fuel in the proper sequence, thereby "tuning" the experiments to accommodate inadequate knowledge of the fuel EOS. The question remains whether the existing discrepancies above 1 Mbar indicate a misunderstanding of the behavior of hydrogen at the extreme pressures that occur later in an ICF implosion. Near stagnation and during burn, the EOS and conductivity of the highly compressed fuel can have a significant influence on the behavior and performance of an ICF implosion.

Knowledge of the high-pressure EOS of laser ablator materials is critical to ICF target design. CH is a favored ablator material because spherical shells can readily be made with high uniformity, smoothness, and precise sizes. CH and CD (deuterized CH) shells are transparent (permitting optical cryogenic-layer characterization) and are sufficiently strong to hold high-pressure fills. Polymers have been studied extensively to support their uses as ablators.

Early studies of the polymers of interest to ICF were limited to low-pressure gas-gun data[685–689] and low-precision laser-driven data[690–692] for polystyrene. The latter suggested that, above 2 Mbar, CH was considerably less compressible than the models predicted. Using quartz as a standard, Barrios *et al.*[693,694] made systematic high-precision (~1%), impedance-matching measurements of a number of polymer materials relevant to ICF target design, including polystyrene (CH), polypropylene (CH_2), glow-discharge polymer (GDP) (CHO), and germanium-doped GDP (Ge-GDP). The study

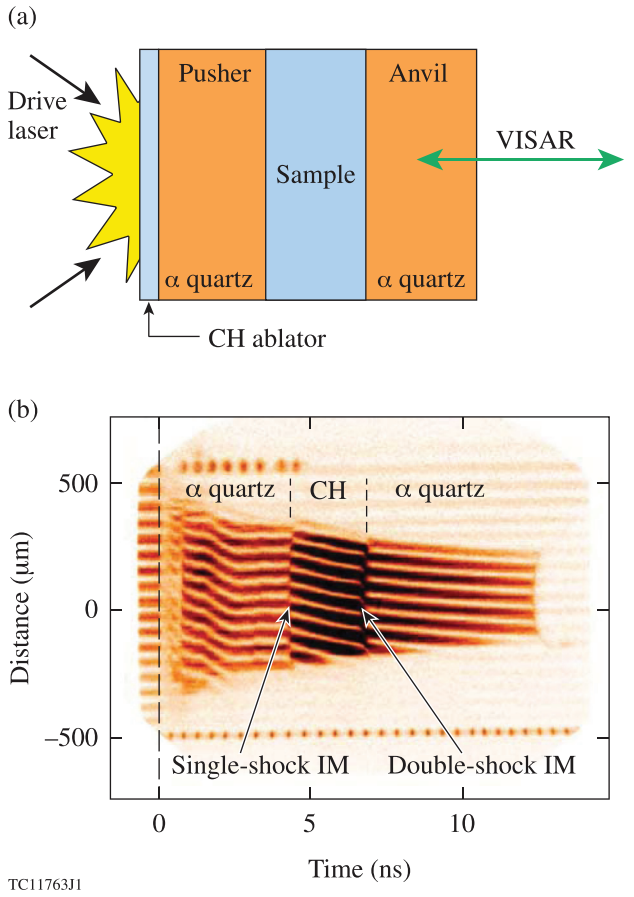

FIG. 12-6. (a) Schematic of a typical target used in the equation-of-state (EOS) experiments. The laser drive irradiates the CH ablator from the left, producing a shock wave that traverses the pusher, the sample, and the anvil. VISAR probes the target from the right. (b) VISAR data for a target with an anvil. Single- and double-shock impedance-matching (IM) measurements are made as the shock crosses the two interfaces. Reproduced with permission from Phys. Plasmas **17**, 056307 (2010). Copyright 2010 AIP Publishing LLC.

evaluated the effects of hydrogen:carbon ratio, chemical composition, and mid-*Z* doping on the material response to high-pressure compression.

A typical experiment is shown schematically in Fig. 12-6(a) (from Ref. 693). Shock pressures of 1–10 Mbar were produced by 1–12 OMEGA laser beams delivering a total energy between 200 J and 1130 J in 2-ns temporally square pulses. The average overlapped laser intensity was between 0.3 and 1.1×10^{14} W/cm^2. The targets consisted of 90-μm-thick pushers made of *z*-cut α quartz (the reference material), with a 20-μm CH ablator on the laser side and the samples mounted on the rear side. The samples were 50-μm-thick foils, typically CH, CH_2, GDP, and Ge-GDP. In some targets (as shown in Fig. 12-6), a second piece of *z*-cut α quartz was glued onto the back of the 50-μm CH sample to serve as an "anvil." For all targets, single-shock measurements were obtained at the first interface (quartz-to-sample). For the anvil targets, reshock measurements were obtained at the second interface (sample-to-quartz), where the shock in the sample reflected off the denser quartz, producing a double-shocked sample. The shock waves originated from laser-produced plasmas with temperatures of 1–2 keV. The soft and mid-energy x rays from these plasmas were absorbed in the first half (laser side) of the quartz pusher. X-ray production was minimized by using a low-*Z* ablator.

Shock velocities were measured using VISAR. The drive pressures were sufficient to produce optically reflective shock fronts in both the quartz and the polymer samples. This resulted in direct, time-resolved measurements of the shock velocity to a precision of ~1% in the pusher, the samples, and the anvil. The SOP measured the visible and near-infrared self-emission from the shock front as it propagated through the target. Figure 12-6(b) shows VISAR data for a target with an anvil. Before time $t = 0$, the time at which the laser starts, the VISAR fringes are horizontal and constant. The x rays from the laser-driven plasma then cause the CH ablator to "blank," i.e., to become opaque.[695] As a result, the VISAR fringes are barely visible from $t = 0$ to ~0.7 ns. At 0.7 ns the shock wave enters the quartz, where little or no blanking occurs. This, together with the highly reflective shock, provides ample return signal and the VISAR data (moving fringes) are clearly visible. The shock-wave strength decays as it transits the quartz but soon stabilizes as the rarefactions equilibrate the pressure between the shock front and the ablation front driven by the laser. Ultimately a relatively steady shock forms from 2 to 4.3 ns. At 4.3 ns, the shock wave transits the quartz–CH interface and enters the CH, where its velocity changes. This is seen as a jump in the position of the VISAR fringes and an abrupt change in their intensity. The latter is a result of the difference in the reflectivities of the shock waves in quartz and CH. The single-shock impedance-matching measurement is made across this interface and determines the particle velocity and pressure in the sample. The shock wave reaches the quartz anvil at 6.7 ns, when the fringe position and intensity change again. The double-shock (reshock) impedance-matching measurement is made at this interface.

Results for single-shocked CH are shown in Fig. 12-7 in the pressure–density plane [Barrios (2010)][693] together with a compilation of previous results from gas-gun experiments[685–689] that used aluminum flyer plates as standards, the absolute measurements on Nova [Cauble (1997)],[690] and impedance-matching measurements on GEKKO using first an aluminum reference [Ozaki (2005)][691] and then a quartz reference [Ozaki (2009)].[692] The predictions of three *SESAME* models[638] and the QEOS model[639] are also shown. The OMEGA data agree fairly well with the *SESAME* 7592 model and do not exhibit the "stiff" (less-compressible) behavior suggested by Cauble (1997) and Ozaki (2005). These authors stated, post publication, that their results probably suffered from x-ray preheating of the samples.[696] Subsequent data [Ozaki (2009)] that used thicker pushers and low-*Z* ablators to reduce preheat (green inverted triangles in Fig. 12-7) showed behavior closer to the OMEGA results.

XIII. CRYOGENIC TARGET FORMATION AND CHARACTERIZATION

Development of cryogenic equipment for making direct-drive ICF cryogenic targets began once it was realized that

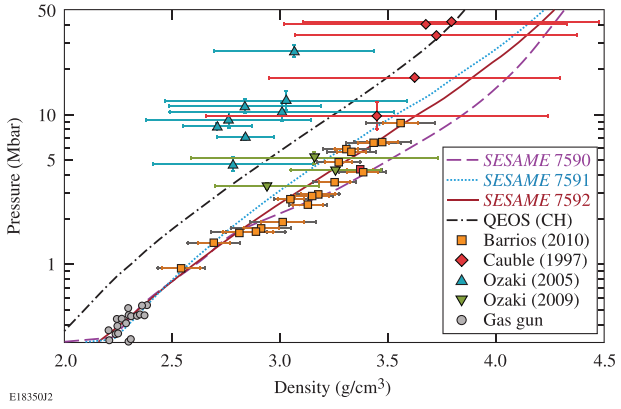

FIG. 12-7. Principal Hugoniot data in the pressure–density plane for polystyrene (CH) (orange squares), using impedance matching on OMEGA with a quartz reference. Data from previous studies are included along with predictions of three *SESAME* models and the QEOS model. The high-precision OMEGA data show that CH is more compressible than suggested by earlier data. Reproduced with permission from Phys. Plasmas **17**, 056307 (2010). Copyright 2010 AIP Publishing LLC.

the DT fuel must be in the form of a solid shell with an inner gas void to achieve the hot-spot mass and areal density needed for ignition. The equipment developed since the late 1970s ranges from large-scale engineering systems integrated into the target chamber to simpler, smaller systems used to study the behavior and properties of solid hydrogen isotopes.

Laser-facility–based cryogenic target systems were developed for use at KMS Fusion,[304,697] Shiva,[698,699] Novette,[700] OMEGA-24,[307,701] GEKKO XII,[312] OMEGA-60,[320] Nike,[702] and the NIF.[703] Many smaller cryogenic systems (too many to enumerate) were also developed to conduct target science, test cryogenic concepts, and qualify designs for inclusion in the larger systems. The major systems used for implosion experiments are described in Sec. XIII A. Direct-drive experiments carried out at these facilities are described in Sec. VIII B. A comprehensive historical review of the development of cryogenic target systems is given in Ref. 320.

The methods for producing cryogenic targets evolved as target designs evolved and as the understanding of the properties and behavior of solid DT developed. The first experiments[304] used liquid DT layers. Thereafter, early targets (1970s and 1980s) were typically glass shells with DT ice layers. The ice layers (of thickness up to $\sim 5\,\mu$m) were formed by the "flash-heat and refreeze" technique, first demonstrated by Miller *et al.*,[704,705] wherein a frozen "lump" of DT inside the cold target was vaporized with a pulse from a continuous wave (cw) laser and forced to cool rapidly. This resulted in an ice-thickness uniformity of $\lesssim$20% and typically an uncharacterized small-scale roughness. Woerner and Hendricks[698] adapted the technique of Miller *et al.* to use an electrical heat pulse rather than a laser.

Improved understanding of the implosion physics together with the availability of higher-power lasers redirected target designs toward plastic shells with a thicker DT ice layer and tighter specifications. Ice layers of $\sim$100-μm thickness were required for the 60-beam OMEGA laser (Sec. VIII B) and thicker layers will be required for ignition and high-gain targets (Secs. III and XVI). An ice-layer uniformity of $\sim$1-μm rms is required both for OMEGA (Ref. 706) and the NIF (Ref. 197). Section XIII B 1 describes new methods for fielding cryogenic targets and forming smoother, more-uniform ice layers. The flash-heat and refreeze layer-forming process was replaced by a radiation-induced sublimation process (β-particle heating from tritium decay), known as β-layering. This produced a single DT crystal structure that provided a smoother surface. Improved methods for characterizing the ice layer are addressed in Sec. XIII B 2. Understanding how the ice layer behaves in the final time interval before the implosion when the thermal shrouds are retracted is addressed in Sec. XIII B 3.

A. Cryogenic target systems

This discussion is limited to five large-scale cryogenic systems that were developed for imploding DT/D_2-filled targets using the major lasers available in the U.S. and Japan. The systems are shown schematically in Fig. 13-1.

The first system was developed in the late 1970s for imploding glass microspheres using Shiva.[698,699] The target was fielded on an $\sim$2-m-long cryogenic target pylon that used an electromagnetic system for retracting the thermally protective cryogenic shrouds [Fig. 13-1(a)]. The targets (100 μm in diameter and 4 μm thick) contained an $\sim$1-μm-thick DT ice layer. The thickness uniformity of the layer was measured to be better than 20% (the resolution limit) using an optical-interference characterization technique.

The second system [Fig. 13-1(b)] was developed at KMS,[697] used for implosion physics experiments at KMS,[305,310] and adapted by LLE for use on the 24-beam OMEGA laser.[307,701] The targets imploded on OMEGA were larger (300-μm diameter) and had thicker ice layers (5 μm) than previously. They were mounted on a low-mass target support structure (spider silk). The target's exposure to ambient radiation was limited to $\sim$10 ms by rapidly retracting the shroud using a linear motor retractor.[701] The equipment used liquid helium to cool the target-positioning stage and shroud and an argon laser to melt the DT, which was then allowed to rapidly refreeze to form the ice layer. A pair of shearing interferometers was used to characterize the ice layer. Estimates of the uniformity of the ice layer were obtained by comparing interferograms with ray-tracing simulations; these images demonstrated the symmetry of the interferogram to within 0.5 fringes, implying a fuel-layer uniformity with a $\lesssim$20% variation in layer thickness.

The third system [Fig. 13-1(c)] was developed for GEKKO XII and typically used 500- to 700-μm-diam, 4-μm-thick plastic shell targets containing a 10-μm layer of foam filled with liquid D_2 (Ref. 312). The plastic shells were permeation filled within a cryostat inside the target chamber and then cooled. The filling was accomplished by moving the pressure vessel in Fig. 13-1(c) upward over the target to mate with the lower surface of the target support. Liquid deuterium was wicked into the foam to create a uniformly thick layer that was characterized using interferometry. The

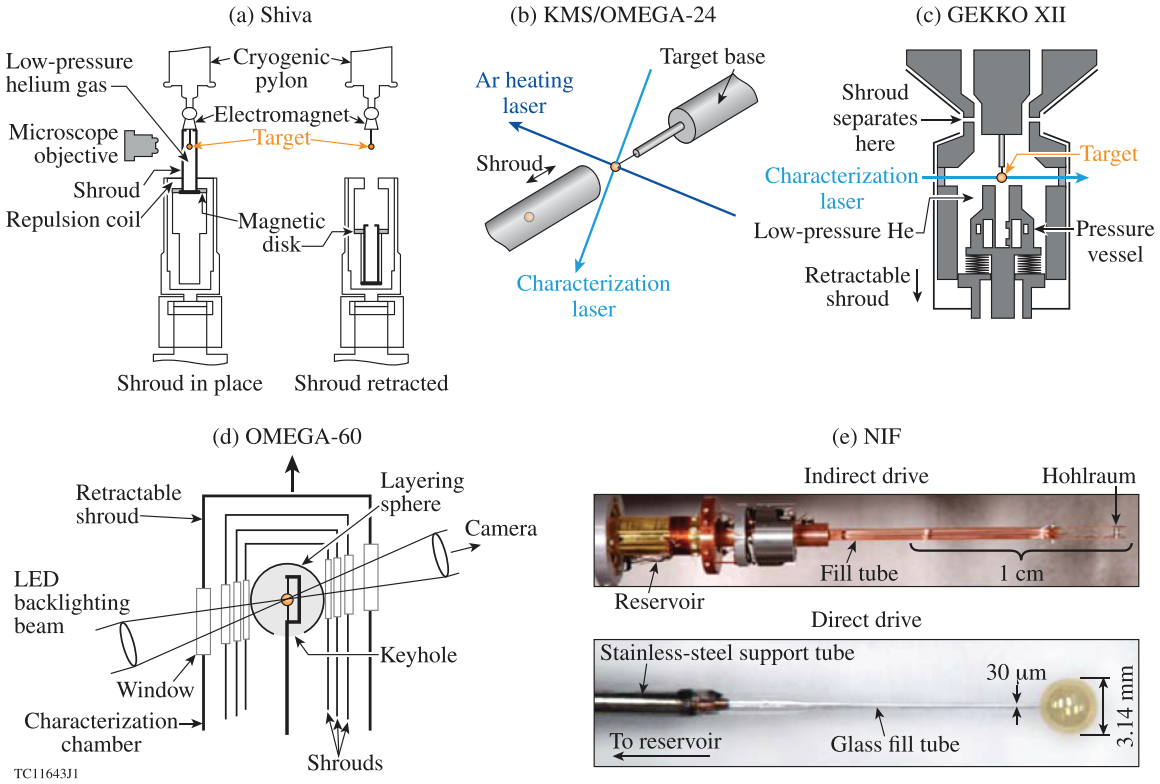

FIG. 13-1 Schematic showing significant features of five major cryogenic target systems: (a) Shiva (1 μm DT inside 4-μm-thick SiO_2 with diameter $d \sim 100\,\mu$m); (b) KMS (1 μm DT inside polyvinyl alcohol, $d \sim 130\,\mu$m) and OMEGA-24 (5 μm DT inside 4-μm-thick SiO_2, $d \sim 300\,\mu$m); (c) GEKKO XII (10 μm CH foam filled with liquid D_2 inside 4 μm CH, $d \sim 500$ to 700 μm); (d) OMEGA-60 ($\lesssim 100\,\mu$m DT inside 2 to 12 μm CD, $d \sim 700$ to 1000 μm); and (e) the NIF (typically 70 to 80 μm DT inside 160 to 190 μm CH, $d \sim 2$ mm for indirect drive; 150 to 300 μm DT inside $\sim 30\,\mu$m CH, $d \sim 3$ mm for direct drive). The indirect-drive portion of (e) is from Ref. 707.

shroud was removed ~20 ms prior to implosion. This system was also used to make solid D_2 layers.

The fourth system [Fig. 13-1(d)] was a collaborative endeavor between LLE and General Atomics and was developed for current use on the 60-beam OMEGA laser (2000);[320] LANL provided technical support on tritium issues. The design incorporated experience from earlier systems and knowledge acquired in separate cryogenic studies. The targets have plastic walls as thin as 2 μm and are larger (~1 mm in diameter) and contain more DT (up to 95 μm thick) than before. Added capabilities include (a) pressurizing thin-wall plastic shells to higher DT pressures (1000 atm) than used before; (b) forming a uniformly thick ice layer inside a layering sphere using β-layering, obviating the need for a foam shell and replacing the flash-heat and refreeze technique; and (c) preparing multiple cryogenic targets (up to five) outside the target chamber for delivery and implosion in a single day (to allow other laser-driven experiments to proceed during the cryogenic-target preparation process). An optical shadowgraphy system is included that allows for 80% of the ice surface to be characterized, enabling an ice-surface roughness of $<1\,\mu$m (rms) to be demonstrated. The system employs the same linear-motor shroud-retraction concept of the previous design with the same short target-exposure time (<70 ms) to prevent ambient radiation from damaging the ice. The spherical layering sphere surrounding the target retracts with the shroud, with the target and its mount passing through the "keyhole" in the bottom of the layering sphere.

The most-recent cryogenic target system [Fig. 13-1(e)] (Refs. 703 and 707) is designed for achieving ignition using indirect drive at the NIF. The design and capabilities of this system differ from those of earlier systems because of the presence of the hohlraum, which simplifies some aspects of the cryogenic engineering task while complicating others—specifically, the ability to form and characterize the ice layer. This design differs from earlier designs by filling the targets through a fill tube and characterizing the ice layer using x-ray phase-contrast imaging (Sec. XIII B 2). While this design supports ongoing indirect-drive–ignition experiments, alternative designs that will allow direct-drive–ignition experiments on the NIF are being developed;[708] these designs add the DT-filling and layering requirements for direct drive and will be retrofitted to the existing NIF cryogenic target system. The target is attached to a fill tube that doubles as a support structure and is connected to a reservoir containing the DT fuel supply [Fig. 13-1(e)]. The cryogenic environment for the target and reservoir assembly shown for direct drive is being developed in a dedicated experimental facility at LLE.

B. Cryogenic target science

This subject entails three distinct areas of scientific study: forming the ice layer, characterizing the ice layer, and

determining the ice smoothness and inner gas density at the moment of the implosion.

1. Ice-layer formation

Heating a small frozen lump of DT and allowing it to rapidly recondense on the cold inner surface of the target was an effective method used originally to redistribute DT around the target and attain an approximately uniform mass distribution. This technique became impractical as increasingly thick DT layers (above the 5 μm used on the 24-beam OMEGA laser) were needed because of the difficulty of rapidly refreezing the DT vapor into a uniformly thick layer. This was related to the large amount of heat that needed to be removed and the intrinsically low heat-flow rate from the target. Also, as the DT transitioned from a gas to a solid, the intermediate liquid state would be subject to sagging,[697,705,709] further limiting the layer uniformity.

An alternative process, known as β-layering, was developed as a more controlled and effective method for forming the ice layer. This process was proposed by Martin *et al.*[710,711] and demonstrated first in a cylindrical geometry by Hoffer and Foreman[712] and then in a spherical geometry.[713] It relies on the energy from the beta decay of the tritium atom (5.7 keV mean, 18.6 keV max) being reabsorbed in the ice, heating the ice. The process, carried out near the triple-point temperature (19.79 K), is used to layer targets for implosion experiments on the 60-beam OMEGA Laser System and the NIF.

Beta-layering involves the redistribution of ice from warmer to cooler regions within the target, as illustrated in Fig. 13-2. This is achieved by placing the target at the center of an isothermal layering sphere as shown in Fig. 13-1(d). This causes the thicker regions of the ice to be warmer than the thinner regions. Solid DT sublimes from warmer regions and deposits in cooler regions. Heat is conducted away from the target by helium (~0.1 Torr). The dimensions of the target and cavity ensure that, once a uniform layer is formed, the radial heat flux is to the first order constant over the surface of the target so that the target surface is isothermal. The spherical uniformity of the isotherms in the layering sphere controls the low-spatial-mode uniformity of the ice layer ($\lambda < 50$), while the high-spatial-mode uniformity is determined by the quality of the ice crystal: a layer consisting of a single crystal is preferable to a polycrystalline morphology with multiple grain boundaries.

The quality of the ice crystal is measured by the absence of visible defects (typically shallow grooves in the inner surface of the ice) and is achieved by growing the crystal from a single initial seed. This seed is typically formed at the top of the target (the coldest region when an unlayered target is melted to form the seed) [Fig. 13-3(a)]. It first grows toward the equator [Fig. 13-3(b)] and then expands to fill the target. The layering process produces a uniformly thick ice layer over a period of 5–14 h [Fig. 13-3(c)], as evidenced by the uniformity of the bright ring. Using the bright-ring–based shadowgraphic characterization technique described in Sec. XIII B 2, this layer has a uniformity of 1.5% rms. The smoothness and quality of the

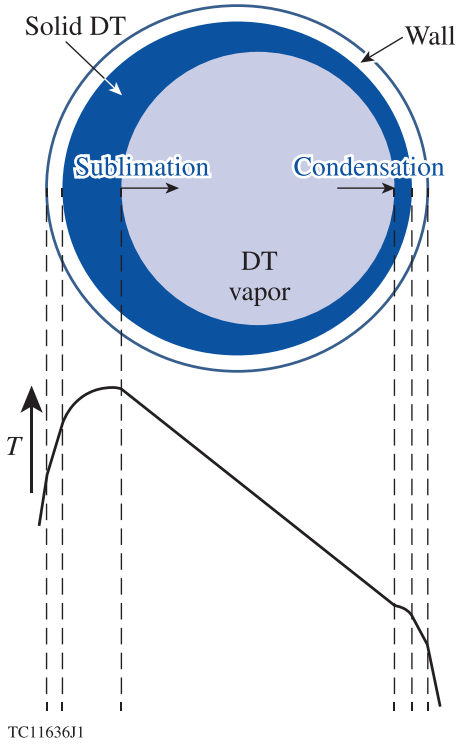

FIG. 13-2. Illustration of the β-layering process, together with a lineout (not to scale) of the temperature profile across the center of the target at an early stage in the process. The solid DT is heated by electrons resulting from the β decay of tritium atoms. The temperature of the solid DT is greater wherever the solid is thicker. The higher temperature corresponds to a higher vapor pressure, so mass sublimes from thicker regions and deposits at cooler, thinner regions.

crystal are determined by the rate at which the crystal grows, which is controlled by the rate at which heat flows from the target. Shorter growth times are possible (as short as 1 h), but the resulting ice layer will typically possess multiple crystallites and a greater overall roughness because of discontinuities at the crystallite grain boundaries. The horizontal elliptical ring seen in the front and rear surfaces of the ice layer [Fig. 13-3(b)] defines the interface between the liquid and solid phases and lies in the *a* plane of the hcp (hexagonal close packed) ice crystal.[714]

Beta-layering has also been used successfully with foam targets. An example [for a target layered at LLE with a 0.9-mm-diam, 55-μm resorcinol-formaldehyde, low-density (~0.1-g/cm^3) foam wall containing DT] is shown in Fig. 13-4. Analysis of the bright ring (barely perceptible in the image) indicates an inner-ice-surface uniformity of <1-μm rms. The target is transparent because the foam cells are filled and the DT ice forms as a single crystal surrounding their walls.

An alternative layering technique[715,716] that used infrared heating of D_2-filled targets in place of β-layering was employed for several years at LLE to study the formation of D_2 ice layers without the radiological complications of using tritium. Infrared emission from an optical parametric oscillator (OPO) tuned to the $Q_1(0) + S_0(0)$ D_2 absorption band (3165 cm^{-1}) of the ice was injected into the layering sphere through an optical fiber.[715–717] The inner surface of the layering sphere was made diffusive in an attempt to provide uniform heating. However, the ice uniformity, especially in

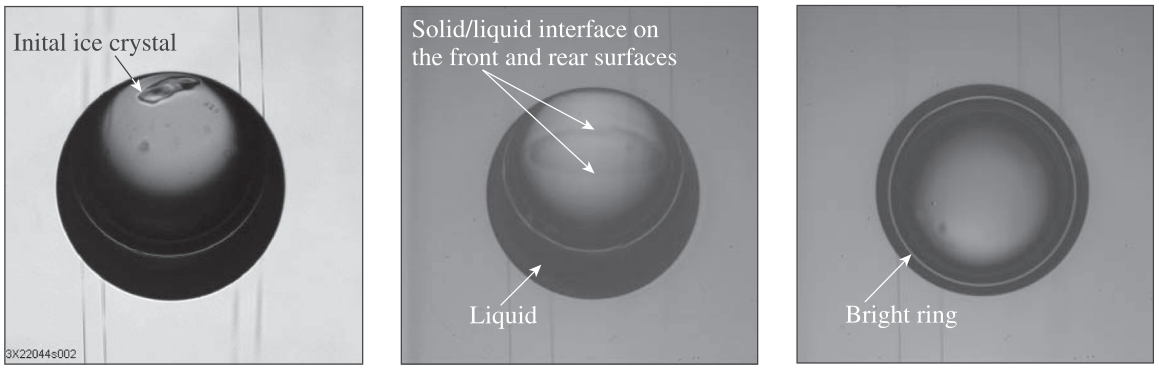

FIG. 13-3. Sequence of images showing the growth of a DT ice layer in a 960-μm-diam OMEGA target formed using β-layering. (a) Initial, mostly liquid target with a seed crystal at the north pole; (b) intermediate, showing the expanding crystal; and (c) the final target with a uniformly thick ice layer of 95 μm.

the low spectral modes ($\lambda < 10$), did not approach the uniformity achieved with β-layering, and it was impossible to produce D_2 layers with roughness below 2 μm (rms). For this reason cryogenic implosion experiments at LLE with D_2 were discontinued in 2008.

Another method proposed to improve the smoothness of the DT ice surface used the layering sphere as a high-Q microwave cavity to energize electrons from β decay in the DT vapor and electrically heat ("fire-polish") the inner ice surface.[718–720] While effective at improving the roughness of a multicrystalline ice layer, experience demonstrated that the most-effective method for achieving a smooth inner ice surface is to control the crystal growth process.[721,722]

2. Ice-layer characterization

Initially, interferometry was used for characterizing the ice layer. Examples of interferograms of a cryogenic target before and after the fast-refreeze layering technique was applied, taken from Ref. 307, are shown in Fig. 13-5. In Ref. 307 it was estimated that the ice layer uniformity was within 20%. However, for the larger targets and thicker ice layers of current interest, a more-suitable method was needed to determine the roughness to the desired specification (1-μm rms).

Two improved techniques were developed for characterizing the uniformity of the ice layer: optical shadowgraphy,[715,716,723,724] which can be used with transparent ablators, and x-ray phase contrast imaging,[725,726] which can be used with opaque ablators (such as beryllium, high-density carbon, and thick plastic), as well as transparent targets. A shadowgraphic image of a cryogenic target (with a DT ice layer) is shown in Fig. 13-6(a) with the corresponding ray trace of the visible rays that pass through the target in Fig. 13-6(b). There are two primary types of rays: "A rays" that propagate through the center of the target and are used to identify defects in the front and rear surfaces of the ice, and "B rays" that reflect off the inner surface of the ice near the limb of the target and form a bright ring[723] when projected back to the central plane of the target, which forms the object plane of the imaging system. Additional rings with lower intensity are seen in good-quality targets, corresponding to the "D-ray" and "U-ray" trajectories of Fig. 13-6(b). The bright ring formed by B rays contains the positional information used to determine the roughness of the ice around a great circle of the target. The inner-ice radius is determined from the bright ring radius through ray-tracing simulations such as that shown in Fig. 13-6(b). As described by Edgell *et al.*,[724] the circular image is unwrapped to a lineout of ice thickness as a function of angle around the great circle [Fig. 13-7(a)]. The small deviations from the mean illustrate the quality of the inner ice surface. A Fourier analysis of lineouts taken from many views is used to determine the spectral power of each mode. This is shown in Fig. 13.7(b), together with the spectral power obtained from measurements of the outer edge of the target

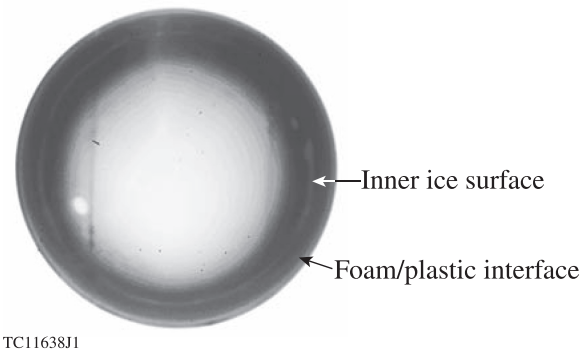

FIG. 13-4. Image of a 55-μm DT ice layer inside a 45-μm-thick resorcinol-formaldehyde foam shell that is covered with a 5-μm solid plastic wall. The inner ice surface has a 1-μm (rms) roughness.

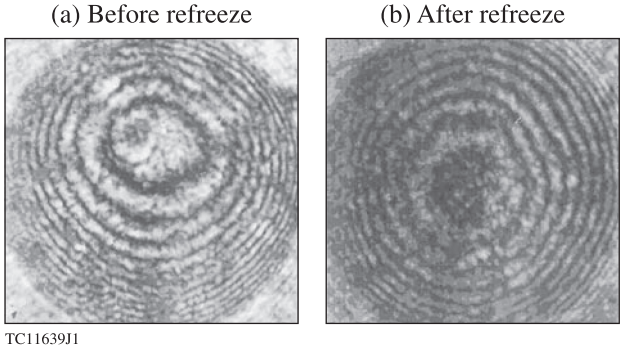

FIG. 13-5. A comparison of the interferograms of a 300-μm-diam glass shell with a 5-μm DT ice layer, (a) before and (b) after the flash-heat and refreeze technique as implemented in the OMEGA-24 cryogenic system. Reprinted with permission from Marshall *et al.*, Phys. Rev. A **40**, 2547 (1989). Copyright 1989 American Physical Society.

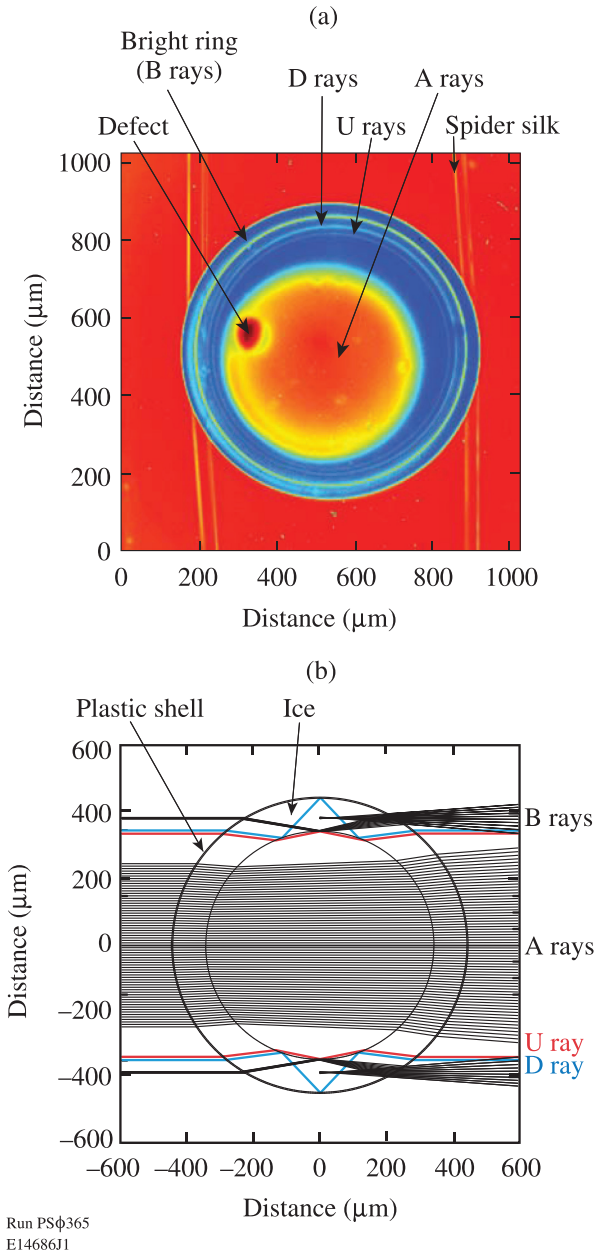

FIG. 13-6. (a) Shadowgraphic image of a representative cryogenic DT target, including the bright ring used for uniformity characterization and two lower-intensity rings. (b) Ray trace of a similar target indicating the origins of the rings. The bright ring is formed by "B" rays that reflect from the inner ice surface and, when projected back to the central plane, appear to come from a well-defined radius. The lower-intensity rings are formed from the U rays (red) and D rays (blue).

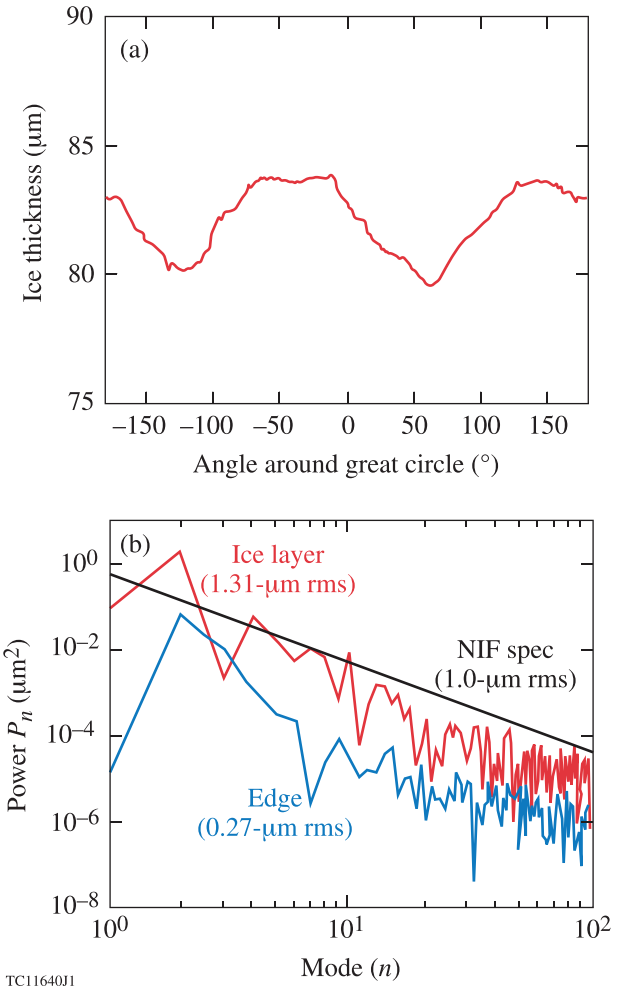

FIG. 13-7. (a) Ice thickness determined from the bright ring radius of Fig. 13-6(a) as a function of angle around the image. (b) Fourier decompositions of the bright ring and the edge of the target, combining many views, used to determine the ice roughness.

from the same images. The ignition smoothness specification, with an rms uniformity of 1%, is shown for comparison. Targets of this quality have been routinely imploded on OMEGA since 2006.

A schematic of the equipment configuration used at LLE for x-ray phase-contrast imaging is shown in Fig. 13-8(a). A beam of x rays (of energy typically ~30 keV) passes through the target. Refraction causes the x rays to experience deflections that are negligible except for a small group of rays just below the ice–vapor interface that are almost tangent to this interface, as shown in the ray trace of Fig. 13-8(b), resulting in intensity modulations in the image on the charge-coupled–device (CCD) camera. The camera is placed far from the target (typically at a distance of 1 m) since the x-ray deflections are small. A typical phase-contrast image of a NIF-scale target containing a cryogenic D_2 layer is shown in Fig. 13-8(c). The nonuniformity results from the difficulty of obtaining uniform infrared heating in the absence of β-layering and from the fill tube absorbing the IR light and heating the target.

Both techniques analyze a 2-D slice (~10 to 20 μm thick, perpendicular to the viewing axis) through the target. Optical shadowgraphy additionally provides information (from the A rays) about the presence of grain boundaries and large-scale dislocations in the front and rear surfaces of the ice, and techniques exist that allow the length and depth of these features to be quantified.[727] Rotating the target around the axis used to support it in a sequence of steps (typically 15° per step), and acquiring a 2-D image at each position, allows for the complete surface to be analyzed by averaging the discrete 2-D slices. These images can be combined into a 3-D reconstruction of the ice surface (Fig. 13-9) and quantified by spherical-harmonic coefficients (Y_{lm}) (Ref. 724). The locations of the target support and viewing axes in the OMEGA cryogenic target system are not orthogonal, so the

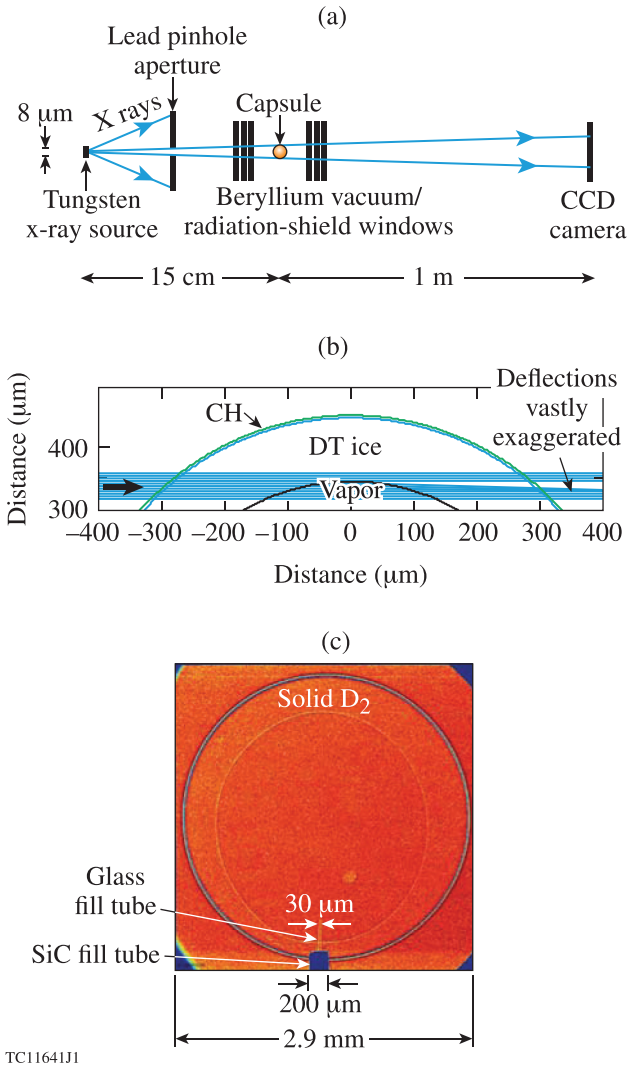

FIG. 13-8. (a) Schematic of the x-ray phase-contrast imaging system used at LLE; (b) a ray trace of the x rays through the target; and (c) an x-ray phase-contrast image of a D_2 ice layer inside a NIF-scale direct-drive target. CCD: charge-coupled device.

ice surfaces at the north and south polar regions (~20% of the surface) are not visible and remain uncharacterized. This limitation does not apply to the NIF system or to the cryogenic test facility at LLE used to characterize direct-drive NIF targets, where the entire surface is characterized. The latter facility was constructed with optical shadowgraphy and x-ray phase-contrast imaging on orthogonal axes. A comparison of the resolution and sensitivity of these techniques (Fig. 13-10) shows good agreement.[708]

In this experiment, the D_2 gas used to fill the target was contained in a 4-cm^3 reservoir, held at a higher temperature (<5 K differential) than the target to provide the pressure differential needed to force the gas into the target. Liquid was contained in the target by cooling the fill tube to create an ice plug. Further information on the fill-tube/reservoir system being developed for the NIF is found in Ref. 708.

The viability of using acoustic spectroscopy to determine the uniformity of the ice layer was assessed[728] but not pursued because it lacked sensitivity to higher-mode roughness.

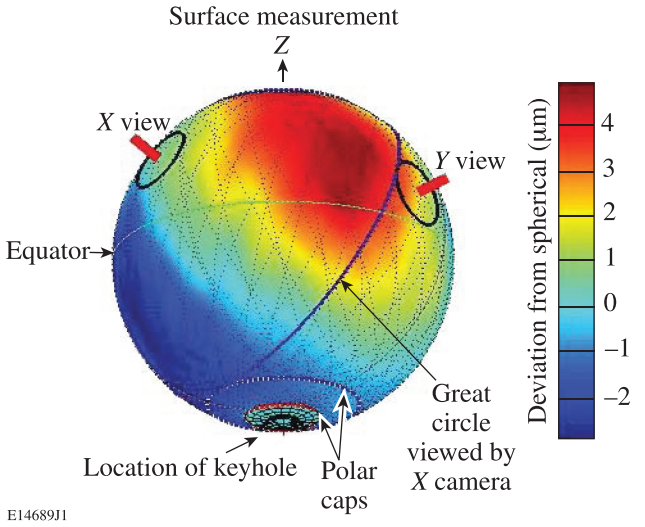

FIG. 13-9. Three-dimensional reconstruction of the thickness uniformity of a cryogenic D_2 target on OMEGA, showing the great circles viewed by the two cameras for different target orientations and "polar caps," within which no data are available.

3. Target properties at the moment of implosion

The DT ice layers in direct-drive cryogenic targets that are imploded at OMEGA, and in indirect-drive targets that are imploded at the NIF, are formed and characterized well

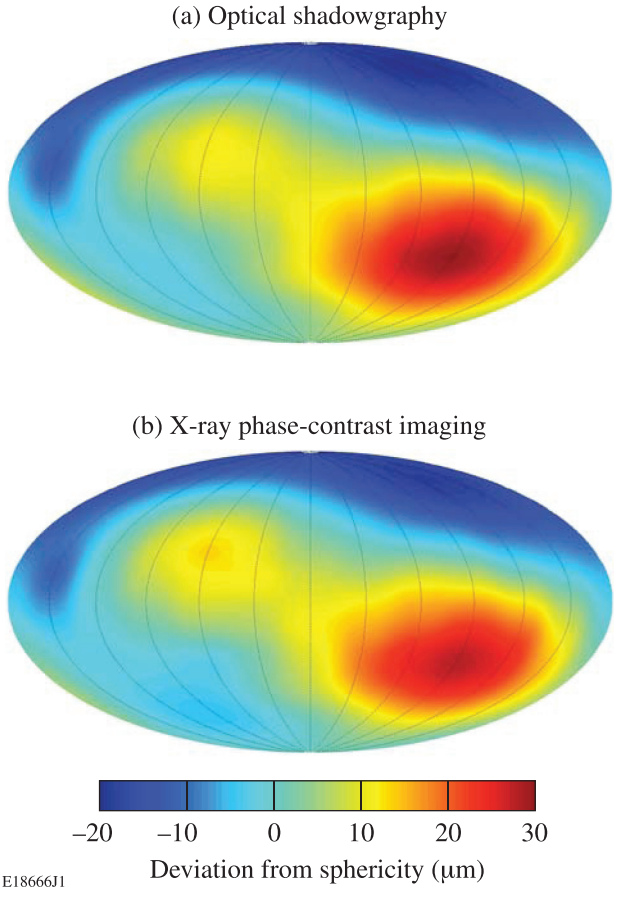

FIG. 13-10. Aitoff projections of the nonuniformity of the cryogenic D_2 target in Fig. 13-8 as determined from (a) optical shadowgraphy and (b) x-ray phase-contrast imaging. The large deviations from sphericity result from nonuniform infrared heating of the D_2 ice and the C-mount.

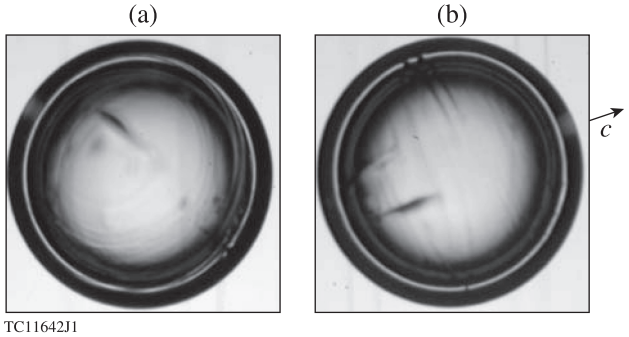

FIG. 13-11. Two perpendicular shadowgraphic images of an OMEGA cryogenic DT target showing the results of cooling the target more than 1 K below the triple-point temperature. The observed cracks are caused by stress-induced plastic failure between the *a* planes of the hcp crystal resulting from the differential volumetric contraction of the ice and the plastic ablator. These features are the faint circular lines seen (a) when looking at an angle of ~20° to the *c* axis of the crystal and (b) when looking perpendicular to the *c* axis.

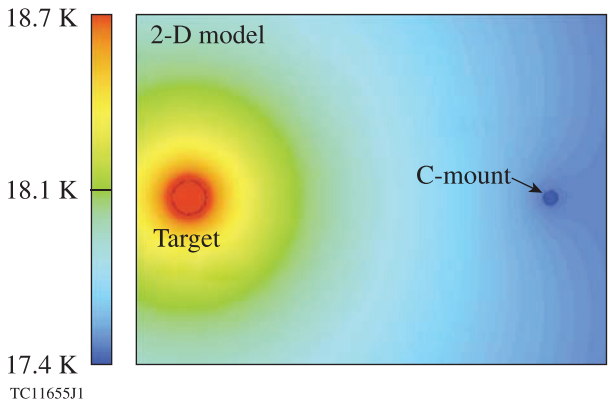

FIG. 13-12. A *FLUENT*™ calculation of the thermal nonuniformities around an OMEGA-size D_2-filled target. The image shows the thermal profile in a horizontal plane through the target and the C-mount used to support the target. The target is cooler on the side nearer the C-mount by 0.3 mK, causing the ice to be thicker on that side.

before the implosion and then transported to the center of the target chamber. They are maintained in a controlled thermal environment until they are imploded and intermittent inspection of the ice layer shows that the roughness does not change during this time.

One requirement on the direct-drive cryogenic system being developed for the NIF is that the inner gas density of the target should be lower than the vapor density (~0.6 mg/cm^3) at the triple-point temperature (19.79 K) used to form the crystal. Collins *et al.*[197] presented simulations of NIF ignition designs showing that the gain increases as the inner gas density is decreased. They suggested operating at 18 K, where the density is 0.26 mg/cm^2. Forming the ice layer at this temperature would result in a multicrystalline structure with unacceptable ice roughness. Cooling a target with acceptable smoothness (one that was layered at the optimal temperature) to the desired temperature induces thermal stresses because of the differential volumetric contraction of the ice and plastic. This cracks the ice and creates roughness. An example of a target cooled more than 1 K is shown in Fig. 13-11 from two views. The faint circular features are regions of high strain where the ice has plastically deformed and are seen in the plane perpendicular to the *c* axis of the crystal. The ice deforms and cracks regardless of how slowly the target cools.

One path to achieving both the desired ice smoothness and gas density is to rapidly cool the target immediately before the implosion and implode it before the induced thermal stresses crack the ice. Timing this process requires knowing the time-dependent temperature and gas density within the target, which have not been measured directly. These and related issues are discussed in Refs. 721, 722, 729, and 730. Compounding this complexity is the heat load to the target from thermal radiation and β-decay once the shrouds are retracted and the target is exposed without any conductive gas surrounding it to remove this heat. These effects are being studied using surrogate target designs that allow the results to be extrapolated to actual targets.

Predicting how the DT layer will behave between the removal of the helium gas and the implosion relies on computational fluid dynamics (CFD) models such as *FLUENT*™ (Ref. 731) and experimental input from scaled experiments. The latest version of the *FLUENT* CFD model includes the relevant physical properties for D_2, DT, and T_2, accounts for heat and mass transport, and simulates the β-layering process and the temporal response of the target to radiant heat load and changing temperatures (such as result from rapid cooling and shroud retraction). An earlier version of the model was used to guide the design of the layering sphere for the OMEGA cryogenic target and its support, and the results were consistent with experimental results. Figure 13-12 shows a 2-D *FLUENT* calculation for a cryogenic D_2 target supported by a beryllium C-mount, in a plane perpendicular to the C-mount [a horizontal plane with respect to Fig. 13-1(d)]. The C-mount locally reduces the temperature of the helium gas, resulting in thicker ice on the side of the target facing the C-mount. In reality, infrared radiation from the OPO (not included in the calculation) heated the C-mount, causing the ice-layer nonuniformity seen in Fig. 13-9.

A more-recent 3-D version of the model was used to calculate the DT ice-thickness uniformity of a NIF direct-drive target attached to a fill tube and positioned inside the prototype cryogenic system[708] [Fig. 13-1(e)]. The target diameter is 3.3 mm and the fill-tube diameter at the target is 30 μm. A representative calculation is shown in Fig. 13-13 for the prototype parameters. The *FLUENT* calculation includes the target, layering sphere, helium gas, fill tube, and gas reservoir. It predicts uniform ice around the target except for the vicinity of the fill tube, where the ice is slightly thicker by ~8% (28 μm for a 350-μm ice layer). Heating the fill tube with a laser is proposed to eliminate this nonuniformity. [This was demonstrated in Fig. 13-8(c), where the fill tube was heated by the OPO laser, resulting in thinner ice in the vicinity of the tube.] The *FLUENT* model was also used to evaluate the effect on the ice layer of not having the target optimally positioned in the layering sphere.[708]

The following three topics remain active areas of study because they can affect the implosion performance: (1) the presence of ^{3}He resulting from tritium decay; (2) fractionation of the D_2, DT, and T_2 isotopes during crystal growth (radial variation of the isotopic ratio because of the triple-point

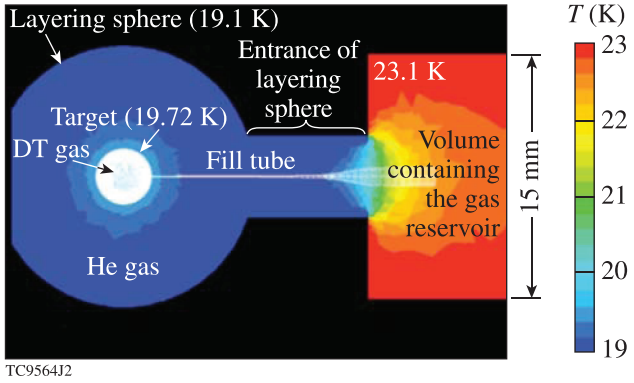

FIG. 13-13. *FLUENT* simulation of the thermal profile of a NIF-size (3.3-mm-diam) direct-drive DT-filled target (including the fill tube and reservoir) inside a prototype cryogenic system that is being developed at LLE for use at the NIF. The fill tube has a diameter of 30 μm where it attaches to the target. The slightly thicker ice at the fill tube can be effectively removed by heating the fill tube using a laser. The target and fill tube are white to show their positions.

differences); and (3) formation of the initial seed crystal used to grow a single-crystal ice layer. Accumulation of ^{3}He is minimized by purifying the tritium source using a Pd permeation membrane,[329] filling the target rapidly through a fill tube, and minimizing the life span of the target. The accumulation of ^{3}He in the ice layer does not affect the ice roughness if the ice layer is less than one week old.[732,733] Fractionation of H_2 and D_2 isotopes (used as a surrogate for D_2, DT, and T_2) when gradually frozen in a cryogenic cell with a similar temperature profile to a cryogenic target has been measured to be less than 10% (Ref. 734); this small degree of fractionation is consistent with the low-mode ice thickness amplitude variation ($\sim$1 μm) seen in OMEGA-size cryogenic targets. This estimate for D:T fractionation remains a subject of ongoing research because a higher ratio of deuterium at the inner surface of the ice layer will affect the isotopic content of the gas void and the D:T ratio in the hot spot. The ability to form an ice layer without the grain boundaries and dislocations that affect the higher-mode surface roughness is directly connected to the ability to form an initial seed crystal; presently this is a "hit-or-miss" process of heating an ice layer until it is almost fully melted and reversing the thermal cycle. It is desirable to be able to deterministically induce nucleation at a specified location and avoid supercooling and uncontrolled crystal growth.

XIV. FAST IGNITION

Fast ignition is an advanced laser-fusion concept that has the potential to provide significantly higher gains than conventional hot-spot ignition. First, a fuel shell is imploded with low implosion velocity, ideally forming an isochoric (uniform density) compressed core. Then a high-energy, high-intensity laser initiates ignition in a small region of the compressed core with high-energy electrons or ions generated in laser–target interactions. Because the implosion occurs at a much lower velocity than conventional hot-spot ignition, significantly more mass can be assembled for the same laser energy, leading to higher gain if the fuel can be ignited.

In a review paper, Tabak *et al.*[735] described some of the background and history of the fast-ignition concept. The basic concept of separating the compression and ignition phases was published in 1975 by Maschke[736] in the context of heavy ion fusion. Maschke mentions a compression system employing lasers, macro-particles, or heavy ion beams and an ignition system based on a large-aperture, high-energy superconductor storage/accelerator ring. In 1983, Shcherbakov[737] proposed using a low-intensity laser pulse to compress a spherical shell followed by a high-intensity laser pulse to launch a focusing shock wave into the target that would ignite the fuel in the center of the target. However, no detailed target designs were given in either proposal. Around the same time as Ref. 737, Yamanaka[738] proposed using a long (nanosecond) pulse to compress a target followed by a short, intense pulse that would use a combination of self-focusing and hot electrons to heat the compressed fuel to ignition temperatures. Again, few details were given. Later, Basov *et al.*[739] suggested a similar idea wherein, in place of the spherical shock, a very small spot on the target surface would be irradiated at an intensity of $\sim 10^{18}$ W/cm^2 to ignite precompressed fuel, but, yet again, no details were given as to how ignition could be achieved. The spherical shock approach, now known as shock ignition, is reviewed in Sec. XV.

The current interest in fast ignition was triggered by the work of Tabak *et al.*,[740] in which a three-step scheme was proposed. First, a DT capsule would be imploded with a nanosecond pulsed driver to achieve a cold, isochoric, and dense (several hundred g/cm^3) fuel assembly. Second, a powerful short-pulse laser would be injected to form a channel through the plasma corona to bring sufficient short-pulse energy close to the dense core. The ponderomotive force associated with the high laser intensity would displace the plasma, forming the channel. Third, fast electrons would be produced by the short-pulse laser to ignite the fuel. In that sense the term "fast ignition" was coined to reflect that the dense core is ignited by particles (electrons, protons, or other ions) that are generated by a short, ultra-intense, high-energy laser pulse. Fast ignition relies on the localized deposition of the particle energy in the core, isochorically heating a small portion of the fuel to temperatures $\sim$10 keV so that sufficient fusion reactions are generated to trigger ignition. Tabak *et al.* envisaged a 10-μm radius of the DT at 300 g/cm^3 in the central part of the target and suggested that ignition might be possible with a total energy of a few tens of kilojoules of laser light. Later studies refined how much energy is required for fast ignition. The required compression laser energy for an implosion amounts to several hundred kilojoules,[741,742] while the minimum ignition energy that must be coupled into the DT fuel to initiate a burn wave is $\sim$10 kJ for an idealized target design.[740,742,743] Gain curves illustrate the high gains that are potentially available using fast ignition,[741–746] with one example from Ref. 741 being reproduced in Fig. 14-1.

A variant of the channeling concept, known as the "cone-in-shell" concept, was described by Stephens *et al.*[747] and Hatchett.[748] In this concept, the channel is formed by the interior of a hollow cone placed in the initial target. The short-pulse ignitor laser beam propagates to the tip of the

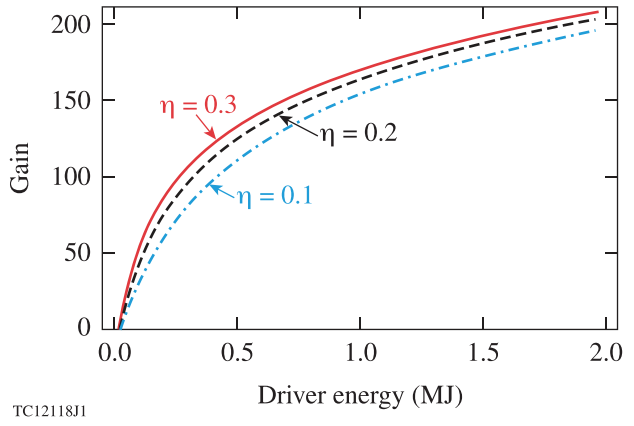

FIG. 14-1. Predicted gain (energy yield/total energy on target) versus compression driver energy for fast-ignition targets with various assumed coupling efficiencies η from the short-pulse laser into collimated fast particles. In each case 15 kJ of fast-particle energy is assumed to be coupled into the compressed core. Reproduced with permission from Phys. Plasmas **13**, 100703 (2006). Copyright 2006 AIP Publishing LLC.

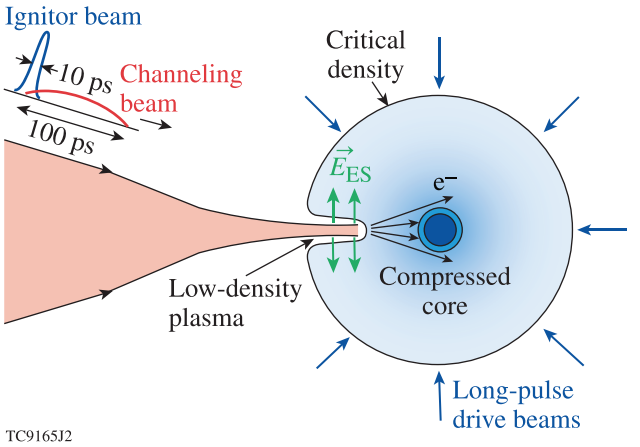

FIG. 14-2. Schematic illustration of the channeling concept for fast ignition. Reproduced with permission from Phys. Plasmas **18**, 082703 (2011). Copyright 2011 AIP Publishing LLC.

cone, where fast electrons are generated close to the compressed core. Both Stephens *et al*. and Hatchett considered geometries in which the capsules were compressed using indirect drive, but most subsequent work has used direct-drive compression. Hatchett ascribed the cone-in-shell concept to Tabak and Wilks. In Ref. 735, Tabak *et al*. mentioned that in 1985 Tabak developed gain models for precompressed fuel that is ignited with various schemes including one with a cone. Tabak *et al*. stated that "purely hydrodynamic ignition/burn propagation schemes were considered… At this time, the concept of ignition with lasers was rejected because such ultrapowerful lasers did not seem credible." Around the same time, Feoktistov[749] described a similar cone-in-shell concept in which the cone had an open tip. A short (~100-ps) laser pulse with high energy (~1 MJ) propagated through the cone just before the inner surface of the imploding fuel shell reached the origin, directly heating the inside of the shell.

The discussion in this section is restricted to direct-drive fast-ignition schemes and focuses on work that is immediately relevant to integrated experiments and ignition designs. It is recognized that a substantial body of work has been done over the last 20 years to study the physics of fast-particle generation with short-pulse lasers and the transport and deposition of the particle energy in the plasma. Sections XIV A and XIV B discuss the channeling and cone-in-shell concepts, respectively, and Sec. XIV C briefly indicates some alternative concepts. Sections XIV D and XIV E review cone-in-shell implosion experiments and ignition-scale designs, respectively.

A. Channeling concept

The scheme proposed in Ref. 740 envisioned a high-intensity laser pulse with a duration of the order of several hundred picoseconds to form a channel prior to the generation of hot electrons by an ultrahigh-intensity trailing portion of the pulse. Figure 14-2 (from Ref. 750) shows a schematic of this concept in which the pulse is represented as separate channeling and ignitor beams (whose durations should be considered only as nominal). The ponderomotive force of the channeling pulse on the electrons results in a strong electrostatic field (E_{ES}) that drags plasma ions after the electrons, leading to the evacuation of a channel in the coronal plasma of the compressed core up to the critical density. The trailing portion of the pulse ramps up to a spike (with intensity of the order of 10^{19}–10^{20} W/cm^2 for 1-μm radiation). The light pressure on the critical surface (I/c for completely absorbed light, where I is the laser intensity and c is the speed of light in vacuum) is immense, quoted by Tabak *et al*.[740] as 100 Gbar at 3×10^{20} W/cm^2, and pushes the critical density farther into the plasma. In addition, the critical density is increased because of the mass increase of electrons oscillating in the laser field at velocities close to the speed of light. This combined process is known as hole boring and pushes the critical density closer to the dense fuel.

The hole-boring process was observed in 2-D particle-in-cell (PIC) simulations used by Wilks *et al*.[751] to investigate the interaction of ultra-intense laser pulses with plasmas for laser intensities $>10^{18}$ W/cm^2. In these simulations, a substantial fraction of the laser energy was absorbed into suprathermal electrons, with a characteristic temperature that scaled with intensity I and laser wavelength λ as $(I\lambda^2)^{1/2}$. The fast-electron temperature is determined by the ponderomotive energy, the cycle-averaged oscillation energy of an electron in an electromagnetic field. The high-intensity portion of the ignition pulse generates ~MeV electrons, some of which deposit energy in the highly compressed core leading to ignition.

The channeling laser pulse must penetrate a distance of the order of ~1 mm in the plasma. The coupling of electron energy into the core depends critically on the standoff distance between the location where the electrons are generated and the compressed fuel and the divergence of the fast-electron beam. Since electrons produced in relativistic laser–plasma interactions are emitted into a large solid angle, it is important that the high-intensity pulse comes as close as possible to the dense core.

Another important consideration is that the electron energy must be coupled efficiently and localized into the

compressed core, where the cold DT fuel has a density >300 g/cm^3 and an areal density >1.5 g/cm^2 (Ref. 742). The assembly will stop fast electrons with energies up to ~2 MeV (Ref. 752). Higher-energy electrons will lose some fraction of their kinetic energy but not all of it. Based on the scaling given by Wilks *et al.*,[751] the average kinetic energy of the electrons that are produced by the laser is ~1 MeV at $I\lambda^2 \sim 10^{19}$ W/cm^2 · μm^2. A critical issue in fast ignition is that the suprathermal electrons are not monoenergetic, but their kinetic energy is distributed in a broad spectrum. Only a fraction of the electrons will have energies in the range of 1–3 MeV that is optimal for ignition.

The channeling concept uses standard spherical implosions and is therefore consistent with current cryogenic target manufacturing processes (Sec. XIII). Other fast-ignition concepts (such as the cone-in-shell concept) that use more-complicated target designs are technically challenging to fabricate with uniform cryogenic DT ice layers and have not yet been demonstrated.

Many physics issues must be overcome to demonstrate that the channeling approach is viable for laser fusion. The laser–plasma interactions that are relevant to the channeling approach, in particular laser transport, fast-electron generation, and fast-electron transport, are far from being completely understood. Laser transport in the plasma must efficiently couple the laser energy near the critical-density surface while minimizing losses in the extended corona. Early research related to the propagation of a high-intensity, short-pulse laser in underdense plasma started soon after the fast-ignition concept of Tabak *et al.*[740] was proposed. Young and Bolton[753] experimentally investigated laser-induced channels and the propagation of low-energy (~J), high-intensity (5×10^{18} W/cm^2) light through underdense plasmas produced from thin exploding-foil targets. They observed beam breakup above a threshold intensity consistent with relativistic filamentation, leading to a finding that the transmission was greatly reduced in the channeling regime. Previous studies by Young *et al.*[754] with a lower intensity (5×10^{16} W/cm^2) and longer pulse durations (100 ps to 1000 ps) demonstrated successful channel formation in underdense plasmas produced from exploding thin foils. It was found that longer pulses increased the extent of the channel before the onset of the filamentation instability terminated the channeling process.

Relativistic whole-beam self-focusing is another highly nonlinear effect that is important for channeling. The first experimental observation of relativistic self-channeling of a high-power (~50-TW) subpicosecond laser pulse in underdense plasma was reported by Monot *et al.*[755] in 1995. These experiments were performed at low densities. At higher densities and especially when propagating over a large distance in the corona of a compressed target, small-scale self-focusing can easily break the beam into many filaments. Indications of this process were found in experiments by Tanaka *et al.*[756] recording the back-reflected image of a 100-TW laser pulse incident on a long-scale-length plasma. Multiple highly intense spots were observed inside the original focal spot. Pukhov and Meyer-ter-Vehn[757] performed 3-D PIC simulations to study these effects in more detail for laser pulses with relativistic intensity propagating in slightly underdense plasmas. The production of relativistic electrons axially co-moving with the pulse and the generation of strong magnetic fields were observed. After an initial filamentation phase, the simulations showed that the magnetic field pinched the electron current. The light followed the currents, and multiple filaments eventually merged into a single channel.

The first experimental study of laser channeling into an overdense plasma at intensities >10^{17} W/cm^2 was reported by Kodama *et al.*[758] A 1-μm-wavelength laser pulse (2×10^{17} W/cm^2, 100 ps) was focused onto a preformed plasma created by a UV laser on a 100-μm-thick plastic foil. X-ray pinhole images, time-resolved optical spectra, and the temporal profiles and angular distribution of the backscattered light all indicated laser hole boring in the preformed plasma. In similar experiments with flat foil targets using a 1-μm-wavelength laser (2×10^{17} W/cm^2, 100 ps), Tanaka *et al.*[759] and Takahashi *et al.*[760] studied whole-beam focusing and hole boring in preformed, overdense plasmas. In Ref. 760, the hole boring was diagnosed using an x-ray laser. In later experiments by the same group, Lei *et al.*[761] studied self-focusing and channeling of a subpicosecond laser beam near the critical density. A 0.6-ps, 250-J, 1-μm-wavelength laser pulse with an intensity of ~10^{19} W/cm^2 was focused into a plasma produced from a thin plastic foil target irradiated by a nanosecond laser pulse. Laser light transmittance and x-ray pinhole camera measurements suggested the formation of a channel by the relativistic laser pulse into the preformed plasma.

Willingale *et al.*[762] performed channeling experiments on the OMEGA EP laser using ~0.7-kJ, 8-ps laser pulses with considerably higher laser energy and longer pulse duration than in previous experiments. The pulse propagated through a millimeter-size underdense plasma plume, with a maximum electron density estimated to be 2.5×10^{19} cm^{-3}, corresponding to 2.5% of the critical density. The channel was imaged with proton radiography (Fig. 14-3), showing the temporal evolution of the channel formation as well as beam filamentation, self-correction, and density modulations on the channel wall attributed to surface waves.

Li *et al.*[763] used 2-D PIC simulations to study laser channeling in millimeter-size, inhomogeneous plasmas with electron densities initially between 10% and 100% of the critical density. Their simulations showed that the front of the laser pulse piles up plasma, significantly reducing the channeling speed as the pulse progresses to higher density. Other nonlinear effects such as laser hosing, channel bifurcation and self-correction, and electron heating to relativistic temperatures were observed. The simulations established scaling laws for the laser energy and pulse duration to extend a channel through a millimeter-size coronal plasma to the critical density. Later work by the same group[764] indicated substantially faster channeling in 3-D versus 2-D PIC simulations.

The first channeling experiment in an imploded plasma was performed by Fujita *et al.*[765] at the GEKKO XII laser, where twelve 0.53-μm-wavelength beams with a total energy of 0.8 kJ and pulse duration of 1.3 ns imploded a 500-μm-

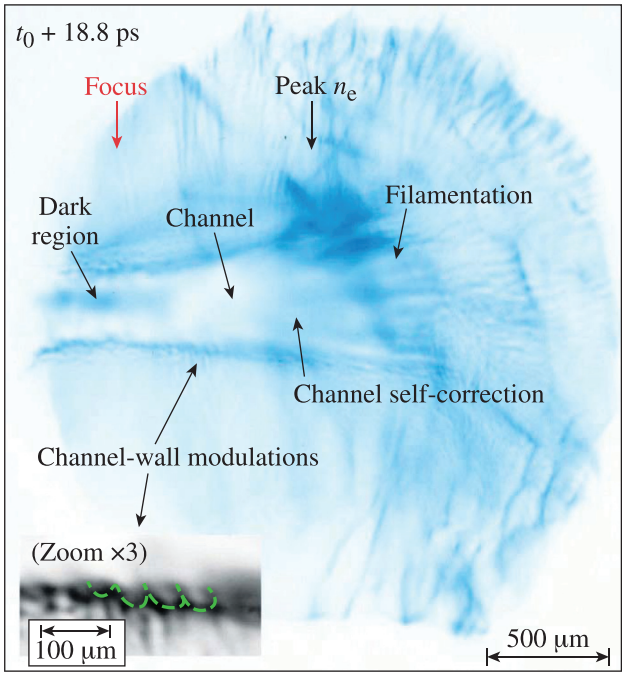

FIG. 14-3. Proton probe image of a channel that was created by an ~0.7-kJ, 8-ps laser pulse from OMEGA EP. The laser propagated through plasma with an electron density of 2.5×10^{19} cm^{-3}. The image was taken at 18.8 ps after the start of the channeling pulse. This image is part of a series of images taken at different times showing the temporal evolution of the channel. The inset shows a zoomed region of the channel wall. The laser pulse was traveling from left to right. Reprinted with permission from Willingale *et al.*, Phys. Rev. Lett. **106**, 105002 (2011). Copyright 2011 American Physical Society.

diam, 7-μm-thick, deuterated plastic shell. The imploded plasma was then heated by two 100-ps, 1-μm-wavelength laser pulses separated by 300 ps. Slight enhancements in neutron yield and x-ray emission were reported, but overall the experimental results were not conclusive. Several years later, the same group performed an experiment with a single, ultrashort pulse focused onto an imploded shell.[766] The 1-μm-wavelength laser, with an energy of 190 J and a 0.6-ps pulse length, was focused to a 30-μm-diam spot on the target, providing a vacuum peak intensity of 1×10^{19} W/cm^2. The beam was focused at the predicted location of the critical density, 200 μm from the target center—a distance that was shorter than the Rayleigh length of the beam (670 μm). The short pulse generated energetic electrons within a narrow cone of full angle 30°, which heated the imploded CD shell and enhanced the thermal neutron yield. A total neutron yield of 4×10^6 was measured—a factor of 4 more than from the implosion alone. The enhancement appeared when the short-pulse laser was injected in a narrow time window of 80 ps close to peak compression.

Integrated experiments are required to study the formation of a channel by a longer (~100-ps) laser pulse in an imploded target followed by the guiding of an intense short (~10-ps) laser pulse through the channel and the subsequent heating of the compressed core. New diagnostics are needed to permit the channel to be observed at densities much higher than the critical density.

B. Cone-in-shell concept

The complications encountered in the early work on the channeling concept triggered the development of alternative designs that could circumvent detrimental laser–plasma processes and maximize the fast-electron generation efficiency. The most successful of these designs contained a re-entrant cone, shown in Fig. 14-4(a), to guide the short-pulse laser and generate the fast electrons closer to the compressed core without the need to channel through a large plasma corona.[747,748,767] The concept relies on a high-energy petawatt laser beam that initiates ignition through the creation at the cone tip of an intense current of MeV electrons that is directed toward the compressed core. In this design, a segment is cut out of a spherical shell and a hollow gold cone is inserted to keep a path clear for the short-pulse beam to reach the imploded plasma at stagnation. In an alternative design [Fig. 14-4(b)], Norreys *et al.*[767] proposed to mount a shell segment over the mouth of a hollow gold cone and to implode the shell segment into the cone. The ignitor beam interacts with the cone tip from the outside, producing electrons that stream into

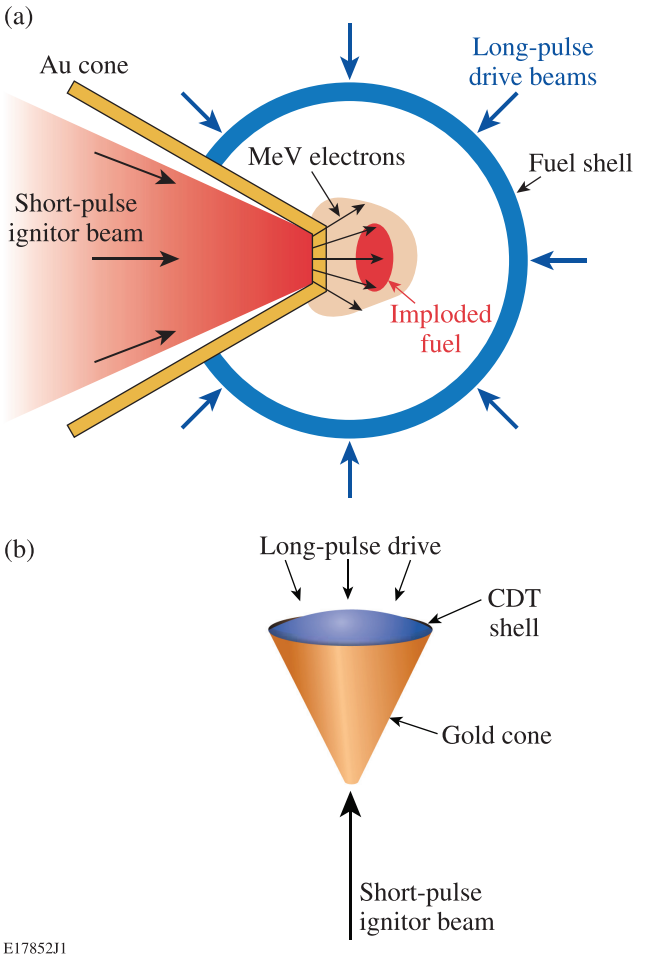

FIG. 14-4. Schematic illustration of the cone-in-shell concept for fast ignition. This concept, involving nonspherically symmetric implosions, was suggested to avoid problems related to the channeling concept. Two schemes are shown: (a) implosion of a spherical shell that has a segment cut out, into which a hollow gold cone is inserted to provide a path for the short-pulse beam to reach the imploded plasma at stagnation; and (b) implosion of a shell segment into a hollow gold cone with the ignitor beam interacting from the outside with the cone tip. Adapted from Ref. 767.

the cone to heat the compressed matter inside. Beside some initial experiments exploring the second concept,[767] most of the simulation and experimental work has been devoted to the first design.[745] The cone-in-shell concept is of significant interest because of the promising initial, integrated experiments carried out at Osaka (Sec. XIV D 1).

The coupling efficiency of the hot-electron energy into the dense core depends on the standoff distance from the cone tip to the target center, the size of the pre-plasma in the cone, the fast-electron distribution function, the transport dynamics of the fast electrons through the cone tip and the dense plasma, and the formation of sufficient areal density for electron stopping. The survival of the cone tip up to the point of sufficient compression is another important issue. Detrimental effects of the cone collapse in the context of reactor designs have been discussed by Shmatov.[768]

The source electron distribution function is typically characterized by parameters such as the mean electron kinetic energy, the energy spread, and the angular distribution. Experiments with flat foil targets irradiated with high-intensity laser pulses have measured the angular spread of fast electrons using various diagnostics including K_α imaging,[769] transition-radiation emission,[770,771] optical probing,[772] and hard x-ray emission.[773,774] These measurements indicate a smaller divergence angle than obtained from simulations of the fast-electron source—a result consistent with collimating effects from resistive magnetic fields,[775] known as resistive collimation, as the electrons traversed solid-density material toward a buried fluorescence layer or diagnostics on the rear of the target.

Experiments with flat foil targets irradiated by Green *et al.*[772] at laser intensities from $\sim 5 \times 10^{18}$ to $\sim 5 \times 10^{20}$ W/cm^2 showed that the full divergence angle increases with laser intensity from $\sim 25°$ to $\sim 55°$. Adam *et al.*[776] used multidimensional PIC simulations to study the angular distribution of relativistic electrons in the case of laser interaction with a steep-density-gradient plasma and identified that inhomogeneous, large static magnetic fields located in the interaction layer are one cause of the spread. Simulations that included a pre-plasma[777] showed that the beam divergence strongly increases with the scale length and the laser intensity. The collisionless Weibel instability develops in lower-density plasma, increasing the scattering of fast electrons in stochastic magnetic fields and leading to a larger angular spread of the fast electrons. The dispersion angle is enhanced for lower background density. In the presence of a pre-plasma, the radial beam deviation increases as a result of the electrons being accelerated in a larger volume. These effects work against collimating effects arising during the electron transport in the dense material.

The interaction of intense petawatt laser pulses with overdense plasma was studied by Kemp and Divol[778] using 2-D and 3-D PIC simulations over several picoseconds and under conditions that are relevant to both the cone-in-shell and channeling approaches. Kemp and Divol assumed a laser with an intensity of 1.4×10^{20} W/cm^2, a 40-μm-diam focal spot, a 10-ps pulse duration, and a 1-μm wavelength. The laser drives surface-density perturbations into nonlinear saturation, causing a periodic release of plasma and the formation of an extended underdense plasma shelf. Up to 80% of the laser energy is absorbed and up to ~65% of the laser energy is converted into fast electrons. The dynamics lead to the acceleration of three distinct groups of electrons, some with energies many times the laser ponderomotive energy. The lower-energy group is limited by the ponderomotive energy with a temperature of ~5 MeV, the second group consists of electrons with a hotter distribution in the range from ~7 to ~15 MeV, and the third group is a superhot distribution with an ~17-MeV slope temperature. The divergence (full angle of ~100°) seemed to approach a steady-state value after a few picoseconds, making these simulations relevant for ignition pulses.

The transport of the fast electrons in the dense plasma shares similar issues with the channeling concept. It was pointed out by Bell *et al.*[779] that the transport of short-pulse–produced fast electrons in solid targets is affected by self-generated electrostatic fields and the electrical conductivity of the background plasma. The theoretical study of the transport of intense relativistic electron beams in dense plasma requires 3-D simulations that include a fluid-model description of the background plasma including collisional effects and the self-generated electromagnetic fields induced by the target resistivity.[780] These simulations show how beams with small transverse velocity dispersion in cold targets are sensitive to fragmentation because of the resistive filamentation instability. As the fast-electron beam propagates through the target, ohmic heating increases the background temperature, which in turn modifies the electrical conductivity of the plasma and therefore affects the target heating rate and the energy loss of the fast-electron beam.[781] The azimuthal magnetic fields that are generated around the fast-electron beam can provide some resistive collimation under certain beam and plasma conditions. This collimation effect might also be exploited in a different way by making use of two materials with different electrical conductivities.[782] Experiments by Kar *et al.*[783] on fast-electron transport in solid planar targets demonstrated the confinement of fast electrons in a low-conductivity tin layer sandwiched transversely between two high-conductivity aluminum slabs.

The control of the electron divergence is a key issue in fast ignition. Strozzi *et al.*[784] have suggested that this might be accomplished by placing a strong external axial magnetic field between the cone tip and the compressed fuel, but it is currently unclear how such a magnetic field could be integrated into a fast-ignition–relevant design.

C. Alternative concepts

Theoretical studies have considered the ignition of imploded fuel with heavy ion beams or macroparticles,[785] short-pulse laser-produced protons,[786] and short-pulse laser-produced light ions.[787] A similar concept was proposed by Naumova *et al.*[788] using ultra-relativistic laser intensities of $>1 \times 10^{22}$ W/cm^2. Such a laser pulse might penetrate deeply through the corona into the compressed core because of an efficient ponderomotive acceleration of ions in the forward direction, creating a channel for the laser pulse. Simulations show efficient (~20% conversion efficiency of laser energy) ion acceleration in the channel in the forward direction that

could initiate ignition in the core. Simple estimates show that this scheme would require a 60-PW laser facility with a laser energy of ~45 kJ that is delivered in an ~1-ps pulse.[788] Hain and Mulser[789] have suggested that ignition might be achieved without channeling by depositing sufficient energy (~10 kJ) at the critical-density layer of the corona of the imploded fuel using a petawatt laser ("coronal ignition").

Winterberg[790] proposed in 1968 that ignition could be achieved by colliding two macroscopic DT pellets. A related concept was proposed by Murakami and Nagatomo[791] for an impact-ignition scheme by using a cone-in-shell geometry similar to that shown in Fig. 14-4. The target consists of a cryogenic fuel shell with an embedded hollow metal cone. The mouth of the cone is covered by another fuel-shell segment and the cone tip contains a small hole to allow the passage of material within the cone after acceleration. The main shell is imploded to form a dense fuel assembly in front of the open cone tip, and the shell inside the cone (the impactor shell) is accelerated to a high velocity ($>10^8$ cm/s) to collide with the compressed fuel at stagnation. The temperature and density reach ignition conditions during the collision.

Azechi *et al.*[792] carried out integrated experiments to explore this concept with warm CD cone-in-shell targets, demonstrating a factor-of-100 increase in fusion neutron yield for optimum timing of the impactor laser pulse relative to the implosion laser pulse. The main shell (7-μm-thick CD) and the impactor shell (10-μm-thick CD), both with a 500-μm diameter, were irradiated by a 1.3-ns laser pulse with a wavelength of 0.53 μm. The impactor shell was attached to the entrance of a gold cone with a full opening angle of 90°. The cone had an open apex with a diameter of 50 μm. Nine out of the 12 GEKKO XII beams imploded the main shell with an energy of 3 kJ. The three remaining beams (with an energy of 0.4 kJ) were focused at a higher intensity (7×10^{14} W/cm^2) onto the impactor shell to accelerate a small portion of this shell to a velocity of $\sim 6 \times 10^7$ cm/s. With the impactor properly timed, the implosion produced 2×10^6 neutrons, while just 3×10^4 neutrons were produced when only the main shell was imploded. In planar-target experiments using the Nike KrF laser, Karasik *et al.*[793] demonstrated that it is possible to accelerate near-solid-density plastic foils to speeds close to 10^8 cm/s. The subsequent collision with a stationary deuterated plastic foil produced ~Gbar shock pressures and heated the ions to 2–3 keV. Although the foil was accelerated close to the required speed, the pressures produced were still significantly below ignition values. One challenge of this scheme is that the required speed exceeds the exhaust velocity, requiring most of the target mass to be ablated. For limited laser energy, the foils are necessarily thin, making them prone to breakup from the Rayleigh–Taylor instability.

D. Cone-in-shell implosion experiments

This section describes cone-in-shell experiments at Osaka and LLE that have demonstrated through neutron-yield enhancement that short-pulse laser energy is coupled into the implosion. A number of issues have been identified including early cone-tip destruction and the formation of pre-plasma inside the cone. The pre-plasma increases the standoff distance of the electrons and degrades their coupling.

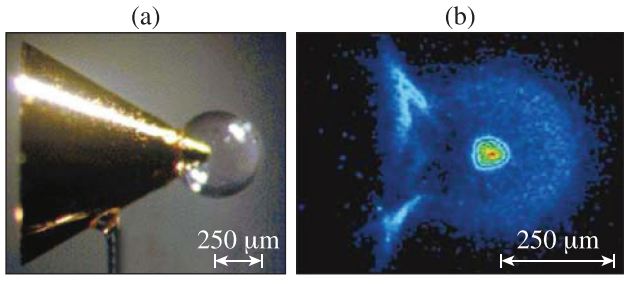

FIG. 14-5. (a) Photograph of the target used for the first integrated cone-in-shell experiments at Osaka. A hollow gold cone is attached to a deuterated polystyrene (CD) shell (500-μm diameter, 7-μm wall thickness). Nine 1-ns laser beams were used to implode the shell at the tip of the cone. The 100-TW short-pulse laser was injected from the open side of the cone. (b) X-ray self-emission image showing the imploded core plasma on the tip of the cone. The dimmer features correspond to the outline of the cone (left). The halo concentric with the bright core feature is emitted from the imploding shell. Reprinted with permission from Kodama *et al.*, Nature **412**, 798 (2001). Copyright 2001 Macmillan Publishers Ltd.

1. Osaka integrated cone-in-shell experiments

The cone-guided implosion concept was first tested on the GEKKO XII laser by Kodama *et al.*[794] Figure 14-5 shows (a) the target and (b) a time-integrated x-ray image of the implosion without injection of the short-pulse laser. Initial experiments with the 0.53-μm-wavelength laser used nine 1-ns pulses with a total energy of 1.2 kJ to implode a 500-μm-diam, 7-μm-thick CD shell around a hollow Au cone. The inner cone (full) angle was 60° and the outside of the tip was placed 50 μm away from the center of the sphere. A 1.05-μm-wavelength, 60-J, 0.6-ps, 100-TW laser pulse was focused inside the cone tip to produce fast electrons that deposited a fraction of their energy into the compressed plasma. The heating produced 2.45-MeV neutrons from D_2 fusion reactions, which were measured with neutron time-of-flight detectors. The observed yield was 2×10^5—about an order of magnitude higher than the yield without injection of the short-pulse laser. Follow-up experiments with slightly higher implosion energy (2.5 kJ) and higher short-pulse laser energy (300 J) resulted in neutron yields of up to 2×10^7 (Ref. 795), enhanced by about three orders of magnitude above the yield of $2–5 \times 10^4$ for no short pulse. Figure 14-6 shows the measured (relative) neutron enhancement as a function of injection timing of the short pulse, indicating correlation with the predicted compressed density. Time zero marks the maximum yield enhancement. The enhancement was observed during a ±40-ps window.

In later experiments in the same configuration, Yabuuchi *et al.*[796] spectrally resolved hot electrons passing forward through the compressed core with an electron spectrometer at 20° from the short-pulse laser axis. On those shots when the short pulse was timed to produce an enhanced neutron yield, they found a significant reduction of hot electrons with energies below 15 MeV, beyond what would be

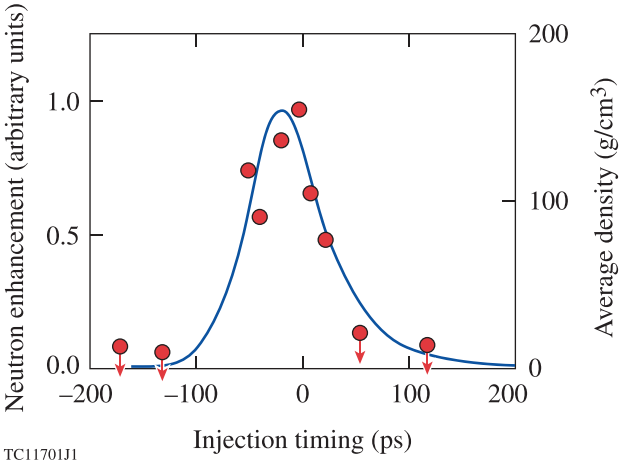

FIG. 14-6. Normalized neutron enhancement as a function of injection timing of the heating pulse for the Osaka integrated cone-in-shell experiments. Time zero marks the maximum yield enhancement (about three orders of magnitude). The line represents the temporal profile of the average density of the compressed plasma from a hydrodynamic simulation. The arrows indicate data points at or below the noise level. Reprinted with permission from Kodama *et al.*, Nature **418**, 933 (2002). Copyright 2002 Macmillan Publishers Ltd.

expected for classical slowing down, and proposed an anomalous stopping mechanism based on electron magnetohydrodynamic shock formation.

2. LLE cone-in-shell fuel-assembly experiments

Fuel-assembly experiments with cone-in-shell targets were performed on the OMEGA laser by Stoeckl *et al.*[797] to study the erosion of the cone tip. The targets were 24-μm-thick CH shells of ~870-μm outer diameter, with a hollow gold cone having full opening angles of 70° or 35° inserted through a hole in the shell (Fig. 14-7). A shelf built into the cone rests on the shell and determines the distance between the tip of the cone and the center of the shell, typically 30 μm. The inner cone had a wall thickness of 10 μm and a pointed tip.

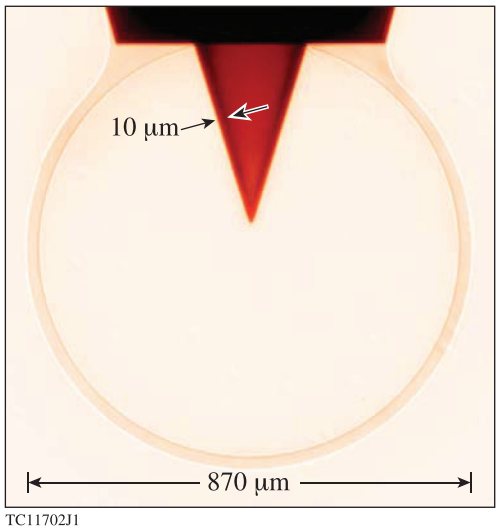

FIG. 14-7. X-ray radiograph of a gas-tight cone-in-shell target with a 35° opening (full angle), showing the outline of the 24-μm-thick CH shell and the opaque gold cone with 10-μm wall thickness. A shelf was built into the cone for accurate mounting of the shell. Reproduced with permission from Phys. Plasmas **14**, 112702 (2007). Copyright 2007 AIP Publishing LLC.

The implosion was imaged with temporal resolution using x-ray backlighting with an x-ray framing camera. The shell, filled with 10 atm D_2 gas, was irradiated with 35 OMEGA beams using 1-THz smoothing by spectral dispersion (SSD) (Sec. VI C) and polarization smoothing (Sec. VI D) with a 1-ns pulse and ~11 kJ of laser energy. The energy of 15 of the 35 beams was reduced to ~50% of the maximum to provide nearly uniform illumination of the shell. An additional 15 full-energy beams with a total energy of ~6 kJ irradiated a backlighter foil (V or Fe) to generate the x-ray radiation. Figure 14-8 shows three frames of the measurement, separated by 250 ps, showing the assembly of the core and the erosion of the cone tip. The central image is close to peak compression. Similar experiments with unfilled targets show that the cone erosion appears later when the target is empty. These experiments demonstrate that the compressing shell pushes a jet of plasma material toward the cone that leads to the destruction of the tip. Similar results were obtained in indirectly driven cone-in-shell target experiments on OMEGA,[798,799] showing cone-tip destruction and the ablation of gold material from the cone.

3. LLE integrated cone-in-shell experiments

Integrated fast-ignition experiments started at LLE in 2008 (Ref. 800), shortly after the commissioning of the OMEGA EP laser. The targets were 40-μm-thick, ~870-μm-outer-diam, deuterated-plastic (CD) shells with an

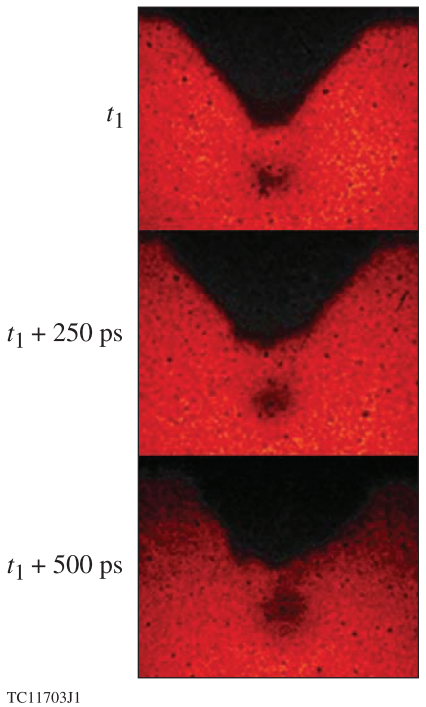

FIG. 14-8. Backlit framing camera images obtained on OMEGA of a 70° cone-in-shell target filled with 10 atm D_2, using a V backlighter (predominantly He_α line emission at 4.95 keV). Three images spaced ~250 ps apart show the assembly of the core and the erosion of the cone tip, with the central image close to the time of peak compression. Reproduced with permission from Phys. Plasmas **14**, 112702 (2007). Copyright 2007 AIP Publishing LLC.

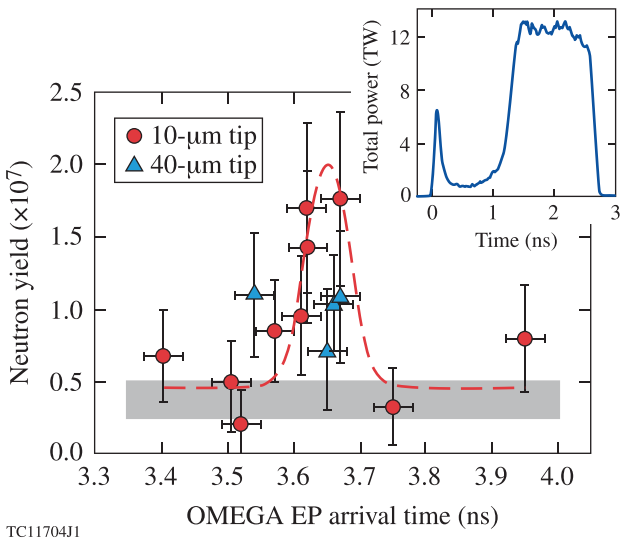

FIG. 14-9. Measured neutron yield for LLE integrated cone-in-shell experiments as a function of the arrival time of the short-pulse OMEGA EP laser beam for targets with tip diameters of 10 μm and 40 μm. The plotted yield excludes neutrons generated in the corona. The gray area represents data without the short-pulse beam. The inset displays the pulse shape of the implosion drive laser. Reproduced with permission from Phys. Plasmas **18**, 056305 (2011). Copyright 2011 AIP Publishing LLC.

inserted hollow gold cone. The cone had an inner full opening angle of 34°, a side-wall thickness of 10 μm, and a small circular flat tip. The tip diameter was either 10 or 40 μm. The tip thickness ranged from 5 μm to 15 μm. The shells were imploded with a 2.7-ns shaped pulse (inset in Fig. 14-9) using 54 of the 60 UV OMEGA beams (0.35-μm wavelength) with a total energy of ~20 kJ. The laser used polarization smoothing and phase plates but no SSD. The 1.05-μm-wavelength short pulse from OMEGA EP had an energy of ~1 kJ and a 10-ps duration and was focused inside the cone to a spot with a radius of $R_{80} = (26 \pm 2)$ μm containing 80% of the laser energy. More than 30% of the laser energy had an intensity $>10^{19}$ W/cm^2, while the average intensity within R_{80} was $\sim 6 \times 10^{18}$ W/cm^2. A nanosecond prepulse with an intensity of $\sim 2 \times 10^{12}$ W/cm^2 (and energy ~20 mJ) preceded the short pulse.

Thermonuclear neutrons were produced from the plasma corona as well as from the hot, dense core surrounded by the cold shell. The entire shell was deuterated and the region between the critical and ablation surfaces was heated to temperatures >1 keV, generating a significant amount of neutrons. The corona yield was measured in a series of shots with cone-in-shell targets without a short-pulse laser, where the inside of the shell was coated with a CH plastic layer (1–5 μm) to quench the yield from the target center. The neutron yield was ~35% lower compared with pure CD shells and did not depend on the thickness of the CH layer. The corona yield of 7×10^6 measured in this way was subtracted from the measured total yield.

Figure 14-9 shows the neutron yield from the compressed plasma as a function of the arrival time of the short pulse in the cone for targets with two tip sizes (10 μm and 40 μm). The 10-μm data show a peak in neutron yield at a time of 3.65 ± 0.05 ns. The dashed curve is a fit of a Gaussian profile to the red circles. The gray bar represents the yield from several shots without the short-pulse beam. The 10-μm data show an enhancement in neutron yield by a factor of 4 for a properly timed short-pulse beam. It was not clear why the targets with the 40-μm tip size, which should have had smaller pre-plasma problems, performed less well.

Stoeckl *et al.*[797] and Theobald *et al.*[800] described shock-breakout measurements performed by imploding the shell without a short-pulse beam. The jet of plasma from the compressing shell that strikes the tip of the cone launches a shock wave into the cone. When this shock wave reaches the inner cone surface (i.e., the surface that the short-pulse beam will strike), it generates optical emission inside the hollow cone, which is measured temporally and spatially resolved. The breakout is delayed with increasing tip thickness. The breakout time for the 10-μm-diam, 15-μm-thick tip was measured to be 3.72 ± 0.03 ns on the same time axis as Fig. 14-9, which is close to the measured peak of neutron production. The possibility of premature cone destruction is a significant issue that must be taken into account in ignition designs.

Pre-plasma formation inside the cone by a laser prepulse is another issue. Two-dimensional simulations were performed with the radiation–hydrodynamics code *HYDRA* to study this issue for the OMEGA experiment using the measured prepulse.[800] Figure 14-10 shows simulated density contours for the smaller 10-μm-diam tip. As pre-plasma expands in the cone, the IR critical density shifts ~100 μm away from the original inner cone wall by the time the main ignitor pulse is incident. The cone geometry exacerbates the effect by laterally confining the plasma in the cavity and therefore increasing the longitudinal scale length. This increases the standoff distance between the location where the fast electrons are produced and the dense core. Similar conclusions were drawn from short-pulse experiments with cone-like structures at the LULI 100-TW laser in France. Experiments by Baton *et al.*[801] revealed the presence of pre-plasma over

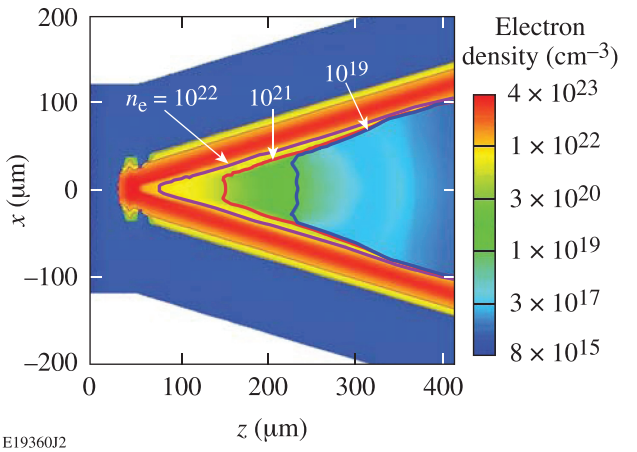

FIG. 14-10. Electron-density contours at the time of the short-pulse interaction from a 2-D *HYDRA* simulation of the pre-plasma formation in a gold cone. (The short main pulse was not included in the simulation.) The solid red curve is the IR critical-density contour and shows that the location of the laser interaction is shifted ~100 μm away from the cone tip. Reproduced with permission from Phys. Plasmas **18**, 056305 (2011). Copyright 2011 AIP Publishing LLC.

100 μm away from the cone tip for similar laser contrast to that in the OMEGA experiment. It was shown by MacPhee *et al.*[802] that a preformed plasma in a hollow cone strongly affects the ultra-intense laser–plasma interaction and hot-electron generation. The prepulse eliminates the forward-going component of 2- to 4-MeV electrons. All of the laser energy is diverted from the cone tip by the preformed plasma and the laser beam is split into multiple filaments far from best focus. Two-dimensional PIC simulations by Li *et al.*[803] of the experiments of Ref. 800 also showed a significant fraction of the hot-electron flux propagating sideways through the cone wall.

Future experiments require minimization of the size of the pre-plasma in the cone through the application of lasers with an ultrahigh intensity contrast ratio and improvements to the target designs to delay the cone-tip breakout as late as possible. It is also important to know where in the compressed plasma the fast electrons deposit their energy. Unfortunately, the low neutron yield from these experiments precludes the application of neutron imaging, so spatially resolving diagnostics that are sensitive to fast electrons are required. Possibilities include using plastic shells that are doped with an appropriate higher-Z material (e.g., copper) and imaging the fast-electron–excited K_α fluorescence emission.

E. Ignition-scale designs

A first estimate of the ignition criteria of precompressed, cold fuel by a pulsed fast-electron beam was given by Tabak *et al.*[740] It was later refined by Atzeni[743] in a parameter study that analyzed the dependence of the pulse parameters on the particle range in the fuel. However, both of these studies assumed an idealized monoenergetic, parallel particle beam. The laser–plasma interaction, which is necessary to create the particles, was not discussed. Atzeni found the minimum energy for ignition to be ~14 kJ for a beam with a radius of 20 μm, a particle range of 0.6 g/cm^2, negligible divergence, and a target density of 300 g/cm^3. The particle range of 0.6 g/cm^2 in compressed DT with a density of 300 g/cm^3 corresponds to an electron energy of ~1 MeV (Ref. 752). Improved design studies were performed by Solodov *et al.*[742,804] with integrated simulations coupling a hydrodynamics code (*DRACO*) with a hybrid PIC code (*LSP*). The simulations indicated that electron-beam energies ranging from ~40 to 100 kJ are required for ignition, assuming a Gaussian-shaped fast-electron beam with 30-μm spot diameter, 10-ps duration, and a relativistic Maxwellian distribution with 2-MeV mean energy. The beam is injected 125 μm from the target center into a compressed deuterium–tritium (DT) core with peak density $\rho = 500$ g/cm^3 and areal density $\rho R = 1$ g/cm^2. It was found that the ignition threshold depends on the initial beam's full divergence angle, which was varied from 40° to 80° in the simulation. Similar ignition electron-beam energies have been obtained in other design studies.[746,805] These studies included self-generated electric and magnetic fields but still lacked a detailed description of the laser–plasma interaction, which is complex and requires large-scale, 3-D PIC simulations.

Target design studies have been performed by Atzeni *et al.*[746] for the proposed European High Power Laser Energy Research (HiPER) Facility.[806] HiPER was proposed to deliver a 0.35-μm-wavelength, multibeam, multinanosecond pulse with an energy of 250 kJ to implode a capsule, followed by a short (15-ps) pulse with a wavelength of 0.53 μm or 0.35 μm and an energy of 70–100 kJ for ignition. The baseline target concept was a direct-drive single-shell capsule, ignited by hot electrons generated by a cone-guided ultra-intense laser beam. Atzeni *et al.*[746] presented ignition and compression requirements for HiPER, including gain curves based on an integrated model that includes ablative drive, compression, ignition, and burn, and took the coupling efficiency of the igniting beam as a parameter. Ignition and a gain of up to 100 were predicted for a design that included adiabat shaping (Sec. III) in the compression phase and assumed that a fraction >20% of the laser energy was coupled into the fuel via hot electrons.

Two-dimensional hydrodynamic simulations of an indirect-drive–ignition target design were performed by Shay *et al.*,[807] who explored a number of design parameters (common to both direct and indirect drive) including two different capsule sizes, the shape of the cone tip, the cone-tip offset, and various cone-tip materials (diamond, copper, gold) inserted into the nose of an Au cone. They demonstrated that, while the asymmetry of the implosion can degrade the peak DT density and ρR, there are designs that do approach 1-D parameters and give reasonably efficient DT burn if ignited. Targets were designed that produce areal densities of 1.5–2.0 g/cm^2 along the fast-electron path with an ~100- to 200-μm standoff distance from the electron source to the core. Because the implosion adjacent to the cone surface lags, the chance of cone material being swept to the center of convergence was reduced.

Simulations performed at LLNL by Strozzi *et al.*[784] indicate that significantly higher short-pulse laser energies are required than previously estimated based on simpler models. Using the electron source from large-scale 3-D PIC simulations (~130° divergence full angle and a two-temperature distribution function), Strozzi *et al.* studied the transport of the fast electrons in an ignition-scale target using a hybrid PIC code (*Zuma*) coupled to the hydrodynamics code *HYDRA*. The simulations indicate that even with a dense core in direct contact with the cone tip (i.e., optimum implosion), the electron coupling to the core is poor. In addition to the large divergence, another major detrimental factor is the fast-electron temperature (or mean energy). High-energy electrons can propagate through the dense core without depositing much of their energy. The simulations show no ignition even for >1 MJ of fast-electron energy for a 140-μm standoff distance between the electron source and the center of the core when using a frequency-doubled, 0.5-μm-wavelength laser. The poor coupling is partially attributed to the too-energetic electron energy spectrum, although the electron temperature was already reduced by using a 0.5-μm wavelength. Figure 14-11 shows the simulated fusion yield versus the total injected fast-electron energy when the electrons were artificially collimated to a beam with 15° full-angle divergence. Even in this case, however, the electron

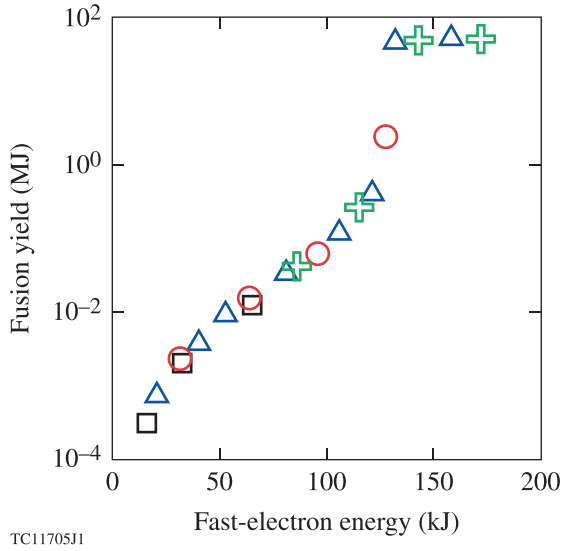

FIG. 14-11. Fusion yield versus the total injected fast-electron energy from *Zuma–HYDRA* simulations assuming a 0.5-μm-wavelength ignitor beam. The electron spectrum was obtained from PIC simulations. The electrons were artificially collimated to a beam with 15° full-angle divergence. The different symbols mark different electron source diameters. Reproduced with permission from Phys. Plasmas **19**, 072711 (2012). Copyright 2012 AIP Publishing LLC.

beam energy required for ignition is ~135 kJ, requiring a petawatt laser with an estimated energy of 300–400 kJ. By placing an external magnetic field in the target, Strozzi *et al.* were able to reduce the required electron energy to ~100 kJ. The question here is how such large magnetic fields can be generated and how uniform they must be to efficiently couple the fast electrons into the core.

In a parameter study without magnetic collimation, Bellei *et al.*[808] calculated the ignition laser energy, extending the previous work by Atzeni[743] with a more-realistic electron source extracted from a 3-D PIC simulation. Bellei *et al.* used an electron transport model similar to the one described by Strozzi *et al.*[784] and calculated the ignition energy for two different laser wavelengths (0.527 and 0.351 μm) as a function of the source–fuel distance, the laser focus size, and the density of a precompressed, idealized DT fuel assembly. As a result of the large divergence of the electron beam, they found that the scaling of ignition energy with the DT density ρ is weaker than the ρ^{-2} scaling for an idealized beam.[743] The required laser energies were calculated to be above ~500 kJ, even for a small separation of 25 μm between the fuel (location of the 50% peak density point) and the electron source.

The major challenges for fast ignition include the control of the kinetic energy distribution and divergence of the fast electrons. A too-energetic electron spectrum and a large divergence result in poor coupling to the core. Future work must address how to control the fast-electron generation and transport so that reasonable ignition energies can be achieved.

XV. SHOCK IGNITION

Following the proposals described in Sec. XIV to separate the compression and ignition phases, most work along these lines has focused on the fast-ignition concept (Sec. XIV), rather than the suggestion of Shcherbakov[737] to use a shock for the ignition phase. However, since the work of Betti *et al.*[809] in 2007, the shock-ignition (SI) concept has emerged as a viable approach worthy of serious consideration.

In SI, the ignition phase is accomplished through a modification of a typical hot-spot laser pulse design (such as that described in Sec. III), adding a high-intensity spike pulse (Fig. 15-1 from Ref. 810) to the end of the main compression pulse. The main drive pulse is typically reduced in power, resulting in a slower shell velocity at the end of the acceleration phase and allowing a greater compressed fuel mass for a given laser energy. The late-time shock dynamics of a typical shock-ignition target with a plastic ablator are illustrated in Fig. 15-2. As the target implodes, the shock from the main pulse [Fig. 15-2(a)] propagates inward, eventually rebounding off the center [Fig. 15-2(b)]. The late-time laser spike then launches a strong, spherically symmetric shock wave into the precompressed target. The late-time shock propagates through the compressed shell material and amplifies through spherical convergence until it collides with the rebound shock [Fig. 15-2(c)]. This shock collision typically occurs near the inner portion of the dense shell material and increases the shock pressure transmitted into the hot-spot gas, leading to a higher stagnation-time hot-spot pressure than exists in standard hot-spot designs with no late-time laser spike. Extensive references to theoretical and simulation work on shock ignition can be found in Ref. 810.

To create this strong spherical shock, the laser intensity is increased substantially above the main-drive laser intensity. This may be accomplished by using the same laser beams that drive the target compression and ramping up the laser power late in time (as in Fig. 15-1) or by using (in addition to the compression beams) dedicated high-peak-power beams arranged in a spherically symmetric pattern. The first approach has a possible advantage over fast ignition in that a separate short-pulse laser system is not required. Either approach may be performed on current laser facilities, such

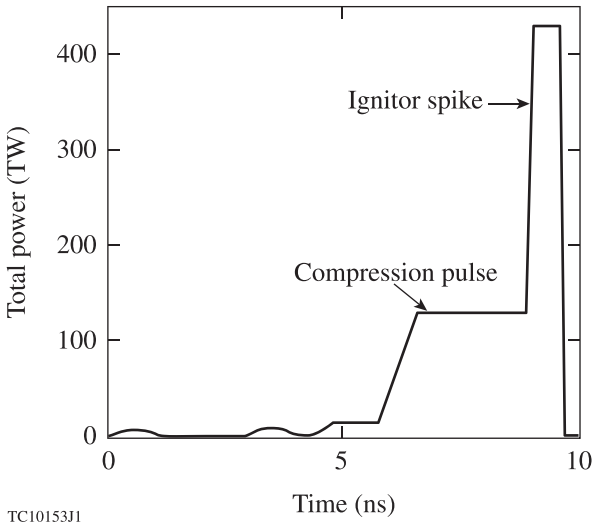

FIG. 15-1. Typical pulse shape for a NIF-scale shock-ignition experiment, consisting of a main compression drive pulse followed by an ignitor spike. Reproduced with permission from Phys. Plasmas **20**, 056312 (2013). Copyright 2013 AIP Publishing LLC.

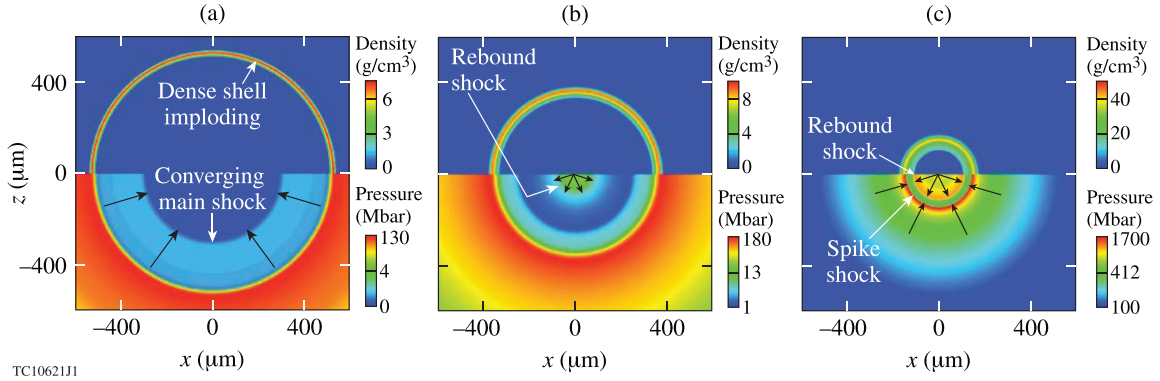

FIG. 15-2. An illustration of the shock dynamics for a typical plastic-ablator shock-ignition target. Mass density is plotted on top and pressure on a logarithmic scale at the bottom. (a) The main-drive shock converges toward the center of the gas fill. (b) The main-drive shock rebounds and moves outward. (c) The spike shock is driven inward and collides with the rebound shock in the inner portion of the dense shell. In all cases the black arrows indicate fluid motion.

as the NIF, the second approach requiring some subset of the compression beams to be retasked as spike-pulse beams. In the first approach, it is desirable to have the spike portion of the pulse focused to a smaller spot than the compression portion. This can be accomplished with KrF lasers configured to use echelon-free induced spatial incoherence (ISI) (Sec. VI B) since they can be dynamically zoomed (as demonstrated in Fig. 16-7 below). Schmitt *et al.*[811] found this to lower the constraints on laser power. If a second set of beams is used for the spike pulse, it is straightforward to use a tighter focus for these beams, but there will be some loss of uniformity if this is done with a smaller number of beams. It should be noted that an optimized SI laser facility will have a higher peak laser power than an optimized hot-spot laser facility. Perkins *et al.*[812] pointed out that it will not be possible to achieve shock ignition on the NIF using indirect drive in a hohlraum since the radiation drive rises too slowly.

Shock ignition offers distinct advantages over standard hot-spot implosions. In comparison with hot-spot targets driven by the same input laser energy, SI targets can be more massive, leading to higher areal densities and gains. These more-massive targets have lower acceleration, reducing the growth rates of the Rayleigh–Taylor instability (Sec. IX). Furthermore, the target's in-flight aspect ratio (IFAR) (Sec. III) is reduced for a given driver energy and in-flight adiabat, providing more robustness against hydrodynamic instability.

Several potential physics issues in the SI scheme have yet to be adequately explored, particularly in the appropriate regimes of laser intensity and scale length. Spike-pulse laser intensities are typically several times 10^{15}–10^{16} W/cm^2. Laser–plasma instabilities can impact laser–shock coupling and potentially lead to target preheat through the acceleration of suprathermal electrons in the corona.

Section XV A reviews existing 1-D designs and the physics modeling currently used to simulate SI implosions. Section XV B summarizes 2-D simulation work done in the context of characterizing the effect of hydrodynamic instabilities and other nonuniformities. Section XV C focuses on the modeling of laser–plasma interactions and hot-electron transport. Section XV D reviews SI experiments and comments on their relevance in the context of ignition-scale target designs.

A. One-dimensional analysis and simulations

In typical direct-drive hot-spot ignition designs, targets implode with velocities at or near 4×10^7 cm/s with an average fuel adiabat of 2–3. The SI target of Betti *et al.*[809] implodes at a much-slower velocity of 2.25×10^7 cm/s, with an average fuel adiabat of 2, and relies on a spike pulse with intensity 6×10^{15} W/cm^2 to ignite the fuel assembly. Betti *et al.* indicated that a hot-spot pressure enhancement of 70% compared with that expected in typical hot-spot implosions can lead to a fourfold reduction in the energy required for ignition. Ribeyre *et al.*[813] derived a criterion for ignition based on the strong-shock velocity and pre-spike fuel-assembly density and radius. One-dimensional theoretical models of shock propagation and shock collision in planar[814] and spherical[813,815–817] geometries have characterized parameters for achieving maximum amplification of the hot-spot pressure. A detailed analysis by Vallet *et al.*[817] produced equations for shock and fluid-particle trajectories during shock convergence and reflection using a Guderley[818] solution with first-order corrections and characterized the effects of a finite shock Mach number. Davie and Evans[819] studied numerically the stability of spherical shocks in two dimensions and found only modest departures from sphericity after shock reflection due to self-healing in the expanding shock wave. Nora and Betti[814] suggested the possibility of multiple strong shocks to achieve higher hot-spot pressure.

These results have been confirmed by simulations of similar designs by Perkins *et al.*,[812] Terry *et al.*,[820] and Anderson *et al.*[810] for the NIF; Canaud and Temporal[821] and Temporal *et al.*[822] for the Laser Mégajoule (LMJ); Ribeyre *et al.*[823,824] and Atzeni *et al.*[825] for HiPER;[806] and Schmitt *et al.*[811,826] and Bates *et al.*[827] for KrF lasers. Earlier work used all-DT designs or wetted-foam ablators, but most recent work has focused on CH-ablator targets for keeping the generation of hot electrons from laser–plasma interactions low during the main drive pulse. In these designs, shock pressures at shock launch time vary from ~300 Mbar to ~700 Mbar. The shocks are strongly amplified by spherical convergence by amounts that depend on the details of the implosion[813,816] and may reach pressures of the order of 1–3 Gbar at shock collision time.[809,816] The shock is further amplified by the shock collision.[813,816] All SI designs discussed here

involve cryogenic targets, although Canaud *et al.*[828] have proposed using noncryogenic double shells.

Gain curves for SI have been developed from both analytical models[815,824,826] and 1-D simulations.[811,812,815,824,826] One such gain curve,[812] reproduced in Fig. 15-3(a) for wetted-foam targets driven at 0.35 μm, indicates that SI is capable of achieving higher gains in 1-D than direct- or indirect-drive hot-spot implosions of similar driver energy. These findings are consistent with Fig. 15-3(b), taken from Ref. 826, which shows a gain curve at 0.248 μm, also for wetted-foam targets, and with other simulated[811,824] and analytical[815] gain curves. Perkins *et al.*[812] and Schmitt *et al.*[811] have noted that the SI scheme would make a good candidate for inertial fusion energy (IFE) reactor-scale implosions because of its potential for high gain.

It is important to recognize that a long-scale-length hot corona surrounding the target has been formed by the onset of the spike pulse. The standoff distance between the laser-absorption region (near the critical-density surface) and the ablation front may be large, of the order of 200 μm (beginning of the spike) to 300 μm (end of the spike) in CH, all-DT, and wetted-foam ablators. This may present an issue for laser coupling to the ablation surface and ultimately to strong shock generation. Radiation–hydrodynamics simulations have mostly used flux-limited thermal conduction to model heat transport. However, coronal temperatures in these simulations may exceed 8 keV, and a nonlocal treatment of heat flow is probably required (Sec. XI). For example, it was shown by Bell and Tzoufras[829] that the peak pressure is higher in Vlasov–Fokker–Planck simulations than in hydrodynamic simulations with Spitzer thermal conductivity in the intensity regime of interest for SI. There are indications that fuel preheat in SI targets from nonlocal thermal electrons may be significant,[830] but these simulations should be treated with caution since the various nonlocal thermal conduction models exhibit very different levels of preheat.[615]

The large standoff distance between the absorption region and the ablation surface improves the smoothing of laser nonuniformities. It also increases the ratio of surface area between the quarter-critical and ablation surfaces, which is expected to reduce hot-electron coupling to the target, particularly for less-directional hot-electron acceleration mechanisms such as the TPD instability (Sec. X A). The target's areal density increases by the onset of the spike pulse, providing the target with resistance to preheat from lower-energy ($\lesssim$100-keV) hot electrons generated during the spike pulse (Sec. XV C).

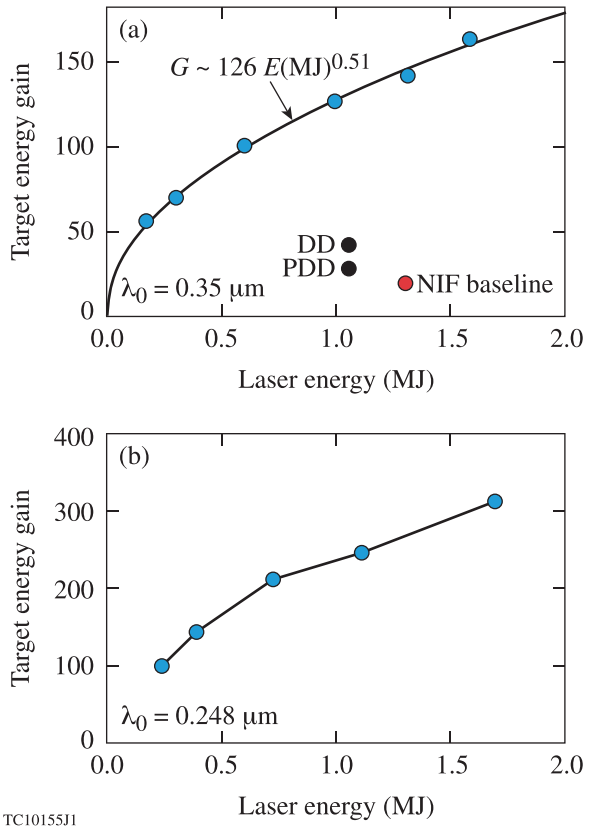

FIG. 15-3. (a) Predicted 1-D gain versus input laser energy for a family of self-similar shock-ignition implosions from simulations of Perkins *et al.*[812] for wetted-foam targets driven at a laser wavelength of 0.35 μm. Simulation points for conventional direct-drive (DD) and polar-direct-drive (PDD) hot-spot designs at 1 MJ and the indirect-drive NIF National Ignition Campaign baseline are shown for comparison. Reprinted with permission from Perkins *et al.*, Phys. Rev. Lett. **103**, 045004 (2009). Copyright 2009 American Physical Society. (b) One-dimensional shock-ignition gain calculations for wetted-foam targets driven at a laser wavelength of 0.248 μm. Reproduced with permission from Phys. Plasmas **17**, 042701 (2010). Copyright 2010 AIP Publishing LLC.

B. Two-dimensional hydrodynamics

One advantage of SI over hot-spot designs with respect to hydrodynamic instabilities is that IFARs are smaller in SI designs. As a result, instabilities must grow larger to affect hot-spot formation. However, SI designs typically use lower fuel adiabats, leading to less-effective ablative stabilization of the Rayleigh–Taylor instability (Sec. IX). This may be mitigated through adiabat-shaping techniques (Sec. III). SI targets typically have somewhat higher convergence ratios; for example, the convergence ratio is 32 for the shock-ignition design of Ref. 810 and 26 for the hot-spot design of Ref. 197. Therefore, multidimensional hydrodynamic stability simulations are necessary to quantify the robustness of SI designs.

Several studies have indicated a sensitivity to small-scale perturbations, but they have also suggested that these nonuniformities do not preclude the robust formation of a hot spot and ignition. For example, detailed 2-D simulations were performed by Schmitt *et al.*[826] of an IFE-scale SI design using a wetted-foam ablator imploded with a KrF laser. The total laser energy was 490 kJ and the ignitor pulse delivered 10^{15} W over 200 ps. The simulations modeled perturbations up to mode 512, including perturbations from inner ice and outer target roughness consistent with "NIF-spec" spectra,[831] with nominal (rms) amplitudes of 1.0 and 0.125 μm, respectively. Laser imprint was included, based on 300 overlapped and mutually incoherent 1-THz ISI beams. Figure 15-4 illustrates the time evolution of the nonuniformities in one simulation. The final image is dominated by low-mode perturbations. The gain was 102, indicating robust ignition. Similar results were published by Bates *et al.*[827]

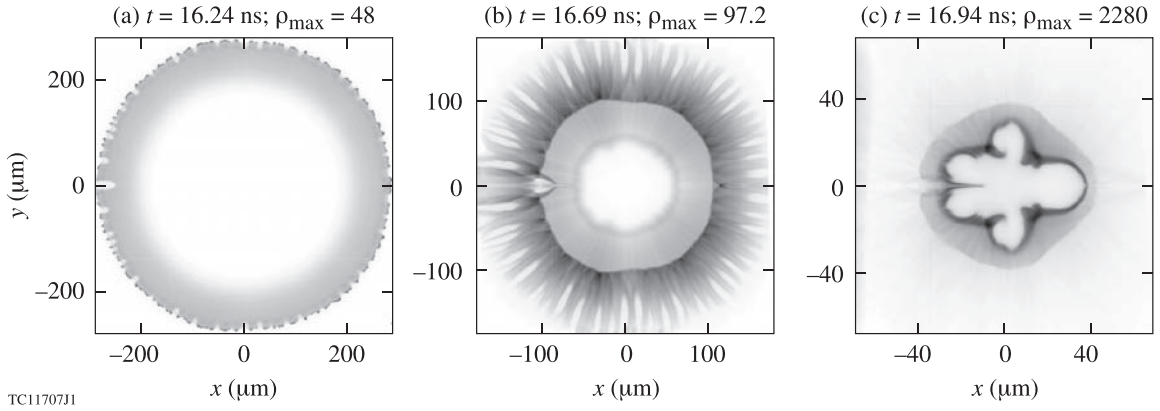

FIG. 15-4. Images representing the density of an imploding target at times (a) 100 ps after the ignitor starts; (b) when the ignitor shock is halfway through the shell; and (c) at stagnation as the burn begins. In each case the maximum density ρ_{max} is given in g/cm^3. The target was initially perturbed on the outer and inner surfaces with "NIF-spec" spectra and was subject to laser imprinting from 300 overlapped and mutually incoherent 1-THz ISI beams. The resulting gain was 102. Reproduced with permission from Phys. Plasmas **17**, 042701 (2010). Copyright 2010 AIP Publishing LLC.

Given the small stagnation hot-spot radii in SI implosions, low-mode asymmetries may also be problematic, particularly those from target offset and beam geometry. Simulations[810,825] indicate that SI targets can tolerate offsets only of the order of half their stagnation radii, or about 10–15 μm. The beam geometries of facilities like the NIF and LMJ, which are optimized for indirect drive and therefore lack spherical symmetry, have led to "polar-drive" beam-repointing schemes (Sec. VIII C) that introduce low-mode asymmetries. A polar-drive point design for the NIF using a CH ablator was proposed by Anderson *et al.*[810] This design used 760 kJ of energy with 300 kJ in the ignitor pulse at 430 TW over 675 ps. Detailed 2-D simulations of this design, including polar-drive beam geometry, beam mispointing, beam-to-beam mistiming, outer and inner surface roughness, laser imprint, and target offset, indicated that ignition would be achieved. Schmitt *et al.*[826] showed that additional margin in SI designs can be recovered by increasing the power and energy in the ignitor beam. This was confirmed in 1-D simulations by Anderson *et al.*[810]

Polar-drive geometries also have the potential to compromise the uniformity of the strong shock. It is therefore important to quantify the effect of this polar-drive ignitor shock on SI implosion performance. Simulations by Ribeyre *et al.*[823] and Canaud *et al.*[832] have indicated that late-time thermal smoothing is large enough to maintain shock uniformity even in a configuration where only the polar rings on LMJ contribute to the shock pulse. Simulations by Anderson *et al.*[810] also indicated substantial thermal smoothing. Anderson *et al.* found that the largest contribution to shock nonuniformity was from the target nonuniformities at the end of the main drive rather than from the shock-beam geometry. These 2-D studies[810,823,832] suggest that SI is feasible in a polar-drive configuration, but the extent to which the polar-drive beam geometry impacts the target's nonuniformity budget remains to be seen. Simulations reported by Ribeyre *et al.*[823] and Atzeni *et al.*[833] indicate that the spike shock may have a stabilizing effect on low-mode asymmetries.

C. Laser–plasma instability simulations

Several groups have studied laser–plasma interactions in SI-relevant plasmas using 1-D or 2-D particle-in-cell (PIC) simulations. Of greatest interest to SI in these simulations are the total energy and temperature of suprathermal (hot) electrons generated by the stimulated Raman scattering (SRS) (Sec. X C) and two-plasmon-decay (TPD) instabilities (Sec. X A), as well as the balance between absorbed and reflected laser power. These simulations generally predict laser–plasma coupling consistent with that required in radiation–hydrodynamics simulations for strong-shock generation and ignition. These studies, however, are limited in scope and scale, and many of the assumptions and approximations used have not been validated experimentally.

Most hot-electron production in SI plasmas appears to be dominated by SRS. Weber *et al.*[834] found this to be the case in their 2-D PIC simulations, which indicated a fast suppression of TPD in the presence of SRS under SI plasma conditions. These SRS hot electrons are generally shown in simulations to have energies of the order of 25–60 keV. One-dimensional simulations by Klimo *et al.*[835,836] at a laser wavelength of 0.35 μm showed SRS hot-electron conversion efficiencies of up to 5% with spectral temperatures of ~25 keV at intensities of 10^{15}–10^{16} W/cm^2. SBS (Sec. X B) reflectivity in Refs. 835 and 836 was initially very strong, exhibiting pulse-like behavior, but its intensity decreased in time. These simulations indicated a total of 35% of the incident laser energy scattered at 8×10^{15} W/cm^2, with the remaining 65% absorbed in the plasma.[836] Two-dimensional PIC simulations by Klimo and Tikhonchuk[837] at the same laser wavelength indicated an overall absorption into inverse bremsstrahlung and hot electrons of 69% at 2.4×10^{15} W/cm^2 at $\lambda = 0.35$ μm, with 50% absorption into hot electrons of temperature 30 keV. These simulations, like those of Ref. 834, indicated a suppression of TPD after a few picoseconds. Riconda *et al.*[838] showed that filamentation was present in single-speckle simulations for $\lambda = 0.35$ μm and $I \sim 10^{16}$ W/cm^2, leading to self-focusing and SBS bursts. Cavitation has been shown to have an important effect on the laser absorption.[834,835,838]

These PIC simulations are by necessity limited in both the spatial extent of the computational domain and the duration of the simulations because of the computational resources required. Typically they use either plane-wave

approximations[834–836,838] for the laser field or model a single speckle,[834,838] ignoring speckle–speckle interaction, which may be important.[839] Whereas the spike-pulse duration for typical SI implosions is of the order of 400–700 ps, PIC simulation times are generally between 20 and 60 ps for 1-D simulations and ~5 ps for 2-D simulations. It is unclear whether the early-time plasma response in these simulations is representative of the entire pulse.

The coupling of instability-generated hot electrons to the capsule and shock has been studied numerically. Generally, simulations indicate that ignition designs have sufficient areal density during the spike laser pulse to resist preheat from hot electrons with spectral temperatures of less than 100 keV, stopping most electrons in the ablator or outer portion of the fuel.[810,840] Indeed, several researchers have indicated that electrons of such energies may be beneficial to SI since they deposit energy near the shock-formation region and, therefore, may amplify the shock pressures above those anticipated by including only inverse bremsstrahlung absorption and flux-limited thermal heat conduction.[809,810,812,840–843] Some authors have gone further to propose using hot electrons as the primary shock-launching mechanism.[844,845]

D. Experiments

SI-relevant experiments have been performed at various facilities, examining target stability and yield, strong-shock generation, and laser–plasma interactions at spike-pulse laser intensities. These experiments have shown enhanced fusion reactions from the addition of an SI laser spike in subscale SI implosions along with laser light scattering and hot-electron temperatures within design constraints.

Symmetric SI implosions[846] were carried out on OMEGA and compared with similar no-spike implosions. These experiments used all 60 OMEGA beams with the same laser pulse shape for each beam [Fig. 15-5(a)]. The targets were 40-μm-thick, 860-μm-diam plastic shells filled with D_2. Implosions with a late-time spike pulse and with no spike were compared at the same total laser energy. Results showed that the spike-pulse shots had neutron yields up to 4× higher than those without a spike [Fig. 15-5(b)]. Shots with two different picket timings (t_p) were included in the dataset, but the effect of picket timing was secondary. These experiments showed higher ratios of the yield-over-clean [(YOC), defined as the ratio of the experimental yield to the simulated, 1-D yield] than their no-shock counterparts, particularly at a higher convergence ratio [Fig. 15-6(a)]. The convergence ratio was varied by changing the pressure of the gas fill. Higher areal densities were measured with the spike pulses [Fig. 15-6(b)]. These results indicate that the targets imploded with an intensity spike at the end of the pulse were more stable than the no-spike targets. However, the late shock was weak and the spike intensity was less than 10^{15} W/cm^2, so potential problems with plasma instabilities may have been avoided.

Spherical laser–plasma interaction experiments on OMEGA at SI-relevant laser intensities[847–849] were performed using 40 beams to compress the target and 20 tightly focused beams to generate a shock and to study laser–plasma interactions. Results indicate that the main mechanism of hot-electron acceleration is SRS, with SRS backscatter varying from ~8% of the incident laser energy at 0.9×10^{15} W/cm^2 up to ~36% at 8×10^{15} W/cm^2. Suprathermal electron temperatures inferred from hard x-ray signals were generally ~30 keV, which is not expected to be detrimental to SI. The hot-electron temperature was insensitive to laser intensity. SBS backscatter was also measured and found to vary from ~8% to 12% at high intensity. Cross-beam energy transfer (Sec. X B) was unlikely to have been a factor during the spike pulse since there was little to no overlap in the high-intensity shock beams. No TPD 3/2-harmonic signature was measured. However, the experiments did not use SSD beam smoothing (Sec. VI C) and the tight-focus conditions may not be representative (since the optimal geometry for shock ignition will probably involve overlapping spike beams to maximize spherical uniformity), so these results should be treated with caution.

Several planar laser–plasma interaction experiments have been performed at other facilities at wavelengths varying from 1 μm to 0.35 μm (Refs. 850–853). These experiments generally produced SRS backscatter of up to 5% of

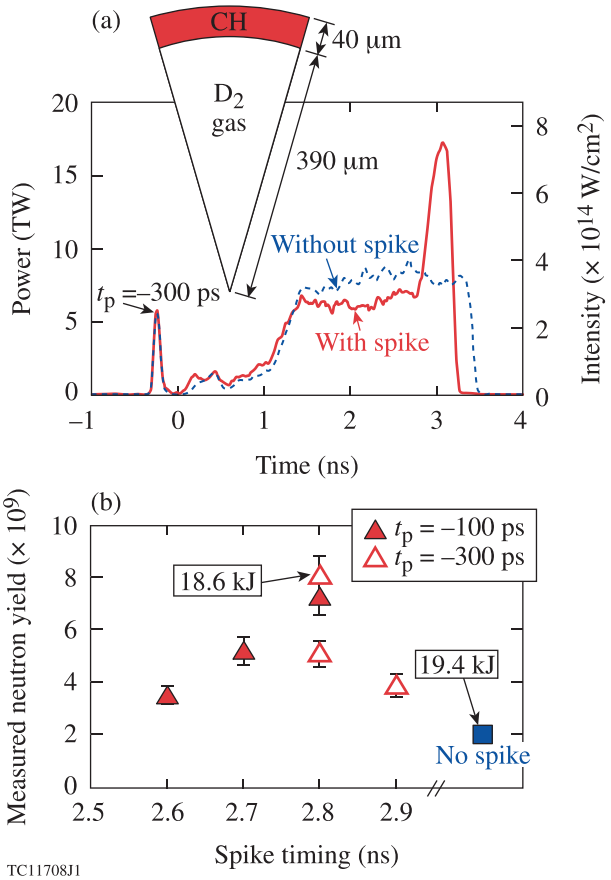

FIG. 15-5. (a) Target parameters and representative pulse shapes, with and without spike, for shock-ignition implosion experiments on OMEGA. The targets were typically filled with 25 atm of D_2. (b) Measured neutron yield as a function of the onset of the spike pulse for two different picket-pulse timings t_p. The pulse without a spike is shown as a reference and was shot with $t_p = -300$ ps. Reproduced with permission from Phys. Plasmas **15**, 056306 (2008). Copyright 2008 AIP Publishing LLC.

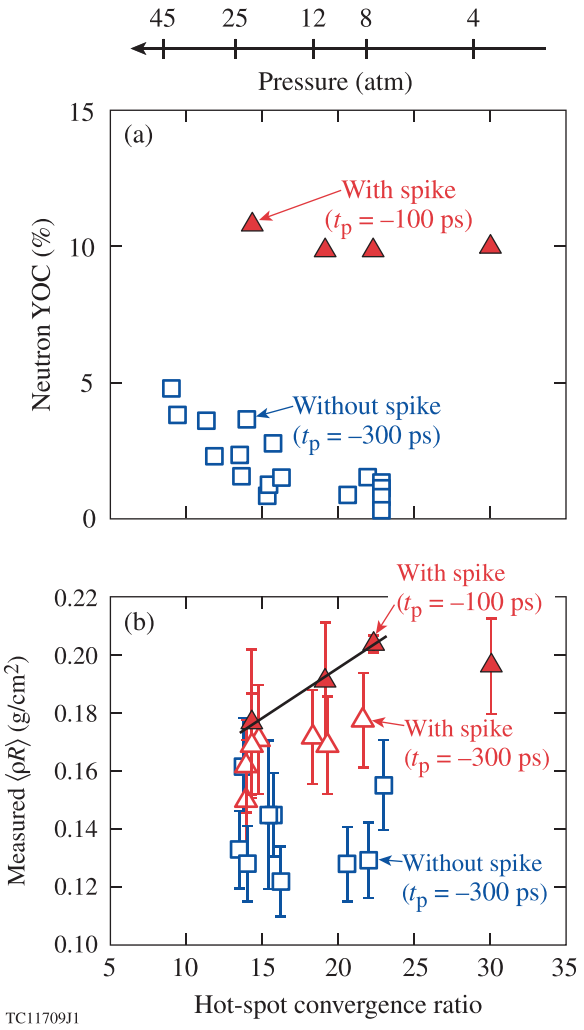

FIG. 15-6. (a) Neutron yield-over-clean (YOC) versus the 1-D calculated hot-spot convergence ratio with and without a spike. With a spike, the YOC is close to 10% for a hot-spot convergence ratio of up to 30. (b) Areal density $\langle \rho R \rangle$ versus convergence ratio for implosions with a spike (2.8-ns timing) and without a spike. Reproduced with permission from Phys. Plasmas **15**, 056306 (2008). Copyright 2008 AIP Publishing LLC.

the incident laser energy at intensities up to 3×10^{15} W/cm^2. In Ref. 852, less than 0.01% of the laser energy went into electrons of energy greater than 60 keV. SBS backscatter varied from ~7% to ~20%. The density-gradient scale lengths at quarter critical in these experiments varied widely from ~100 to ~420 μm. The small spot size and the lack of multibeam overlap may affect the relevance of these experiments to SI.

SI experiments have so far been limited to short-scale, planar, and/or sub-ignition laser platforms. The encouraging results from the OMEGA implosions make scaled-up experiments on the NIF of primary importance. In addition, laser-energy coupling must be investigated under more-relevant plasma conditions. Shock pressures generated by high-intensity pulses in long-scale-length plasmas must be quantified. The energy spectra and angular spread of hot electrons and their coupling to the target, including fuel preheat, must be more accurately characterized. In short, to adequately validate the SI concept, experiments are needed on an ignition-scale laser facility.

XVI. IGNITION AND HIGH-GAIN TARGET DESIGNS

The goal of achieving ignition and eventual high gain is at the heart of every direct-drive target design. Ignition itself is a complex combination of a high-temperature source of thermonuclear (TN) alpha particles interacting with a cold dense hydrogenic fuel layer surrounding it. Fraley *et al.*[854] outlined the process very clearly and discussed the significant improvement in gain when a central hot spot can be heated to ignition temperatures and allowed to burn outward through a cold dense fuel mass. Ignition typically occurs within a simulation when the ion temperature at the edge of the hot spot, defined by the point at which the areal density integrated from the center of the target equals 300 mg/cm^2, reaches ~5 keV. Timing is crucial because typical TN burns last only a few hundred picoseconds at most. The burn time is determined from the time at which the imploding cold fuel layer first begins to decelerate until the time at which it stagnates at the center of the system. As the shell begins to decelerate, it transfers its kinetic energy into compressional work on the hot spot, raising its temperature and pressure. The shell decelerates when the hot-spot pressure opposes the momentum of the incoming shell.

A minimum amount of kinetic energy in the imploding target shell is needed to produce ignition. Below this threshold value, the central hot spot does not produce and trap enough fusion alpha particles to sustain itself or to initiate a thermonuclear burn wave into the surrounding dense fuel. The ratio of the shell's kinetic energy to this threshold value is defined as the fuel margin. Levedahl and Lindl[855] compiled results from an extensive set of 2-D *LASNEX* ignition simulations, examining the dependence of the fuel burnup fraction on the fuel margin at ignition. Their results clearly demonstrated an ignition "cliff" below which the burnup fraction approaches zero. The fuel margin must be at least 2 to attain a high burnup fraction.

Levedahl and Lindl observed that the minimum kinetic energy needed for ignition (at a constant implosion pressure) scaled as $\sim v_{\rm imp}^{-5.5\pm0.5} \alpha^{1.7\pm0.2}$, where α is the shell adiabat (the ratio of the fuel shell pressure to the Fermi-degenerate pressure) and $v_{\rm imp}$ is the shell's implosion velocity. This implies that low-adiabat, high-velocity implosions are needed for ignition at minimum kinetic energy. While later studies found somewhat different scalings using different assumptions,[856,857] the low-adiabat, high-velocity scaling for the minimum shell kinetic energy was confirmed.

Many promising target configurations have been studied over the years using 1-D radiation–hydrodynamics codes, with ignition and high gain demonstrated over a wide range of input laser conditions. Some of the earliest 1-D studies included CH shells with inner layers of DT ice[367,858] and DT-wetted CH foam shells[859] and indicated that high gain could be achieved. However, researchers began to realize that Rayleigh–Taylor (RT) instabilities would significantly constrain their target designs. For example, Tabak *et al.*[367] estimated that surface finishes of 100–300 Å and an adiabat of ~3 would be needed for ignition and gain to occur.

From this realization, two important design specifications, dealing with the growth of perturbations during the

acceleration and deceleration phases of the implosion, were put forth. The first characterizes the susceptibility of the accelerating shell to breakup resulting from the growth of a perturbation exceeding the overall thickness of the in-flight shell. The in-flight aspect ratio (IFAR) is defined as the ratio of the mean radius of the peak density of the shell to the overall thickness of the shell. The IFAR for an implosion is usually evaluated when the shell has moved roughly a third of its radius. It has been found that if the IFAR exceeds a value of ~30, the shell is in danger of breaking apart during the acceleration phase of the implosion.[2,3] Keeping the IFAR below 30 requires careful consideration of the initial shell thickness and laser drive, while maintaining the high velocity necessary for ignition later in the implosion.

The second design parameter is the convergence ratio, defined as the ratio of the initial inner radius of the shell to its final radius at peak compression with alpha-particle deposition turned off. This parameter places a constraint on the drive uniformity to ensure that all portions of the shell will converge at the center, forming a spherically igniting hot spot. The convergence ratio is also related to the RT growth during the deceleration phase of the implosion, which can delay or preclude ignition. Target designs that require high convergence ratios (small hot spots) to reach ignition conditions can be at a high risk for failure. As such, it is generally considered that the convergence ratio should not exceed ~30. Rosen[36] pointed out that an excellent symmetry (at a 1% to 2% time-integrated uniformity level) is required for convergence ratios above 20. Targets with convergence ratios higher than 30 require exquisite control of all sources of nonuniformities in both the laser illumination and the target surface.

Multidimensional modeling of the effects of a multitude of physical imperfections in both the target and laser systems is essential to provide robust ignition target designs. Surface-quality limitations on the target interfaces (the outer surface of the target, the interface between the ablator and the DT-ice fuel, and the inner surface of the ice), power-balance limitations of the laser-irradiation system, and the single-beam nonuniformities associated with high-power laser beams all contribute to the degradation of target performance. Many authors have made approximations to these perturbations and, using analytic models describing perturbation growth, have determined the effects that the applied nonuniformities can have on target performance.

A useful example is that of Kishony and Shvarts,[860] who defined a "clean-volume" approach to the hot-spot formation. From Fig. 16-1 (taken from Ref. 58), the concept asserts that only the unperturbed central volume (of radius $R_{3\text{-D}}$) will participate in ignition. The evolving perturbations on the perimeter resulting from the deceleration-phase instability can prevent the hot spot from reaching ignition conditions in a timely manner. This requires the hot spot to be driven to an even smaller radius, which implicitly delays ignition, translates into a loss of fuel margin, and can precipitously lower the burnup fraction, leading to a much smaller gain. Ignition itself is precluded if the central clean volume becomes too small.

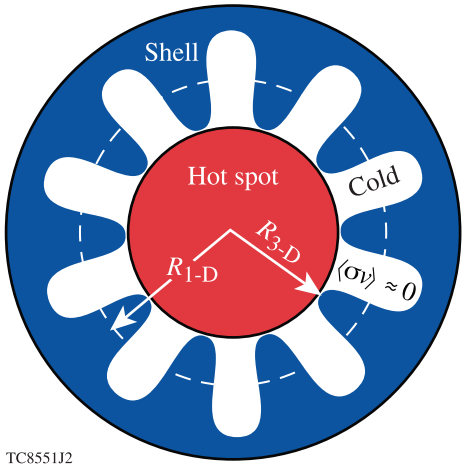

FIG. 16-1. Schematic of a typical ICF ignition hot spot, consisting of a central "clean" volume surrounded by a perturbed ice/vapor interface. The dashed line (of radius $R_{1\text{-D}}$) indicates the extent of the hot spot from a 1-D simulation. Only the clean volume (of radius $R_{3\text{-D}}$) can participate in ignition because of the increased thermal conduction and cooling in the vapor trapped between the growing spikes from the Rayleigh–Taylor instability. Reproduced with permission from Phys. Plasmas **17**, 058102 (2010). Copyright 2010 AIP Publishing LLC.

The various perturbations affecting direct-drive capsule implosions can generally be divided into those that are active during the acceleration phase and those that are active during the deceleration phase. The acceleration-phase perturbations, combining mainly the nonuniformity of laser drive and the surface roughness of the target, are particularly dangerous since they grow over long times and distances and can cause a complete breakup of the shell before deceleration begins. Additionally, even when shell breakup is avoided, much of the modulation spectrum acquired at the end of the acceleration phase feeds through the shell to the inner surface of the ice. Here, the ablation-front feedthrough couples in quadrature with the initial inner ice surface roughness to set the seed for perturbation growth during the deceleration phase. As such, significant effort has been focused on mitigating acceleration-mode perturbations.

Direct-drive–ignition designs start with relatively simple target and laser specifications. The earliest designs for which hydrodynamic instabilities were explicitly simulated in 2-D were originated by Verdon[861] and known as "all-DT designs." Details of the designs are given in Ref. 862. The targets are simply DT ice shells (of 325-μm thickness and 1.69-mm outer radius) with a very thin (~3-μm) CH overcoat. These designs are attractive because of their simplicity, the lack of a potentially unstable ablator-fuel interface, and high hydrodynamic efficiency. However, the relatively low absorption of the laser light in DT is not optimum for high-gain designs, particularly at lower energies, and preheat resulting from the two-plasmon–decay instability (Sec. X A) is greater for the lower-Z ablator. Early 2-D simulations of this design evaluated the effects of laser imprint and surface roughness and established the necessary specifications for a plausible attempt at ignition on the then-proposed NIF Laser System.[333] The simulations of Ref. 862 set stringent requirements for the quadrature sum of nonuniformities at the start of the acceleration phase to be ~0.2 μm (rms).

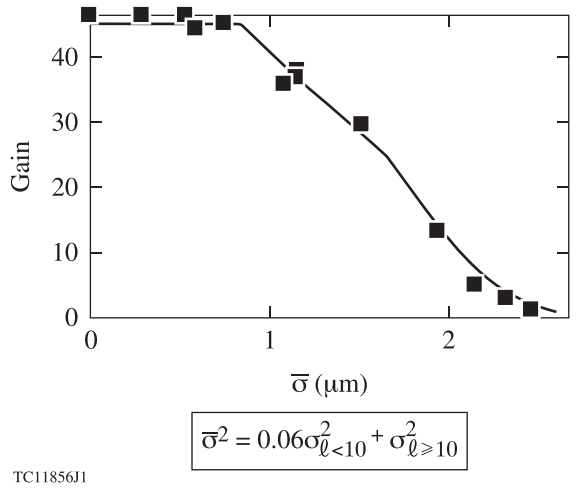

FIG. 16-2. Capsule gain as a function of $\bar{\sigma}$, defined as a weighted quadrature sum of modal amplitudes taken from the ice–vapor interface at the end of the acceleration phase of the implosion. Reproduced with permission from Phys. Plasmas **8**, 2315 (2001). Copyright 2001 AIP Publishing LLC.

Expanding on Verdon's analysis of the all-DT design, McKenty *et al.*[863] defined a single effective-nonuniformity parameter $\bar{\sigma}$ that added the spectral amplitudes of different nonuniformity sources in a weighted quadrature. This quantity was defined at the ice–vapor interface at the end of the acceleration phase. From 2-D simulations including the various nonuniformity sources, the target gain was found to depend on $\bar{\sigma}$, as shown in Fig. 16-2. This scaling led to a method to directly relate target performance of the OMEGA implosions to those proposed for the NIF.[318]

McKenty *et al.*[863] found that, in the absence of beam smoothing, perturbations resulting from laser imprint grew sufficiently to cause complete shell disruption and ignition failure. Figure 16-3(a) shows the density contours around the end of the acceleration phase for this case. In contrast, with SSD (Sec. VI C) at 1-THz bandwidth [Fig. 16-3(b)], the outer shell maintained its integrity and the implosion returned almost 70% of the 1-D predicted yield.

Another early design, by Gardner *et al.*[864] at NRL, is shown in Fig. 16-4. It employed a CH-foam ablator surrounding an inner layer of DT ice and was driven by a KrF laser pulse with a long, low-intensity foot. The low-density

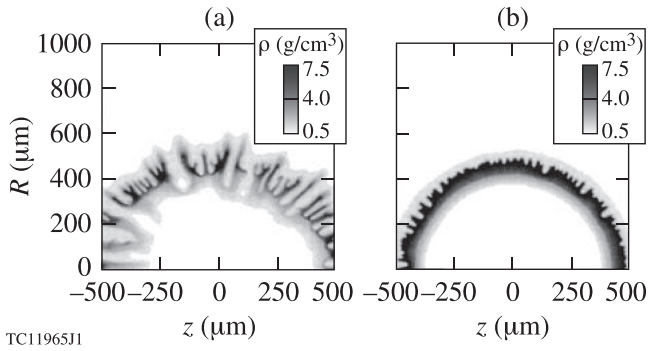

FIG. 16-3. Simulated density contours of the NIF all-DT ignition design at the end of the acceleration phase, (a) without SSD and (b) with 1-THz SSD. Reproduced with permission from Phys. Plasmas **8**, 2315 (2001). Copyright 2001 AIP Publishing LLC.

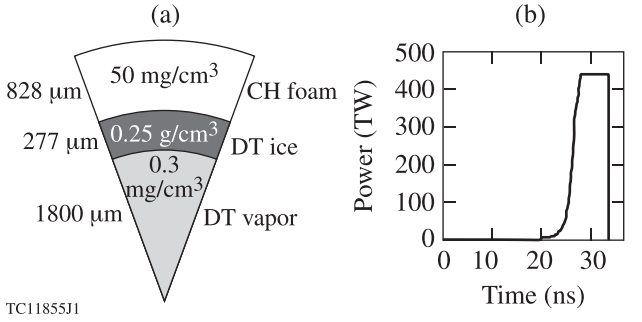

FIG. 16-4. (a) Sample wetted-foam ignition capsule and (b) its laser drive pulse, illustrating the relative simplicity of the target design. Reproduced with permission from Phys. Plasmas **5**, 1935 (1998). Copyright 1998 AIP Publishing LLC.

foam ablator (50 mg/cm^3) was used as an early attempt at adiabat shaping. Adiabat shaping (described in Sec. III A) involves setting the adiabat high at the ablation surface to mitigate the RT instability but keeping the adiabat low at the inner surface of the shell to maximize compression. In the design of Gardner *et al.*, the initial shock would be partially reflected at the foam–DT interface and preferentially raise the ablator adiabat above that of the fuel. However, the significant challenges of manufacturing such a target, as well as the subsequent development of laser pulses with adiabat-shaping pickets (Sec. III A), caused this design concept to be dropped.

NRL moved to incorporating high-Z overcoats in their designs, in an attempt to reduce laser imprint (Sec. VII B 2) and to increase the ablator adiabat relative to that of the fuel.[48,826,865] These designs had a thin (300-Å) Au layer on a DT-wetted CH-foam ablator on top of DT ice. NRL also began to exploit the zooming feature of echelon-free ISI smoothing (Sec. VI B) that enabled the laser spot to shrink during the implosion. With these modifications, simulations predicted that a 1.3-MJ KrF laser pulse would give a 1-D gain of 125, while the shell perturbations were predicted to be less than 20% for initial perturbations of 500 Å (Refs. 865 and 866).

Wetted-foam targets were first described by Sacks and Darling[867] in 1987. They have the advantage of higher absorption than all-DT targets because of the higher-Z carbon and may be desirable for inertial fusion energy applications because of their potential for mass production (Sec. XVII C 3). One-dimensional simulations by Skupsky *et al.*[859] demonstrated the improved target performance possible using wetted foam because of increased laser absorption. Collins *et al.*[868] presented a 1-MJ ignition design using a CH wetted-foam ablator that produced a gain of 32. This design combined decaying-shock adiabat shaping (Sec. III A) with the higher laser absorption of foam (86%, compared with 65% for the all-DT design). Using 2-D simulations and a $\bar{\sigma}$ analysis as in Fig. 16-2, this design was shown to be robust to the primary sources of implosion nonuniformity when 2-D SSD (Sec. VI C) was used. Several different implementations of SSD were modeled and compared. Three examples are shown in Fig. 16-5, where 2-D SSD with bandwidths of 1.3, 0.6, and 0.3 THz led to $\bar{\sigma}$ values of 0.37, 0.96, and 2.3 μm, respectively. Similar to the results found in Fig. 16-3, the

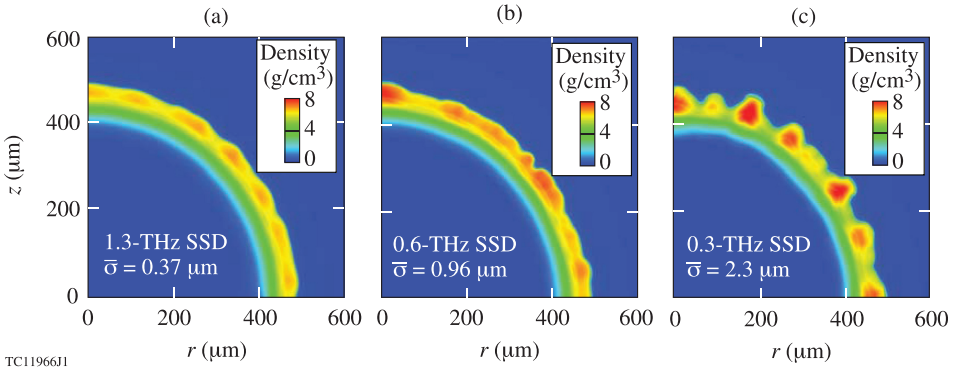

FIG. 16-5. Simulated density contours of the wetted-foam design of Ref. 868 at the end of the acceleration phase including 2-D SSD with bandwidths (a) 1.3, (b) 0.6, and (c) 0.3 THz. Reproduced with permission from Phys. Plasmas **14**, 056308 (2007). Copyright 2007 AIP Publishing LLC.

shell is intact and relatively unperturbed in the high-bandwidth case [Fig. 16-5(a)] but completely broken up in the lowest-bandwidth case [Fig. 16-5(c)].

Schmitt *et al.*[869] described a 2.5-MJ, KrF, wetted-foam target (2.375-mm outer radius with a 5-μm CH layer overcoating two concentric fuel layers, a 256-μm-thick wetted-foam layer over a 344-μm-thick DT shell). As shown in Fig. 16-6, density modulations resulting from a laser pulse without an early-time picket (spike) [Fig. 16-6(a)] can be mitigated with the addition of a picket pulse [Fig. 16-6(b)]. Schmitt *et al.* found that 2-D simulations of 1-D ignition designs not using the early-time laser picket could fail to reach breakeven. However, when the initial picket was applied, fully integrated 2-D simulations recovered 90% of the 1-D gain of 160. Schmitt *et al.* suggested that the main effect of the picket was to decrease the Richtmyer–Meshkov growth of surface perturbations, leaving a smaller seed perturbation for the RT instability to amplify. Picket pulses are now routinely included in most direct-drive–ignition designs. The design of Ref. 869 was one of those employed by the High Average Power Laser (HAPL) Program (Sec. XVII B 7).

Other researchers have investigated ablator systems that use radiation to reduce the impact of the RT instability [through either imprint mitigation (Sec. VII B) or adiabat shaping]. For example, Fujioka *et al.*[236] demonstrated stabilization of RT growth using brominated-plastic (CHBr) foils

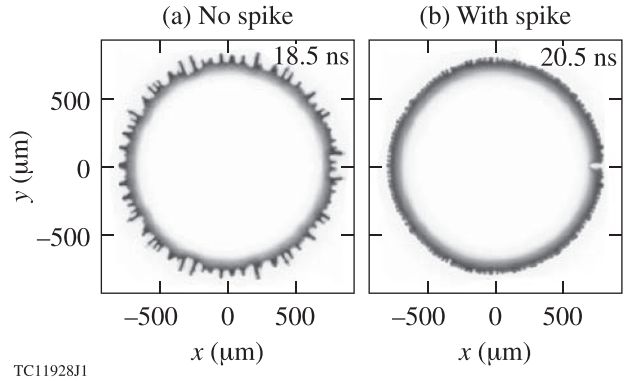

FIG. 16-6. Isodensity contours of two simulations of the same 2.5-MJ, KrF ignition design, both displayed after the shell has moved ~1600 μm. (a) Shell perturbations when a standard pulse is used. (b) Perturbations for the same shell and pulse except for the addition of an early-time laser picket. Reproduced with permission from Phys. Plasmas **11**, 2716 (2004). Copyright 2004 AIP Publishing LLC.

(Fig. 7-8). They incorporated this concept into an ignition design for the NIF that returned a gain of ~23 for an incident laser energy of 1.8 MJ.

With the development of triple-picket designs for adiabat shaping (Sec. III A), LLE moved away from wetted-foam designs and concentrated on CH ablators. By using the pickets to put the CH on a high adiabat, many of the benefits of foam were maintained (such as high absorption and low IFAR) without introducing new target fabrication issues. Most of this design work[197] has been applied to plans for polar-drive–ignition experiments on the NIF (Sec. VIII C).

High-gain designs have been developed for shock ignition (Sec. XV). The separation of the ignition pulse from the compression pulse in shock ignition makes it easier to ignite and produce high gains at smaller drive energies. For example, Schmitt *et al.*[811] obtained a 2-D gain of 102 using a total laser energy of 0.52 MJ and an ignitor pulse delivering 1000 TW in 200 ps. The 1-D gain curve from this design study also showed gains greater than 300 at less than 2 MJ of laser energy. Shock-ignition designs are reviewed in more detail in Secs. XV A and XV B.

Researchers at NRL leveraged the knowledge gained from the HAPL Program to call for the initiation of an intermediate, direct-drive, sub-MJ Fusion Test Facility (FTF).[870] This is intended to serve as a low-cost, high-repetition-rate ignition facility, providing an intermediate step from the proof-of-principle ignition experiments at the NIF to an eventual inertial fusion energy (IFE) reactor. The facility design incorporated and extended the HAPL database but required a target design energy scaled down from the original 2.5 MJ to the anticipated 500-kJ KrF laser. Colombant *et al.*[871] accomplished this, predicting 1-D target gains of just over 50. Other attractive features of the FTF include the implementation and testing of 5-Hz implosion operation and the application of functional focal-spot zooming. In support of the proposed FTF, Kehne *et al.*[872] at NRL demonstrated focal-spot zooming by a margin (4.5:1) that exceeds what would be required by the FTF. This is illustrated in Fig. 16-7, which shows a streaked image of light from the rear of a 60-μm CH target irradiated by the Nike laser. The target was initially irradiated with a large (~1.3-mm) focal spot (at time zero in Fig. 16-7). The spot was then changed mid-pulse to a small, zoomed spot (~0.3 mm), which launched a shock that was invisible until it overtook the first shock at ~2.9 ns and subsequently broke out of the rear of the target at ~3.5 ns.

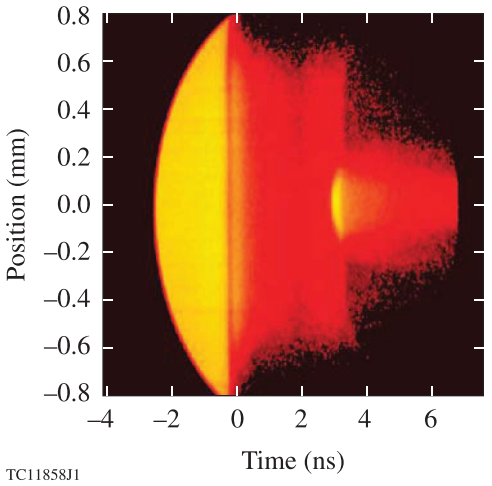

FIG. 16-7. Streak-camera image of the rear surface of a 60-μm-thick CH target, irradiated with an ~1.3-mm-diam spot that was later zoomed to ~0.3 mm; $t<0$: low-level prepulse effects; $0\,\text{ns}<t\leq 3\,\text{ns}$: large-spot effects; $t>3$ ns: small-spot effects. Reproduced with permission from Rev. Sci. Instrum. **84**, 013509 (2013). Copyright 2013 AIP Publishing LLC.

The eventual use of IFE as a viable energy source will require stable and robust target gains. Betti and Zhou[873] examined the scaling of target gain with MJ laser drivers and showed that the gain scales roughly as the burnup fraction divided by $v_{\text{imp}}^{1.3}$. Figure 16-8, taken from Ref. 38, schematically shows the relation between gain and v_{imp}, with the $v_{\text{imp}}^{-1.3}$ scaling. Conventional hot-spot ignition requires that v_{imp} be at least $\sim 3\times 10^7$ cm/s to produce a sufficient hot-spot temperature, but less than $\sim 5\times 10^7$ cm/s to avoid hydrodynamic instabilities that would quench the gain. The region below

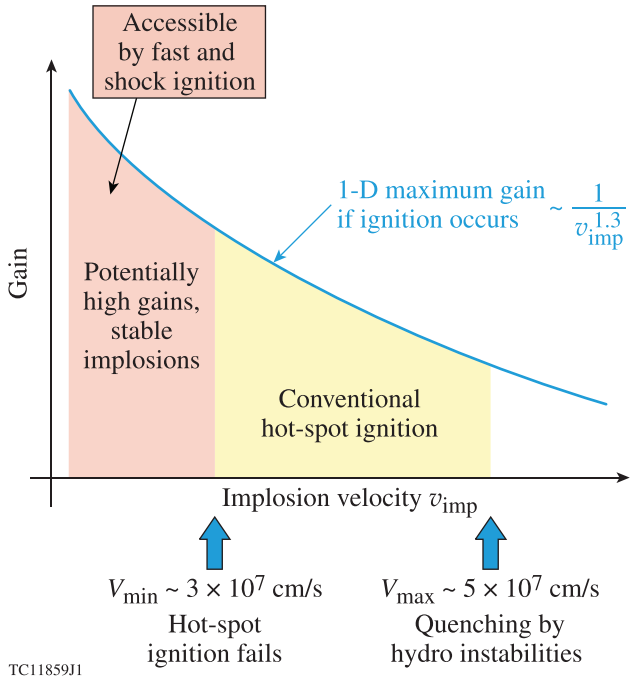

FIG. 16-8. Schematic illustrating the dependence of target gain G on the implosion velocity v_{imp}. The operational range of conventional hot-spot designs is limited to velocities between 3 and 5×10^7 cm/s with maximum target gains approaching 100. Reproduced with permission from Phys. Plasmas **15**, 055503 (2008). Copyright 2008 AIP Publishing LLC.

$\sim 3\times 10^7$ cm/s is accessible by either fast ignition (Sec. XIV) or shock ignition (Sec. XV).

Target gains in the conventional hot-spot ignition window generally fall in the range of ~50 to ~150. Hot-spot designs are therefore consistent with the requirements for inertial fusion energy (Sec. XVII). Higher gains are found for shock ignition, for shorter wavelengths, and with focal-spot zooming. A 1-D design study using shock ignition at lower laser energies (~250 to 600 kJ) found an ~70% increase in gain for a laser wavelength of 0.248 μm versus 0.35 μm and a similar increase in gain when comparing zooming with no zooming.[811] High-gain, shock-ignition designs are discussed in Sec. XV.

XVII. INERTIAL FUSION ENERGY (IFE)

The development of high-gain direct-drive target designs increases the prospects of a practical source of power from inertial confinement fusion. An IFE electrical power plant would emit no greenhouse emissions, have an abundant fuel supply, and produce limited and controllable radioactive waste. The potential of ICF has led to a multi-decade quest to design a suitable IFE-based power plant.

The first IFE reactor concept was published in Scientific American in 1971 by Lubin and Fraas.[874] Since that time, considerable progress has been made. While there is still much work to be done, the accomplishments to date, in virtually all the required technological areas, make a compelling case for advancing the development of IFE reactor concepts.

Section XVII A outlines the fundamental components of an IFE reactor and their function. Section XVII B describes the history of laser-driven IFE reactor design studies. Early designs adopted untested concepts for the laser technology, target physics, and other components, and then set about to produce the most economically attractive reactor. More recent studies have set out to establish viable concepts based on knowledge gained through experiments. Section XVII C discusses the current state of the art of the key technologies described in Sec. XVII A.

A. Fundamental IFE reactor components

In any direct-drive laser IFE system, an array of lasers precisely and uniformly illuminates a target that has been injected into a chamber. A generic drawing of a laser IFE chamber is shown in Fig. 17-1. The illumination is usually spherically symmetric, but other geometries have been considered. Upon ignition and burn, the target releases its fusion energy in the form of neutrons, charged particles, and x rays. The walls of the chamber collect this energy and, through a surrounding blanket, convert the energy into useful heat and breed tritium to close the fuel cycle. The process is repeated several times per second. The realization of this concept entails far more than just the development of a high-gain target.

Among the science and technologies that need to be developed are the following:

- A target gain with sufficient energy to power the laser and the energy conversion process and still produce enough electricity to make the process economically feasible.

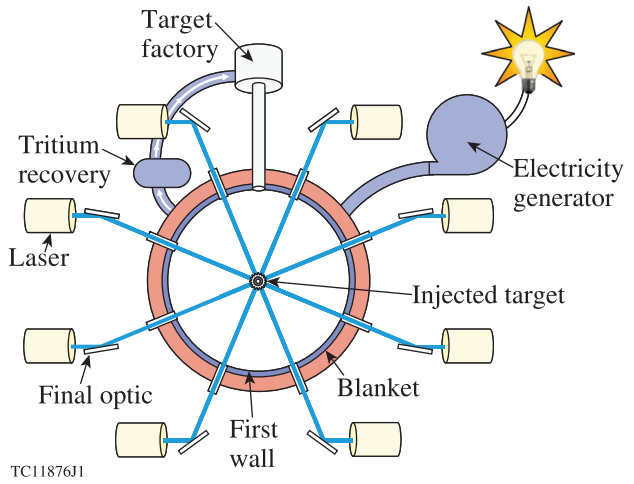

FIG. 17-1. Main components of the core of a direct-drive laser inertial fusion energy (IFE) reactor.

Conventional wisdom is that the product of laser efficiency (η) and gain (G) should be greater than 10, assuming 40% electrical conversion efficiency and an additional 10% energy gain in the blanket, to keep the recirculating power below 25%.

- A laser driver that can meet the fusion energy requirements for repetition rate, durability, efficiency, and cost, as well as the target-physics requirements for beam uniformity, wavelength, bandwidth, and pulse shape.
- An ability to manufacture targets economically at a shot rate of between 5 and 15 Hz.
- An ability to recycle, or preferably render completely gaseous, the target materials.
- A means to ensure that the (presumed) cryogenically cold targets survive injection into the hot chamber. Typically the chamber wall operates above 800 K for good thermal efficiency.
- An ability to place the target and/or steer the laser beams to achieve the illumination precision, accuracy, and uniformity required by the target physics.
- A final optic that withstands the high optical fluence of the incoming laser beams as well as the emissions from the target.
- A chamber first wall capable of repetitively withstanding the x-ray, ion, and neutron emissions from the fusion target.
- A mechanism to "restore" the chamber environment after each shot.
- A lithium-bearing chamber "blanket" (the layer outside the first wall) that can capture the neutrons, breed sufficient tritium to maintain a self-sufficient fuel cycle, and efficiently carry the reaction heat to the electricity generator.
- A system to process the tritium bred from the blanket and transport it to the target supply chain.

These requirements are interdependent, and any viable reactor concept must take them all into account. Other critical items such as reactor economics and issues related to obtaining regulatory approval are outside the scope of this review.

B. IFE reactor concepts

Many laser direct-drive IFE reactor concepts have been proposed over the years. The more-prominent concepts are described in this section.

1. BLASCON

BLASCON[874,875] (Fig. 17-2) was described by Lubin of the University of Rochester and Fraas of Oak Ridge National Laboratory in an article entitled simply, "Fusion by Laser," published in 1971 (Ref. 874) before the declassification of the concept of laser-induced compression. The authors stated, "Experiments indicate that energy-releasing fusion reactions can be initiated and to some extent controlled without a confining magnetic field by focusing a powerful laser pulse on a frozen pellet of fuel." In this concept, a flash-lamp–pumped Nd:glass laser, operating at a 1-μm wavelength, was proposed to perform two functions: The leading edge of the laser pulse would vaporize the pellet, while the main part of the pulse would heat the resulting plasma to fusion conditions. The duration of the main laser pulse was 0.1 ns. The reaction chamber was 5 m in diameter, and the inner wall of the chamber was protected from the neutrons by a vortex of liquid lithium. Bubbles in the lithium absorbed the shock of the target. The liquid lithium also provided the tritium breeding and the heat transfer for the steam cycle. The repetition rate was anticipated to be one pulse every 10 s.

While many of the details were unrealistic, a quick comparison with Fig. 17-1 shows that this paper outlined the approach to an IFE reactor that is still being followed today.

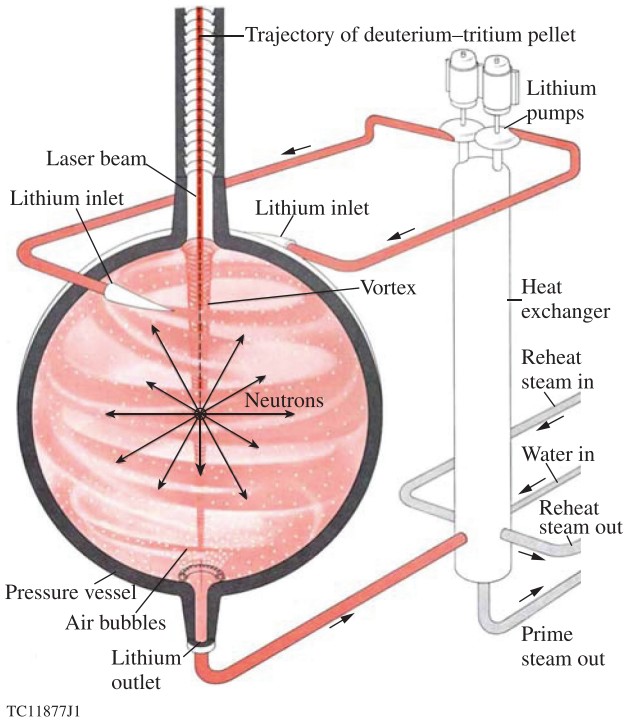

FIG. 17-2. Lubin/Fraas IFE reactor concept from June 1971 Scientific American.[874] Note the single-sided illumination and the laser and pellet injection along the same axis. Reproduced with permission from M. J. Lubin and A. P. Fraas, Sci. Am. **224**, 21 (1971). Copyright 1971 Scientific American, Inc.

The design included a nanosecond-pulse high-energy laser with pulse shaping (the laser power was varied with time) to drive the fusion reactions, a frozen DT target injected into a hot chamber, optics to guide the (single) laser beam to precisely illuminate the target, repetitively pulsed operation, a means to absorb the neutrons in a tritium-breeding blanket, and the need to protect the reaction chamber wall from the target emissions. Several reactor-concept design studies soon followed. They all recognized the challenges of developing a durable first wall and efficiently breeding tritium. As a result, most of these were distinguished largely by variations in the chamber/first-wall breeder design. Later concepts included economic models, some of which are still used today. However, all these concepts had two major shortcomings: they were woefully optimistic when it came to the (largely unknown) target physics, and they did not understand the laser requirements/capabilities. In addition, they all used only paper designs for the key technologies, none of which were tested at some level to see if they might work. One could argue that this was not the fault of the design studies since the target physics and laser technologies were unknown, and the design studies were not funded to test anything. Nevertheless, it was not until 1999–2009 that a reactor approach emerged that was based on better understood target-physics and illumination requirements, the state of the art in laser development, and the demonstration of the required technologies at some level in the laboratory.

Shortly after Ref. 874, a number of other papers appeared on the topic of laser-driven fusion energy. In 1973, Nuckolls *et al.*[86] concentrated on the implosion physics, quantitatively setting out the need for pulse shaping and short-wavelength light, and providing estimates of the required implosion velocity, compression ratio, and drive energy. While the latter was woefully optimistic (high gain was predicted at 10 kJ with a 0.5-μm laser wavelength), the authors acknowledged, "The development of new lasers is required if laser-fusion power production is to become a reality." Their Table I lists candidate lasers for fusion, including Nd:glass, CO_2, iodine, and (at the time undeveloped) xenon-based systems. Their table also included a hypothetical laser system that had all the ideal characteristics. Of the lasers that were listed, CO_2, iodine, and xenon are gas lasers and can meet the desired repetition-rate requirements, but xenon was the only one that did not require any frequency conversion. The authors also touched on some of the issues regarding the reaction chamber (including the need to withstand all the target emissions), the breeding blanket, and the power conversion cycle. The latter included a potential magnetohydrodynamic conversion cycle.

Also in 1973, Boyer from Los Alamos published an overview paper[82] that, while not introducing significant new research, gives a good history of the work done to that date, including the early work at Livermore and Los Alamos. The primary laser discussed is the CO_2 gas laser, and the possible need to convert its 10.6-μm wavelength to something shorter is acknowledged. The paper includes a concept for a reactor including a "wetted wall," in which a thin layer of lithium seeps through a porous wall and ablates off during each explosion to protect the inner wall. The paper also considered laser fusion as a means for space propulsion.

In a related paper published in 1973, Brueckner[88] from KMS Fusion took a first-principles approach to a laser fusion system. No specific designs or choices were made for any of the components, but calculations were carried out to define the required laser energy (500 kJ), the target gain (40), the wall loading from the emissions, the neutron load on the structure, and the tritium-breeding requirements. This paper also considered laser IFE for a fusion–fission hybrid and as a means for space propulsion.

2. Los Alamos laser-driven fusion reactor

This concept, shown in Fig. 17-3, was proposed by Booth *et al.*[876] in 1976. They made several seminal advances: They recognized the importance of symmetric illumination of a direct-drive target. They realized that there were many options for the laser drivers. However, even though their Table I acknowledged the use of solid-state lasers in contemporary laser fusion experiments, the only lasers they considered for energy had a gas medium. They were the first to realize that the emissions from the target that are incident on the first wall are not just the primary fusion products, but the secondary ions that are accelerated by these products. They considered a wide range of options to protect the first wall from these emissions, including vacuum, ambient gas, thick liquid, thin liquid wetted walls, and magnetic fields. They were the first to seriously study the materials that could be used in the first wall, chamber, and blanket.

3. SOLASE

SOLASE (Fig. 17-4) was a 1000-MWe IFE design study carried out by the University of Wisconsin.[877] The name was

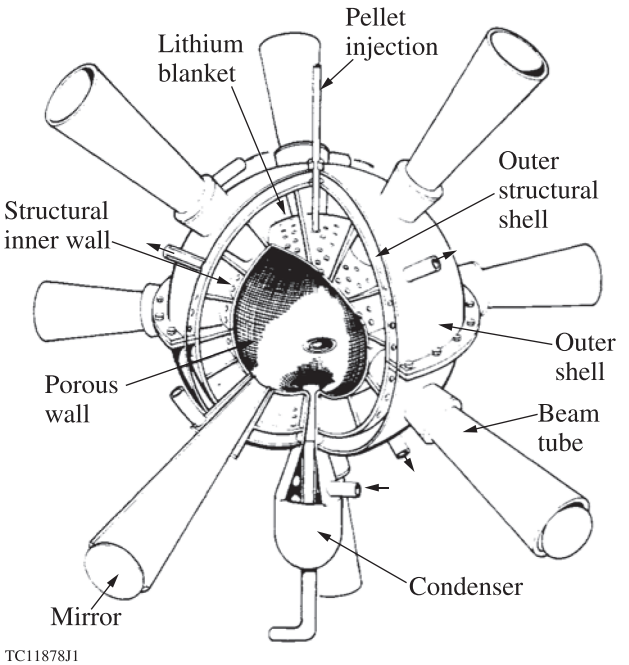

FIG. 17-3. Symmetric-illumination, wetted-liquid-wall reactor concept. Reprinted with permission from Booth *et al.*, Proc. IEEE **64**, 1460 (1976). Copyright 1976 IEEE.

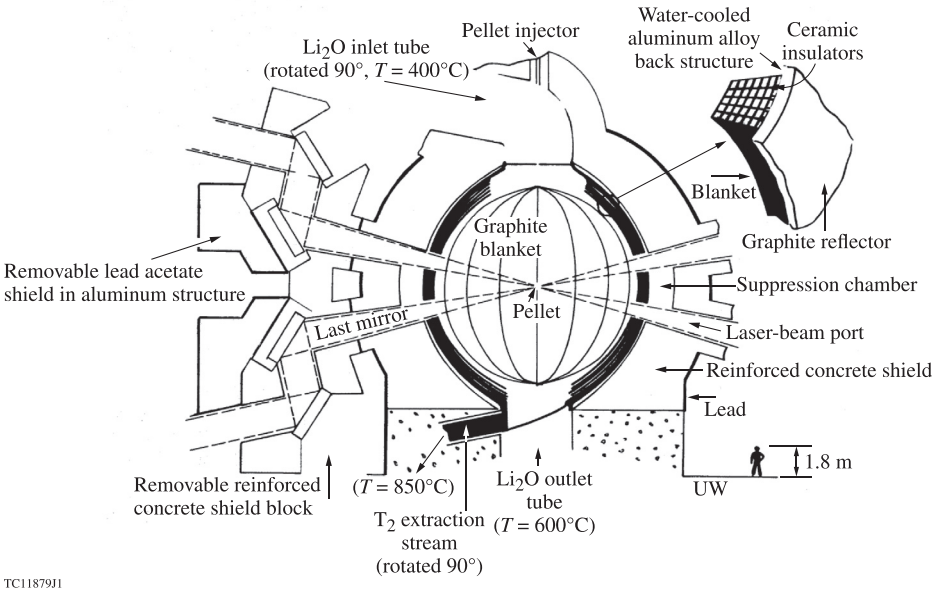

FIG. 17-4. SOLASE IFE reactor design (from Ref. 877).

inspired by a quote from James Joyce's *Finnegans Wake*.[878] The study explored a very wide range of parameters and technologies and was by far the most complete to that date—the report, published in 1977, is over 1100 pages long. No particular laser wavelength was specified, the authors appearing to be unaware of the requirement (not widely recognized in 1977) to go to as short a wavelength as possible. When specificity was required, the authors used a CO_2 gas laser (10.6-μm wavelength) as a stand-in. The laser efficiency was specified to be 6.7%, the repetition rate 20 Hz, and the laser energy on target 1 MJ. The required gain was calculated to be 150. For the first time, target fabrication was considered and costed. The target was composed of multiple layers and the fuel was a frozen DT shell, as in current designs. However, some of the target materials (polyvinyl alcohol, mercury, glass) would not be popular today. The target was injected using a variation of a gas gun. The target was illuminated directly from two sides by 12 laser beams. Unfortunately, the importance of symmetric irradiation was not recognized. Two-sided illumination was chosen because "uniform illumination is not truly compatible with the reactor requirements."

The final optics were copper, diamond turned on an aluminum baseplate and actively cooled to 50 °C to minimize temperature-driven neutron irradiation effects. The optic was protected from target x rays and debris by flowing gas. This was the first time the issue of damage to the final optic from radiation and target debris was considered, but the report missed the optical damage caused by the laser itself, which can be significant. The reaction chamber was 6 m in diameter and used a graphite structure. The wall was protected with a buffer gas of Xe. The Xe gas absorbs the x rays and ionic debris and forms a plasma that reradiates over a longer time, reducing the peak power incident on the wall. The blanket was flowing Li_2O. Extensive work was done on the design of the chamber, neutronics, mechanical design, and maintenance concepts. In many ways this set the methodology for future reactor design studies.

4. SIRIUS-T

SIRIUS-T was developed around 1990 at the University of Wisconsin[879] as a concept for an advanced tritium-production facility. (Two variations, denoted "M" and "C," explored applications as a materials development test bed and a commercial reactor.) It used symmetric illumination, and it was the first to identify the electron-beam–pumped krypton fluoride (KrF) laser as the laser of choice. This choice was based on the recognition that the target physics dictates a short wavelength (KrF lases at 0.248 μm) and on the relative ease in cooling a laser with a gas medium. With a 2.0-MJ laser, the target gain was calculated to be 50. The target was a DT shell illuminated by 92 symmetrically distributed beams around a spherical cavity of 4-m radius. The first wall consisted of graphite tiles bonded to an actively cooled vanadium structure (also a first), and, as in SOLASE, a 1.0-Torr Xe buffer gas protected the first wall. SIRIUS introduced the present-day concept of the grazing-incidence metal mirror (GIMM) for the final optic. With a repetition rate of 10 Hz and a blanket energy multiplication of 1.41 (Sec. XVII C 8), the facility was predicted to be energy self-sufficient with KrF laser efficiencies of 5% or greater. (Sethian *et al.*[880] projected that the overall wall-plug efficiency for an IFE-sized KrF system will be greater than 7%.) The study went into significant engineering detail on the first wall, chamber, blanket, and tritium-breeding components. For the first time, a study performed a detailed economic analysis of an IFE-based system.

5. SOMBRERO

SOMBRERO (solid moving breeder reactor) was developed[881] in 1991 as a conceptual study initially led by W. J. Schafer Associates, teamed with the University of Wisconsin, Bechtel, General Atomics, and Textron. Wisconsin did considerable work refining the concept after the initial study was completed.[881] SOMBRERO, shown in Fig. 17-5, was a

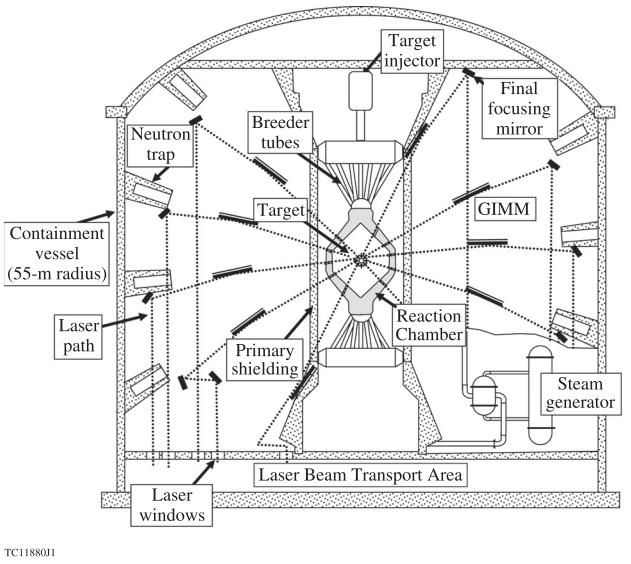

FIG. 17-5. SOMBRERO IFE reactor design (based on Ref. 881).

variation on the SIRIUS series to determine if it would be possible to build a commercially viable IFE-based source of electricity. The concept utilized direct-drive targets with symmetric illumination from 60 laser beams. It used a 3.4-MJ KrF laser, had a target gain of 118, and operated at 6.7 Hz. The laser efficiency was estimated to be 7%. The design used the waste heat from the laser gas to boost the overall efficiency to 9%. The gross power output of 1360 MWe gave a net power output of 1000 MWe. The study showed that direct-drive laser fusion would be economically attractive with these numbers. SOMBRERO was the most-complete design study to that date since it both addressed and identified solutions for virtually every component in the system from target injection to tritium breeding. It was also the first to compute a complete "threat spectrum" of emissions from the target and design a first wall chamber to withstand these emissions. The chamber was constructed of a low-activation carbon/carbon composite and the blanket consisted of a moving bed of solid Li_2O particles ($\sim$400 μm in diameter) flowing through the chamber by gravity. The chamber first wall was conical in shape (to facilitate the moving solid breeder) with a nominal radius of 6.5 m. The wall was protected with a background of 0.5 Torr of Xe gas. A discussion of the economics related to SOMBRERO is given by Meier and von Rosenberg.[882]

6. Prometheus-L

Prometheus-L was a symmetric direct-drive, 4-MJ KrF reactor design based on a concept developed by McDonnell Douglas Aerospace[883] in 1994 (Fig. 17-6). Instead of using $\sim$60 electron-beam–pumped amplifiers, it used 960 electric-discharge laser amplifiers to enhance driver reliability by allowing for random outages of one (or several) amplifiers. Pulse shaping was carried out through optical switchyards. None of these technologies had been tried on the required scale. The target gain was estimated to be 124, and the total plant power was 1000 MWe. The final optical elements were GIMMs, as in SIRIUS, and the chamber first wall and blanket structure were made of low-activation SiC. A thin liquid-lead layer protected the wall. This film was expected to be evaporated by the target emissions and then uniformly recondense as a liquid film on the wall in time for the next pulse. Helium was used as the heat exchange fluid (along with the lead from the first wall protection) and the breeder was lithium-oxide pellets.

7. High Average Power Laser (HAPL) Program

The HAPL Program was jointly initiated by NRL and the Lawrence Livermore National Laboratory to develop high-average-power KrF and diode-pumped solid-state lasers (DPSSL) that could meet the requirements for IFE. The NRL component grew into a multi-institutional, multidisciplinary program[884] dedicated to addressing the broad range of scientific and technological issues related to IFE. The program, which operated from 1999 to 2009, departed from previous studies in that its goal was to demonstrate the technologies needed for IFE in scalable tests. Its design studies took into account scientific and technological realities. The program used the Sombrero Design Study, particularly its economic analysis, as the starting point. The program was multidisciplinary and, for the first time in the development of laser-driven IFE approaches, the physics and components were developed together as an integrated

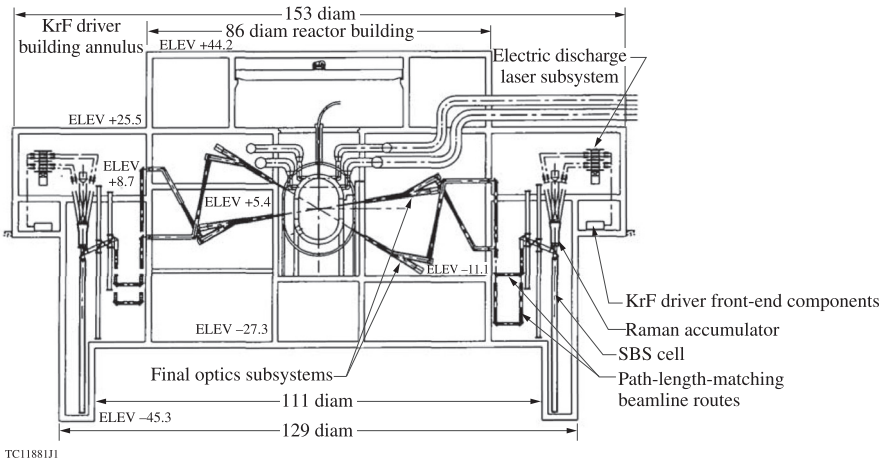

FIG. 17-6. Prometheus-L IFE reactor design. Reprinted with permission from L. M. Waganer, Fusion Eng. Des. **25**, 125 (1994). Copyright 1994 Elsevier.

coherent system. The HAPL Program addressed the breeding, structural, and materials requirements that are unique to direct-drive IFE. It did not address issues beyond the first wall such as materials damage and the energy conversion cycle, as these are common to other approaches and are being addressed within the much-larger worldwide magnetic fusion program. For the first time, multiple technology solutions for the same component were evaluated. The resulting natural competition between potential technologies had the beneficial effect of accelerating progress. When the program ended in 2009, solutions to almost all the key components had been identified and many had been evaluated with scalable tests.

One notable accomplishment of the HAPL Program was the development of two different laser technologies—the electron-beam–pumped KrF laser[880] and the DPSSL.[885] It was the first time that a solid-state laser had been considered for an IFE reactor since the original BLASCON design in 1971. By the time the HAPL Program ended, it had demonstrated that both laser architectures could run at the required repetition rate, and that both have the potential to be scaled to IFE energies while meeting the requirements for durability and efficiency.

C. IFE technologies

This section provides brief summaries of the state of the art of key components needed for laser direct drive, shown schematically in Fig. 17-1. Many of these were developed under the HAPL Program, and alternative solutions were developed in other endeavors.

1. Lasers

According to present understanding, a laser for a fusion power plant should have a total energy of around 0.5–1.5 MJ, a wavelength $\lesssim 0.35\ \mu$m, a smooth-enough focal profile to minimize the modulations that can seed hydrodynamic instabilities, an ability to produce the pulse shapes required by the target physics, and an efficiency greater than 6% to 7%. These numbers are based on recent high-performance target designs (Secs. XV and XVI). The efficiency requirement is based on projected target gains of at least 150 and the requirement that the gain–efficiency product exceed 10.

Both the KrF and DPSSL lasers have been developed sufficiently for one to confidently predict that they can meet both the target-physics and reactor requirements for direct-drive laser fusion. The KrF laser naturally has a very smooth focal profile. The fundamental wavelength of the DPSSL is 1.05 μm, requiring it to be frequency converted to 0.35 μm. Also, the DPSSL beam focal profile must be smoothed with SSD (Sec. VI C). The KrF laser has a ready ability to decrease (zoom) the laser spot to follow the imploding pellet (see Sec. VI B and the discussion of Fig. 16-7). Zooming can be implemented on DPSSL laser systems by using separate beams for different portions of the laser pulse as described in the introduction to Sec. XV. KrF lasers, because of their inherent attributes (beam smoothing, high bandwidth, short wavelength), are predicted by Schmitt *et al.*[811] to produce higher gain than a frequency-tripled DPSSL for shock-ignition targets (Sec. XV). For example, from Fig. 15-3, a KrF-driven shock-ignition target is predicted to have a 1-D gain of 200 at 1 MJ, while the gain for a similar DPSSL target is 150 at 1.5 MJ. Nevertheless, the best choice for IFE must also be based on factors such as cost and reliability, the achieved and demonstrated overall laser efficiency, and most importantly, a demonstration of a power-plant–sized laser beamline.

2. Final optics and illumination geometry

It is generally considered that a large number of beams are required for adequate uniformity (Sec. VI). The OMEGA Laser System uses 60 beams that are symmetrically distributed around the target chamber in a "stretched soccer-ball" geometry,[164] located at the vertices of the hexagons and pentagons. The HAPL Program, like SOMBRERO, also adopted a 60-beam geometry,[884] but it is entirely possible that an IFE reactor could use a different number of beams, depending on the laser technology selected.

The final optical element is the only one that is directly exposed to the steady barrage of pulsed x rays, ions, and neutrons from the fusion reactions. The upstream optics can be protected somewhat by means of a series of reflectors and labyrinths. Of the three emission species, neutrons cause the most damage since they displace atoms and cause the optic to swell, thereby compromising the high optical quality needed to precisely illuminate the target. A solution developed at the University of California at San Diego (UCSD) is to make the final optic from a thin, high-reflective coating on a silicon-carbide or aluminum base. Both are known to be resistant to neutron-induced swelling. Orienting the optic at a grazing incidence (5°) to the incoming laser beams minimizes the laser fluence on the reflector. The design of the optical train calls for this GIMM to withstand a laser fluence of 1.5–2 J/cm^2 per pulse. Research has shown that a reflector made of a solid solution alloy of aluminum with 5% copper can withstand well above 3.5 J/cm^2 for over 10^7 pulses with no damage.[886] Neutrons scattering off the GIMM will be incident on the upstream optics. GIMMs are large (typically 3.44 m × 4.05 m, at a distance of 24 m from the target[884]), so it is desirable to make these upstream optics using something other than a GIMM. Studies at Oak Ridge National Laboratory, in conjunction with Penn State University, have shown that a tailored high-reflectivity, high-laser-damage-threshold, dielectric mirror can withstand the expected neutron flux for the 30-year life of the plant.[887] Further research may show that it is possible to use a dielectric as the final optical element.

An alternative to the GIMM is to use two large (1-m-diam) Fresnel lenses on either side of a thick shielded neutron "pinhole." These have the advantage of being considerably more compact. Studies by Livermore showed that maintaining the optic at 500 °C will anneal the neutron damage from each pulse if the lens is less than 1 cm thick.[888] This approach only works at the DPSSL wavelength of 0.35 μm since no annealing was observed at 0.248 μm.

3. Target fabrication

A typical high-gain target used for IFE reactor studies has a foam shell filled with frozen DT (Sec. XVI). The shell has a few-microns-thick seal coat on its outer surface that is coated with an Au–Pd alloy several hundred angstroms thick. The Au–Pd provides an IR reflector to protect the target from thermal loading from the wall during injection and helps the target physics (Sec. VII B 2). The inner surface of the DT is smooth (Sec. XIII) to minimize the seed for hydrodynamic instabilities. The foam helps the target physics (Sec. XVI) and also allows for a more thermally robust DT ice layer as shown by Hoffer *et al.*[889] The smoothness of the DT surface grown over foam in a toroidal geometry that serves as a surrogate for millimeter-size foam shells was demonstrated in Ref. 889 to be fairly constant over a broad range of temperatures—15 K to 19 K. (This experiment must be repeated with a spherical foam shell to ensure that there are no geometry-dependent differences.) Experiments with OMEGA-scale foam shells (0.9-mm diameter) show that a uniformly thick and smooth DT ice layer with an rms roughness $\lesssim 1\,\mu$m can be achieved inside a spherical foam target (Fig. 13-4). To allow for the inevitable warm-up that occurs during injection into the chamber, the target can be injected at 16 K, allowed to heat up to 19 K, and still be below the triple point and possess an acceptable DT layer.

IFE targets must be made on a mass-production basis (of the order of 10^6 per day depending on the repetition rate). In one approach, the shells have been made in a triple-orifice droplet generator. This has produced up to 22 shells per minute and has demonstrated the precision called for by current high-gain target designs.[890] Methods to apply both a seal coat and an Au–Pd overcoat have been demonstrated.[884] Using chemical plant analysis, the total cost of a target was estimated to be less than \$0.17 (Ref. 891). A concept for mass layering has been developed based on a fluidized bed and shown to work with a room-temperature surrogate.[892] In another approach, the science of microfluidics is used to make the foam shells.[893,894] Electric fields are used to dispense, create, and manipulate minute oil and water droplets to produce a spherically concentric layer, which can then be polymerized with heat or light. The step in which the foam shell is formed is shown in Fig. 17-7. This approach has the potential to mass produce very high precision shells at low cost and to combine some of the other target fabrication steps including, possibly, filling with DT and layering.

The tritium inventory of an IFE power plant has been estimated by Schwendt *et al.*[895] to be less than 1 kg.

4. Target injection

A new target can be injected into the chamber only after the blast from the preceding explosion has cleared. At 5 Hz, this suggests a velocity of 50–400 m/s, depending on the chamber configuration and recovery time. The target is both fragile and cryogenic, so an insulating sabot is required in the injector. General Atomics demonstrated a gas-gun approach in which the sabot is separated and captured before entering the chamber.[896] With non-cryogenic targets the system ran at 5 Hz and achieved velocities of 400 m/s. Another approach, proposed by Robson,[897] is to accelerate a ferromagnetic sabot in a fixed magnetic field gradient. Analysis showed that this could stably accelerate the sabot to the required velocities. The cup-shaped sabot would be rapidly slowed and captured by a reversed magnetic field at the muzzle, thereby allowing the target to continue into the chamber.

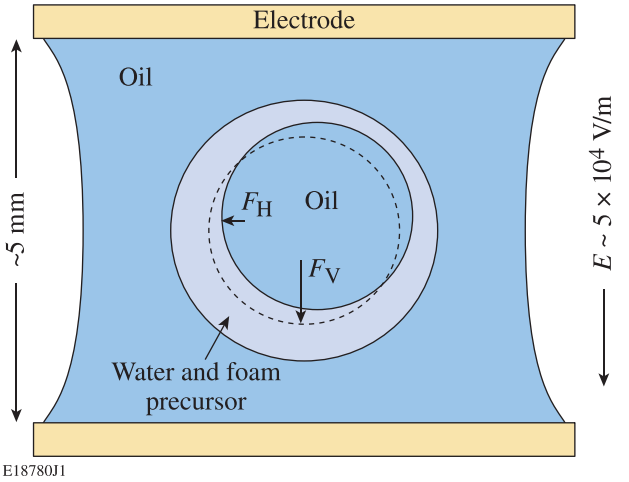

FIG. 17-7. Concept for the formation of a concentric foam shell for a direct-drive target. A solution containing the chemicals needed to make the foam is suspended between two oil droplets. An oscillating electric field at 20 MHz causes the inner oil droplet to center itself by virtue of the horizontal and vertical dielectrophoretic forces F_H and F_V, respectively. Heat or infrared light is then used to initiate the polymerization.

5. Target tracking/placement

As part of the HAPL program, General Atomics and UCSD demonstrated a tracking concept that meets the target design specifications for pointing accuracy.[898] The concept uses a low-intensity laser to reflect off the Au–Pd coating on the target surface. This glint reflection is then used to direct the final steering mirrors to precisely illuminate the target. The glint uniquely defines the position of the target and can be clearly seen from all angles in one half of the target chamber, so only two glint lasers are needed. The system was demonstrated using a surrogate target in free fall and steered a low-power laser beam to engage the target with an accuracy of better than 28 μm, very close to the estimate of 1% of the target radius that is believed to be required.[162]

6. Target survival into the chamber

The target must not heat up above the triple point of DT (19.79 K) as it is injected into a chamber. The HAPL designs called for starting the target at 16 K and allowing it to warm up to 19 K during injection. This is still comfortably below the triple point. As discussed above, this can be done for a foam target without compromising the DT surface smoothness. As discussed in Sec. XVII C 7, the preferred chamber designs have a near-vacuum background, so the only heat load on the target is from the wall at ~1000 K, or ~0.2 W/cm^2. For a long time, getting the target to survive this journey into the

chamber was considered quite daunting. However, simulations from UCSD[899] and experiments at Los Alamos[900] suggest that this is indeed feasible. These experiments used cylindrical geometry as a surrogate for a spherical target and applied a sudden heat flux (60% of the prototypical value) to a DT ice layer. The initial target temperature was 19 K and the target contained no foam (so was not as robust to temperature swings). The layer did not degrade for over 20 ms, the time that the target is expected to take to traverse the 5.5-m-radius chamber. During this time, the target is expected to warm up by 3 K. It is therefore expected that an IFE target in which the DT is wicked into a foam shell and capable of starting at temperatures as low as 16 K should survive injection into the chamber.

7. First wall

The reaction chamber is one of the most challenging aspects in developing any practical fusion power plant. It has six primary functions: (1) ensure that the target survives injection and/or placement (i.e., does not deform or melt); (2) allow the driver energy to be coupled to the target with the required precision; (3) repeatedly withstand the pulsed emissions of x rays, ions, and neutrons from the fusion reactions; (4) recover conditions to allow the next target to be shot; (5) provide a means to convert heat to electrical power; and (6) provide a means to breed and recover tritium.

A typical chamber design has a first wall that directly sees the target emissions, an encasing lithium-bearing blanket, and a structure to hold everything together. The chamber and target design depend on each other since each target design produces a distinct "threat spectrum" (energy partitioning among the reaction products) that must be withstood by the chamber's first wall. In a direct-drive IFE power plant, about 75% of the fusion energy is incident on the wall as neutrons, about 23% as energetic ions, and the remaining 2% as x rays.[901] (See also Table I of Ref. 884.) The major challenge for short-term first wall survival is the heat loading from x rays and ions, as these deposit their considerable energy in a shallow depth ($<5\,\mu$m) and in short periods of time ($<1\,\mu$s). Neutrons, while a long-term problem, deposit their energy volumetrically throughout the wall and blanket and therefore do not contribute to the instantaneous heat load. The average neutron loading is similar to that of a magnetic fusion reactor, the main difference being that one is pulsed and the other is continuous.

Five main chamber configurations have been considered for direct-drive IFE (see Ref. 884 and references therein): (1) solid wall—vacuum in chamber; (2) magnetic intervention—vacuum in chamber; (3) solid wall—gas in chamber; (4) replaceable solid wall—vacuum in chamber; and (5) thick liquid walls (or thin liquid-protected walls). To date, the first three configurations have had the most development.

The most appealing chamber configuration (option 1) uses a solid wall and maintains the chamber in vacuum. This ensures high-fidelity laser propagation, puts the least strain on cryogenic target survival during injection, and is the easiest to restore to the same conditions before the next shot. The major issues are the extreme cyclical heat loading on the first wall and helium retention. The heat loading appears to be solved by making the first wall from a 1-mm-thick tungsten armor layer bonded to a ferritic-steel substrate structure. Experiments in subscale tests,[899] backed with modeling,[902] show that this morphology can survive the continual cyclical heat load.

Helium retention occurs when the high-energy (several-MeV) helium ions produced by the target are driven 2–5 μm deep into the surface. Because the helium migration distance is 50–100 nm, comparable to the grain dimensions, the helium coalesces into bubbles at the grain boundaries. The resulting buildup in helium pressure exfoliates the surface. Experiments at Oak Ridge and the University of North Carolina showed that the problem is somewhat mitigated because the natural IFE cycle of pulsed implantation followed by a high-temperature pulse can enhance the helium diffusion.[903] Another solution conceived by UCSD and tested on a small-scale electrostatic trap at the University of Wisconsin was to make the first wall of a fibrous tungsten material whose diameter is smaller than the migration distance. Then, no matter where the helium is stopped, it is always less than a migration length from a free surface. Experiments showed that the expected mass loss from an IFE-sized chamber would be only the equivalent of a 1-μm layer of solid material over the equivalent of 450 days of operation.[904]

8. Blanket

Both Pb-17Li (83% lead, 17% lithium) and FLIBE (fluorine–lithium–beryllium) blankets have been evaluated specifically for laser-direct-drive IFE tritium breeding and power conversion. Tritium is produced when the neutrons react with lithium in one of two ways. One reaction is exothermic (i.e., boosts the fusion energy): $^6\mathrm{Li} + \mathrm{n} = \mathrm{T} + \mathrm{He}^4 + 4.78\,\mathrm{MeV}$. The other is endothermic and results in a neutron n′ (of lower energy) along with the triton: $^7\mathrm{Li} + \mathrm{n} = \mathrm{T} + \mathrm{He}^4 + \mathrm{n}' - 2.47\,\mathrm{MeV}$. Since the natural abundances are 7.42% ^{6}Li, 92.58% ^{7}Li, it might appear that the blanket will consume net energy. However, because the cross sections are dramatically different, there is a net energy release. The cross section for the ^{6}Li reaction increases with decreasing energy and is large even at thermal energies, while the ^{7}Li reaction is suppressed below 2.5 MeV. Therefore, all the lower-energy daughter neutrons produced by the ^{7}Li reaction will eventually take part in subsequent ^{6}Li reactions (Ref. 905 and references therein). This means that the blanket can convert each 14-MeV neutron into more than one triton, as well as increase the energy output. Neutrons can be multiplied, to increase the tritium production or boost the blanket energy, by adding Be or Pb to the blanket and making use of the reaction $\mathrm{n} + {}^9\mathrm{Be} + 3\,\mathrm{MeV} = 2\,\mathrm{He}^4 + \mathrm{n}' + \mathrm{n}''$, or $\mathrm{n} + \mathrm{Pb} + 10\,\mathrm{MeV} = \mathrm{Pb} + \mathrm{n}' + \mathrm{n}''$. Here n′ and n″ denote lower-energy neutrons.

Breeder systems are designed using simulation codes that have been benchmarked with experiments with a neutron emitter in the center of a lithium sphere.[906] The goal is to minimize the 14.1-MeV neutrons that are lost in the blanket support structure, through optical ports, etc. In principle, all that is needed is an average tritium-breeding ratio (TBR)

greater than 1, but more may be needed when fusion is first introduced into the economy to provide a surplus of tritium to fuel the startup of new reactors.[907] In continuous operation, an average TBR of 1.05 should suffice. From the discussion above, a breeder can readily have a local TBR ~ 1.5 (Ref. 908) and, since the beam ports take up less than 2% of the solid angle, there are generally no issues meeting this requirement.[909] A discussion of plasma, nuclear, material, and technological conditions in which tritium self-sufficiency can be obtained is given in Ref. 910. A complete conceptual tritium recovery and purification system has been designed for direct-drive IFE.[911]

In addition to the power conversion schemes from the earlier studies, three new power conversion concepts have recently been evaluated (Ref. 912 and references therein). All are based on a three-compressor/two-intercooler Brayton Cycle.[912] One solid wall concept uses a more-conventional reduced-activation F82H steel wall and tungsten armor. The initial chamber temperature is 550 °C and the electrical conversion efficiency is estimated to be 38%. A second solid-wall concept uses a more-advanced ferritic steel wall and tungsten armor. The chamber operates at 700 °C, and the electrical conversion efficiency can be as high as 49%. For a magnetic intervention chamber concept (in which magnetic fields divert the ions away from the chamber first wall), the first wall is a SiC/SiC composite, which runs at 1000 °C, and the conversion efficiency is predicted to be 50%.

ACKNOWLEDGMENTS

The contributions of A. R. Bell, R. Epstein, D. H. Froula, I. V. Igumenshchev, T. J. Kessler, R. H. Lehmberg, C. K. Li, F. J. Marshall, P. M. Nilson, C. Ren, A. L. Velikovich, S. C. Wilks, and M. D. Wittman in reviewing portions of this manuscript and providing many valuable suggestions are greatly appreciated. A useful discussion with R. G. Evans is acknowledged. The authors appreciate the considerable contributions of the referee in providing a very thorough review and suggesting numerous improvements. The authors are also very much aware of the efforts, dedication, and ingenuity of many thousands of people over many decades who have contributed to the growth of the direct-drive ICF program.

This material is based upon work supported by the Department of Energy National Nuclear Security Administration under Award Number DE-NA0001944, the University of Rochester, and the New York State Energy Research and Development Authority. The support of the DOE does not constitute an endorsement by the DOE of the views expressed in this article.

[1]J. Nuckolls, L. Wood, A. Thiessen, and G. Zimmerman, "Laser compression of matter to super-high densities: Thermonuclear (CTR) applications," Nature **239**, 139 (1972).
[2]J. D. Lindl, "Development of the indirect-drive approach to inertial confinement fusion and the target physics basis for ignition and gain," Phys. Plasmas **2**, 3933 (1995).
[3]J. D. Lindl, *Inertial Confinement Fusion: The Quest for Ignition and Energy Gain Using Indirect Drive* (Springer-Verlag, New York, 1998).
[4]D. R. Speck, E. S. Bliss, J. A. Glaze, J. W. Herris, F. W. Holloway, J. T. Hunt, B. C. Johnson, D. J. Kuizenga, R. G. Ozarski, H. G. Patton, P. R. Rupert, G. J. Suski, C. D. Swift, and C. E. Thompson, "The Shiva Laser-Fusion Facility," IEEE J. Quantum Electron. **17**, 1599 (1981).
[5]E. M. Campbell, J. T. Hunt, E. S. Bliss, D. R. Speck, and R. P. Drake, "Nova experimental facility (invited)," Rev. Sci. Instrum. **57**, 2101 (1986).
[6]C. A. Haynam, P. J. Wegner, J. M. Auerbach, M. W. Bowers, S. N. Dixit, G. V. Erbert, G. M. Heestand, M. A. Henesian, M. R. Hermann, K. S. Jancaitis, K. R. Manes, C. D. Marshall, N. C. Mehta, J. Menapace, E. Moses, J. R. Murray, M. C. Nostrand, C. D. Orth, R. Patterson, R. A. Sacks, M. J. Shaw, M. Spaeth, S. B. Sutton, W. H. Williams, C. C. Widmayer, R. K. White, S. T. Yang, and B. M. Van Wonterghem, "National Ignition Facility laser performance status," Appl. Opt. **46**, 3276 (2007).
[7]M. Lubin, E. Goldman, J. Soures, L. Goldman, W. Friedman, S. Letzring, J. Albritton, P. Koch, and B. Yaakobi, "Single- and multi-beam laser pellet fusion experiments," in *Plasma Physics and Controlled Nuclear Fusion Research 1974* (IAEA, Vienna, 1975), Vol. II, pp. 459–477.
[8]J. M. Soures, T. C. Bristow, H. Deckman, J. Delettrez, A. Entenberg, W. Friedman, J. Forsyth, Y. Gazit, G. Halpern, F. Kalk, S. Letzring, R. McCrory, D. Peiffer, J. Rizzo, W. Seka, S. Skupsky, E. Thorsos, B. Yaakobi, and T. Yamanaka, "A review of high density, laser driven, implosion experiments at the Laboratory for Laser Energetics," in *Laser Interaction and Related Plasma Phenomena*, edited by H. J. Schwarz, H. Hora, M. J. Lubin, and B. Yaakobi (Plenum Press, New York, 1981), Vol. 5, pp. 463–481.
[9]J. M. Soures, R. J. Hutchison, S. D. Jacobs, L. D. Lund, R. L. McCrory, and M. C. Richardson, "OMEGA: A short-wavelength laser for fusion experiments," in *Proceedings of the 10th IEEE/NPSS Symposium on Fusion Engineering, SOFE'83* (IEEE, New York, 1983), pp. 1392–1397.
[10]T. R. Boehly, D. L. Brown, R. S. Craxton, R. L. Keck, J. P. Knauer, J. H. Kelly, T. J. Kessler, S. A. Kumpan, S. J. Loucks, S. A. Letzring, F. J. Marshall, R. L. McCrory, S. F. B. Morse, W. Seka, J. M. Soures, and C. P. Verdon, "Initial performance results of the OMEGA laser system," Opt. Commun. **133**, 495 (1997).
[11]J. S. Ladish, "Helios, a 20 TW CO_2 Laser Fusion Facility," in *Laser 79 Opto-Electronics: Proceedings of the Fourth Conference* (IPC Science and Technology Press, Ltd., Guildford, England, 1979), pp. 294–301.
[12]C. Yamanaka, Y. Kato, Y. Izawa, K. Yoshida, T. Yamanaka, T. Sasaki, M. Nakatsuka, T. Mochizuki, J. Kuroda, and S. Nakai, "Nd-doped phosphate glass laser systems for laser-fusion research," IEEE J. Quantum Electron. **17**, 1639 (1981).
[13]C. Yamanaka, S. Nakai, T. Yamanaka, Y. Izawa, K. Mima, K. Nishihara, Y. Kato, T. Mochizuki, M. Yamanaka, M. Nakatsuka, and T. Yabe, "Pellet implosion and interaction studies by GEKKO XII green laser," in *Laser Interaction and Related Plasma Phenomena*, edited by H. Hora and G. H. Miley (Plenum Press, New York, 1986), Vol. 7, pp. 395–419.
[14]I. Ross, M. White, J. Boon, D. Craddock, A. Damerell, R. Day, A. F. Gibson, P. Gottfeldt, D. J. Nicholas, and C. Reason, "Vulcan—A versatile high-power glass laser for multiuser experiments," IEEE J. Quantum Electron. **17**, 1653 (1981).
[15]M. Andre, J. C. Courteille, J. Y. Le Gall, and P. Rovati, "OCTAL: A new neodymium glass laser built in the Centre d'Etudes de Limeil for laser fusion experiments," Proc. SPIE **164**, 8–16 (1979).
[16]N. G. Basov, O. N. Krokhin, G. V. Sklizkov, S. I. Fedotov, and A. S. Shikanov, "A powerful laser setup and investigation of the efficiency of high temperature heating of a plasma," Sov. Phys.-JETP **35**, 109 (1972).
[17]N. Hopps, C. Danson, S. Duffield, D. Egan, S. Elsmere, M. Girling, E. Harvey, D. Hillier, M. L. Norman, S. P. Parker, P. Treadwell, D. Winter, and T. H. Bett, "Overview of laser systems for the Orion facility at the AWE," Appl. Opt. **52**, 3597 (2013).
[18]G. A. Kirillov, V. M. Murugov, V. T. Punin, and V. I. Shemyakin, "High power laser system ISKRA V," Laser Part. Beams **8**, 827 (1990).
[19]J. Ebrardt and J. M. Chaput, "LMJ project status," J. Phys.: Conf. Ser. **112**, 032005 (2008).
[20]G. A. Kirillov, G. G. Kocheasov, A. V. Bessarab, S. G. Garanin, L. S. Mkhitarian, V. M. Murugov, S. A. Sukharev, and N. V. Zhidkov, "Status of laser fusion research at VNIIEF (Arzamas-16)," Laser Part. Beams **18**, 219 (2000).
[21]X. T. He, W. Y. Zhang, and the Chinese ICF team, "Advances in the national inertial fusion program of China," EPJ Web Conf. **59**, 01009 (2013).
[22]S. P. Obenschain, S. E. Bodner, D. Colombant, K. Gerber, R. H. Lehmberg, E. A. McLean, A. N. Mostovych, M. S. Pronko, C. J. Pawley, A. J. Schmitt, J. D. Sethian, V. Serlin, J. A. Stamper, C. A. Sullivan, J. P.

Dahlburg, J. H. Gardner, Y. Chan, A. V. Deniz, J. Hardgrove, T. Lehecka, and M. Klapisch, "The Nike KrF Laser Facility: Performance and initial target experiments," Phys. Plasmas **3**, 2098 (1996).
[23]E. Fabre, F. Amiranoff, R. Fabbro, C. Garban-Labaune, J. Virmont, M. Weinfeld, F. David, and R. Pellat, "Effect of laser wavelength on interaction studies for inertial fusion," in *Plasma Physics and Controlled Nuclear Fusion Research 1980* (IAEA, Vienna, 1981), Vol. 2, pp. 263–272.
[24]G. Velarde and N. Carpintero-Santamaría, *Inertial Confinement Nuclear Fusion: A Historical Approach by Its Pioneers* (Foxwell & Davies (UK) Ltd., London, 2007).
[25]S. Atzeni and J. Meyer-ter-Vehn, *The Physics of Inertial Fusion: Beam Plasma Interaction, Hydrodynamics, Hot Dense Matter*, International Series of Monographs on Physics (Clarendon Press, Oxford, 2004).
[26]*La Fusion Thermonucléaire Inertielle par Laser* (Part 1: L'Interaction Laser-Matière; Part 2: La Fusion par Confinement Inertiel; Part 3: Les Techniques Exp érimentales et Numériques), edited by R. Dautray and J.-P. Watteau (Eyrolles, Paris, 1993).
[27]J. J. Duderstadt and G. A. Moses, *Inertial Confinement Fusion* (Wiley, New York, 1982).
[28]W. L. Kruer, *The Physics of Laser Plasma Interactions*, Frontiers in Physics Vol. 73, edited by D. Pines (Addison-Wesley, Redwood City, CA, 1988).
[29]C. Yamanaka, *Introduction to Laser Fusion* (Harwood Academic Publishers, New York, 1991).
[30]*Nuclear Fusion by Inertial Confinement: A Comprehensive Treatise*, edited by G. Velarde, Y. Ronen, and J. M. Martínez-Val (CRC Press, Boca Raton, FL, 1993).
[31]R. P. Drake, *High-Energy-Density Physics: Fundamentals, Inertial Fusion, and Experimental Astrophysics, Shock Wave and High Pressure Phenomena* (Springer, Berlin, 2006).
[32]S. Pfalzner, *An Introduction to Inertial Confinement Fusion*, Series in Plasma Physics (Taylor & Francis, New York, 2006).
[33]K. A. Brueckner and S. Jorna, "Laser-driven fusion," Rev. Mod. Phys. **46**, 325 (1974).
[34]G. H. McCall, "Laser-driven implosion experiments," Plasma Phys. **25**, 237 (1983).
[35]R. L. McCrory and J. M. Soures, "Inertially confined fusion," in *Laser-Induced Plasmas and Applications*, edited by L. J. Radziemski and D. A. Cremers (Marcel Dekker, New York, 1989), pp. 207–268.
[36]M. D. Rosen, "The physics issues that determine inertial confinement fusion target gain and driver requirements: A tutorial," Phys. Plasmas **6**, 1690 (1999).
[37]J. D. Lindl, P. Amendt, R. L. Berger, S. G. Glendinning, S. H. Glenzer, S. W. Haan, R. L. Kauffman, O. L. Landen, and L. J. Suter, "The physics basis for ignition using indirect-drive targets on the National Ignition Facility," Phys. Plasmas **11**, 339 (2004).
[38]R. L. McCrory, D. D. Meyerhofer, R. Betti, R. S. Craxton, J. A. Delettrez, D. H. Edgell, V. Yu. Glebov, V. N. Goncharov, D. R. Harding, D. W. Jacobs-Perkins, J. P. Knauer, F. J. Marshall, P. W. McKenty, P. B. Radha, S. P. Regan, T. C. Sangster, W. Seka, R. W. Short, S. Skupsky, V. A. Smalyuk, J. M. Soures, C. Stoeckl, B. Yaakobi, D. Shvarts, J. A. Frenje, C. K. Li, R. D. Petrasso, and F. H. Séguin, "Progress in direct-drive inertial confinement fusion research," Phys. Plasmas **15**, 055503 (2008).
[39]S. E. Bodner, "Critical elements of high gain laser fusion," J. Fusion Energy **1**, 221 (1981).
[40]J. D. Huba, "NRL Plasma Formulary," Naval Research Laboratory, Washington, DC, Report No. NRL/PU/6790–13-589 (2013).
[41]H. Azechi, N. Miyanaga, R. O. Stapf, K. Itoga, H. Nakaishi, M. Yamanaka, H. Shiraga, R. Tsuji, S. Ido, K. Nishihara, Y. Izawa, T. Yamanaka, and C. Yamanaka, "Experimental determination of fuel density-radius product of inertial confinement fusion targets using secondary nuclear fusion reactions," Appl. Phys. Lett. **49**, 555 (1986).
[42]V. N. Goncharov, T. C. Sangster, T. R. Boehly, S. X. Hu, I. V. Igumenshchev, F. J. Marshall, R. L. McCrory, D. D. Meyerhofer, P. B. Radha, W. Seka, S. Skupsky, C. Stoeckl, D. T. Casey, J. A. Frenje, and R. D. Petrasso, "Demonstration of the highest deuterium-tritium areal density using multiple-picket cryogenic designs on OMEGA," Phys. Rev. Lett. **104**, 165001 (2010).
[43]V. N. Goncharov, "Cryogenic deuterium and deuterium-tritium direct–drive implosions on Omega," in *Laser-Plasma Interactions and Applications*, Scottish Graduate Series, edited by P. McKenna, D. Neely, R. Bingham, and D. A. Jaroszynski (Springer, Switzerland, 2013), Chap. 7, pp. 135–183.
[44]J. D. Lindl and W. C. Mead, "Two-dimensional simulation of fluid instability in laser-fusion pellets," Phys. Rev. Lett. **34**, 1273 (1975).
[45]R. Betti, M. Umansky, V. Lobatchev, V. N. Goncharov, and R. L. McCrory, "Hot-spot dynamics and deceleration-phase Rayleigh–Taylor instability of imploding inertial confinement fusion capsules," Phys. Plasmas **8**, 5257 (2001).
[46]R. Betti, K. Anderson, V. N. Goncharov, R. L. McCrory, D. D. Meyerhofer, S. Skupsky, and R. P. J. Town, "Deceleration phase of inertial confinement fusion implosions," Phys. Plasmas **9**, 2277 (2002).
[47]J. H. Gardner, S. E. Bodner, and J. P. Dahlburg, "Numerical simulation of ablative Rayleigh–Taylor instability," Phys. Fluids B **3**, 1070 (1991).
[48]S. E. Bodner, D. G. Colombant, J. H. Gardner, R. H. Lehmberg, S. P. Obenschain, L. Phillips, A. J. Schmitt, J. D. Sethian, R. L. McCrory, W. Seka, C. P. Verdon, J. P. Knauer, B. B. Afeyan, and H. T. Powell, "Direct-drive laser fusion: Status and prospects," Phys. Plasmas **5**, 1901 (1998).
[49]T. J. B. Collins, A. Poludnenko, A. Cunningham, and A. Frank, "Shock propagation in deuterium-tritium-saturated foam," Phys. Plasmas **12**, 062705 (2005).
[50]Ya. B. Zel'dovich and Yu. P. Raĭzer, "Introduction to the gasdynamics of shock waves," in *Physics of Shock Waves and High-Temperature Hydrodynamic Phenomena*, edited by W. D. Hayes and R. F. Probstein (Dover Publications, Mineola, NY, 2002), Vol. I, Chap. I, pp. 45–49.
[51]V. N. Goncharov, J. P. Knauer, P. W. McKenty, P. B. Radha, T. C. Sangster, S. Skupsky, R. Betti, R. L. McCrory, and D. D. Meyerhofer, "Improved performance of direct-drive inertial confinement fusion target designs with adiabat shaping using an intensity picket," Phys. Plasmas **10**, 1906 (2003).
[52]K. Anderson and R. Betti, "Laser-induced adiabat shaping by relaxation in inertial fusion implosions," Phys. Plasmas **11**, 5 (2004).
[53]T. J. B. Collins, J. P. Knauer, R. Betti, T. R. Boehly, J. A. Delettrez, V. N. Goncharov, D. D. Meyerhofer, P. W. McKenty, S. Skupsky, and R. P. J. Town, "Reduction of the ablative Rayleigh–Taylor growth rate with Gaussian picket pulses," Phys. Plasmas **11**, 1569 (2004).
[54]J. P. Knauer, K. Anderson, R. Betti, T. J. B. Collins, V. N. Goncharov, P. W. McKenty, D. D. Meyerhofer, P. B. Radha, S. P. Regan, T. C. Sangster, V. A. Smalyuk, J. A. Frenje, C. K. Li, R. D. Petrasso, and F. H. Séguin, "Improved target stability using picket pulses to increase and shape the ablator adiabat," Phys. Plasmas **12**, 056306 (2005).
[55]M. Tabak, Lawrence Livermore National Laboratory, private communication (2005).
[56]K. Anderson and R. Betti, "Theory of laser-induced adiabat shaping in inertial fusion implosions: The decaying shock," Phys. Plasmas **10**, 4448 (2003).
[57]R. Betti, K. Anderson, J. Knauer, T. J. B. Collins, R. L. McCrory, P. W. McKenty, and S. Skupsky, "Theory of laser-induced adiabat shaping in inertial fusion implosions: The relaxation method," Phys. Plasmas **12**, 042703 (2005).
[58]R. Betti, P. Y. Chang, B. K. Spears, K. S. Anderson, J. Edwards, M. Fatenejad, J. D. Lindl, R. L. McCrory, R. Nora, and D. Shvarts, "Thermonuclear ignition in inertial confinement fusion and comparison with magnetic confinement," Phys. Plasmas **17**, 058102 (2010).
[59]C. D. Zhou and R. Betti, "Hydrodynamic relations for direct-drive fast-ignition and conventional inertial confinement fusion implosions," Phys. Plasmas **14**, 072703 (2007).
[60]P. Franken, "Optical masers: Engineering phase beginning for lasers," Electronic Design (15 March 1962), pp. 24–26.
[61]W. I. Linlor, "Plasmas produced by laser bursts," Bull. Am. Phys. Soc. **7**, 440 (1962).
[62]J. M. Dawson, "On the production of plasma by giant pulse lasers," Phys. Fluids **7**, 981 (1964).
[63]J. Dawson, P. Kaw, and B. Green, "Optical absorption and expansion of laser-produced plasmas," Phys. Fluids **12**, 875 (1969).
[64]N. G. Basov and O. N. Krokhin, "The conditions of plasma heating by the optical generator radiation," in *Quantum Electronics: Proceedings of the Third International Congress*, edited by P. Grivet and N. Bloembergen (Dunod Éditeur, Paris, 1964), Vol. 1, pp. 1373–1377.
[65]N. G. Basov and O. N. Krokhin, "Conditions for heating up of a plasma by the radiation from an optical generator," Sov. Phys.-JETP **19**, 123 (1964).
[66]N. G. Basov, S. D. Zakharov, P. G. Kryukov, Yu. V. Senatskii, and S. V. Chekalin, "Experiments of neutron observation by focusing power laser emission on the surface of lithium deuteride," JETP Lett. **8**, 14 (1968).

[67]N. G. Basov, P. G. Kriukov, S. D. Zakharov, Yu. V. Senatsky, and S. V. Tchekalin, "O-11–Experiments on the observation of neutron emission at a focus of high-power laser radiation on a lithium deuteride surface," IEEE J. Quantum Electron. **4**, 864 (1968).
[68]G. W. Gobeli, J. C. Bushnell, P. S. Peercy, and E. D. Jones, "Observation of neutrons produced by laser irradiation of lithium deuteride," Phys. Rev. **188**, 300 (1969).
[69]F. Floux, D. Cognard, L. G. Denoeud, G. Piar, D. Parisot, J. L. Bobin, F. Delobeau, and C. Fauquignon, "Nuclear fusion reactions in solid-deuterium laser-produced plasma," Phys. Rev. A **1**, 821 (1970).
[70]N. G. Basov, V. A. Boiko, S. M. Zakharov, O. N. Krokhin, and G. V. Sklizkov, "Generation of neutrons in a laser CD_2 plasma heated by pulses of nanosecond duration," JETP Lett. **13**, 489 (1971).
[71]S. W. Mead, R. E. Kidder, J. E. Swain, F. Rainer, and J. Petruzzi, "Preliminary measurements of x-ray and neutron emission from laser-produced plasmas," Appl. Opt. **11**, 345 (1972).
[72]K. Büchl, K. Eidmann, P. Mulser, H. Salzmann, and R. Sigel, "Plasma production with a Nd laser and non-thermal effects," in *Laser Interaction and Related Plasma Phenomena*, edited by H. J. Schwarz and H. Hora (Plenum Press, New York, 1972), Vol. 2, pp. 503–514.
[73]F. Floux, J. F. Benard, D. Cognard, and A. Saleres, "Nuclear DD reactions in solid deuterium laser created plasma," in *Laser Interaction and Related Plasma Phenomena*, edited by H. J. Schwarz and H. Hora (Plenum Press, New York, 1972), Vol. 2, pp. 409–431.
[74]J. W. Shearer and W. S. Barnes, "Mechanisms for production of neutron-emitting plasma by subnanosecond laser-pulse heating," Phys. Rev. Lett. **24**, 92 (1970); **24**, 432(E) (1970).
[75]N. G. Basov, Yu. S. Ivanov, O. N. Krokhin, Yu. A. Mikhailov, G. V. Sklizkov, and S. I. Fedotov, "Neutron generation in spherical irradiation of a target by high-power laser radiation," JETP Lett. **15**, 417 (1972).
[76]G. H. McCall, F. Young, A. W. Ehler, J. F. Kephart, and R. P. Godwin, "Neutron emission from laser-produced plasmas," Phys. Rev. Lett. **30**, 1116 (1973).
[77]C. Yamanaka, T. Yamanaka, T. Sasaki, K. Yoshida, M. Waki, and H. B. Kang, "Anomalous heating of a plasma by a laser," Phys. Rev. A **6**, 2335 (1972).
[78]N. G. Basov, V. A. Boiko, S. M. Zakharov, O. N. Krokhin, Yu. A. Mikhailov, G. V. Sklizkov, and S. I. Fedotov, "Mechanisms of neutron generation in a laser plasma," JETP Lett. **18**, 184 (1973).
[79]J. Soures, L. M. Goldman, and M. Lubin, "Short-pulse-laser-heated plasma experiments," Nucl. Fusion **13**, 829 (1973).
[80]N. G. Basov, E. G. Gamaly, O. N. Krokhin, Yu. A. Mikhailov, G. V. Sklizkov, and S. I. Fedotov, "Investigation of plasma parameters at the spherical heating of the isolated solid target by high-power laser radiation," in *Laser Interaction and Related Plasma Phenomena*, edited by H. J. Schwarz and H. Hora (Plenum Press, New York, 1974), Vol. 3B, pp. 553–590.
[81]S. E. Bodner, G. F. Chapline, and J. DeGroot, "Anomalous ion heating in a laser heated plasma," Plasma Phys. **15**, 21 (1973).
[82]K. Boyer, "Laser-initiated fusion—Key experiments looming," Astronaut. Aeronaut. **11**, 28 (1973).
[83]J. W. Daiber, A. Hertzberg, and C. E. Wittliff, "Laser-generated implosions," Phys. Fluids **9**, 617 (1966).
[84]R. E. Kidder, "Application of lasers to the production of high-temperature and high-pressure plasma," Nucl. Fusion **8**, 3 (1968).
[85]S. W. Mead, "Plasma production with a multibeam laser system," Phys. Fluids **13**, 1510 (1970).
[86]J. Nuckolls, J. Emmett, and L. Wood, "Laser-induced thermonuclear fusion," Phys. Today **26**(8), 46 (1973).
[87]M. N. Rosenbluth and R. Z. Sagdeev, "Laser fusion and parametric instabilities," Comments Plasma Phys. Controlled Fusion **1**, 129 (1972).
[88]K. A. Brueckner, "Laser driven fusion," IEEE Trans. Plasma Sci. **1**, 13 (1973).
[89]R. R. Johnson, "Observation of *D–T* neutron production from laser driven implosions," Bull. Am. Phys. Soc. **19**, 886 (1974).
[90]G. Charatis, J. Downward, R. Goforth, B. Guscott, T. Henderson, S. Hildum, R. Johnson, K. Moncur, T. A. Leonard, F. Mayer, S. Segall, L. Siebert, D. Solomon, and C. Thomas, "Experimental study of laser driven compression of spherical glass shells," in *Plasma Physics and Controlled Nuclear Fusion Research 1974* (IAEA, Vienna, 1974), Vol. II, pp. 317–335.
[91]C. E. Thomas, "Laser fusion target illumination system," Appl. Opt. **14**, 1267 (1975).
[92]P. M. Campbell, G. Charatis, and G. R. Montry, "Laser-driven compression of glass microspheres," Phys. Rev. Lett. **34**, 74 (1975).
[93]V. W. Slivinsky, H. G. Ahlstrom, K. G. Tirsell, J. Larsen, S. Glaros, G. Zimmerman, and H. Shay, "Measurement of the ion temperature in laser-driven fusion," Phys. Rev. Lett. **35**, 1083 (1975).
[94]N. M. Ceglio and L. W. Coleman, "Spatially resolved α emission from laser fusion targets," Phys. Rev. Lett. **39**, 20 (1977).
[95]R. A. Lerche, L. W. Coleman, J. W. Houghton, D. R. Speck, and E. K. Storm, "Laser fusion ion temperatures determined by neutron time-of-flight techniques," Appl. Phys. Lett. **31**, 645 (1977).
[96]W. I. Linlor, "Ion energies produced by laser giant pulse," Appl. Phys. Lett. **3**, 210 (1963).
[97]P. Langer, G. Tonon, F. Floux, and A. Ducauze, "7A11–Laser induced emission of electrons, ions, and x rays from solid targets," IEEE J. Quantum Electron. **2**, 499 (1966).
[98]J. W. Shearer, S. W. Mead, J. Petruzzi, F. Rainer, J. E. Swain, and C. E. Violet, "Experimental indications of plasma instabilities induced by laser heating," Phys. Rev. A **6**, 764 (1972).
[99]J. N. Olsen, G. W. Kuswa, and E. D. Jones, "Ion-expansion energy spectra correlated to laser plasma parameters," J. Appl. Phys. **44**, 2275 (1973).
[100]A. W. Ehler, "High-energy ions from a CO_2 laser-produced plasma," J. Appl. Phys. **46**, 2464 (1975).
[101]B. H. Ripin, P. G. Burkhalter, F. C. Young, J. M. McMahon, D. G. Colombant, S. E. Bodner, R. R. Whitlock, D. J. Nagel, D. J. Johnson, N. K. Winsor, C. M. Dozier, R. D. Bleach, J. A. Stamper, and E. A. McLean, "X-ray emission spectra from high-power-laser-produced plasmas," Phys. Rev. Lett. **34**, 1313 (1975).
[102]N. K. Winsor and D. A. Tidman, "Laser target model," Phys. Rev. Lett. **31**, 1044 (1973).
[103]R. E. Kidder and J. W. Zink, "Decoupling of corona and core of laser-heated pellets," Nucl. Fusion **12**, 325 (1972).
[104]J. S. Clarke, H. N. Fisher, and R. J. Mason, "Laser-driven implosion of spherical DT targets to thermonuclear burn conditions," Phys. Rev. Lett. **30**, 89 (1973); **30**, 249(E) (1973).
[105]R. J. Mason, "The calculated performance of structured laser fusion pellets," Nucl. Fusion **15**, 1031 (1975).
[106]W. C. Mead, R. A. Haas, W. L. Kruer, D. W. Phillion, H. N. Kornblum, J. D. Lindl, D. R. MacQuigg, and V. C. Rupert, "Observation and simulation of effects on parylene disks irradiated at high intensities with a 1.06-μm laser," Phys. Rev. Lett. **37**, 489 (1976).
[107]V. W. Slivinsky, H. N. Kornblum, and H. D. Shay, "Determination of suprathermal electron distributions in laser-produced plasmas," J. Appl. Phys. **46**, 1973 (1975).
[108]J. F. Kephart, R. P. Godwin, and G. H. McCall, "Bremsstrahlung emission from laser–produced plasmas," Appl. Phys. Lett. **25**, 108 (1974).
[109]K. A. Brueckner, "Energy deposition in laser-heated plasmas," Phys. Rev. Lett. **36**, 677 (1976).
[110]K. A. Brueckner, "Fast-electron production in laser-heated plasma," Nucl. Fusion **17**, 1257 (1977).
[111]E. L. Lindman, "Absorption and transport in laser plasmas," J. Phys. **38**, C6–9 (1977).
[112]D. W. Forslund, J. M. Kindel, K. Lee, E. L. Lindman, and R. L. Morse, "Theory and simulation of resonant absorption in a hot plasma," Phys. Rev. A **11**, 679 (1975).
[113]D. W. Forslund, J. M. Kindel, and K. Lee, "Theory of hot-electron spectra at high laser intensity," Phys. Rev. Lett. **39**, 284 (1977).
[114]K. Estabrook and W. L. Kruer, "Properties of resonantly heated electron distributions," Phys. Rev. Lett. **40**, 42 (1978).
[115]H. Hora, "Nonlinear confining and deconfining forces associated with the interaction of laser radiation with plasma," Phys. Fluids **12**, 182 (1969).
[116]K. G. Estabrook, E. J. Valeo, and W. L. Kruer, "Two-dimensional relativistic simulations of resonance absorption," Phys. Fluids **18**, 1151 (1975).
[117]N. M. Ceglio and J. T. Larsen, "Spatially resolved suprathermal x-ray emission from laser-fusion targets," Phys. Rev. Lett. **44**, 579 (1980).
[118]See National Technical Information Service Document No. UCRL79788 (E. K. Storm, J. T. Larsen, J. H. Nuckolls, H. G. Ahlstrom, and K. R. Manes, "Simple scaling model for exploding pusher targets," Lawrence Livermore National Laboratory, Livermore, CA, UCRL-79788, 1977). Copies may be obtained from the National Technical Information Service, Springfield, VA 22161.
[119]See National Technical Information Service Document No. LA7218MS (D. V. Giovanielli and C. W. Cranfill, "Simple model for exploding pusher targets," Los Alamos National Laboratory, Los Alamos, NM, LA-

7218-MS, 1978). Copies may be obtained from the National Technical Information Service, Springfield, VA 22161.
[120]M. D. Rosen and J. H. Nuckolls, "Exploding pusher performance—A theoretical model," Phys. Fluids **22**, 1393 (1979).
[121]B. Ahlborn and M. H. Key, "Scaling laws for laser driven exploding pusher targets," Plasma Phys. **23**, 435 (1981).
[122]N. G. Denisov, "On a singularity of the field of an electromagnetic wave propagated in an inhomogeneous plasma," Sov. Phys.-JETP **4**, 544 (1957).
[123]V. L. Ginzburg, *Propagation of Electromagnetic Waves in Plasmas*, edited by W. L. Sadowski and D. M. Gallik (Gordon and Breach, New York, 1961), Sec. 20, pp. 377–403.
[124]J. P. Freidberg, R. W. Mitchell, R. L. Morse, and L. I. Rudsinski, "Resonant absorption of laser light by plasma targets," Phys. Rev. Lett. **28**, 795 (1972).
[125]K. R. Manes, V. C. Rupert, J. M. Auerbach, P. Lee, and J. E. Swain, "Polarization and angular dependence of 1.06-μm laser-light absorption by planar plasmas," Phys. Rev. Lett. **39**, 281 (1977).
[126]See National Technical Information Service Document No. UCRL5002177V2 [J. J. Thomson, W. L. Kruer, A. B. Langdon, C. E. Max, and W. C. Mead, "Laser light absorption on a steepened, rippled critical-density surface," *Laser Program Annual Report 1977*, Lawrence Livermore National Laboratory, Livermore, CA, UCRL-50021-77 (1978), Vol. 2, pp. 4-40–4-43]. Copies may be obtained from the National Technical Information Service, Springfield, VA 22161.
[127]R. P. Godwin, R. Sachsenmaier, and R. Sigel, "Angle-dependent reflectance of laser-produced plasmas," Phys. Rev. Lett. **39**, 1198 (1977).
[128]A. G. M. Maaswinkel, K. Eidmann, and R. Sigel, "Comparative reflectance measurements on laser-produced plasmas at 1.06 and 0.53 μm," Phys. Rev. Lett. **42**, 1625 (1979).
[129]S. Jackel, B. Perry, and M. Lubin, "Dynamics of laser-produced plasmas through time-resolved observations of the $2\omega_0$ and $3/2\omega_0$ harmonic light emission," Phys. Rev. Lett. **37**, 95 (1976).
[130]M. Decroisette, B. Meyer, and G. Piar, "Observation de l'harmonique 2 dans un plasma créé par laser," J. Phys. Colloq. **32**, C5b-119 (1971).
[131]A. Saleres, M. Decroisette, and C. Patou, "Plasma density scale length determination in a deuterium, laser generated plasma," Opt. Commun. **13**, 321 (1975).
[132]D. T. Attwood, D. W. Sweeney, J. M. Auerbach, and P. H. Y. Lee, "Interferometric confirmation of radiation-pressure effects in laser-plasma interactions," Phys. Rev. Lett. **40**, 184 (1978).
[133]R. Fedosejevs, I. V. Tomov, N. H. Burnett, G. D. Enright, and M. C. Richardson, "Self-steepening of the density profile of a CO_2-laser-produced plasma," Phys. Rev. Lett. **39**, 932 (1977).
[134]W. Brown, "Reevaluation of interferometric plasma density profiles incorporating refractive effects," in 1993 Summer Research Program for High School Juniors at the University of Rochester's Laboratory for Laser Energetics, Rochester, NY (1993).
[135]D. T. Attwood, "Diagnostics for the laser fusion program—Plasma physics on the scale of microns and picoseconds," IEEE J. Quantum Electron. **14**, 909 (1978).
[136]D. T. Attwood, L. W. Coleman, M. J. Boyle, J. T. Larsen, D. W. Phillion, and K. R. Manes, "Space-time implosion characteristics of laser-irradiated fusion targets," Phys. Rev. Lett. **38**, 282 (1977).
[137]D. Billon, P. A. Holstein, J. Launspach, C. Patou, J. M. Reisse, and D. Schirmann, "Laser driven implosion experiments at Limeil," in *Laser Interaction and Related Plasma Phenomena*, edited by H. J. Schwarz and H. Hora (Plenum Press, New York, 1977), Vol. 4A, pp. 503–534.
[138]M. H. Key, C. L. S. Lewis, J. G. Lunney, A. Moore, T. A. Hall, and R. G. Evans, "Pulsed-x-ray shadowgraphy of dense, cool, laser-imploded plasma," Phys. Rev. Lett. **41**, 1467 (1978).
[139]M. H. Key, P. T. Rumsby, R. G. Evans, C. L. S. Lewis, J. M. Ward, and R. L. Cooke, "Study of ablatively imploded spherical shells," Phys. Rev. Lett. **45**, 1801 (1980).
[140]H. G. Ahlstrom, "Laser fusion experiments, facilities, and diagnostics at Lawrence Livermore National Laboratory," Appl. Opt. **20**, 1902 (1981).
[141]W. Seka, S. D. Jacobs, J. E. Rizzo, R. Boni, and R. S. Craxton, "Demonstration of high efficiency third harmonic conversion of high power Nd-glass laser radiation," Opt. Commun. **34**, 469 (1980).
[142]R. S. Craxton, "Theory of high efficiency third harmonic generation of high power Nd-glass laser radiation," Opt. Commun. **34**, 474 (1980).
[143]J. M. Soures, R. L. McCrory, C. P. Verdon, A. Babushkin, R. E. Bahr, T. R. Boehly, R. Boni, D. K. Bradley, D. L. Brown, R. S. Craxton, J. A. Delettrez, W. R. Donaldson, R. Epstein, P. A. Jaanimagi, S. D. Jacobs, K. Kearney, R. L. Keck, J. H. Kelly, T. J. Kessler, R. L. Kremens, J. P. Knauer, S. A. Kumpan, S. A. Letzring, D. J. Lonobile, S. J. Loucks, L. D. Lund, F. J. Marshall, P. W. McKenty, D. D. Meyerhofer, S. F. B. Morse, A. Okishev, S. Papernov, G. Pien, W. Seka, R. Short, M. J. Shoup III, M. Skeldon, S. Skupsky, A. W. Schmid, D. J. Smith, S. Swales, M. Wittman, and B. Yaakobi, "Direct-drive laser-fusion experiments with the OMEGA, 60-beam, >40-kJ, ultraviolet laser system," Phys. Plasmas **3**, 2108 (1996).
[144]W. Seka, R. S. Craxton, J. Delettrez, L. Goldman, R. Keck, R. L. McCrory, D. Shvarts, J. M. Soures, and R. Boni, "Measurements and interpretation of the absorption of 0.35 μm laser radiation on planar targets," Opt. Commun. **40**, 437 (1982).
[145]S. R. Gunn and V. C. Rupert, "Calorimeters for measurement of ions, x-rays, and scattered radiation in laser-fusion experiments," Rev. Sci. Instrum. **48**, 1375 (1977).
[146]C. Garban-Labaune, E. Fabre, C. E. Max, R. Fabbro, F. Amiranoff, J. Virmont, M. Weinfeld, and A. Michard, "Effect of laser wavelength and pulse duration on laser-light absorption and back reflection," Phys. Rev. Lett. **48**, 1018 (1982).
[147]C. Garban-Labaune, E. Fabre, C. Max, F. Amiranoff, R. Fabbro, J. Virmont, and W. C. Mead, "Experimental results and theoretical analysis of the effect of wavelength on absorption and hot-electron generation in laser-plasma interaction," Phys. Fluids **28**, 2580 (1985).
[148]W. C. Mead, E. M. Campbell, K. G. Estabrook, R. E. Turner, W. L. Kruer, P. H. Y. Lee, B. Pruett, V. C. Rupert, K. G. Tirsell, G. L. Stradling, F. Ze, C. E. Max, and M. D. Rosen, "Laser-plasma interactions at 0.53 μm for disk targets of varying Z," Phys. Rev. Lett. **47**, 1289 (1981).
[149]D. C. Slater, G. E. Busch, G. Charatis, R. R. Johnson, F. J. Mayer, R. J. Schroeder, J. D. Simpson, D. Sullivan, J. A. Tarvin, and C. E. Thomas, "Absorption and hot-electron production for 1.05 and 0.53 μm light on spherical targets," Phys. Rev. Lett. **46**, 1199 (1981).
[150]M. C. Richardson, R. S. Craxton, J. Delettrez, R. L. Keck, R. L. McCrory, W. Seka, and J. M. Soures, "Absorption physics at 351 nm in spherical geometry," Phys. Rev. Lett. **54**, 1656 (1985).
[151]R. S. Craxton and R. L. McCrory, "Calculations of the wavelength dependence of absorption," Laboratory for Laser Energetics, University of Rochester, Rochester, NY, LLE Report No. 108, 1980.
[152]W. C. Mead, E. M. Campbell, K. G. Estabrook, R. E. Turner, W. L. Kruer, P. H. Y. Lee, B. Pruett, V. C. Rupert, K. G. Tirsell, G. L. Stradling, F. Ze, C. E. Max, M. D. Rosen, and B. F. Lasinski, "Laser irradiation of disk targets at 0.53 μm wavelength," Phys. Fluids **26**, 2316 (1983).
[153]R. P. Drake, R. L. Kauffman, B. F. Lasinski, M. D. Cable, L. J. Suter, and F. Ze, "The angular dependence of the absorption of 0.35 μm laser light by high-Z, laser-produced plasmas," Phys. Fluids B **3**, 3477 (1991).
[154]W. Seka, unpublished results (2006).
[155]W. Seka, D. H. Edgell, J. P. Knauer, J. F. Myatt, A. V. Maximov, R. W. Short, T. C. Sangster, C. Stoeckl, R. E. Bahr, R. S. Craxton, J. A. Delettrez, V. N. Goncharov, I. V. Igumenshchev, and D. Shvarts, "Time-resolved absorption in cryogenic and room-temperature direct-drive implosions," Phys. Plasmas **15**, 056312 (2008).
[156]T. Dewandre, J. R. Albritton, and E. A. Williams, "Doppler shift of laser light reflected from expanding plasmas," Phys. Fluids **24**, 528 (1981).
[157]V. N. Goncharov, O. V. Gotchev, E. Vianello, T. R. Boehly, J. P. Knauer, P. W. McKenty, P. B. Radha, S. P. Regan, T. C. Sangster, S. Skupsky, V. A. Smalyuk, R. Betti, R. L. McCrory, D. D. Meyerhofer, and C. Cherfils-Clérouin, "Early stage of implosion in inertial confinement fusion: Shock timing and perturbation evolution," Phys. Plasmas **13**, 012702 (2006).
[158]I. V. Igumenshchev, D. H. Edgell, V. N. Goncharov, J. A. Delettrez, A. V. Maximov, J. F. Myatt, W. Seka, A. Shvydky, S. Skupsky, and C. Stoeckl, "Crossed-beam energy transfer in implosion experiments on OMEGA," Phys. Plasmas **17**, 122708 (2010).
[159]S. Skupsky and K. Lee, "Uniformity of energy deposition of laser driven fusion," J. Appl. Phys. **54**, 3662 (1983).
[160]L. Iwan, ed., "Illumination-uniformity considerations for direct-drive fusion reactors," LLE Review Quarterly Report **19**, 120 (1984), Laboratory for Laser Energetics, University of Rochester, Rochester, NY, LLE Document No. DOE/DP/40124-43.
[161]A. J. Schmitt, "Absolutely uniform illumination of laser fusion pellets," Appl. Phys. Lett. **44**, 399 (1984).
[162]A. J. Schmitt and J. H. Gardner, "Illumination uniformity of laser-fusion pellets using induced spatial incoherence," J. Appl. Phys. **60**, 6 (1986).

[163]J. E. Howard, "Uniform illumination of spherical laser fusion targets," Appl. Opt. **16**, 2764 (1977).
[164]See National Technical Information Service Document No. DE92008915 [R. S. Craxton, ed., *OMEGA Upgrade Preliminary Design*, Laboratory for Laser Energetics, University of Rochester, Rochester, NY, LLE Document No. DOE/DP 40200-101 (1989)]. Copies may be obtained from the National Technical Information Service, Springfield, VA 22161.
[165]J. F. Holzrichter and D. R. Speck, "Laser focusing limitations from nonlinear beam instabilities," J. Appl. Phys. **47**, 2459 (1976).
[166]S. Skupsky and T. Kessler, "A source of hot spots in frequency-tripled laser light," Opt. Commun. **70**, 123 (1989).
[167]Y. Kato and K. Mima, "Random phase shifting of laser beam for absorption profile smoothing and instability suppression in laser produced plasmas," Appl. Phys. B **29**, 186 (1982).
[168]Y. Kato, K. Mima, N. Miyanaga, S. Arinaga, Y. Kitagawa, M. Nakatsuka, and C. Yamanaka, "Random phasing of high-power lasers for uniform target acceleration and plasma-instability suppression," Phys. Rev. Lett. **53**, 1057 (1984).
[169]See National Technical Information Service Document No. DE88008065 [Laboratory for Laser Energetics, "OMEGA phase conversion with distributed phase plates," Laboratory for Laser Energetics Review Quarterly Report (University of Rochester, Rochester, NY, 1987), Vol. 33, p. 1, LLE Document No. DOE/DP/40200-65]. Copies may be obtained from the National Technical Information Service, Springfield, VA 22161.
[170]T. J. Kessler, Y. Lin, J. J. Armstrong, and B. Velazquez, "Phase conversion of lasers with low-loss distributed phase plates," Proc. SPIE **1870**, 95–104 (1993).
[171]S. N. Dixit, I. M. Thomas, B. W. Woods, A. J. Morgan, M. A. Henesian, P. J. Wegner, and H. T. Powell, "Random phase plates for beam smoothing on the Nova laser," Appl. Opt. **32**, 2543 (1993).
[172]S. N. Dixit, J. K. Lawson, K. R. Manes, H. T. Powell, and K. A. Nugent, "Kinoform phase plates for focal plane irradiance profile control," Opt. Lett. **19**, 417 (1994).
[173]J. A. Menapace, S. N. Dixit, F. Y. Genin, and W. F. Brocious, "Magnetorheological finishing for imprinting continuous-phase plate structures onto optical surfaces," Proc. SPIE **5273**, 220–230 (2003).
[174]X. Deng, X. Liang, Z. Chen, W. Yu, and R. Ma, "Uniform illumination of large targets using a lens array," Appl. Opt. **25**, 377 (1986).
[175]R. H. Lehmberg and S. P. Obenschain, "Use of induced spatial incoherence for uniform illumination of laser fusion targets," Opt. Commun. **46**, 27 (1983).
[176]R. H. Lehmberg, A. J. Schmitt, and S. E. Bodner, "Theory of induced spatial incoherence," J. Appl. Phys. **62**, 2680 (1987).
[177]S. P. Obenschain, J. Grun, M. J. Herbst, K. J. Kearney, C. K. Manka, E. A. McLean, A. N. Mostovych, J. A. Stamper, R. R. Whitlock, S. E. Bodner, J. H. Gardner, and R. H. Lehmberg, "Laser-target interaction with induced spatial incoherence," Phys. Rev. Lett. **56**, 2807 (1986).
[178]A. N. Mostovych, S. P. Obenschain, J. H. Gardner, J. Grun, K. J. Kearney, C. K. Manka, E. A. McLean, and C. J. Pawley, "Brillouin-scattering measurements from plasma irradiated with spatially and temporally incoherent laser light," Phys. Rev. Lett. **59**, 1193 (1987).
[179]T. A. Peyser, C. K. Manka, S. P. Obenschain, and K. J. Kearney, "Reduction of $3\omega_0/2$ emission from laser-produced plasmas with broad bandwidth, induced spatial incoherence at 0.53 μm," Phys. Fluids B **3**, 1479 (1991).
[180]R. H. Lehmberg and J. Goldhar, "Use of incoherence to produce smooth and controllable irradiation profiles with KrF fusion lasers," Fusion Technol. **11**, 532 (1987).
[181]H. Nakano, T. Kanabe, K. Yagi, K. Tsubakimoto, M. Nakatsuka, and S. Nakai, "Amplification and propagation of partially coherent amplified spontaneous emission from Nd:glass," Opt. Commun. **78**, 123 (1990).
[182]H. Nakano, K. Tsubakimoto, N. Miyanaga, M. Nakatsuka, T. Kanabe, H. Azechi, T. Jitsuno, and S. Nakai, "Spectrally dispersed amplified spontaneous emission for improving irradiation uniformity into high power Nd:glass laser system," J. Appl. Phys. **73**, 2122 (1993).
[183]H. Nakano, N. Miyanaga, K. Yagi, K. Tsubakimoto, T. Kanabe, M. Nakatsuka, and S. Nakai, "Partially coherent light generated by using single and multimode optical fibers in a high-power Nd:glass laser system," Appl. Phys. Lett. **63**, 580 (1993).
[184]D. Véron, H. Ayral, C. Gouedard, D. Husson, J. Lauriou, O. Martin, B. Meyer, M. Rostaing, and C. Sauteret, "Optical spatial smoothing of Nd-glass laser beam," Opt. Commun. **65**, 42 (1988).
[185]D. Véron, G. Thiell, and C. Gouedard, "Optical smoothing of the high power PHEBUS Nd-glass laser using the multimode optical fiber technique," Opt. Commun. **97**, 259 (1993).
[186]S. Skupsky, R. W. Short, T. Kessler, R. S. Craxton, S. Letzring, and J. M. Soures, "Improved laser-beam uniformity using the angular dispersion of frequency-modulated light," J. Appl. Phys. **66**, 3456 (1989).
[187]S. G. Glendinning, S. V. Weber, P. Bell, L. B. Da Silva, S. N. Dixit, M. A. Henesian, D. R. Kania, J. D. Kilkenny, H. T. Powell, R. J. Wallace, P. J. Wegner, J. P. Knauer, and C. P. Verdon, "Laser-driven planar Rayleigh–Taylor instability experiments," Phys. Rev. Lett. **69**, 1201 (1992).
[188]D. M. Pennington, S. N. Dixit, T. L. Weiland, R. B. Ehrlich, and J. E. Rothenberg, "Implementation and performance of beam smoothing on 10 beams of the Nova laser," Proc. SPIE **3047**, 725–735 (1997).
[189]D. Eimerl, J. M. Auerbach, C. E. Barker, D. Milam, and P. W. Milonni, "Multicrystal designs for efficient third-harmonic generation," Opt. Lett. **22**, 1208 (1997).
[190]A. Babushkin, R. S. Craxton, S. Oskoui, M. J. Guardalben, R. L. Keck, and W. Seka, "Demonstration of the dual-tripler scheme for increased-bandwidth third-harmonic generation," Opt. Lett. **23**, 927 (1998).
[191]S. Skupsky and R. S. Craxton, "Irradiation uniformity for high-compression laser-fusion experiments," Phys. Plasmas **6**, 2157 (1999).
[192]S. P. Regan, J. A. Marozas, R. S. Craxton, J. H. Kelly, W. R. Donaldson, P. A. Jaanimagi, D. Jacobs-Perkins, R. L. Keck, T. J. Kessler, D. D. Meyerhofer, T. C. Sangster, W. Seka, V. A. Smalyuk, S. Skupsky, and J. D. Zuegel, "Performance of 1-THz-bandwidth, two-dimensional smoothing by spectral dispersion and polarization smoothing of high-power, solid-state laser beams," J. Opt. Soc. Am. B **22**, 998 (2005).
[193]G. Miyaji, N. Miyanaga, S. Urushihara, K. Suzuki, S. Matsuoka, M. Nakatsuka, A. Morimoto, and T. Kobayashi, "Three-directional spectral dispersion for smoothing of a laser irradiance profile," Opt. Lett. **27**, 725 (2002).
[194]N. Miyanaga, M. Nakatsuka, H. Azechi, H. Shiraga, T. Kanabe, H. Asahara, H. Daido, H. Fujita, K. Fujita, Y. Izawa, T. Jitsuno, T. Kawasaki, H. Kitamura, S. Matsuo, K. Mima, N. Morio, M. Nakai, S. Nakai, K. Nishihara, H. Nishimura, T. Sakamoto, K. Shigemori, K. Sueda, K. Suzuki, K. Tsubakimoto, H. Takabe, S. Urushihara, H. Yoshida, T. Yamanaka, and C. Yamanaka, "The GEKKO XII-HIPER (high intensity plasma experimental research) system relevant to ignition targets," in *Proceedings of the 18th International Conference on Fusion Energy* (IAEA, Vienna, 2000), Paper No. IFP/14(R), IAEA-CN-77.
[195]J. E. Rothenberg, "Comparison of beam-smoothing methods for direct-drive inertial confinement fusion," J. Opt. Soc. Am. B **14**, 1664 (1997).
[196]See National Technical Information Service Document No. DE2008935224 [Laboratory for Laser Energetics, "Multiple-FM smoothing by spectral dispersion—An augmented laser speckle smoothing scheme," Laboratory for Laser Energetics Review Quarterly Report (University of Rochester, Rochester, NY, 2008), Vol. 114, p. 73, LLE Document No. DOE/NA/28302-826]. Copies may be obtained from the National Technical Information Services, Springfield, VA 22161.
[197]T. J. B. Collins, J. A. Marozas, K. S. Anderson, R. Betti, R. S. Craxton, J. A. Delettrez, V. N. Goncharov, D. R. Harding, F. J. Marshall, R. L. McCrory, D. D. Meyerhofer, P. W. McKenty, P. B. Radha, A. Shvydky, S. Skupsky, and J. D. Zuegel, "A polar-drive–ignition design for the National Ignition Facility," Phys. Plasmas **19**, 056308 (2012).
[198]Y. Kato, unpublished notes from work at LLE, July 1984.
[199]T. E. Gunderman, J.-C. Lee, T. J. Kessler, S. D. Jacobs, D. J. Smith, and S. Skupsky, "Liquid crystal distributed polarization rotator for improved uniformity of focused laser light," in *Conference on Lasers and Electro-Optics*, Vol. 7, 1990 OSA Technical Digest Series (Optical Society of America, Washington, DC, 1990), p. 354.
[200]K. Tsubakimoto, M. Nakatsuka, H. Nakano, T. Kanabe, T. Jitsuno, and S. Nakai, "Suppression of interference speckles produced by a random phase plate, using a polarization control plate," Opt. Commun. **91**, 9 (1992).
[201]See National Technical Information Service Document No. DE91010027 [Laboratory for Laser Energetics, "Phase conversion using distributed polarization rotation," Laboratory for Laser Energetics, Review Quarterly Report (University of Rochester, Rochester, NY, 1990), Vol. 45, p. 1, LLE Document No. DOE/DP40200-149]. Copies may be obtained from the National Technical Information Service, Springfield, VA 22161.
[202]T. R. Boehly, V. A. Smalyuk, D. D. Meyerhofer, J. P. Knauer, D. K. Bradley, R. S. Craxton, M. J. Guardalben, S. Skupsky, and T. J. Kessler, "Reduction of laser imprinting using polarization smoothing on a solid-state fusion laser," J. Appl. Phys. **85**, 3444 (1999).
[203]V. N. Goncharov, "Theory of the ablative Richtmyer–Meshkov instability," Phys. Rev. Lett. **82**, 2091 (1999).

[204]R. D. Richtmyer, "Taylor instability in shock acceleration of compressible fluids," Commun. Pure Appl. Math. **XIII**, 297 (1960).
[205]E. E. Meshkov, "Instability of the interface of two gases accelerated by a shock wave," Fluid Dyn. **4**(5), 101 (1969).
[206]R. Betti, V. Lobatchev, and R. L. McCrory, "Feedout and Rayleigh–Taylor seeding induced by long wavelength perturbations in accelerated planar foils," Phys. Rev. Lett. **81**, 5560 (1998).
[207]Y. Aglitskiy, A. L. Velikovich, M. Karasik, N. Metzler, S. T. Zalesak, A. J. Schmitt, L. Phillips, J. H. Gardner, V. Serlin, J. L. Weaver, and S. P. Obenschain, "Basic hydrodynamics of Richtmyer–Meshkov-type growth and oscillations in the inertial confinement fusion-relevant conditions," Philos. Trans. R. Soc. A **368**, 1739 (2010).
[208]R. Ishizaki and K. Nishihara, "Propagation of a rippled shock wave driven by nonuniform laser ablation," Phys. Rev. Lett. **78**, 1920 (1997).
[209]R. Ishizaki and K. Nishihara, "Model of hydrodynamic perturbation growth in the start-up phase of laser implosion," Phys. Rev. E **58**, 3744 (1998).
[210]V. N. Goncharov, S. Skupsky, T. R. Boehly, J. P. Knauer, P. McKenty, V. A. Smalyuk, R. P. J. Town, O. V. Gotchev, R. Betti, and D. D. Meyerhofer, "A model of laser imprinting," Phys. Plasmas **7**, 2062 (2000).
[211]See National Technical Information Service Document No. DE2001761211 [Laboratory for Laser Energetics, "Modeling laser imprint for inertial confinement fusion targets," Laboratory for Laser Energetics Review Quarterly Report (University of Rochester, Rochester, NY, 1999), Vol. 80, p. 185, LLE Document No. DOE/SF/19460-321]. Copies may be obtained from the National Technical Information Service, Springfield, VA 22161.
[212]J. Sanz, J. A. Nicolas, J. R. Sanmartin, and J. Hilario, "Nonuniform target illumination in the deflagration regime: Thermal smoothing," Phys. Fluids **31**, 2320 (1988).
[213]J. Sanz, "Self-consistent analytical model of the Rayleigh–Taylor instability in inertial confinement fusion," Phys. Rev. E **53**, 4026 (1996).
[214]V. N. Goncharov, R. Betti, R. L. McCrory, P. Sorotokin, and C. P. Verdon, "Self-consistent stability analysis of ablation fronts with large Froude numbers," Phys. Plasmas **3**, 1402 (1996).
[215]R. J. Taylor, A. L. Velikovich, J. P. Dahlburg, and J. H. Gardner, "Saturation of laser imprint on ablatively driven plastic targets," Phys. Rev. Lett. **79**, 1861 (1997).
[216]V. A. Smalyuk, T. R. Boehly, D. K. Bradley, V. N. Goncharov, J. A. Delettrez, J. P. Knauer, D. D. Meyerhofer, D. Oron, D. Shvarts, Y. Srebro, and R. P. J. Town, "Nonlinear evolution of broad-bandwidth, laser-imprinted nonuniformities in planar targets accelerated by 351-nm laser light," Phys. Plasmas **6**, 4022 (1999).
[217]A. J. Cole, J. D. Kilkenny, P. T. Rumsby, R. G. Evans, C. J. Hooker, and M. H. Key, "Measurement of Rayleigh–Taylor instability in a laser-accelerated target," Nature **299**, 329 (1982).
[218]D. H. Kalantar, M. H. Key, L. B. Da Silva, S. G. Glendinning, J. P. Knauer, B. A. Remington, F. Weber, and S. V. Weber, "Measurement of 0.35 μm laser imprint in a thin Si foil using an x-ray laser backlighter," Phys. Rev. Lett. **76**, 3574 (1996).
[219]S. G. Glendinning, S. N. Dixit, B. A. Hammel, D. H. Kalantar, M. H. Key, J. D. Kilkenny, J. P. Knauer, D. M. Pennington, B. A. Remington, R. J. Wallace, and S. V. Weber, "Measurements of laser-speckle-induced perturbations in laser-driven foils," Phys. Rev. E **54**, 4473 (1996).
[220]C. J. Pawley, K. Gerber, R. H. Lehmberg, E. A. McLean, A. N. Mostovych, S. P. Obenschain, J. D. Sethian, V. Serlin, J. A. Stamper, C. A. Sullivan, S. E. Bodner, D. Colombant, J. P. Dahlburg, A. J. Schmitt, J. H. Gardner, C. Brown, J. F. Seely, T. Lehecka, Y. Aglitskiy, A. V. Deniz, Y. Chan, N. Metzler, and M. Klapisch, "Measurements of laser-imprinted perturbations and Rayleigh–Taylor growth with the Nike KrF laser," Phys. Plasmas **4**, 1969 (1997).
[221]Y. Aglitskiy, T. Lehecka, S. Obenschain, S. Bodner, C. Pawley, K. Gerber, J. Sethian, C. M. Brown, J. Seely, U. Feldman, and G. Holland, "High-resolution monochromatic x-ray imaging system based on spherically bent crystals," Appl. Opt. **37**, 5253 (1998).
[222]T. R. Boehly, V. N. Goncharov, O. Gotchev, J. P. Knauer, D. D. Meyerhofer, D. Oron, S. P. Regan, Y. Srebro, W. Seka, D. Shvarts, S. Skupsky, and V. A. Smalyuk, "Optical and plasma smoothing of laser imprinting in targets driven by lasers with SSD bandwidths up to 1 THz," Phys. Plasmas **8**, 2331 (2001).
[223]M. Nakai, H. Azechi, N. Miyanaga, K. Shigemori, T. Kawasaki, T. Nagaya, M. Nishikino, Y. Kanai, D. Ohnuki, H. Nishimura, H. Shiraga, O. Maegawa, R. Ishizaki, K. Nishihara, H. Takabe, and T. Yamanaka, "Single spatial mode experiments on initial laser imprint on direct-driven planar targets," Phys. Plasmas **9**, 1734 (2002).
[224]K. Okada, T. Mochizuki, S. Sakabe, H. Shiraga, T. Yabe, and C. Yamanaka, "Laser implosion of thick low-*Z* foam coated glass microballoon," Appl. Phys. Lett. **42**, 231 (1983).
[225]M. H. Emery, J. H. Gardner, R. H. Lehmberg, and S. P. Obsenschain, "Hydrodynamic target response to an induced spatial incoherence-smoothed laser beam," Phys. Fluids B **3**, 2640 (1991).
[226]M. Desselberger, M. W. Jones, J. Edwards, M. Dunne, and O. Willi, "Use of x-ray preheated foam layers to reduce beam structure imprint in laser-driven targets," Phys. Rev. Lett. **74**, 2961 (1995).
[227]M. Dunne, M. Borghesi, A. Iwase, M. W. Jones, R. Taylor, O. Willi, R. Gibson, S. R. Goldman, J. Mack, and R. G. Watt, "Evaluation of a foam buffer target design for spatially uniform ablation of laser-irradiated plasmas," Phys. Rev. Lett. **75**, 3858 (1995).
[228]R. G. Watt, D. C. Wilson, R. E. Chrien, R. V. Hollis, P. L. Gobby, R. J. Mason, R. A. Kopp, R. A. Lerche, D. H. Kalantar, B. MacGowan, M. B. Nelson, T. Phillips, P. W. McKenty, and O. Willi, "Foam-buffered spherical implosions at 527 nm," Phys. Plasmas **4**, 1379 (1997).
[229]R. G. Watt, J. Duke, C. J. Fontes, P. L. Gobby, R. V. Hollis, R. A. Kopp, R. J. Mason, D. C. Wilson, C. P. Verdon, T. R. Boehly, J. P. Knauer, D. D. Meyerhofer, V. Smalyuk, R. P. J. Town, A. Iwase, and O. Willi, "Laser imprint reduction using a low-density foam buffer as a thermal smoothing layer at 351-nm wavelength," Phys. Rev. Lett. **81**, 4644 (1998).
[230]S. Depierreux, C. Labaune, D. T. Michel, C. Stenz, P. Nicolaï, M. Grech, G. Riazuelo, S. Weber, C. Riconda, V. T. Tikhonchuk, P. Loiseau, N. G. Borisenko, W. Nazarov, S. Hüller, D. Pesme, M. Casanova, J. Limpouch, C. Meyer, P. Di-Nicola, R. Wrobel, E. Alozy, P. Romary, G. Thiell, G. Soullié, C. Reverdin, and B. Villette, "Laser smoothing and imprint reduction with a foam layer in the multikilojoule regime," Phys. Rev. Lett. **102**, 195005 (2009).
[231]S. Yu. Gus'kov, J. Limpouch, Ph. Nicolaï, and V. T. Tikhonchuk, "Laser-supported ionization wave in under-dense gases and foams," Phys. Plasmas **18**, 103114 (2011).
[232]K. A. Tanaka, B. Boswell, R. S. Craxton, L. M. Goldman, F. Guglielmi, W. Seka, R. W. Short, and J. M. Soures, "Brillouin scattering, two-plasmon decay, and self-focusing in underdense ultraviolet laser-produced plasmas," Phys. Fluids **28**, 2910 (1985).
[233]J. L. Bocher, M. Decroisette, P. A. Holstein, M. Louis-Jacquet, B. Meyer, A. Salères, and G. Thiell, "Improvement of beam nonuniformity smoothing due to x radiation in laser-driven layered targets," Phys. Rev. Lett. **52**, 823 (1984).
[234]S. P. Obenschain, D. G. Colombant, M. Karasik, C. J. Pawley, V. Serlin, A. J. Schmitt, J. L. Weaver, J. H. Gardner, L. Phillips, Y. Aglitskiy, Y. Chan, J. P. Dahlburg, and M. Klapisch, "Effects of thin high-*Z* layers on the hydrodynamics of laser-accelerated plastic targets," Phys. Plasmas **9**, 2234 (2002).
[235]A. N. Mostovych, D. G. Colombant, M. Karasik, J. P. Knauer, A. J. Schmitt, and J. L. Weaver, "Enhanced direct-drive implosions with thin high-*Z* ablation layers," Phys. Rev. Lett. **100**, 075002 (2008).
[236]S. Fujioka, A. Sunahara, K. Nishihara, N. Ohnishi, T. Johzaki, H. Shiraga, K. Shigemori, M. Nakai, T. Ikegawa, M. Murakami, K. Nagai, T. Norimatsu, H. Azechi, and T. Yamanaka, "Suppression of the Rayleigh–Taylor instability due to self-radiation in a multiablation target," Phys. Rev. Lett. **92**, 195001 (2004).
[237]S. X. Hu, G. Fiksel, V. N. Goncharov, S. Skupsky, D. D. Meyerhofer, and V. A. Smalyuk, "Mitigating laser imprint in direct-drive inertial confinement fusion implosions with high-*Z* dopants," Phys. Rev. Lett. **108**, 195003 (2012).
[238]G. Fiksel, S. X. Hu, V. N. Goncharov, D. D. Meyerhofer, T. C. Sangster, V. A. Smalyuk, B. Yaakobi, M. J. Bonino, and R. Jungquist, "Experimental reduction of laser imprinting and Rayleigh–Taylor growth in spherically compressed, medium-*Z*-doped plastic targets," Phys. Plasmas **19**, 062704 (2012).
[239]V. A. Smalyuk, S. X. Hu, J. D. Hager, J. A. Delettrez, D. D. Meyerhofer, T. C. Sangster, and D. Shvarts, "Rayleigh–Taylor growth measurements in the acceleration phase of spherical implosions on OMEGA," Phys. Rev. Lett. **103**, 105001 (2009).
[240]H. Nishimura, H. Shiraga, H. Azechi, N. Miyanaga, M. Nakai, N. Izumi, M. Nishikino, M. Heya, K. Fujita, Y. Ochi, K. Shigemori, N. Ohnishi, M. Murakami, K. Nishihara, R. Ishizaki, H. Takabe, K. Nagai, T. Norimatsu, M. Nakatsuka, T. Yamanaka, S. Nakai, C. Yamanaka, and K. Mima,

"Indirect-direct hybrid target experiments with the GEKKO XII laser," Nucl. Fusion **40**, 547 (2000).
[241]M. Nishikino, H. Shiraga, N. Miyanaga, H. Nishimura, K. Shigemori, M. Heya, H. Azechi, M. Nakai, K. Mima, H. Takabe, S. Nakai, and T. Yamanaka, "Indirect/direct-hybrid drive implosion experiments with x-ray pre-irradiation," Proc. SPIE **3886**, 465–472 (2000).
[242]M. Nishikino, H. Shiraga, N. Maiyanaga, N. Ohnishi, K. Shigemori, S. Fujikoa, M. Nakai, H. Nishimura, H. Azechi, K. Mima, H. Takabe, S. Nakai, and T. Yamanaka, "Imprint reduction in a plasma layer preformed with x-ray irradiation," Phys. Plasmas **9**, 1381 (2002).
[243]M. Desselberger, T. Afshar-rad, F. Khattak, S. Viana, and O. Willi, "Nonuniformity imprint on the ablation surface of laser-irradiated targets," Phys. Rev. Lett. **68**, 1539 (1992).
[244]J. H. Nuckolls, "Laser-induced implosion and thermonuclear burn," in *Laser Interaction and Related Plasma Phenomena*, edited by H. J. Schwarz and H. Hora (Plenum Press, New York, 1974), Vol. 3B, pp. 399–425.
[245]A. B. Iskakov, V. F. Tishkin, I. G. Lebo, J. Limpouch, K. Mašek, and K. Rohlena, "Two-dimensional model of thermal smoothing of laser imprint in a double-pulse plasma," Phys. Rev. E **61**, 842 (2000).
[246]E. Krouský, O. Renner, K. Mašek, M. Pfeiffer, O. Pacherová, B. Králiková, J. Skála, and K. Rohlena, "Experimental evidence of thermal smoothing in a double-pulse produced plasma," Laser Part. Beams **18**, 87 (2000).
[247]T. J. B. Collins and S. Skupsky, "Imprint reduction using an intensity spike in OMEGA cryogenic targets," Phys. Plasmas **9**, 275 (2002).
[248]V. A. Smalyuk, V. N. Goncharov, K. S. Anderson, R. Betti, R. S. Craxton, J. A. Delettrez, D. D. Meyerhofer, S. P. Regan, and T. C. Sangster, "Measurements of the effects of the intensity pickets on laser imprinting for direct-drive, adiabat-shaping designs on OMEGA," Phys. Plasmas **14**, 032702 (2007).
[249]L. D. Landau and E. M. Lifshitz, *Fluid Mechanics*, 2nd ed. (Butterworth-Heinemann, Oxford, 1987), pp. 488–489.
[250]A. R. Piriz and R. F. Portugues, "Landau–Darrieus instability in an ablation front," Phys. Plasmas **10**, 2449 (2003).
[251]P. Clavin and L. Masse, "Instabilities of ablation fronts in inertial confinement fusion: A comparison with flames," Phys. Plasmas **11**, 690 (2004).
[252]A. L. Velikovich, J. P. Dahlburg, A. J. Schmitt, J. H. Gardner, L. Phillips, F. L. Cochran, Y. K. Chong, G. Dimonte, and N. Metzler, "Richtmyer–Meshkov-like instabilities and early-time perturbation growth in laser targets and Z-pinch loads," Phys. Plasmas **7**, 1662 (2000).
[253]T. Endo, K. Shigemori, H. Azechi, A. Nishiguchi, K. Mima, M. Sate, M. Nakai, S. Nakaji, N. Miyanaga, S. Matsuoka, A. Ando, K. A. Tanaka, and S. Nakai, "Dynamic behavior of rippled shock waves and subsequently induced areal-density-perturbation growth in laser-irradiation foils," Phys. Rev. Lett. **74**, 3608 (1995); **75**, 2908(E) (1995).
[254]N. Matsui, K. Mima, M. Honda, and A. Nishiguchi, "Analysis of rippled shock-wave propagation and ablation-front stability by theory and hydrodynamic simulation," J. Plasma Phys. **61**, 43 (1999).
[255]Y. Aglitskiy, A. L. Velikovich, M. Karasik, V. Serlin, C. J. Pawley, A. J. Schmitt, S. P. Obenschain, A. N. Mostovych, J. H. Gardner, and N. Metzler, "Direct observation of mass oscillations due to ablative Richtmyer–Meshkov instability in plastic targets," Phys. Rev. Lett. **87**, 265001 (2001).
[256]O. Gotchev, V. N. Goncharov, J. P. Knauer, T. R. Boehly, T. J. B. Collins, R. Epstein, P. A. Jaanimagi, and D. D. Meyerhofer, "Test of thermal transport models through dynamic overpressure stabilization of ablation-front perturbation growth in laser-driven CH foils," Phys. Rev. Lett. **96**, 115005 (2006).
[257]K. O. Mikaelian, "Richtmyer-Meshkov instabilities in stratified fluids," Phys. Rev. A **31**, 410 (1985).
[258]A. L. Velikovich, A. J. Schmitt, J. H. Gardner, and N. Metzler, "Feedout and Richtmyer–Meshkov instability at large density difference," Phys. Plasmas **8**, 592 (2001).
[259]A. Velikovich and L. Phillips, "Instability of a plane centered rarefaction wave," Phys. Fluids **8**, 1107 (1996).
[260]D. P. Smitherman, R. E. Chrien, N. M. Hoffman, and G. R. Magelssen, "The feedout process: Rayleigh–Taylor and Richtmyer–Meshkov instabilities in uniform, radiation-driven foils," Phys. Plasmas **6**, 932 (1999).
[261]K. Shigemori, M. Nakai, H. Azechi, K. Nishihara, R. Ishizaki, T. Nagaya, H. Nagatomo, and K. Mima, "Feed-out of rear surface perturbation due to rarefaction wave in laser-irradiated targets," Phys. Rev. Lett. **84**, 5331 (2000).
[262]Y. Aglitskiy, A. L. Velikovich, M. Karasik, V. Serlin, C. J. Pawley, A. J. Schmitt, S. P. Obenschain, A. N. Mostovych, J. H. Gardner, and N. Metzler, "Direct observation of feedout-related mass oscillations in plastic targets," Phys. Rev. Lett. **87**, 265002 (2001).
[263]B. Yaakobi, D. Steel, E. Thorsos, A. Hauer, and B. Perry, "Direct measurement of compression of laser-imploded targets using x-ray spectroscopy," Phys. Rev. Lett. **39**, 1526 (1977).
[264]B. Yaakobi, S. Skupsky, R. L. McCrory, C. F. Hooper, H. Deckman, P. Bourke, and J. M. Soures, "Symmetric laser compression of argon-filled glass shells to densities of 4–6 g/cm^3," Phys. Rev. Lett. **44**, 1072 (1980).
[265]S. P. Regan, B. Yaakobi, T. R. Boehly, R. Epstein, J. A. Delettrez, V. Yu. Glebov, V. N. Goncharov, P. A. Jaanimagi, J. P. Knauer, F. J. Marshall, R. L. McCrory, D. D. Meyerhofer, P. B. Radha, T. C. Sangster, V. A. Smalyuk, J. Soures, C. Stoeckl, R. C. Mancini, D. A. Haynes, Jr., L. Welser-Sherrill, J. A. Koch, R. Tommasini, and H. Sawada, "Applied plasma spectroscopy: Laser-fusion experiments," High Energy Density Phys. **5**, 234 (2009).
[266]B. Yaakobi, I. Pelah, and J. Hoose, "Preheat by fast electrons in laser-fusion experiments," Phys. Rev. Lett. **37**, 836 (1976).
[267]J. D. Hares, J. D. Kilkenny, M. H. Key, and J. G. Lunney, "Measurement of fast-electron energy spectra and preheating in laser-irradiated targets," Phys. Rev. Lett. **42**, 1216 (1979).
[268]J. M. Auerbach, W. C. Mead, E. M. Campbell, D. L. Matthews, D. S. Bailey, C. W. Hatcher, L. N. Koppel, S. M. Lane, P. H. Y. Lee, K. R. Manes, G. McClellan, D. W. Phillion, R. H. Price, V. C. Rupert, V. W. Slivinsky, and C. D. Swift, "Compression of polymer-coated laser-fusion targets to ten times liquid DT density," Phys. Rev. Lett. **44**, 1672 (1980).
[269]D. W. Phillion, D. L. Banner, E. M. Campbell, R. E. Turner, and K. G. Estabrook, "Stimulated Raman scattering in large plasmas," Phys. Fluids **25**, 1434 (1982).
[270]G. B. Zimmerman and W. L. Kruer, "Numerical simulation of laser-initiated fusion," Comments Plasma Phys. Controlled Fusion **2**, 51 (1975).
[271]T. H. Tan, G. H. McCall, R. Kopp, T. Ganley, D. van Hulsteyn, A. Hauer, A. Williams, K. Mitchell, J. S. Ladish, D. Giovanielli, E. Linnebur, and R. J. Fries, "CO_2 laser-driven high-density implosion experiments," Phys. Fluids **24**, 754 (1981).
[272]E. G. Gamaliĭ, S. Yu. Gus'kov, O. N. Krokhin, and V. B. Rozanov, "Possibility of determining the characteristics of laser plasma by measuring the neutrons of the DT-reaction," JETP Lett. **21**, 70 (1975).
[273]H. Azechi, R. O. Stapf, N. Miyanaga, R. Tsuji, M. Yamanaka, S. Ido, K. Nishihara, T. Yabe, and C. Yamanaka, "Study of fuel-pusher mixing in laser-driven implosions, using secondary nuclear fusion reactions," Phys. Rev. Lett. **59**, 2635 (1987).
[274]H. Azechi, T. Jitsuno, T. Kanabe, M. Katayama, K. Mima, N. Miyanaga, M. Nakai, S. Nakai, M. Nakatsuka, A. Nishiguchi, P. A. Norrays, Y. Setsuhara, M. Takagi, M. Yamanaka, and C. Yamanaka, "High-density compression experiments at ILE, Osaka," Laser Part. Beams **9**, 193 (1991).
[275]E. M. Campbell, W. M. Ploeger, P. H. Lee, and S. M. Lane, "Exploding-pusher-tamper areal density measurement by neutron activation," Appl. Phys. Lett. **36**, 965 (1980).
[276]S. Skupsky and S. Kacenjar, "Measuring fuel ρR for inertial fusion experiments using neutron elastic-scattering reactions," J. Appl. Phys. **52**, 2608 (1981).
[277]S. Kacenjar, S. Skupsky, A. Entenberg, L. Goldman, and M. Richardson, "Direct measurement of the fuel density-radius product in laser-fusion experiments," Phys. Rev. Lett. **49**, 463 (1982).
[278]D. K. Bradley, J. A. Delettrez, and C. P. Verdon, "Measurements of the effect of laser beam smoothing on direct-drive inertial-confinement-fusion capsule implosions," Phys. Rev. Lett. **68**, 2774 (1992).
[279]M. Heya, H. Shiraga, A. Sunahara, M. Nakasuji, M. Nishikino, H. Honda, N. Izumi, N. Miyanaga, H. Nishimura, H. Azechi, S. Naruo, H. Takabe, T. Yamanaka, and K. Mima, "Implosion experiments of gas-filled plastic-shell targets with $\ell = 1$ drive nonuniformity at the Gekko-XII glass laser," Laser Part. Beams **19**, 267 (2001).
[280]D. D. Meyerhofer, J. A. Delettrez, R. Epstein, V. Yu. Glebov, V. N. Goncharov, R. L. Keck, R. L. McCrory, P. W. McKenty, F. J. Marshall, P. B. Radha, S. P. Regan, S. Roberts, W. Seka, S. Skupsky, V. A. Smalyuk, C. Sorce, C. Stoeckl, J. M. Soures, R. P. J. Town, B. Yaakobi, J. D. Zuegel, J. Frenje, C. K. Li, R. D. Petrasso, D. G. Hicks, F. H. Séguin, K. Fletcher, S. Padalino, C. Freeman, N. Izumi, R. Lerche, T. W. Phillips, and T. C. Sangster, "Core performance and mix in direct-drive

spherical implosions with high uniformity," Phys. Plasmas **8**, 2251 (2001).
[281]D. D. Meyerhofer, J. A. Delettrez, R. Epstein, V. Yu. Glebov, V. N. Goncharov, R. L. Keck, R. L. McCrory, P. W. McKenty, F. J. Marshall, P. B. Radha, S. P. Regan, S. Roberts, W. Seka, S. Skupsky, V. A. Smalyuk, C. Sorce, C. Stoeckl, J. M. Soures, R. P. J. Town, B. Yaakobi, J. Frenje, C. K. Li, R. D. Petrasso, F. H. Séguin, K. Fletcher, S. Padalino, C. Freeman, N. Izumi, R. A. Lerche, T. W. Phillips, and T. C. Sangster, "Inferences of mix in direct-drive spherical implosions with high uniformity," Plasma Phys. Controlled Fusion **43**, A277 (2001).
[282]P. B. Radha, J. Delettrez, R. Epstein, V. Yu. Glebov, R. Keck, R. L. McCrory, P. McKenty, D. D. Meyerhofer, F. Marshall, S. P. Regan, S. Roberts, T. C. Sangster, W. Seka, S. Skupsky, V. Smalyuk, C. Sorce, C. Stoeckl, J. Soures, R. P. J. Town, B. Yaakobi, J. Frenje, C. K. Li, R. Petrasso, F. Séguin, K. Fletcher, S. Padalino, C. Freeman, N. Izumi, R. Lerche, and T. W. Phillips, "Inference of mix in direct-drive implosions on OMEGA," Phys. Plasmas **9**, 2208 (2002).
[283]C. K. Li, F. H. Séguin, J. A. Frenje, S. Kurebayashi, R. D. Petrasso, D. D. Meyerhofer, J. M. Soures, J. A. Delettrez, V. Yu. Glebov, P. B. Radha, F. J. Marshall, S. P. Regan, S. Roberts, T. C. Sangster, and C. Stoeckl, "Effects of fuel-shell mix upon direct-drive, spherical implosions on OMEGA," Phys. Rev. Lett. **89**, 165002 (2002).
[284]B. Yaakobi, F. J. Marshall, D. K. Bradley, J. A. Delettrez, R. S. Craxton, and R. Epstein, "Signatures of target performance and mixing in titanium-doped, laser-driven target implosions," Phys. Plasmas **4**, 3021 (1997).
[285]D. K. Bradley, J. A. Delettrez, R. Epstein, R. P. J. Town, C. P. Verdon, B. Yaakobi, S. Regan, F. J. Marshall, T. R. Boehly, J. P. Knauer, D. D. Meyerhofer, V. A. Smalyuk, W. Seka, D. A. Haynes, Jr., M. Gunderson, G. Junkel, C. F. Hooper, Jr., P. M. Bell, T. J. Ognibene, and R. A. Lerche, "Measurements of core and pusher conditions in surrogate capsule implosions on the OMEGA laser system," Phys. Plasmas **5**, 1870 (1998).
[286]S. P. Regan, J. A. Delettrez, R. Epstein, P. A. Jaanimagi, B. Yaakobi, V. A. Smalyuk, F. J. Marshall, D. D. Meyerhofer, W. Seka, D. A. Haynes, Jr., I. E. Golovkin, and C. F. Hooper, Jr., "Characterization of direct-drive-implosion core conditions on OMEGA with time-resolved Ar *K*-shell spectroscopy," Phys. Plasmas **9**, 1357 (2002).
[287]S. P. Regan, J. A. Delettrez, F. J. Marshall, J. M. Soures, V. A. Smalyuk, B. Yaakobi, V. Yu. Glebov, P. A. Jaanimagi, D. D. Meyerhofer, P. B. Radha, W. Seka, S. Skupsky, C. Stoeckl, R. P. J. Town, D. A. Haynes, Jr., I. E. Golovkin, C. F. Hooper, Jr., J. A. Frenje, C. K. Li, R. D. Petrasso, and F. H. Séguin, "Shell mix in the compressed core of spherical implosions," Phys. Rev. Lett. **89**, 085003 (2002).
[288]S. P. Regan, J. A. Delettrez, V. N. Goncharov, F. J. Marshall, J. M. Soures, V. A. Smalyuk, P. B. Radha, B. Yaakobi, R. Epstein, V. Yu. Glebov, P. A. Jaanimagi, D. D. Meyerhofer, T. C. Sangster, W. Seka, S. Skupsky, C. Stoeckl, D. A. Haynes, Jr., J. A. Frenje, C. K. Li, R. D. Petrasso, and F. H. Séguin, "Dependence of shell mix on feedthrough in direct drive inertial confinement fusion," Phys. Rev. Lett. **92**, 185002 (2004).
[289]J. R. Rygg, J. A. Frenje, C. K. Li, F. H. Séguin, R. D. Petrasso, V. Yu. Glebov, D. D. Meyerhofer, T. C. Sangster, and C. Stoeckl, "Time-dependent nuclear measurements of mix in inertial confinement fusion," Phys. Rev. Lett. **98**, 215002 (2007).
[290]D. C. Wilson, P. S. Ebey, T. C. Sangster, W. T. Shmayda, V. Yu. Glebov, and R. A. Lerche, "Atomic mix in directly driven inertial confinement implosions," Phys. Plasmas **18**, 112707 (2011).
[291]P. B. Radha, C. Stoeckl, V. N. Goncharov, J. A. Delettrez, D. H. Edgell, J. A. Frenje, I. V. Igumenshchev, J. P. Knauer, J. A. Marozas, R. L. McCrory, D. D. Meyerhofer, R. D. Petrasso, S. P. Regan, T. C. Sangster, W. Seka, and S. Skupsky, "Triple-picket warm plastic-shell implosions on OMEGA," Phys. Plasmas **18**, 012705 (2011).
[292]B. Yaakobi, V. A. Smalyuk, J. A. Delettrez, F. J. Marshall, D. D. Meyerhofer, and W. Seka, "Measurement of areal density modulation of laser-imploded shells through *K*-edge imaging," Phys. Plasmas **7**, 3727 (2000).
[293]V. A. Smalyuk, B. Yaakobi, J. A. Delettrez, F. J. Marshall, and D. D. Meyerhofer, "Compressed-shell integrity measurements in spherical implosion experiments," Phys. Plasmas **8**, 2872 (2001).
[294]V. A. Smalyuk, V. N. Goncharov, J. A. Delettrez, F. J. Marshall, D. D. Meyerhofer, S. P. Regan, and B. Yaakobi, "Evolution of shell nonuniformities near peak compression of a spherical implosion," Phys. Rev. Lett. **87**, 155002 (2001).
[295]V. A. Smalyuk, J. A. Delettrez, V. N. Goncharov, F. J. Marshall, D. D. Meyerhofer, S. P. Regan, T. C. Sangster, R. P. J. Town, and B. Yaakobi, "Rayleigh–Taylor instability in the deceleration phase of spherical implosion experiments," Phys. Plasmas **9**, 2738 (2002).
[296]V. A. Smalyuk, J. A. Delettrez, S. B. Dumanis, V. Yu. Glebov, V. N. Goncharov, J. P. Knauer, F. J. Marshall, D. D. Meyerhofer, P. B. Radha, S. P. Regan, S. Roberts, T. C. Sangster, S. Skupsky, J. M. Soures, C. Stoeckl, R. P. J. Town, B. Yaakobi, J. A. Frenje, C. K. Li, R. D. Petrasso, F. H. Séguin, D. L. McCrorey, R. C. Mancini, and J. A. Koch, "Hydrodynamic growth of shell modulations in the deceleration phase of spherical direct-drive implosions," Phys. Plasmas **10**, 1861 (2003).
[297]V. A. Smalyuk, T. R. Boehly, L. S. Iwan, T. J. Kessler, J. P. Knauer, F. J. Marshall, D. D. Meyerhofer, C. Stoeckl, B. Yaakobi, and D. K. Bradley, "Fourier-space image processing for spherical experiments on OMEGA," Rev. Sci. Instrum. **72**, 635 (2001).
[298]V. A. Smalyuk, S. B. Dumanis, F. J. Marshall, J. A. Delettrez, D. D. Meyerhofer, S. P. Regan, T. C. Sangster, B. Yaakobi, and J. A. Koch, "Radial structure of shell modulations near peak compression of spherical implosions," Phys. Plasmas **10**, 830 (2003).
[299]R. Tommasini, J. A. Koch, N. Izumi, L. A. Welser, R. C. Mancini, J. Delettrez, S. Regan, and V. Smalyuk, "Multispectral x-ray imaging for core temperature and density maps retrieval in direct drive implosions," Rev. Sci. Instrum. **77**, 10E303 (2006).
[300]T. Nagayama, R. C. Mancini, R. Florido, D. Mayes, R. Tommasini, J. A. Koch, J. A. Delettrez, S. P. Regan, and V. A. Smalyuk, "Investigation of a polychromatic tomography method for the extraction of the three-dimensional spatial structure of implosion core plasmas," Phys. Plasmas **19**, 082705 (2012).
[301]F. H. Séguin, C. K. Li, J. A. Frenje, D. G. Hicks, K. M. Green, S. Kurebayashi, R. D. Petrasso, J. M. Soures, D. D. Meyerhofer, V. Yu. Glebov, P. B. Radha, C. Stoeckl, S. Roberts, C. Sorce, T. C. Sangster, M. D. Cable, K. Fletcher, and S. Padalino, "Using secondary-proton spectra to study the compression and symmetry of deuterium-filled capsules at OMEGA," Phys. Plasmas **9**, 2725 (2002).
[302]F. H. Séguin, C. K. Li, J. A. Frenje, S. Kurebayashi, R. D. Petrasso, F. J. Marshall, D. D. Meyerhofer, J. M. Soures, T. C. Sangster, C. Stoeckl, J. A. Delettrez, P. B. Radha, V. A. Smalyuk, and S. Roberts, "Measurements of ρR asymmetries at burn time in inertial-confinement-fusion capsules," Phys. Plasmas **9**, 3558 (2002).
[303]C. K. Li, F. H. Séguin, J. A. Frenje, R. D. Petrasso, J. A. Delettrez, P. W. McKenty, T. C. Sangster, R. L. Keck, J. M. Soures, F. J. Marshall, D. D. Meyerhofer, V. N. Goncharov, J. P. Knauer, P. B. Radha, S. P. Regan, and W. Seka, "Effects of nonuniform illumination on implosion asymmetry in direct-drive inertial confinement fusion," Phys. Rev. Lett. **92**, 205001 (2004).
[304]T. M. Henderson and R. R. Johnson, "The implosion of cryogenic spherical shell targets," Appl. Phys. Lett. **31**, 18 (1977).
[305]E. Storm and Technical Staff, "Laser fusion experiments at KMS," in *Proceedings of the Japan-U.S. Seminar on Theory and Application of Multiply-Ionized Plasmas Produced by Laser and Particle Beams*, edited by C. Yamanaka (Institute of Laser Engineering, Osaka University, Nara, Japan, 1982), pp. 96–114.
[306]R. L. McCrory, J. M. Soures, C. P. Verdon, F. J. Marshall, S. A. Letzring, S. Skupsky, T. J. Kessler, R. L. Kremens, J. P. Knauer, H. Kim, J. Delettrez, R. L. Keck, and D. K. Bradley, "Laser-driven implosion of thermonuclear fuel to 20 to 40 g cm^{-3}," Nature **335**, 225 (1988).
[307]F. J. Marshall, S. A. Letzring, C. P. Verdon, S. Skupsky, R. L. Keck, J. P. Knauer, R. L. Kremens, D. K. Bradley, T. Kessler, J. Delettrez, H. Kim, J. M. Soures, and R. L. McCrory, "Cryogenic-laser-fusion target implosion studies performed with the OMEGA UV-laser system," Phys. Rev. A **40**, 2547 (1989).
[308]J. D. Kilkenny, P. M. Bell, B. A. Hammel, R. L. Hanks, O. L. Landen, T. E. McEwan, D. S. Montgomery, R. E. Turner, J. D. Wiedwald, and D. K. Bradley, "Sub 100 psec x-ray gating cameras for ICF imaging applications," Proc. SPIE **1358**, 117–133 (1990).
[309]J. D. Kilkenny, P. Bell, R. Hanks, G. Power, R. E. Turner, and J. D. Wiedwald, "High-speed gated x-ray images," Rev. Sci. Instrum. **59**, 1793 (1988).
[310]R. R. Johnson, L. V. Powers, B. H. Failor, E. F. Gabl, C. L. Shepard, Gar E. Busch, P. Hammerling, J. T. Larsen, P. D. Rockett, R. J. Schroeder, and D. Sullivan, "Low-preheat cryogenic implosion experiments with a shaped 0.53-μm laser pulse," Phys. Rev. A **41**, 1058 (1990).
[311]S. Nakai, K. Mima, M. Yamanaka, H. Azechi, N. Miyanaga, A. Nishiguchi, H. Nakaishi, Y. W. Chen, Y. Setsuhara, P. A. Norreys, T.

Yamanaka, K. Nishihara, K. A. Tanaka, M. Nakai, R. Kodama, M. Katayama, Y. Kato, H. Takabe, H. Nishimura, H. Shiraga, T. Endo, K. Kondo, M. Nakatsuka, T. Sasaki, T. Jitsuno, K. Yoshida, T. Kanabe, A. Yokotani, T. Norimatsu, M. Takagi, H. Katayama, Y. Izawa, and C. Yamanaka, "High density compression of hollow-shell target by GEKKO XII and laser fusion research at ILE, Osaka University," in *Laser Interaction and Related Plasma Phenomena*, edited by H. Hora and G. H. Miley (Plenum Press, New York, 1991), Vol. 9, pp. 25–67.

[312]K. A. Tanaka, T. Yamanaka, K. Nishihara, T. Norimatsu, N. Miyanaga, H. Shiraga, M. Nakai, Y. Kitagawa, R. Kodama, T. Kanabe, H. Azechi, M. Heya, T. Jitsuno, M. Kado, K. Mima, M. Nakatsuka, A. Nishiguchi, H. Takabe, M. Takagi, K. Tsubakimoto, M. Tsukamoto, Y. Kato, Y. Izawa, and S. Nakai, "Cryogenic deuterium target experiments with the GEKKO XII, green laser system," Phys. Plasmas **2**, 2495 (1995).

[313]Y. Kitagawa, K. A. Tanaka, M. Nakai, T. Yamanaka, K. Nishihara, H. Azechi, N. Miyanaga, T. Norimatsu, T. Kanabe, C. Chen, A. Richard, M. Sato, H. Furukawa, and S. Nakai, "Areal density measurement of imploded cryogenic target by energy peak shift of DD-produced protons," Phys. Rev. Lett. **75**, 3130 (1995).

[314]H. Azechi, M. D. Cable, and R. O. Stapf, "Review of secondary and tertiary reactions, and neutron scattering as diagnostic techniques for inertial confinement fusion targets," Laser Part. Beams **9**, 119 (1991).

[315]C. Stoeckl, C. Chiritescu, J. A. Delettrez, R. Epstein, V. Yu. Glebov, D. R. Harding, R. L. Keck, S. J. Loucks, L. D. Lund, R. L. McCrory, P. W. McKenty, F. J. Marshall, D. D. Meyerhofer, S. F. B. Morse, S. P. Regan, P. B. Radha, S. Roberts, T. C. Sangster, W. Seka, S. Skupsky, V. A. Smalyuk, C. Sorce, J. M. Soures, R. P. J. Town, J. A. Frenje, C. K. Li, R. D. Petrasso, F. H. Séguin, K. Fletcher, S. Padalino, C. Freeman, N. Izumi, R. Lerche, and T. W. Phillips, "First results from cryogenic target implosions on OMEGA," Phys. Plasmas **9**, 2195 (2002).

[316]T. C. Sangster, J. A. Delettrez, R. Epstein, V. Yu. Glebov, V. N. Goncharov, D. R. Harding, J. P. Knauer, R. L. Keck, J. D. Kilkenny, S. J. Loucks, L. D. Lund, R. L. McCrory, P. W. McKenty, F. J. Marshall, D. D. Meyerhofer, S. F. B. Morse, S. P. Regan, P. B. Radha, S. Roberts, W. Seka, S. Skupsky, V. A. Smalyuk, C. Sorce, J. M. Soures, C. Stoeckl, K. Thorp, J. A. Frenje, C. K. Li, R. D. Petrasso, F. H. Séguin, K. A. Fletcher, S. Padalino, C. Freeman, N. Izumi, J. A. Koch, R. A. Lerche, M. J. Moran, T. W. Phillips, and G. J. Schmid, "Direct-drive cryogenic target implosion performance on OMEGA," Phys. Plasmas **10**, 1937 (2003).

[317]T. C. Sangster, V. N. Goncharov, R. Betti, T. R. Boehly, D. T. Casey, T. J. B. Collins, R. S. Craxton, J. A. Delettrez, D. H. Edgell, R. Epstein, K. A. Fletcher, J. A. Frenje, V. Yu. Glebov, D. R. Harding, S. X. Hu, I. V. Igumenshchev, J. P. Knauer, S. J. Loucks, C. K. Li, J. A. Marozas, F. J. Marshall, R. L. McCrory, P. W. McKenty, D. D. Meyerhofer, P. M. Nilson, S. P. Padalino, R. D. Petrasso, P. B. Radha, S. P. Regan, F. H. Seguin, W. Seka, R. W. Short, D. Shvarts, S. Skupsky, V. A. Smalyuk, J. M. Soures, C. Stoeckl, W. Theobald, and B. Yaakobi, "Shock-tuned cryogenic-deuterium-tritium implosion performance on Omega," Phys. Plasmas **17**, 056312 (2010).

[318]P. W. McKenty, T. C. Sangster, M. Alexander, R. Betti, R. S. Craxton, J. A. Delettrez, L. Elasky, R. Epstein, A. Frank, V. Yu. Glebov, V. N. Goncharov, D. R. Harding, S. Jin, J. P. Knauer, R. L. Keck, S. J. Loucks, L. D. Lund, R. L. McCrory, F. J. Marshall, D. D. Meyerhofer, S. P. Regan, P. B. Radha, S. Roberts, W. Seka, S. Skupsky, V. A. Smalyuk, J. M. Soures, K. A. Thorp, M. Wozniak, J. A. Frenje, C. K. Li, R. D. Petrasso, F. H. Séguin, K. A. Fletcher, S. Padalino, C. Freeman, N. Izumi, J. A. Koch, R. A. Lerche, M. J. Moran, T. W. Phillips, G. J. Schmid, and C. Sorce, "Direct-drive cryogenic target implosion performance on OMEGA," Phys. Plasmas **11**, 2790 (2004).

[319]F. J. Marshall, R. S. Craxton, J. A. Delettrez, D. H. Edgell, L. M. Elasky, R. Epstein, V. Yu. Glebov, V. N. Goncharov, D. R. Harding, R. Janezic, R. L. Keck, J. D. Kilkenny, J. P. Knauer, S. J. Loucks, L. D. Lund, R. L. McCrory, P. W. McKenty, D. D. Meyerhofer, P. B. Radha, S. P. Regan, T. C. Sangster, W. Seka, V. A. Smalyuk, J. M. Soures, C. Stoeckl, S. Skupsky, J. A. Frenje, C. K. Li, R. D. Petrasso, and F. H. Séguin, "Direct-drive, cryogenic target implosions on OMEGA," Phys. Plasmas **12**, 056302 (2005).

[320]T. C. Sangster, R. Betti, R. S. Craxton, J. A. Delettrez, D. H. Edgell, L. M. Elasky, V. Yu. Glebov, V. N. Goncharov, D. R. Harding, D. Jacobs-Perkins, R. Janezic, R. L. Keck, J. P. Knauer, S. J. Loucks, L. D. Lund, F. J. Marshall, R. L. McCrory, P. W. McKenty, D. D. Meyerhofer, P. B. Radha, S. P. Regan, W. Seka, W. T. Shmayda, S. Skupsky, V. A. Smalyuk, J. M. Soures, C. Stoeckl, B. Yaakobi, J. A. Frenje, C. K. Li, R. D. Petrasso, F. H. Séguin, J. D. Moody, J. A. Atherton, B. D. MacGowan, J. D. Kilkenny, T. P. Bernat, and D. S. Montgomery, "Cryogenic DT and D_2 targets for inertial confinement fusion," Phys. Plasmas **14**, 058101 (2007).

[321]T. C. Sangster, V. N. Goncharov, P. B. Radha, V. A. Smalyuk, R. Betti, R. S. Craxton, J. A. Delettrez, D. H. Edgell, V. Yu. Glebov, D. R. Harding, D. Jacobs-Perkins, J. P. Knauer, F. J. Marshall, R. L. McCrory, P. W. McKenty, D. D. Meyerhofer, S. P. Regan, W. Seka, R. W. Short, S. Skupsky, J. M. Soures, C. Stoeckl, B. Yaakobi, D. Shvarts, J. A. Frenje, C. K. Li, R. D. Petrasso, and F. H. Séguin, "High-areal-density fuel assembly in direct-drive cryogenic implosions," Phys. Rev. Lett. **100**, 185006 (2008).

[322]V. N. Goncharov, T. C. Sangster, P. B. Radha, R. Betti, T. R. Boehly, T. J. B. Collins, R. S. Craxton, J. A. Delettrez, R. Epstein, V. Yu. Glebov, S. X. Hu, I. V. Igumenshchev, J. P. Knauer, S. J. Loucks, J. A. Marozas, F. J. Marshall, R. L. McCrory, P. W. McKenty, D. D. Meyerhofer, S. P. Regan, W. Seka, S. Skupsky, V. A. Smalyuk, J. M. Soures, C. Stoeckl, D. Shvarts, J. A. Frenje, R. D. Petrasso, C. K. Li, F. Séguin, W. Manheimer, and D. G. Colombant, "Performance of direct-drive cryogenic targets on OMEGA," Phys. Plasmas **15**, 056310 (2008).

[323]V. A. Smalyuk, D. Shvarts, R. Betti, J. A. Delettrez, D. H. Edgell, V. Yu. Glebov, V. N. Goncharov, R. L. McCrory, D. D. Meyerhofer, P. B. Radha, S. P. Regan, T. C. Sangster, W. Seka, S. Skupsky, C. Stoeckl, B. Yaakobi, J. A. Frenje, C. K. Li, R. D. Petrasso, and F. H. Séguin, "Role of hot-electron preheating in the compression of direct-drive imploding targets with cryogenic D_2 ablators," Phys. Rev. Lett. **100**, 185005 (2008).

[324]V. A. Smalyuk, R. Betti, T. R. Boehly, R. S. Craxton, J. A. Delettrez, D. H. Edgell, V. Yu. Glebov, V. N. Goncharov, D. R. Harding, S. X. Hu, J. P. Knauer, F. J. Marshall, R. L. McCrory, P. W. McKenty, D. D. Meyerhofer, P. B. Radha, S. P. Regan, T. C. Sangster, W. Seka, R. W. Short, D. Shvarts, S. Skupsky, J. M. Soures, C. Stoeckl, B. Yaakobi, J. A. Frenje, C. K. Li, R. D. Petrasso, and F. H. Séguin, "Cryogenic-target performance and implosion physics studies on OMEGA," Phys. Plasmas **16**, 056301 (2009).

[325]J. A. Frenje, K. M. Green, D. G. Hicks, C. K. Li, F. H. Séguin, R. D. Petrasso, T. C. Sangster, T. W. Phillips, V. Yu. Glebov, D. D. Meyerhofer, S. Roberts, J. M. Soures, C. Stoeckl, K. Fletcher, S. Padalino, and R. J. Leeper, "A neutron spectrometer for precise measurements of DT neutrons from 10 to 18 MeV at OMEGA and the National Ignition Facility," Rev. Sci. Instrum. **72**, 854 (2001).

[326]J. A. Frenje, D. T. Casey, C. K. Li, F. H. Séguin, R. D. Petrasso, V. Yu. Glebov, P. B. Radha, T. C. Sangster, D. D. Meyerhofer, S. P. Hatchett, S. W. Haan, C. J. Cerjan, O. L. Landen, K. A. Fletcher, and R. J. Leeper, "Probing high areal-density cryogenic deuterium-tritium implosions using downscattered neutron spectra measured by the magnetic recoil spectrometer," Phys. Plasmas **17**, 056311 (2010).

[327]F. J. Marshall, R. S. Craxton, M. J. Bonino, R. Epstein, V. Yu. Glebov, D. Jacobs-Perkins, J. P. Knauer, J. A. Marozas, P. W. McKenty, S. G. Noyes, P. B. Radha, W. Seka, S. Skupsky, and V. A. Smalyuk, "Polar-direct-drive experiments on OMEGA," J. Phys. IV **133**, 153 (2006).

[328]I. V. Igumenshchev, F. J. Marshall, J. A. Marozas, V. A. Smalyuk, R. Epstein, V. N. Goncharov, T. J. B. Collins, T. C. Sangster, and S. Skupsky, "The effects of target mounts in direct-drive implosions on OMEGA," Phys. Plasmas **16**, 082701 (2009).

[329]T. C. Sangster, V. N. Goncharov, R. Betti, P. B. Radha, T. R. Boehly, D. T. Casey, T. J. B. Collins, R. S. Craxton, J. A. Delettrez, D. H. Edgell, R. Epstein, C. J. Forrest, J. A. Frenje, D. H. Froula, M. Gatu-Johnson, V. Yu. Glebov, D. R. Harding, M. Hohenberger, S. X. Hu, I. V. Igumenshchev, R. Janezic, J. H. Kelly, T. J. Kessler, C. Kingsley, T. Z. Kosc, J. P. Knauer, S. J. Loucks, J. A. Marozas, F. J. Marshall, A. V. Maximov, R. L. McCrory, P. W. McKenty, D. D. Meyerhofer, D. T. Michel, J. F. Myatt, R. D. Petrasso, S. P. Regan, W. Seka, W. T. Shmayda, R. W. Short, A. Shvydky, S. Skupsky, J. M. Soures, C. Stoeckl, W. Theobald, V. Versteeg, B. Yaakobi, and J. D. Zuegel, "Improving cryogenic deuterium–tritium implosion performance on OMEGA," Phys. Plasmas **20**, 056317 (2013).

[330]T. Ma, P. K. Patel, N. Izumi, P. T. Springer, M. H. Key, L. J. Atherton, L. R. Benedetti, D. K. Bradley, D. A. Callahan, P. M. Celliers, C. J. Cerjan, D. S. Clark, E. L. Dewald, S. N. Dixit, T. Döppner, D. H. Edgell, R. Epstein, S. Glenn, G. Grim, S. W. Haan, B. A. Hammel, D. Hicks, W. W. Hsing, O. S. Jones, S. F. Khan, J. D. Kilkenny, J. L. Kline, G. A. Kyrala, O. L. Landen, S. Le Pape, B. J. MacGowan, A. J. Mackinnon, A. G. MacPhee, N. B. Meezan, J. D. Moody, A. Pak, T. Parham, H.-S. Park, J. E. Ralph, S. P. Regan, B. A. Remington, H. F. Robey, J. S. Ross, B. K. Spears, V. Smalyuk, L. J. Suter, R. Tommasini, R. P. Town, S. V. Weber,

J. D. Lindl, M. J. Edwards, S. H. Glenzer, and E. I. Moses, "Onset of hydrodynamic mix in high-velocity, highly compressed inertial confinement fusion implosions," Phys. Rev. Lett. **111**, 085004 (2013).
[331]See National Technical Information Service Document No. UCRL5002178V2 [K. R. Manes, "Laser irradiation on target (LITAR) code," Laser Program Annual Report 1978, Lawrence Livermore National Laboratory, Livermore, CA, UCRL-50021-78 (1979), Vol. 2, pp. 6-66–6-67]. Copies may be obtained from the National Technical Information Service, Springfield, VA 22161.
[332]D. Eimerl, J. Rothenberg, M. Key, S. Weber, C. Verdon, S. Skupsky, J. Soures, and S. Craxton, "Configuring NIF for direct drive experiments," Proc. SPIE **2633**, 170–182 (1995).
[333]See National Technical Information Service Document No. DE95017854 ("Configuring the National Ignition Facility for direct-drive experiments," edited by D. Eimerl, Lawrence Livermore National Laboratory, Livermore, CA, UCRL-ID-120758, 1995). Copies may be obtained from the National Technical Information Service, Springfield, VA 22161.
[334]R. S. Craxton, F. J. Marshall, M. J. Bonino, R. Epstein, P. W. McKenty, S. Skupsky, J. A. Delettrez, I. V. Igumenshchev, D. W. Jacobs-Perkins, J. P. Knauer, J. A. Marozas, P. B. Radha, and W. Seka, "Polar direct drive: Proof-of-principle experiments on OMEGA and prospects for ignition on the National Ignition Facility," Phys. Plasmas **12**, 056304 (2005).
[335]J. D. Kilkenny, Lawrence Livermore National Laboratory, private communication (2002).
[336]R. S. Craxton, "Two-dimensional *SAGE* simulations of polar direct drive on the NIF," paper presented at the 33rd Anomalous Absorption Conference, Lake Placid, NY, 22–27 June 2003, Paper No. WO3.
[337]R. S. Craxton and R. L. McCrory, "Hydrodynamics of thermal self-focusing in laser plasmas," J. Appl. Phys. **56**, 108 (1984).
[338]A. M. Cok, R. S. Craxton, and P. W. McKenty, "Polar-drive designs for optimizing neutron yields on the National Ignition Facility," Phys. Plasmas **15**, 082705 (2008).
[339]S. Skupsky, J. A. Marozas, R. S. Craxton, R. Betti, T. J. B. Collins, J. A. Delettrez, V. N. Goncharov, P. W. McKenty, P. B. Radha, T. R. Boehly, J. P. Knauer, F. J. Marshall, D. R. Harding, J. D. Kilkenny, D. D. Meyerhofer, T. C. Sangster, and R. L. McCrory, "Polar direct drive on the National Ignition Facility," Phys. Plasmas **11**, 2763 (2004).
[340]S. G. Glendinning, Lawrence Livermore National Laboratory, private communication (2003).
[341]G. Kyrala, N. Delamater, D. Wilson, J. Guzik, D. Haynes, M. Gunderson, K. Klare, R. W. Watt, W. M. Wood, and W. Varnum, "Direct drive double shell target implosion hydrodynamics on OMEGA," Laser Part. Beams **23**, 187 (2005).
[342]J. J. MacFarlane, I. E. Golovkin, P. R. Woodruff, D. R. Welch, B. V. Oliver, T. A. Mehlhorn, and R. B. Campbell, "Simulation of the ionization dynamics of aluminum irradiated by intense short-pulse lasers," in *Inertial Fusion Sciences and Applications 2003*, edited by B. A. Hammel, D. D. Meyerhofer, J. Meyer-ter-Vehn, and H. Azechi (American Nuclear Society, La Grange Park, IL, 2004), pp. 457–460.
[343]J. A. Marozas, F. J. Marshall, R. S. Craxton, I. V. Igumenshchev, S. Skupsky, M. J. Bonino, T. J. B. Collins, R. Epstein, V. Yu. Glebov, D. Jacobs-Perkins, J. P. Knauer, R. L. McCrory, P. W. McKenty, D. D. Meyerhofer, S. G. Noyes, P. B. Radha, T. C. Sangster, W. Seka, and V. A. Smalyuk, "Polar-direct-drive simulations and experiments," Phys. Plasmas **13**, 056311 (2006).
[344]P. B. Radha, F. J. Marshall, J. A. Marozas, A. Shvydky, I. Gabalski, T. R. Boehly, T. J. B. Collins, R. S. Craxton, D. H. Edgell, R. Epstein, J. A. Frenje, D. H. Froula, V. N. Goncharov, M. Hohenberger, R. L. McCrory, P. W. McKenty, D. D. Meyerhofer, R. D. Petrasso, T. C. Sangster, and S. Skupsky, "Polar-drive implosions on OMEGA and the National Ignition Facility," Phys. Plasmas **20**, 056306 (2013).
[345]F. J. Marshall, P. W. McKenty, J. A. Delettrez, R. Epstein, J. P. Knauer, V. A. Smalyuk, J. A. Frenje, C. K. Li, R. D. Petrasso, F. H. Séguin, and R. C. Mancini, "Plasma-density determination from x-ray radiography of laser-driven spherical implosions," Phys. Rev. Lett. **102**, 185004 (2009).
[346]J. A. Cobble, T. J. Murphy, M. J. Schmitt, P. A. Bradley, N. S. Krasheninnikova, K. A. Obrey, S. C. Hsu, I. L. Tregillis, G. R. Magelssen, F. J. Wysocki, and S. H. Batha, "Asymmetric directly driven capsule implosions: Modeling and experiments—A requirement for the National Ignition Facility," Phys. Plasmas **19**, 122713 (2012).
[347]M. M. Marinak, R. E. Tipton, O. L. Landen, T. J. Murphy, P. Amendt, S. W. Haan, S. P. Hatchett, C. J. Keane, R. McEachern, and R. Wallace, "Three-dimensional simulations of Nova high growth factor capsule implosion experiments," Phys. Plasmas **3**, 2070 (1996).
[348]S. Skupsky, R. S. Craxton, F. J. Marshall, R. Betti, T. J. B. Collins, R. Epstein, V. N. Goncharov, I. V. Igumenshchev, J. A. Marozas, P. W. McKenty, P. B. Radha, J. D. Kilkenny, D. D. Meyerhofer, T. C. Sangster, and R. L. McCrory, "Polar direct drive—Ignition at 1 MJ," J. Phys. IV **133**, 233 (2006).
[349]R. S. Craxton and D. W. Jacobs-Perkins, "The Saturn target for polar direct drive on the National Ignition Facility," Phys. Rev. Lett. **94**, 095002 (2005).
[350]M. J. Schmitt, P. A. Bradley, J. A. Cobble, J. R. Fincke, P. Hakel, S. C. Hsu, N. S. Krasheninnikova, G. A. Kyrala, G. R. Magelssen, D. S. Montgomery, T. J. Murphy, K. A. Obrey, R. C. Shah, I. L. Tregillis, J. A. Baumgaertel, F. J. Wysocki, S. H. Batha, R. S. Craxton, P. W. McKenty, P. Fitzsimmons, A. Nikroo, and R. Wallace, "Development of a polar direct-drive platform for studying inertial confinement fusion implosion mix on the National Ignition Facility," Phys. Plasmas **20**, 056310 (2013).
[351]N. S. Krasheninnikova, S. M. Finnegan, and M. J. Schmitt, "An initial assessment for three-dimensional polar direct drive capsule asymmetries for implosions at the National Ignition Facility," Phys. Plasmas **19**, 012702 (2012).
[352]P. B. Radha, J. A. Marozas, F. J. Marshall, A. Shvydky, T. J. B. Collins, V. N. Goncharov, R. L. McCrory, P. W. McKenty, D. D. Meyerhofer, T. C. Sangster, and S. Skupsky, "OMEGA polar-drive target designs," Phys. Plasmas **19**, 082704 (2012).
[353]Lord Rayleigh, "Investigation of the character of the equilibrium of an incompressible heavy fluid of variable density," in *Scientific Papers* (Cambridge University Press, Cambridge, England, 1900), Vol. II, pp. 200–207.
[354]G. Taylor, "The instability of liquid surfaces when accelerated in a direction perpendicular to their planes. I," Proc. R. Soc. London, Ser. A **201**, 192 (1950).
[355]J. D. Kilkenny, S. G. Glendinning, S. W. Haan, B. A. Hammel, J. D. Lindl, D. Munro, B. A. Remington, S. V. Weber, J. P. Knauer, and C. P. Verdon, "A review of the ablative stabilization of the Rayleigh–Taylor instability in regimes relevant to inertial confinement fusion," Phys. Plasmas **1**, 1379 (1994).
[356]R. L. McCrory, L. Montierth, R. L. Morse, and C. P. Verdon, "Taylor instability in fusion targets," in *Laser Interaction and Related Plasma Phenomena*, edited by H. J. Schwarz, H. Hora, M. Lubin, and B. Yaakobi (Plenum Press, New York, 1981), Vol. 5, pp. 713–742.
[357]J. N. Shiau, E. B. Goldman, and C. I. Weng, "Linear stability analysis of laser-driven spherical implosions," Phys. Rev. Lett. **32**, 352 (1974).
[358]D. B. Henderson and R. L. Morse, "Symmetry of laser-driven implosions," Phys. Rev. Lett. **32**, 355 (1974).
[359]S. E. Bodner, "Rayleigh–Taylor instability and laser-pellet fusion," Phys. Rev. Lett. **33**, 761 (1974).
[360]R. L. McCrory, L. Montierth, R. L. Morse, and C. P. Verdon, "Nonlinear evolution of ablation-driven Rayleigh–Taylor instability," Phys. Rev. Lett. **46**, 336 (1981).
[361]C. P. Verdon, R. L. McCrory, R. L. Morse, G. R. Baker, D. I. Meiron, and S. A. Orszag, "Nonlinear effects of multifrequency hydrodynamic instabilities on ablatively accelerated thin shells," Phys. Fluids **25**, 1653 (1982).
[362]H. Takabe and K. Mima, "Effects of thermal conduction and compressibility on Rayleigh-Taylor instability," J. Phys. Soc. Jpn. **48**, 1793 (1980).
[363]L. Baker, "Propagation and smoothing of nonuniform thermal fronts," Phys. Rev. A **26**, 461 (1982).
[364]M. H. Emery, J. H. Gardner, J. P. Boris, and A. L. Cooper, "Vortex shedding due to laser ablation," Phys. Fluids **27**, 1338 (1984).
[365]H. Takabe, L. Montierth, and R. L. Morse, "Self-consistent eigenvalue analysis of Rayleigh–Taylor instability in an ablating plasma," Phys. Fluids **26**, 2299 (1983).
[366]H. Takabe, K. Mima, L. Montierth, and R. L. Morse, "Self-consistent growth rate of the Rayleigh–Taylor instability in an ablatively accelerating plasma," Phys. Fluids **28**, 3676 (1985).
[367]M. Tabak, D. H. Munro, and J. D. Lindl, "Hydrodynamic stability and the direct drive approach to laser fusion," Phys. Fluids B **2**, 1007 (1990).
[368]H. J. Kull, "Incompressible description of Rayleigh–Taylor instabilities in laser-ablated plasmas," Phys. Fluids B **1**, 170 (1989).
[369]M. A. Liberman, V. V. Bychkov, S. M. Golberg, and D. L. Book, "Stability of a planar flame front in the slow-combustion regime," Phys. Rev. E **49**, 445 (1994).
[370]V. V. Bychkov, S. M. Golberg, and M. A. Liberman, "Self-consistent model of the Rayleigh–Taylor instability in ablatively accelerated laser plasma," Phys. Plasmas **1**, 2976 (1994).

[371]J. Sanz, "Self-consistent analytical model of the Rayleigh–Taylor instability in inertial confinement fusion," Phys. Rev. Lett. **73**, 2700 (1994).
[372]R. Betti, V. N. Goncharov, R. L. McCrory, and C. P. Verdon, "Self-consistent cutoff wave number of the ablative Rayleigh–Taylor instability," Phys. Plasmas **2**, 3844 (1995).
[373]V. N. Goncharov, R. Betti, R. L. McCrory, and C. P. Verdon, "Self-consistent stability analysis of ablation fronts with small Froude numbers," Phys. Plasmas **3**, 4665 (1996).
[374]R. Betti, V. N. Goncharov, R. L. McCrory, P. Sorotokin, and C. P. Verdon, "Self-consistent stability analysis of ablation fronts in inertial confinement fusion," Phys. Plasmas **3**, 2122 (1996).
[375]A. B. Bud'ko and M. A. Liberman, "Stabilization of the Rayleigh–Taylor instability by convection in smooth density gradient: Wentzel–Kramers–Brillouin analysis," Phys. Fluids B **4**, 3499 (1992).
[376]R. Betti, V. N. Goncharov, R. L. McCrory, and C. P. Verdon, "Growth rates of the ablative Rayleigh–Taylor instability in inertial confinement fusion," Phys. Plasmas **5**, 1446 (1998).
[377]J. Sanz and R. Betti, "Analytical model of the ablative Rayleigh–Taylor instability in the deceleration phase," Phys. Plasmas **12**, 042704 (2005).
[378]J. Sanz, J. Garnier, C. Cherfils, B. Canaud, L. Masse, and M. Temporal, "Self-consistent analysis of the hot spot dynamics for inertial confinement fusion capsules," Phys. Plasmas **12**, 112702 (2005).
[379]R. Decoste, S. E. Bodner, B. H. Ripin, E. A. McLean, S. P. Obenschain, and C. M. Armstrong, "Ablative acceleration of laser-irradiated thin-foil targets," Phys. Rev. Lett. **42**, 1673 (1979).
[380]S. P. Obenschain, J. Grun, B. H. Ripin, and E. A. McLean, "Uniformity of laser-driven, ablatively accelerated targets," Phys. Rev. Lett. **46**, 1402 (1981); **48**, 709(E) (1982).
[381]J. Grun, S. P. Obenschain, B. H. Ripin, R. R. Whitlock, E. A. McLean, J. Gardner, M. J. Herbst, and J. A. Stamper, "Ablative acceleration of planar targets to high velocities," Phys. Fluids **26**, 588 (1983).
[382]S. P. Obenschain, R. R. Whitlock, E. A. McLean, B. H. Ripin, R. H. Price, D. W. Phillion, E. M. Campbell, M. D. Rosen, and J. M. Auerbach, "Uniform ablative acceleration of targets by laser irradiation at 10^{14} W/cm^2," Phys. Rev. Lett. **50**, 44 (1983).
[383]A. Raven, H. Azechi, T. Yamanaka, and C. Yamanaka, "Stability of ablatively accelerated thin foils," Phys. Rev. Lett. **47**, 1049 (1981).
[384]J. Grun, M. E. Emery, C. K. Manka, T. N. Lee, E. A. McLean, A. Mostovych, J. Stamper, S. Bodner, S. P. Obenschain, and B. H. Ripin, "Rayleigh–Taylor instability growth rates in targets accelerated with a laser beam smoothed by induced spatial incoherence," Phys. Rev. Lett. **58**, 2672 (1987).
[385]M. Desselberger, O. Willi, M. Savage, and M. J. Lamb, "Measurement of the Rayleigh–Taylor instability in targets driven by optically smoothed laser beams," Phys. Rev. Lett. **65**, 2997 (1990).
[386]J. P. Knauer, R. Betti, D. K. Bradley, T. R. Boehly, T. J. B. Collins, V. N. Goncharov, P. W. McKenty, D. D. Meyerhofer, V. A. Smalyuk, C. P. Verdon, S. G. Glendinning, D. H. Kalantar, and R. G. Watt, "Single-mode, Rayleigh–Taylor growth-rate measurements on the OMEGA laser system," Phys. Plasmas **7**, 338 (2000).
[387]H. Azechi, T. Sakaiya, S. Fujioka, Y. Tamari, K. Otani, K. Shigemori, M. Nakai, H. Shiraga, N. Miyanaga, and K. Mima, "Comprehensive diagnosis of growth rates of the ablative Rayleigh–Taylor instability," Phys. Rev. Lett. **98**, 045002 (2007).
[388]K. Shigemori, H. Azechi, M. Nakai, M. Honda, K. Meguro, N. Miyanaga, H. Takabe, and K. Mimi, "Measurements of Rayleigh–Taylor growth rate of planar targets irradiated directly by partially coherent light," Phys. Rev. Lett. **78**, 250 (1997).
[389]H. Azechi, M. Nakai, K. Shigemori, N. Miyanaga, H. Shiraga, H. Nishimura, M. Honda, R. Ishizaki, J. G. Wouchuk, H. Takabe, K. Nishihara, K. Mima, A. Nishiguchi, and T. Endo, "Direct-drive hydrodynamic instability experiments on the GEKKO XII laser," Phys. Plasmas **4**, 4079 (1997).
[390]R. R. Whitlock, M. H. Emery, J. A. Stamper, E. A. McLean, S. P. Obenschain, and M. C. Peckerar, "Observation of Rayleigh-Taylor-like structures in a laser-accelerated foil," Phys. Rev. Lett. **52**, 819 (1984).
[391]J. Grun and S. Kacenjar, "Novel x-ray backlighting method for measuring areal densities of Rayleigh–Taylor unstable, ablatively driven targets," Appl. Phys. Lett. **44**, 497 (1984).
[392]J. Grun, M. H. Emery, S. Kacenjar, C. B. Opal, E. A. McLean, S. P. Obenschain, B. H. Ripin, and A. Schmitt, "Observation of the Rayleigh–Taylor instability in ablatively accelerated foils," Phys. Rev. Lett. **53**, 1352 (1984).
[393]S. G. Glendinning, S. N. Dixit, B. A. Hammel, D. H. Kalantar, M. H. Key, J. D. Kilkenny, J. P. Knauer, D. M. Pennington, B. A. Remington, R. J. Wallace, and S. V. Weber, "Measurement of a dispersion curve for linear-regime Rayleigh–Taylor growth rates in laser-driven planar targets," Phys. Rev. Lett. **78**, 3318 (1997).
[394]T. Sakaiya, H. Azechi, M. Matsuoka, N. Izumi, M. Nakai, K. Shigemori, H. Shiraga, A. Sunahara, H. Takabe, and T. Yamanaka, "Ablative Rayleigh–Taylor instability at short wavelengths observed with moiré interferometry," Phys. Rev. Lett. **88**, 145003 (2002).
[395]M. Matsuoka, H. Azechi, M. Nakai, N. Izumi, K. Shigemori, T. Nagaya, and N. Miyanaga, "Moiré interferometry of short wavelength Rayleigh–Taylor growth," Rev. Sci. Instrum. **70**, 637 (1999).
[396]K. Otani, K. Shigemori, T. Sakaiya, S. Fujioka, A. Sunahara, M. Nakai, H. Shiraga, H. Azechi, and K. Mima, "Reduction of Rayleigh–Taylor instability growth with cocktail color irradiation," Phys. Plasmas **14**, 122702 (2007).
[397]C. J. Pawley, S. E. Bodner, J. P. Dahlburg, S. P. Obenschain, A. J. Schmitt, J. D. Sethian, C. A. Sullivan, J. H. Gardner, Y. Aglitskiy, Y. Chan, and T. Lehecka, "Observation of Rayleigh–Taylor growth to short wavelengths on Nike," Phys. Plasmas **6**, 565 (1999).
[398]V. A. Smalyuk, S. X. Hu, V. N. Goncharov, D. D. Meyerhofer, T. C. Sangster, D. Shvarts, C. Stoeckl, B. Yaakobi, J. A. Frenje, and R. D. Petrasso, "Rayleigh–Taylor growth stabilization in direct-drive plastic targets at laser intensities of $\sim 1 \times 10^{15}$ W/cm^2," Phys. Rev. Lett. **101**, 025002 (2008).
[399]V. A. Smalyuk, S. X. Hu, V. N. Goncharov, D. D. Meyerhofer, T. C. Sangster, C. Stoeckl, and B. Yaakobi, "Systematic study of Rayleigh–Taylor growth in directly driven plastic targets in a laser-intensity range of $\sim 2 \times 10^{14}$ W/cm^2 to $\sim 1.5 \times 10^{15}$ W/cm^2," Phys. Plasmas **15**, 082703 (2008).
[400]J. D. Hager, T. J. B. Collins, V. A. Smalyuk, J. P. Knauer, D. D. Meyerhofer, and T. C. Sangster, "Study of Rayleigh–Taylor growth in laser irradiated planar SiO_2 targets at ignition-relevant conditions," Phys. Plasmas **20**, 072707 (2013).
[401]D. L. Tubbs, C. W. Barnes, J. B. Beck, N. M. Hoffman, J. A. Oertel, R. G. Watt, T. Boehly, D. Bradley, P. Jaanimagi, and J. Knauer, "Cylindrical implosion experiments using laser direct drive," Phys. Plasmas **6**, 2095 (1999).
[402]M. V. Goldman, "Parametric plasmon-photon interactions: Part II. Analysis of plasmon propagator and correlation functions," Ann. Phys. **38**, 117 (1966).
[403]E. A. Jackson, "Parametric effects of radiation on a plasma," Phys. Rev. **153**, 235 (1967).
[404]A. A. Galeev, V. N. Oraevskii, and R. Z. Sagdeev, "Anomalous absorption of electromagnetic radiation at double the plasma frequency," JETP Lett. **16**, 136 (1972).
[405]M. N. Rosenbluth, "Parametric instabilities in inhomogeneous media," Phys. Rev. Lett. **29**, 565 (1972).
[406]J. I. Katz, J. Weinstock, W. L. Kruer, J. S. DeGroot, and R. J. Faehl, "Turbulently heated distribution functions and perturbed orbit theory," Phys. Fluids **16**, 1519 (1973).
[407]J. J. Thomson, R. J. Faehl, W. L. Kruer, and S. Bodner, "Electron heating due to parametric-instability turbulence," Phys. Fluids **17**, 973 (1974).
[408]J. M. Dawson, "Nonlinear electron oscillations in a cold plasma," Phys. Rev. **113**, 383 (1959).
[409]A. Simon, R. W. Short, E. A. Williams, and T. Dewandre, "On the inhomogeneous two-plasmon instability," Phys. Fluids **26**, 3107 (1983).
[410]Y. C. Lee and P. K. Kaw, "Temporal electrostatic instabilities in inhomogeneous plasmas," Phys. Rev. Lett. **32**, 135 (1974).
[411]C. S. Liu and M. N. Rosenbluth, "Parametric decay of electromagnetic waves into two plasmons and its consequences," Phys. Fluids **19**, 967 (1976).
[412]See National Technical Information Service Document No. UCRL5002177V2 [B. F. Lasinski and A. B. Langdon, "Linear theory of the $2\omega_{pe}$ instability in inhomongeneous plasmas," Laser Program Annual Report 1977, Lawrence Livermore National Laboratory, Livermore, CA, UCRL-50021-77 (1978), Vol. 2, pp. 4-49–4-51]. Copies may be obtained from the National Technical Information Service, Springfield, VA 22161.
[413]B. B. Afeyan and E. A. Williams, "A variational approach to parametric instabilities in inhomogeneous plasmas III: Two-plasmon decay," Phys. Plasmas **4**, 3827 (1997).
[414]J. L. Bobin, M. Decroisette, B. Meyer, and Y. Vitel, "Harmonic generation and parametric excitation of waves in a laser-created plasma," Phys. Rev. Lett. **30**, 594 (1973).

[415]H. C. Pant, K. Eidmann, P. Sachsenmaier, and R. Sigel, "Threshold of the $2\omega_{pe}$ instability in a laser produced plasma," Opt. Commun. **16**, 396 (1976).
[416]A. I. Avrov, V. Yu. Bychenkov, O. N. Krokhin, V. V. Pustovalov, A. A. Rupasov, V. P. Silin, G. V. Sklizkov, V. T. Tikhonchuk, and A. S. Shikanov, "Generation of the $(3/2)\omega_0$ harmonic of the neodymium-laser radiation during the heating of spherical targets," Sov. Phys.-JETP **45**, 507 (1977).
[417]B. B. Afeyan and E. A. Williams, "Unified theory of stimulated Raman scattering and two-plasmon decay in inhomogeneous plasmas: High frequency hybrid instability," Phys. Rev. Lett. **75**, 4218 (1995).
[418]J. J. Schuss, T. K. Chu, and L. C. Johnson, "Measurements of the parametric decay of CO_2-laser radiation into plasma waves at quarter-critical density using ruby-laser Thomson scattering," Phys. Rev. Lett. **40**, 27 (1978); **40**, 350(E) (1978).
[419]H. A. Baldis, J. C. Samson, and P. B. Corkum, "Two-plasmon decay and profile modification produced by 10.6-μm radiation at quarter-critical density," Phys. Rev. Lett. **41**, 1719 (1978).
[420]N. A. Ebrahim, H. A. Baldis, C. Joshi, and R. Benesch, "Hot electron generation by the two-plasmon decay instability in the laser-plasma interaction at 10.6 μm," Phys. Rev. Lett. **45**, 1179 (1980).
[421]D. M. Villeneuve, R. L. Keck, B. B. Afeyan, W. Seka, and E. A. Williams, "Production of hot electrons by two-plasmon decay instability in UV laser plasmas," Phys. Fluids **27**, 721 (1984).
[422]R. L. Keck, L. M. Goldman, M. C. Richardson, W. Seka, and K. Tanaka, "Observations of high-energy electron distributions in laser plasmas," Phys. Fluids **27**, 2762 (1984).
[423]W. C. Mead, E. M. Campbell, W. L. Kruer, R. E. Turner, C. W. Hatcher, D. S. Bailey, P. H. Y. Lee, J. Foster, K. G. Tirsell, B. Pruett, N. C. Holmes, J. T. Trainor, G. L. Stradling, B. F. Lasinski, C. E. Max, and F. Ze, "Characteristics of lateral and axial transport in laser irradiations of layered-disk targets at 1.06 and 0.35 μm wavelengths," Phys. Fluids B **27**, 1301 (1984).
[424]D. W. Phillion, E. M. Campbell, K. G. Estabrook, G. E. Phillips, and F. Ze, "High-energy electron production by the Raman and $2\omega_{pe}$ instabilities in a 1.064-μm-laser-produced underdense plasma," Phys. Rev. Lett. **49**, 1405 (1982).
[425]C. Stoeckl, R. E. Bahr, B. Yaakobi, W. Seka, S. P. Regan, R. S. Craxton, J. A. Delettrez, R. W. Short, J. Myatt, A. V. Maximov, and H. Baldis, "Multibeam effects on fast-electron generation from two-plasmon-decay instability," Phys. Rev. Lett. **90**, 235002 (2003).
[426]D. H. Froula, B. Yaakobi, S. X. Hu, P.-Y. Chang, R. S. Craxton, D. H. Edgell, R. Follett, D. T. Michel, J. F. Myatt, W. Seka, R. W. Short, A. Solodov, and C. Stoeckl, "Saturation of the two-plasmon decay instability in long-scale-length plasmas relevant to direct-drive inertial confinement fusion," Phys. Rev. Lett. **108**, 165003 (2012).
[427]D. F. DuBois, B. Bezzerides, and H. A. Rose, "Collective parametric instabilities of many overlapping laser beams with finite bandwidth," Phys. Fluids B **4**, 241 (1992).
[428]W. Seka, D. H. Edgell, J. F. Myatt, A. V. Maximov, R. W. Short, V. N. Goncharov, and H. A. Baldis, "Two-plasmon-decay instability in direct-drive inertial confinement fusion experiments," Phys. Plasmas **16**, 052701 (2009).
[429]V. A. Smalyuk, R. Betti, J. A. Delettrez, V. Yu. Glebov, D. D. Meyerhofer, P. B. Radha, S. P. Regan, T. C. Sangster, J. Sanz, W. Seka, C. Stoeckl, B. Yaakobi, J. A. Frenje, C. K. Li, R. D. Petrasso, and F. H. Séguin, "Implosion experiments using glass ablators for direct-drive inertial confinement fusion," Phys. Rev. Lett. **104**, 165002 (2010).
[430]S. X. Hu, D. T. Michel, D. H. Edgell, D. H. Froula, R. K. Follett, V. N. Goncharov, J. F. Myatt, S. Skupsky, and B. Yaakobi, "Hydrodynamic simulations of long-scale-length two-plasmon–decay experiments at the Omega Laser Facility," Phys. Plasmas **20**, 032704 (2013).
[431]J. Meyer and Y. Zhu, "Measurement of two plasmon decay instability development in k space of a laser produced plasma and its relation to 3/2-harmonic generation," Phys. Rev. Lett. **71**, 2915 (1993).
[432]B. Yaakobi, P.-Y. Chang, A. A. Solodov, C. Stoeckl, D. H. Edgell, R. S. Craxton, S. X. Hu, J. F. Myatt, F. J. Marshall, W. Seka, and D. H. Froula, "Fast-electron generation in long-scale-length plasmas," Phys. Plasmas **19**, 012704 (2012).
[433]D. T. Michel, A. V. Maximov, R. W. Short, J. A. Delettrez, D. Edgell, S. X. Hu, I. V. Igumenshchev, J. F. Myatt, A. A. Solodov, C. Stoeckl, B. Yaakobi, and D. H. Froula, "Measured hot-electron intensity threshold quantified by a two-plasmon-decay resonant common-wave gain in various experimental configurations," Phys. Plasmas **20**, 055703 (2013).
[434]D. T. Michel, A. V. Maximov, R. W. Short, S. X. Hu, J. F. Myatt, W. Seka, A. A. Solodov, B. Yaakobi, and D. H. Froula, "Experimental validation of the two-plasmon-decay common-wave process," Phys. Rev. Lett. **109**, 155007 (2012).
[435]B. Yaakobi, A. A. Solodov, J. F. Myatt, J. A. Delettrez, C. Stoeckl, and D. H. Froula, "Measurements of the divergence of fast electrons in laser-irradiated spherical targets," Phys. Plasmas **20**, 092706 (2013).
[436]A. B. Langdon, B. F. Lasinski, and W. L. Kruer, "Nonlinear saturation and recurrence of the two-plasmon decay instability," Phys. Rev. Lett. **43**, 133 (1979).
[437]R. Yan, A. V. Maximov, C. Ren, and F. S. Tsung, "Growth and saturation of convective modes of the two-plasmon decay instability in inertial confinement fusion," Phys. Rev. Lett. **103**, 175002 (2009).
[438]H. X. Vu, D. F. DuBois, D. A. Russell, and J. F. Myatt, "The reduced-description particle-in-cell model for the two plasmon decay instability," Phys. Plasmas **17**, 072701 (2010).
[439]D. F. DuBois, D. A. Russell, and H. A. Rose, "Saturation spectra of the two-plasmon decay instability," Phys. Rev. Lett. **74**, 3983 (1995).
[440]D. A. Russell and D. F. DuBois, "$3/2\omega_0$ radiation from the laser-driven two-plasmon decay instability in an inhomogeneous plasma," Phys. Rev. Lett. **86**, 428 (2001).
[441]J. F. Myatt, H. X. Vu, D. F. DuBois, D. A. Russell, J. Zhang, R. W. Short, and A. V. Maximov, "Mitigation of two-plasmon decay in direct-drive inertial confinement fusion through the manipulation of ion-acoustic and Langmuir wave damping," Phys. Plasmas **20**, 052705 (2013).
[442]R. Yan, C. Ren, J. Li, A. V. Maximov, W. B. Mori, Z.-M. Sheng, and F. S. Tsung, "Generating energetic electrons through staged acceleration in the two-plasmon-decay instability in inertial confinement fusion," Phys. Rev. Lett. **108**, 175002 (2012).
[443]H. X. Vu, D. F. DuBois, D. A. Russell, and J. F. Myatt, "Hot-electron generation by "cavitating" Langmuir turbulence in the nonlinear stage of the two-plasmon–decay instability," Phys. Plasmas **19**, 102708 (2012).
[444]H. X. Vu, D. F. DuBois, J. F. Myatt, and D. A. Russell, "Hot-electron production and suprathermal heat flux scaling with laser intensity from the two-plasmon-decay instability," Phys. Plasmas **19**, 102703 (2012).
[445]L. Brillouin, "Diffusion de la lumière et des rayons x par un corps transparent homogène: Influence de l'agitation thermique," Ann. Phys. (France) **17**, 88 (1922).
[446]N. M. Kroll, "Excitation of hypersonic vibrations by means of photoelastic coupling of high-intensity light waves to elastic waves," J. Appl. Phys. **36**, 34 (1965).
[447]C. S. Liu, M. N. Rosenbluth, and R. B. White, "Raman and Brillouin scattering of electromagnetic waves in homogeneous plasmas," Phys. Fluids **17**, 1211 (1974).
[448]D. W. Forslund, J. M. Kindel, and E. L. Lindman, "Theory of stimulated scattering processes in laser-irradiated plasmas," Phys. Fluids **18**, 1002 (1975).
[449]D. W. Forslund, J. M. Kindel, and E. L. Lindman, "Nonlinear behavior of stimulated Brillouin and Raman scattering in laser-irradiated plasmas," Phys. Rev. Lett. **30**, 739 (1973).
[450]D. W. Forslund, J. M. Kindel, and E. L. Lindman, "Plasma simulation studies of stimulated scattering processes in laser-irradiated plasmas," Phys. Fluids **18**, 1017 (1975).
[451]W. L. Kruer, K. G. Estabrook, and K. H. Sinz, "Instability-generated laser reflection in plasmas," Nucl. Fusion **13**, 952 (1973).
[452]A. A. Galeev, G. Laval, T. M. O'Neil, M. N. Rosenbluth, and R. Z. Sagdeev, "Parametric back scattering of a linear electromagnetic wave in a plasma," JETP Lett. **17**, 35 (1973).
[453]K. Eidmann and R. Sigel, "Backscatter experiments," in *Laser Interaction and Related Plasma Phenomena*, edited by H. J. Schwarz and H. Hora (Plenum Press, New York, 1974), Vol. 3B, pp. 667–690.
[454]B. H. Ripin, F. C. Young, J. A. Stamper, C. M. Armstrong, R. Decoste, E. A. McLean, and S. E. Bodner, "Enhanced backscatter with a structured laser pulse," Phys. Rev. Lett. **39**, 611 (1977).
[455]R. H. Lehmberg, "Theory of optical ray retracing in laser-plasma backscatter," Phys. Rev. Lett. **41**, 863 (1978).
[456]R. A. Haas, H. D. Shay, W. L. Kruer, M. J. Boyle, D. W. Phillion, F. Rainer, V. C. Rupert, and H. N. Kornblum, "Interaction of 1.06-μm laser radiation with planar targets," Phys. Rev. Lett. **39**, 1533 (1977).
[457]D. W. Phillion, W. L. Kruer, and V. C. Rupert, "Brillouin scatter in laser-produced plasmas," Phys. Rev. Lett. **39**, 1529 (1977).
[458]H. D. Shay, R. A. Haas, W. L. Kruer, M. J. Boyle, D. W. Phillion, V. C. Rupert, H. N. Kornblum, F. Rainer, V. W. Slivinsky, L. N. Koppel,

L. Richards, and K. G. Tirsell, "Interaction of 1.06 μm laser radiation with variable $\bar{Z}$ targets," Phys. Fluids **21**, 1634 (1978).
[459]M. D. Rosen, D. W. Phillion, V. C. Rupert, W. C. Mead, W. L. Kruer, J. J. Thomson, H. N. Kornblum, V. W. Slivinsky, G. J. Caporaso, M. J. Boyle, and K. G. Tirsell, "The interaction of 1.06 μm laser radiation with high Z disk targets," Phys. Fluids **22**, 2020 (1979).
[460]L. M. Goldman, J. Soures, and M. J. Lubin, "Saturation of stimulated backscattered radiation in laser plasmas," Phys. Rev. Lett. **31**, 1184 (1973).
[461]K. Büchl, K. Eidmann, H. Salzmann, and R. Sigel, "Spectral investigation of light reflected from a laser-produced deuterium plasma," Appl. Phys. Lett. **20**, 3 (1972).
[462]J. A. Tarvin and R. J. Schroeder, "Time-resolved spectrum of light reflected from laser-produced plasmas," Phys. Rev. Lett. **47**, 341 (1981).
[463]S. P. Regan, D. K. Bradley, A. V. Chirokikh, R. S. Craxton, D. D. Meyerhofer, W. Seka, R. W. Short, A. Simon, R. P. J. Town, B. Yaakobi, J. J. Carroll III, and R. P. Drake, "Laser-plasma interactions in long-scale-length plasmas under direct-drive National Ignition Facility conditions," Phys. Plasmas **6**, 2072 (1999).
[464]J. Myatt, A. V. Maximov, W. Seka, R. S. Craxton, and R. W. Short, "Modeling stimulated Brillouin scattering in the underdense corona of a direct drive inertial confinement fusion target," Phys. Plasmas **11**, 3394 (2004).
[465]W. Seka, H. A. Baldis, J. Fuchs, S. P. Regan, D. D. Meyerhofer, C. Stoeckl, B. Yaakobi, R. S. Craxton, and R. W. Short, "Multibeam stimulated Brillouin scattering from hot, solid-target plasmas," Phys. Rev. Lett. **89**, 175002 (2002).
[466]A. V. Maximov, J. Myatt, W. Seka, R. W. Short, and R. S. Craxton, "Modeling of stimulated Brillouin scattering near the critical-density surface in the plasmas of direct-drive inertial confinement fusion targets," Phys. Plasmas **11**, 2994 (2004).
[467]W. Seka, R. S. Craxton, R. L. Keck, J. P. Knauer, D. D. Meyerhofer, S. P. Regan, C. Stoeckl, B. Yaakobi, R. E. Bahr, D. Montgomery, H. Baldis, and R. Kirkwood, "Laser-plasma interaction diagnostics for ICF fusion research," in *Advanced Diagnostics for Magnetic and Inertial Fusion*, edited by P. E. Stott, A. Wootton, G. Gorini, E. Sindoni, and D. Batani (Kluwer Academic/Plenum Publishers, New York, 2002), pp. 27–30.
[468]I. M. Begg and R. A. Cairns, "Enhanced reflection of laser light from an expanding plasma," J. Phys. D: Appl. Phys. **9**, 2341 (1976).
[469]C. J. Randall, J. J. Thomson, and K. G. Estabrook, "Enhancement of stimulated Brillouin scattering due to reflection of light from plasma critical surface," Phys. Rev. Lett. **43**, 924 (1979).
[470]W. L. Kruer, S. C. Wilks, B. B. Afeyan, and R. K. Kirkwood, "Energy transfer between crossing laser beams," Phys. Plasmas **3**, 382 (1996).
[471]R. K. Kirkwood, B. B. Afeyan, W. L. Kruer, B. J. MacGowan, J. D. Moody, D. S. Montgomery, D. M. Pennington, T. L. Weiland, and S. C. Wilks, "Observation of energy transfer between frequency-mismatched laser beams in a large-scale plasma," Phys. Rev. Lett. **76**, 2065 (1996).
[472]W. Seka, S. P. Regan, D. D. Meyerhofer, B. Yaakobi, C. Stoeckl, R. S. Craxton, R. W. Short, H. Baldis, J. Fuchs, and C. Labaune, "Stimulated Brillouin sidescatter and backscatter in NIF scale direct-drive plasmas," Bull. Am. Phys. Soc. **46**, 283 (2001).
[473]S. H. Glenzer, B. J. MacGowan, P. Michel, N. B. Meezan, L. J. Suter, S. N. Dixit, J. L. Kline, G. A. Kyrala, D. K. Bradley, D. A. Callahan, E. L. Dewald, L. Divol, E. Dzenitis, M. J. Edwards, A. V. Hamza, C. A. Haynam, D. E. Hinkel, D. H. Kalantar, J. D. Kilkenny, O. L. Landen, J. D. Lindl, S. LePape, J. D. Moody, A. Nikroo, T. Parham, M. B. Schneider, R. P. J. Town, P. Wegner, K. Widmann, P. Whitman, B. K. F. Young, B. Van Wonterghem, L. J. Atherton, and E. I. Moses, "Symmetric inertial confinement fusion implosions at ultra-high laser energies," Science **327**, 1228 (2010).
[474]P. Michel, S. H. Glenzer, L. Divol, D. K. Bradley, D. Callahan, S. Dixit, S. Glenn, D. Hinkel, R. K. Kirkwood, J. L. Kline, W. L. Kruer, G. A. Kyrala, S. Le Pape, N. B. Meezan, R. Town, K. Widmann, E. A. Williams, B. J. MacGowan, J. Lindl, and L. J. Suter, "Symmetry tuning via controlled crossed-beam energy transfer on the National Ignition Facility," Phys. Plasmas **17**, 056305 (2010).
[475]I. V. Igumenshchev, W. Seka, D. H. Edgell, D. T. Michel, D. H. Froula, V. N. Goncharov, R. S. Craxton, L. Divol, R. Epstein, R. Follett, J. H. Kelly, T. Z. Kosc, A. V. Maximov, R. L. McCrory, D. D. Meyerhofer, P. Michel, J. F. Myatt, T. C. Sangster, A. Shvydky, S. Skupsky, and C. Stoeckl, "Crossed-beam energy transfer in direct-drive implosions," Phys. Plasmas **19**, 056314 (2012).
[476]D. H. Froula, I. V. Igumenshchev, D. T. Michel, D. H. Edgell, R. Follett, V. Yu. Glebov, V. N. Goncharov, J. Kwiatkowski, F. J. Marshall, P. B. Radha, W. Seka, C. Sorce, S. Stagnitto, C. Stoeckl, and T. C. Sangster, "Increasing hydrodynamic efficiency by reducing cross-beam energy transfer in direct-drive implosion experiments," Phys. Rev. Lett. **108**, 125003 (2012).
[477]R. K. Kirkwood, P. Michel, R. London, J. D. Moody, E. Dewald, L. Yin, J. Kline, D. Hinkel, D. Callahan, N. Meezan, E. Williams, L. Divol, B. L. Albright, K. J. Bowers, E. Bond, H. Rose, Y. Ping, T. L. Wang, C. Joshi, W. Seka, N. J. Fisch, D. Turnbull, S. Suckewer, J. S. Wurtele, S. Glenzer, L. Suter, C. Haynam, O. Landen, and B. J. Macgowan, "Multi-beam effects on backscatter and its saturation in experiments with conditions relevant to ignition," Phys. Plasmas **18**, 056311 (2011).
[478]R. K. Kirkwood, J. D. Moody, J. Kline, E. Dewald, S. Glenzer, L. Divol, P. Michel, D. Hinkel, R. Berger, E. Williams, J. Milovich, L. Yin, H. Rose, B. MacGowan, O. Landen, M. Rosen, and J. Lindl, "A review of laser–plasma interaction physics of indirect-drive fusion," Plasma Phys. Controlled Fusion **55**, 103001 (2013).
[479]A. Smekal, "Zur quantentheorie der dispersion," Naturwissenschaften **11**, 873 (1923).
[480]C. V. Raman, "A new radiation," Indian J. Phys. **2**, 387 (1928).
[481]G. Landsberg and L. Mandelstam, "Eine neue erscheinung bei der lichtzerstreuung in krystallen," Naturwissenschaften **16**, 557 (1928).
[482]R. W. Hellwarth, "Theory of stimulated Raman scattering," Phys. Rev. **130**, 1850 (1963).
[483]G. G. Comisar, "Theory of the stimulated Raman effect in plasmas," Phys. Rev. **141**, 200 (1966).
[484]M. V. Goldman and D. F. Du Bois, "Stimulated incoherent scattering of light from plasmas," Phys. Fluids **8**, 1404 (1965).
[485]N. Bloembergen and Y. R. Shen, "Optical nonlinearities of a plasma," Phys. Rev. **141**, 298 (1966).
[486]See National Technical Information Service Document No. DE81026589 (D. W. Phillion and D. L. Banner, "Stimulated Raman scattering in large plasmas," Lawrence Livermore National Laboratory, Livermore, CA, UCRL-84854, 1980). Copies may be obtained from the National Technical Information Service, Springfield, VA 22161.
[487]J. F. Drake and Y. C. Lee, "Temporally growing Raman backscattering instabilities in an inhomogeneous plasma," Phys. Rev. Lett. **31**, 1197 (1973).
[488]W. L. Kruer, K. Estabrook, B. F. Lasinski, and A. B. Langdon, "Raman backscatter in high temperature, inhomogeneous plasmas," Phys. Fluids **23**, 1326 (1980).
[489]K. Estabrook, W. L. Kruer, and B. F. Lasinski, "Heating by Raman backscatter and forward scatter," Phys. Rev. Lett. **45**, 1399 (1980).
[490]C. E. Max, E. M. Campbell, W. C. Mead, W. L. Kruer, D. W. Phillion, R. E. Turner, B. F. Lasinski, and K. G. Estabrook, "Scaling of laser-plasma interactions with laser wavelength and plasma size," in *Laser Interaction and Related Plasma Phenomena*, edited by H. Hora and G. H. Miley (Plenum Press, New York, 1984), Vol. 6, pp. 507–526.
[491]J. M. Manley and H. E. Rowe, "Some general properties of nonlinear elements—Part I. General energy relations," Proc. IRE **44**, 904 (1956).
[492]W. Seka, B. B. Afeyan, R. Boni, L. M. Goldman, R. W. Short, K. Tanaka, and T. W. Johnston, "Diagnostic value of odd-integer half-harmonic emission from laser-produced plasmas," Phys. Fluids **28**, 2570 (1985).
[493]R. L. Berger and L. V. Powers, "Emission of light at half-integer harmonics of the laser frequency," Phys. Fluids **28**, 2895 (1985).
[494]R. E. Turner, D. W. Phillion, E. M. Campbell, and K. G. Estabrook, "Time-resolved observations of stimulated Raman scattering from laser-produced plasmas," Phys. Fluids **26**, 579 (1983).
[495]R. P. Drake, R. E. Turner, B. F. Lasinski, K. G. Estabrook, E. M. Campbell, C. L. Wang, D. W. Phillion, E. A. Williams, and W. L. Kruer, "Efficient Raman sidescatter and hot-electron production in laser-plasma interaction experiments," Phys. Rev. Lett. **53**, 1739 (1984).
[496]K. Tanaka, L. M. Goldman, W. Seka, M. C. Richardson, J. M. Soures, and E. A. Williams, "Stimulated Raman scattering from UV-laser-produced plasmas," Phys. Rev. Lett. **48**, 1179 (1982).
[497]R. P. Drake, E. A. Williams, P. E. Young, K. Estabrook, W. L. Kruer, D. S. Montgomery, H. A. Baldis, and T. W. Johnston, "Narrow Raman spectra: The competition between collisional and Landau damping," Phys. Fluids B **1**, 2217 (1989).
[498]H. Figueroa, C. Joshi, H. Azechi, N. A. Ebrahim, and K. Estabrook, "Stimulated Raman scattering, two-plasmon decay, and hot electron

generation from underdense plasmas at 0.35 μm," Phys. Fluids **27**, 1887 (1984).
[499]R. E. Turner, K. Estabrook, R. L. Kauffman, D. R. Bach, R. P. Drake, D. W. Phillion, B. F. Lasinski, E. M. Campbell, W. L. Kruer, and E. A. Williams, "Evidence for collisional damping in high-energy Raman-scattering experiments at 0.26 μm," Phys. Rev. Lett. **54**, 189 (1985); **54**, 1878(E) (1985).
[500]R. W. Short, W. Seka, and R. Bahr, "Stimulated Raman scattering in self-focused light filaments in laser-produced plasmas," Phys. Fluids **30**, 3245 (1987).
[501]S. P. Obenschain, C. J. Pawley, A. N. Mostovych, J. A. Stamper, J. H. Gardner, A. J. Schmitt, and S. E. Bodner, "Reduction of Raman scattering in a plasma to convective levels using induced spatial incoherence," Phys. Rev. Lett. **62**, 768 (1989).
[502]S. E. Coe, T. Afshar-rad, M. Desselberger, F. Khattak, O. Willi, A. Giulietti, Z. Q. Lin, W. Yu, and C. Danson, "Suppression of instabilities in a long-scalelength preformed plasma," Europhys. Lett. **10**, 31 (1989).
[503]W. Seka, R. E. Bahr, R. W. Short, A. Simon, R. S. Craxton, D. S. Montgomery, and A. E. Rubenchik, "Nonlinear laser-matter interaction processes in long-scale-length plasmas," Phys. Fluids B **4**, 2232 (1992).
[504]W. Seka, unpublished results (2003).
[505]W. Seka, D. H. Edgell, J. F. Myatt, R. S. Craxton, A. V. Maximov, and R. W. Short, "SBS, SRS, and TPD in planar target experiments relevant to direct-drive ICF," paper presented at the 40th Annual Anomalous Absorption Conference, Snowmass Village, CO, 13–18 June 2010.
[506]C. B. Darrow, R. P. Drake, D. S. Montgomery, P. E. Young, K. Estabrook, W. L. Kruer, and T. W. Johnston, "Experimental studies of stimulated Raman scattering in reactor-size laser-produced plasmas," Phys. Fluids B **3**, 1473 (1991).
[507]G. A. Askar'yan, "Effects of the gradient of a strong electromagnetic beam on electrons and atoms," Sov. Phys.-JETP **15**, 1088 (1962).
[508]P. Kaw, G. Schmidt, and T. Wilcox, "Filamentation and trapping of electromagnetic radiation in plasmas," Phys. Fluids **16**, 1522 (1973).
[509]F. W. Perkins and E. J. Valeo, "Thermal self-focusing of electromagnetic waves in plasmas," Phys. Rev. Lett. **32**, 1234 (1974).
[510]W. L. Kruer, "Ponderomotive and thermal filamentation of laser light," Comments Plasma Phys. Controlled Fusion **9**, 63 (1985).
[511]E. M. Epperlein, "Kinetic theory of laser filamentation in plasmas," Phys. Rev. Lett. **65**, 2145 (1990).
[512]P. E. Young, H. A. Baldis, R. P. Drake, E. M. Campbell, and K. G. Estabrook, "Direct evidence of ponderomotive filamentation in a laser-produced plasma," Phys. Rev. Lett. **61**, 2336 (1988).
[513]P. E. Young, "Characterization of filamentation in laser-produced plasmas," Comments Plasma Phys. Controlled Fusion **12**, 53 (1988).
[514]H. A. Rose and D. F. DuBois, "Initial development of ponderomotive filaments in plasma from intense hot spots produced by a random phase plate," Phys. Fluids B **5**, 3337 (1993).
[515]R. Y. Chiao, E. Garmire, and C. H. Townes, "Self-trapping of optical beams," Phys. Rev. Lett. **13**, 479 (1964); **14**, 1056(E) (1965).
[516]K. Estabrook, W. L. Kruer, and D. S. Bailey, "Two-dimensional ray-trace calculations of thermal whole beam self-focusing," Phys. Fluids **28**, 19 (1985).
[517]D. J. Nicholas and S. G. Sajjadi, "Numerical simulation of filamentation in laser-plasma interactions," J. Phys. D: Appl. Phys. **19**, 737 (1986).
[518]A. J. Schmitt, "The effects of optical smoothing techniques on filamentation in laser plasmas," Phys. Fluids **31**, 3079 (1988).
[519]R. Rankin, C. E. Capjack, and C. R. James, "Numerical simulations of induced spatial incoherence laser light self-focusing," Phys. Fluids B **1**, 2437 (1989).
[520]A. J. Schmitt, "Three-dimensional filamentation of light in laser plasmas," Phys. Fluids B **3**, 186 (1991).
[521]R. L. Berger, B. F. Lasinski, T. B. Kaiser, E. A. Williams, A. B. Langdon, and B. I. Cohen, "Theory and three-dimensional simulation of light filamentation in laser-produced plasma," Phys. Fluids B **5**, 2243 (1993).
[522]A. J. Schmitt and B. B. Afeyan, "Time-dependent filamentation and stimulated Brillouin forward scattering in inertial confinement fusion plasmas," Phys. Plasmas **5**, 503 (1998).
[523]R. L. Berger, C. H. Still, E. A. Williams, and A. B. Langdon, "On the dominant and subdominant behavior of stimulated Raman and Brillouin scattering driven by nonuniform laser beams," Phys. Plasmas **5**, 4337 (1998).
[524]S. Hüller, Ph. Mounaix, and V. T. Tikhonchuk, "SBS reflectivity from spatially smoothed laser beams: Random phase plates versus polarization smoothing," Phys. Plasmas **5**, 2706 (1998).
[525]L. C. Johnson and T. K. Chu, "Measurements of electron density evolution and beam self-focusing in a laser-produced plasma," Phys. Rev. Lett. **32**, 517 (1974).
[526]B. Grek, F. Martin, T. W. Johnston, H. Pépin, G. Mitchel, and F. Rheault, "Fine-scale structures in plasmas stimulated by a CO_2 laser," Phys. Rev. Lett. **41**, 1811 (1978).
[527]C. Joshi, C. E. Clayton, A. Yasuda, and F. F. Chen, "Direct observation of laser beam filamentation in an underdense plasma," J. Appl. Phys. **53**, 215 (1982).
[528]O. Willi, P. T. Rumsby, and S. Sartang, "Optical probe observations of nonuniformities in laser-produced plasmas," IEEE J. Quantum Electron. **17**, 1909 (1981).
[529]O. Willi and P. T. Rumsby, "Filamentation on laser irradiated spherical targets," Opt. Commun. **37**, 45 (1981).
[530]M. G. Haines, "Thermal instability and magnetic field generated by large heat flow in a plasma, especially under laser-fusion conditions," Phys. Rev. Lett. **47**, 917 (1981).
[531]R. A. Haas, M. J. Boyle, K. R. Manes, and J. E. Swain, "Evidence of localized heating in CO_2-laser-produced plasmas," J. Appl. Phys. **47**, 1318 (1976).
[532]O. Willi and P. H. Y. Lee, "Filamentation of an annular laser beam in a short wavelength laser produced plasma," Opt. Commun. **55**, 120 (1985).
[533]M. J. Herbst, J. A. Stamper, R. R. Whitlock, R. H. Lehmberg, and B. H. Ripin, "Evidence from x-ray, 3/2 ω_0, and $2\omega_0$ emission for laser filamentation in a plasma," Phys. Rev. Lett. **46**, 328 (1981).
[534]M. J. Herbst, R. R. Whitlock, and F. C. Young, "Unusual structures observed in x-ray emission from laser-irradiated targets," Phys. Rev. Lett. **47**, 91 (1981); **47**, 1568(E) (1981).
[535]Z. Xu, P. H. Y. Lee, Y. Xu, W. Zhang, and L. Wang, "Intense laser self-focusing in plasmas," Sci. Sin. Ser. A **26**, 435 (1983).
[536]J. A. Stamper, R. H. Lehmberg, A. Schmitt, M. J. Herbst, F. C. Young, J. H. Gardner, and S. P. Obenschain, "Evidence in the second-harmonic emission for self-focusing of a laser pulse in a plasma," Phys. Fluids **28**, 2563 (1985).
[537]Z. Lin, O. Willi, and P. T. Rumsby, "Evidence for beam self-focusing in the corona of laser-irradiated spherical targets," J. Phys. D: Appl. Phys. **14**, L35 (1981).
[538]P. E. Young, "Experimental study of filamentation in laser-plasma interactions," Phys. Fluids B **3**, 2331 (1991).
[539]S. E. Coe, T. Afshar-rad, and O. Willi, "Direct observations of filamentation and self-focusing in a large underdense plasma," Opt. Commun. **73**, 299 (1989).
[540]S. E. Coe, T. Afshar-rad, and O. Willi, "Experimental observations of thermal whole beam self-focusing," Europhys. Lett. **13**, 251 (1990).
[541]O. Willi, T. Afshar-rad, S. Coe, and A. Giulietti, "Study of instabilities in long scale-length plasmas with and without laser-beam-smoothing techniques," Phys. Fluids B **2**, 1318 (1990).
[542]T. Afshar-rad, S. E. Coe, O. Willi, and M. Desselberger, "Evidence of stimulated Raman scattering occurring in laser filaments in long-scale-length plasmas," Phys. Fluids B **4**, 1301 (1992).
[543]J. A. Armstrong, N. Bloembergen, J. Ducuing, and P. S. Pershan, "Interactions between light waves in a nonlinear dielectric," Phys. Rev. **127**, 1918 (1962).
[544]V. P. Silin, "Parametric resonance in a plasma," Sov. Phys.-JETP **21**, 1127 (1965).
[545]D. F. DuBois and M. V. Goldman, "Radiation-induced instability of electron plasma oscillations," Phys. Rev. Lett. **14**, 544 (1965).
[546]V. N. Oraevskii and R. Z. Sagdeev, "Stability of steady-state longitudinal plasma oscillations," Sov. Phys.-Tech. Phys. **7**, 955 (1963).
[547]M. V. Goldman, "Parametric plasmon-photon interaction: Part I. Threshold for amplification of plasmons," Ann. Phys. **38**, 95 (1966).
[548]R. A. Stern and N. Tzoar, "Parametric coupling between electron-plasma and ion-acoustic oscillations," Phys. Rev. Lett. **17**, 903 (1966).
[549]D. F. DuBois and M. V. Goldman, "Parametrically excited plasma fluctuations," Phys. Rev. **164**, 207 (1967).
[550]K. Nishikawa, "Parametric excitation of coupled waves. II. Parametric plasmon-photon interaction," J. Phys. Soc. Jpn. **24**, 1152 (1968).
[551]W. L. Kruer, P. K. Kaw, J. M. Dawson, and C. Oberman, "Anomalous high-frequency resistivity and heating of a plasma," Phys. Rev. Lett. **24**, 987 (1970).
[552]T. Amano and M. Okamoto, "Parametric effects of an alternating field on inhomogeneous plasmas," J. Phys. Soc. Jpn. **26**, 529 (1969).
[553]W. L. Kruer and J. M. Dawson, "Anomalous high-frequency resistivity of a plasma," Phys. Fluids **15**, 446 (1972).

[554]A. Y. Wong, F. F. Chen, N. Booth, D. L. Jassby, R. Stenzel, D. Baker, and C. S. Liu, "Remote plasma control, heating and measurements of electron distribution and trapped particles by non-linear electromagnetic interactions," in *Plasma Physics and Controlled Nuclear Fusion Research 1971* (IAEA, Vienna, 1971), Vol. I, pp. 335–342.
[555]K. Mizuno, J. S. DeGroot, and K. G. Estabrook, "Electron heating due to *s*-polarized microwave (laser) driven parametric instabilities," Phys. Rev. Lett. **52**, 271 (1984).
[556]K. Mizuno, F. Kehl, and J. S. DeGroot, "Investigations of the angular distribution of parametrically driven ion acoustic waves," Phys. Rev. Lett. **56**, 2184 (1986).
[557]K. Mizuno, P. E. Young, W. Seka, R. Bahr, J. S. De Groot, R. P. Drake, and K. G. Estabrook, "Investigation of ion-acoustic-decay instability thresholds in laser-plasma interactions," Phys. Rev. Lett. **65**, 428 (1990).
[558]K. Mizuno, R. Bahr, B. S. Bauer, R. S. Craxton, J. S. DeGroot, R. P. Drake, W. Seka, and B. Sleaford, "Direct measurements of the ion acoustic decay instability in a laser-produced, large-scale, hot plasma," Phys. Rev. Lett. **73**, 2704 (1994).
[559]V. V. Korobkin and R. V. Serov, "Investigation of the magnetic field of a spark produced by focusing laser radiation," JETP Lett. **4**, 70 (1966).
[560]G. A. Askar'yan, M. S. Rabinovich, A. D. Smirnova, and V. B. Studenov, "Currents produced by light pressure when a laser beam acts on matter," JETP Lett. **5**, 93 (1967).
[561]J. A. Stamper, K. Papadopoulos, R. N. Sudan, S. O. Dean, E. A. McLean, and J. M. Dawson, "Spontaneous magnetic fields in laser-produced plasmas," Phys. Rev. Lett. **26**, 1012 (1971).
[562]L. Biermann and A. Schlüter, "Cosmic radiation and cosmic magnetic fields. II. Origin of cosmic magnetic fields," Phys. Rev. **82**, 863 (1951).
[563]M. G. Haines, "Magnetic-field generation in laser fusion and hot-electron transport," Can. J. Phys. **64**, 912 (1986).
[564]J. A. Stamper, "Review on spontaneous magnetic fields in laser-produced plasmas: Phenomena and measurements," Laser Part. Beams **9**, 841 (1991).
[565]F. Schwirzke, "Measurements of spontaneous magnetic fields in laser-produced plasmas," in *Laser Interaction and Related Plasma Phenomena*, edited by H. J. Schwarz and H. Hora (Plenum Press, New York, 1974), Vol. 3A, pp. 213–235.
[566]J. A. Stamper and B. H. Ripin, "Faraday-rotation measurements of megagauss magnetic fields in laser-produced plasmas," Phys. Rev. Lett. **34**, 138 (1975).
[567]A. Raven, O. Willi, and P. T. Rumsby, "Megagauss magnetic field profiles in laser-produced plasmas," Phys. Rev. Lett. **41**, 554 (1978); **41**, 1002(E) (1978).
[568]J. A. Stamper, E. A. McLean, and B. H. Ripin, "Studies of spontaneous magnetic fields in laser-produced plasmas by Faraday rotation," Phys. Rev. Lett. **40**, 1177 (1978).
[569]A. Raven, P. T. Rumsby, J. A. Stamper, O. Willi, R. Illingworth, and R. Thareja, "Dependence of spontaneous magnetic fields in laser produced plasmas on target size and structure," Appl. Phys. Lett. **35**, 526 (1979).
[570]O. Willi, P. T. Rumsby, and C. Duncan, "Megagauss magnetic fields on laser irradiated spherical targets," Opt. Commun. **37**, 40 (1981).
[571]E. A. McLean, J. A. Stamper, C. K. Manka, H. R. Griem, D. W. Droemer, and B. H. Ripin, "Observation of magnetic fields in laser-produced plasma using the Zeeman effect," Phys. Fluids **27**, 1327 (1984).
[572]M. A. Yates, D. B. van Hulsteyn, H. Rutkowski, G. Kyrala, and J. U. Brackbill, "Experimental evidence for self-generated magnetic fields and remote energy deposition in laser-irradiated targets," Phys. Rev. Lett. **49**, 1702 (1982).
[573]D. W. Forslund and J. U. Brackbill, "Magnetic-field-induced surface transport on laser-irradiated foils," Phys. Rev. Lett. **48**, 1614 (1982).
[574]K. Mima, T. Tajima, and J. N. Leboeuf, "Magnetic field generation by the Rayleigh–Taylor instability," Phys. Rev. Lett. **41**, 1715 (1978).
[575]M. J.-E. Manuel, C. K. Li, F. H. Séguin, J. Frenje, D. T. Casey, R. D. Petrasso, S. X. Hu, R. Betti, J. D. Hager, D. D. Meyerhofer, and V. A. Smalyuk, "First measurements of Rayleigh-Taylor-induced magnetic fields in laser-produced plasmas," Phys. Rev. Lett. **108**, 255006 (2012).
[576]M. J.-E. Manuel, C. K. Li, F. H. Séguin, J. A. Frenje, D. T. Casey, R. D. Petrasso, S. X. Hu, R. Betti, J. D. Hager, D. D. Meyerhofer, and V. Smalyuk, "Rayleigh-Taylor-induced magnetic fields in laser-irradiated plastic foils," Phys. Plasmas **19**, 082710 (2012).
[577]L. Gao, P. M. Nilson, I. V. Igumenshchev, S. X. Hu, J. R. Davies, C. Stoeckl, M. G. Haines, D. H. Froula, R. Betti, and D. D. Meyerhofer, "Magnetic field generation by the Rayleigh-Taylor instability in laser-driven planar plastic targets," Phys. Rev. Lett. **109**, 115001 (2012).
[578]L. Gao, P. M. Nilson, I. V. Igumenshchev, G. Fiksel, R. Yan, J. R. Davies, D. Martinez, V. Smalyuk, M. G. Haines, E. G. Blackman, D. H. Froula, R. Betti, and D. D. Meyerhofer, "Observation of self-similarity in the magnetic fields generated by the ablative nonlinear Rayleigh-Taylor instability," Phys. Rev. Lett. **110**, 185003 (2013).
[579]L. Spitzer, Jr. and R. Härm, "Transport phenomena in a completely ionized gas," Phys. Rev. **89**, 977 (1953).
[580]E. N. Parker, "Dynamical properties of stellar coronas and stellar winds. II. Integration of the heat-flow equation," Astrophys. J. **139**, 93 (1964).
[581]R. E. Harrington, "Application of the theory of heat conduction to the absorption of blackbody radiation," J. Appl. Phys. **38**, 3266 (1967).
[582]H. Salzmann, "The applicability of Fourier's theory of heat conduction on laser produced plasmas," Phys. Lett. A **41**, 363 (1972).
[583]See National Technical Information Service Document No. UCID15745 (J. W. Shearer, "A survey of the physics of plasma heating by laser light," Lawrence Radiation Laboratory, University of California, Livermore, CA, Report UCID-15745, 1970). Copies may be obtained from the National Technical Information Service, Springfield, VA 22161.
[584]D. R. Gray and J. D. Kilkenny, "The measurement of ion acoustic turbulence and reduced thermal conductivity caused by a large temperature gradient in a laser heated plasma," Plasma Phys. **22**, 81 (1980).
[585]J. Delettrez, "Thermal electron transport in direct-drive laser fusion," Can. J. Phys. **64**, 932 (1986).
[586]R. L. Morse and C. W. Nielson, "Occurrence of high-energy electrons and surface expansion in laser-heated target plasmas," Phys. Fluids **16**, 909 (1973).
[587]R. J. Bickerton, "Thermal conduction limitations in laser fusion," Nucl. Fusion **13**, 457 (1973).
[588]D. W. Forslund, "Instabilities associated with heat conduction in the solar wind and their consequences," J. Geophys. Res, A, Space Phys. **75**, 17 (1970).
[589]C. T. Dum, "Anomalous electron transport equations for ion sound and related turbulent spectra," Phys. Fluids **21**, 956 (1978).
[590]See National Technical Information Service Document No. LA5611MS (A. W. Ehler, D. V. Giovanielli, R. P. Godwin, G. H. McCall, R. L. Morse, and S. D. Rockwood, "Evidence of anomalously reduced electron thermal conduction in laser-produced plasmas," Los Alamos Scientific Laboratory, Los Alamos, NM, LA-5611-MS, 1974). Copies may be obtained from the National Technical Information Service, Springfield, VA 22161.
[591]R. C. Malone, R. L. McCrory, and R. L. Morse, "Indications of strongly flux-limited electron thermal conduction in laser-target experiments," Phys. Rev. Lett. **34**, 721 (1975).
[592]S. J. Gitomer and D. B. Henderson, "Re-examination of strongly flux limited thermal conduction in laser produced plasmas," Phys. Fluids **22**, 364 (1979).
[593]D. R. Gray, J. D. Kilkenny, M. S. White, P. Blyth, and D. Hull, "Observation of severe heat-flux limitation and ion-acoustic turbulence in a laser-heated plasma," Phys. Rev. Lett. **39**, 1270 (1977).
[594]M. S. White, J. D. Kilkenny, and A. E. Dangor, "Measurement of thermal conductivity in a laser-heated plasma," Phys. Rev. Lett. **35**, 524 (1975).
[595]A. R. Bell, R. G. Evans, and D. J. Nicholas, "Electron energy transport in steep temperature gradients in laser-produced plasmas," Phys. Rev. Lett. **46**, 243 (1981).
[596]D. Shvarts, J. Delettrez, R. L. McCrory, and C. P. Verdon, "Self-consistent reduction of the Spitzer–Härm electron thermal heat flux in steep temperature gradients in laser-produced plasmas," Phys. Rev. Lett. **47**, 247 (1981).
[597]S. A. Khan and T. D. Rognlien, "Thermal heat flux in a plasma for arbitrary collisionality," Phys. Fluids **24**, 1442 (1981).
[598]M. H. Shirazian and L. C. Steinhauer, "Kinetic-theory description of electron heat transfer in a plasma," Phys. Fluids **24**, 843 (1981).
[599]J. P. Matte and J. Virmont, "Electron heat transport down steep temperature gradients," Phys. Rev. Lett. **49**, 1936 (1982).
[600]J. R. Albritton, "Laser absorption and heat transport by non-Maxwell-Boltzmann electron distributions," Phys. Rev. Lett. **50**, 2078 (1983).
[601]J. P. Matte, T. W. Johnston, J. Delettrez, and R. L. McCrory, "Electron heat flow with inverse bremsstrahlung and ion motion," Phys. Rev. Lett. **53**, 1461 (1984).
[602]J. F. Luciani, P. Mora, and J. Virmont, "Nonlocal heat transport due to steep temperature gradients," Phys. Rev. Lett. **51**, 1664 (1983).
[603]A. R. Bell, "Electron energy transport in ion waves and its relevance to laser-produced plasmas," Phys. Fluids **26**, 279 (1983).

[604]J. F. Luciani, P. Mora, and R. Pellat, "Quasistatic heat front and delocalized heat flux," Phys. Fluids **28**, 835 (1985).
[605]T. J. Goldsack, J. D. Kilkenny, B. J. MacGowan, P. F. Cunningham, C. L. S. Lewis, M. H. Key, and P. T. Rumsby, "Evidence for large heat fluxes from the mass ablation rate of laser-irradiated spherical targets," Phys. Fluids **25**, 1634 (1982).
[606]W. B. Fechner, C. L. Shepard, Gar. E. Busch, R. J. Schroeder, and J. A. Tarvin, "Analysis of plasma density profiles and thermal transport in laser-irradiated spherical targets," Phys. Fluids **27**, 1552 (1984).
[607]R. L. McCrory, J. M. Soures, C. Verdon, M. Richardson, P. Audebert, D. Bradley, J. Delettrez, L. Goldman, R. Hutchison, S. Jacobs, P. Jaanimagi, R. Keck, H. Kim, T. Kessler, J. Knauer, R. Kremens, S. Letzring, F. Marshall, P. McKenty, W. Seka, S. Skupsky, and B. Yaakobi, "High-density laser-fusion experiments at the Laboratory for Laser Energetics," in *Laser Interaction and Related Plasma Phenomena*, edited by H. Hora and G. H. Miley (Plenum Press, New York, 1988), Vol. 8, pp. 483–502.
[608]E. M. Epperlein, "Kinetic simulations of laser filamentation in plasmas," Phys. Fluids B **3**, 3082 (1991).
[609]A. Nishiguchi, K. Mima, H. Azechi, N. Miyanaga, and S. Nakai, "Kinetic effects of electron thermal conduction on implosion hydrodynamics," Phys. Fluids B **4**, 417 (1992).
[610]J. Li, B. Zhao, H. Li, and J. Zheng, "Study of flux limiter using Fokker–Planck and fluid simulations of planar laser-driven ablation," Plasma Phys. Controlled Fusion **52**, 085008 (2010).
[611]P. L. Bhatnagar, E. P. Gross, and M. Krook, "A model for collision processes in gases. I. Small amplitude processes in charged and neutral one-component systems," Phys. Rev. **94**, 511 (1954).
[612]S. X. Hu, V. Smalyuk, V. N. Goncharov, S. Skupsky, T. C. Sangster, D. D. Meyerhofer, and D. Shvarts, "Validation of thermal-transport modeling with direct-drive, planar-foil acceleration experiments on OMEGA," Phys. Rev. Lett. **101**, 055002 (2008).
[613]G. P. Schurtz, Ph. D. Nicolaï, and M. Busquet, "A nonlocal electron conduction model for multidimensional radiation hydrodynamics codes," Phys. Plasmas **7**, 4238 (2000).
[614]A. Sunahara, J. A. Delettrez, C. Stoeckl, R. W. Short, and S. Skupsky, "Time-dependent electron thermal flux inhibition in direct-drive laser implosions," Phys. Rev. Lett. **91**, 095003 (2003).
[615]A. Marocchino, M. Tzoufras, S. Atzeni, A. Schiavi, Ph. D. Nicolaï, J. Mallet, V. Tikhonchuk, and J.-L. Feugeas, "Comparison for non-local hydrodynamic thermal conduction models," Phys. Plasmas **20**, 022702 (2013).
[616]W. Manheimer, D. Colombant, and V. Goncharov, "The development of a Krook model for nonlocal transport in laser produced plasmas. I. Basic theory," Phys. Plasmas **15**, 083103 (2008).
[617]D. Colombant and W. Manheimer, "The development of a Krook model for nonlocal transport in laser produced plasmas. II. Application of the theory and comparisons with other models," Phys. Plasmas **15**, 083104 (2008).
[618]D. Colombant and W. Manheimer, "Krook model for nonthermal electron energy transport. III. Spherical configurations," Phys. Plasmas **16**, 062705 (2009).
[619]E. S. Weibel, "Spontaneously growing transverse waves in a plasma due to an anisotropic velocity distribution," Phys. Rev. Lett. **2**, 83 (1959).
[620]V. T. Tikhonchuk, W. Rozmus, V. Yu. Bychenkov, C. E. Capjack, and E. Epperlein, "Return current instability in laser heated plasmas," Phys. Plasmas **2**, 4169 (1995).
[621]V. Yu Bychenkov, V. P. Silin, and S. A. Uryupin, "Ion-acoustic turbulence and anomalous transport," Phys. Rep. **164**, 119 (1988).
[622]A. B. Langdon, "Nonlinear inverse bremsstrahlung and heated-electron distributions," Phys. Rev. Lett. **44**, 575 (1980).
[623]G. J. Rickard, A. R. Bell, and E. M. Epperlein, "2D Fokker–Planck simulations of short-pulse laser-plasma interactions," Phys. Rev. Lett. **62**, 2687 (1989).
[624]P. M. Celliers, G. W. Collins, L. B. Da Silva, D. M. Gold, and R. Cauble, "Accurate measurement of laser-driven shock trajectories with velocity interferometry," Appl. Phys. Lett. **73**, 1320 (1998).
[625]D. H. Munro, P. M. Celliers, G. W. Collins, D. M. Gold, L. B. Da Silva, S. W. Haan, R. C. Cauble, B. A. Hammel, and W. W. Hsing, "Shock timing techniques for the National Ignition Facility," Phys. Plasmas **8**, 2245 (2001).
[626]P. M. Celliers, D. K. Bradley, G. W. Collins, D. G. Hicks, T. R. Boehly, and W. J. Armstrong, "Line-imaging velocimeter for shock diagnostics at the Omega Laser Facility," Rev. Sci. Instrum. **75**, 4916 (2004).
[627]J. E. Miller, T. R. Boehly, A. Melchior, D. D. Meyerhofer, P. M. Celliers, J. H. Eggert, D. G. Hicks, C. M. Sorce, J. A. Oertel, and P. M. Emmel, "Streaked optical pyrometer system for laser-driven shock-wave experiments on OMEGA," Rev. Sci. Instrum. **78**, 034903 (2007).
[628]L. M. Barker and R. E. Hollenbach, "Laser interferometer for measuring high velocities of any reflecting surface," J. Appl. Phys. **43**, 4669 (1972).
[629]D. D. Bloomquist and S. A. Sheffield, "Optically recording interferometer for velocity measurements with subnanosecond resolution," J. Appl. Phys. **54**, 1717 (1983).
[630]T. R. Boehly, D. H. Munro, P. M. Celliers, R. E. Olson, D. G. Hicks, V. N. Goncharov, G. W. Collins, H. F. Robey, S. X. Hu, J. A. Marozas, T. C. Sangster, O. L. Landen, and D. D. Meyerhofer, "Demonstration of the shock-timing technique for ignition targets on the National Ignition Facility," Phys. Plasmas **16**, 056302 (2009).
[631]T. R. Boehly, V. N. Goncharov, W. Seka, M. A. Barrios, P. M. Celliers, D. G. Hicks, G. W. Collins, S. X. Hu, J. A. Marozas, and D. D. Meyerhofer, "Velocity and timing of multiple spherically converging shock waves in liquid deuterium," Phys. Rev. Lett. **106**, 195005 (2011).
[632]T. R. Boehly, V. N. Goncharov, W. Seka, S. X. Hu, J. A. Marozas, D. D. Meyerhofer, P. M. Celliers, D. G. Hicks, M. A. Barrios, D. Fratanduono, and G. W. Collins, "Multiple spherically converging shock waves in liquid deuterium," Phys. Plasmas **18**, 092706 (2011).
[633]H. F. Robey, T. R. Boehly, P. M. Celliers, J. H. Eggert, D. Hicks, R. F. Smith, R. Collins, M. W. Bowers, K. G. Krauter, P. S. Datte, D. H. Munro, J. L. Milovich, O. S. Jones, P. A. Michel, C. A. Thomas, R. E. Olson, S. Pollaine, R. P. J. Town, S. Haan, D. Callahan, D. Clark, J. Edwards, J. L. Kline, S. Dixit, M. B. Schneider, E. L. Dewald, K. Widmann, J. D. Moody, T. Döppner, H. B. Radousky, A. Throop, D. Kalantar, P. DiNicola, A. Nikroo, J. J. Kroll, A. V. Hamza, J. B. Horner, S. D. Bhandarkar, E. Dzenitis, E. Alger, E. Giraldez, C. Castro, K. Moreno, C. Haynam, K. N. LaFortune, C. Widmayer, M. Shaw, K. Jancaitis, T. Parham, D. M. Holungal, C. F. Walters, B. Haid, E. R. Mapoles, J. Sater, C. R. Gibson, T. Malsbury, J. Fair, D. Trummer, K. R. Coffee, B. Burr, L. V. Berzins, C. Choate, S. J. Brereton, S. Azevedo, H. Chandrasekaran, D. C. Eder, N. D. Masters, A. C. Fisher, P. A. Sterne, B. K. Young, O. L. Landen, B. M. Van Wonterghem, B. J. MacGowan, J. Atherton, J. D. Lindl, D. D. Meyerhofer, and E. Moses, "Shock timing experiments on the National Ignition Facility: Initial results and comparison with simulation," Phys. Plasmas **19**, 042706 (2012).
[634]H. F. Robey, J. D. Moody, P. M. Celliers, J. S. Ross, J. Ralph, S. Le Pape, L. Berzak Hopkins, T. Parham, J. Sater, E. R. Mapoles, D. M. Holunga, C. F. Walters, B. J. Haid, B. J. Kozioziemski, R. J. Dylla-Spears, K. G. Krauter, G. Frieders, G. Ross, M. W. Bowers, D. J. Strozzi, B. E. Yoxall, A. V. Hamza, B. Dzenitis, S. D. Bhandarkar, B. Young, B. M. Van Wonterghem, L. J. Atherton, O. L. Landen, M. J. Edwards, and T. R. Boehly, "Measurement of high-pressure shock waves in cryogenic deuterium-tritium ice layered capsule implosions on NIF," Phys. Rev. Lett. **111**, 065003 (2013).
[635]J. D. Moody, H. F. Robey, P. M. Celliers, D. H. Munro, D. A. Barker, K. L. Baker, T. Döppner, N. L. Hash, L. Berzak Hopkins, K. LaFortune, O. L. Landen, S. LePape, B. J. MacGowan, J. E. Ralph, J. S. Ross, C. Widmayer, A. Nikroo, E. Giraldez, and T. Boehly, "Early time implosion symmetry from two-axis shock-timing measurements on indirect drive NIF experiments," Phys. Plasmas **21**, 092702 (2014).
[636]G. I. Kerley, "Equation of state and phase diagram of dense hydrogen," Phys. Earth Planet. Inter. **6**, 78 (1972).
[637]See National Technical Information Service Document No. LA7130 (B. I. Bennett, J. D. Johnson, G. I. Kerley, and G. T. Rood, "Recent development in the *SESAME* equation-of-state library," Los Alamos National Laboratory, Los Alamos, NM, LA-7130, 1978). Copies may be obtained from the National Technical Information Service, Springfield, VA 22161.
[638]S. P. Lyon and J. D. Johnson, "T-1 handbook of the *SESAME* equation of state library," Los Alamos National Laboratory, Los Alamos, NM, LA-CP-98-100, 1998.
[639]R. M. More, K. H. Warren, D. A. Young, and G. B. Zimmerman, "A new quotidian equation of state (QEOS) for hot dense matter," Phys. Fluids **31**, 3059 (1988).
[640]T. J. Lenosky, J. D. Kress, and L. A. Collins, "Molecular-dynamics modeling of the Hugoniot of shocked liquid deuterium," Phys. Rev. B **56**, 5164 (1997).
[641]Ya. B. Zel'dovich and Yu. P. Raĭzer, "Hugoniot curves," in *Physics of Shock Waves and High-Temperature Hydrodynamic Phenomena*, edited by W. D. Hayes and R. F. Probstein (Dover Publications, Mineola, NY, 2002), Vol. I, Chap. I, pp. 49–50.

[642]L. Collins, I. Kwon, J. Kress, N. Troullier, and D. Lynch, "Quantum molecular dynamics simulations of hot, dense hydrogen," Phys. Rev. E **52**, 6202 (1995).
[643]T. J. Lenosky, S. R. Bickham, J. D. Kress, and L. A. Collins, "Density-functional calculation of the Hugoniot of shocked liquid deuterium," Phys. Rev. B **61**, 1 (2000).
[644]L. A. Collins, S. R. Bickham, J. D. Kress, S. Mazevet, T. J. Lenosky, N. J. Troullier, and W. Windl, "Dynamical and optical properties of warm dense hydrogen," Phys. Rev. B **63**, 184110 (2001).
[645]J. Clérouin and J.-F. Dufrêche, "*Ab initio* study of deuterium in the dissociating regime: Sound speed and transport properties," Phys. Rev. E **64**, 066406 (2001).
[646]S. A. Bonev, B. Militzer, and G. Galli, "*Ab initio* simulations of dense liquid deuterium: Comparison with gas-gun shock-wave experiments," Phys. Rev. B **69**, 014101 (2004).
[647]B. Holst, R. Redmer, and M. P. Desjarlais, "Thermophysical properties of warm dense hydrogen using quantum molecular dynamics simulations," Phys. Rev. B **77**, 184201 (2008).
[648]M. P. Desjarlais, "Density-functional calculations of the liquid deuterium Hugoniot, reshock, and reverberation timing," Phys. Rev. B **68**, 064204 (2003).
[649]W. R. Magro, D. M. Ceperley, C. Pierleoni, and B. Bernu, "Molecular dissociation in hot, dense hydrogen," Phys. Rev. Lett. **76**, 1240 (1996).
[650]B. Militzer and D. M. Ceperley, "Path integral Monte Carlo calculation of the deuterium Hugoniot," Phys. Rev. Lett. **85**, 1890 (2000).
[651]B. Militzer, D. M. Ceperley, J. D. Kress, J. D. Johnson, L. A. Collins, and S. Mazevet, "Calculation of a deuterium double shock Hugoniot from *ab initio* simulations," Phys. Rev. Lett. **87**, 275502 (2001).
[652]B. Militzer, W. Magro, and D. Ceperley, "Characterization of the state of hydrogen at high temperature and density," Contrib. Plasma Phys. **39**, 151 (1999).
[653]V. Bezkrovniy, V. S. Filinov, D. Kremp, M. Bonitz, M. Schlanges, W. D. Kraeft, P. R. Levashov, and V. E. Fortov, "Monte Carlo results for the hydrogen Hugoniot," Phys. Rev. E **70**, 057401 (2004).
[654]V. S. Filinov, P. R. Levashov, M. Bonitz, and V. E. Fortov, "Calculation of the shock Hugoniot of deuterium at pressures above 1 Mbar by the path-integral Monte Carlo method," Plasma Phys. Rep. **31**, 700 (2005).
[655]L. Caillabet, S. Mazevet, and P. Loubeyre, "Multiphase equation of state of hydrogen from *ab initio* calculations in the range 0.2 to 5 g/cc up to 10 eV," Phys. Rev. B **83**, 094101 (2011).
[656]M. A. Morales, L. X. Benedict, D. S. Clark, E. Schwegler, I. Tamblyn, S. A. Bonev, A. A. Correa, and S. W. Haan, "*Ab initio* calculations of the equation of state of hydrogen in a regime relevant for inertial fusion applications," High Energy Density Phys. **8**, 5 (2012).
[657]S. X. Hu, B. Militzer, V. N. Goncharov, and S. Skupsky, "First-principles equation-of-state table of deuterium for inertial confinement fusion applications," Phys. Rev. B **84**, 224109 (2011).
[658]S. X. Hu, B. Militzer, V. N. Goncharov, and S. Skupsky, "Strong coupling and degeneracy effects in inertial confinement fusion implosions," Phys. Rev. Lett. **104**, 235003 (2010).
[659]L. Caillabet, B. Canaud, G. Salin, S. Mazevet, and P. Loubeyre, "Change in inertial confinement fusion implosions upon using an *ab initio* multiphase DT equation of state," Phys. Rev. Lett. **107**, 115004 (2011).
[660]P. Loubeyre, P. M. Celliers, D. G. Hicks, E. Henry, A. Dewaele, J. Pasley, J. Eggert, M. Koenig, F. Occelli, K. M. Lee, R. Jeanloz, D. Neely, A. Benuzzi-Mounaix, D. Bradley, M. Bastea, S. Moon, and G. W. Collins, "Coupling static and dynamic compressions: First measurements in dense hydrogen," High Press. Res. **24**, 25 (2004).
[661]R. Jeanloz, P. M. Celliers, G. W. Collins, J. H. Eggert, K. K. M. Lee, R. S. McWilliams, S. Brygoo, and P. Loubeyre, "Achieving high-density states through shock-wave loading of precompressed samples," Proc. Natl. Acad. Sci. U. S. A. **104**, 9172 (2007).
[662]K. K. M. Lee, L. R. Benedetti, A. Mackinnon, D. Hicks, S. J. Moon, P. Loubeyre, F. Occelli, A. Dewaele, G. W. Collins, and R. Jeanloz, "Taking thin diamonds to their limit: Coupling static-compression and laser-shock techniques to generate dense water," AIP Conf. Proc. **620**, 1363 (2002).
[663]K. K. M. Lee, L. R. Benedetti, R. Jeanloz, P. M. Celliers, J. H. Eggert, D. G. Hicks, S. J. Moon, A. Mackinnon, L. B. Da Silva, D. K. Bradley, W. Unites, G. W. Collins, E. Henry, M. Koenig, A. Benuzzi-Mounaix, J. Pasley, and D. Neely, "Laser-driven shock experiments on precompressed water: Implications for "icy" giant planets," J. Chem. Phys. **125**, 014701 (2006).
[664]J. Edwards, K. T. Lorenz, B. A. Remington, S. Pollaine, J. Colvin, D. Braun, B. F. Lasinski, D. Reisman, J. M. McNaney, J. A. Greenough, R. Wallace, H. Louis, and D. Kalantar, "Laser-driven plasma loader for shockless compression and acceleration of samples in the solid state," Phys. Rev. Lett. **92**, 075002 (2004).
[665]D. C. Swift and R. P. Johnson, "Quasi-isentropic compression by ablative laser loading: Response of materials to dynamic loading on nanosecond time scales," Phys. Rev. E **71**, 066401 (2005).
[666]D. C. Swift, R. G. Kraus, E. N. Loomis, D. G. Hicks, J. M. McNaney, and R. P. Johnson, "Shock formation and the ideal shape of ramp compression waves," Phys. Rev. E **78**, 066115 (2008).
[667]D. E. Fratanduono, T. R. Boehly, M. A. Barrios, D. D. Meyerhofer, J. H. Eggert, R. F. Smith, D. G. Hicks, P. M. Celliers, D. G. Braun, and G. W. Collins, "Refractive index of lithium fluoride ramp compressed to 800 GPa," J. Appl. Phys. **109**, 123521 (2011).
[668]D. E. Fratanduono, T. R. Boehly, P. M. Celliers, M. A. Barrios, J. H. Eggert, R. F. Smith, D. G. Hicks, G. W. Collins, and D. D. Meyerhofer, "The direct measurement of ablation pressure driven by 351-nm laser radiation," J. Appl. Phys. **110**, 073110 (2011).
[669]D. K. Bradley, J. H. Eggert, R. F. Smith, S. T. Prisbrey, D. G. Hicks, D. G. Braun, J. Biener, A. V. Hamza, R. E. Rudd, and G. W. Collins, "Diamond at 800 GPa," Phys. Rev. Lett. **102**, 075503 (2009).
[670]J. R. Rygg, J. H. Eggert, A. E. Lazicki, F. Coppari, J. A. Hawreliak, D. G. Hicks, R. F. Smith, C. M. Sorce, T. M. Uphaus, B. Yaakobi, and G. W. Collins, "Powder diffraction from solids in the terapascal regime," Rev. Sci. Instrum. **83**, 113904 (2012).
[671]M. D. Knudson, D. L. Hanson, J. E. Bailey, C. A. Hall, J. R. Asay, and W. W. Anderson, "Equation of state measurements in liquid deuterium to 70 GPa," Phys. Rev. Lett. **87**, 225501 (2001).
[672]R. W. Lemke, M. R. Martin, R. D. McBride, J.-P. Davis, M. D. Knudson, D. Sinars, I. C. Smith, M. Savage, W. Stygar, K. Killebrew, D. G. Flicker, and M. Herrmann, "Determination of pressure and density of shocklessly compressed beryllium from x-ray radiography of a magnetically driven cylindrical liner implosion," AIP Conf. Proc. **1426**, 473 (2012).
[673]M. D. Knudson, M. P. Desjarlais, and D. H. Dolan, "Shock-wave exploration of the high-pressure phases of carbon," Science **322**, 1822 (2008).
[674]M. D. Knudson and M. P. Desjarlais, "Adiabatic release measurements in α-quartz between 300 and 1200 GPa: Characterization of α-quartz as a shock standard in the multimegabar regime," Phys. Rev. B **88**, 184107 (2013).
[675]L. B. Da Silva, P. Celliers, G. W. Collins, K. S. Budil, N. C. Holmes, T. W. Barbee, Jr., B. A. Hammel, J. D. Kilkenny, R. J. Wallace, M. Ross, R. Cauble, A. Ng, and G. Chiu, "Absolute equation of state measurements on shocked liquid deuterium up to 200 GPa (2 Mbar)," Phys. Rev. Lett. **78**, 483 (1997).
[676]G. W. Collins, L. B. Da Silva, P. Celliers, D. M. Gold, M. E. Foord, R. J. Wallace, A. Ng, S. V. Weber, K. S. Budil, and R. Cauble, "Measurements of the equation of state of deuterium at the fluid insulator-metal transition," Science **281**, 1178 (1998).
[677]G. W. Collins, P. Celliers, L. B. Da Silva, R. Cauble, D. Gold, M. Foord, K. S. Budil, R. Stewart, N. C. Holmes, M. Ross, B. A. Hammel, J. D. Kilkenny, R. J. Wallace, and A. Ng, "Equation of state measurements of hydrogen isotopes on Nova," Phys. Plasmas **5**, 1864 (1998).
[678]See Office of Scientific and Technical Information Document No. 917468 (G. I. Kerley, "Equations of state for hydrogen and deuterium," Sandia National Laboratory, Albuquerque, NM, SAND2003-3613, 2003). Copies may be obtained from the Office of Scientific and Technical Information at http://www.osti.gov/home/reportform.html.)
[679]A. N. Mostovych, Y. Chan, T. Lehecha, A. Schmitt, and J. D. Sethian, "Reflected shock experiments on the equation-of-state properties of liquid deuterium at 100–600 GPa (1–6 Mbar)," Phys. Rev. Lett. **85**, 3870 (2000).
[680]A. N. Mostovych, Y. Chan, T. Lehecha, L. Phillips, A. Schmitt, and J. D. Sethian, "Reflected shock experiments on the equation-of-state properties of liquid deuterium at 100–600 GPa (1–6 Mbar)," Phys. Plasmas **8**, 2281 (2001).
[681]A. N. Mostovych, Naval Research Laboratory, private communication (2004).
[682]T. R. Boehly, D. G. Hicks, P. M. Celliers, T. J. B. Collins, R. Earley, J. H. Eggert, D. Jacobs-Perkins, S. J. Moon, E. Vianello, D. D. Meyerhofer, and G. W. Collins, "Properties of fluid deuterium under double-shock compression to several Mbar," Phys. Plasmas **11**, L49 (2004).

[683]D. G. Hicks, T. R. Boehly, P. M. Celliers, J. H. Eggert, S. J. Moon, D. D. Meyerhofer, and G. W. Collins, "Laser-driven single shock compression of fluid deuterium from 45 to 220 GPa," Phys. Rev. B **79**, 014112 (2009); **85**, 099901(E) (2012).
[684]M. Ross, "Linear-mixing model for shock-compressed liquid deuterium," Phys. Rev. B **58**, 669 (1998).
[685]*LASL Shock Hugoniot Data*, Los Alamos Series on Dynamic Material Properties, edited by S. P. Marsh (University of California Press, Berkeley, CA, 1980).
[686]I. P. Dudoladov, V. I. Rakitin, Yu. N. Sutulov, and G. S. Telegin, "Shock compressibility of polystyrene with varying initial densities," J. Appl. Mech. Tech. Phys. **10**, 673 (1969).
[687]R. G. McQueen, S. P. Marsh, J. W. Taylor, J. N. Fritz, and W. J. Carter, "The equation of state of solids from shock wave studies," in *High-Velocity Impact Phenomena*, edited by R. Kinslow (Academic Press, New York, 1970), Chap. VII, Sec. II, pp. 293–417.
[688]See National Technical Information Service Document No. UCRL50108V1 [M. van Thiel, J. Shaner, and E. Salinas, "Compendium of shock wave data," Lawrence Livermore National Laboratory, Livermore, CA, UCRL-50108 (1977), Vol. 1, Rev. 1]. Copies may be obtained from the National Technical Information Service, Springfield, VA 22161.
[689]A. V. Bushman, I. V. Lomonosov, V. E. Fortov, K. V. Khishchenko, M. V. Zhernokletov, and Yu. N. Sutulov, "Experimental investigation of phenylene and polystyrene under conditions of shock loading and isentropic expansion. Equations of state of plastics at high energy densities," JETP Lett. **82**, 895 (1996).
[690]R. Cauble, L. B. Da Silva, T. S. Perry, D. R. Bach, K. S. Budil, P. Celliers, G. W. Collins, A. Ng, T. W. Barbee, Jr., B. A. Hammel, N. C. Holmes, J. D. Kilkenny, R. J. Wallace, G. Chiu, and N. C. Woolsey, "Absolute measurements of the equations of state of low-*Z* materials in the multi-Mbar regime using laser-driven shocks," Phys. Plasmas **4**, 1857 (1997).
[691]N. Ozaki, T. Ono, K. Takamatsu, K. A. Tanaka, M. Nakano, T. Kataoka, M. Yoshida, K. Wakabayashi, M. Nakai, K. Nagai, K. Shigemori, T. Yamanaka, and K. Kondo, "Equation-of-state measurements for polystyrene at multi-TPa pressures in laser direct-drive experiments," Phys. Plasmas **12**, 124503 (2005).
[692]N. Ozaki, T. Sano, M. Ikoma, K. Shigemori, T. Kimura, K. Miyanishi, T. Vinci, F. H. Ree, H. Azechi, T. Endo, Y. Hironaka, Y. Hori, A. Iwamoto, T. Kadono, H. Nagatomo, M. Nakai, T. Norimatsu, T. Okuchi, K. Otani, T. Sakaiya, K. Shimizu, A. Shiroshita, A. Sunahara, H. Takahashi, and R. Kodama, "Shock Hugoniot and temperature data for polystyrene obtained with quartz standard," Phys. Plasmas **16**, 062702 (2009).
[693]M. A. Barrios, D. G. Hicks, T. R. Boehly, D. E. Fratanduono, J. H. Eggert, P. M. Celliers, G. W. Collins, and D. D. Meyerhofer, "High-precision measurements of the equation of state of hydrocarbons at 1–10 Mbar using laser-driven shock waves," Phys. Plasmas **17**, 056307 (2010).
[694]M. A. Barrios, T. R. Boehly, D. G. Hicks, D. E. Fratanduono, J. H. Eggert, G. W. Collins, and D. D. Meyerhofer, "Precision equation-of-state measurements on National Ignition Facility ablator materials from 1 to 12 Mbar using laser-driven shock waves," J. Appl. Phys. **111**, 093515 (2012).
[695]W. Theobald, J. E. Miller, T. R. Boehly, E. Vianello, D. D. Meyerhofer, T. C. Sangster, J. Eggert, and P. M. Celliers, "X-ray preheating of window materials in direct-drive shock-wave timing experiments," Phys. Plasmas **13**, 122702 (2006).
[696]R. C. Cauble, Lawrence Livermore National Laboratory, private communication (2009); N. Ozaki, Institute of Laser Engineering, Osaka University, private communication (2009).
[697]D. L. Musinski, T. M. Henderson, R. J. Simms, T. R. Pattinson, and R. B. Jacobs, "Technological aspects of cryogenic laser-fusion targets," J. Appl. Phys. **51**, 1394 (1980).
[698]See National Technical Information Service Document No. UCRL79442 (R. L. Woerner and C. D. Hendricks, "Fabrication of cryogenic laser fusion targets," Lawrence Livermore National Laboratory, Livermore, CA, UCRL-79442, 1978). Copies may be obtained from the National Technical Information Service, Springfield, VA 22161.
[699]See National Technical Information Service Document No. UCRL80877 (R. L. Woerner, J. W. Bell, and W. G. Steward, "Fabrication and delivery of cryogenic targets for laser fusion experiments," Lawrence Livermore National Laboratory, Livermore, CA, UCRL-80877, 1978). Copies may be obtained from the National Technical Information Service, Springfield, VA 22161.
[700]See National Technical Information Service Document No. DE84017287 [T. Bernat, "Novette Cryogenic Target Support System," Laser Program Annual Report 1983, Lawrence Livermore National Laboratory, Livermore, CA, UCRL-50021-83 (1984), pp. 4-5–4-7]. Copies may be obtained from the National Technical Information Service, Springfield, VA 22161.
[701]See National Technical Information Service Document No. DE88008065 [Laboratory for Laser Energetics, "An advanced cryogenic target-positioning system," Laboratory for Laser Energetics Review Quarterly Report (University of Rochester, Rochester, NY, 1987), Vol. 33, p. 11, LLE Document No. DOE/DP/40200-65]. Copies may be obtained from the National Technical Information Service, Springfield, VA 22161.
[702]A. N. Mostovych, Y. Aglitskiy, S. E. Bodner, Y. Chan, D. G. Colombant, A. V. Deniz, U. Feldman, J. H. Gardner, M. Karasik, M. Klapisch, R. H. Lehmberg, E. A. McLean, S. P. Obenschain, C. J. Pawley, L. Phillips, A. J. Schmitt, J. F. Seely, J. D. Sethian, J. A. Stamper, A. Velikovich, and J. L. Weaver, "Nike direct-drive ICF program," Proc. SPIE **4424**, 15–22 (2001).
[703]C. R. Gibson, D. P. Atkinson, J. A. Baltz, V. P. Brugman, F. E. Coffield, O. D. Edwards, B. J. Haid, S. F. Locke, T. N. Malsbury, S. J. Shiromizu, and K. M. Skulina, "Design of the NIF cryogenic target system," Fusion Sci. Technol. **55**, 233 (2009).
[704]J. R. Miller, "A new method for producing cryogenic laser fusion targets," in *Advances in Cryogenic Engineering*, edited by K. D. Timmerhaus (Plenum Press, New York, 1978), Vol. 23, pp. 669–675.
[705]J. R. Miller, R. J. Fries, and W. J. Press, "Cryogenic laser fusion target material design considerations," J. Nucl. Mater. **85–86**, 121 (1979).
[706]S. X. Hu, V. N. Goncharov, P. B. Radha, J. A. Marozas, S. Skupsky, T. R. Boehly, T. C. Sangster, D. D. Meyerhofer, and R. L. McCrory, "Two-dimensional simulations of the neutron yield in cryogenic deuterium-tritium implosions on OMEGA," Phys. Plasmas **17**, 102706 (2010).
[707]See National Technical Information Service Document No. PB2009115568 (C. Gibson, J. Baltz, T. Malsbury, D. Atkinson, V. Brugmann, F. Coffield, O. Edwards, B. Haid, S. Locke, S. Shiromizu, and K. Skulina, "Design of the NIF cryogenic target system," Lawrence Livermore National Laboratory, Livermore, CA, LLNL-JRNL-404974, 2008). Copies may be obtained from the National Technical Information Service, Springfield, VA 22161.
[708]D. R. Harding, M. D. Wittman, and D. H. Edgell, "Considerations and requirements for providing cryogenic targets for direct-drive inertial fusion implosions at the National Ignition Facility," Fusion Sci. Technol. **63**, 95 (2013).
[709]T. M. Henderson, R. J. Simms, and R. B. Jacobs, "Cryogenic pellets for laser-fusion research—Theoretical and practical considerations," in *Advances in Cryogenic Engineering*, edited by K. D. Timmerhaus (Plenum Press, New York, 1978), Vol. 23, pp. 682–689.
[710]A. J. Martin, R. J. Simms, and D. L. Musinski, "Production of uniform DT ice layers in large shells: Tritium β-decay heating model," *KMS Annual Technical Report*, 99–102, KMS Fusion, Inc., Ann Arbor, MI, KMSF Report No. 1348 (1985).
[711]A. J. Martin, R. J. Simms, and R. B. Jacobs, "Beta energy driven uniform deuterium-tritium ice laser in reactor-size cryogenic inertial fusion targets," J. Vac. Sci. Technol. A **6**, 1885 (1988).
[712]J. K. Hoffer and L. R. Foreman, "Radioactively induced sublimation in solid tritium," Phys. Rev. Lett. **60**, 1310 (1988).
[713]J. K. Hoffer, L. R. Foreman, J. D. Simpson, and T. R. Pattinson, "The effects of exchange gas temperature and pressure on the beta-layering process in solid deuterium-tritium fusion fuel," Physica B **165–166**, 163 (1990).
[714]A. A. Chernov, B. J. Kozioziemski, J. A. Koch, L. J. Atherton, M. A. Johnson, A. V. Hamza, S. O. Kucheyev, J. B. Lugten, E. A. Mapoles, J. D. Moody, J. D. Salmonson, and J. D. Sater, "Single crystal growth and formation of defects in deuterium-tritium layers for inertial confinement nuclear fusion," Appl. Phys. Lett. **94**, 064105 (2009).
[715]G. W. Collins, D. N. Bittner, E. Monsler, S. Letts, E. R. Mapoles, and T. P. Bernat, "Infrared redistribution of D_2 and HD layers for inertial confinement fusion," J. Vac. Sci. Technol. A **14**, 2897 (1996).
[716]D. N. Bittner, G. W. Collins, E. Monsler, and S. Letts, "Forming uniform HD layers in shells using infrared radiation," Fusion Technol. **35**, 244 (1999).
[717]D. R. Harding, D. D. Meyerhofer, S. J. Loucks, L. D. Lund, R. Janezic, L. M. Elasky, T. H. Hinterman, D. H. Edgell, W. Seka, M. D. Wittman, R.

Q. Gram, D. Jacobs-Perkins, R. Earley, T. Duffy, and M. J. Bonino, "Forming cryogenic targets for direct-drive experiments," Phys. Plasmas **13**, 056316 (2006).
[718]C. M. Chen, T. Norimatsu, Y. Tsuda, T. Yamanaka, and S. Nakai, "Redistribution of solid fuel in inertial confinement fusion target by plasma," J. Vac. Sci. Technol. A **11**, 509 (1993).
[719]C. M. Chen, T. Norimatsu, Y. Izawa, T. Yamanaka, and S. Nakai, "Heating uniformity of a microwave discharge plasma to redistribute a solid fuel layer inside a cryogenic target for inertial confinement fusion," J. Vac. Sci. Technol. A **13**, 2908 (1995).
[720]E. R. Mapoles, J. Sater, J. Pipes, and E. Monsler, "Smoothing of deuterium-tritium ice by electrical heating of the saturated vapor," Phys. Rev. E **55**, 3473 (1997).
[721]See National Technical Information Service Document No. DE2008935224 [Laboratory for Laser Energetics, "Cryogenic targets: Current status and future development," Laboratory for Laser Energetics Review Quarterly Report (University of Rochester, Rochester, NY, 2008), Vol. 114, p. 57, LLE Document No. DOE/NA/28302/826]. Copies may be obtained from the National Technical Information Service, Springfield, VA 22161.
[722]B. J. Kozioziemski, S. O. Kucheyev, J. B. Lugten, J. A. Koch, J. D. Moody, A. A. Chernov, E. A. Mapoles, A. V. Hamza, and L. J. Atherton, "Plastic deformation of solid hydrogen in fusion targets," J. Appl. Phys. **105**, 093512 (2009).
[723]J. A. Koch, T. P. Bernat, G. W. Collins, B. A. Hammel, A. J. MacKinnon, C. H. Still, J. D. Sater, and D. N. Bittner, "Numerical raytrace verification of optical diagnostics of ice surface roughness for inertial confinement fusion experiments," Fusion Sci. Technol. **43**, 55 (2003).
[724]D. H. Edgell, W. Seka, R. S. Craxton, L. M. Elasky, D. R. Harding, R. L. Keck, and M. D. Wittman, "Three-dimensional characterization of cryogenic target ice layers using multiple shadowgraph views," Fusion Sci. Technol. **49**, 616 (2006).
[725]D. S. Montgomery, A. Nobile, and P. J. Walsh, "Characterization of National Ignition Facility cryogenic beryllium capsules using x-ray phase contrast imaging," Rev. Sci. Instrum. **75**, 3986 (2004).
[726]B. J. Kozioziemski, J. D. Sater, J. D. Moody, J. J. Sanchez, R. A. London, A. Barty, H. E. Martz, and D. S. Montgomery, "X-ray imaging of cryogenic deuterium-tritium layers in a beryllium shell," J. Appl. Phys. **98**, 103105 (2005).
[727]J. A. Koch, B. J. Kozioziemski, J. Salmonson, A. Chernov, L. J. Atherton, E. Dewald, N. Izumi, M. A. Johnson, S. Kucheyev, J. Lugten, E. Mapoles, J. D. Moody, J. W. Pipes, J. D. Sater, and D. Stefanescu, "Optical and x-ray characterization of groove profiles in DT ice layers," Lawrence Livermore National Laboratory, Livermore, CA, Report No. LLNL-PROC-405206 (2008).
[728]T. J. Asaki, J. K. Hoffer, and J. D. Sheliak, "Characterization of inertial confinement fusion targets," J. Acoust. Soc. Am. **99**, 2581 (1996).
[729]M. Martin, C. Gauvin, A. Choux, P. Baclet, and G. Pascal, "The cryogenic target for ignition on the LMJ: Useful tools to achieve nominal temperature and roughness conditions of the DT solid layer," Fusion Sci. Technol. **49**, 600 (2006).
[730]J. D. Moody, B. J. Kozioziemski, E. R. Mapoles, J. D. Sater, E. L. Dewald, J. A. Koch, N. Izumi, A. Chernov, J. Salmonson, R. C. Montesanti, L. J. Atherton, J. A. Burmann, J. W. Pipes, D. Stefanescu, K. Salari, T. Weisgrabber, J. Reynolds, C. Castro, J. Klingmann, and B. Dzenitis, "Status of cryogenic layering for NIF ignition targets," J. Phys.: Conf. Ser. **112**, 032064 (2008).
[731]W. Baumann, *FLUENT 6.2 User's Guide* (Fluent USA, Inc., Lebanon, NH 03766, 2003).
[732]See National Technical Information Service Document No. DE91017920 [T. P. Bernat, E. R. Mapoles, and J. J. Sanchez, "Temperature- and age-dependence of redistribution rates of frozen deuterium–tritium," ICF Quarterly Report (Lawrence Livermore National Laboratory, Livermore, CA, 1991), Vol. 1, p. 57, UCRL-LR-105821-91-2]. Copies may be obtained from the National Technical Information Service, Springfield, VA 22161.
[733]J. D. Simpson, J. K. Hoffer, and L. R. Foreman, "Beta-layering of solid deuterium-tritium in a spherical polycarbonate shell," Fusion Technol. **21**, 330 (1992).
[734]P. W. McKenty, M. D. Wittman, and D. R. Harding, "Effect of experimentally observed hydrogenic fractionation on inertial confinement fusion ignition target performance," J. Appl. Phys. **100**, 073302 (2006).
[735]M. Tabak, D. Hinkel, S. Atzeni, E. M. Campbell, and K. Tanaka, "Fast ignition: Overview and background," Fusion Sci. Technol. **49**, 254 (2006).
[736]A. W. Maschke, "Relativistic heavy ions for fusion applications," IEEE Trans. Nucl. Sci. **NS-22**, 1825 (1975).
[737]V. A. Shcherbakov, "Ignition of a laser-fusion target by a focusing shock wave," Sov. J. Plasma Phys. **9**, 240 (1983).
[738]T. Yamanaka, "Additional heating by a picosecond pulse," in *Inertial Confinement Fusion Research Plan—Kongo Plan (First Phase) Investigative Operation Separate Report*, Osaka University Laser Confinement Fusion Research Center, Suita, Japan (1983) (internal report, unpublished).
[739]N. G. Basov, S. Yu. Gus'kov, and L. P. Feokistov, "Thermonuclear gain of ICF targets with direct heating of ignitor," J. Sov. Laser Res. **13**, 396 (1992).
[740]M. Tabak, J. Hammer, M. E. Glinsky, W. L. Kruer, S. C. Wilks, J. Woodworth, E. M. Campbell, M. D. Perry, and R. J. Mason, "Ignition and high gain with ultrapowerful lasers," Phys. Plasmas **1**, 1626 (1994).
[741]R. Betti, A. A. Solodov, J. A. Delettrez, and C. Zhou, "Gain curves for direct-drive fast ignition at densities around 300 g/cc," Phys. Plasmas **13**, 100703 (2006).
[742]A. A. Solodov, R. Betti, J. A. Delettrez, and C. D. Zhou, "Gain curves and hydrodynamic simulations of ignition and burn for direct-drive fast-ignition fusion targets," Phys. Plasmas **14**, 062701 (2007).
[743]S. Atzeni, "Inertial fusion fast ignitor: Igniting pulse parameter window vs the penetration depth of the heating particles and the density of the pre-compressed fuel," Phys. Plasmas **6**, 3316 (1999).
[744]M. Tabak, D. S. Clark, S. P. Hatchett, M. H. Key, B. F. Lasinski, R. A. Snavely, R. Stephens, E. M. Campbell, R. Kodama, K. Mima, K. A. Tanaka, S. Atzeni, and R. Freeman, "Review of progress in fast ignition," Phys. Plasmas **12**, 057305 (2005).
[745]M. H. Key, "Status of and prospects for the fast ignition inertial fusion concept," Phys. Plasmas **14**, 055502 (2007).
[746]S. Atzeni, A. Schiavi, J. J. Honrubia, X. Ribeyre, G. Schurtz, Ph. Nicolaï, M. Olazabal–Loumé, C. Bellei, R. G. Evans, and J. R. Davies, "Fast ignitor target studies for the HiPER project," Phys. Plasmas **15**, 056311 (2008).
[747]See National Technical Information Service Document No. DE200114592 (R. B. Stephens, M. Key, W. Meier, R. Moir, and M. Tabak, "The case for fast ignition as an IFE concept exploration program," Lawrence Livermore National Laboratory, Livermore, CA, UCRL-JC-135800, 1999). Copies may be obtained from the National Technical Information Service, Springfield, VA 22161.
[748]S. Hatchett, "Cone-focussed target design for fast ignition," paper presented at the 30th Anomalous Absorption Conference, Ocean City, MD, 21–26 2000.
[749]L. P. Feoktistov, "Horizons of laser thermonuclear fusion," in *Budustchee Nauki (Future of Science)* (Znanie, Moscow, 1985), Vol. 18, pp. 168–182 (in Russian).
[750]J.-H. Yang and R. S. Craxton, "An empirical model of collective electrostatic effects for laser-beam channeling in long-scale-length relativistic plasmas," Phys. Plasmas **18**, 082703 (2011).
[751]S. C. Wilks, W. L. Kruer, M. Tabak, and A. B. Langdon, "Absorption of ultra-intense laser-pulses," Phys. Rev. Lett. **69**, 1383 (1992).
[752]A. A. Solodov and R. Betti, "Stopping power and range of energetic electrons in dense plasmas of fast-ignition fusion targets," Phys. Plasmas **15**, 042707 (2008).
[753]P. E. Young and P. R. Bolton, "Propagation of subpicosecond laser pulses through a fully ionized plasma," Phys. Rev. Lett. **77**, 4556 (1996).
[754]P. E. Young, M. E. Foord, J. H. Hammer, W. L. Kruer, M. Tabak, and S. C. Wilks, "Time-dependent channel formation in a laser-produced plasma," Phys. Rev. Lett. **75**, 1082 (1995).
[755]P. Monot, T. Auguste, P. Gibbon, F. Jakober, G. Mainfray, A. Dulieu, M. Louis-Jacquet, G. Malka, and J. L. Miquel, "Experimental demonstration of relativistic self-channeling of a multiterawatt laser pulse in an underdense plasma," Phys. Rev. Lett. **74**, 2953 (1995).
[756]K. A. Tanaka, M. M. Allen, A. Pukhov, R. Kodama, H. Fujita, Y. Kato, T. Kawasaki, Y. Kitagawa, K. Mima, N. Morio, H. Shiraga, M. Iwata, T. Miyakoshi, and T. Yamanaka, "Evidence of relativistic laser beam filamentation in back-reflected images," Phys. Rev. E **62**, 2672 (2000).
[757]A. Pukhov and J. Meyer-ter-Vehn, "Relativistic magnetic self-channeling of light in near-critical plasma: Three-dimensional particle-in-cell simulation," Phys. Rev. Lett. **76**, 3975 (1996).
[758]R. Kodama, K. Takahashi, K. A. Tanaka, M. Tsukamoto, H. Hashimoto, Y. Kato, and K. Mima, "Study of laser-hole boring into overdense plasmas," Phys. Rev. Lett. **77**, 4906 (1996).

[759]K. A. Tanaka, H. Hashimoto, R. Kodama, K. Mima, Y. Sentoku, and K. Takahashi, "Performance comparison of self-focusing with 1053- and 351-nm laser pulses," Phys. Rev. E **60**, 3283 (1999).
[760]K. Takahashi, R. Kodama, K. A. Tanaka, H. Hashimoto, Y. Kato, K. Mima, F. A. Weber, T. W. Barbee, Jr., and L. B. Da Silva, "Laser-hole boring into overdense plasma measured with soft x-ray laser probing," Phys. Rev. Lett. **84**, 2405 (2000).
[761]A. L. Lei, A. Pukhov, R. Kodama, T. Yabuuchi, K. Adumi, K. Endo, R. R. Freeman, H. Habara, Y. Kitagawa, K. Kondo, G. R. Kumar, T. Matsuoka, K. Mima, H. Nagatomo, T. Norimatsu, O. Shorokhov, R. Snavely, X. Q. Yang, J. Zheng, and K. A. Tanaka, "Relativistic laser channeling in plasmas for fast ignition," Phys. Rev. E **76**, 066403 (2007).
[762]L. Willingale, P. M. Nilson, A. G. R. Thomas, J. Cobble, R. S. Craxton, A. Maksimchuk, P. A. Norreys, T. C. Sangster, R. H. H. Scott, C. Stoeckl, C. Zulick, and K. Krushelnick, "High-power, kilojoule class laser channeling in millimeter-scale underdense plasma," Phys. Rev. Lett. **106**, 105002 (2011).
[763]G. Li, R. Yan, C. Ren, T.-L. Wang, J. Tonge, and W. B. Mori, "Laser channeling in millimeter-scale underdense plasma of fast-ignition targets," Phys. Rev. Lett. **100**, 125002 (2008).
[764]G. Li, R. Yan, C. Ren, J. Tonge, and W. B. Mori, "Three-dimensional particle-in-cell simulations of laser channeling in fast ignition," Phys. Plasmas **18**, 042703 (2011).
[765]K. Fujita, A. Sunahara, K. A. Tanaka, N. Izumi, T. Jitsuno, N. Miyanaga, T. Miyakoshi, H. Otani, M. Fukao, M. Heya, Y. Ochi, Y. Kitagawa, R. Kodama, K. Mima, H. Nishimura, T. Norimatsu, Y. Sentoku, H. Takabe, and T. Yamanaka, "Model experiments of fast ignition with coaxial high-power laser beams," Proc. SPIE **4424**, 37–44 (2001).
[766]Y. Kitagawa, Y. Sentoku, S. Akamatsu, W. Sakamoto, K. A. Tanaka, R. Kodama, H. Nishimura, Y. Inubushi, M. Nakai, T. Watari, T. Norimatsu, and A. Sunahara, "Petawatt-laser direct heating of uniformly imploded deuterated-polystyrene shell target," Phys. Rev. E **71**, 016403 (2005).
[767]P. A. Norreys, R. Allott, R. J. Clarke, J. Collier, D. Neely, S. J. Rose, M. Zepf, M. Santala, A. R. Bell, K. Krushelnick, A. E. Dangor, N. C. Woolsey, R. G. Evans, H. Habara, T. Norimatsu, and R. Kodama, "Experimental studies of the advanced fast ignitor scheme," Phys. Plasmas **7**, 3721 (2000).
[768]M. L. Shmatov, "Some problems related to heating the compressed thermonuclear fuel through the cone," Fusion Sci. Technol. **43**, 456 (2003).
[769]R. B. Stephens, R. A. Snavely, Y. Aglitskiy, F. Amiranoff, C. Andersen, D. Batani, S. D. Baton, T. Cowan, R. R. Freeman, T. Hall, S. P. Hatchett, J. M. Hill, M. H. Key, J. A. King, J. A. Koch, M. Koenig, A. J. MacKinnon, K. L. Lancaster, E. Martinolli, P. Norreys, E. Perelli-Cippo, M. Rabec Le Gloahec, C. Rousseaux, J. J. Santos, and F. Scianitti, "K_α fluorescence measurement of relativistic electron transport in the context of fast ignition," Phys. Rev. E **69**, 066414 (2004).
[770]J. J. Santos, F. Amiranoff, S. D. Baton, L. Gremillet, M. Koenig, E. Martinolli, M. Rabec Le Gloahec, C. Rousseaux, D. Batani, A. Bernardinello, G. Greison, and T. Hall, "Fast electron transport in ultraintense laser pulse interactions with solid targets by rear-side self-radiation diagnostics," Phys. Rev. Lett. **89**, 025001 (2002).
[771]M. Storm, A. A. Solodov, J. F. Myatt, D. D. Meyerhofer, C. Stoeckl, C. Mileham, R. Betti, P. M. Nilson, T. C. Sangster, W. Theobald, and C. Guo, "High-current, relativistic electron-beam transport in metals and the role of magnetic collimation," Phys. Rev. Lett. **102**, 235004 (2009).
[772]J. S. Green, V. M. Ovchinnikov, R. G. Evans, K. U. Akli, H. Azechi, F. N. Beg, C. Bellei, R. R. Freeman, H. Habara, R. Heathcote, M. H. Key, J. A. King, K. L. Lancaster, N. C. Lopes, T. Ma, A. J. MacKinnon, K. Markey, A. McPhee, Z. Najmudin, P. Nilson, R. Onofrei, R. Stephens, K. Takeda, K. A. Tanaka, W. Theobald, T. Tanimoto, J. Waugh, L. Van Woerkom, N. C. Woolsey, M. Zepf, J. R. Davies, and P. A. Norreys, "Effect of laser intensity on the fast-electron-beam divergence in solid-density plasmas," Phys. Rev. Lett. **100**, 015003 (2008).
[773]M. I. K. Santala, M. Zepf, I. Watts, F. N. Beg, E. Clark, M. Tatarakis, K. Krushelnick, A. E. Dangor, T. McCanny, I. Spencer, R. P. Singhal, K. W. D. Ledingham, S. C. Wilks, A. C. Machacek, J. S. Wark, R. Allott, R. J. Clarke, and P. A. Norreys, "Effect of the plasma density scale length on the direction of fast electrons in relativistic laser-solid interactions," Phys. Rev. Lett. **84**, 1459 (2000).
[774]S. P. Hatchett, C. G. Brown, T. E. Cowan, E. A. Henry, J. S. Johnson, M. H. Key, J. A. Koch, A. B. Langdon, B. F. Lasinski, R. W. Lee, A. J. MacKinnon, D. M. Pennington, M. D. Perry, T. W. Phillips, M. Roth, T. C. Sangster, M. S. Singh, R. A. Snavely, M. A. Stoyer, S. C. Wilks, and K. Yasuike, "Electron, photon, and ion beams from the relativistic interaction of petawatt laser pulses with solid targets," Phys. Plasmas **7**, 2076 (2000).
[775]A. R. Bell and R. J. Kingham, "Resistive collimation of electron beams in laser-produced plasmas," Phys. Rev. Lett. **91**, 035003 (2003).
[776]J. C. Adam, A. Héron, and G. Laval, "Dispersion and transport of energetic particles due to the interaction of intense laser pulses with overdense plasmas," Phys. Rev. Lett. **97**, 205006 (2006).
[777]A. Debayle, J. J. Honrubia, E. d'Humières, and V. T. Tikhonchuk, "Divergence of laser-driven relativistic electron beams," Phys. Rev. E **82**, 036405 (2010).
[778]A. J. Kemp and L. Divol, "Interaction physics of multipicosecond petawatt laser pulses with overdense plasma," Phys. Rev. Lett. **109**, 195005 (2012).
[779]A. R. Bell, J. R. Davies, S. Guerin, and H. Ruhl, "Fast-electron transport in high-intensity short-pulse laser-solid experiments," Plasma Phys. Controlled Fusion **39**, 653 (1997).
[780]L. Gremillet, G. Bonnaud, and F. Amiranoff, "Filamented transport of laser-generated relativistic electrons penetrating a solid target," Phys. Plasmas **9**, 941 (2002).
[781]J. R. Davies, "Electric and magnetic field generation and target heating by laser-generated fast electrons," Phys. Rev. E **68**, 056404 (2003).
[782]A. P. L. Robinson and M. Sherlock, "Magnetic collimation of fast electrons produced by ultraintense laser irradiation by structuring the target composition," Phys. Plasmas **14**, 083105 (2007).
[783]S. Kar, A. P. L. Robinson, D. C. Carroll, O. Lundh, K. Markey, P. McKenna, P. Norreys, and M. Zepf, "Guiding of relativistic electron beams in solid targets by resistively controlled magnetic fields," Phys. Rev. Lett. **102**, 055001 (2009).
[784]D. J. Strozzi, M. Tabak, D. J. Larson, L. Divol, A. J. Kemp, C. Bellei, M. M. Marinak, and M. H. Key, "Fast-ignition transport studies: Realistic electron source, integrated particle-in-cell and hydrodynamic modeling, imposed magnetic fields," Phys. Plasmas **19**, 072711 (2012).
[785]A. Caruso and V. A. Pais, "The ignition of dense DT fuel by injected triggers," Nucl. Fusion **36**, 745 (1996).
[786]M. Roth, T. E. Cowan, M. H. Key, S. P. Hatchett, C. Brown, W. Fountain, J. Johnson, D. M. Pennington, R. A. Snavely, S. C. Wilks, K. Yasuike, H. Ruhl, E. Pegoraro, S. V. Bulanov, E. M. Campbell, M. D. Perry, and H. Powell, "Fast ignition by intense laser-accelerated proton beams," Phys. Rev. Lett. **86**, 436 (2001).
[787]V. Yu. Bychenkov, W. Rozmus, A. Maksimchuk, D. Umstadter, and C. E. Capjack, "Fast ignitor concept with light ions," Plasma Phys. Rep. **27**, 1017 (2001).
[788]N. Naumova, T. Schlegel, V. T. Tikhonchuk, C. Labaune, I. V. Sokolov, and G. Mourou, "Hole boring in a DT pellet and fast-ion ignition with ultraintense laser pulses," Phys. Rev. Lett. **102**, 025002 (2009).
[789]S. Hain and P. Mulser, "Fast ignition without hole boring," Phys. Rev. Lett. **86**, 1015 (2001).
[790]F. Winterberg, "Implosion of a dense plasma by hypervelocity impact," Plasma Phys. **10**, 55 (1968).
[791]M. Murakami and H. Nagatomo, "A new twist for inertial fusion energy: Impact ignition," Nucl. Instrum. Methods Phys. Res. A **544**, 67 (2005).
[792]H. Azechi, T. Sakaiya, T. Watari, M. Karasik, H. Saito, K. Ohtani, K. Takeda, H. Hosoda, H. Shiraga, M. Nakai, K. Shigemori, S. Fujioka, M. Murakami, H. Nagatomo, T. Johzaki, J. Gardner, D. G. Colombant, J. W. Bates, A. L. Velikovich, Y. Aglitskiy, J. Weaver, S. Obenschain, S. Eliezer, R. Kodama, T. Norimatsu, H. Fujita, K. Mima, and H. Kan, "Experimental evidence of impact ignition: 100-fold increase of neutron yield by impactor collision," Phys. Rev. Lett. **102**, 235002 (2009).
[793]M. Karasik, J. L. Weaver, Y. Aglitskiy, T. Watari, Y. Arikawa, T. Sakaiya, J. Oh, A. L. Velikovich, S. T. Zalesak, J. W. Bates, S. P. Obenschain, A. J. Schmitt, M. Murakami, and H. Azechi, "Acceleration to high velocities and heating by impact using Nike KrF laser," Phys. Plasmas **17**, 056317 (2010).
[794]R. Kodama, P. A. Norreys, K. Mima, A. E. Dangor, R. G. Evans, H. Fujita, Y. Kitagawa, K. Krushelnick, T. Miyakoshi, N. Miyanaga, T. Norimatsu, S. J. Rose, T. Shozaki, K. Shigemori, A. Sunahara, M. Tampo, K. A. Tanaka, Y. Toyama, T. Yamanaka, and M. Zepf, "Fast heating of ultrahigh-density plasma as a step towards laser fusion ignition," Nature **412**, 798 (2001).
[795]R. Kodama, H. Shiraga, K. Shigemori, Y. Toyama, S. Fujioka, H. Azechi, H. Fujita, H. Habara, T. Hall, Y. Izawa, T. Jitsuno, Y. Kitagawa, K. M. Krushelnick, K. L. Lancaster, K. Mima, K. Nagai, M. Nakai, H. Nishimura, T. Norimatsu, P. A. Norreys, S. Sakabe, K. A. Tanaka, A. Youssef,

M. Zepf, and T. Yamanaka, "Nuclear fusion: Fast heating scalable to laser fusion ignition," Nature **418**, 933 (2002).
[796]T. Yabuuchi, A. Das, G. R. Kumar, H. Habara, P. K. Kaw, R. Kodama, K. Mima, P. A. Norreys, S. Sengupta, and K. A. Tanaka, "Evidence of anomalous resistivity for hot electron propagation through a dense fusion core in fast ignition experiments," New J. Phys. **11**, 093031 (2009).
[797]C. Stoeckl, T. R. Boehly, J. A. Delettrez, S. P. Hatchett, J. A. Frenje, V. Yu. Glebov, C. K. Li, J. E. Miller, R. D. Petrasso, F. H. Séguin, V. A. Smalyuk, R. B. Stephens, W. Theobald, B. Yaakobi, and T. C. Sangster, "Hydrodynamics studies of direct-drive cone-in-shell, fast-ignitor targets on OMEGA," Phys. Plasmas **14**, 112702 (2007).
[798]R. B. Stephens, S. P. Hatchett, R. E. Turner, K. A. Tanaka, and R. Kodama, "Implosion of indirectly driven reentrant-cone shell target," Phys. Rev. Lett. **91**, 185001 (2003).
[799]S. P. Hatchett, D. Clark, M. Tabak, R. E. Turner, C. Stoeckl, R. B. Stephens, H. Shiraga, and K. Tanaka, "Hydrodynamics of conically guided fast ignition targets," Fusion Sci. Technol. **49**, 327 (2006).
[800]W. Theobald, A. A. Solodov, C. Stoeckl, K. S. Anderson, R. Betti, T. R. Boehly, R. S. Craxton, J. A. Delettrez, C. Dorrer, J. A. Frenje, V. Yu. Glebov, H. Habara, K. A. Tanaka, J. P. Knauer, R. Lauck, F. J. Marshall, K. L. Marshall, D. D. Meyerhofer, P. M. Nilson, P. K. Patel, H. Chen, T. C. Sangster, W. Seka, N. Sinenian, T. Ma, F. N. Beg, E. Giraldez, and R. B. Stephens, "Initial cone-in-shell fast-ignition experiments on OMEGA," Phys. Plasmas **18**, 056305 (2011).
[801]S. D. Baton, M. Koenig, J. Fuchs, A. Benuzzi-Mounaix, P. Guillou, B. Loupias, T. Vinci, L. Gremillet, C. Rousseaux, M. Drouin, E. Lefebvre, F. Dorchies, C. Fourment, J. J. Santos, D. Batani, A. Morace, R. Redaelli, M. Nakatsutsumi, R. Kodama, A. Nishida, N. Ozaki, T. Norimatsu, Y. Aglitskiy, S. Atzeni, and A. Schiavi, "Inhibition of fast electron energy deposition due to preplasma filling of cone-attached targets," Phys. Plasmas **15**, 042706 (2008).
[802]A. G. MacPhee, L. Divol, A. J. Kemp, K. U. Akli, F. N. Beg, C. D. Chen, H. Chen, D. S. Hey, R. J. Fedosejevs, R. R. Freeman, M. Henesian, M. H. Key, S. Le Pape, A. Link, T. Ma, A. J. Mackinnon, V. M. Ovchinnikov, P. K. Patel, T. W. Phillips, R. B. Stephens, M. Tabak, R. Town, Y. Y. Tsui, L. D. Van Woerkom, M. S. Wei, and S. C. Wilks, "Limitation on prepulse level for cone-guided fast-ignition inertial confinement fusion," Phys. Rev. Lett. **104**, 055002 (2010).
[803]J. Li, J. R. Davies, T. Ma, W. B. Mori, C. Ren, A. A. Solodov, W. Theobald, and J. Tonge, "Hot-electron generation from laser–pre-plasma interactions in cone-guided fast ignition," Phys. Plasmas **20**, 052706 (2013).
[804]A. A. Solodov, K. S. Anderson, R. Betti, V. Gotcheva, J. Myatt, J. A. Delettrez, S. Skupsky, W. Theobald, and C. Stoeckl, "Simulations of electron transport and ignition for direct-drive fast-ignition targets," Phys. Plasmas **15**, 112702 (2008).
[805]J. J. Honrubia and J. Meyer-ter-Vehn, "Fast ignition of fusion targets by laser-driven electrons," Plasma Phys. Controlled Fusion **51**, 014008 (2009).
[806]M. Dunne, "A high-power laser fusion facility for Europe," Nat. Phys. **2**, 2 (2006).
[807]H. D. Shay, P. Amendt, D. Clark, D. Ho, M. Key, J. Koning, M. Marinak, D. Strozzi, and M. Tabak, "Implosion and burn of fast ignition capsules—calculations with HYDRA," Phys. Plasmas **19**, 092706 (2012).
[808]C. Bellei, L. Divol, A. J. Kemp, M. H. Key, D. J. Larson, D. J. Strozzi, M. M. Marinak, M. Tabak, and P. K. Patel, "Fast ignition: Dependence of the ignition energy on source and target parameters for particle-in-cell-modelled energy and angular distributions of the fast electrons," Phys. Plasmas **20**, 052704 (2013).
[809]R. Betti, C. D. Zhou, K. S. Anderson, L. J. Perkins, W. Theobald, and A. A. Solodov, "Shock ignition of thermonuclear fuel with high areal density," Phys. Rev. Lett. **98**, 155001 (2007).
[810]K. S. Anderson, R. Betti, P. W. McKenty, T. J. B. Collins, M. Hohenberger, W. Theobald, R. S. Craxton, J. A. Delettrez, M. Lafon, J. A. Marozas, R. Nora, S. Skupsky, and A. Shvydky, "A polar-drive shock-ignition design for the National Ignition Facility," Phys. Plasmas **20**, 056312 (2013).
[811]A. J. Schmitt, J. W. Bates, S. P. Obenschain, S. T. Zalesak, D. E. Fyfe, and R. Betti, "Direct drive fusion energy shock ignition designs for sub-MJ lasers," Fusion Sci. Technol. **56**, 377 (2009).
[812]L. J. Perkins, R. Betti, K. N. LaFortune, and W. H. Williams, "Shock ignition: A new approach to high gain inertial confinement fusion on the National Ignition Facility," Phys. Rev. Lett. **103**, 045004 (2009).
[813]X. Ribeyre, V. T. Tikhonchuk, J. Breil, M. Lafon, and E. Le Bel, "Analytic criteria for shock ignition of fusion reactions in a central hot spot," Phys. Plasmas **18**, 102702 (2011).
[814]R. Nora and R. Betti, "One-dimensional planar hydrodynamic theory of shock ignition," Phys. Plasmas **18**, 082710 (2011).
[815]M. Lafon, X. Ribeyre, and G. Schurtz, "Gain curves and hydrodynamic modeling for shock ignition," Phys. Plasmas **17**, 052704 (2010).
[816]M. Lafon, X. Ribeyre, and G. Schurtz, "Optimal conditions for shock ignition of scaled cryogenic deuterium–tritium targets," Phys. Plasmas **20**, 022708 (2013).
[817]A. Vallet, X. Ribeyre, and V. Tikhonchuk, "Finite Mach number spherical shock wave, application to shock ignition," Phys. Plasmas **20**, 082702 (2013).
[818]G. Guderley, "Starke kugelige und zylindrische verdichtungsstöße in der nähe des kugelmittelpunktes bzw. Der zylinderachse," Luftfahrtforschung **19**, 302 (1942).
[819]C. J. Davie and R. G. Evans, "Symmetry of spherically converging shock waves through reflection, relating to the shock ignition fusion energy scheme," Phys. Rev. Lett. **110**, 185002 (2013).
[820]M. R. Terry, L. J. Perkins, and S. M. Sepke, "Design of a deuterium and tritium-ablator shock ignition target for the National Ignition Facility," Phys. Plasmas **19**, 112705 (2012).
[821]B. Canaud and M. Temporal, "High-gain shock ignition of direct-drive ICF targets for the Laser Mégajoule," New J. Phys. **12**, 043037 (2010).
[822]M. Temporal, R. Ramis, B. Canaud, V. Brandon, S. Laffite, and B. J. Le Garrec, "Irradiation uniformity of directly driven inertial confinement fusion targets in the context of the shock-ignition scheme," Plasma Phys. Controlled Fusion **53**, 124008 (2011).
[823]X. Ribeyre, G. Schurtz, M. Lafon, S. Galera, and S. Weber, "Shock ignition: An alternative scheme for HiPER," Plasma Phys. Controlled Fusion **51**, 015013 (2009).
[824]X. Ribeyre, M. Lafon, G. Schurtz, M. Olazabal-Loume, J. Breil, S. Galera, and S. Weber, "Shock ignition: Modelling and target design robustness," Plasma Phys. Controlled Fusion **51**, 124030 (2009).
[825]S. Atzeni, A. Schiavi, and A. Marocchino, "Studies on the robustness of shock-ignited laser fusion targets," Plasma Phys. Controlled Fusion **53**, 035010 (2011).
[826]A. J. Schmitt, J. W. Bates, S. P. Obenschain, S. T. Zalesak, and D. E. Fyfe, "Shock ignition target design for inertial fusion energy," Phys. Plasmas **17**, 042701 (2010).
[827]J. W. Bates, A. J. Schmitt, D. E. Fyfe, S. P. Obenschain, and S. T. Zalesak, "Simulations of high-gain shock-ignited inertial-confinement-fusion implosions using less than 1 MJ of direct KrF-laser energy," High Energy Density Phys. **6**, 128 (2010).
[828]B. Canaud, S. Laffite, and M. Temporal, "Shock ignition of direct-drive double-shell targets," Nucl. Fusion **51**, 062001 (2011).
[829]A. R. Bell and M. Tzoufras, "Electron transport and shock ignition," Plasma Phys. Controlled Fusion **53**, 045010 (2011).
[830]W. Manheimer, D. Colombant, and A. J. Schmitt, "Calculations of nonlocal electron energy transport in laser produced plasmas in one and two dimensions using the velocity dependent Krook model," Phys. Plasmas **19**, 056317 (2012).
[831]A. Nikroo, J. Bousquet, R. Cook, B. W. McQuillan, R. Paguio, and M. Takagi, "Progress in 2 mm glow discharge polymer mandrel development for NIF," Fusion Sci. Technol. **45**, 165 (2004).
[832]B. Canaud, S. Laffite, V. Brandon, and M. Temporal, "2D analysis of direct-drive shock-ignited HiPER-like target implosions with the full Laser Megajoule," Laser Part. Beams **30**, 183 (2012).
[833]S. Atzeni, J. R. Davies, L. Hallo, J. J. Honrubia, P. H. Maire, M. Olazabal-Loumé, J. L. Feugeas, X. Ribeyre, A. Schiavi, G. Schurtz, J. Breil, and P. Nicolaï, "Studies on targets for inertial fusion ignition demonstration at the HiPER facility," Nucl. Fusion **49**, 055008 (2009).
[834]S. Weber, C. Riconda, O. Klimo, A. Héron, and V. T. Tikhonchuk, "Fast saturation of the two-plasmon-decay instability for shock-ignition conditions," Phys. Rev. E **85**, 016403 (2012).
[835]O. Klimo, S. Weber, V. T. Tikhonchuk, and J. Limpouch, "Particle-in-cell simulations of laser-plasma interaction for the shock ignition scenario," Plasma Phys. Controlled Fusion **52**, 055013 (2010).
[836]O. Klimo, V. T. Tikhonchuk, X. Ribeyre, G. Schurtz, C. Riconda, S. Weber, and J. Limpouch, "Laser plasma interaction studies in the context of shock ignition—Transition from collisional to collisionless absorption," Phys. Plasmas **18**, 082709 (2011).
[837]O. Klimo and V. T. Tikhonchuk, "Laser–plasma interaction studies in the context of shock ignition: The regime dominated by parametric instabilities," Plasma Phys. Controlled Fusion **55**, 095002 (2013).

[838]C. Riconda, S. Weber, V. T. Tikhonchuk, and A. Héron, "Kinetic simulations of stimulated Raman backscattering and related processes for the shock-ignition approach to inertial confinement fusion," Phys. Plasmas **18**, 092701 (2011).
[839]L. Yin, B. J. Albright, H. A. Rose, K. J. Bowers, B. Bergen, and R. K. Kirkwood, "Self-organized bursts of coherent stimulated Raman scattering and hot electron transport in speckled laser plasma media," Phys. Rev. Lett. **108**, 245004 (2012).
[840]R. Betti, W. Theobald, C. D. Zhou, K. S. Anderson, P. W. McKenty, S. Skupsky, D. Shvarts, V. N. Goncharov, J. A. Delettrez, P. B. Radha, T. C. Sangster, C. Stoeckl, and D. D. Meyerhofer, "Shock ignition of thermonuclear fuel with high areal densities," J. Phys.: Conf. Ser. **112**, 022024 (2008).
[841]A. R. Piriz, G. Rodriguez Prieto, N. A. Tahir, Y. Zhang, S. D. Liu, and Y. T. Zhao, "Ablation driven by hot electrons generated during the ignitor laser pulse in shock ignition," Phys. Plasmas **19**, 122705 (2012).
[842]N. H. Burnett, G. Josin, B. Ahlborn, and R. Evans, "Generation of shock waves by hot electron explosions driven by a CO_2 laser," Appl. Phys. Lett. **38**, 226 (1981).
[843]S. Yu. Gus'kov, V. V. Zverev, and V. B. Rozanov, "Steady-state model of the corona of spherical laser targets allowing for energy transfer by fast electrons," Sov. J. Quantum Electron. **13**, 498 (1983).
[844]S. Gus'kov, X. Ribeyre, M. Touati, J. L. Feugeas, Ph. Nicolaï, and V. Tikhonchuk, "Ablation pressure driven by an energetic electron beam in a dense plasma," Phys. Rev. Lett. **109**, 255004 (2012).
[845]X. Ribeyre, S. Gus'kov, J.-L. Feugeas, Ph. Nicolaï, and V. T. Tikhonchuk, "Dense plasma heating and Gbar shock formation by a high intensity flux of energetic electrons," Phys. Plasmas **20**, 062705 (2013).
[846]W. Theobald, R. Betti, C. Stoeckl, K. S. Anderson, J. A. Delettrez, V. Yu. Glebov, V. N. Goncharov, F. J. Marshall, D. N. Maywar, R. L. McCrory, D. D. Meyerhofer, P. B. Radha, T. C. Sangster, W. Seka, D. Shvarts, V. A. Smalyuk, A. A. Solodov, B. Yaakobi, C. D. Zhou, J. A. Frenje, C. K. Li, F. H. Séguin, R. D. Petrasso, and L. J. Perkins, "Initial experiments on the shock-ignition inertial confinement fusion concept," Phys. Plasmas **15**, 056306 (2008).
[847]W. Theobald, K. S. Anderson, R. Betti, R. S. Craxton, J. A. Delettrez, J. A. Frenje, V. Yu. Glebov, O. V. Gotchev, J. H. Kelly, C. K. Li, A. J. Mackinnon, F. J. Marshall, R. L. McCrory, D. D. Meyerhofer, J. F. Myatt, P. A. Norreys, P. M. Nilson, P. K. Patel, R. D. Petrasso, P. B. Radha, C. Ren, T. C. Sangster, W. Seka, V. A. Smalyuk, A. A. Solodov, R. B. Stephens, C. Stoeckl, and B. Yaakobi, "Advanced-ignition-concept exploration on OMEGA," Plasma Phys. Controlled Fusion **51**, 124052 (2009).
[848]W. Theobald, R. Nora, M. Lafon, A. Casner, X. Ribeyre, K. S. Anderson, R. Betti, J. A. Delettrez, J. A. Frenje, V. Yu. Glebov, O. V. Gotchev, M. Hohenberger, S. X. Hu, F. J. Marshall, D. D. Meyerhofer, T. C. Sangster, G. Schurtz, W. Seka, V. A. Smalyuk, C. Stoeckl, and B. Yaakobi, "Spherical shock-ignition experiments with the $40+20$-beam configuration on OMEGA," Phys. Plasmas **19**, 102706 (2012).
[849]W. Theobald, A. Casner, R. Nora, X. Ribeyre, M. Lafon, K. S. Anderson, R. Betti, R. S. Craxton, J. A. Delettrez, J. A. Frenje, V. Yu. Glebov, O. V. Gotchev, M. Hohenberger, S. X. Hu, F. J. Marshall, R. L. McCrory, D. D. Meyerhofer, L. J. Perkins, T. C. Sangster, G. Schurtz, W. Seka, V. A. Smalyuk, C. Stoeckl, and B. Yaakobi, "Progress in the shock-ignition inertial confinement fusion concept," EPJ Web Conf. **59**, 03001 (2013).
[850]S. Depierreux, C. Goyon, K. Lewis, H. Bandulet, D. T. Michel, G. Loisel, V. Yahia, V. Tassin, C. Stenz, N. G. Borisenko, W. Nazarov, J. Limpouch, P. E. Masson Laborde, P. Loiseau, M. Casanova, Ph. Nicolaï, S. Hüller, D. Pesme, C. Riconda, V. T. Tikhonchuk, and C. Labaune, "Interaction physics for the shock ignition scheme of inertial confinement fusion targets," Plasma Phys. Controlled Fusion **53**, 124034 (2011).
[851]S. Depierreux, P. Loiseau, D. T. Michel, V. Tassin, C. Stenz, P. E. Masson-Laborde, C. Goyon, V. Yahia, and C. Labaune, "Experimental investigation of the stimulated Brillouin scattering growth and saturation at 526 and 351 nm for direct drive and shock ignition," Phys. Plasmas **19**, 012705 (2012).
[852]S. D. Baton, M. Koenig, E. Brambrink, H. P. Schlenvoigt, C. Rousseaux, G. Debras, S. Laffite, P. Loiseau, F. Philippe, X. Ribeyre, and G. Schurtz, "Experiment in planar geometry for shock ignition studies," Phys. Rev. Lett. **108**, 195002 (2012).
[853]D. Batani, G. Malka, G. Schurtz, X. Ribeyre, E. Lebel, L. Giuffrida, V. Tikhonchuk, L. Volpe, A. Patria, P. Koester, L. Labate, L. A. Gizzi, L. Antonelli, M. Richetta, J. Nejdl, M. Sawicka, D. Margarone, M. Krus, E. Krousky, J. Skala, R. Dudzak, A. Velyhan, J. Ullshmied, O. Renner, M. Smid, O. Klimo, S. Atzeni, A. Marocchino, A. Schiavi, C. Spindloe, T. O'Dell, T. Vinci, J. Wolowski, J. Badziak, T. Pysarcizck, M. Rosinski, Z. Kalinowska, and T. Chodukowski, "Preliminary results from recent experiments and future roadmap to shock ignition of fusion targets," J. Phys.: Conf. Ser. **399**, 012005 (2012).
[854]G. S. Fraley, E. J. Linnebur, R. J. Mason, and R. L. Morse, "Thermonuclear burn characteristics of compressed deuterium-tritium microspheres," Phys. Fluids **17**, 474 (1974).
[855]W. K. Levedahl and J. D. Lindl, "Energy scaling of inertial confinement fusion targets for ignition and high gain," Nucl. Fusion **37**, 165 (1997).
[856]M. C. Herrmann, M. Tabak, and J. D. Lindl, "Ignition scaling laws and their application to capsule design," Phys. Plasmas **8**, 2296 (2001).
[857]A. Kemp, J. Meyer-ter-Vehn, and S. Atzeni, "Stagnation pressure of imploding shells and ignition energy scaling of inertial confinement fusion targets," Phys. Rev. Lett. **86**, 3336 (2001).
[858]S. M. Pollaine and J. D. Lindl, "Effect of capsule aspect ratio on hydrodynamic efficiency," Nucl. Fusion **26**, 1719 (1986).
[859]S. Skupsky, R. Betti, T. J. B. Collins, V. N. Goncharov, D. R. Harding, R. L. McCrory, P. W. McKenty, D. D. Meyerhofer, and R. P. J. Town, "High-gain direct-drive target designs for the National Ignition Facility," in *Inertial Fusion Sciences and Applications 2001*, edited by K. Tanaka, D. D. Meyerhofer, and J. Meyer-ter-Vehn (Elsevier, Paris, 2002), pp. 240–245.
[860]R. Kishony and D. Shvarts, "Ignition condition and gain prediction for perturbed inertial confinement fusion targets," Phys. Plasmas **8**, 4925 (2001).
[861]C. P. Verdon, "High-performance direct-drive capsule designs for the National Ignition Facility," Bull. Am. Phys. Soc. **38**, 2010 (1993).
[862]S. V. Weber, S. G. Glendinning, D. H. Kalantar, M. H. Key, B. A. Remington, J. E. Rothenberg, E. Wolfrum, C. P. Verdon, and J. P. Knauer, "Simulations of laser imprint for Nova experiments and for ignition capsules," Phys. Plasmas **4**, 1978 (1997).
[863]P. W. McKenty, V. N. Goncharov, R. P. J. Town, S. Skupsky, R. Betti, and R. L. McCrory, "Analysis of a direct-drive ignition capsule designed for the National Ignition Facility," Phys. Plasmas **8**, 2315 (2001).
[864]J. H. Gardner, A. J. Schmitt, J. P. Dahlburg, C. J. Pawley, S. E. Bodner, S. P. Obenschain, V. Serlin, and Y. Aglitskiy, "Computational modeling of direct-drive fusion pellets and KrF-driven foil experiments," Phys. Plasmas **5**, 1935 (1998).
[865]S. E. Bodner, D. G. Colombant, A. J. Schmitt, and M. Klapisch, "High-gain direct-drive target design for laser fusion," Phys. Plasmas **7**, 2298 (2000).
[866]S. E. Bodner, D. G. Colombant, A. J. Schmitt, J. H. Gardner, R. H. Lehmberg, and S. P. Obenschain, "Overview of new high gain target design for a laser fusion power plant," Fusion Eng. Des. **60**, 93 (2002).
[867]R. A. Sacks and D. H. Darling, "Direct drive cryogenic ICF capsules employing DT wetted foam," Nucl. Fusion **27**, 447 (1987).
[868]T. J. B. Collins, J. A. Marozas, R. Betti, D. R. Harding, P. W. McKenty, P. B. Radha, S. Skupsky, V. N. Goncharov, J. P. Knauer, and R. L. McCrory, "One-megajoule, wetted-foam target design performance for the National Ignition Facility," Phys. Plasmas **14**, 056308 (2007).
[869]A. J. Schmitt, D. G. Colombant, A. L. Velikovich, S. T. Zalesak, J. H. Gardner, D. E. Fyfe, and N. Metzler, "Large-scale high-resolution simulations of high gain direct-drive inertial confinement fusion targets," Phys. Plasmas **11**, 2716 (2004).
[870]S. P. Obenschain, D. G. Colombant, A. J. Schmitt, J. D. Sethian, and M. W. McGeoch, "Pathway to a lower cost high repetition rate ignition facility," Phys. Plasmas **13**, 056320 (2006).
[871]D. Colombant, A. J. Schmitt, S. P. Obenschain, S. T. Zalesak, A. L. Velikovich, J. W. Bates, D. E. Fyfe, J. H. Gardner, and W. Manheimer, "Direct-drive laser target designs for sub-megajoule energies," Phys. Plasmas **14**, 056317 (2007).
[872]D. M. Kehne, M. Karasik, Y. Aglitsky, Z. Smyth, S. Terrell, J. L. Weaver, Y. Chan, R. H. Lehmberg, and S. P. Obenschain, "Implementation of focal zooming on the Nike KrF laser," Rev. Sci. Instrum. **84**, 013509 (2013).
[873]R. Betti and C. Zhou, "High-density and high-ρR fuel assembly for fast-ignition inertial confinement fusion," Phys. Plasmas **12**, 110702 (2005).
[874]M. J. Lubin and A. P. Fraas, "Fusion by laser," Sci. Am. **224**, 21 (1971).
[875]See National Technical Information Service Document No. ORNLTM3231 (A. P. Fraas, "The BLASCON—An exploding pellet fusion reactor," Oak Ridge National Laboratory, Oak Ridge, TN, ORNL-TM-3231, 1971). Copies may be obtained from the National Technical Information Service, Springfield, VA 22161.

[876]L. A. Booth, D. A. Freiwald, T. G. Frank, and F. T. Finch, "Prospects of generating power with laser-driven fusion," Proc. IEEE **64**, 1460 (1976).
[877]See National Technical Information Service Document No. UWFDM220V1 and UWFDM220V2 (R. W. Conn, S. I. Abdel-Khalik, G. A. Moses, F. Beranek, E. T. Cheng, G. W. Cooper, R. B. Droll, T. Henderson, J. Howard, T. O. Hunter, E. M. Larsen, G. J. Kulcinski, E. G. Lovell, G. R. Magelssen, C. W. Maynard, K. R. Okula, M. Ortman, M. Ragheb, W. B. Rensel, D. Solomon, R. Spencer, I. N. Sviatoslavsky, W. F. Vogelsang, R. D. Watson, and W. G. Wolfer, "SOLASE—A conceptual laser fusion reactor design," The University of Wisconsin, Madison, WI, UWFDM-220, 1977). Copies may be obtained from the National Technical Information Service, Springfield, VA 22161.
[878]"…in their solase in dorckaness, and splattering together, joyously the plaps of their tappyhands as, with a cry of genuine distress, so prettly prattly pollylogue, they viewed him, the just one, their darling, away." J. Joyce, *Finnegans Wake* (The Viking Press, New York, 1939), p. 470.
[879]I. N. Sviatoslavsky, G. L. Kulcinski, G. A. Moses, M. E. Sawan, R. L. Engelstad, E. Larsen, E. Lovell, J. MacFarlane, E. Mogahed, R. R. Peterson, J. W. Powers, and L. J. Wittenberg, "SIRIUS-T, an advanced tritium production facility utilizing symmetrically illuminated inertial confinement fusion," Fusion Sci. Technol. **19**, 634 (1991).
[880]J. D. Sethian, M. C. Myers, J. L. Giuliani, Jr., R. H. Lehmberg, P. C. Kepple, S. P. Obenschain, F. Hegeler, M. Friedman, M. F. Wolford, R. V. Smilgys, S. B. Swanekamp, D. Weidenheimer, D. Giorgi, D. R. Welch, D. V. Rose, and S. Searles, "Electron beam pumped krypton fluoride lasers for fusion energy," Proc. IEEE **92**, 1043 (2004).
[881]I. N. Sviatoslavsky, M. E. Sawan, R. R. Peterson, G. L. Kulcinski, J. J. MacFarlane, L. J. Wittenberg, E. A. Mogahed, S. C. Rutledge, S. Ghose, and R. F. Bourque, "SOMBRERO—A solid breeder moving bed KrF laser driven IFE power reactor," in *Proceedings of 14th IEEE/NPSS Symposium on Fusion Engineering, SOFE'91* (IEEE, New York, 1991), Vol. 2, pp. 646–649.
[882]W. R. Meier and C. W. von Rosenberg, Jr., "Economic modeling and parametric studies for SOMBRERO—A laser-driven IFE power plant," Fusion Technol. **21**, 1552 (1992).
[883]L. M. Waganer, "Innovation leads the way to attractive inertial fusion energy reactors–Prometheus-L and Prometheus-H," Fusion Eng. Des. **25**, 125 (1994).
[884]J. D. Sethian, D. G. Colombant, Jr., J. L. Giuliani, R. H. Lehmberg, M. C. Myers, S. P. Obenschain, A. J. Schmitt, J. Weaver, M. F. Wolford, F. Hegeler, M. Friedman, A. E. Robson, A. Bayramian, J. Caird, C. Ebbers, J. Latkowski, W. Hogan, W. R. Meier, L. J. Perkins, K. Schaffers, S. Abdel Kahlik, K. Schoonover, D. Sadowski, K. Boehm, L. Carlson, J. Pulsifer, F. Najmabadi, A. R. Raffray, M. S. Tillack, G. Kulcinski, J. P. Blanchard, T. Heltemes, A. Ibrahim, E. Marriott, G. Moses, R. Radell, M. Sawan, J. Santarius, G. Sviatoslavsky, S. Zenobia, N. M. Ghoniem, S. Sharafat, J. El-Awady, Q. Hu, C. Duty, K. Leonard, G. Romanoski, L. L. Snead, S. J. Zinkle, C. Gentile, W. Parsells, C. Prinksi, T. Kozub, T. Dodson, D. V. Rose, T. Renk, C. Olson, N. Alexander, A. Bozek, G. Flint, D. T. Goodin, J. Hund, R. Paguio, R. W. Petzoldt, D. G. Schroen, J. Sheliak, T. Bernat, D. Bittner, J. Karnes, N. Petta, J. Streit, D. Geller, J. K. Hoffer, M. W. McGeoch, S. C. Glidden, H. Sanders, D. Weidenheimer, D. Morton, I. D. Smith, M. Bobecia, D. Harding, T. Lehecka, S. B. Gilliam, S. M. Gidcumb, D. Forsythe, N. R. Parikh, S. O'Dell, and M. Gorensek, "The science and technologies for fusion energy with lasers and direct-drive targets," IEEE Trans. Plasma Sci. **38**, 690 (2010).
[885]A. Bayramian, P. Armstrong, E. Ault, R. Beach, C. Bibeau, J. Caird, R. Campbell, B. Chai, J. Dawson, C. Ebbers, A. Erlandson, Y. Fei, B. Freitas, R. Kent, Z. Liao, T. Ladran, J. Menapace, B. Molander, S. Payne, N. Peterson, M. Randles, K. Schaffers, S. Sutton, J. Tassano, S. Telford, and E. Utterback, "The Mercury project: A high average power, gas-cooled laser for inertial fusion energy development," Fusion Sci. Technol. **52**, 383 (2007).
[886]M. S. Tillack and J. E. Pulsifer, "Long-term survival of grazing-incidence metal mirrors for laser fusion," Fusion Sci. Technol. **56**, 446 (2009).
[887]L. L. Snead, K. J. Leonard, G. E. Jellison, Jr., M. Sawan, and T. Lehecka, "Irradiation effects on dielectric mirrors for fusion power reactor application," Fusion Sci. Technol. **56**, 1069 (2009).
[888]J. F. Latkowski, A. Kubota, M. J. Caturla, S. N. Dixit, J. A. Speth, and S. A. Payne, "Fused silica final optics for inertial fusion energy: Radiation studies and system-level analysis," Fusion Sci. Technol. **43**, 540 (2003).
[889]J. K. Hoffer, J. D. Sheliak, D. A. Geller, D. Schroen, and P. S. Ebey, "Beta-layering in foam-lined surrogate IFE targets," Fusion Sci. Technol. **50**, 15 (2006).
[890]B. A. Vermillion, B. W. McQuillan, L. C. Brown, D. T. Goodin, R. Paguio, J. E. Streit, D. G. Schroen, P. C. Goodman, and W. Maksaereekul, "Mass production methods for IFE targets," Fusion Sci. Technol. **47**, 1139 (2005).
[891]D. T. Goodin, N. B. Alexander, L. C. Brown, D. T. Frey, R. Gallix, C. R. Gibson, J. L. Maxwell, A. Nobile, C. Olson, R. W. Petzoldt, R. Raffray, G. Rochau, D. G. Schroen, M. Tillack, W. S. Rickman, and B. Vermillion, "A cost-effective target supply for inertial fusion energy," Nucl. Fusion **44**, S254 (2004).
[892]K. J. Boehm, A. R. Raffray, N. B. Alexander, D. T. Frey, and D. T. Goodin, "Numerical and experimental analysis of a fluidized bed for IFE target layering," Fusion Sci. Technol. **56**, 422 (2009).
[893]W. Wang, T. B. Jones, and D. R. Harding, "On-chip double emulsion droplet assembly using electrowetting-on-dielectric and dielectrophoresis," Fusion Sci. Technol. **59**, 240 (2011).
[894]Z.-M. Bei, T. B. Jones, A. Tucker-Schwartz, and D. R. Harding, "Electric field mediated droplet centering," Appl. Phys. Lett. **93**, 184101 (2008).
[895]A. M. Schwendt, A. Nobile, P. L. Gobby, W. P. Steckle, Jr., D. G. Colombant, J. D. Sethian, D. T. Goodin, and G. E. A. Besenbruch, "Tritium inventory of inertial fusion energy target fabrication facilities: Effect of foam density and consideration of target yield of direct drive targets," Fusion Sci. Technol. **43**, 217 (2003).
[896]D. T. Goodin, C. R. Gibson, R. W. Petzoldt, N. P. Siegel, L. Thompson, A. Nobile, G. E. Besenbruch, and K. R. Schultz, "Developing the basis for target injection and tracking in inertial fusion energy power plants," Fusion Eng. Des. **60**, 27 (2002).
[897]A. E. Robson, Consultant to Naval Research Laboratory, private communication (2007).
[898]R. Petzoldt, N. Alexander, L. Carlson, G. Flint, D. Goodin, J. Spalding, and M. Tillack, "A continuous, in-chamber target tracking and engagement approach for laser fusion," Fusion Sci. Technol. **52**, 454 (2007).
[899]A. R. Raffray and The HAPL Team, "Threats, design limits and design windows for laser IFE dry wall chambers," J. Nucl. Mater. **347**, 178 (2005).
[900]J. Hoffer, Los Alamos National Laboratory, private communication (2006).
[901]L. J. Perkins, Lawrence Livermore National Laboratory, private communication (2005).
[902]J. P. Blanchard, Q. Hu, and N. Ghoniem, "A unified model for ion deposition and theromomechanical response in dry wall laser IFE chambers," Fusion Sci. Technol. **56**, 341 (2009).
[903]N. Hashimoto, J. D. Hunn, N. Parikh, S. Gilliam, S. Gidcumb, B. Patnaik, and L. L. Snead, "Microstructural analysis on helium retention of ion-irradiated and annealed tungsten foils," J. Nucl. Mater. **347**, 307 (2005).
[904]S. J. Zenobia and G. L. Kulcinski, "Retention and surface pore formation in helium implanted tungsten as a fusion first wall material," Fusion Sci. Technol. **56**, 352 (2009).
[905]R. A. Gross, *Fusion Energy* (Wiley, New York, 1984), pp. 18–19.
[906]H. Bachmann, U. Fritscher, F. W. Kappler, D. Rusch, H. Werle, and H. W. Wiese, "Neutron spectra and tritium production measurements in a lithium sphere to check fusion reaction blanket calculations," Nucl. Sci. Eng. **67**, 74 (1978).
[907]M. A. Abdou, "Tritium breeding in fusion reactors," in *Nuclear Data for Science and Technology*, edited by K. H. Böckhoff (Springer, Netherlands, 1983), pp. 293–312.
[908]M. E. Sawan, I. N. Sviatoslavsky, A. R. Raffray, and X. Wang, "Neutronics assessment of blanket options for the HAPL laser inertial fusion energy chamber," in *Proceedings of the Twenty-First IEEE/NPSS Symposium on Fusion Engineering, SOFE'05* (IEEE, New York, 2005).
[909]S. Fukada, Y. Edao, S. Yamaguti, and T. Norimatsu, "Tritium recovery system for Li–Pb loop of inertial fusion reactor," Fusion Eng. Des. **83**, 747 (2008).
[910]M. E. Sawan and M. A. Abdou, "Physics and technology conditions for attaining tritium self-sufficiency for the DT fuel cycle," Fusion Eng. Des. **81**, 1131 (2006).
[911]C. A. Gentile, S. W. Langish, T. Kozub, C. Priniski, T. Dodson, G. Gettelfinger, B. Paul, L. Ciebiera, J. Wermer, A. Nobile, K. Sessions, J. Sethian, and A. E. Robson, "Conceptual design of a plasma exhaust and fuel recovery system for an inertial fusion energy (IFE) power reactor," in *Proceedings of the 22nd IEEE/NPSS Symposium on Fusion Engineering, SOFE'07* (IEEE, New York, 2007).
[912]A. R. Raffray, A. E. Robson, M. E. Sawan, G. Sviatoslavsky, I. N. Sviatoslavsky, and X. Wang, "A self-cooled liquid breeder blanket for a laser IFE power plant with magnetic intervention," Fusion Sci. Technol. **52**, 603 (2007).